Dissertation

Search for Dark Matter Production in Association with a Higgs Boson with the ATLAS Detector at the LHC

von

Rainer-Christian Röhrig

erstellt am

Max-Planck-Institut für Physik

(Werner-Heisenberg-Institut)

eingereicht an der

Fakultät für Physik

der

Technischen Universität München

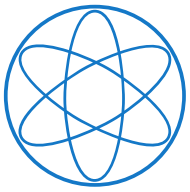

München

Februar 2019

Fakultät für Physik der Technischen Universität München

Max-Planck-Institut für Physik
(Werner-Heisenberg-Institut)

Search for Dark Matter Production in Association with a Higgs Boson with the ATLAS Detector at the LHC

Rainer-Christian Röhrig

Vollständiger Abdruck der von der Fakultät für Physik der Technischen Universität München zur Erlangung des akademischen Grades eines

Doktors der Naturwissenschaften (Dr. rer. nat.)

genehmigten Dissertation.

Vorsitzender: Prof. Dr. N. Kaiser
Prüfer der Dissertation:
1. Prof. Dr. H. Kroha
2. Prof. Dr. S. Schönert

Die Dissertation wurde am 27. Februar 2019 bei der Technischen Universität München eingereicht und durch die Fakultät für Physik am XX. März 2019 angenommen.

Für meine Großmütter
Anna Dück
und
Johanna Röhrig

Abstract

Many cosmological and astrophysical observations indicate the existence of Dark Matter (DM) in the Universe with an abundance of about five times the one of visible matter. Several theories beyond the Standard Model of particle physics predict the existence of DM particles, and in particular, their associated production with a Higgs boson at the Large Hadron Collider (LHC). A search for DM particles has been performed in the mono-Higgs channel in proton-proton collisions at a center-of-mass energy of 13 TeV. The Higgs boson decaying into a $b\bar{b}$ quark pair is produced in association with large missing transverse energy related to the DM particles. The search for DM in the mono-Higgs channel is complementary to searches for DM in association with other Standard Model particles at the LHC. For high missing transverse energy, the Higgs boson can be highly boosted requiring novel jet substructure analysis techniques for the reconstruction of the $h \to b\bar{b}$ decays.

Data of the ATLAS experiment at the LHC corresponding to integrated luminosities of 36.1 fb^{-1} and 79.8 fb^{-1} recorded from 2015 to 2017 have been analysed. In the absence of a signal, the results are interpreted in terms of exclusion limits for simplified DM models with heavy mediators of the interaction between DM and Standard Model particles, including models with a Z'_{B} boson from a $\mathrm{U}(1)_{\mathrm{B}}$ gauge symmetry generated by baryon number B or with additional vector or pseudoscalar mediators in two Higgs-doublet models. Vector mediator masses up to 2.6 TeV are excluded at 95 % CL and pseudoscalar mediator masses up to 260 GeV based on the 36.1 fb^{-1} dataset. 90 % CL upper limits on the spin-independent DM-nucleon scattering cross section in the Z'_{B} model have been derived and compared with direct search results. For DM masses below 4 GeV, the constraints on the Z'_{B} mediated DM-nucleon cross section are more stringent than direct detection limits. Furthermore, upper limits on the visible production cross section with reduced model dependence are placed for associated production of DM particles with the Higgs boson.

Using the increased dataset of 79.8 fb^{-1} and improved reconstruction techniques for the boosted Higgs decays into $b\bar{b}$ based on variable-radius jets, vector mediator masses up to 2.8 TeV have been excluded at 95 % CL.

Contents

Introduction

The origin of Dark Matter is a longstanding open question in particle physics and cosmology. First evidence for the existence of Dark Matter starts from the early 1930s [1]. Over the years more astrophysical observations, ranging from the rotational speed of stars in galaxies [2], the formation of large scale structures [3] and the fluctuations in the Cosmic Microwave Background [4,5] to gravitational lensing measurements [6,7] indicate the existence of Dark Matter.
The abundance of Dark Matter in the Universe is expected to be five times larger then the one of baryonic matter. All these astrophysical observations are based on the gravitational effects of Dark Matter. Up to now, there are no experimental hints about the particle nature of Dark Matter. Nevertheless, the properties of hypothetical Dark Matter particles are constrained by the astrophysical observations. Dark Matter must be non-luminous and non-baryonic, i.e. it does not interact electromagnetically and strongly. Dark Matter particles must be massive and have to have very large lifetimes, comparable with the age of the Universe.

Despite the great success of the Standard Model of particle physics in describing all known fundamental interactions and elementary particles, it does not provide a particle candidate for Dark Matter.
Many attempts have been made to search for Dark Matter particles interacting not only gravitationally but also weakly with Standard Model particles, so-called Weakly Interacting Massive Particles (WIMPs). If they have masses around the electroweak scale, their expected abundance in the Universe corresponds to the observed Dark Matter density. Searches for WIMPs are performed based on their elastic scattering off the nuclei in a detector and their annihilations or decays, and via their production at high-energy colliders like the Large Hadron Collider (LHC).

With the discovery of the Higgs boson with a mass of 125 GeV by the ATLAS and CMS experiments [8, 9] at the LHC at CERN in 2012, the verification of the particle content of the theory is completed. The focus of the current and upcoming runs of the LHC is to search for physics beyond the Standard Model, e.g. for new heavy mediators of the interactions between Standard Model and Dark Matter particles. The signatures

for Dark Matter production at the LHC is the missing transverse energy caused by the Dark Matter particles recoiling against visible Standard Model particles produced in association with the Dark Matter. The Higgs boson can also be used as a tag for Dark Matter production. It is natural to assume that heavy Dark Matter particles couple to the Higgs boson, especially if their mass is around the electroweak scale.
There are different ways to use the Higgs boson in searches for Dark Matter. The Higgs boson may act as a mediator decaying into a Dark Matter particle pair. These invisible Higgs boson decays are possible, if the Dark Matter particle mass is smaller then half the Higgs mass. Or it is may be produced in association with Dark Matter via an additional heavy mediator particle. The latter scenario is called *mono-Higgs production*. It probes directly the hard interaction process producing the Dark Matter particles, since initial-state radiation of Higgs bosons is suppressed due to the very small Yukawa coupling to light quarks. The mono-Higgs channel, therefore, is complementary to other Dark Matter searches at the LHC, where the tag particle is mainly produced via initial-state radiation.
The Higgs decay mode into $b\bar{b}$ pairs is most suitable for Dark Matter searches because it has the highest branching fraction of 58 %. The mono-Higgs to $b\bar{b}$ channel has been used in this thesis to search for Dark Matter in 36.1 fb^{-1} and 79.8 fb^{-1} of proton-proton collision data recorded by the ATLAS detector at a center-of-mass energy of 13 TeV during Run 2 of the LHC.

Chapter 1 introduces the Standard Model of particle physics, discusses the phenomenology of high-energy proton-proton interactions, and summarises the latest measurements of the Higgs boson properties. In Chapter 2, experimental evidence for Dark Matter, possible Dark Matter particle candidates and the mono-Higgs ($b\bar{b}$) channel are discussed. A description of the LHC and of the ATLAS detector and of the reconstruction methods of the physics objects used in the analysis is given in Chapter 3. In Chapter 4, the mono-Higgs ($b\bar{b}$) analysis is described. The results of the search are summarised in Chapter 5. In Chapter 6, an improved identification technique for strongly boosted Higgs boson decays, based on jets reconstructed from inner detector tracks with variable radius parameter is discussed. Finally, the results of Chapter 5 are reinterpreted in the context of two other simplified Dark Matter production models and to derive upper limits on the visible cross section for Higgs ($b\bar{b}$) + $E_{\text{T}}^{\text{miss}}$ events with reduced model dependence (see Chapter 7).

Chapter 1

The Standard Model and Particle Physics at the LHC

This Chapter introduces the theoretical framework of this thesis. Since the mid 1970s, it is established that the elementary particles that make up the ordinary matter are *fermions* with spin-$\frac{1}{2}$, while the forces between them are mediated by *bosons* with spin-1. Three forces are described by the *Standard Model* of particle physics: the strong, weak and electromagnetic interactions. The strong interaction is responsible for binding the constituents of nucleons, while the weak interaction is responsible for the radioactive decays of nuclei. All charged particles are subject to the electromagnetic interaction.
The elementary fermions include the *leptons*, i.e. the electron (e) and its heavier variants the muon (μ) and the tau (τ), as well as the electrically neutral and very light neutrinos (ν), one for each charged lepton, and the *quarks*, which form bound states of mesons (spin-0 or 1) and baryons (spin-$\frac{1}{2}$ or $\frac{3}{2}$) via the strong force. Mesons and baryons are collectively called *hadrons* and consist of a quark-anti quark pairs and triplets of quarks, respectively. The lightest baryons are the protons and neutrons.
More details about the Standard Model are discussed in Section 1.1 (see also Refs. [10, 11]). In Section 1.2, the *BEH mechanism* for the generation of fermion and weak vector boson masses is explained. Open questions of the Standard Model are discussed in Section 1.3. In Section 1.4, the phenomenology of proton-proton interactions at a hadron collider are discussed, including the theoretical predictions for *Higgs boson* production cross sections at the LHC and the Higgs boson decay branching ratios as well as the measured properties of the Higgs boson by the ATLAS and CMS experiments.
Throughout this thesis natural units ($\hbar = c = 1$) are used.

1.1 The Standard Model of Particle Physics

The Standard Model [12–15] is a relativistic quantum field theory based on the gauge symmetry group

$$\mathrm{SU(3)_C} \otimes \mathrm{SU(2)_L} \otimes \mathrm{U(1)_Y} \quad , \tag{1.1}$$

which is a direct product of the three simplest special unitary Lie groups [16], describing the strong and electroweak interactions between elementary particles, while the gravitational force is not part of it. The properties of the interactions are determined by the structure of the local non-Abelian* gauge symmetry group (Yang-Mills theory [17]).
Interactions between coloured quarks and gluons are described by quantum chromodynamics (QCD) [18–20] with the symmetry group $\mathrm{SU(3)_C}$. The electroweak gauge theory, introduced by Glashow [12], Salam [14,21] and Weinberg [13], unifies the electromagnetic interaction described by quantum electrodynamics (QED) [22–27] and the week interaction of quarks and leptons based on the gauge symmetry group $\mathrm{SU(2)_L} \otimes \mathrm{U(1)_Y}$ of weak isospin and hypercharge.
The latter is spontaneously broken to the Abelian electromagnetic gauge group $\mathrm{U(1)_Q}$ according to the *Brout-Englert-Higgs (BEH) mechanism* [28–33] (see Section 1.2). The BEH mechanism gives masses to the weak vector bosons and the fermions without violating the weak gauge symmetry of the Lagrangian. It has been proven by t'Hooft and Veltman that the Standard Model with the BEH mechanism is a renormalisable field theory [34,35] which allows for precise predictions in perturbation theory (see Section 1.4). The Standard Model has been tested in many experiments and so far no significant deviations from its predictions have been found.

Particle Content and Gauge Interactions
All particles described by the Standard Model have been observed, including the Higgs boson as the last one in July 2012 by the ATLAS and CMS collaborations [8,9]. The fermions and bosons of the Standard Model are summarised in Table 1.1.
The local gauge symmetry of the Standard Model determines the electroweak and the strong interactions via minimal gauge invariant couplings of the gauge fields to the matter fields, as described below at the example of the quantum field theory of electromagnetism.

Quantum Electrodynamics
The matter constituents are electrically charged spin-$\frac{1}{2}$ fermions. QED describes the electromagnetic interaction between them, mediated by the massless spin-1 photon. Free fermion fields ψ with mass m are described the Dirac equation:

$$(i\gamma^\mu \partial_\mu - m)\psi = 0 \quad , \tag{1.2}$$

which can be derived according to Hamilton's principle from the Lagrangian density

$$\mathcal{L}_0 = \bar{\psi}(i\gamma^\mu \partial_\mu - m)\psi \quad , \tag{1.3}$$

*This implies interactions between the gauge bosons.

Table 1.1: Overview of the particle content of the Standard Model. J denotes the spin and P the parity quantum numbers of the particle. The mass values are taken from Ref. [36]. The uncertainties in the lepton masses are below 0.01 %. For each fermion there is an anti-fermion with opposite charge and parity.

			Name	Symbol	Charge [e]	Mass
Fermions	Leptons	$J^P = \frac{1}{2}^+$	Electron neutrino	ν_e	0	< 2 eV
			Electron	e	-1	0.511 MeV
			Muon neutrino	ν_μ	0	< 0.12 MeV
			Muon	μ	-1	105.7 MeV
			Tau neutrino	ν_τ	0	< 18.2 MeV
			Tau	τ	-1	1.777 GeV
	Quarks	$J^P = \frac{1}{2}^+$	Up	u	+2/3	$2.2^{+0.6}_{-0.4}$ MeV
			Down	d	-1/3	$4.7^{+0.5}_{-0.4}$ MeV
			Strange	s	+2/3	96^{+8}_{-4} MeV
			Charm	c	-1/3	1.27 ± 0.03 GeV
			Bottom	b	+2/3	$4.18^{+0.04}_{-0.03}$ GeV
			Top	t	-1/3	173.21 ± 0.87 GeV
Bosons	Vector	$J^P = 1^-$	8 gluons	g	0	0
			Photon	γ	0	0
			W bosons	$W^\pm$	± 1	80.385 ± 0.015 GeV
			Z boson	Z	0	91.1876 ± 0.0021 GeV
	Scalar	$J^P = 0^+$	Higgs boson	h	0	125.09 ± 0.24 GeV

which is invariant under a global U(1) gauge symmetry transformation $\psi' = \exp(iQ\alpha)\psi$. It can be made invariant under local U(1) gauge symmetry transformations, $\psi'(x) = \exp(iQ\alpha(x))\psi(x)$, by introducing an interaction of the fermions with a gauge vector field $A_\mu(x)$, which couples to the electric charge Q with strength e (elementary charge). In addition, the derivative ∂_μ is replaced by the covariant derivative

$$\partial_\mu \rightarrow D_\mu = \partial_\mu + iQA_\mu(x) \quad . \tag{1.4}$$

The vector field transforms via

$$A_\mu(x) \rightarrow A'_\mu(x) = A_\mu(x) - \frac{1}{Q}\partial_\mu\alpha(x) \tag{1.5}$$

under the gauge transformations. The Lagrangian of the free Dirac field in Eq. (1.3) is modified to

$$\mathcal{L} = \bar{\psi}(i\gamma^\mu D_\mu - m)\psi = \mathcal{L}_0 + \underbrace{Q\bar{\psi}\gamma^\mu\psi A_\mu}_{\mathcal{L}_{\text{int}}} \quad , \tag{1.6}$$

with the minimal gauge invariant coupling term $\mathcal{L}_{\text{int}}$ of the conserved electromagnetic current $j^\mu = Q\bar{\psi}\gamma^\mu\psi$ of the charged fermions. The gauge invariant Lagrangian of the photon field $A_\mu(x)$ is

$$\mathcal{L}_{\text{photon}} = -\frac{1}{4}F_{\mu\nu}F^{\mu\nu} \quad , \tag{1.7}$$

with the electromagnetic field tensor $F_{\mu\nu} = \partial_\mu A_\nu - \partial_\nu A_\mu$. The Lagrangian of QED, therefore is given by

$$\begin{aligned}\mathcal{L}_{\text{QED}} &= \mathcal{L}_0 + \mathcal{L}_{\text{int}} + \mathcal{L}_{\text{photon}} \\ &= \bar{\psi}(i\gamma^\mu\partial_\mu - m)\psi + Q\bar{\psi}\gamma^\mu\psi A_\mu - \frac{1}{4}F_{\mu\nu}F^{\mu\nu} \quad ,\end{aligned} \tag{1.8}$$

which preserves the local U(1) gauge symmetry.

Weak Interaction

The weak interaction, is responsible for the β-decay of the neutron. In the Glashow-Salam-Weinberg theory [12–14, 21], it is combined with QED to the unified electroweak interaction described by the local gauge symmetry group $\mathrm{SU(2)_L} \otimes \mathrm{U(1)_Y}$. $\mathrm{SU(2)_L}$ is the weak isospin gauge group with three charges $\vec{I} = (I_{1,2,3}) = \frac{1}{2}\sigma_{1,2,3}$ with $\sigma_{1,2,3}$ the three 2×2 Pauli matrices in the fundamental doublet representation. $\mathrm{U(1)_Y}$ is the gauge group of the *weak hypercharge*, Y. The electric charge, Q, the third component of the weak isospin, I_3, and the weak hypercharge, Y, of the fermions are related by the Gell-Mann-Nishijima relation [37, 38]

$$Y = 2 \cdot (Q - I_3) \quad . \tag{1.9}$$

The associated quantum numbers of the fermions in the doublet and singlet representation of the $\mathrm{SU(2)_L}$ are summarised in Table 1.2. The Lagrangian of the free weak gauge vector fields is given by

$$\mathcal{L} = -\frac{1}{4}W^i_{\mu\nu}W^{i,\,\mu\nu} - \frac{1}{4}B_{\mu\nu}B^{\mu\nu} \quad , \tag{1.10}$$

where $W_\mu^{i=1,2,3}$ (a weak isospin triplet) and B_μ (a weak isospin singlet) are the gauge fields of the $\mathrm{SU(2)_L}$ and the $\mathrm{U(1)_Y}$ symmetry, respectively. The field strength tensors

Table 1.2: Overview of the fundamental fermions of the Standard Model grouped in doublets (left-handed fermions) and singlets (right-handed fermions) of the weak isospin I. Its third component I_3, the electric charge Q and the weak hypercharge Y of the particles are also given.

	Fermions			I	I_3	Q [e]	Y
Leptons	$\begin{pmatrix}\nu_e\\ e\end{pmatrix}_L$	$\begin{pmatrix}\nu_\mu\\ \mu\end{pmatrix}_L$	$\begin{pmatrix}\nu_\tau\\ \tau\end{pmatrix}_L$	$\frac{1}{2}$ $\frac{1}{2}$	$+\frac{1}{2}$ $-\frac{1}{2}$	0 -1	-1
	e_R	μ_R	τ_R	0	0	-1	-2
Quarks	$\begin{pmatrix}u\\ d\end{pmatrix}_L$	$\begin{pmatrix}c\\ s\end{pmatrix}_L$	$\begin{pmatrix}t\\ b\end{pmatrix}_L$	$\frac{1}{2}$ $\frac{1}{2}$	$+\frac{1}{2}$ $-\frac{1}{2}$	$+\frac{2}{3}$ $-\frac{1}{3}$	$+\frac{1}{3}$ $+\frac{1}{3}$
	u_R	c_R	t_R	0	0	$+\frac{2}{3}$	$+\frac{4}{3}$
	d_R	s_R	b_R	0	0	$-\frac{1}{3}$	$-\frac{2}{3}$

of the electroweak gauge field theory are given by

$$\begin{aligned} W^i_{\mu\nu} &= \partial_\mu W^i_\nu - \partial_\nu W^i_\mu + g\epsilon^{ijk} W^j_\mu W^k_\nu \quad \text{and} \\ B_{\mu\nu} &= \partial_\mu B_\nu - \partial_\nu B_\mu \quad . \end{aligned} \tag{1.11}$$

where g is the gauge coupling constant and ϵ^{ijk} ($i,\ j,\ k = 1, 2, 3$) represents the structure constants of the $\mathrm{SU(2)_L}$ group. The term proportional to g in Eq. (1.11) is required for gauge invariance of the Lagrangian and is responsible for weak interactions among the non-Abelian $\mathrm{SU(2)_L}$ gauge fields $W^i_{\mu\nu}$. It only couples to left-handed fermion states leading to the observed maximum parity violation in the weak interaction. The covariant derivative of the theory is given by

$$D_\mu = \partial_\mu + ig\vec{I}\cdot\vec{W}_\mu + ig'\frac{Y}{2}B_\mu \quad , \tag{1.12}$$

where g' is the gauge coupling constant of the $\mathrm{U(1)_Y}$ gauge group. The mass eigenstates of the weak gauge bosons are two charged ones, W^+ and W^-, and one neutral, Z. The latter is the heavy partner of the photon in the electroweak unification.

Quantum Chromodynamics

QCD with the non-Abelian symmetry group $\mathrm{SU(3)_C}$ describes the interaction between coloured quarks and gluons. The quarks are colour triplet states, $\Psi = (q_r,\, q_g,\, q_b)^{\mathrm{T}}$, under $\mathrm{SU(3)_C}$, where r, g, and b indicates the colour quantum numbers. Leptons are colour neutral and form colour singlets, and, therefore, do not interact strongly. The $\mathrm{SU(3)_C}$ symmetry group has eight charge operators

$$T^a = \frac{\lambda^a}{2} \quad , \tag{1.13}$$

where λ^a ($a = 1, ..., 8$) are the 3×3 Gell-Mann matrices in the fundamental triplet representation. Correspondingly, there are eight gauge fields, G^a_μ, coupling to coloured particles, including to themselves. The gauge covariant derivative is

$$D_\mu = \partial_\mu + i g_s T^a G^a_\mu \quad , \tag{1.14}$$

with the field strength tensors

$$G^a_{\mu\nu} = \partial_\mu G^a_\nu - \partial_\nu G^a_\mu + g_s f^{abc} G^b_\mu G^c_\nu \quad . \tag{1.15}$$

The QCD Lagrangian is given by

$$\mathcal{L}_{\mathrm{QCD}} = \bar{\Psi}(i\gamma^\mu D_\mu - m)\Psi - \frac{1}{4} G^a_{\mu\nu} G^{a,\mu\nu} \tag{1.16}$$

with the antisymmetric structure constant f^{abc} of the $\mathrm{SU(3)_C}$ symmetry group and the strong gauge coupling constant g_s. Without violating gauge invariance, an additional term $\theta \epsilon^{\mu\nu\alpha\beta} G^a_{\mu\nu} G^a_{\alpha\beta}$ can be added to the QCD Lagrangian in Eq. (1.16) leading to strong CP violation and a non-vanishing electric dipole moment of the neutron. The fact that the latter is experimentally not observed, and the need for an explanation why the phase parameter, θ, is so small ($\theta \ll 10^{-9}$ [39]) is known as the *strong CP problem*. A possible solution is the introduction of a new global U(1) symmetry which is broken, leading to a new scalar particle, the so-called *axion*, which can serve as a Dark Matter candidate (see Section 2.4). The last term of Eq. (1.15) leads to self-coupling of the massless gluons carrying colour charges themselves.

Local gauge theories predict massless gauge bosons mediating the interactions, as it is the case for the photon and the gluons. The observed large masses of the weak gauge bosons $W^\pm$ and Z are in conflict with the electroweak gauge symmetry. Fermion mass terms ($m\bar{\psi}\psi = m(\psi^\dagger_{\mathrm{L}}\psi_{\mathrm{R}} + \psi^\dagger_{\mathrm{R}}\psi_{\mathrm{L}})$) in the Standard Model Lagrangian violate global $\mathrm{SU(2)_L}$ gauge invariance, as left-handed (ψ_{L}) and right-handed (ψ_{R}) fermion fields transform differently under $\mathrm{SU(2)_L}$ transformations. The theory of the electroweak interaction, unifying the electromagnetic and weak forces, provides a mechanism to overcome these problems. The BEH mechanism spontaneously breaks the electroweak gauge symmetry in the ground state while the gauge invariance of the Lagrangian is preserved.

1.2 Electroweak Symmetry Breaking and the Higgs Boson

The electroweak gauge symmetry $\mathrm{SU(2)_L} \otimes \mathrm{U(1)_Y}$ is spontaneously broken down to the $\mathrm{U(1)_Q}$ symmetry of the electromagnetic interaction, giving masses to the weak gauge

bosons $W^{\pm}$ and Z, while the photon corresponding to the unbroken $\mathrm{U(1)_Q}$ symmetry of QED stays massless. Spontaneous electroweak symmetry breaking is generated by introducing a new complex scalar field Φ in the Standard Model. The masses of the leptons and quarks are generated by Yukawa couplings of the fermion fields to Φ [13,40,41]. The symmetry breaking mechanism, called BEH or *Higgs* mechanism, was independently proposed by Brout, Englert, Higgs, Guralnik, Hagen and Kibble [28–33]. In its minimal version, the BEH mechanism introduces two complex scalar fields, ϕ^+ and ϕ^0, which form a $\mathrm{SU(2)_L}$ isospin doublet

$$\Phi = \begin{pmatrix} \phi^+ \\ \phi^0 \end{pmatrix}, \quad \text{with} \quad \begin{matrix} Q & I_3 & Y \\ +1 & +\frac{1}{2} & +1 \\ 0 & -\frac{1}{2} & +1 \end{matrix} \quad . \tag{1.17}$$

The Lagrangian of the scalar field

$$\mathcal{L} = (D^{\mu}\Phi)^{\dagger}(D_{\mu}\Phi) - V(\Phi) \tag{1.18}$$

consists of the kinetic term with the covariant derivative from Eq. (1.12) and of the Higgs potential,

$$V(\Phi) = \mu^2\Phi^{\dagger}\Phi + \lambda(\Phi^{\dagger}\Phi)^2 \quad , \tag{1.19}$$

with μ the mass parameter and λ the self-coupling constant. From unitarity arguments, the constants μ^2 and λ must be real, and vacuum stability demands that $\lambda > 0$. The choices of $\mu^2 > 0$ and $\mu^2 < 0$ change the shape of the potential as illustrated in Fig. 1.1a and Fig. 1.1b, respectively. The scalar field develops a non-vanishing vacuum expectation

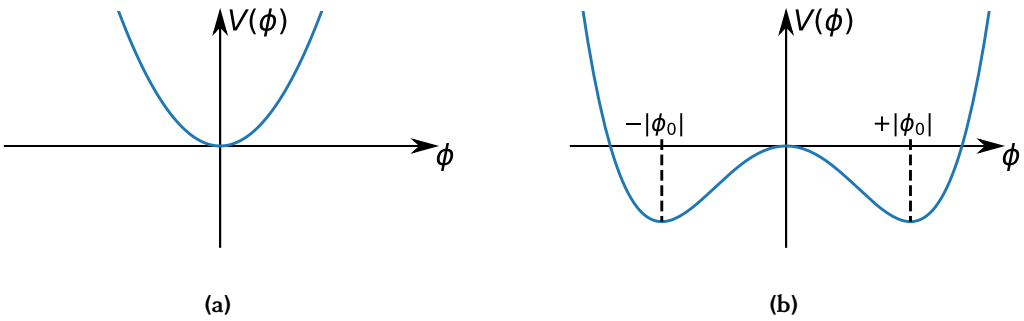

Figure 1.1: Illustration of the Higgs potential, $V(\phi)$, in one dimension for the case (a) $\mu^2 > 0$ and (b) $\mu^2 < 0$. A vacuum expectation value, $v = \sqrt{2}|\Phi_0|$, different from zero of the scalar field breaks the gauge symmetry of the ground state.

value (VEV), $v = \sqrt{2}|\Phi_0|$, for $\mu^2 < 0$, which spontaneously breaks the gauge symmetry

in the ground state. The potential has a degenerated minimum for $|\Phi_0| = \sqrt{\frac{-\mu^2}{2\lambda}} = \frac{v}{\sqrt{2}}$. The gauge symmetry is broken by choosing a particular ground state

$$\Phi_0 = \frac{1}{\sqrt{2}} \begin{pmatrix} 0 \\ v \end{pmatrix} \quad . \tag{1.20}$$

In the unitarity gauge, which eliminates massless Goldstone excitations [42, 43], small excitations around the VEV can be parametrised as

$$\Phi(x) = \frac{1}{\sqrt{2}} \begin{pmatrix} 0 \\ v + h(x) \end{pmatrix} \quad , \tag{1.21}$$

where $h(x)$ is a massive excitation orthogonal to the set of ground states called the *Higgs boson* field.
Mass terms of the weak gauge bosons and of the Higgs boson are generated by inserting the scalar field of Eq. (1.21) into the Lagrangian of Eq. (1.18). The masses of the weak gauge bosons and of the Higgs boson are given by the relations

$$\begin{aligned} m_W &= \frac{gv}{2} \quad , \\ m_Z &= \frac{m_W}{\cos\theta_{\mathrm{W}}} \quad \text{and} \\ m_h &= v\sqrt{2\lambda} \quad , \end{aligned} \tag{1.22}$$

where θ_{W} is the weak mixing angle or *Weinberg angle* with $\sin^2\theta_{\mathrm{W}} \backsimeq 0.23$ [36]. The measured mass values are given in Table 1.1. The VEV in Eq. (1.22) can be determined from the *Fermi coupling constant*, G_F, precisely measured in muon decays [44] and is related to:

$$v = (\sqrt{2}G_F)^{-1/2} \backsimeq 246\,\mathrm{GeV} \quad . \tag{1.23}$$

The fermions acquire their masses by *Yukawa interactions* with the Higgs field. Assuming massless neutrinos, the Yukawa interaction Lagrangian is given by

$$\mathcal{L}_{\text{Yukawa}} = - \sum_{i,j=\{1,2,3\}\ \text{generations}} h^d_{ij} \bar{q}_{L_i} \Phi d_{R_j} + h^u_{ij} \bar{q}_{L_i} \tilde{\Phi} u_{R_j} + h^\ell_{ij} \bar{\ell}_{L_i} \Phi e_{R_j} + h.c. \quad , \tag{1.24}$$

where $\tilde{\Phi} = -i\sigma_2\Phi^*$ and $q_L\,(\ell_L)$ and u_R, $d_R\,(e_R)$ are the quark (lepton) $\mathrm{SU(2)_L}$ doublets and singlets, respectively, and $h^{d,\,u,\,\ell}_{ij}$ the Yukawa couplings. For the charged leptons, the coupling and mass matrices can be diagonalised, while for the quarks a mixing of the mass eigenstates occur in the flavour space via the unitary Cabibbo-Kobayashi-Maskawa (CKM) matrix. The measured values of the CKM matrix elements, $|V_{ij}|$ with $i = u,\, c,\, t$ and $j = d,\, s,\, b$, are given in Fig. 1.2, and with massive neutrinos also neutrino

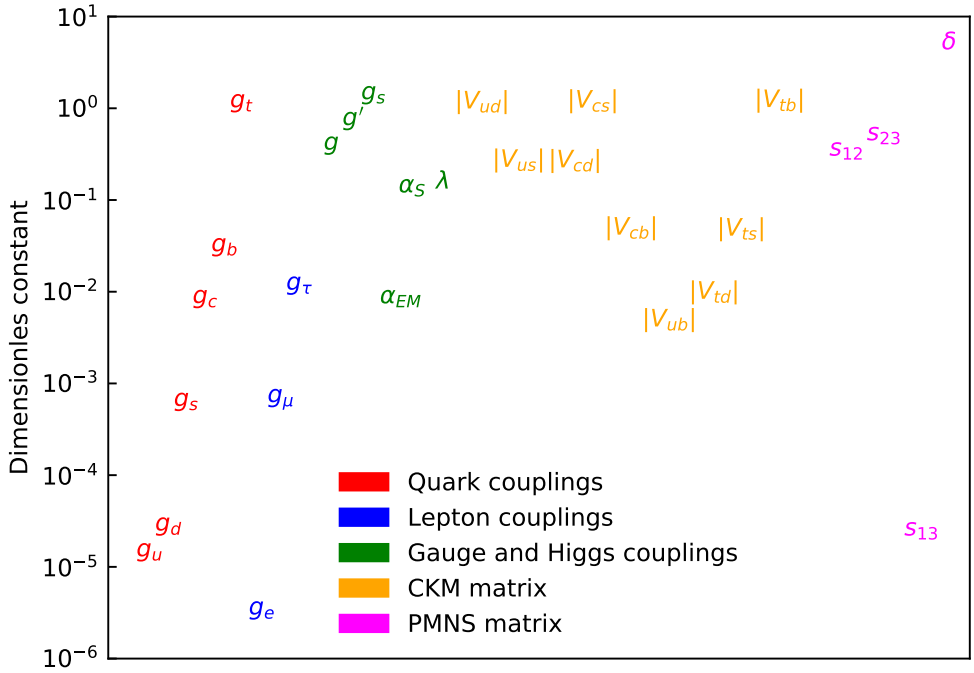

Figure 1.2: A comparison [36] of the dimensionless constants of the Standard Model, the nine quark (red) and three lepton (blue) Yukawa couplings. The three gauge couplings $g = e/\cos\theta_W$, $g' = e/\sin\theta_W$ and g_s, and $\alpha_{EM} = \frac{e^2}{4\pi} \approx 1/137$ and $\alpha_s = \frac{g_s^2}{4\pi} \approx 0.1$, and the Higgs self-interaction strength λ (green). The measured magnitudes of the CKM matrix elements and values of the PMNS mixing angles s_{ij} (with $i, j = 1, 2, 3$) and of the CP violating phase δ are indicated in orange and magenta, respectively.

flavour mixing via the Pontecorvo-Maki-Nakagawa-Sakata (PMNS) matrix is introduced. After spontaneous symmetry breaking the fermion masses m_f are given by

$$m_f = g_f \cdot \frac{v}{\sqrt{2}} \quad , \tag{1.25}$$

where g_f are the Yukawa coupling constants of the fermions f. The stronger the coupling to the Higgs field the heavier is the fermion. The fermion masses and Yukawa couplings, respectively, are free parameters of the theory like the Higgs boson mass and self-coupling and must be measured. The Higgs boson has been finally successfully discovered in 2012 and its mass measured to be about 125 GeV [36] (see Section 1.4.5).

1.3 Open Questions of the Standard Model

The Standard Model of particle physics is an extremely successful theory. Its predictions have been tested with very high accuracy in many experiments. One of its latest triumphs is the discovery of the Higgs boson with properties as predicted by the Standard Model. Nevertheless, there are phenomena wich cannot be explained by the Standard Model and requires new physics beyond the Standard Model (BSM physics).
In the Standard Model, neutrinos are treated as massless particles, but the measurement of neutrino oscillations [36] indicate that they actually have very small masses. The mass scale and the mass hierarchy of the three neutrinos is still unknown.
Another problem of the Standard Model is the *hierarchy problem*, caused by the large differences between the electroweak symmetry breaking scale ($\mathcal{O}$(100 GeV)) and the unification scale of the electroweak and strong forces (10^{16} GeV) as well as the Planck scale (10^{19} GeV) where the gravitational force is expected to be unified with the other forces in a quantum field theory of gravity. The hierarchy of these very different scales leads to the *fine tuning* problem of radiative corrections of the Higgs boson mass in the Standard Model. Additional particles are needed to cancel quadratically diverging loop-corrections to the mass of the scalar Higgs boson in order to avoid fine tuning of the connected mass parameter. Possible solutions are provided for example by supersymmetric [45] or technicolor [46] extensions of the Standard Model.
Furthermore, the origin of the difference between the amounts of matter and antimatter in the Universe, which should have been the same at the Big Bang, is another open question. The universe is dominated by matter and only a tiny part consists of antimatter. Any mechanism generating a matter-antimatter asymmetry requires a rather strong violation of *CP symmetry*. The known sources of CP violation in the Standard Model from the CKM matrix are not sufficient to explain the asymmetry.
The most striking problem of the Standard Model is that it describes only about 4.9 % of the energy content of the Universe which is the fraction of baryonic matter surrounding us on Earth. Around 68.3 % is so-called *Dark Energy* and 26.8 % is Dark Matter which is discussed in Chapter 2. Dark Energy is responsible for the observed accelerated expansion of the Universe.

1.4 Physics at Hadron Colliders

1.4.1 Phenomenology of Proton-Proton Interactions

Proton-proton (pp) collisions at the LHC can be classified as either a *hard* or a *soft scattering processes* depending on the momentum transfer, Q^2. In both cases, the strong interaction dominates, but hard scattering processes can also be mediated by electroweak

vector bosons. The precision calculation of the hard processes, e.g. the Higgs boson production or the production of potential new heavy particles, is much more advanced then for soft processes, since for large momentum transfers and small strong coupling, $\alpha_s(Q^2)$, QCD perturbation theory is valid. For soft processes, the non-perturbative QCD effects must be taken into account. However, soft processes dominate the total cross section and the underlying event at hadron colliders, due to the interaction of the spectator quarks to the hard process and soft gluon radiation in initial (ISR) and final (FSR) state.

As protons are composite particles, not the entire center-of-mass energy, $\sqrt{s}$, of the two protons is available in the hard process. Only a fraction of the proton momentum is carried by the interacting partons. The *Parton Distribution Function* (PDF), $f_{a/A}(x_a, Q^2)$, is the probability density function of the momentum fraction x_a of the parton a in proton A at momentum transfer Q^2. The PDFs have to be obtained from deep inelastic scattering (DIS) data.

The interaction of two protons A and B is illustrated in Fig. 1.3. Only the two partons a

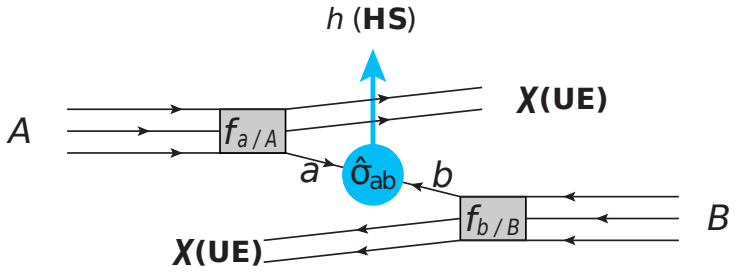

Figure 1.3: Illustration of proton-proton collisions with factorisation into a hard scattering process (HS) of partons a and b, $ab \to h$, with cross section $\hat{\sigma}_{ab\to h}$ and the soft scattering products X making the underlying event (UE). The momentum distribution of the parton a and b in the proton A and B, respectively, are given by the parton distribution functions $f_{a/A}$ and $f_{b/B}$.

and b participate in the hard process. The remaining partons and the underlying event are denoted by X. The soft and the hard contribution to the process can in general be factorised in the cross section calculation [47]. The hadronic cross section, $\sigma_{AB\to hX}$, of producing for example a Higgs boson, h, in association with hadronic particles X, can be separated into the hard scattering cross section $\hat{\sigma}_{ab\to h}$, which can be calculated perturbatively and convolved with the measured PDFs $f_{a/A}$ and $f_{b/B}$ of the protons:

$$\sigma_{AB\to hX} = \iint \mathrm{d}x_a \mathrm{d}x_b f_{a/A}(x_a, \mu_F^2) f_{b/B}(x_b, \mu_F^2) \hat{\sigma}_{ab\to h}(\mu_R^2) \quad . \tag{1.26}$$

In Eq. (1.26), μ_F is the fragmentation scale separating hard and soft processes and μ_R the renormalisation scale which originates from the truncation of the perturbative expansion of the hard cross section. A common choice of the two scales is μ_F and μ_R equal to the mass of the heavy particle produced in the hard process, like a Z or h boson. The proper choice helps to avoid large logarithms in the perturbation calculation. First order corrections in powers of α_s usually reduce the μ_R dependence.
The PDFs are parametrised depending on the energy scale and have to be measured from DIS data. Figure 1.4 shows two sets of PDFs at two scales, 2 GeV and 100 GeV, as determined by the CT14 collaboration [48]. At small Q ($= 2\,\text{GeV}$) and large $x \geq 0.1$, the

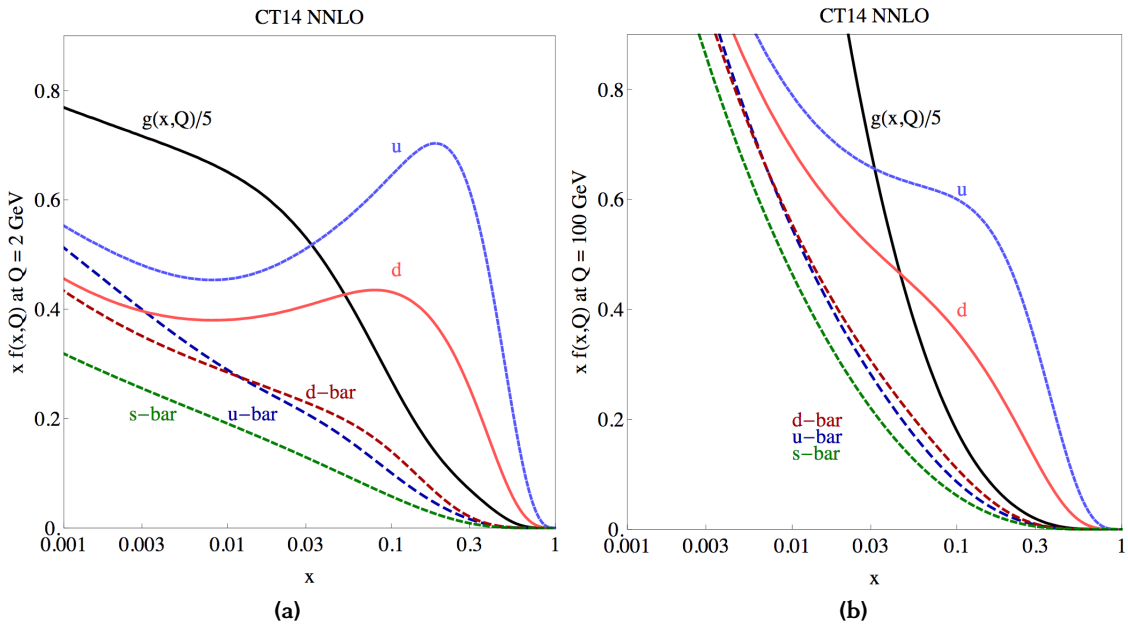

Figure 1.4: Parton distribution functions multiplied by x as determined by the CT14 collaboration [48] at next-to-next-to-leading-order QCD for the factorisation scales of (a) 2 and (b) 100 GeV.

fraction of u and d quarks is largest and heavier sea quarks are suppressed. At larger momentum transfer (see Fig. 1.4b) quark and gluon distributions rise rapidly towards low x and become increasingly flavour symmetric.
The cross sections of the most important Standard Model processes at the LHC are shown in Fig. 1.5. The total pp cross section at a center-of-mass energy of 13 TeV is approximately 80 mb, while the cross sections for the production of heavy particles like the Higgs boson are much lower (51 pb).

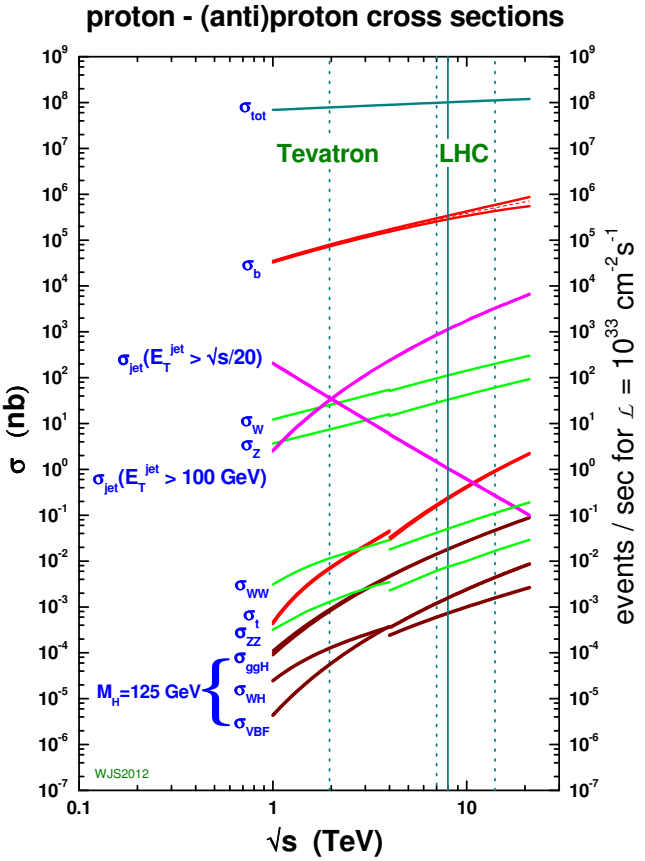

Figure 1.5: Next-leading-order or next-to-next-to-leading-order QCD calculations of the cross sections and the event rates of Standard Model processes in pp and $p\bar{p}$ collisions as a function of the center-of-mass energy $\sqrt{s}$ [49] using the MSTW2008 parton distribution functions [50]. The discontinuities at a center-of-mass energy of 4 TeV is due to the transition from $p\bar{p}$ collisions (at the Tevatron) to pp collisions (at the LHC).

1.4.2 Simulation of Hadronic Collision Events

For the estimation of the Standard Model backgrounds for searches for new physics, a large amount of simulated pp collision events is required. This is a computing intense task at the LHC due to the higher order QCD corrections and the large number of particles produced including multiple pp interactions per bunch crossing increasing with luminosity.

The final state particles and the cross section of a process are simulated by Monte-Carlo (MC) event generators. The PDFs recommended for the LHC are provided by the LHAPDF library [51]. Many different Monte-Carlo generators are used specialised for each application (see Ref. [52]). The hard scattering process is simulated first at leading-order (LO) or next-to-leading order (NLO) in perturbation theory. Another generator usually is

used to simulate QCD soft corrections with a parton shower (PS) algorithm, followed the hadronisation of the partons into colour neutral hadrons. As a final step, the underlying event due to the proton beam remnants and multiple parton interactions (pile-up) are added to the event.
The generated so-called truth particles in an event are then propagated through the ATLAS detector simulation [52]. Event filters may already be applied at the truth level to save computation time. The interactions of the particles in the detector are simulated using the GEANT4 package [53]. The response of the detector components to the particle interactions and the digitisation of the electronics signals are simulated as well and passed through the same particle reconstruction algorithms as used for pp collision data (see Section 3.3). The event generators used for the mono-Higgs search are given in Table 1.3.

Table 1.3: Overview of the used Monte-Carlo generators used for the mono-Higgs ($b\bar{b}$) search. The multi-purpose generators SHERPA and PYTHIA simulate in addition to the hard scattering (HS) processes also the parton shower (PS), hadronisation (had.) and the underlying event (UE). POWHEG and MADGRAPH generators are used to describe the hard scattering processes only and must be interfaced to PYTHIA.

Precision	Name	Application	Remarks
NLO	POWHEG [54–58]	HS	Used in combination with PYTHIA
	SHERPA [59]	HS, PS, had., UE	
LO	MADGRAPH [60–62]	HS	Signal process generation
	PYTHIA 6/8 [63, 64]	HS, PS, had., UE	

PYTHIA 6/8 [63, 64] and SHERPA [59] are multi-purpose event generators at leading and next-to-leading order in perturbation theory, respectively, which include the parton shower and hadronisation. The specialised leading-order signal generator MADGRAPH [60–62, 65] is interfaced to PYTHIA 8 for parton showering and for simulating the underlying event of the signal process (see Section 2.6). The POWHEG [54–58] generator describes the hard processes at next-to-leading order and is interfaced to PYTHIA 6 for parton showering, hadronisation and the underlying event simulation. More details on general-purpose event generators are given in Ref. [66]. Additional information on generators used for the mono-Higgs ($b\bar{b}$) search are given in Sections 4.2 and 4.3.1 for the signal

and the background processes, respectively.

1.4.3 Higgs Boson Production at the Large Hadron Collider

The properties of the Standard Model Higgs boson, such as the production cross sections, the decay rates to fermions and gauge bosons, and the total decay width, are completely determined once the Higgs boson mass, m_h, is known. The Higgs boson mass has been measured precisely by the ATLAS and CMS experiments. A combination of the two measurements has been performed for Run 1 of the LHC, resulting in a measured mass of $125.09 \pm 0.24\,\text{GeV}$ [67]. Measurements for Run 2 data have been performed separately by ATLAS [68] and CMS [69], both being in agreement with the Run 1 results.
In the following, V (with $V = W, Z$) indicate both real and virtual weak bosons, and no distinction is made between particles and anti-particles. The Standard Model Higgs boson, h, can be produced via several production channels at the LHC. The Higgs boson coupling to fermions

$$g_{hff} \propto \frac{m_f}{v} \tag{1.27}$$

and weak vector bosons

$$g_{hVV} \propto \frac{2m_V^2}{v} \tag{1.28}$$

indicate that the Higgs boson couples primarily to heavy particles like W and Z bosons and top and bottom quarks [70]. The dominant production channels are illustrated by the Feynman diagrams in Fig. 1.6. The predicted cross sections of the production channels at $\sqrt{s} = 13\,\text{TeV}$ are shown in Fig. 1.7a as a function of the Higgs boson mass.
The dominant production process for a Higgs boson with mass around 125 GeV is via gluon-gluon fusion, ggF, where the Higgs boson is produced via an intermediate top quark or W boson loop (see Fig. 1.6a), as the massless gluons do not directly couple to the Higgs boson. The second largest and an order of magnitude smaller production cross section is provided by vector boson fusion *VBF* (see Fig. 1.6b). The cross section of the associated production with weak vector bosons Vh (see Fig. 1.6c) is a factor of two (W) to four (Z) smaller than for the VBF production. Zh production with the Z decaying into a pair of neutrinos is an irreducible background for the mono-Higgs search. Higgs boson production in association with a top or a bottom quark pair, $t\bar{t}h/b\bar{b}h$, (see Fig. 1.6d) has an even lower cross section. Single top quark production in association with the Higgs boson (th) has a very small cross section and is not shown in Fig. 1.6.

1.4.4 Higgs Boson Decay Channels

The Higgs boson couplings to fermions and weak vector bosons (see Eq. (1.27) and Eq. (1.28), respectively) are proportional to the masses of the particles such that the Higgs boson

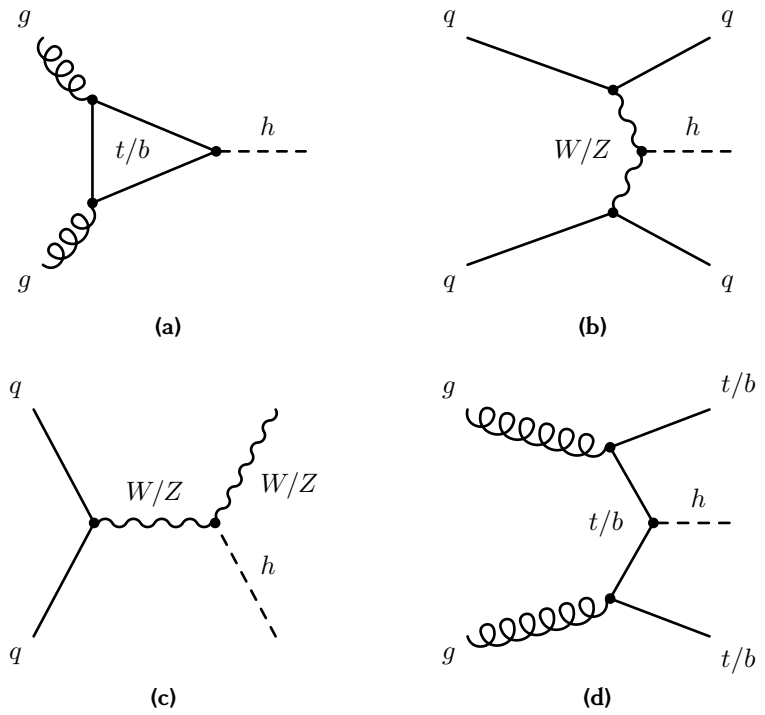

Figure 1.6: Tree-level Feynman diagrams for dominant Higgs boson production mechanisms at the LHC: (a) the gluon-gluon fusion (ggF), (b) vector boson fusion (VBF), (c) associated production of a vector boson (Vh) and (d) the associated production with a top or a bottom quark pair ($t\bar{t}h/b\bar{b}h$).

decays predominantly into the heaviest one allowed by phase space. Figure 1.7b shows the decay branching ratios of the Standard Model Higgs boson as a function of its mass in the range of 120 to 130 GeV. For a Higgs boson mass of 125.09 GeV, the decay into pairs of b quarks is the most dominant decay channel with a predicted branching ratio of 58.09 ± 0.38 % [71]. The detection of this decay mode at the LHC is very difficult due to overwhelming hadronic background. Associated production of the Higgs boson with a W or Z (see Fig. 1.6c) is the best channel to use. It allows for triggering and sufficient background suppression.
The decays into gauge boson pairs, $\gamma\gamma$ and W^+W^-/ZZ, shown in Figs. 1.8a and 1.8b, respectively, lead to the discovery of the Higgs boson in 2012. The Higgs boson decay into a fermion pair (see Fig. 1.8c) was discovered first in the $h \to \tau^+\tau^-$ channel [72–74].

1.4.5 Higgs Boson Discovery and Measurements

The ATLAS and CMS experiments reported in July 2012 the independent discovery of a new boson with a mass around 125 GeV and properties compatible with the expectations for the Standard Model Higgs boson [8, 9]. The measurements of the properties of the

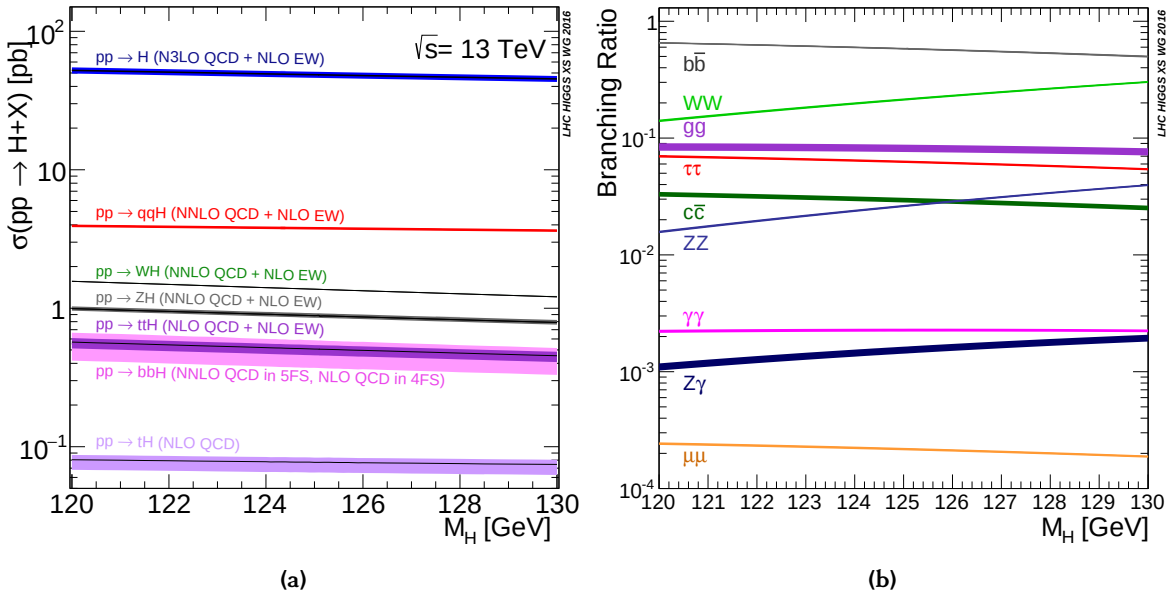

Figure 1.7: The Higgs boson production cross sections for pp collisions at $\sqrt{s} = 13\,\text{TeV}$ (a) and branching ratios of the most important Higgs boson decay channels (b) as a function of the Higgs boson mass [71], which is shown around the measured value of 125 GeV.

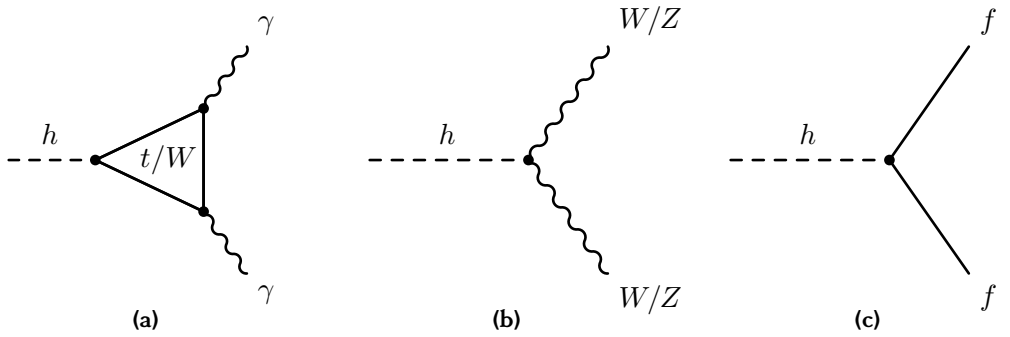

Figure 1.8: The main Higgs boson decay channels into a pair of photons via top quark or W boson loop (a), into weak gauge boson pairs (b) and into fermion pairs (c).

Higgs boson by the two experiments in Run 1 and Run 2 of the LHC including spin and CP quantum numbers and coupling strengths are in very good agreement with each other and with the predictions of the Standard Model. The latest results are summarised in the following.

The Higgs boson property measurements by the ATLAS and CMS experiments have been performed with pp collision data recorded in Run 1 at $\sqrt{s} = 7\,\text{TeV}$ in 2011 and at 8 TeV in 2012 corresponding to approximately $25\,\text{fb}^{-1}$ for each of the two experiments [72], and in Run 2 at $\sqrt{s} = 13\,\text{TeV}$ corresponding to $36\,\text{fb}^{-1}$ and $80\,\text{fb}^{-1}$ [75–77].

The spin and CP quantum numbers of the Standard Model Higgs boson, $J^P = 0^{++}$,

have been tested against several alternative spin-0 and spin-2 and CP hypotheses*. All of them are disfavoured and the Standard Model hypothesis is favoured with high confidence level (CL) [80, 81].

In the Standard Model, the mass of the Higgs boson is a free parameter. It has been measured by the ATLAS and CMS experiments in Run 1 to $125.09 \pm 0.24\,\text{GeV}$ [67]. With the mass of the Higgs boson determined, all of its production and decay properties are defined, including the total decay width of 4 MeV [70]. The ATLAS collaboration placed upper limits on the total width of 14.4 MeV at 95 % CL in Run 2 [82].

In order to probe the production and decay mechanism of the Higgs boson, the signal strength parameter $\mu = \frac{\sigma \cdot \mathcal{B}}{\sigma_{\text{SM}} \cdot \mathcal{B}_{\text{SM}}}$ is measured for the different production channels, ggF, VBF, Wh, Zh and $t\bar{t}h$ in the observed $\gamma\gamma$, W^+W^-, $\tau^+\tau^-$ and $b\bar{b}$ decay modes. The decay into a pair of b quarks is not considered in the ggF and VBF case, because of the overwhelming hadronic background. The rare decay into ZZ is only considered for ggF and VBF production. Figure 1.9 shows the combined signal strength measurements by the ATLAS experiment in Run 2 [77], which are consistent with the Standard Model expectations within two standard deviations.

In order to study the mass generation for weak vector bosons and fermions as given in in the Standard Model, it is of fundamental importance to measure their direct couplings to the Higgs boson and its quadratic dependence or proportionality, respectively, to identify if any deviation from the predicted properties exist. Deviations from the Standard Model are parametrised by coupling scale factors, κ_F, for the fermions and κ_V for the massive vector bosons. The linear scaling of these parameters as a function of the particle masses is shown in Fig. 1.10, which impressively supports the Standard Model BEH mechanism.

The measurement of the Higgs boson coupling to the heaviest quark, the top quark, is an important test of the Standard Model. Both, the ATLAS and the CMS collaboration observed Higgs boson production in association with a top quark pair in decays to $\gamma\gamma$, W^+W^-, ZZ, $\tau^+\tau^-$ and $b\bar{b}$ with an significance of 6.3σ [83] and 5.2σ [84], respectively, in combination with results from Run 1 and Run 2.

Of special interest for this thesis is the decay of the Higgs boson into a pair of b quarks. It has the largest branching ratio. First evidence was found in associated production with a vector boson (Vh) at Fermilab at the $p\bar{p}$ Tevatron collider by the CDF and D$\emptyset$ experiments with a global significance of 3.1 standard deviations [85].

The $h \to b\bar{b}$ decay was first observed by the ATLAS collaboration with an observed (expected) significance of 5.4 (5.5) [86] standard deviations by combining the VBF, ggF, Vh and $t\bar{t}h$ production channels and the Run 1 and the Run 2 datasets of $25\,\text{fb}^{-1}$ and

*The spin-1 hypothesis is excluded by the discovery of the Higgs boson decay into $\gamma\gamma$ according to the Landau-Yang theorem [78, 79], which forbids the decay of a massive particle with spin-1 into two photons.

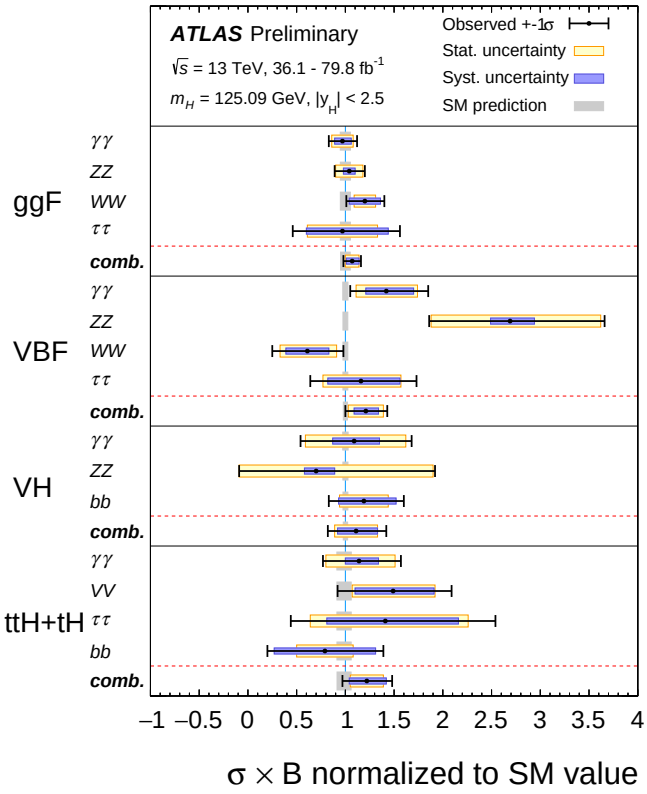

Figure 1.9: The best fit values of the Higgs boson production cross section, for the ggF, VBF, Vh and $t\bar{t}h + th$ processes, times the decay branching ratio of each specific channel, in detail the decay into $\gamma\gamma$, W^+W^-, ZZ, $\tau\tau$ and $b\bar{b}$, normalised to the Standard Model prediction measured by the ATLAS collaboration [77].

$80\,\text{fb}^{-1}$, respectively. The CMS experiment also observed $h \to b\bar{b}$ decays with an observed (expected) significance of 5.6 (5.5) standard deviations and a signal strength of 1.04 ± 0.20 [87].

These results confirm the coupling of the Higgs boson to b quarks assumed for the Dark Matter mono-Higgs ($b\bar{b}$) search in this thesis and also the existence of the irreducible Vh ($h \to b\bar{b}$) background process.

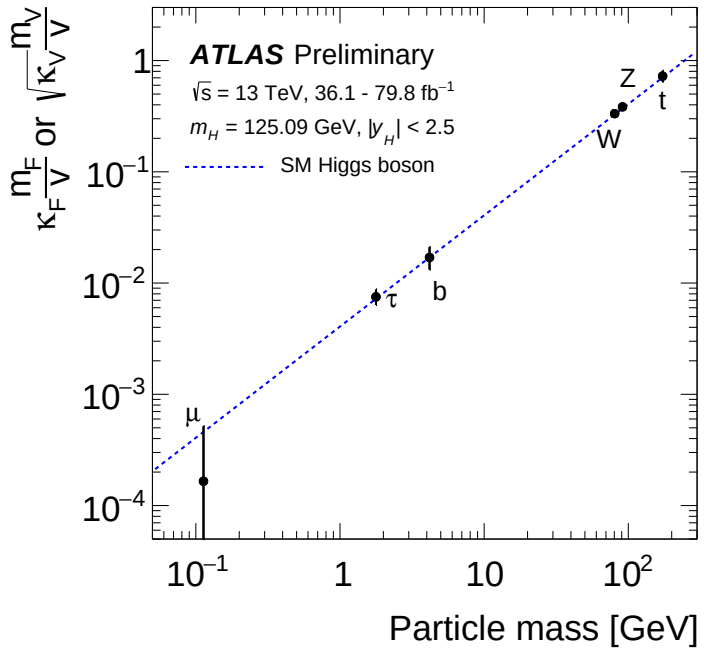

Figure 1.10: The best fit values of the coupling scale factors κ_F and $\sqrt{\kappa_V}$ for fermions and vector bosons, respectively, as a function of $m_{F/V}$. The blue dashed line indicates the expected dependence in the Standard Model for the vacuum expectation value $v = 246\,\text{GeV}$ and a Higgs boson mass of 125.09 GeV in the region $|y_H| < 2.5$ of the Higgs boson rapidity [77].

Chapter 2

Dark Matter

This Chapter introduces the basic concepts of Dark Matter. In Section 2.1, a short introduction to the Standard Model of cosmology is given. The estimate of the relic abundance of Dark Matter is discussed in Section 2.2, followed by the main evidence for the existence of Dark Matter in Section 2.3 and a discussion about the most promising Dark Matter particle candidates in Section 2.4. Section 2.5 gives an overview of Dark Matter searches by direct and indirect detection experiments and at the LHC. The discussion in this Chapter is based on Ref. [88].

2.1 The Cosmological Standard Model

The *Big Bang* is the starting point of the Universe roughly $13.8 \cdot 10^9$ years ago. The cosmological Standard Model describes the observations of the accelerated expansion of the Universe, the Cosmic Microwave Background (CMB), the abundance of the light elements, the large scale structure and the energy content of the Universe. It includes Hubble's law [89, 90], the existence of Dark Matter and a non-vanishing cosmological constant Λ. The Λ Cold Dark Matter (ΛCDM) model includes Einstein's theory of General Relativity. Einstein's gravitational field equations [91] have the form

$$R_{\mu\nu} - \frac{1}{2} g_{\mu\nu} R = -8\pi G_N T_{\mu\nu} + \Lambda g_{\mu\nu} \quad , \tag{2.1}$$

where $R_{\mu\nu}$ and $R \equiv g_{\mu\nu} R^{\mu\nu}$ is the Ricci tensor and scalar, respectively, $g_{\mu\nu}$ the metric tensor, G_N Newton's constant, $T_{\mu\nu}$ the energy-momentum tensor and Λ the cosmological constant responsible in the theory for the accelerated expansion of the Universe.
The cosmological constant term in Eq. (2.1) was originally introduced by Einstein to obtain a static solution for the Universe and abandoned when the expansion of the Universe was discovered. It corresponds to a constant and homogeneous *vacuum energy* and can describe the accelerated expansion of the Universe discovered by the study of type Ia supernova data [92]. This vacuum energy is also referred to as the Dark Energy [93].

In order to find solutions to Einstein's equation for the Universe, homogeneity and isotropy is assumed, the so-called *cosmological principle*, which is in agreement with observations (see Section 2.2). Under these assumptions, the Friedmann-Lemaître-Robertson-Walker (FLRW) metric provides as an exact solution of Eq. (2.1), with the line element

$$\mathrm{d}s^2 = -\mathrm{d}t^2 + a(t)^2 \left(\frac{\mathrm{d}r^2}{1-kr^2} + r^2 \mathrm{d}\Omega^2 \right) \quad , \tag{2.2}$$

where $a(t)$ is the spatial *scale factor* describing the relative expansion of the Universe, the curvature parameter $k = 0, +1, -1$ (see Table 2.1) distinguishes between flat, closed and open universes, respectively, and $\mathrm{d}\Omega^2 = \mathrm{d}\theta^2 + \sin^2\theta\,\mathrm{d}\phi^2$.

Table 2.1: Classification of Friedmann universes with $\Lambda = 0$.

Geometry	k	Ω
open	-1	< 1
flat	0	$= 1$
closed	$+1$	> 1

The time dependence of the scale factors for $\Lambda = 0$ is given by the *Friedmann equation* [94, 95]:

$$H^2(t) \equiv \left(\frac{\dot{a}(t)}{a(t)} \right)^2 = \frac{8\pi G_N}{3} \rho_{\mathrm{tot}} - \frac{k}{a^2} \quad , \tag{2.3}$$

where ρ_{tot} is the homogeneous energy density of the Universe and $H(t)$ the Hubble parameter. Its current value, the *Hubble constant*, is measured to be $H_0 \approx 67.7\,\mathrm{km\,s^{-1}\,Mpc^{-1}}$ [96]. For the critical density $\rho_c \equiv \frac{3H^2}{8\pi G_N}$, the Universe is flat ($k = 0$). Matter and energy densities ρ_i in the Universe are often given in units of the critical density, defining

$$\Omega_i = \frac{\rho_i}{\rho_c} \quad , \tag{2.4}$$

with

$$\Omega = \sum_i \Omega_i = \frac{\rho_{\mathrm{tot}}}{\rho_c} \quad . \tag{2.5}$$

The Friedmann equation in Eq. (2.3) takes then the form

$$\Omega - 1 = \frac{k}{H(t)^2 a(t)^2} \tag{2.6}$$

and for a flat Universe this results in $\Omega = 1$ (see Table 2.1). Measurements of the angular fluctuations of the temperature of the CMB radiation allows to distinguishing between the different curvature models (see Section 2.2). The CMB radiation was emitted at the time of the decoupling of matter and radiation, with the potential *freeze-out* also of

Dark Matter particles, and cooled down with the expansion of the Universe since then. A short summary of the history of the Universe is given in Appendix A.

2.2 Dark Matter Relic Density

The evolution of the Universe depends on the amount of Dark Matter in the Universe. In the ΛCDM model, a non-vanishing cosmological constant Λ and cold Dark Matter consisting of non-relativistic particles after decoupling from Standard Model particles are assumed. The *relic density* is the present Dark Matter density. After the Big Band, Dark Matter particles, χ, were in thermal equilibrium with Standard Model particles, f, via creation and annihilation processes

$$\chi\bar{\chi} \longleftrightarrow f\bar{f} \quad , \tag{2.7}$$

which is illustrated in Fig. 2.1. With the expansion of the Universe, the Dark Matter

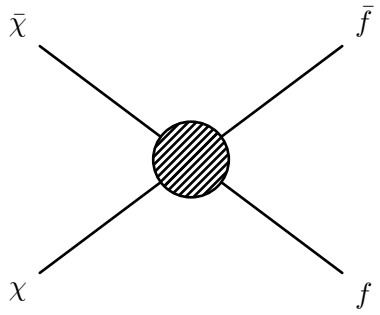

Figure 2.1: Illustrations of Dark Matter particle interactions in the Universe.

density and, therefore, the creation and the annihilation rate becomes so small that the Dark Matter particles *freeze-out* of the thermal equilibrium at a temperature T_F and the Dark Matter density becomes constant, i.e. the relic density. The evolution of the Dark Matter particle number density, n, is described by the Boltzmann equation

$$\frac{\mathrm{d}n}{\mathrm{d}t} = -3Hn - \langle\sigma v\rangle \left(n^2 - n_{\mathrm{eq}}^2\right) \quad , \tag{2.8}$$

where n_{eq} is the equilibrium particle number density at which the evolutions starts, and $\langle\sigma v\rangle$ the average of the annihilation cross section, σ, times the particle velocity, v. The first term on the right-hand side of Eq. (2.8) accounts for the dilution due to the expansion of the Universe, while the n^2 term arises from the interactions in Eq. (2.7).

Eq. (2.8) can be solved numerically, resulting in a Dark Matter relic density [97] of

$$\Omega_{\mathrm{DM}} h^2 \approx \frac{3 \cdot 10^{-27}\,\mathrm{cm}^3\,\mathrm{s}^{-1}}{\langle \sigma v \rangle} \quad , \tag{2.9}$$

with $h = \frac{H_0}{100\,\mathrm{km\,s^{-1}\,Mpc^{-1}}}$. The freeze-out behaviour is illustrated in Fig. 2.2: the Dark Matter particle number density decreases exponentially with decreasing temperature and increasing time until the Dark Matter interaction rate becomes too small and freezes-out and becomes constant. In the calculations above, simplifying assumptions have been made, i.e. that the Dark Matter particle is stable and elementary (not considering co-annihilations of an extended Dark Matter sector) and non-relativistic.
From Eq. (2.9) it can be seen, that the right Dark Matter relic density $\Omega_{\mathrm{DM}} h^2 \approx 0.1188$ [96] (see Eq. (2.14)) observed today is obtained for a typical weak interaction cross section of about $\langle \sigma v \rangle \approx 3 \cdot 10^{-26}\,\mathrm{cm}^3\,\mathrm{s}^{-1} = 1\,\mathrm{pb}$ for Dark Matter particle masses at the electroweak scale of about 10 to 1000 GeV. This coincidence is often referred to as the *WIMP miracle*. Weakly interacting massive particles in this mass range are called WIMPs (see Section 2.4).

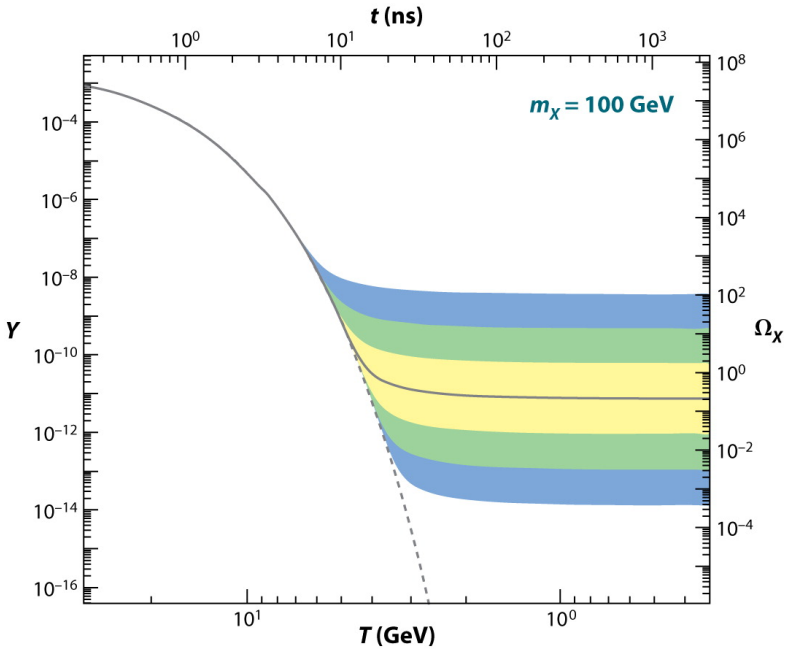

Figure 2.2: The comoving number density, Y, and the thermal relic density, Ω_X, of a Dark Matter particle with $m_\chi = 100\,\mathrm{GeV}$ as a function of the temperature, T, and time, t, in the evolution of the Universe. The solid gray line corresponds to a creation and annihilation cross section yielding the relic density observed today. The coloured regions correspond to cross sections varied up or down by factors of 10, 100 and 1000 from this reference value. The dashed gray line represents the number density of a particle remaining in thermal equilibrium [98].

2.3 Evidence for Dark Matter

The existence of Dark Matter is firmly established by a variety of astrophysical observations at different distance scales. The most important cases are described in the following.

Galactic Scales

One of the first hints of Dark Matter was found by Jan Hendrik Oort in 1932. He noted that the amount of visible matter from stars and interstellar gas, near the solar system falls short of explaining the motions of the stars perpendicular to the Milky Way disk. Luminous matter does not provide sufficient restoring gravitational force attraction such that additional unobserved matter must account for the discrepancy. This observation is known as the *Oort Discrepancy* [99].

More evidence for Dark Matter was found in the following year 1933, when Fritz Zwicky investigated the Coma cluster [1] measuring the velocity distribution of galaxies inside the cluster via Doppler-shift of their visible light spectra. By applying the virial theorem, he estimated the gravitational potential and thereby the mass of the cluster. Comparing that to the amount of luminous matter, he derived a mass-to-light ratio for the Coma cluster that was larger by two orders of magnitude than the one in the solar neighbourhood. This phenomenon, Zwicky could only explain by assuming the existence of a new type of non-luminous matter, which he called Dark Matter. These observations of the Coma cluster have been confirmed later by the measurement of the X-ray spectrum of the gas inside the cluster by the ROSAT satellite [100]. The observed high temperature of the gas can only be explained by a large Dark Matter component producing a large gravitational field in the center of the cluster, which attracts the gas heating it up and leading to the increased X-ray emission.

Inter-Galactic Scales

Another hint for Dark Matter came from Kent Ford and Vera Rubin in the mid 1960s [101], with the observation that luminous objects, like stars or hot gas, move faster than one would expect, if they were only attracted by the gravitational force of other visible objects. This was observed in the study of *rotation curves* of galaxies, which give the orbital velocity of the stars or the gas as a function of the distance from the galactic center. The rotation curves are usually obtained from measurements of the Doppler-shift of the 21 cm hyperfine structure line of neutral hydrogen and optical surface photometry of stars.

In the classical Newtonian theory of gravity, the rotation velocity, $v(r)$, is given by

$$v(r) = \sqrt{\frac{G_N M(r)}{r}} \propto \frac{1}{\sqrt{r}} \quad , \tag{2.10}$$

where $M(r) = 4\pi \int \mathrm{d}r \rho(r) r^2$ is the total mass of the galaxy with the radius r. However, the observed rotation curves, e.g. the one for the spiral galaxy NGC 6503 [2] shown in Fig. 2.3, flattens out at large radii in contradiction to the predicted curve from the visible matter in the disk and the gas. This is compelling evidence for the existence in

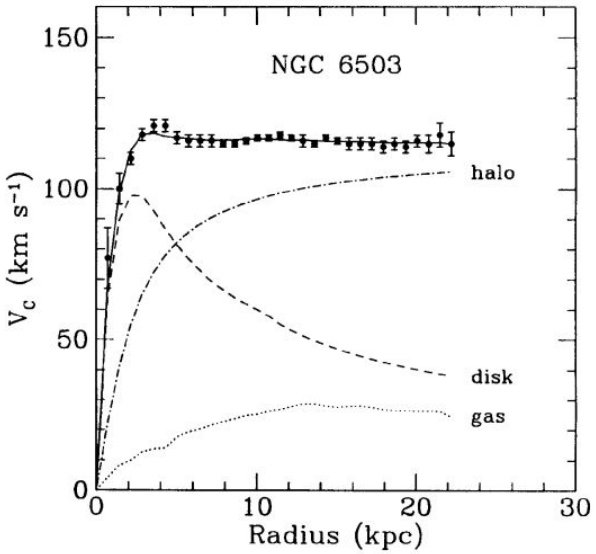

Figure 2.3: Rotation curve of the galaxy NGC 6503 with the predictions from visible matter in the galactic disk and in the form of gas [2]. The prediction for the additional Dark Matter needed to explain the observation is also shown.

the form of an invisible halo of Dark Matter surrounding the galaxy. In order to describe the flat rotation curve in Fig. 2.3, the mass distribution $M(r)$ in Eq. (2.10) must be proportional to r and thus $\rho_{\mathrm{DM}}(r) \propto r^{-2}$. This supports the existence of spherical Dark Matter halos around galaxies.
A different explanation for the observed rotation curves is given by modified Newton dynamics (MOND) models [102] and its relativistic extension TeVeS [103], which modify Newton's and Einstein's laws of gravity for this purpose. The empirical MOND and TeVeS models in general cannot describe observations in contrast to Newton's and Einstein's theory of gravity by including Dark Matter, but they are also not completely excluded.

The Bullet Cluster

The Bullet Cluster [7] provides one of the most striking indications for Dark Matter. It is the product of the collision of two galaxy clusters. Figure 2.4a shows the optical image

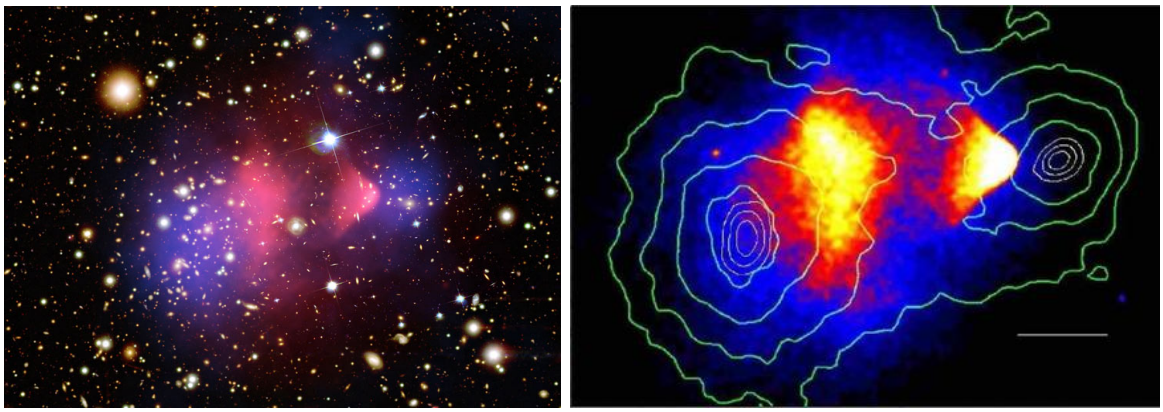

(a) (b)

Figure 2.4: The *Bullet Cluster* from the collision of two galaxy clusters with (a) the optical overlayed Dark Matter distribution (blue) determined from gravitational lensing of the light of the background galaxies and with the hot X-ray emitting intergalactic gas (pink) measured by the Chandra X-ray Observatory [104] and (b) the gravitational potential contours from gravitational lensing overlayed on the heated gas distribution [7].

of the cluster, with an overlay in pink of the hot gas, detected by its X-rays emission by the Chandra satellite. The two blue clouds represent the Dark Matter distributions inferred from gravitational lensing of the two colliding galaxies of the light of background galaxies. The gravitational potential in the cluster has been precisely determined and is shown in Fig. 2.4b. The majority of the mass of the cluster must be due to Dark Matter. There is an offset between the center of the gravitational potential and the center of the visible matter of the colliding galaxy clusters which can be explained by the existence of Dark Matter. This spatial offset cannot be explained with modifications of the gravitational force law and has a significance of 8 standard deviations [7]. From this observation, upper limits on the Dark Matter self-interaction cross section, σ, can be derived [105–107]:

$$\frac{\sigma}{m_\chi} < 1\,\mathrm{cm}^2\,\mathrm{g}^{-1} \quad , \tag{2.11}$$

with m_χ the Dark Matter particle mass.

Cosmological Scale - Cosmic Microwave Background

The evidence for Dark Matter discussed so far does not allow to quantify the amount of Dark Matter in the Universe. The CMB is a relic of thermal radiation which was emitted at the time when matter and radiation decoupled at around 380 000 years after the Big Bang and cooled down with the expansion of the Universe since then (see Appendix A). At the time when neutral atoms got formed and the Universe became transparent, its temperature was around 3000 K. Since then, the Universe expanded by

a red-shift factor of $z = 1100$ cooling to a temperature of approximately 2.7 K. The CMB radiation now has a perfect isotropic blackbody spectrum with a associated temperature of 2.7255 ± 0.0006 K [108]. Georg Gamow predicted the existence of the CMB radiation in 1948 [109,110] and it was first discovered by Penzias and Wilson in 1965 [4,5].
Before the decoupling of matter and radiation, the Universe was filled with a hot plasma of baryons and photons, and likely with Dark Matter. Density waves in the plasma (acoustic waves) created characteristic temperature fluctuations imprinted in the observed CMB. Measurements of the angular temperature fluctuations of the CMB by the Planck satellite [3] are shown in Fig. 2.5. Their amplitude is of the order of a few 100 µK.

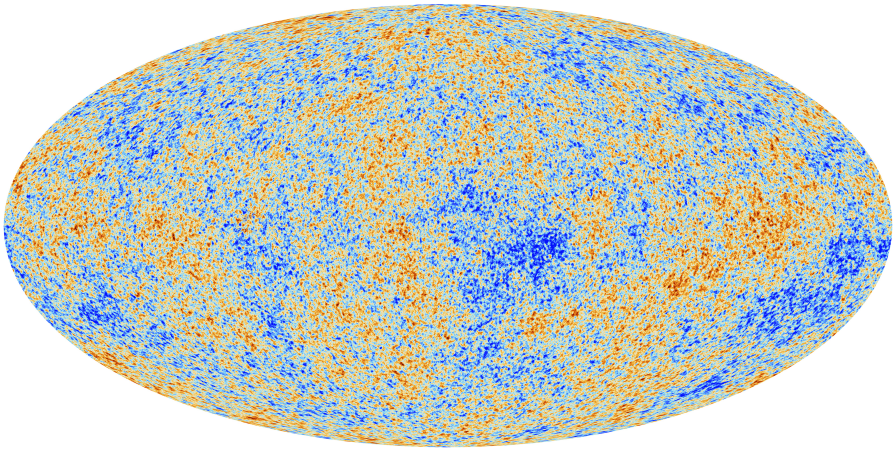

Figure 2.5: Sky map of the temperature of the Cosmic Microwave Background radiation measured by the Planck satellite [3,111]. The colour code indicates temperature fluctuations from –300 µK (dark blue) to 300 µK (red) corresponding to anisotropies in the hot plasma filling the Universe around 380 000 years after the Big Bang.

The analysis of the CMB temperature fluctuation spectrum allows for accurate tests of cosmological models and precise determination of the parameters of the ΛCDM model. The temperature anisotropies are described by expanding them into spherical harmonics

$$\frac{\Delta T}{T} = \sum_{l,m} a_{lm} Y_{lm}(\theta, \phi) \quad , \tag{2.12}$$

with the inclination and declination angles θ and ϕ on the sky and the multipole moments $l = 1, 2, .., \infty$ and $-l \leq m \leq l$ increasing with decreasing angular scale of the temperature fluctuations. The power spectrum of the fluctuations is shown in Fig. 2.6. The locations and the amplitudes of the acoustic peaks provide direct information about the energy-matter content of the Universe.
The position of the first peak at $l \approx 200$ is sensitive to the total energy density Ω and, therefore, the curvature of the Universe. The measurements by the Planck collaboration [96] indicate that the Universe is flat and its energy density is close to

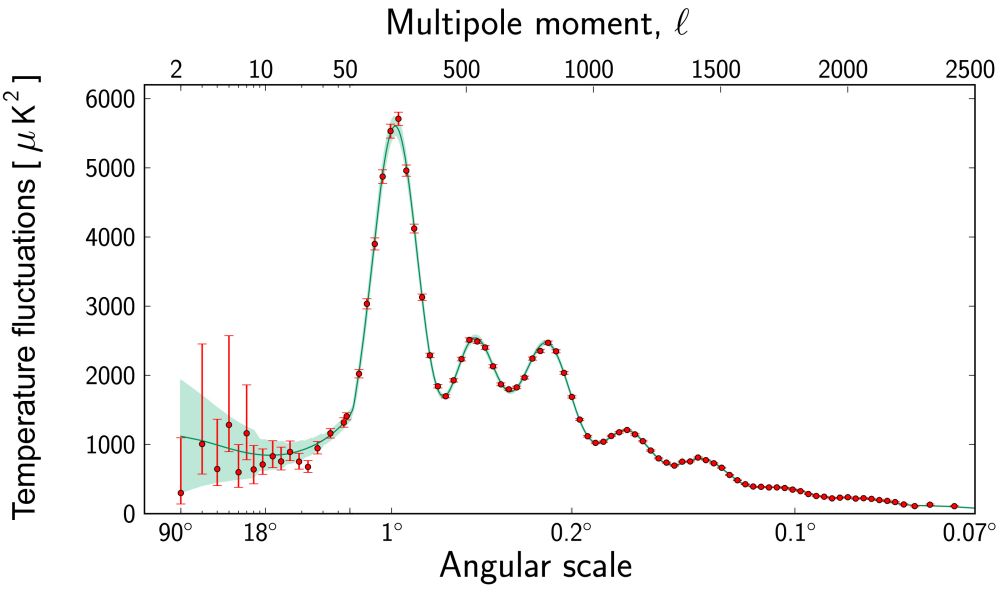

Figure 2.6: The Cosmic Microwave Background power spectrum measured by the Planck satellite [111, 112]. The data points (red) are fitted with the prediction of the ΛCDM model (green curve).

the critical one (see Section 2.1). From the positions of the second and third and their relative height, the baryon and Dark Matter density can be extracted

$$\Omega_b h^2 = 0.022\,30 \pm 0.000\,14 \tag{2.13}$$

and

$$\Omega_{\mathrm{DM}} h^2 = 0.1188 \pm 0.0010 \quad , \tag{2.14}$$

respectively, with $h = \frac{H_0}{100\,\mathrm{km\,s^{-1}\,Mpc^{-1}}}$. Within the ΛCDM model, this requires a large amount of Dark Energy

$$\Omega_\Lambda = 0.683 \pm 0.013 \quad . \tag{2.15}$$

The best fit values to the Planck data yield the following picture of the energy composition of the Universe: 68.3 % Dark Energy, 26.8 % Dark Matter and only 4.9 % ordinary matter.

Dark Matter is also required for the formation of the observed large scale structures, like galaxies and galaxy clusters, of the Universe [113]. Models of the Big Bang nucleosynthesis predict the right amount of baryonic matter, i.e. the right amount of light elements such as hydrogen and helium, when Dark Matter is taken into account in the model [3].

2.4 Dark Matter Candidates

Many candidates for Dark Matter have been proposed, either as astrophysical objects or elementary particles in theories beyond the Standard Model. From the experimental observations outlined in Section 2.3, important constraints on the particle nature of Dark Matter are provided.

One class of Dark Matter particles is referred to as *cold*[*] Dark Matter, inferred from the structure formation and the CMB spectrum, which means that the thermal velocities where non-relativistic in the early Universe, such that structures could form and have not been washed out. This also means that Dark Matter particles are massive. Furthermore, Dark Matter particles are required to be stable, i.e. they must have a lifetime comparable with the age of the Universe, otherwise they would have decayed by now. Moreover, as their name suggest, Dark Matter particles do not interact electrically and do not radiate photons. At most they can have very weak interaction with Standard Model particles besides gravity. Dark Matter particles are by definition non-baryonic[†] and their abundance must be in accordance with the relic density. Finally, their self-interaction and annihilation cross section of the particle candidate is constrained by Eq. (2.11). Possible Dark Matter particle candidates are discussed below.

Neutrinos

Within the Standard Model, possible Dark Matter candidates are the neutrinos. Measurements of the Planck satellite constrains the sum of the neutrino masses to $\sum m_\nu < 0.23\,\text{eV}$ and the energy fraction in the Universe to $\Omega_\nu h^2 < 0.0025$ [3]. Neutrinos make up hot Dark Matter, due to their small masses and relativistic velocities, resulting in different structure formation predominantly on smaller scales. Even though neutrinos have a very high abundance in the Universe, they cannot contribute significantly to the required Dark Matter density in Eq. (2.14), at most 2 % of the required Dark Matter abundance.

So-called *sterile neutrinos* [115], denoted by $\tilde{\nu}$, which extend the Standard Model neutrino sector by an additional right-handed neutrino neutral under the electroweak interaction[‡] behave like the Standard Model neutrinos (or *active* neutrinos) and, therefore, are candidates for Dark Matter [116] with mass in the keV range. LEP measurements of the Z resonance constrain the number of light neutrino species to three [117]. This is not in contradiction with the existence of sterile neutrinos, since they contribute only to

[*]Other models assume *warm* or *hot* Dark Matter.

[†]Dark Matter could be partially made of massive compact halo objects (MACHOs) of condensed baryons, fulfilling the requirement of being dark and gravitationally interacting, e.g. black holes, neutron stars, brown dwarfs or faint stars, but they cannot account for the large amount of Dark Matter in the Universe [114].

[‡]Right-handed fermions have zero weak isospin and like neutrinos they carry no electric charge, and, therefore, their hypercharge is also zero.

invisible Z boson decays and if they mix only weakly with active neutrinos or if their mass is larger than the Z boson mass [118]. A small mixing between active and sterile neutrinos breaks the sterility and allows sterile neutrinos to decay into Standard Model particles, e.g. via $\tilde{\nu} \to \gamma\nu$. Such a process would change the abundance of neutrinos and photons in the Universe and is constrained by the CMB measurements and by Big Bang nucleosynthesis. Highly energetic photons from sterile neutrino decay are a characteristic signature in searches for Dark Matter (see Section 2.5.2).

Axions

Axions [119,120], denoted by a, are pseudoscalar particles and were originally motivated by the so-called *strong CP problem* (see Section 1.1), and, therefore, are referred to as *QCD axions*. Astrophysical observations provide mass limits of $1\,\mu\text{eV} < m_a < 10\,\text{meV}$ [121,122], which lead to a too short lifetime for a Dark Matter particle candidate. For stable axions, the mass is required to be $\lesssim 20\,\text{eV}$ [98] in disagreement with the right relic abundance. However, with the fine tunning of the axion coupling to photons, axions can comply to all constraints for a Dark Matter candidate in agreement with QCD axion properties only in a small parameter range. But axion-like particles (ALPs) maybe provide an attractive Dark Matter scenario. Searches for axions are currently performed by many experiments including ADMX [123]. Recently, the MADMAX [124] experiment has been proposed which searches for axions in the meV mass range compatible with cosmological and CMB constraints.

Weakly Interacting Massive Particles (WIMPs)

The most favoured Dark Matter candidates are *Weakly Interacting Massive Particles* (WIMPs) [125-128], denoted by χ, with masses at the electroweak scale from a few GeV to $\mathcal{O}(\text{TeV})$. Their production cross sections would be similar to the ones of typical electroweak processes (see Section 2.2), matching the right relic abundance. WIMPs are assumed to have only weak couplings to Standard Model particles. They can be either a fermions or scalars leading to different signatures at colliders. An upper bound on the WIMP mass of $m_\chi \lesssim 100\,\text{TeV}$ [129,130] derives from perturbative unitarity, while a lower bound of $m_\chi \gtrsim 10\,\text{GeV}$ [96] results from the validity of the Dark Matter thermal freeze-out scenario.

Many models beyond the Standard Model predict WIMPs. The most prominent example is Supersymmetry (SUSY) (see Ref. [45]), which extends the Standard Model particle content by a fermionic partner for each boson and visa versa. In the minimal supersymmetric extension of the Standard Model (MSSM), R parity* conservation predict a

*The R parity quantum number is defined by $R = 3(B-L)+2S$, with B the baryon number, L the lepton number and S the spin of the particle. The R parity transformation is given by $\hat{P}_R = (-1)^R$ such that Standard Model particles have an R parity eigenvalue of +1 and their supersymmetric particles −1.

lightest supersymmetric particle (LSP) which is stable. The LSP is a perfect Dark Matter candidate if it is electrically neutral. In many supersymmetric models, neutralinos (a mixture of the superpartners of the Higgs bosons and the weak vector bosons), sneutrinos (superpartners of the Standard Model neutrinos) or gravitinos (superpartners of the graviton) are the LSPs. The scattering cross section of sneutrinos with nucleons is much larger than the limits from direct Dark Matter searches [131]. Gravitinos are very difficult to detect as they interact only via gravity [132]. The most promising SUSY Dark Matter candidate, therefore, is the lightest neutralino. SUSY models provide a consistent and ultra-violet complete theory with many new particles and free parameters, which is motivated as a solution to the hierarchy problem [133–136].
There are also Dark Matter candidates in many other extensions of the Standard Model, like *Kaluza-Klein particles* [137,138] excitations in theories with extra dimensions, new particles in *Little Higgs* [139–142] and *Technicolor* [143] models, *WIMPzillas* [144, 145], *QBalls* [146,147], *self-interacting Dark Matter* [148,149], *fuzzy Dark Matter* [150] and many others (see Ref. [88]).
Simplified models are often used for interpreting searches for WIMPs at the LHC assuming only a minimal set of new particles and free parameters (see Section 2.6). An overview of searches for Dark Matter is given in Section 2.5.

2.5 Dark Matter Searches

So far, Dark Matter has only been observed through its gravitational interaction in galaxies and on even larger scales. Not much is known about its particle nature. Several complementary experimental approaches are used to search for Dark Matter particles, which can be divided into three classes: (i) *direct detection* experiments which look for nuclear recoils from the interaction of WIMPs of the galactic halo with the detector material, (ii) *indirect detection* experiments searching for the annihilation products of WIMP pairs and (iii) *collider searches* looking for WIMP pair production in pp collisions with the signature of missing transverse energy. The different approaches are illustrated in Fig. 2.7. The experimental methods and latest results of direct and indirect detection experiments are discussed in Section 2.5.1 and Section 2.5.2, respectively. Section 2.6 focuses on collider searches and on different signal signatures.

2.5.1 Direct Detection

Direct detection (DD) of Dark Matter is based on the elastic scattering of Dark Matter particles from the galactic halo of the Milky Way on the nuclei in a detector as illustrated in Fig. 2.7. The resulting nuclear recoils are on the order of 1 to 100 keV for WIMPs with masses of 10 to 1000 GeV, respectively.

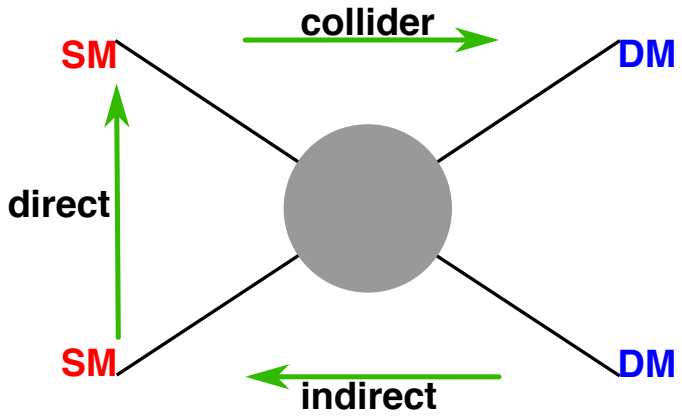

Figure 2.7: The three types of WIMP Dark Matter particle (in blue) detection via an interaction with Standard Model particles (in red): from right to left the annihilation of Dark Matter particles into Standard Model particles (indirect detection), from bottom to top the scattering of Dark Matter particles off a nuclei (direct detection), and from left to right the production of Dark Matter particles at high energy colliders like the LHC.

The expected event rate of a Dark Matter-nucleon interactions is given by:

$$R \simeq \frac{N \rho_\chi \langle \sigma_{\chi-N} \rangle}{m_\chi} \quad , \tag{2.16}$$

where N is the number of target nucleons, ρ_χ the halo Dark Matter density, $\langle \sigma_{\chi-N} \rangle$ the interaction cross section of Dark Matter and the nuclei N averaged over protons and neutrons, and m_χ the Dark Matter particle mass. The Dark Matter density in the Milky Way can be derived from the so-called *Standard Halo Model* (SHM) [151], which is an isothermal sphere with density profile $\rho_\chi(r) \propto r^{-2}$. The standard parameter values at the Solar radius $r = R_0$ used for the SHM are the local Dark Matter density $\rho_\chi^{\text{Milky Way}} \simeq 0.3\,\text{GeV}\,\text{cm}^{-3}$, the local circular speed $v \simeq 220\,\text{km}\,\text{s}^{-1}$ and the local escape speed $v \simeq 544\,\text{km}\,\text{s}^{-1}$ [152,153]. The sensitivity of DD experiments depends on the detector material, and is best for target nuclei masses close to the WIMP mass. For very light Dark Matter particles the dependence on the target nuclei and the interaction cross sections are small, while for heavier particles the recoil energy is higher but the detection rate is suppressed as the flux scales with m_χ^{-1} (see Eq. (2.16)).
Depending on the coupling structure between Dark Matter and nuclei the scattering cross section can be either *spin-independent* or *spin-dependent*. In the spin-independent scenario, scalar or vector particles serve as the mediators between Dark Matter particles and nuclei. The spin-independent cross section increases approximately as A^2, making heavy target nuclei like germanium or xenon preferential. The spin-dependent cross section is proportional to $\frac{J+1}{J}$, where J is the nuclear spin, and rather independent of the mass of the target nuclei, which often are polarised, e.g. fluorine. Spin-dependent in-

teractions remit from axial-vector or pseudo-scalar couplings. Usually, spin-independent interactions are stronger then spin-dependent ones, due to the A^2 dependence.
The event rates in Eq. (2.16) are very low, approximately one event per year per kg detector material, requiring a large detector mass and a good background discrimination, which is the main experimental challenge. The detector is usually shielded against cosmic radiation in deep underground laboratories. The detector material itself must provide a very low intrinsic radioactivity.
To further discriminate a hypothetical Dark Matter signal from competing background processes, usually two different detection channels are exploited, for example combinations of energy deposition (phonons) in cryogenic crystal calorimeters, scintillation light (photons), or ionisation (electrons) by scattered nuclei. This enables for instance the discrimination against neutron scattering or electronic recoils (e.g. photon interactions or β decays).

Spin-Independent Interaction

An overview of the current status of the direct detection experiments for the spin-independent case is given in Fig. 2.8. The DAMA/NaI experiment and its predecessor DAMA/LIBRA make a long standing claim of detection of a Dark Matter signal (see Fig. 2.8). The experiment uses thallium-doped sodium iodide crystals and measures the expected annual modulation of the Dark Matter flux in the halo as a consequence of the Earth's rotation around the Sun on top of a large but time-independent background from cosmic radiation and radioactive decays [173]. The DAMA experiments observed an annual modulation of the signal with a significance of 12.9 standard deviations over 20 independent annual cycles [170,171,174]. Despite the very high reported significance, the DAMA signal is controversial, it has already been excluded by other experiments (see Fig. 2.8). To better understand the DAMA, new experiments using NaI (Tl) like ANAIS [175], COSINE [176], COSINUS [177] and SABRE [178] are under preparation. In order to avoid seasonal Dark Matter halo effects, experiments are build in the northern and southern hemispheres as part of the DM-ICE collaboration [179].
Other experiments, GoGeNT [180] and CDMS-II Si [160] have also claimed observation of WIMP signals but with a lower significance than DAMA. All are excluded by other DD experiments.
Experiments with very low energy thresholds provide the best limits in the low Dark Matter mass region, for example CRESST [154,155], CDEX [156] and EDELWEISS [157], DAMIC [158], CDMS [160,160], SuperCDMS [161,162] and ZEPLIN [159], while liquid Xenon detectors such LUX [167], PandaX-II [168] and XENON1T [169,181] and the liquid Argon detectors DarkSide [165,166] provide the strongest cross section limits in the WIMP mass region above 10 GeV.

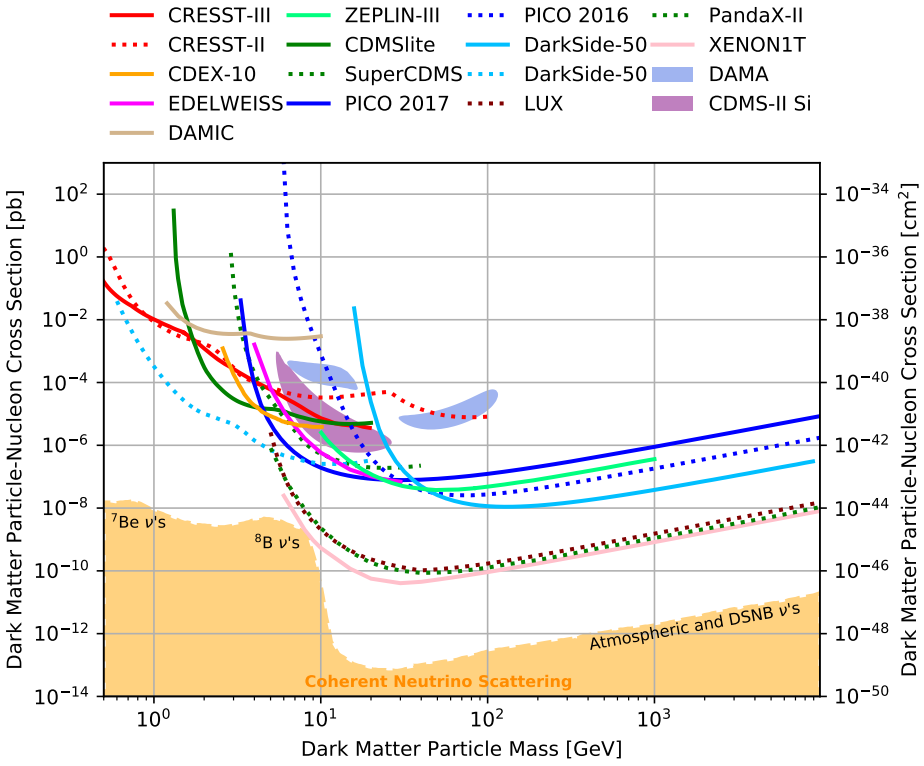

Figure 2.8: The latest 90 % confidence level exclusion upper limits on the spin-independent WIMP-nucleon cross section, from the experiments: CRESST [154,155], CDEX [156], EDELWEISS [157], DAMIC [158], ZEPLIN [159], CDMS-II [160], SuperCDMS [161,162], PICO [163,164], DarkSide [165,166], LUX [167], PandaX-II [168] and XENONIT [169]. The contours of DAMA/NaI and DAMA/LIBRA [170,171] and of CDMS-II Si [160] experiments correspond to claims of Dark Matter signals observed. The expected signal from coherent solar and atmospheric neutrino scattering [172] which marks the limitation for the current direct detection experiments is indicated as the orange region.

Spin-Dependent Interaction

Liquid-Xe experiments containing spin-even and spin-odd isotopes can also probe spin-dependent interactions. The experiments COUPP [182], PICASSO [183], PICO [164] and SIMPLE [184] are operated as bubble chambers containing polarised fluorine molecules to detect spin-dependent interaction. The results on spin-dependent WIMP-proton cross section limits are summarised in Fig. 2.9. The best limits in the mass range 5 to 50 GeV are provided by the fluorine experiments PICASSO [183] and SIMPLE [184]. The IceCube [188,189] experiment, primarily designed for high-energy neutrino detection, now places the overall strongest limits for spin-dependent interactions (see for more details in Section 2.5.2).

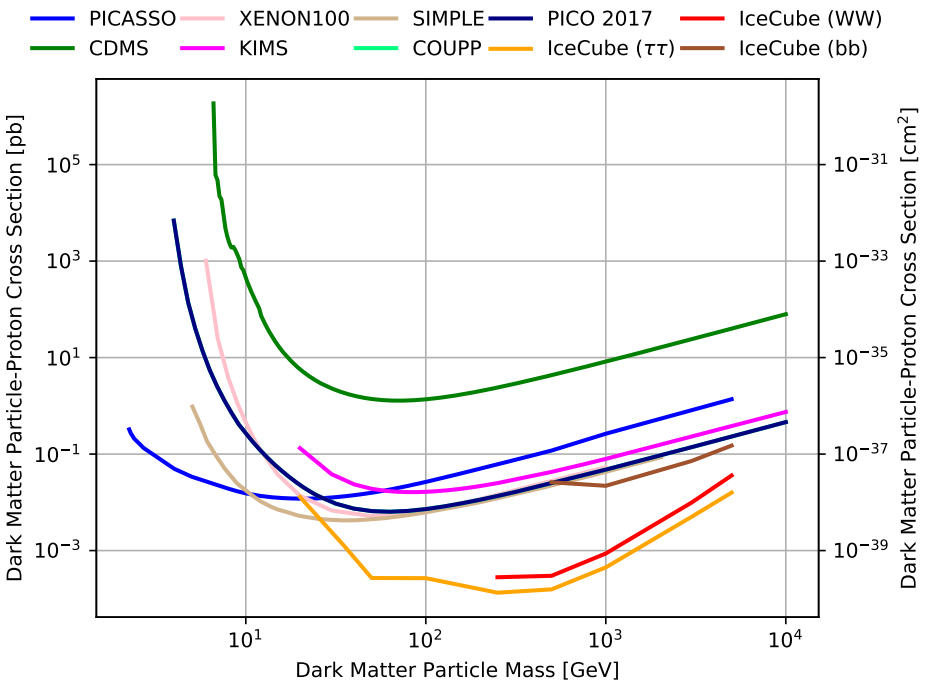

Figure 2.9: The latest 90 % confidence level exclusion upper limits on the spin-dependent WIMP-nucleon cross section by the PICASSO [183], CDMS [185] XENON [186], KIMS [187], SIMPLE [184], COUPP [182], PICO [164] and IceCube [188–190]. The strongest limits are now provided by IceCube in several channels like $\chi\bar{\chi} \to \tau^+\tau^- / b\bar{b} / W^+W^-$, which produce in subsequent decays highly energetic neutrinos. The neutrino energies and fluxes depend on the production mechanism.

2.5.2 Indirect Detection

Dark Matter can also reveal its existence indirectly. The total number of Dark Matter particles did not change significantly after freeze-out in the early Universe, but their spatial distribution changed considerably during structure formation.
Indirect Detection (ID) experiments attempt to identify products of possible Dark Matter self-annihilation*, in the form of highly energetic Standard Model particles in space reaching in energy up to the mass of the Dark Matter particle, which is expected in the few hundred GeV up to TeV range. It is assumed that the Dark Matter particles annihilate into pairs of Standard Model particles via

$$\begin{aligned} \chi\bar{\chi} &\to \gamma\gamma\,, \gamma Z\,, \gamma h \quad \text{or} \\ \chi\bar{\chi} &\to W^+W^-\,, ZZ\,, b\bar{b}\,, t\bar{t}\,, \mu^+\mu^-\,, \tau^+\tau^-\,, \nu\bar{\nu} \quad , \end{aligned} \tag{2.17}$$

as illustrated in Fig. 2.7, where the decay products may decay further into e^+e^-, photons or neutrinos or produce hadrons like protons and neutrons. The different decay

*WIMP decays with very long lifetimes can also provide a indirect Dark Matter signal [191].

channels have different branching ratios and depend on the Dark Matter particle mass. Furthermore, the resulting energy spectra of the secondary particles, e.g. of neutrinos, depend on the production channel, such that neutrinos from decays $W \to \ell\nu$ and $Z \to \nu\bar{\nu}$ decays give neutrino lines in the reference frame of the decaying boson, while the direct production $\chi\bar{\chi} \to \nu\bar{\nu}$ would produce a line at $E_\nu = m_\chi$.
For these searches, it is natural to look in regions of high gravitational attraction and thus high Dark Matter concentration like the center of galaxies, or in stars or in spheroidal dwarf galaxies*, as the Dark Matter annihilation cross section scales with the square of the Dark Matter density. Inside these dense Dark Matter regions, the Dark Matter particles are slowed down and more likely to annihilate with each other possibly into Standard Model particles (see Eq. (2.17)).
A characteristic ID signal is the excess of secondary Standard Model anti-particles like e^+ or $\bar{p}$ in the cosmic ray spectrum studied by satellite or balloon experiments or highly energetic γ-rays or neutrinos measured also by ground based detectors. Charged cosmic ray particles are deflected by the interstellar and intergalactic magnetic fields loosing information about their origin. In contrast, γ-rays and neutrinos point back to their production source. Different to neutrinos, γ-rays are also scattered by the interstellar medium.
ID experiments face large astrophysical backgrounds and large systematic uncertainties due to the modelling of the Dark Matter distribution. But they can study much higher energy ranges and, therefore, are complementary to DD experiments. The ID experiments usually provide exclusion limits on $\langle\sigma v\rangle$, the Dark Matter annihilation cross section averaged over the velocity distribution.

γ-Ray Astronomy

A mono-energetic line in the cosmic γ spectrum at an energy around the electroweak scale or an excess in the γ-ray flux from dwarf galaxies or galaxy clusters provide another indication of Dark Matter annihilation in the processes $\chi\bar{\chi} \to \gamma\gamma$ or γZ†.
The ground based telescopes HESS [193–195], MAGIC [196–199] and VERITAS [200,201] so far did not observe such signals in the γ-ray spectrum up 30 TeV of different astrophysical sources. The HESS experiment, for example, sets an upper limit on the Dark Matter mass of 300 GeV for $\langle\sigma v\rangle = 1.5 \cdot 10^{-28}\,\mathrm{cm}^3\,\mathrm{s}^{-1}$ [195] from the γ-ray spectrum of the galactic center, while VERITAS excludes $\langle\sigma v\rangle > 1.32 \cdot 10^{-25}\,\mathrm{cm}^3\,\mathrm{s}^{-1}$ at $m_\chi = 1\,\mathrm{TeV}$ [201] from observations of spheroidal dwarf galaxies. The most stringent bounds for weak-scale Dark Matter particles come from measurements of softer γ-rays from spheroidal dwarf galaxies in the Milky Way by the Fermi satellite detector, excluding Dark Matter particles

*Spheroidal dwarf galaxies are among the oldest structures in the Universe very faint and strongly Dark Matter dominated [192].
†These processes are only possible via loop diagrams as the Dark Matter particles are electrically neutral.

masses below 100 GeV for $\langle \sigma v \rangle = 2.2 \cdot 10^{-26}\,\mathrm{cm}^3\,\mathrm{s}^{-1}$ [202, 203].

Neutrino Astronomy

Cosmic neutrino detectors like Super-Kamiokande [204], ANTARES [205] or IceCube [206] are sensitive to WIMP annihilations in the core of the earth or sun, where the WIMPS have been gravitationally captured and their density is significantly enhanced which increases the probability for Dark Matter pair annihilation into neutrinos.
The neutrino telescopes look for highly energetic neutrinos which usually interact with the detector through the processes $\nu q \to \mu q'$ or $\nu q \to \nu q$, such that the neutrino is detected through secondary objects like a muon or a hadronic shower. A muon from the direction of the center of the earth would be an indication for Dark Matter.
The limits obtained by neutrino telescopes are generally weaker than for γ-ray telescopes, but become important at very high Dark Matter masses above 5 TeV [190].

Charged Particle Astronomy

The abundance of charged particles like protons, anti-protons, electrons and positrons in the Universe is studied by satellites in space. In contrast to photons and neutrinos, charged particles are deflected during their way through the galactic magnetic fields. As the modelling of the magnetic fields is very difficult, because it is impossible to infer the original source of the particle.
Measurements of the cosmic positron and electron flux by the PAMELA [207] and Fermi [208] satellites and the AMS-02 experiment [209] on the International Space Station show an excess of the positron fraction in the energy range of 10 to 250 GeV. The observed spectrum could also be explained by nearby astrophysical objects like pulsars or secondary sources like highly energetic photons interacting with the interstellar medium [210]. This is indicated by the results of the HAWC telescope [211, 212], which can be described by pulsars as the dominant contribution of the excess of cosmic positrons.
A comprehensive review of ID experiments and their results is given in Ref. [191].

2.5.3 Signatures at Colliders

The searches for Dark Matter particles at colliders can be performed either indirectly by high precision measurements of electroweak observables as new particles can contribute through loop corrections or directly by producing Dark Matter particles in the collision. Dark Matter particles must have been in thermal equilibrium in interactions with Standard Model particles in the early Universe [213], for colliders to produce them. The production mechanism of Dark Matter particles at colliders, like the LHC, is illustrated in Fig. 2.1.

WIMP particles are assumed to be pair produced at colliders. The Dark Matter particles traverse the detector without interaction. Thus, the particle pairs must be produced in association with a detectable Standard Model against the Dark Matter particles recoil. Dark Matter pair production is characterised by large momentum imbalance in the transverse plane, i.e. large missing transverse energy $E_{\mathrm{T}}^{\mathrm{miss}}$. Such a signature is referred to as mono-X or $E_{\mathrm{T}}^{\mathrm{miss}}$ + X signature and is shown in Fig. 2.10a.
Collider searches can probe different models describing the interaction between Dark Matter and Standard Model particles with different assumptions on mediators and coupling parameters. They are complementary to direct and indirect detection experiments [214], and will be of special importance in case of a discovery to study the particle nature of Dark Matter in detail. The LHC Dark Matter working group as well as the ATLAS-CMS Dark Matter forum [215] formulated various benchmark signal models to be probed during Run 1 and Run 2 of the LHC, where the Dark Matter-Standard Model particle interactions are either described by contact interaction operators in an Effective Field Theory (EFT) approach [216–218] or by *simplified models* [219]. In EFTs it is assumed that new physics effects appear only at a high energy scale and are suppressed at the collision energy. The EFT approach is model independent and allows for a direct comparison between collider and non-collider Dark Matter searches. During Run 1, mainly the EFT approach has been used. But its validity is not always guaranteed, in particular when the typical momentum exchange in the process is much higher than the suppression scale of the EFT [220], which is often the case at the LHC.
In simplified models, new heavy mediators responsible for the interaction between Dark Matter and Standard Model particles with a certain coupling structure are introduced. They have been mainly used for the interpretation of the Run 2 data of the LHC.
The X in mono-X searches can be any detectable object, i.e. a jet, bottom/top quarks, a vector boson or the Standard Model Higgs boson (see Fig. 2.10a and Fig. 2.10b, respectively). The Standard Model particle is dominantly produced by initial-state-radiation (ISR) of gluons or vector bosons, $V = \gamma$, $W^{\pm}$, Z. The so-called mono-jet signature* has the highest cross section, but is accompanied by background. In contrast, the Higgs boson is not produced via ISR as the Yukawa to light quarks are very small (see Fig. 1.2). Instead, the Higgs boson is always directly involved in the production mechanism of the Dark Matter particles as indicated in Fig. 2.10b.
The ATLAS and CMS experiments at the LHC have performed searches for Dark Matter in various $pp \to \chi\bar{\chi} + X$ channels, where the X is either a jet [221–223], a photon [224,225], a hadronically decaying $W^{\pm}$ or Z boson [223,226], a leptonically decaying Z boson [227,228], a heavy flavour quark pair ($b\bar{b}$ or $t\bar{t}$) [229–235], a hadronically de-

*The name is misleading, because the probability to produce just one highly energetic jet is rather low and in reality one looks for several jets.

caying heavy Z' boson [226] or the Higgs boson (see Section 2.6). Besides the mono-X searches for Dark Matter in events with large $E_{\mathrm{T}}^{\mathrm{miss}}$, searches for heavy dijet [236–245] or dilepton [246] resonances give also information about Dark Matter models by looking for the mediators of the Dark Matter-Standard Model interaction as shown in Fig. 2.10c.

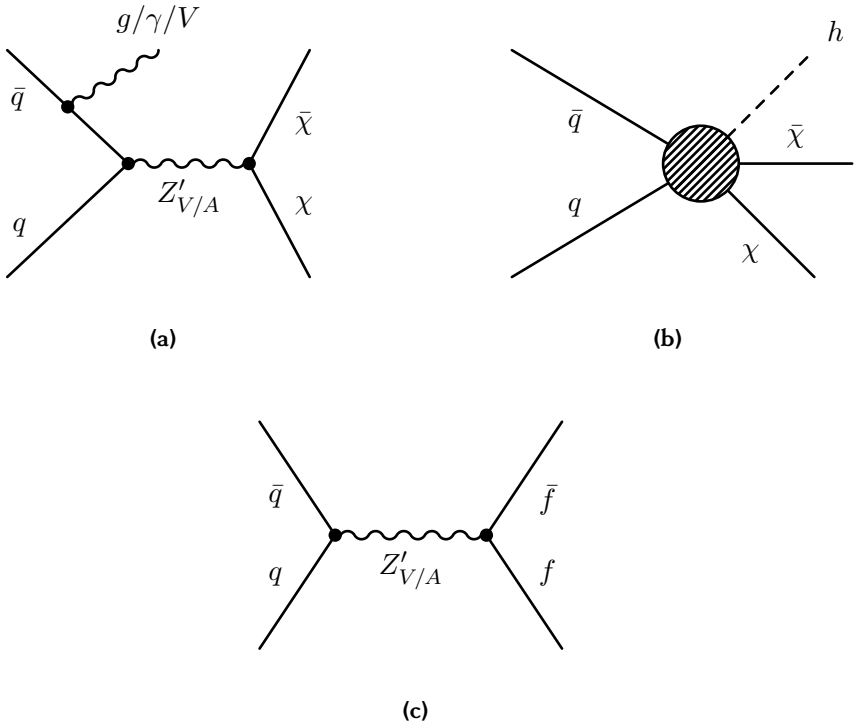

Figure 2.10: Representative Feynman diagram showing (a) the pair production of Dark Matter particles in association with a gluon (g), a photon (γ), or a weak vector boson $V = W^{\pm}, Z$ from initial-state-radiation of a quark or (b) a Higgs boson (h) as part of the vertex and (c) the production of fermion pairs via a vector or axial-vector spin-1 mediator.

The Higgs boson plays a special role in Dark Matter searches. It allows to search for Dark Matter either via invisible Higgs boson decays into Dark Matter, either directly or indirectly via missing decay width, where the Higgs boson is the only mediator of interactions between Dark Matter and Standard Model particles (so-called *Higgs portals* [247–249]), or via the mono-Higgs searches (see Section 2.6).
The search for invisible Higgs boson decays covers light Dark Matter particles with $\mathrm{m}_{\chi} < m_h/2$. The invisible Higgs boson branching ratio, $\mathcal{B}(h \to \text{inv.})$, can be measured either directly by searching for invisible Higgs boson decays or by precisely measuring the visible decay channels of the Higgs boson and comparing with the Standard Model prediction. Indirect searches for Dark Matter via invisible Higgs boson decays assume that there are couplings between Dark Matter particles and the Higgs boson which contribute to the total Higgs boson decay width leading to deviations from the Standard

Model expectation. The only Standard Model contribution to the invisible branching ratio originates from $h \to ZZ^\star \to 4\nu$ decays [70] with a branching fraction of only 0.1 % [71]. Thus, any deviation from the Standard Model expectation indicates additional invisible decay modes of the Higgs boson.

Direct searches for invisible Higgs boson decays are performed in the Vh production channel [226, 250, 251] with leptonic or hadronic Z decays or hadronic W decays, the VBF [252, 253] channel or the ggF [250] channel with additional ISR jets (see Fig. 1.6 with $h \to \chi\bar{\chi}$).

The WIMPs in Higgs portal models are assumed to be either scalar, fermionic or vector particles. The sensitivity of Higgs portal model searches at the LHC is compared to Direct Detection experiments in Fig. 2.11. The WIMP-nucleon cross section upper

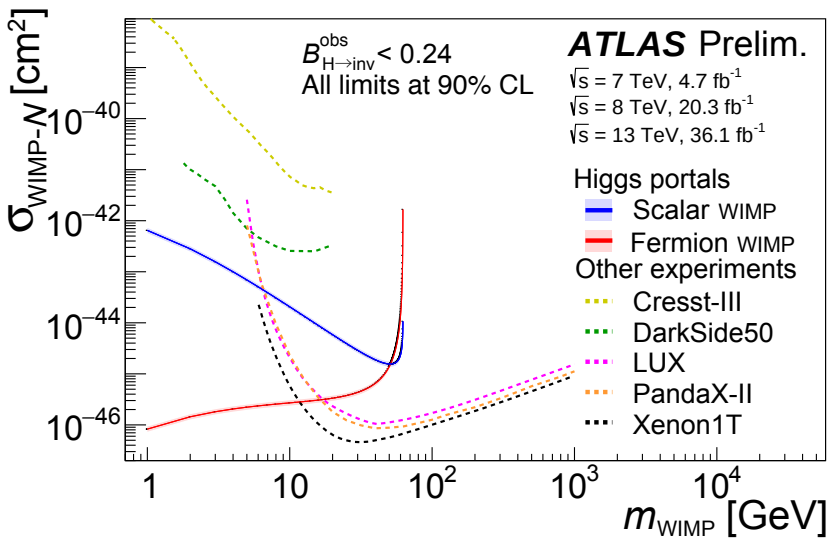

Figure 2.11: 90 % upper limits on the spin-independent WIMP-nucleon cross section for ATLAS indirect searches for invisible Higgs decays with $\mathcal{B}(h \to \text{inv.}) < 0.24$ in Run 1 and Run 2 in Higgs portal models as a function of the WIMP mass for scalar (blue) and fermion (red) WIMPs compared to Direct Detection results [254].

limits decrease from scalar to fermion WIMP assumptions. The sensitivity vanishes for $m_\chi > m_h/2$ [254].

The currently best ATLAS observed (expected) upper limits on $\mathcal{B}(h \to \text{inv.})$ are 0.23 (0.24) [255] at 95 % CL, from a Run 1 and Run 2 combination of the VBF, $Z(\to \ell\ell)h$ and W, $Z(\to jj)h$ production channels for direct search and for indirect search the decay channels $h \to \gamma\gamma$, ZZ, W^+W^-, $Z\gamma$, $\tau^+\tau^-$, $\mu^+\mu^-$ and $b\bar{b}$ resulting in upper limits of 0.26 (0.17) at 95 % CL [254]. The CMS experiment obtained similar results with upper limits of 0.24 (0.23) at 95 % CL [251] using Run 1 data and of 0.24 (0.18) at 95 % CL [256] using Run 2 data.

2.6 Mono-Higgs Events as Dark Matter Signature

Searches for Dark Matter particles produced in association with the Standard Model Higgs boson referred to as *mono-Higgs* searches, have become particularly interesting after the discovery of the Higgs boson at the LHC in 2012 and provide a new opportunity to search for Dark Matter. Compared to typical mono-X Dark Matter searches with X =jets, γ, W, Z from ISR (see Section 2.5.3), the mono-Higgs signature (see Fig. 2.10b) is complementary due to the non-ISR production of the Higgs boson and its direct involvement in the Dark Matter production mechanism and coupling structure. The mono-Higgs search can go beyond the limit of $m_h/2$ of searches for invisible Higgs boson decays, as Dark Matter is produced via additional mediators. Searches in the mono-Higgs channel have been performed for Higgs boson decays into $b\bar{b}$ [257–259], $\gamma\gamma$ [260–262], ZZ [263] and $\tau^+\tau^-$ [262]. The highest statistics is obtained in the $b\bar{b}$ final state as the branching ratio is highest for the Higgs boson mass of 125 GeV. But a good background suppression is required in this channel.
The search for Dark Matter particles in the mono-Higgs ($b\bar{b}$) channel with the ATLAS detector is the topic of this thesis. The signal model in the context of an EFT framework is introduced in Section 2.6.2 as basis for the Run 1 and early Run 2 analysis. Explicit models with additional mediators are presented in Section 2.6.3 and Chapter 7, which are used for the Run 2 analysis.

2.6.1 The Mono-Higgs ($b\bar{b}$) Channel

The Dark Matter searches using the mono-Higgs with the $b\bar{b} + E_{\mathrm{T}}^{\mathrm{miss}}$ or $\gamma\gamma + E_{\mathrm{T}}^{\mathrm{miss}}$ final states are motivated in Refs. [264–266]. The expected production cross sections are rather small such that the $b\bar{b}$ channel dominates in spirit of the more difficult background rejection. For the mono-Higgs ($b\bar{b}$) channel efficient identification of the two b quark jets is of major importance to distinguish the signal from the overwhelming QCD-background of the LHC. The invariant mass of the two b-jets (see Section 3.3.5) is required to be around 125 GeV, which helps to reject non-resonant backgrounds containing b quarks, e.g. from $t\bar{t}$ production.
In the Higgs boson production via a heavy mediator (see Section 2.6.3), the Higgs boson can be strongly boosted, such that standard b-jet reconstruction techniques are not efficient to separate the two b-jets and more sophisticated methods using the jet substructure have to be applied. More details on the object reconstruction and the event selection are given in Section 3.3 and Chapter 4, respectively.

2.6.2 Effective Field Theory

In the EFT approach, non-renormalisable effective interaction operators are introduced producing $E_{\mathrm{T}}^{\mathrm{miss}}$+X final states, without specifying the underlying ultraviolet (UV) physics, e.g. new heavy mediators. Due to the non-renormalisability, the operators are suppressed by Λ^{-1}, where Λ is the mass scale of the particles that have been integrated out. In contrast, in the simplified model approach, the UV particles are kept as degrees of freedom of the theory with explicit assumptions about the structure of the interaction, coupling parameters and the masses of the mediators (see Section 2.6.3). The EFT approach is most model-independent with only a small number of free parameters, but its validity is limited to momentum transfers between the two colliding partons below Λ.

In all models, χ is assumed to be the only Dark Matter particle and a singlet under the Standard Model gauge symmetry group. The Dark Matter particle can be either a scalar, a fermion or a vector boson. EFT models have been for Dark Matter searches in the mono-Higgs ($b\bar{b}$) channel with Run 1 [267] and early Run 2 data [257].

The simplest EFT operators, providing a mono-Higgs ($b\bar{b}$) signature described in Ref. [265] and illustrated in Fig. 2.12, involve direct couplings between Dark Matter particles and the Higgs boson through the so-called Higgs portal model [268–274]. For scalar Dark

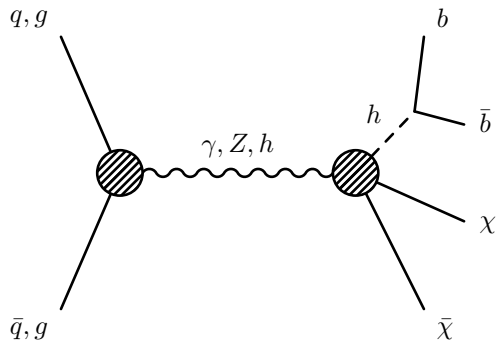

Figure 2.12: Feynman diagram for a mono-Higgs ($b\bar{b}$) signature in EFT. The left circle represents the coupling of an electroweak boson (γ, Z, h) to $q\bar{q}$ or gg, and the right circle the Dark Matter and Higgs boson coupling to the electroweak bosons.

Matter particles, the simplest and renormalisable operator describing the interaction is of dimension 4:

$$\lambda |h|^2 \chi^2 \quad , \tag{2.18}$$

where χ is a real scalar field, h the Standard Model Higgs doublet field and λ a dimensionless coupling constant. For fermionic (Dirac) Dark Matter particles, two non-

renormalisable operators of dimension 5 exist:

$$\begin{aligned} &\frac{1}{\Lambda}|h|^2\bar{\chi}\chi \quad \text{and} \\ &\frac{1}{\Lambda}|h|^2\bar{\chi}i\gamma_5\chi \quad , \end{aligned} \tag{2.19}$$

where Λ is the energy suppression scale. The mono-Higgs ($b\bar{b}$) signature arises from the operators given in Eq. (2.18) and Eq. (2.19) via $gg \to h^* \to h\chi\bar{\chi}$. These interactions also lead to invisible Higgs boson decays for $m_\chi < m_h/2$. In the case of kinematically allowed invisible Higgs decays, it is required that $\lambda \lesssim 0.016$ ($\Lambda \gtrsim 10\,\text{TeV}$) for scalar (fermionic) Dark Matter particles in order to satisfy the bound on the invisible Higgs branching fraction of 38 % from Ref. [275]. Otherwise, e.g. if $m_\chi > m_h/2$, the Dark Matter-Higgs couplings (suppression scale) can be much larger (smaller). The first operator in Eq. (2.19) results in too high Dark Matter density incompatible with the relic density discussed in Section 2.2, in particular for $m_\chi < 2\,\text{TeV}$ [248,276]. The second operator in Eq. (2.19) is parity violating, but results in the observed relic Dark Matter abundance. Thus, it is the only dimension 5 operator considered.

At dimension 6, there are several operators leading to a mono-Higgs ($b\bar{b}$) signature through an effective h-Z-Dark Matter coupling. In the case of scalar Dark Matter particles, the operator is given by

$$\frac{1}{\Lambda^2}\chi^\dagger i\overleftrightarrow{\partial^\mu}\chi h^\dagger iD_\mu h \quad , \tag{2.20}$$

while for fermionic Dark Matter particles, the two operators

$$\frac{1}{\Lambda^2}\bar{\chi}\gamma^\mu\chi h^\dagger iD_\mu h \quad \text{and} \quad \frac{1}{\Lambda^2}\bar{\chi}\gamma^\mu\gamma_5\chi h^\dagger iD_\mu h \tag{2.21}$$

are possible. The coupling to the Z boson arises from the Standard Model covariant derivative D_μ (see Eq. (1.12)). The Z-Dark Matter interactions lead to invisible Z boson decays for $m_\chi < m_Z/2$. In this case, it is required that $\Lambda \gtrsim 400\,\text{GeV}\,(550\,\text{GeV})$ for scalar (fermionic) Dark Matter particles to fulfil constraint from the measured invisible Z boson decay width. Hence, the operator for scalar Dark Matter particles in Eq. (2.20) with lower constraint on the suppression scale is considered.

Finally, many dimension 8 operators involving additional Standard Model fields can be constructed. One of them, providing the highest kinematic acceptance at high missing transverse energy [277], is given by

$$\frac{1}{\Lambda^4}\bar{\chi}\gamma^\mu\chi B_{\mu\nu}h^\dagger D^\nu h \quad , \tag{2.22}$$

where $B^{\mu\nu}$ is the $U(1)_Y$ gauge field strength tensor of the Standard Model. The mono-Higgs ($b\bar{b}$) signal is generated via the process $q\bar{q} \to Z^*/\gamma^* \to h\chi\bar{\chi}$, which is not constrained by invisible Higgs boson decay measurements.

Validity of Effective Field Theory

EFT is a powerful method to describe physical processes at a given energy scale involving only the degrees of freedom active at this scale, e.g. a single Dark Matter particle without additional mediators. The effective interactions are usually non-normalisable and can sometimes violate Standard Model gauge symmetries. The suppression scale, Λ, is the maximum experimental energy scale at which the EFT operator expansion is applicable. Typically, Λ must be higher then the momentum transfer, Q_{tr}, in the process of interest. For example, the approach is justified for the low momentum transfers in Direct Detection experiments. In collider searches especially at the LHC, this is not the case. A general discussion of the validity of EFTs is given in Refs. [220, 278].

In the scenario of a mediator interaction with both Dark Matter and Standard Model particles, the s-channel Dark Matter production cross section is given by

$$\sigma(pp \to \chi\bar{\chi}) \simeq \frac{g_q^2 g_\chi^2}{(Q_{\text{tr}}^2 - m_{\text{med}}^2)^2 + \Gamma_{\text{med}}^2 m_{\text{med}}^2} \simeq \frac{g_q^2 g_\chi^2}{m_{\text{med}}^4} \quad , \tag{2.23}$$

where g_q and g_χ are the flavour universal coupling parameters of the mediator to quarks and to the Dark Matter particle, respectively, m_{med} the mediator mass and Γ_{med} its width, and $Q_{\text{tr}} \ll m_{\text{med}}$ is the momentum transfer between partons in the proton-proton collision. The width of the mediator is neglected, far away from the resonance in the EFT approach for a heavy mediator. The lowest-order term in the $Q_{\text{tr}}^2/m_{\text{med}}^2$ expansion of the cross section corresponds to the EFT case and is given by the last term in Eq. (2.23). The suppression scale is then given by

$$\Lambda = \frac{m_{\text{med}}}{\sqrt{g_q g_\chi}} \quad . \tag{2.24}$$

The coupling parameters have to fulfil the additional requirement g_q, $g_\chi < 4\pi$ in order to stay in the perturbative regime. With $Q_{\text{tr}} < m_{\text{med}}$ this results in

$$\Lambda > \frac{Q_{\text{tr}}}{\sqrt{g_q g_\chi}} > \frac{Q_{\text{tr}}}{4\pi} \quad . \tag{2.25}$$

A common coupling choice is $\sqrt{g_q g_\chi} = 1$, resulting in an important criterion for the validity of the EFT: $Q_{\text{tr}} < \Lambda$ [278]. For the s-channel cross section in Eq. (2.23), the mediator mass must be larger then twice the Dark Matter particle mass, $m_{\text{med}} > 2m_\chi$, which leads to a second validity requirement, $\Lambda > 2m_\chi$, from Eq. (2.24) with $\sqrt{g_q g_\chi} = 1$.

Mono-Higgs ($b\bar{b}$) Results in the Framework of Effective Field Theories

With Run 1 and early Run 2 data, a search for Dark Matter in the mono-Higgs ($b\bar{b}$) channel has been performed interpreted in EFT. The results of the early Run 2 analysis based on a dataset of 3.2 fb^{-1} are outlined below following Ref. [257]. Cross section limits at

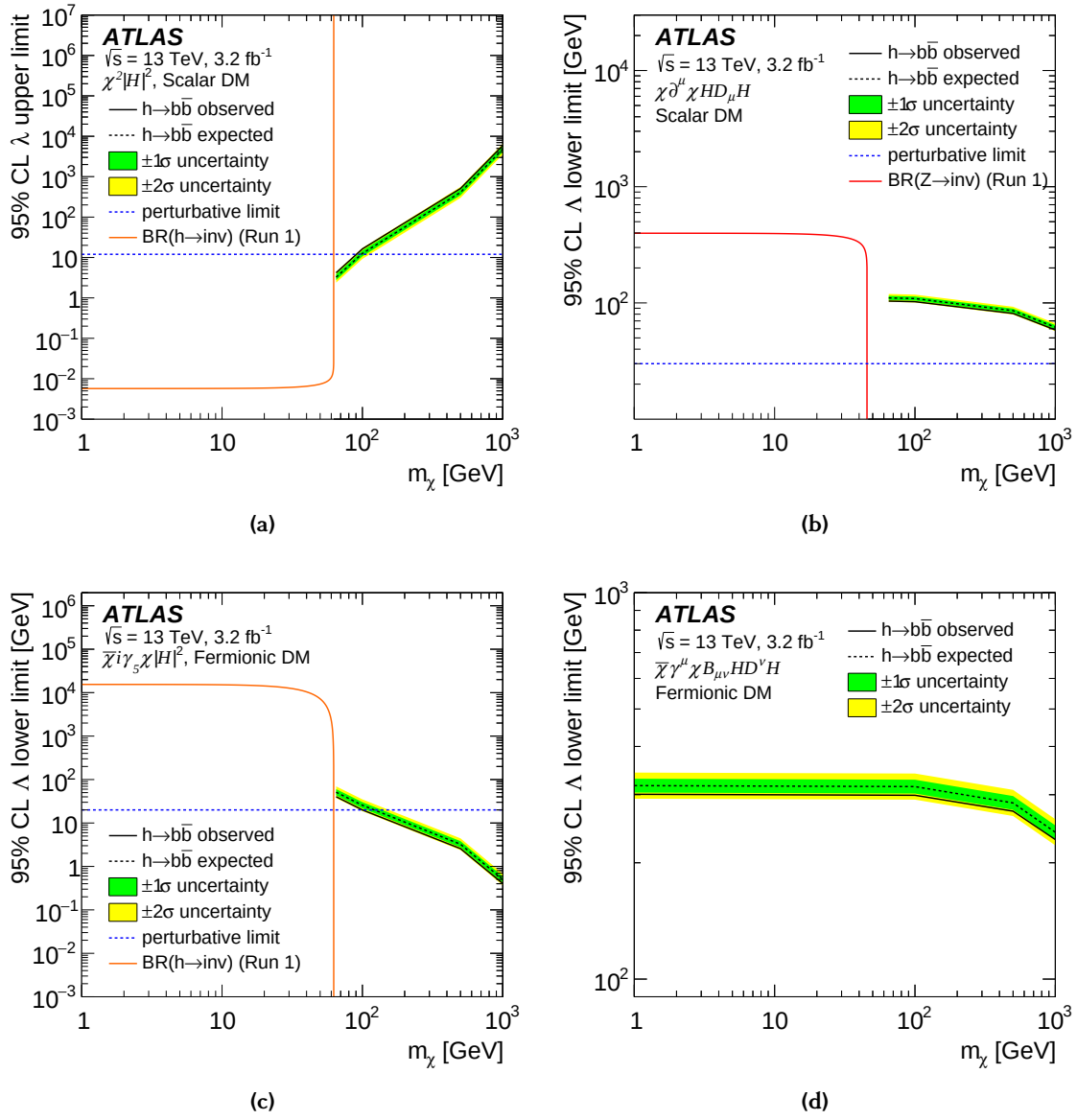

Figure 2.13: Upper (lower) limits at 95 % CL of the ATLAS experiment on the coupling parameter λ (the suppression scale Λ) as a function of the Dark Matter particle mass for EFT effective interaction operators (a) $\lambda|h|^2\chi^2$ (scalar, dimension 4), (b) $\frac{1}{\Lambda^2}\chi^\dagger i\overleftrightarrow{\partial^\mu}\chi h^\dagger iD_\mu h$ (scalar, dimension 5), (c) $\frac{1}{\Lambda}|h|^2\bar{\chi}i\gamma_5\chi$ (fermionic, dimension 6) and (d) $\frac{1}{\Lambda^4}\bar{\chi}\gamma^\mu\chi B_{\mu\nu}h^\dagger D^\nu h$ (fermionic, dimension 8). The regions below the solid black lines are excluded. In addition, constraints due to perturbativity requirement (blue dotted line) and regions excluded due to upper limits on the invisible branching ratio of the h or Z boson (red line) are shown [257].

95 % CL have been derived on the coupling parameter λ or the suppression scale Λ depending on m_χ for the EFT operators given in Eq. (2.18) to (2.22) as shown in Fig. 2.13. For the two EFT models with scalar Dark Matter particles, there is only sensitivity in regions where the kinematic constraints are not valid (see Fig. 2.13a and Fig. 2.13b). Only Dark Matter particle masses below 90 GeV are excluded for $\lambda > 4$ in the case of the dimension 4 operator. For the two operators with fermionic Dark Matter particles in Eq. (2.19) and Eq. (2.22) values of Λ up to 60 GeV and 300 GeV, respectively, are excluded as shown in Fig. 2.13c and Fig. 2.13d.
Further results of non-mono-Higgs Dark Matter searches interpreted in the context of EFT models based on the Run 1 dataset are summarised in Ref. [279].

2.6.3 Simplified Models

Simplified models are complementary to the EFT approach and have been primarily used for Dark Matter searches with Run 2 data. A simplified model is constructed by introducing a new heavy mediator, which is responsible for the interaction between Dark Matter and Standard Model particles. In the EFT formulation, the field has been integrated out. Hence, simplified models are more model dependent and include more free parameters, but they are more self-consistent and are renormalisable over a larger energy range. Compared to full theories like Supersymmetric extension of the Standard Model with $\mathcal{O}(100)$ free parameters, they are described by only few free parameters, namely the masses of the new mediator and of the Dark Matter particle as well as the two coupling parameters between the mediator and Standard Model as well as Dark Matter particles. These models assume a single massive Dark Matter particle, a Dirac fermion, stable and interaction only weakly via the mediator with the detector material. In the context of mono-Higgs searches, often more then one heavy mediator (vector or scalar) is introduced, with subsequent decays to Dark Matter and the Higgs boson.

2.6.3.1 Z'-2HDM Model

For the interaction between WIMPs and Standard Model particles new physics is needed with new heavy mediators potentially inspired by new symmetries. A straight-forward approach is to introduce new gauge bosons. The simplest extension of the Standard Model gauge structure is an additional $U(1)_{Z'}$ gauge group associated with an electrically neutral massive spin-1 gauge boson Z' a heavier copy of the weak Z boson [280–284]. An additional $U(1)_{Z'}$ symmetry is motivated by extensions of the Standard Model, including Grand Unified Theories, models with large extra dimensions, superstring theories and little Higgs models. In the simplest case, generation-independent fermion charges under $U(1)_{Z'}$ are assumed and that only right-handed quarks couple to Z' allowing

for production at the LHC while avoiding strong constraints from dilepton resonance searches.

The Lagrangian of Eq. (1.10) is modified by adding the terms for the Z'^{μ} gauge field, and a mixing term between the two neutral gauge fields B^{μ} and Z'^{μ} associated to $\mathrm{U}(1)_{\mathrm{Y}}$ and $\mathrm{U}(1)_{Z'}$, respectively:

$$\mathcal{L}' = -\frac{1}{4}W^{i}_{\mu\nu}W^{i,\mu\nu} - \frac{1}{4}B_{\mu\nu}B^{\mu\nu} - \frac{1}{4}Z'_{\mu\nu}Z'^{\mu\nu} - \frac{\sin\xi}{2}Z'_{\mu\nu}B^{\mu\nu} \quad , \tag{2.26}$$

where ξ is a mixing angle. These models are usually accompanied by an extended scalar sector to provide a spontaneous symmetry breaking mechanism for the generation of the Z' mass. The spontaneous symmetry breaking of the $\mathrm{U}(1)_{Z'}$ symmetry is introduced by an additional singlet scalar ϕ, with self-coupling z_{ϕ} and VEV v_{ϕ} at a scale above the electroweak symmetry-breaking [285].

Standard Model particle decays into Dark Matter particles due to $Z - Z'$ mixing are experimentally strongly constrained and a Higgs boson of the extended sector can serve as a mediator for Dark Matter particle interaction. The simplest extension of the Standard Model Higgs sector are two-Higgs-doublet models (2HDM) with two complex scalar weak $\mathrm{SU}(2)$ Higgs doublets Φ_u and Φ_d, and five physical Higgs boson fields. Here, a type-II 2HDM is considered where Φ_u couples only to up-type quarks and Φ_d only to down-type quarks and to leptons[*]. The Yukawa couplings of the fermions of a generation to the two Higgs doublets are given by

$$-\mathcal{L}_{Yukawa} = h_u \bar{q}_L \Phi_d d_R + h_d \bar{q}_L \tilde{\Phi}_u u_R + h_e \bar{\ell}_L \Phi_d e_R + h.c. \quad . \tag{2.27}$$

After electroweak symmetry breaking, the Higgs fields, Φ_u and Φ_d, acquire expectation values v_u and v_d, respectively. In the unitary gauge, the doublets can be parametrised as

$$\begin{aligned} \Phi_d &= \frac{1}{\sqrt{2}} \begin{pmatrix} -\sin\beta\ H^+ \\ v_d - \sin\alpha\ h + \cos\alpha\ H - i\sin\beta\ A \end{pmatrix} \quad \text{and} \\ \Phi_u &= \frac{1}{\sqrt{2}} \begin{pmatrix} \cos\beta\ H^+ \\ v_u + \cos\alpha\ h + \sin\alpha\ H + i\cos\beta\ A \end{pmatrix} \quad , \end{aligned} \tag{2.28}$$

where h and H are neutral CP-even scalars, A is a neutral CP-odd scalar with a large branching ratio to Dark Matter, and $H^{\pm}$ two charged scalars. Free parameters of the model are the ratio of the two vacuum expectation values, $\tan\beta = \frac{v_u}{v_d}$[†], and the mixing angle α which diagonalises the $h - H$ mass matrix.

[*] In contrast, in a type-I 2HDM all charged fermions couple to just one Higgs doublet [286].

[†] The vacuum expectation values in the 2HDM are related to the Standard Model one in Eq. (1.23) via $v = \sqrt{v_u^2 + v_d^2} = 246\,\mathrm{GeV}$.

Note, that the Standard Model Higgs boson field is a mixture of the two neutral CP-even scalars and given by

$$h^{\mathrm{SM}} = h \underbrace{\sin(\alpha-\beta)}_{\xlongequal{\alpha=\beta-\frac{\pi}{2}} 1} - H \underbrace{\cos(\alpha-\beta)}_{\xlongequal{\alpha=\beta-\frac{\pi}{2}} 0}, \tag{2.29}$$

and in the so-called *alignment limit*[*] $\alpha = \beta - \frac{\pi}{2}$ [287, 288] the Standard Model Higgs boson, h^{SM}, is denoted as h unless stated otherwise.

The CP-even and charged Higgs bosons are assumed to have masses near or above 300 GeV in accordance with constraints from measurements of the inclusive radiative B-meson decay branching ratio $\mathcal{B}(b \to s\gamma)$ [286,289]. Additionally, it is required that $\tan\beta \geq 0.3$ to fulfil the perturbativity requirement on the Higgs-top Yukawa coupling [290]. The mass of the pseudoscalar Higgs boson, A, is not fixed. A has a large branching ratio $\mathcal{B}(A \to \chi\bar{\chi})$ to Dark Matter particles close to 100 % and serves as a mediator.

The weak Z boson and the newly introduced Z' boson can mix with each other resulting in a modification of the prediction of the precisely measured Z mass and of the ρ parameter[†]. Deviations from the Standard Model value of $\rho = \frac{m_W^2}{m_Z^2 \cos^2\theta_{\mathrm{W}}} = 1$ [291] in the 2HDM are given by

$$\rho = 1 + \epsilon^2 \left(\frac{m_{Z'}^2 - m_Z^2}{m_Z^2} \right) \quad , \tag{2.30}$$

which is accurate up to $\mathcal{O}(\epsilon^2)$, and ϵ is a small mixing parameter given by

$$\begin{aligned} \epsilon &= \frac{1}{m_{Z'}^2 - m_Z^2} \frac{g' g_{Z'}}{2\cos\theta_{\mathrm{W}}} (z_d v_d^2 + z_u v_u^2) \\ &= \frac{(m_Z^0)^2}{m_{Z'}^2 - m_Z^2} \frac{2 g_{Z'} \cos\theta_{\mathrm{W}}}{g'} z_u \sin^2\beta \end{aligned} \tag{2.31}$$

with the Z' gauge coupling constant $g_{Z'}$, and the $\mathrm{U}(1)_{Z'}$ charges to right-handed up- and down-type fermions z_u and z_d, respectively.

The tree-level mass eigenvalues of the Z and Z' bosons are given by

$$\begin{aligned} m_Z^2 &\approx (m_Z^0)^2 - \epsilon^2 \left[(m_{Z'}^0)^2 - (m_Z^0)^2 \right] \quad \text{and} \\ m_{Z'}^2 &\approx (m_{Z'}^0)^2 + \epsilon^2 \left[(m_{Z'}^0)^2 - (m_Z^0)^2 \right] \quad , \end{aligned} \tag{2.32}$$

---

[*] As a result of the alignment limit, the scalar H boson does not interact with W and Z bosons at tree level.

[†] The ρ parameter is measured in the global fit of electroweak precision data from LEP, SLC and hadron colliders to be $\rho = 1.000\,37 \pm 0.000\,23$ [36]. The custodial symmetry in the Standard Model assures that radiative corrections to ρ are small and its value is close to one with only small deviations [291].

where $(m_Z^0)^2 = g'^2(v_d^2 + v_u^2)/(4\cos^2\theta_w)$ and $(m_{Z'}^0)^2 = g_{Z'}^2(z_d^2 v_d^2 + z_u^2 v_u^2 + z_\phi^2 v_\phi^2)$ are the mass-squared values in the absence of mixing.
Upper limits on ρ of 1.0009 [266], from fits of electroweak precision data, can be used to constrain the coupling parameter $g_{Z'}$ as follows:

$$\rho = 1 + \left(\frac{(m_Z^0)^2}{m_{Z'}^2 - m_Z^2}\frac{2g_{Z'}\cos\theta_W}{g'} z_u \sin^2\beta\right)^2 \left(\frac{m_{Z'}^2 - m_Z^2}{m_Z^2}\right) \leq 1.0009 \quad . \tag{2.33}$$

When assuming that only small mixing are allowed, e.g. ϵ is small such that $(m_Z^0)^2 \approx m_Z^2$ and with $z_u = \frac{1}{2}$, the inequality of Eq. (2.33) gets modified to:

$$\begin{aligned} &\left(\frac{m_Z^2}{m_{Z'}^2 - m_Z^2}\frac{g_{Z'}\cos\theta_W}{g'}\sin^2\beta\right)^2 \left(\frac{m_{Z'}^2 - m_Z^2}{m_Z^2}\right) \leq 0.0009 \\ \Longrightarrow \quad &\frac{m_Z^2}{m_{Z'}^2 - m_Z^2}\left(\frac{g_{Z'}\cos\theta_W}{g'}\sin^2\beta\right)^2 \leq 0.0009 \quad . \end{aligned} \tag{2.34}$$

Solving Eq. (2.34) for $g_{Z'}$ results in

$$g_{Z'} \leq 0.03 \cdot \frac{g'}{\cos\theta_W \sin^2\beta} \cdot \sqrt{\frac{m_{Z'}^2 - m_Z^2}{m_Z^2}} \quad , \tag{2.35}$$

depending on the parameters β and $m_{Z'}$.
As the Z' gauge boson couples primarily to quarks, e.g. the dominant production mechanism is via $q\bar{q} \to Z'$, it can also decay to a pair of quarks. Thus, constraints on $g_{Z'}$ exist from searches for dijet resonances at collider experiments. Upper limits from Tevatron and LHC on the coupling parameter $g_{Z'}$ are shown in Fig. 2.14. For Z' masses below 1.3 TeV and large $\tan\beta$, the ρ constraint on $g_{Z'}$ is stronger then the dijet limits, while for $\tan\beta \leq 0.6$, the dijet limits dominate even at low $m_{Z'}$.
The simplified Z'-2HDM model (see Fig. 2.15) is described by five free parameters: $\tan\beta$, the Z' coupling strength $g_{Z'}$, $m_{Z'}$, m_A, and the Dark Matter particle mass m_χ. From the mono-Higgs ($b\bar{b}$) search in Ref. [267], variations of $\tan\beta$ have no effect on the event kinematics as long as $m_A > 2m_\chi$, such that A production is on-shell. Minor kinematic changes are caused by variations of m_χ. The production cross section is independent of m_χ as the Dark Matter particles are produced by on-shell decay of the A boson. Hence, the mass of the Dark Matter particle is fixed in the model to 100 GeV (at the electroweak scale as expected for a WIMP) as recommended by the ATLAS/CMS Dark Matter Forum [215].
The production cross section scales with $\cos\beta^2$. Similarly, variations of $g_{Z'}$ have no influence on the kinematics while the production cross section scales with $(g_{Z'})^2$. The

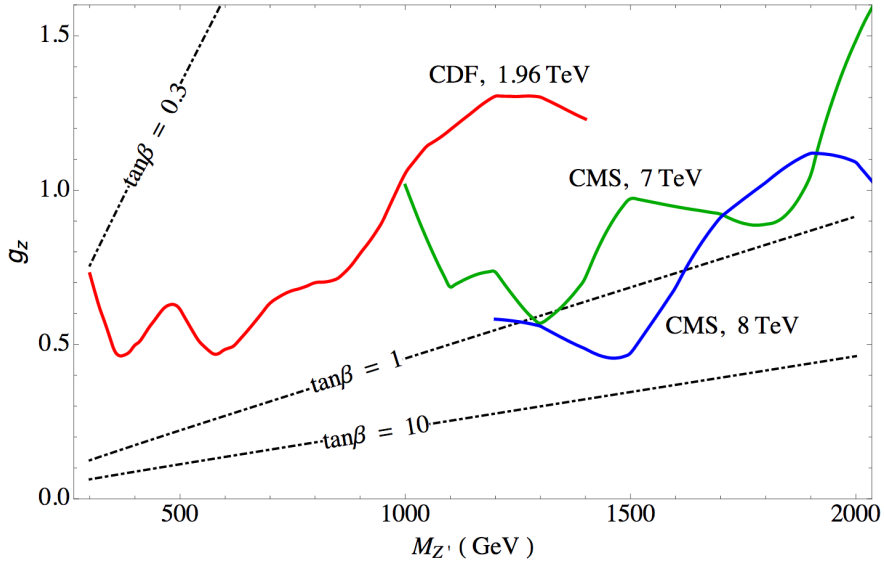

Figure 2.14: The 95 % CL upper bounds on the Z' coupling, $g_{Z'}$, as a function of $m_{Z'}$ from ρ parameter constraints on the $Z - Z'$ mixing strength for $\tan\beta = 0.3$, 1 and 10 (dashed lines), together with upper limits from dijet resonance searches at the Tevatron (red curve) and the LHC (green and blue curves) [266].

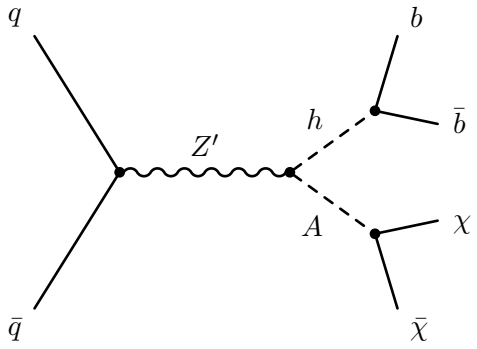

Figure 2.15: Feynman diagram for the production of Dark Matter particles, χ, in association with the Higgs boson in a simplified Z'-2HDM model, where the Z' boson decays into a Higgs boson, h, and a pseudoscalar, A, with subsequent decays of h into a pair of b quarks and of A into a χ pair.

cross section scaling formula is given by

$$\sigma^{\text{Scaled}}_{\text{Run 2 param.}}(q\bar{q} \to Z' \to hA) = \sigma_{\text{Run 2 param.}} \cdot \left(\frac{g_{Z',\text{Run 1}} \cos(\alpha_{\text{Run 1}}) \cos(\beta_{\text{Run 1}})}{g_{Z',\text{Run 2}} \cos(\alpha_{\text{Run 2}}) \cos(\beta_{\text{Run 2}})} \right)^2, \quad (2.36)$$

with $\alpha = \beta - \pi/2$ in the assumed alignment limit. The values of the parameters $g_{Z'}$ and $\tan\beta$ used in the Run 1 and Run 2 analyses are summarised in Table 2.2. They can be translated into each other by using Eq. 2.36, assuming that $g_{Z'}$ and $\tan\beta$ only affect the total rate of the process. Thus, the predicted cross sections for the Run 2

Table 2.2: The coupling parameters $g_{Z'}$ and $\tan\beta$ of the simplified Z'-2HDM model used for the Run 1 and 2 analysis, respectively.

	$g_{Z'}$	$\tan\beta$
Run 1	0.8	1.0
Run 2	0.1	3.0

parameters $(g_{Z'}, \tan\beta) = (0.1, 3.0)$ had been multiplied by 178 to match the ones for Run 1 parameters. More details on the Z'-2HDM signal model can be found in Ref. [266]. The Z'-2HDM signal model is used as a benchmark model for the optimisation of the mono-Higgs ($b\bar{b}$) analysis in Chapter 4.

Chapter 3

The ATLAS Experiment at the Large Hadron Collider

The LHC at CERN[*] near Geneva in Switzerland [292–295] started operation in the year 2008. The LHC is a proton and heavy ion storage ring of 26.7 km circumference located up to 170 m below ground in the tunnel of its predecessor accelerator the Large Electron-Positron Collider (LEP) [296]. It is used to accelerate protons or and lead ions and to collide them at unprecedentedly high energies.
The proton-proton collisions are measured by several experiments, namely ATLAS[†] [297], CMS[‡] [298], ALICE[§] [299] and LHCb[¶] [300]. The multi-purpose detectors ATLAS and CMS have been designed for the search for the Higgs boson and new physics beyond the Standard Model at the highest luminosities. ALICE studies mainly heavy ion collisions and LHCb is specialized B-meson physics.
The maximum design energy of the LHC is 7 TeV per beam, corresponding to a center-of-mass energy ($\sqrt{s}$) of 14 TeV, with a design luminosity of $L = 10^{34}\,\mathrm{cm}^{-2}\,\mathrm{s}^{-1}$. The two proton beams circulate in opposite directions in two vacuum beam pipes and kept in orbit by superconducting magnets. An overview of the CERN accelerator complex and of the LHC operating parameters between 2015 and 2017, when the data for this thesis were taken, is given in Section 3.1. The ATLAS detector is described in Section 3.2 and the particle reconstruction methods in Section 3.3.

3.1 The Large Hadron Collider

The LHC [295] provides the highest collision energies reached with unprecedentedly high collision rates at a hadron collider. Both is required to achieve the goal to discover physics beyond the Standard Model, such as the production of Dark Matter particles.

[*] **C**onseil **E**uropéen pour la **R**echerche **N**ucléaire.
[†] **A** **T**oroidal **L**HC **A**pparatu**S**.
[‡] **C**ompact **M**uon **S**olenoid.
[§] **A** **L**arge **I**on **C**ollider **E**xperiment.
[¶] **L**arge **H**adron **C**ollider **b**eauty.

Before the proton beams are injected into the LHC, they are accelerated in steps up to the injection energy of 450 GeV. A schematic overview of the LHC accelerator complex is shown in Fig. 3.1. Protons are produced by ionising hydrogen atoms, then accelerated to 50 MeV in the linear accelerator (LINAC) 2. The proton beam is then transfered to the Proton Synchrotron Booster (PSB), which consists of four superimposed synchrotron rings, and accelerated to 1.4 GeV. The next step in acceleration is the Proton Synchrotron (PS), which accelerates the proton beam to 25 GeV. The PS also creates the required bunch structure of the proton beam for the LHC, with very bright bunches (high intensity and low emittance). The last step before injection into the LHC, is the acceleration to

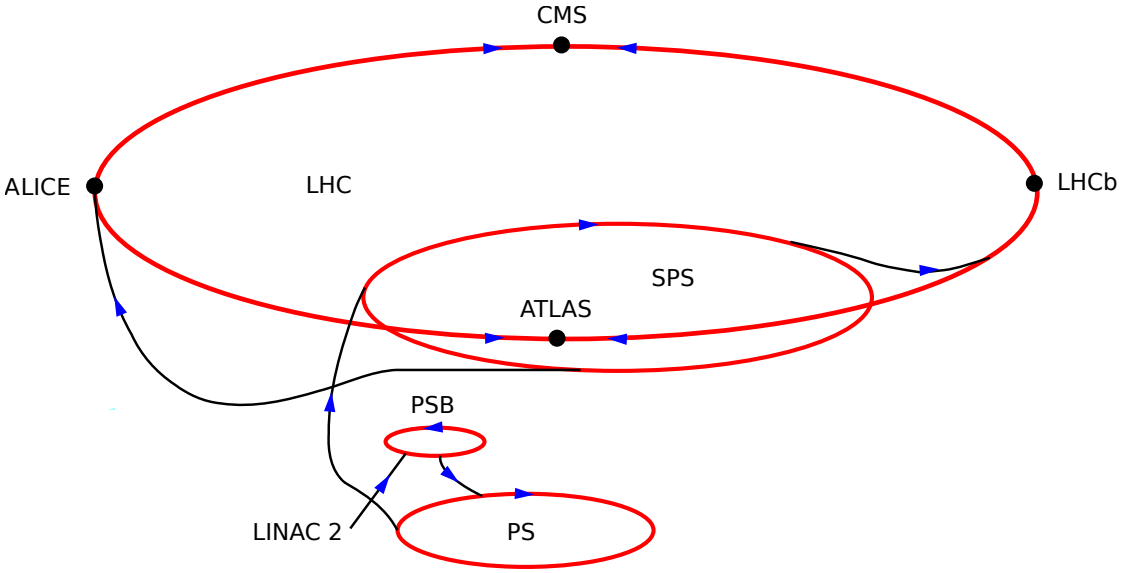

Figure 3.1: Illustration of the CERN accelerator system. The acceleration chain starts with LINAC 2 and followed by the acceleration in the Proton Synchrotron Booster (PSB). The protons are then accelerated further by the Proton Synchrotron (PS) and the Super Proton Synchrotron (SPS) before they are injected into the LHC [301], where they reach their final collision energy. The proton beams cross at four main interaction points, where four large detectors are housed, namely ATLAS, ALICE, CMS and LHCb. For completeness, three smaller experiments, TOTEM [302], LHCf [303] and MoEDAL [304], are located around the LHC, which are not shown here.

450 GeV in the Super Proton Synchrotron (SPS), in the second largest machine in the CERN accelerator complex with a circumference of nearly 7 km. The injection points of the two beams into the LHC are close to ALICE and LHCb, respectively.
In the LHC, the two beams are accelerated in opposite directions to their final energy of up to 6.5 TeV in Run 2 and brought to collision at four interaction points, where the main detectors are located.
The proton beams are accelerated in two separate vacuum beam pipes by eight superconducting radio-frequency cavities. Each of the 16 cavities provides an electric field gradient of 5.5 $\frac{\mathrm{MV}}{\mathrm{m}}$.

Superconducting dipole magnets in so-called *twin-bore design* keep the beams on circular orbits. In this compact design, the two circular beam pipes are integrated into the superconducting magnets and their cryostats. The dipole magnets, using of NbTi cables cooled down to 1.9 K with superfluid helium, provide a maximum magnetic field of 8.33 T. A total of 1232 dipole magnets are installed in the LHC tunnel.
Quadrupole magnets are used to focus the beams and squeeze them near the interaction point to reach high luminosities. Additional kicker magnets are used for beam corrections extraction.

3.1.1 Luminosity

The number of events, N_{events}, generated by a particular process of the LHC depends on the cross section, $\sigma(\sqrt{s})$, of the process and the integrated luminosity, L:

$$N_{\text{events}} = \sigma(\sqrt{s}) \cdot L \quad . \tag{3.1}$$

The cross sections of important Standard Model processes are given in Fig. 1.5 as a function of the center-of-mass energy. The integrated luminosity, L, is related to the instantaneous luminosity, $\mathcal{L}$, by $L = \int \mathrm{d}t\mathcal{L}$.
The instantaneous design luminosity of the LHC with a Gaussian beam particle profile is given by

$$\mathcal{L} = \frac{n_b N_b^2 f_{\text{rev}} \gamma_r F(\theta)}{4\pi\epsilon_n \beta^*} \quad , \tag{3.2}$$

where $n_b = 2808$ is the number of bunches per beam, $N_b = 1.15 \cdot 10^{11}$ the numbers of protons per bunch for 25 ns* bunch spacing. In Eq. (3.2), f_{rev} is the revolution frequency of the protons, γ_r the relativistic gamma-factor, F a geometric luminosity reduction factor taking into account that the beams cross under an angle θ, ϵ_n the normalised beam emittance, and β^* the transverse beam amplitude at the interaction point [305].
The design peak luminosity of the LHC is $10^{34}\,\text{cm}^{-2}\,\text{s}^{-1}$. Due to the large number of protons inside the bunch, the large number of bunches colliding every 25 ns and the large inelastic pp cross section at the LHC collision energy, several inelastic pp interactions can take place in a bunch crossing. As a result, every triggered event in the detector contains also the products of additional soft interactions, referred to as *pile-up* [306], which leads to additional energy contributions to jets or misidentified leptons. There are two contributions to the pile-up. Additional pp interactions in the same bunch crossing are called *in-time* pile-up. Additional interactions which occur in a previous or successive bunch collision are called *out-of-time* pile-up. In-time pile-up has by far the largest

*During Run 2 of the LHC, between the years 2015 and 2018, a bunch spacing of 25 ns is used, while in Run 1 (2011 and 2012), a larger bunch spacing of 50 ns has been used.

impact on the physics analyses. During the LHC Run 2 between 2015 and 2017, the maximum mean was around 32 (see Fig. 3.2a).

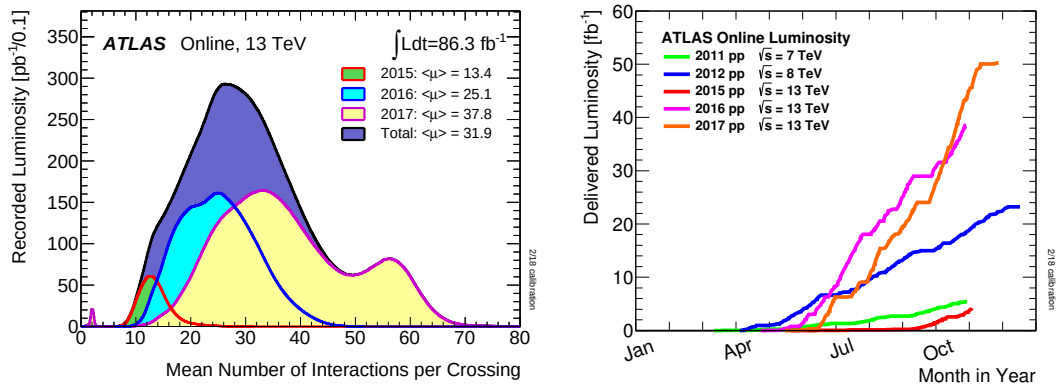

(a) (b)

Figure 3.2: The luminosity weighted distributions of (a) the mean number of interactions per bunch crossing between 2015 and 2017 and (b) the integrated luminosity delivered by the LHC per year from 2011 to 2017 [307].

In addition, so-called *non-collision* background can contribute to the main collision event, for example from beam-gas interactions in the beam pipe and beam interactions with the vacuum pipe, collimators and shielding as well as from neutrons and photons permeating the detector cavern.

3.2 The ATLAS Detector

The ATLAS detector is a multi-purpose detector designed to fully exploit a wide range of physics topics at the LHC. The ATLAS physics program comprises precision measurements of Standard Model processes at the highest energies and the study of new physics phenomena like the search for the Higgs boson, for super-symmetric particles and for Dark Matter particles as well as for new heavy gauge bosons up to the TeV scale. Such massive mediators might be responsible for the interaction between Standard Model and Dark Matter particles.

The high center-of-mass energy and high instantaneous luminosity of the pp collisions at the LHC allow for the study of rare processes, while detector has to cope with very high event rates and particle rates. Therefore, fast detector readout, high granularity and radiation-hard detector technologies and electronics are required. An overview of the ATLAS detector is given in the following [297, 308].

The ATLAS detector is 44 m long and 25 m high and weights approximately 7 t. It has the typical layout of a collider experiment with cylindrical shape and forward-backward

symmetry covering almost the full solid angle. The detector is structured onion-like with cylindrical *barrel* layers concentric with beam pipe and disk-shaped *endcap* detector. A

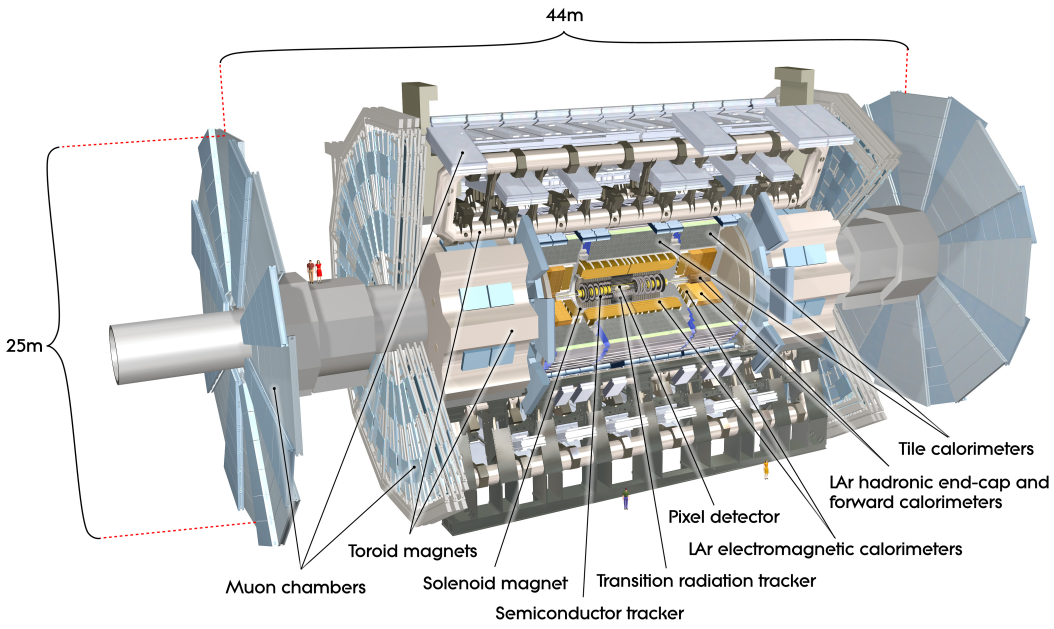

Figure 3.3: Cut-away view of the ATLAS detector with its sub-systems: The Inner Detector consisting of the Pixel Detector, the Semi-Conductor Tracker (SCT) and the Transition Radiation Tracker (TRT), followed by the calorimeter system with the Liquid Argon (LAr) electromagnetic calorimeters, the hadronic LAr endcap and barrel tile calorimeters, and at the outermost radius, the Muon Spectrometer with its large superconducting toroid magnets [297].

schematic overview of the ATLAS detector is shown in Fig. 3.3.

The ATLAS detector is composed of three main components, the inner tracking system [309], the calorimeters [310,311] and the muon spectrometer [312]. The Inner Detector provides track, charge and the momentum measurement of charged particles in a 2 T solenoidal magnetic field of a cylindrical superconducting coil. The calorimeter system surrounds the Inner Detector and allows for the identification of photons, electrons and hadrons and the measurement of their energies. It also measures the missing energy due to neutrinos or other weakly interacting stable particles like Dark Matter not visible in the detector. The Muon Spectrometer is in the outermost part of the detector and it identifies muons and measures their momenta in the field of superconducting toroid magnets.

The energy and momentum resolutions and coverages of the sub-detector systems are given in Table 3.1.

Table 3.1: The energy and transverse momentum resolution and the η coverage of the ATLAS sub-detector systems. [297, 312]. Energies and transverse momenta are given in GeV.

Sub-system	Energy and transverse momentum resolution	η coverage
Inner Detector	$\sigma/p_{\mathrm{T}} = 0.05\,\% p_{\mathrm{T}} \bigoplus 1\,\%$	$\lvert\eta\rvert < 2.5$
Electromagnetic Calorimeter		
barrel and endcap	$\sigma/E = 10\,\%/\sqrt{E} \bigoplus 0.7\,\%$	$\lvert\eta\rvert < 3.2$
Hadronic Calorimeter		
barrel / endcap	$\sigma/E = 50\,\%/\sqrt{E} \bigoplus 3\,\%$	$\lvert\eta\rvert < 3.2$
forward	$\sigma/E = 100\,\%/\sqrt{E} \bigoplus 10\,\%$	$3.1 < \lvert\eta\rvert < 4.9$
Muon Spectrometer	$\sigma/p_{\mathrm{T}} = 4\,\%$ for $p_{\mathrm{T}} = 0.1\,\mathrm{GeV}$	
	$\sigma/p_{\mathrm{T}} = 15\,\%$ for $p_{\mathrm{T}} = 1\,\mathrm{TeV}$	$\lvert\eta\rvert < 2.7$

3.2.1 The ATLAS Coordinate System

The ATLAS detector uses a right-handed coordinate system, with origin at the interaction point. The z-axis points along the beam axis, while the y-axis points upwards and the x-axis towards the center of the LHC ring. The azimuthal angle ϕ is measured around the beam axis from the positive x-axis. The polar angle θ is measured from the z-axis and is related to the *pseudorapidity*[*]

$$\eta = \frac{1}{2} \ln \left(\tan \frac{\theta}{2} \right) \quad , \tag{3.3}$$

which is invariant under Lorentz-boosts along the z-axis. The relation between θ and η is illustrated in Fig. 3.4.
The angular separation between two particles, i and j, is measured by the distance parameter

$$\Delta R := \Delta R_{ij} = \sqrt{(\eta_i - \eta_j)^2 + (\phi_i - \phi_j)^2} = \sqrt{\Delta\eta^2 + \Delta\phi^2} \quad . \tag{3.4}$$

The center-of-mass energy of two colliding partons, the constituents of the colliding protons, is not known. Their initial transverse momenta with respect to the beam direction is negligible. Thus, the sum of the transverse momenta ($p_{\mathrm{T}} = p \cdot \sin\theta$) of the final state particles must be zero too, an important constraint for the event selection. Particles not detected, like neutrinos or Dark Matter, contribute to the missing transverse momentum $E_{\mathrm{T}}^{\mathrm{miss}}$ which, from the momentum conservation, is the absolute value of the

[*]The rapidity $y = \frac{1}{2} \cdot \ln \frac{E+p_z}{E-p_z}$ is equal to the pseudorapidity in the limit of large E/m, where E and m is the energy and mass, respectively, and p_z the momentum in z-direction of the particle.

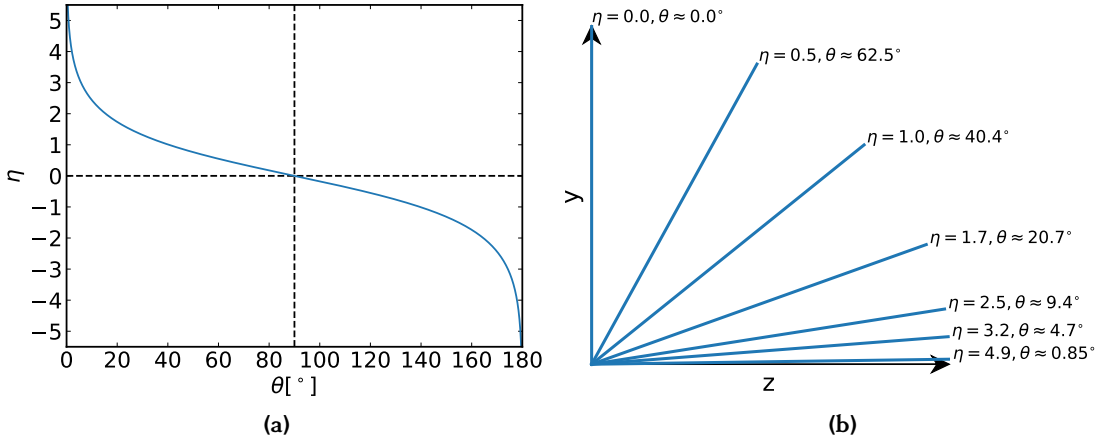

Figure 3.4: The pseudorapidity η as a function of the polar angle θ (a) with examples (b) in the $y-z-$plane.

vector sum of the transverse momenta of all detected particles (see Section 3.3.7).
Other important variables describing charged particle tracks are the transverse and longitudinal impact parameters d_0 and z_0, respectively, defining the point of closest approach of the track to the interaction point (see Ref. [313]). Uncertainties on d_0 and z_0 are given by $\sigma(d_0)$ and $\sigma(z_0)$, respectively.

3.2.2 The Inner Detector

The innermost part of the ATLAS detector is the *Inner Detector* (ID) [314], comprising three independent sub-detector systems [297] (see Fig. 3.5). It combines high spatial resolution silicon detector layers at smaller radii and with continuous tracking with lower granularity at larger radii. The ID is surrounded by a superconducting solenoid magnet providing a homogeneous field in z direction with a strength of 2 T [316].
Tracks of charged particles originating from the interaction point are precisely measured. The track curvature in the transverse plane allows for precise measurement of the particle momentum and charge. Additionally, the primary interaction vertex and possibly secondary decay vertices for the suppression of pile-up interactions and the identification of B-hadron decays, respectively, are reconstructed. This is particularly important at the LHC design luminosity, around 1000 tracks and between 20 to 70 pile-up vertices are produced per proton bunch crossing [297]. Therefore, highly granular tracking detectors are needed to provide sufficient spatial resolution to reconstruct all particle tracks and vertices within these very dense environments while keeping the amount of detector material at a minimum.
The inner tracker covers $|\eta| < 2.5$ with a track p_{T} threshold of 500 MeV. Electron

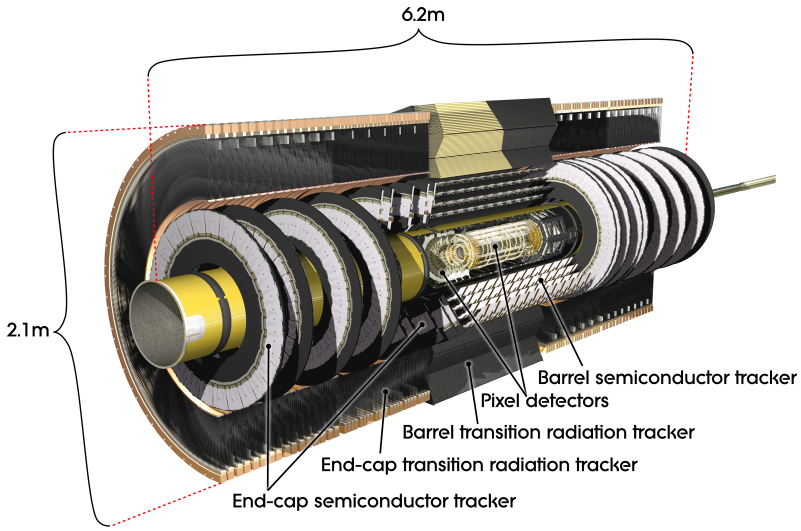

(a)

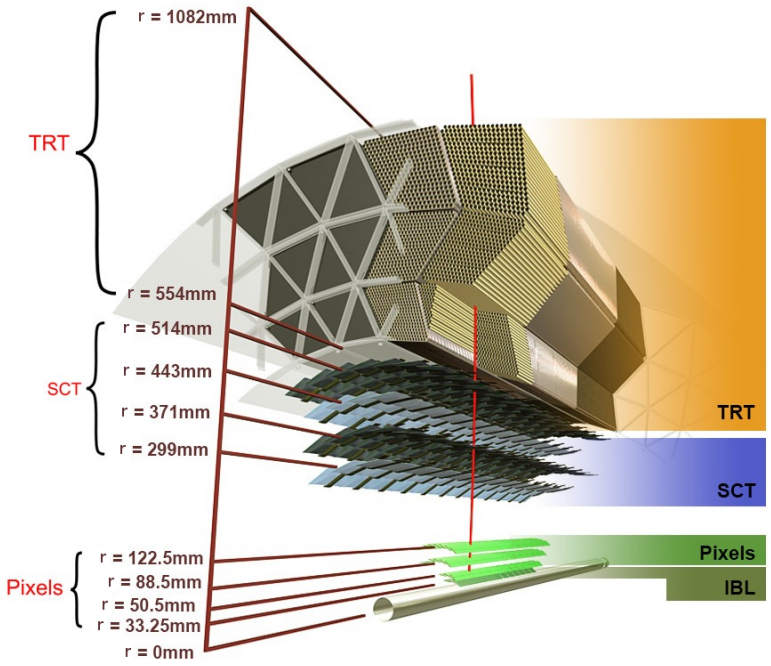

(b)

Figure 3.5: A schematic view of the ATLAS Inner Detector with the barrel and endcap layers of (a) the Pixel Detector, the Semi-Conductor Tracker (SCT) and the Transition Radiation Tracker (TRT) and (b) the new innermost insertable B-layer (IBL) [315].

identification is provided within $|\eta| < 2.0$ by the outermost tracking detector, the Transition Radiation Tracker, over a large energy range from of 0.5 to 150 GeV.

Pixel Detector

Originally, the Pixel Detector [317] consisted of three barrel layers of high-granular pixel sensors at radii of 4 to 14 cm and of four disks in each endcap at distances of 11 to 20 cm from the interaction point completing the angular coverage. In order to have improved track and vertex reconstruction performance and the identification of short lived particles such as B-hadrons and τ-leptons at high instantaneous luminosities during Run 2 and to mitigate the impact of radiation damage to the innermost layer, a fourth layer, the so-called insertable B-layer (IBL) [315, 318], has been added during the LHC shutdown between Run 1 and Run 2 closest to the beam at a radius of 3.57 cm together with a new Beryllium beam pipe (see Fig. 3.5b).

Semi-Conductor Tracker

The Pixel Detector is followed by the Semi-Conductor Tracker (SCT), located at radii between 30 to 51 cm around the beam axis. It provides high-precision track points in four cylindrical layers of silicon strip sensors in the barrel region and nine disks in each of the two endcaps [314]. The strip sensors are mounted back-to-back with a 40 mrad stereo angle to measure (y, z) coordinates in each layer. The endcap layers are arranged such that a charged particles always passed at least four sensor layers.
The spatial resolution of each layer is 16 µm in the azimuthal and 580 µm in the longitudinal direction and similar in the endcaps in the azimuthal and radial directions, respectively. The SCT barrel covers the range $|\eta| \leq 1.5$ and the endcaps extend the acceptance to $|\eta| = 2.5$.

Transition Radiation Tracker (TRT)

The TRT is in the outermost part of the ID. It is composed of 4 mm diameter Kapton straw drift tubes with a length of 150 cm, which can operate up to the very high rates. They contain 30 µm diameter tungsten-rhenium anode wires in their center and are filled with a gas mixture of 70 % Xe, 27 % CO_2 and 3 % O_2. The xenon gas is sensitive to detect transition-radiation photons created in radiator material between the straws, allowing for the discrimination electron tracks. The barrel contains about 50000 straw tubes, each split at $\eta = 0$ in order to reduce the occupancy. The endcaps contain 320000 radial straws. The TRT covers the pseudorapidity range of $|\eta| \leq 2.0$. The spatial resolution of the straw tube is 50 µm [314]. The coordinate along the TRT wire direction is not measured.

3.2.3 The Calorimeter System

The ATLAS calorimeter system [319, 320] surrounds the ID and consists of the electromagnetic and hadron calorimeters both based on sampling principle. The calorimeter

system (see Fig. 3.6) measures the energies of particles and jets by absorbing them (except for neutrinos and muons) in the range of $|\eta| < 4.9$. In addition, the calorimeters provide trigger information (see Section 3.2.6). For this purpose, the minimum number of radiation lengths, X_0, of the electromagnetic calorimeter is 22 in the barrel region and > 24 [297] in the endcaps. The complete calorimeter has a thickness of approximately 10 hadronic interaction lengths.

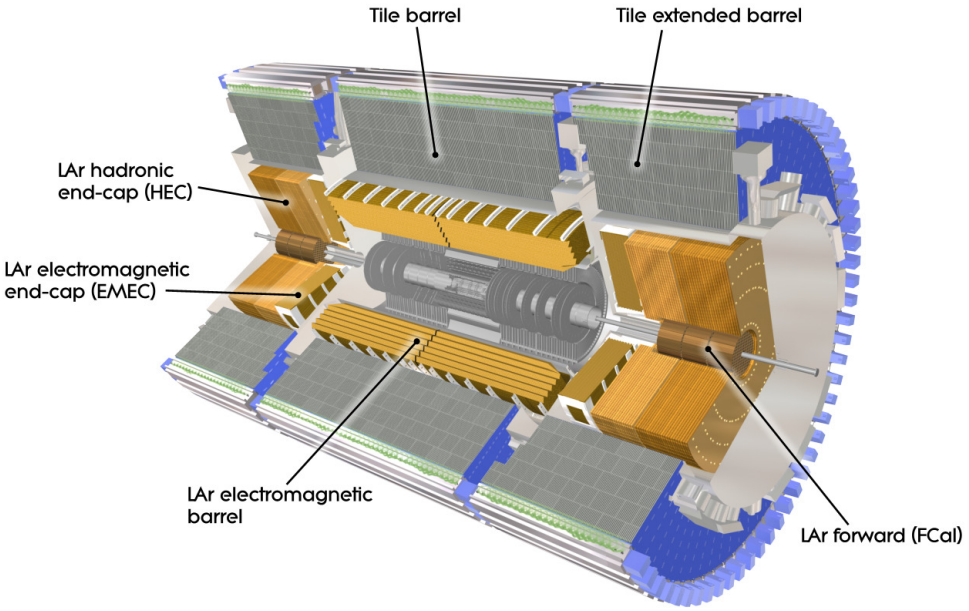

Figure 3.6: Cut-away view of the ATLAS calorimeter system [297]. The inner part is the electromagnetic calorimeter (yellow) surrounded by the hadronic calorimeter (grey).

Electromagnetic Calorimeter

The Electromagnetic Calorimeter (ECAL) is a highly granular sampling calorimeter consisting of lead absorber plates and liquid Argon as active material. Lead has a rather short radiation length of $X_0 = 0.56\,\text{cm}$ [36], such that electromagnetic shower containment is achieved within the available space. The absorbers plates are accordion shaped providing full ϕ coverage without cracks. The barrel calorimeter ($|\eta| < 1.5$), consists of two identical halfs, separated by a small gap at $\eta = 0$, and two endcaps at $1.4 < |\eta| < 3.2$. In the central region of $|\eta| < 1.8$, the ECAL is supplemented by a presampling detector, an instrumented LAr layer, which is used to correct for the energy loss of electrons and photons before they reach the calorimeter.

The transition region $1.375 < |\eta| < 1.52$ between barrel and endcaps region contains a significant amount pf support material for the ID. These services amount to several radiation lengths of inactive material where the energy of the particles cannot be measured.

This region is usually not considered for analyses requiring high precision electron or photon energy measurement.

Hadronic Calorimeter

The Hadronic Calorimeter (HCAL) system comprises three different technologies. In the barrel part the Tile Calorimeter surrounding the ECAL and its extension to larger η, the Hadronic End-cap Calorimeter (HEC) and the Forward Calorimeter (FCal).

The Tile Calorimeter is separated into the central region $|\eta| < 1.0$ and the extended-barrel covering $0.9 < |\eta| < 1.7$. It is a sampling calorimeter with iron absorber plates and scintillating tiles as the active medium. The scintillating plastic tiles are oriented radially. The scintillation photons are collected with wavelength-shifting fibres and measured using photo multipliers.

The HEC calorimeter uses LAr as active material and copper absorber plates covering the range $1.5 < |\eta| < 3.2$. The very forward region $3.1 < |\eta| < 4.9$, is covered by the FCal with a depth of approximately 10 interaction lengths. Each FCal module consists of three sub-modules in beam direction. In the first layer from the IP, the absorber material is copper providing precise electromagnetic shower energy measurement, while tungsten is used for the next two layers to absorb hadronic showers.

3.2.4 The Muon Spectrometer

Muons are the only charged particles, which can traverse the whole detector without being absorbed. The Muon Spectrometer (MS) [321] is the largest detector system of ATLAS, with a length of 44 m and 25 m in diameter, and forms the outermost part of the ATLAS detector. The MS is used for muon identification and precise muon momentum measurement for transverse momenta between 3 GeV up to a few TeV in the magnetic field of superconducting air-core toroid magnets (see Section 3.2.5). For $|\eta| < 1.4$, the magnetic field is provided by eight barrel toroid coils, and for $1.6 < |\eta| < 2.7$[*] with eight toroid coils each in a single cryostat in each endcap.

In addition to high precision tracking chambers, the MS is instrumented with fast muon trigger chambers (see Section 3.2.6). The MS consists of three cylindrical layers of muon chambers around the beam pipe in the barrel and of three wheels in each endcap.

An overview of the MS is given in Fig. 3.7.

Precision Chambers

Monitored drift tube (MDT) chambers measure muon track coordinates in the bending direction perpendicular to the toroidal magnetic field over the range $|\eta| < 2.7$. The MDT

[*]The region $1.4 < |\eta| < 1.6$ is referred to as the *transition region* of the Muon Spectrometer, where the two fields of the barrel and endcap toroids overlap and provide a relatively inhomogeneous magnetic field.

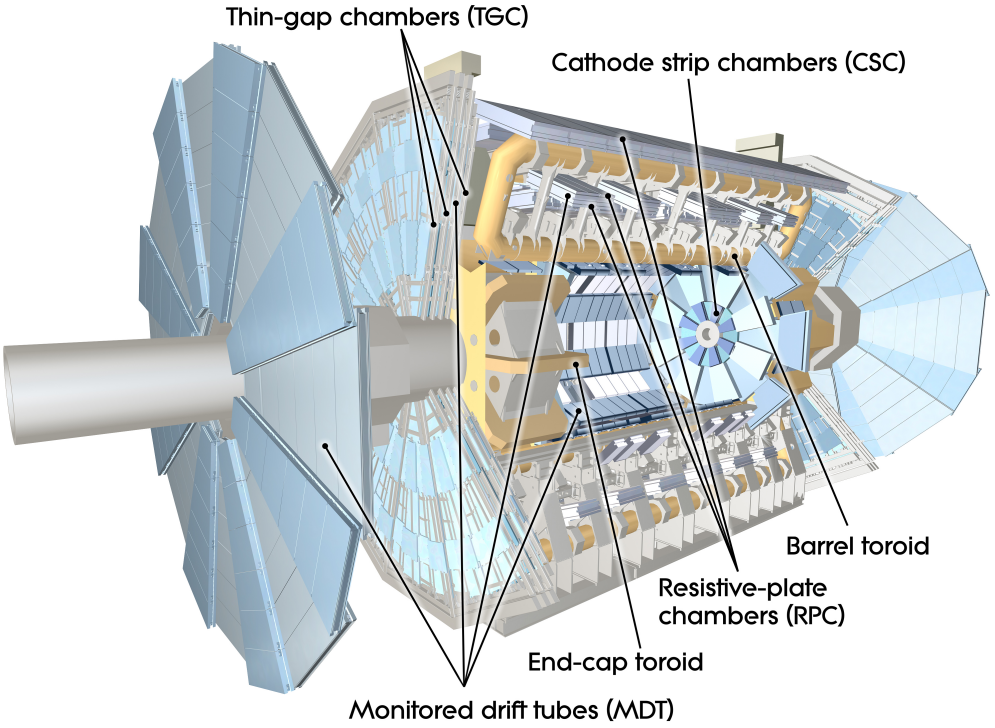

Figure 3.7: Cut-away view of the ATLAS muon system [322].

chambers consist of two multi-layers of drift tubes separated by a spacer frame. The drift tube is an aluminium tube filled with a Ar:CO_2 (93:7) gas mixture at 3 bar pressure, and a tungsten-rhenium anode wire. In the inner layer of the MS, each multi-layer consists of four tube layers, while in the middle and outer layers the multi-layers contain three tube layers.

For the innermost layer in the endcaps, in the region $2.0 < |\eta| < 2.7$, cathode-strip chambers (CSCs) are used for precision tracking, which tolerate the higher background rates in this region. CSCs are multi-wire proportional chambers with segmented cathode strip readout.

Relative alignment of the chambers traversed by a muon with an accuracy of around 50 µm is essential for the measurement of the curvature of the muon trajectory and, therefore, for the momentum of the muon. This is achieved by an optical alignment monitoring system. The momentum measurement in the MS is based on track segments reconstructed in at least two of the three muon precision chamber layers.

Trigger Chambers

Fast muon detectors with a time resolution of a few nanoseconds are used to form the Level-1 muon trigger (see Section 3.2.6) in the range $|\eta| < 2.4$. Resistive Plate Chambers

(RPC) are used in the barrel ($|\eta| < 1.05$) and Thin Gap Chambers (TGC) in the endcaps ($1.05 < |\eta| < 2.4$). RPC's and TGC's also measure the azimuthal coordinates of the muon tracks. The RPCs are parallel electrode-plate gas detectors without wires. TGCs are multi-wire proportional chambers filled with a gas mixture of n-pentane and CO_2.

3.2.5 The Magnet System

The magnetic field of the ATLAS superconducting magnet system [297] deflect charged particles in order to measure their momenta. The magnet system (see Fig. 3.8) consists of the central solenoid (CS) for the ID and a system of toroid magnets for the MS.

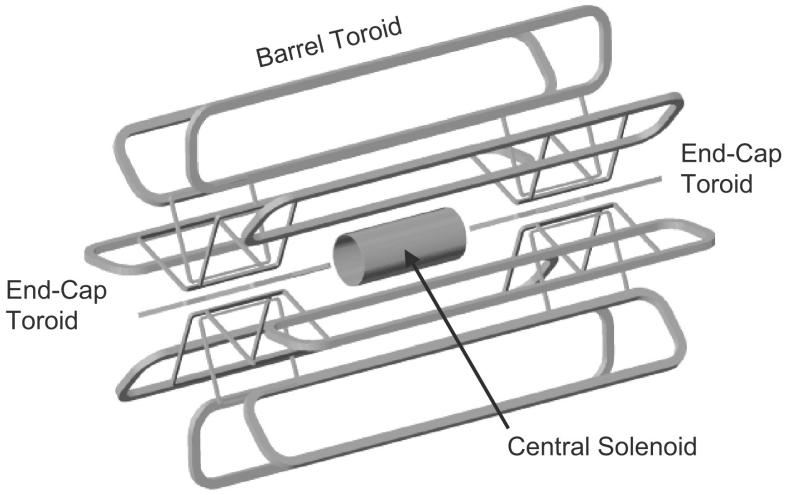

Figure 3.8: Schematic view of the ATLAS magnet system [323].

The CS [323], with a length of 5.3 m and 2.3 m in diameter, is located between the ID and the electromagnetic calorimeter and produces an solenoidal magnetic field of 2 T. The solenoid magnet uses an indirectly cooled aluminum-stabilized NbTi superconducting coil in order to minimise the material thickness in front of the ECAL.
For the barrel and endcap toroid aluminium-stabilised NbTi superconducting coils are used, which are cooled down to 4.5 K using liquid helium. The toroid magnet coils are arranged in eight-fold symmetry around the z-axis. In the barrel, each coil has its own cryostat. In each of the endcaps the eight coils are housed in a single cryostat. The peak toroid fields in barrel and endcaps are 3.9 T and 4.1 T, respectively. The bending power is 2 to 6 T m in the barrel and 4 to 8 T m in the endcaps depending on η.

3.2.6 The Trigger and Data Acquisition System

The LHC bunch crossing rate in 2015, 2016 and 2017 was 25 ns, corresponding to a collision frequency of 40 MHz.The high collision and data rate make it impossible to register every event. A highly selective trigger system is required rejecting efficiently

the overwhelming QCD background.

The schematics of the trigger and data acquisition (TDAQ) system [324] is shown in Fig. 3.9. It consists of a hardware-based Level-1 (L1) trigger and software-based

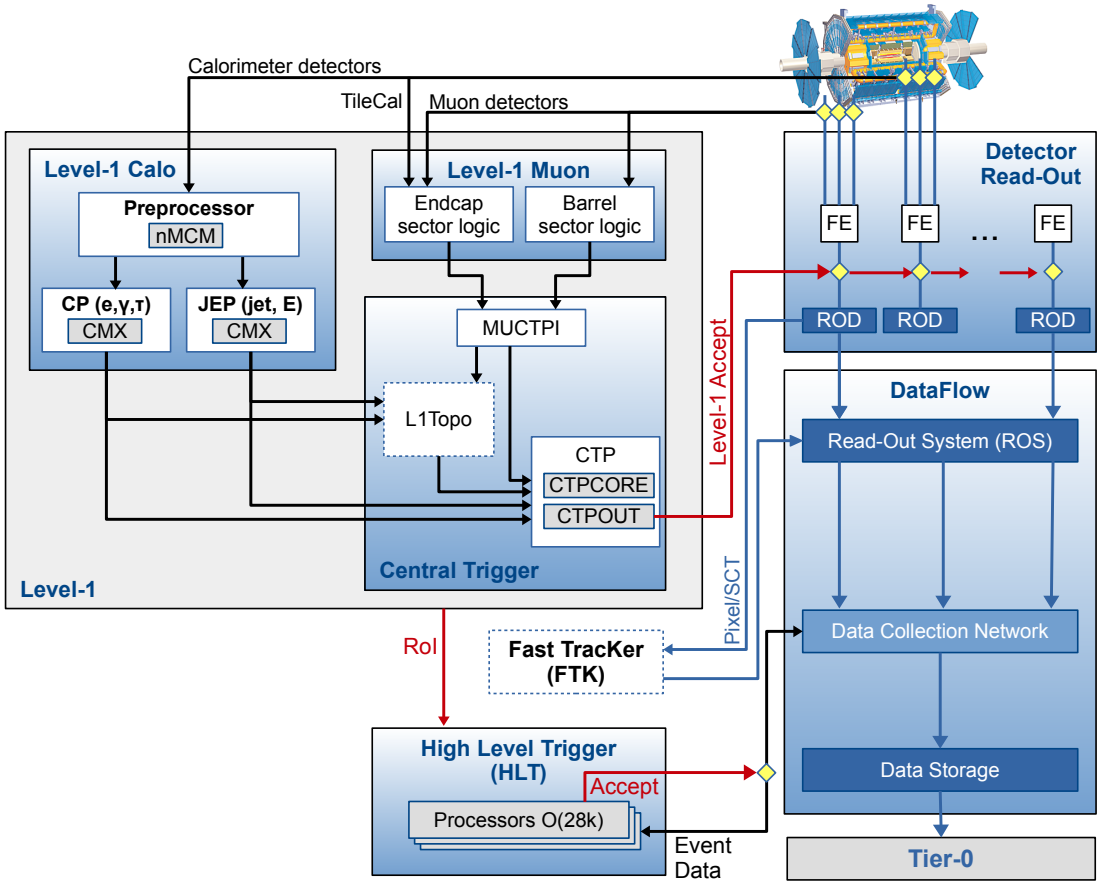

Figure 3.9: The ATLAS Trigger and Data Acquisition (TDAQ) system for Run 2 consists of a hardware-based first-level trigger (Level-1 Calo and Level-1 Muon combined by the Central Trigger) and a software-based high-level trigger (HLT), which reduces the event rate from 40 MHz bunch collision rate to 100 kHz and 1 kHz, respectively [324].

high-level trigger (HLT).

The first decision to readout an event is formed within 2.5 µs by the Central Trigger Processor (CTP), which uses information from the L1 calorimeter (L1 Calo) [325] and L1 muon (L1 Muon) [326] triggers.

The L1 Calo trigger has three sub-systems: the preprocessor system, the Cluster Processor (CP) and the Jet/Energy-sum Processor (JEP). The preprocessor digitises the analogue signals, recorded in the ≈ 7000 trigger towers with a granularity in $\eta \times \phi$ of 0.1×0.1 in the electromagnetic and hadronic calorimeters and applies calibration constants. The CP processor identifies electron, photon and τ lepton candidates above a given E_{T} threshold and satisfying, if required, certain isolation criteria within $|\eta| < 2.5$,

allowing for precise tracking and electromagnetic shower measurement in the HLT. The JEP receives energy sum information from $\eta \times \phi$ cells of size 0.2×0.2 used to identify jets and to determine the total transverse and the missing transverse energy. For the jet triggers, calorimeter information up to $|\eta| = 3.2$ is considered, while for the total and missing transverse energy triggers also the forward calorimeter information up to $|\eta| = 4.9$ is taken into account.
The L1 Muon trigger uses information from three trigger stations of TGCs in the endcaps and RPCs in the barrel region. The trigger algorithms identifies coincidences in the different trigger stations. Both, the L1 Calo and L1 Muon trigger define regions-of-interest used by the software-based HLT algorithms to select interesting physics objects and events, with a further reduced trigger rate of 1 kHz. With this rate, the selected events are stored for the final event reconstruction and analysis using the Worldwide LHC Computing Grid (WLCG).

3.2.7 Luminosity Determination

A precise measurement of the delivered and recorded luminosity is mandatory for precise measurements of Standard Model processes and beyond and to evaluate background contributions to Dark Matter searches.
ATLAS uses two main luminosity detectors, BCM (**B**eam **C**onditions **M**onitor) and LUCID (**LU**minosity measurement using a **C**herenkov **I**ntegrating **D**etector). A detailed description can be found in Ref. [327].
The working principle of the LUCID detector is based on the principle that the detected particle multiplicity is proportional to the number of interactions per bunch crossing [328, 329]. LUCID consists of two identical at each ends of ATLAS at a distance of ± 17 m from the interaction point and at a radius of 10 cm from the beamline corresponding to $|\eta| \approx 5.8$. The detectors consist of twenty aluminium tubes mounted around the beam pipe wich are filled C_4F_{10} gas in which charged particles produce Cherenkov light detected by photo multipliers.
The BCM consists of two sets of four small diamond sensors arranged around the beam pipe in a cross-like pattern on each side of the interaction point at a distance of ± 184 cm. Originally, the BCM was designed for beam monitoring to protect the ID in the case of beam losses by the LHC. Due to its fast readout, the BCM also now provides, like LUCID, a bunch-by-bunch luminosity determination by the measuring the number of inelastic pp interactions per bunch crossing.
Additionally, the ATLAS detector monitors the interaction rate per bunch crossing from which the luminosity can be determined. The measurement is calibrated using dedicated beam-separation scans, so-called *van-der-Meer* scans [330, 331], where the ID measures the number of reconstructed proton-proton interaction vertices (see Section 3.3.1). The

mean of the vertex multiplicity distribution is proportional to the luminosity delivered by the LHC.
The luminosity measurement is recorded typically once per minute corresponding to a so-called *luminosity block* of data. The luminosity blocks are then grouped into *data periods* of uniform detector and triggers configurations Section 3.2.6). The total luminosity is calculated as the sum over all luminosity blocks or of all data taking periods.
The luminosity delivered by the LHC as a function of time is shown in Fig. 3.2b. The total integrated luminosity for the 2015 and 2016 runs has been measured to be 36.1 fb^{-1} with an uncertainty of 3.2 % using van-der-Meer scans [327].

3.3 Reconstruction of Physics Objects

In the mono-Higgs ($b\bar{b}$) search, event level objects like electrons, muons, taus, jets including those with a B-hadron decay and missing transverse energy are reconstructed using the detector information from all sub-detectors of ATLAS (see Section 3.2), based on pp collision data and on Monte-Carlo simulated data.
The Monte-Carlo generated events and the associated particles (see Section 1.4.2) are passed into a simulation of the ATLAS detector [332] based on the `GEANT 4` [53] toolkit. The reconstruction and identification of the physical objects used in the mono-Higgs ($b\bar{b}$) analysis (see Section 4.7) is described in this section.

3.3.1 Track and Vertex Reconstruction

The starting point of the reconstruction of physical objects is the identification of charged particle trajectories recorded in the ID, referred to as *tracks*. The reconstructed tracks are used to identify the primary pp interaction vertex. Only events with a proper reconstructed primary vertex (PV) are considered in the analysis. The PV is particularly important for the identification of B-hadron decays, so-called *b-jets*, produced in the mono-Higgs search by the $h \to b\bar{b}$ decay. In order to identify the Higgs boson decay products, one looks for a secondary vertex inside the B-hadron decay related to the lifetime of the B-hadron. The secondary vertex is also reconstructed within the ID.

Track Reconstruction

A charged particle is bent in the solenoid magnetic field inside the ID and follows a circular trajectory in the transverse plane. The trajectory is parametrised by a set of five parameters, namely the inverse transverse momentum $\frac{q}{p_\text{T}}$ over the particle charge, q, the azimuthal angle ϕ, the polar angle θ, and the transverse and the longitudinal impact parameters, d_0 and z_0 (see Section 3.2.1), respectively.
As the charged particle track reconstruction highly relies on the information of the the

Pixel and SCT detectors, they are only reconstructed in the range $|\eta| < 2.5$. The primary track reconstruction algorithm [333–335] starts from pattern recognition of ID hits with seeding in the inner silicon tracker and performs hit finding towards the outer border of the ID, referred to as the *inside-out* algorithm. Track seeds are built from the hits in the silicon layers within $r \approx 3.5$ to 51 cm. In case of detector hits being in a road window of interest, where additionally other hits are expected, a simplified *Kalman filter* [336, 337] is used for further selection. Detector hits are considered to be part of a track or being rejected, respectively, based on the decision of the Kalman filter, and similar is done for so-called *holes*, where the track traversed a silicon layer without producing an actual hit in the detector material. This procedure results in a collection of several tracks. Track segments can be build by more then one track which share the same hits or holes. Thus, a successive step of resolving these track ambiguities is required that rates the individual tracks by assigning a relative track weight (reward/penalty schema) [333] to each track, depending on the precision of the ID sub-detector. Due to the very large charge particle track density, an additional step is introduced when the pixel clusters are very close to each other. For solving the ambiguity between very close pixel hits to a track, an artificial neural network is trained to identify merged clusters and correctly associate the pixel hits to a track. The surviving track candidates are then extrapolated to search for additional hits in the TRT. The full collection of hits and holes within a certain road corresponding to a track candidate are added iteratively, and the track is refitted every time a new hit or hole is added. The standard track-fit used in ATLAS assumes that tracks come from pions, affecting the fitted momentum through the estimation of their energy loss in the detector.
In order to be sensitive to long-lived particles, e.g. K_S, which do not provide hits in one of the innermost silicon layers, the so-called *outside-in* track finding algorithm is applied. Here, the track finding algorithm is seeded from TRT hits first. In a second step, the algorithm is looking towards the inner part of the ID and selects hits and holes for the final track reconstruction.
Only tracks with $p_{\mathrm{T}} > 500\,\mathrm{MeV}$ are used for the vertex and the object reconstruction.

Primary Vertex Reconstruction

The proper identification of the PV is essential for the reconstruction of the objects in an event and for the understanding of the hard-scattering process in a pp collision, and to discriminate against additional vertices from multiple inelastic pp interactions. The description of the PV reconstruction is fully described in Refs. [338, 339].
For the PV reconstruction, only tracks fulfilling $|d_0| < 4\,\mathrm{mm}$, $\sigma(d_0) < 5\,\mathrm{mm}$ and $\sigma(z_0) < 10\,\mathrm{mm}$, where $\sigma(d_0)$ and $\sigma(z_0)$ are the uncertainties of d_0 and z_0, respectively, are used. The impact parameter requirements are applied to reduce the contamination from tracks,

which originate from secondary pp interactions. Furthermore, the tracks are required to have at least nine silicon hits (at least four of them in the SCT detector) and no holes in the Pixel detector. The reconstruction algorithm consists of two steps, first of the vertex finding, where well reconstructed tracks are matched to a vertex, and second of the vertex fitting step. During the vertex fitting, the actual vertex position closest to the beam spot center is determined. Here, the precise determination of the z-coordinate is very important, since multiple pp interactions are expected along the beam direction. The procedure is repeated until no tracks are left. All vertices with at least two associated tracks are retained as valid PV candidates. The vertex with the largest sum of squared transverse momenta of all of its associated tracks, $\sum p_{\mathrm{T,track}}^2$, is then referred to as the PV in the event.

3.3.2 Muon Reconstruction

Muons produced in pp collisions traverse the full ATLAS detector and leave a detectable signature in all detector parts, without being stopped in the calorimeter. The muon energy deposit in the calorimeter is compatible with the one expected from a minimum ionising particle and is in the range of a few 10 GeV for a muon with $p_{\mathrm{T}} \approx 1\,\mathrm{TeV}$. Muons can be reconstructed independently in the ID and the MS, and, if possible, their information is combined in a later stage to form the full muon track. The combination results in an improved identification efficiency and momentum measurement by exploiting the information of both sub-detectors. Information of the calorimeters is used in the uninstrumented region of the MS ($|\eta| \approx 0$). In the ID, the muon trajectory is reconstructed like any other charged particle track (see Section 3.3.1). In the following, the muon reconstruction in the MS and the combination with ID tracks as well as the reconstruction performance is discussed [312, 340].

The muon reconstruction starts from hits found in the muon chambers. From the hit collection, the tracks are reconstructed by performing a straight-line fit to the hits found in each chamber layer providing six to eight η measurements for a single muon passing the detector within $|\eta| < 2.7$. The trigger chambers (see Section 3.2.4) provide the ϕ coordinate orthogonal to the bending plane.

The ID provides an independent measurement of the muon kinematics close to the interaction point, with very high spatial precision and excellent momentum resolution for muons with $1 < p_{\mathrm{T}} < 100\,\mathrm{GeV}$. The muons can be reconstructed in four different ways depending on the available detector information.

Combined (CB) muons

A combined muon track is reconstructed, if a stand-alone MS track can be successfully associated with an ID track. The hits of independently reconstructed tracks of the ID and

the MS are combined by performing a combined track fit of both. MS hits may be added to or removed from the track to improve the fit quality. The MS dominates the track reconstruction for high-p_{T} muons and the ID for low-p_{T} muons. Information about the track impact parameters are obtained from the measurement of the ID. Possible backgrounds, e.g. from cosmic muons or calorimeter punch-through particles, are efficiently reduced when applying the combination of the ID and MS measurements. Combined muons make up the majority of muons used in ATLAS.

Segment-tagged (ST) muons

Segment tagged muons are similar to CB muons, with the exception that no complete muon track is available in the MS and only one layer of MDT or CSC chambers is traversed, which is possible for low-p_{T} muons or in regions of incomplete MS coverage. The segment tagging starts with an ID track which is extrapolated to at least one chamber of the MS. The muon momentum is measured in the ID and the matched track segments in the MS are used for the muon identification.

Extrapolated (ME) muons

Only detector hits in the MS are used for the muon track reconstruction, and it is required that the muon track can be extrapolated to the interaction point. The track impact parameters z_0 and d_0 are obtained by extrapolating the track back to the interaction point accounting for multiple scattering and energy loss in the calorimeters. Extrapolated muons are mainly used in the region of $2.5 < |\eta| < 2.7$ where the ID is not present. Without the information of the ID, the backgrounds from weak pion and kaon decays are higher.

Calorimeter-tagged (CaloTag) muons

The muon reconstruction is completed by using ID tracks in combination with their energy deposits in the calorimeters, which have to be compatible with the expectation for minimum ionising particles. This method recovers acceptance in the non-instrumented region of the MS mainly at $|\eta| < 0.1$, where ID and calorimeter cables are routed.

Overlaps between the different muon types are resolved before they are used in the analysis. CB muons are always preferred, if they share the same ID track with other muon types, then ST and ME muons, and finally CaloTag muons.

The performance of different muon identification and isolation criteria, as well as the calibration of the muon momenta, is studied based on $3.2\,\mathrm{fb}^{-1}$ of pp collision data recorded in 2015 at $\sqrt{s} = 13\,\mathrm{TeV}$ and is given below.

3.3.2.1 Muon Identification and Isolation

Different muon identification criteria, referred to as a working point (WP), are imposed on muons to reduce backgrounds from non-prompt meson decays. The WPs are optimised to obtain a high muon identification efficiency and a precise measurement of the muon momentum. Two different muon identification WPs are shortly summarised, which are used in the mono-Higgs ($b\bar{b}$) analysis, namely the *Loose* and the *Medium* WP [340]. The muons of both WPs, must satisfy a requirement on the d_0 significance of $|d_0|/\sigma(d_0) < 3$ and of $|\Delta z_0 \sin\theta| < 0.5\,\text{mm}$. The Loose WP is designed to maximise the reconstruction efficiency while having good-quality ID and MS muon tracks. All of the above reconstructed muon types are used within the Loose WP. The ST and CaloTag muons are only used in the region of $|\eta| < 0.1$ to recover efficiency.
More strict quality requirements are applied to muons fulfilling the Medium WP, which is optimised to have a high efficiency and purity while keeping systematic uncertainties at a small level. For the Medium WP, only CB and ME muons are used, while CB muons are required to have at least three hits in at least two MDT layers. In addition, muon tracks with hits in at least one MDT layer but no more than one MDT hole layer are allowed. Furthermore, a requirement on the q/p *significance* is applied, which is the absolute value of the difference between the ratio of the charge and momentum of the muon measured in the ID and MS divided by the sum in quadrature of the corresponding uncertainties. The muons must satisfy $|q/p| < 7$. The requirement on the q/p significance improves the matching of tracks from the ID and the MS, and reduces the hadronic backgrounds where pions and kaons are misidentified as muons.
The resulting reconstruction and identification efficiencies of the Loose and Medium WPs are measured in data and Monte-Carlo simulation from $Z \to \mu\mu$ and $J/\Psi \to \mu\mu$ events by using a so-called *tag-and-probe method* (see Ref. [340]). Here, the *tag muon* is a well-reconstructed and isolated muon, while the *probe muon* can be a CaloTag muon or ME track. The reconstruction and identification efficiency is defined as the fraction of probe to tag muons satisfying the tested criteria. The results of the efficiency measurement are given in Fig. 3.10 and Fig. 3.11 as a function of η and p_T of the muon, respectively. The $J/\Psi \to \mu\mu$ events are used to measure the identification efficiency in the low p_T region of 5 to 20 GeV. The identification efficiency of the Loose and Medium WPs is on average around 98 %, except for the region of $|\eta| < 0.1$.
Prompt muons from W or Z boson decays are usually *isolated*, i.e that no other high-p_T objects are in their vicinity. In contrast, muons from a semileptonic hadron decays, e.g. the decay of a B-mesons via $B \to D^- \mu^+ \nu_\mu$, are embedded inside a hadronic jet, and, therefore, non-isolated. A measure for the muon isolation is related to the activity in the ID or the calorimeter inside a cone with radius parameter, R, around the muon. In the mono-Higgs ($b\bar{b}$) analysis, the muon tracks are required to be isolated. For this, the isola-

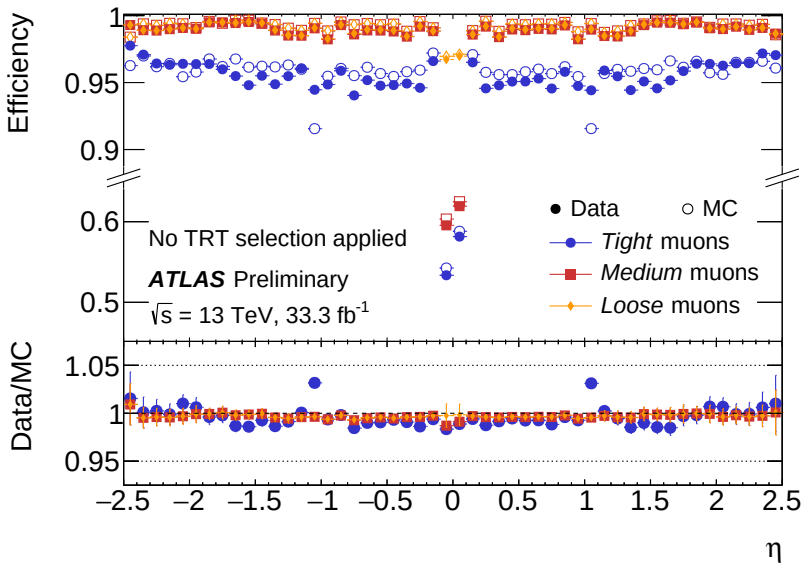

Figure 3.10: Muon reconstruction and identification efficiency in data and Monte-Carlo simulation for the Loose and Medium working points as a function of the pseudorapidity, η, measured in $Z \to \mu\mu$ events for muons with $p_{\mathrm{T}} > 10\,\mathrm{GeV}$. The scale factors, defined as the ratio of the two efficiencies, are shown in the lower panel together with the statistical and systematic uncertainties [34l].

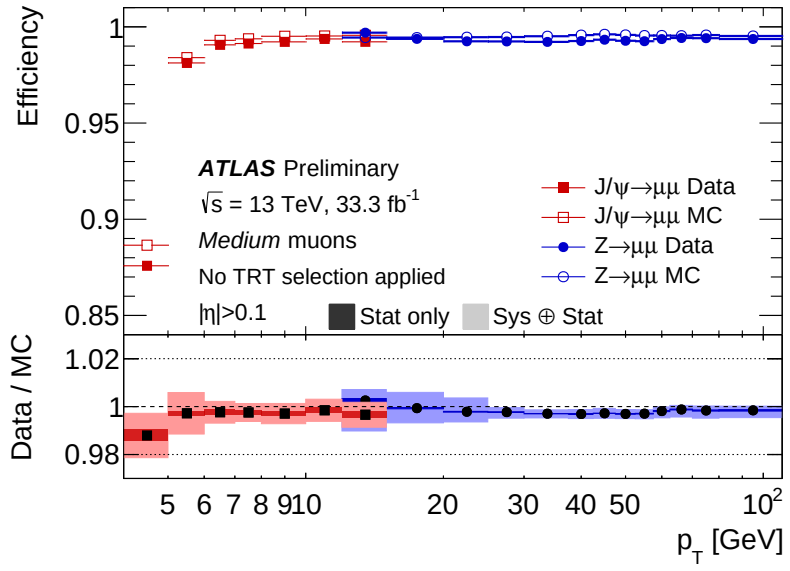

Figure 3.11: Muon reconstruction and identification efficiency in data and Monte-Carlo simulation for the Medium working point as a function of transverse momentum, p_{T}, measured in $J/\Psi \to \mu\mu$ ($5 < p_{\mathrm{T}} < 20\,\mathrm{GeV}$) and $Z \to \mu\mu$ ($20 < p_{\mathrm{T}} < 100\,\mathrm{GeV}$) events. The scale factors, defined as the ratio of the two efficiencies, are shown in the lower panel together with the statistical and systematic uncertainties [34l].

tion variable $p_{\mathrm{T}}^{\mathrm{varcone30}}/p_{\mathrm{T}}^{\mathrm{muon}}$ is defined, where $p_{\mathrm{T}}^{\mathrm{varcone30}}$ is the scalar sum of all tracks with transverse momenta above 1 GeV in a cone of size $\Delta R = \min(10\,\mathrm{GeV}\,/\,p_{\mathrm{T}}^{\mathrm{muon}},\, 0.3)$ around the muon (the muon track itself is excluded) and $p_{\mathrm{T}}^{\mathrm{muon}}$ is the muon momentum. Two muon isolation WPs are used, namely the *LooseTrackOnly* WP, where the requirement on the isolation variable is chosen such that a flat efficiency of 99 % is reached, and the *FixedCutTight* WP with the requirement of $p_{\mathrm{T}}^{\mathrm{varcone30}}/p_{\mathrm{T}}^{\mathrm{muon}} < 0.06$.
The efficiencies of the single-muon triggers in data and Monte-Carlo simulation are measured as well by selecting $Z \to \mu\mu$ events and found to be above 99 % [340] as indicated in Eq. (3.5).
From the derived efficiencies in data and Monte-Carlo simulation so-called *scale factors* (SFs), $\epsilon^{\mathrm{data}}/\epsilon^{\mathrm{MC}}$, are derived which are applied to Monte-Carlo simulation to account for the differences between data and Monte-Carlo simulation. The total SF accounting for the muon identification, isolation and trigger efficiencies is given by :

$$\mathrm{SF} = \frac{\epsilon^{\mathrm{data}}_{\mathrm{identification}}}{\epsilon^{\mathrm{MC}}_{\mathrm{identification}}} \times \frac{\epsilon^{\mathrm{data}}_{\mathrm{isolation}}}{\epsilon^{\mathrm{MC}}_{\mathrm{isolation}}} \times \frac{\epsilon^{\mathrm{data}}_{\mathrm{trigger}}}{\epsilon^{\mathrm{MC}}_{\mathrm{trigger}}} \quad . \tag{3.5}$$

The uncertainties on the SF range between 0.1 to 0.7 % depending on the muon p_{T}. The efficiencies in the high-η region are on average around 90 % with slightly increased systematic uncertainties on the SF compared to the region of $|\eta| < 2.5$.

3.3.2.2 Muon Momentum Calibration

The muon momentum resolution and scale is studied by selecting dimuon events from J/Ψ and Z decays, such that the scale and resolution is measured precisely with the use of a well known resonance. For this purpose, templates from Monte-Carlo simulated events of the invariant dimuon mass, $m_{\mu\mu}^{\mathrm{ID}}$ and $m_{\mu\mu}^{\mathrm{MS}}$, are built as inputs for a fit to data in different bins of p_{T} and η. Corrections from this fit are extracted to match the simulation to the data. The invariant dimuon mass spectrum and the mass resolution are shown in Fig. 3.12 for $Z \to \mu\mu$ events as a function of η of the muon with highest p_{T}. The uncertainties on the muon momentum scale are of the order of 0.2 % and the dimuon mass resolution is about 5 % for small values of η and slightly larger in the endcaps.

3.3.3 Electron Reconstruction

Electrons are reconstructed only in the central region $|\eta| < 2.47$ by using information of the ID and the ECAL. The electron reconstruction and identification is challenging as hadronic jets (see Section 3.3.4) can produce similar signatures in the detector. Secondary electron processes, i.e. electrons from photon conversions, must also be separated from prompt electrons. The procedure of the electron reconstruction as well as the electron

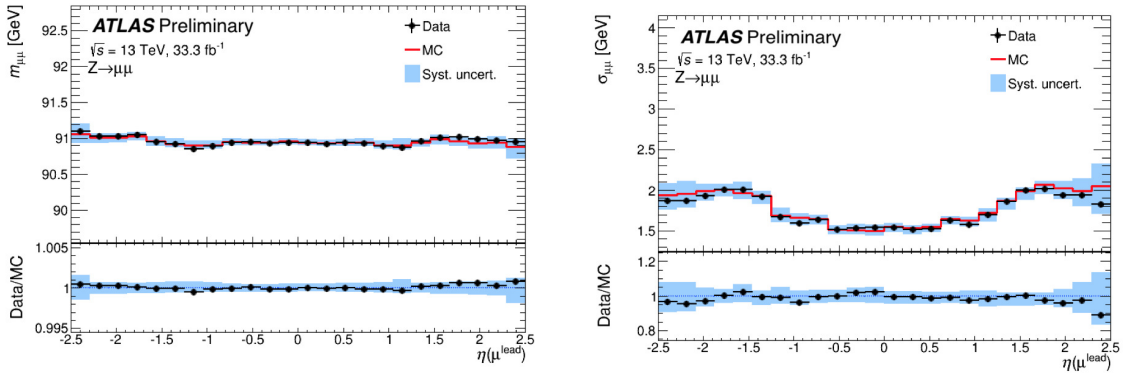

(a) (b)

Figure 3.12: In (a) the dimuon invariant mass distribution and in (b) the corresponding mass resolution for $Z \to \mu\mu$ events as a function of η of the muon with highest p_{T}. The band represents the effect of the systematic uncertainties on the Monte-Carlo momentum corrections. The lower panels show the data to Monte-Carlo ratios [340].

energy calibration is described in more detail in Refs. [342, 343].
Electrons are reconstructed from LAr EM calorimeter cells, where they deposit all of their energy by producing electromagnetic showers, matched to ID tracks. The so-called *sliding window* algorithm [344] is used to find cell seeds with a total cluster transverse energy above 2.5 GeV. The window size is 3×5 in units of $\Delta\eta \times \Delta\phi = 0.025 \times 0.025$, which corresponds to the granularity of the EM middle layer. The selected cells are used to build a cluster, which provide a first estimate of the electron candidate kinematics. ID tracks associated to the primary vertex are matched to the calorimeter cluster, if the longitudinal and transverse shower profile in the EM calorimeter is compatible withe the one expected for electromagnetic showers. The tracks matched to an energy cluster are refitted by applying a *Gaussian-sum filter* [345] which accounts for the electron energy loss from bremsstrahlung produced on their way through the ID. The electron energy is then recomputed from 3×7 (3×7) longitudinal towers in the barrel (endcaps) of the EM calorimeter. Corrections are applied for cases where the EM shower is not fully contained in the calorimeter.
The electron energy is taken from the measurement of the calibrated calorimeter cluster, while the η and ϕ coordinates and the impact parameters are taken from the best fitted track assigned to the cluster. An electron must satisfy requirements on the impact parameters of $|d_0|/\sigma(d_0) < 5$ and $\Delta|z_0 \sin\theta| < 0.5\,\mathrm{mm}$.

3.3.3.1 Electron Identification and Isolation

For separating prompt electrons, i.e. produced in $Z \to ee$ decays, from background objects like hadronic jets and electrons from converted photons electron identification

requirements are applied. In the mono-Higgs ($b\bar{b}$) analysis, the so-called *LooseLLHBLayer* WP is used, which is based on the *LooseLLH* identification criteria, requiring an extra hit in the IBL. This greatly improves the precision in the determination of the impact parameters d_0 and z_0. The underlaying identification algorithm is based on a likelihood-based (LH) method, where signal and background probability density functions are build from the output of a multivariate analysis (MVA) (see Ref. [342]). The MVA separates signal from background electrons by using shower shape information as input variables. The electron reconstruction and identification efficiency is measured in data and Monte-Carlo simulation from $J/\Psi \to ee$ and $Z \to ee$ events by applying a tag-and-probe method. Corresponding scale factors are derived from the ratio of the efficiencies, $\epsilon^{\text{data}}/\epsilon^{\text{MC}}$, similar to Eq. (3.5). The results of the electron efficiency measurements are shown in Fig. 3.13 as a function of the transverse energy and the pseudorapidity of the electron. The most inclusive electron sample, selected by the LooseLLH WP, provides the highest efficiency above 85 %. Scale factors depending on η and p_{T} are applied to Monte-Carlo simulation to match the observed data.
Additional electron isolation criteria are applied to further reduce the contribution of background electrons from hadronic decays. The electrons are required to be track isolated with a variable-cone isolation variable $p_{\text{T}}^{\text{varcone20}}$, defined as the sum of p_{T} of ID tracks within a cone of $\Delta R = \min(10\,\text{GeV} / E_{\text{T}}^{\text{electron}}, 0.2)$ around the electron track, which itself is not included in the calculation. A requirement on the ratio $p_{\text{T}}^{\text{varcone20}} / E_{\text{T}}^{\text{electron}}$ is applied resulting in an flat isolation efficiency of around 99 % for electrons from Z boson decays. In addition to the isolation correction factors, the single-electron trigger inefficiency is also corrected and measured from $Z \to ee$ events. The isolation and the trigger efficiencies corrections are both close to one with uncertainties below 2 % (see Ref. [342]).

3.3.3.2 Electron Energy Calibration

The electron energy scale and resolution in Monte-Carlo simulation is calibrated to match the observed electron kinematics in data. First, a purely Monte-Carlo based correction is applied to account for the non-uniformity of the detector response and for the energy loss in the material upstream of the calorimeter. In the next step, an in-situ procedure is applied, where the electron energy miscalibration between data and Monte-Carlo simulation is parametrised.
The corrections are validated by selecting dielectron pairs in $J/\Psi \to ee$ and $Z \to ee$ events in data and Monte-Carlo simulation. The uncertainties on the electron energy scale are less than one per mill in the barrel and a few per mill in the endcaps (see Ref. [347]).

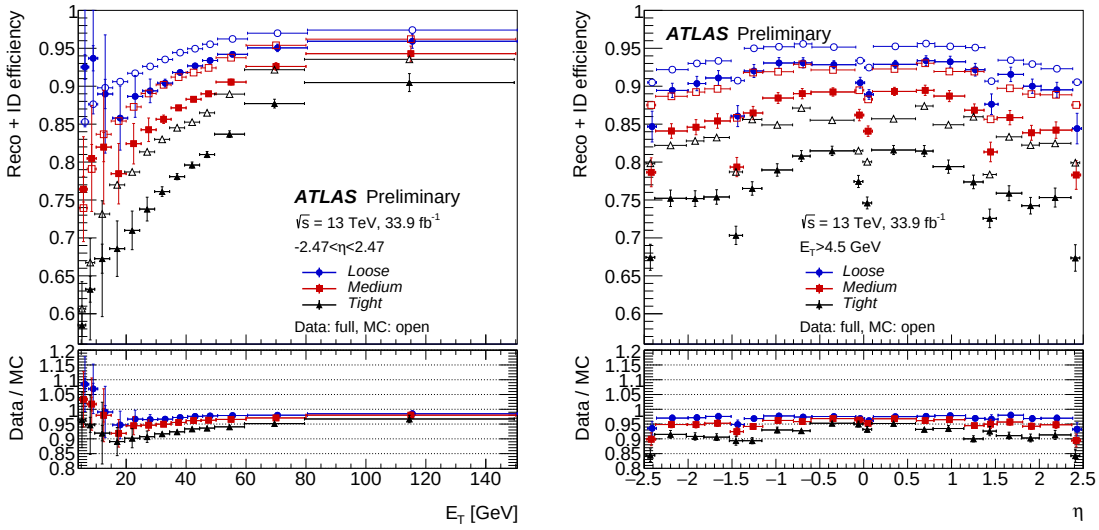

Figure 3.13: Electron reconstruction and identification efficiencies as a function of (a) the electron transverse energy, E_{T}, and (b) the pseudorapidity, η, for $Z \to ee$ events in data and Monte-Carlo simulation [342, 346]. The scale factors in the lower panel are defined as the ratio of the two efficiencies.

3.3.4 Jet Reconstruction and Energy Calibration

Partons, like quarks and gluons, hadronise to colour singlet objects, which form in the subsequent decays a directional and collimated bunch (or spray) of hadrons, referred to as *jets*. Jets are the objects used to identify the products of the Higgs boson decay, $h \to b\bar{b}$, produced in association with Dark Matter particles.

Z'-2HDM signal events can result in two different topologies, depending on the boost of the Higgs boson. The large mass splitting between the Higgs boson and its decay products implies that the Higgs boson can be produced with a large p_{T} resulting in very collimated b quarks. Depending on the transverse momentum of the Higgs boson, $p_{\mathrm{T}}^{\mathrm{Higgs}}$, different Higgs boson identification techniques are applied to efficiently reconstruct its decay products. The angular separation, $\Delta R(b, \bar{b})$, of the two b quarks is approximated by

$$\Delta R(b, \bar{b}) \approx \frac{2m_h}{p_{\mathrm{T}}^{\mathrm{Higgs}}} \quad , \tag{3.6}$$

with $m_h = 125\,\mathrm{GeV}$ [36] the Higgs boson mass. In Eq. (3.6), the two b quarks are assumed to share equally the energy of the Higgs boson, which is true at leading-order without additional gluon emission [348]. For large values of $p_{\mathrm{T}}^{\mathrm{Higgs}}$, the two b quarks become collimated, such that they cannot be well separated anymore inside the calorimeter and overlap. In such a boosted event topology, the Higgs boson is reconstructed as one

single jet with a large radius parameter, R, referred to as large-R jet and for low to intermediate $p_{\mathrm{T}}^{\mathrm{Higgs}}$ below 500 GeV, the Higgs boson decay products are reconstructed as two well separated jets with a small radius parameter (small-R jets) (see Section 3.3.4.1 and Section 3.3.4.2, respectively).

In general, there exist no unique way to reconstruct a jet. A jet is defined by the choice of the *clustering algorithm* and can either be formed from the calorimeter clusters, the ID tracks or from the truth hadrons in Monte-Carlo simulation. A truth jet can be build by taking all truth particles, except for neutrinos, muons and non-interacting particles, within a cone of given size. Sequential jet finders search for the smallest distance d_{ij} or d_{iB} between two clusters i and j or between any cluster i and the beam axis, B, respectively. The two variables d_{ij} and d_{iB} are given by

$$\begin{aligned} d_{ij} &= \min(k_{t,i}^{2p}, k_{t,j}^{2p}) \cdot \frac{\Delta R_{ij}^2}{R^2} \quad \text{and} \\ d_{iB} &= k_{t,i}^{2p} \quad , \end{aligned} \tag{3.7}$$

respectively, with ΔR_{ij}^2 the angular separation of the two clusters i and j (see Eq. (3.4)), R the fixed cone size parameter of the jet and $k_{t,i}$ the transverse momentum of the i-th calorimeter cluster. If the smallest distance d_{ij} is found, the two constituents are recombined, and if d_{iB} is the smallest distance, then the constituent i is considered as a jet and removed from the collection of constituents. The procedure is repeated until no more clusters are found in the collection. In case of two close by and overlapping jets, the one with highest p_{T} will be kept while the contribution of the softer one will be removed.

In Eq. (3.7), the parameter p is of special importance and defines the relative power of the jet energy versus the geometrical scale. For $p = -1$, the algorithm is the so-called anti-k_t algorithm [349], which is primarily used for the reconstruction jets within the ATLAS experiment. The anti-k_t algorithm is a collinear and infrared safe algorithm, making it only minimal sensitive to additional radiation from the underlying event or pile-up. Usually, the anti-k_t algorithm starts from the hardest to the softest constituents and the results are circular jets.

Both types of jets, small-R jets and large-R jets, are build by applying the anti-k_t algorithm. The jet energy calibration, required to precisely determine the jet kinematics and the energy and mass scale and resolution, is described in the following (based on Refs. [350, 351]).

3.3.4.1 Small-Radius Jets

The standard calorimeter jets used within the ATLAS experiment and also one of the primary sort of jets used in the mono-Higgs ($b\bar{b}$) search are small-R jets. The small-R jets are reconstructed using the anti-k_t algorithm with a cone parameter of $R = 0.4$. The algorithm is implemented in the FASTJET [352, 353] software package. Here, the four-momentum scheme is used, where the final jet four-momentum is defined as the sum of the four-momenta of all its constituents. The jets are reconstructed from the energy deposit of massless* three-dimensional topological connected calorimeter clusters, so-called *topo-clusters* [354].

In the topo-cluster formation step, only calorimeter cells with a positive energy above a certain noise threshold are used. The value of the threshold is chosen to what is expected from noise of electronics or pile-up. Each of the calorimeter cells energy is calibrated at the electromagnetic (EM) scale, which is the energy scale produced by particles in an electromagnetic shower, i.e. from $\pi^0 \to \gamma\gamma$ decays.

The jets are then build from the EM calibrated topo-clusters. The energy calibration procedure of small-R jets is based on the corrections derived from Monte-Carlo simulation to match the observed jet energy scale and resolution in data. For example, the precise determination of the jet energy scale (JES) is important, which can be biased if a substantial fraction of hadronic shower energy is not correctly measured or modelled in Monte-Carlo simulated events. In particular, most of the energy is stored as nuclear binding energy of hadrons or is not measured at all due to leaving neutrinos or inactive detector material, such that the jet energy might be different between data and Monte-Carlo simulation. Such effects are hard to model simulation and related corrections are derived in a data-driven approach to correct the Monte-Carlo simulation.

The first step of the jet calibration is to correct the jet four-momentum vector to point into the direction of the hard-scattering PV instead of the center of the ATLAS detector. Here, the jet energy is kept constant, which improves the η resolution of the jet. Afterwards, a pile-up subtraction technique is applied, which corrects the jet four-momentum and the jet shape by an event-by-event basis for additional energy deposition from pile-up contributions. The pile-up corrections depend on the η and ϕ coordinates of the reconstructed jet and on the measured number of primary pp vertices and the mean number of pp interactions per bunch crossing [355].

The absolute JES is determined from Monte-Carlo simulation after applying the pile-up corrections. For this procedure, the jet energy at parton-level, E^{truth}, is compared to the

*The massless particle hypothesis is motivated as there is no appropriate and meaningful cluster mass definition without knowing the origin of the cluster signal. Such that a particle identification of the associated detector signal would be required, which is related to the determination of the particle charge [354] in the ID. This is only done for the identification of hadronic τ and B-hadron decays.

reconstructed jet energy from calorimeter clusters, E^{reco}, while it is assumed that the reconstructed jet can be matched to its counterpart at parton-level. For the calibration, a so-called jet energy response distribution, $R = E^{\text{reco}}/E^{\text{truth}}$, is defined as a function of η and E^{truth} of the jet. The η dependence accounts for biases in the JES related to gaps and transition regions of the calorimeters, where the detector material changes resulting in slightly varying energy resolutions. At the end, each response distribution is fitted by a Gaussian function, which allows to derive correction factors for the energy of the reconstructed jets in Monte-Carlo simulation. This procedure is the so-called EM+JES calibration.
In order to account for residual dependencies of the JES on longitudinal and transverse features of the jet and to improve the energy resolution, an additional calibration step is performed, the so-called *Global Sequential Calibration* (GSC) [356]. The GSC accounts for punch-through jets, which are very high-p_{T} jets that are not fully contained in the calorimeters, resulting in large tails in the jet energy response. In addition, the jet composition and shower shape varies depending on the initiating particles, most notably is the difference between quark- and gluon-initiated jets. The GSC procedure optimises the resolution of the JES response based on observables sensitive to the jet shower shapes. The GSC corrections are applied to jets in Monte-Carlo simulation for different regions of η and as a function of the parton-level jet momentum.
The last step of the JES calibration accounts for differences of the jet response between data and Monte-Carlo simulation referred to as *in-situ* calibrations. The differences can originating from imperfect detector descriptions, the simulation of the hard scattering process and the modelling of electromagnetic and hadronic interactions with the detector material. In order to quantify the difference of the JES in data and Monte-Carlo simulation, are performed. Differences in the jet response between data and Monte-Carlo simulation are studied by selecting events where a high-p_{T} jet balances against a well-measured reference object. The first in-situ calibration corrects for the relative difference in the jet response of jets in the forward region of $0.8 < |\eta| < 4.5$ to that of well-measured jets in the central region of $|\eta| < 0.8$ by using dijet events, where the two jets balance each other in transverse plane, such that the η dependence can be probed in a data-driven way. The η-intercalibration corrects only the relative JES of forward jets, while jets in the central region act only as a reference object without calibrating their energies. Hence, every additional correction derived in the next steps based on the jets in the central region is also applicable the jets in the forward region. An in-situ calibration of central jets with a p_{T} of up to 950 GeV is performed by selecting Z/γ+jets events. In such events, the highest-p_{T} jet recoils against a high energetic Z boson with $Z \to ee/\mu\mu$ decays or against a photon. The Z+jet calibration is statistically limited to jets with $20 < p_{\text{T}} < 500$ GeV, while the γ+jet calibration covers the range of

$36 < p_{\mathrm{T}} < 950\,\mathrm{GeV}$. The lower bound in the γ+jet calibration is related to the photon trigger threshold. The high-p_{T} jet region of $300 < p_{\mathrm{T}} < 2000\,\mathrm{GeV}$ is covered by selecting multijet events. Final states with two or more jets are used to balance against a single high-p_{T} jet by building a a recoil-system composed of the two or more low-p_{T} jets. The highest-p_{T} jet must satisfy $|\eta| < 1.2$. All other subleading jets are combined into a recoil-system with a resulting four-momentum vector. More details on the in-situ calibration techniques and their combinations are given in in [351]. The corrections are calculated by defining a double ratio, $\mathcal{R}^{\mathrm{data/MC}}_{\mathrm{jet/ref}} = (p^{\mathrm{jet}}_{\mathrm{T}}/p^{\mathrm{ref}}_{\mathrm{T}})_{\mathrm{data}}/(p^{\mathrm{jet}}_{\mathrm{T}}/p^{\mathrm{ref}}_{\mathrm{T}})_{\mathrm{MC}}$, of the measured jet responses in data and in Monte-Carlo simulation, where $p^{\mathrm{ref}}_{\mathrm{T}}$ is the p_{T} of the reference object, i.e. either of the Z/γ boson or a jet system. The results of the in-situ corrections are shown in Fig. 3.14. The combined in-situ corrections are of the order of 4 % for low-p_{T} jets and decreases to approximately 2 % for $p_{\mathrm{T}} = 2\,\mathrm{TeV}$. The corrections decrease with increasing jet p_{T} as the multijet calibration dominates in the high-p_{T} region which provides the highest event statistics. Furthermore, in the low-p_{T} region the systematic uncertainties are larger. The total systematic uncertainty on the JES and its main components are shown in Fig. 3.15 as a function of the jet p_{T}. The

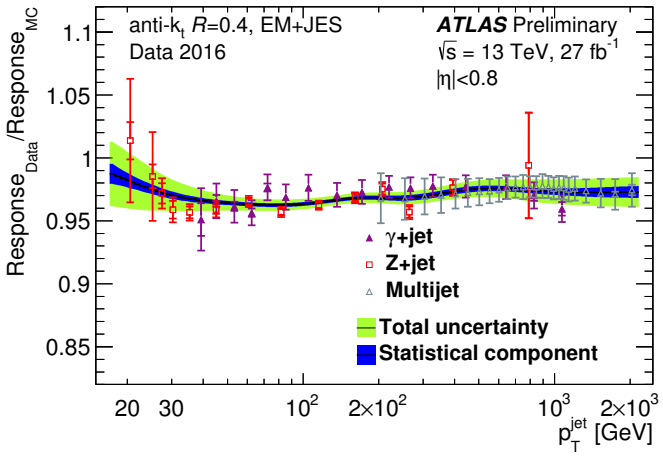

Figure 3.14: The jet response double ratio $\mathcal{R}_{\mathrm{data}}/\mathcal{R}^{\mathrm{MC}}$ as a function of the jet p_{T}, after the EM+JES calibration for the *in-situ* combinations of the Z-jet, γ-jet and multijet calibration techniques. The derived correction (black line) and its statistical (dark blue) and total (light green) uncertainty bands are also shown [357]. The inverse of the combined data-to-Monte-Carlo ratio is taken as the in-situ correction applied to data.

uncertainties shown in Fig. 3.15a for jets with $|\eta| = 0$ are largest at low jet p_{T} starting at 4.5 % and decreases to 1 % at 200 GeV, which then slightly increase due to the statistical uncertainties related to the in-situ calibrations. In comparisons, the uncertainties on the JES as a function of η for $p_{\mathrm{T}} = 60\,\mathrm{GeV}$ in Fig. 3.15b are fairly constant and are at most of the order of 3 %. In both cases, the leading components to the total systematic uncertainty are due to the absolute and relative in-situ calibrations. The corrections

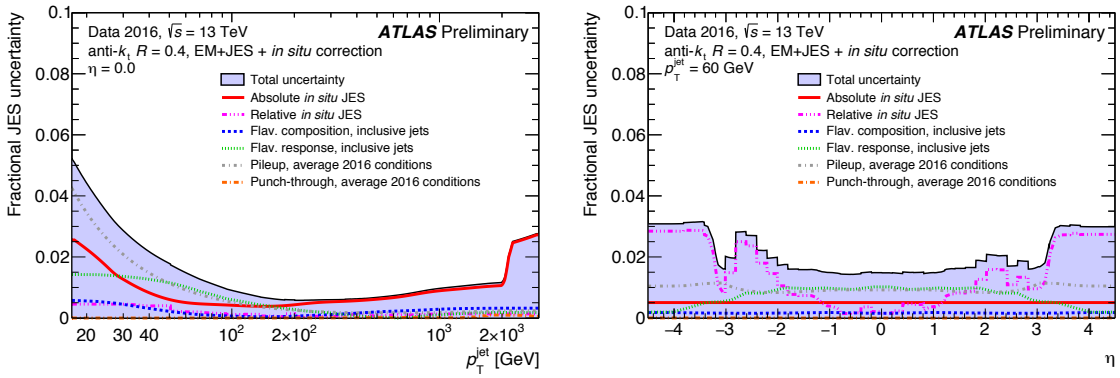

Figure 3.15: Combined uncertainty on the jet energy scale of fully calibrated small-R jets as a function of (a) the p_{T} (with $\eta = 0$) and of (b) the η (with $p_{\mathrm{T}} = 60\,\mathrm{GeV}$). Different systematic sources are also shown, accounting for the effect of pile-up interactions, punch-through jets, the flavour composition of quark and gluons jets and the related difference in their shower shapes, as well as due to the absolute (Z/γ+jets and multijet calibration) and relative (η-intercalibration) in-situ JES calibration [357].

derived from the residual in-situ calibrations are applied only to the data.
In addition to the jet energy scale, the jet energy resolution (JER) found in Monte-Carlo simulation is corrected as well. Besides the impact of the JER on jets, it also impacts the performance of the reconstruction of missing transverse energy (see Section 3.3.7). Similarly to the determination of the JES, the JER is determined by exploiting the transverse momentum balance in dijet events. Uncertainties on the JER of small-R jets are of the order of 1 % for jets with $p_{\mathrm{T}} > 100\,\mathrm{GeV}$ and less than 3 % for $p_{\mathrm{T}} < 100\,\mathrm{GeV}$ [358, 359].

3.3.4.2 Large-Radius Jets

For a Higgs boson with $p_{\mathrm{T}} > 500\,\mathrm{GeV}$, the $h \to b\bar{b}$ decay products can not be reconstructed as two well separated small-R jets anymore and instead they are reconstructed as a single jet with a large radius parameter, a so-called large-R jet. In addition, the usage of large-R jets with underlying jet substructure allows to efficiently reject Standard Model background processes, where often only objects with lower p_{T} are produced. The leading large-R jet, i.e. the one with highest p_{T} in the event, is referred to as the Higgs boson candidate. In particular, the mass of Higgs boson candidate is the one of the leading large-R jet. The identification of the two heavy-flavour jets is done by using so-called *track-jets* (see Section 3.3.4.3).
Large-R jets are reconstructed from topological calorimeter clusters with the anti-k_t algorithm with a radius parameter of $R = 1.0$. The topo-clusters are calibrated using the local cell weighting (LCW) [360–362] scheme, which is different to small-R jets calibrated

to the EM scale. The LCW approach, performs the calibration at the hadronic scale and the cluster energies are corrected for energies not measured in the calorimeters. Such unmeasured energies can arise from nuclear reactions, an energy loss in dead detector material or from the usage of noise thresholds such that energies below the threshold are not measured. In the LCW approach, the measured energy density within a certain volume of cells is classified as mainly an electromagnetic or as a hadronic shower depending on the found cluster shower shape. In accordance to the shower shape, the energy corrections are locally applied to each topo-cluster. This approach results in an improved jet energy resolution compared to small-R jets calibrated to the EM scale, which is especially important when using jets with a larger cone size, and, therefore, since more hadronic activity is contained in the larger volume.
The large-R jet reconstruction is affected by additional hadronic activity provided by pile-up interactions, underlying event and initial state radiation, which are biasing the jet mass scale and resolution. In order to reduce the effect of such biases, a grooming technique [363] is applied to large-R jets to subtract additional calorimeter energy not originating from the hard-scattering process. Large-R jets are groomed by using a so-called *trimming procedure* [364]. Here, all large-R jet constituents are reclustered from the constituents of smaller jets build from the k_T algorithm [365] with a radius parameter of $R_{\text{sub}} = 0.2$. This results in a collection of sub-jets for each large-R jet. The sub-jets must fulfil the requirement of $p_{\text{T}}^{\text{sub-jet}}/p_{\text{T}}^{\text{large}-R\text{ jet}} > 5\,\%$, where $p_{\text{T}}^{\text{sub-jet}}$ is the transverse momentum of the sub-jet and $p_{\text{T}}^{\text{large}-R\text{jet}}$ of the large-R jet. Otherwise, the sub-jet is removed and the final four-momentum of the large-R jet is calculated from the sum of the four-momenta of the remaining sub-jets.
Similarly as for small-R jets (see Section 3.3.4.1), the JER and JES of large-R jets is calibrated by using objects with known energy scale which recoil against the large-R jet. The JER is measured from dijet events, while for the determination of the JES γ+jet [366] and multijet [367] events are selected in data and Monte-Carlo simulation. The two measured response functions are compared to each other. Improved precision of the JES can be achieved by additionally measuring the large-R jet p_{T} in the ID and combining the measurement with the one from the calorimeter [368]. The method ensures high precision even in the high-p_{T} region of 1 to 3 TeV. The results of the JES calibrations are given in Fig. 3.16 as a function of the large-R jet p_{T}. Total uncertainty on the JES of large-R jets approaches 1% for a jet with a p_{T} below 1 TeV, where the γ-jet calibration dominates. For large values of p_{T} up to 2.4 TeV, the systematic uncertainties steadily growth up to 3 %. The systematic uncertainties increase with increasing jet p_{T} as the event statistics significantly decrease.

The large-R jet mass is of major interest for the identification of the Higgs boson

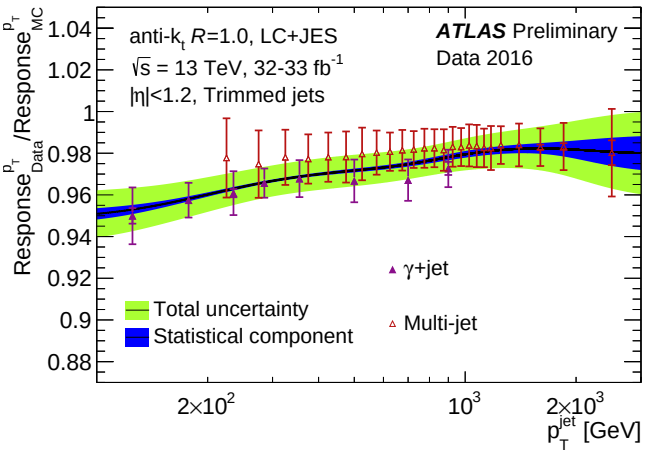

Figure 3.16: The jet response double ratio $\mathcal{R}_{\text{data}}/\mathcal{R}^{\text{MC}}$ as a function of the large-R jet p_{T} showing the final results of the LCW+JES calibration with the *in-situ* combination of the γ-jet and multijet calibration techniques. The derived correction (black line) and its statistical (dark blue) and total (light green) uncertainty bands are also shown [368]. The inverse of the combined data-to-Monte-Carlo ratio is taken as the in-situ correction applied to data. The results apply to trimmed anti-k_t jets with $R = 1$.

candidate, allowing to distinguish a potential signal from a flat background mass distribution. Thus, the large-R jet *mass resolution* (JMR) and *mass scale* (JMS) must be known precisely. The calorimeter-based large-R jet mass

$$m^{\text{calo}} = \sqrt{\left(\sum_{i\in J} E_i\right)^2 - \left(\sum_{i\in J} \vec{p}_i\right)^2} \quad . \tag{3.8}$$

is calculated purely from the energy of calorimeter constituents i associated to the jet, J, with energy $E_i = |\vec{p}_i|$ and momentum $\vec{p}_i$. The precision of the large-R jet mass determination and its associated uncertainties can be improved by combining information of the ID and the calorimeters. For highly boost Higgs boson, the angular separation of the two b quarks is of the same magnitude as the calorimeter granularity. Since the ID provides a better angular resolution compared to the calorimeters, a so-called *track-assisted jet mass*, m^{TA}, is introduced which is given by

$$m^{\text{TA}} = \frac{p_{\text{T}}^{\text{calo}}}{p_{\text{T}}^{\text{track}}} m^{\text{track}} \quad , \tag{3.9}$$

with $p_{\text{T}}^{\text{calo}}$ the transverse momentum of the large-R jet measured in the calorimeters, $p_{\text{T}}^{\text{track}}$ the transverse momentum of the four-momenta sum of all tracks associated with the large-R jet and m^{track} the invariant mass of the four-vector sum of all tracks. The ratio $\frac{p_{\text{T}}^{\text{calo}}}{p_{\text{T}}^{\text{track}}}$ corrects for the fraction of charged to neutral particles associated to a large-R

jet, as the neutral component of the jet is missed by the ID.
A redefined large-R jet mass, the so-called *combined mass*, is obtained as a weighted sum of the calorimeter and the track-assisted jet mass and is given by

$$\begin{aligned} m^{\text{comb}} &= w_{\text{calo}} \cdot m^{\text{calo}} + w_{\text{TA}} \cdot m^{\text{TA}} \quad \text{with} \\ w_{\text{calo}} &= \frac{\sigma_{\text{calo}}^{-2}}{\sigma_{\text{calo}}^{-2} + \sigma_{\text{TA}}^{-2}} \quad \text{and} \quad w_{\text{TA}} = \frac{\sigma_{\text{TA}}^{-2}}{\sigma_{\text{calo}}^{-2} + \sigma_{\text{TA}}^{-2}} \quad , \end{aligned} \tag{3.10}$$

with σ_{calo} the expected calorimeter-based jet mass resolution and σ_{TA} the track-assisted mass resolution. Both resolutions are measured from the jet mass response functions in dijet events [369]. The resolution of the combined mass is always better then either of the two inputs, and the weights are constraint by $w_{\text{calo}} + w_{\text{TA}} = 1$. Figure 3.17 shows the expected improvement in the large-R jet mass resolution* as a function of the truth large-R jet p_{T} reconstructed from hadronically decaying W and Z bosons. The calorimeter-

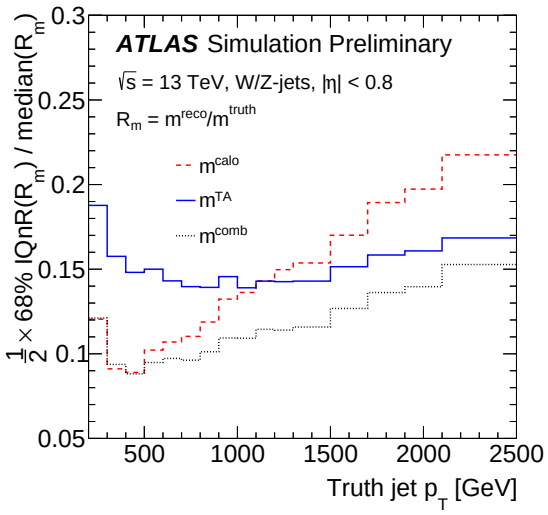

Figure 3.17: The resolution of the jet mass response as a function of truth jet p_{T} for jets from hadronic W and Z boson decays for the calorimeter-based (red dashed line), the track-assisted (blue solid line) and the combined (black dotted line) jet mass. The half of the 69 % interquantile range (IQnR) divided by the median of the jet mass response, $R_m = m^{\text{reco}}/m^{\text{truth}}$, is used as a measure of the jet mass resolution [369], where m^{reco} is the reconstructed jet mass at detector level and m^{truth} of the associated jet at parton-level.

based jet mass resolution degrades at high jet p_{T}, due to the poorer granularity of the calorimeter. In contrast, the track-assisted mass resolution is mostly flat over the whole p_{T} range. The combined mass definition provides the best jet mass resolution over the

*The jet mass resolution is defined as the half of the 68 % interquantile range (IQnR) divided by the median of the response function being a robust definition against outliers of the response function. Here, IQnR is defined as $q_{84\,\%} - q_{16\,\%}$, where $q_{16\,\%}$ and $q_{84\,\%}$ are the 16$^{\text{th}}$ and 84$^{\text{th}}$ percentiles of a given distribution. They relate to the one standard deviation in case of an ideal Gaussian distributed response function.

entire large-R jet p_{T} range and varies between 5 to 35 %.
Systematic uncertainties on the JMS when using the combined mass definition are illustrated in Fig. 3.18, after applying the full large-R jet calibration as outlined in Ref. [368]. The JMS is measured in events with highly boosted W boson or top quark decays captured in large-R jet. For jets with a very high p_{T} the uncertainties on the JMS increases due to the limited size of the used dataset, and ranges between 2 to 6 % for $p_{\mathrm{T}} < 3$ TeV [368].

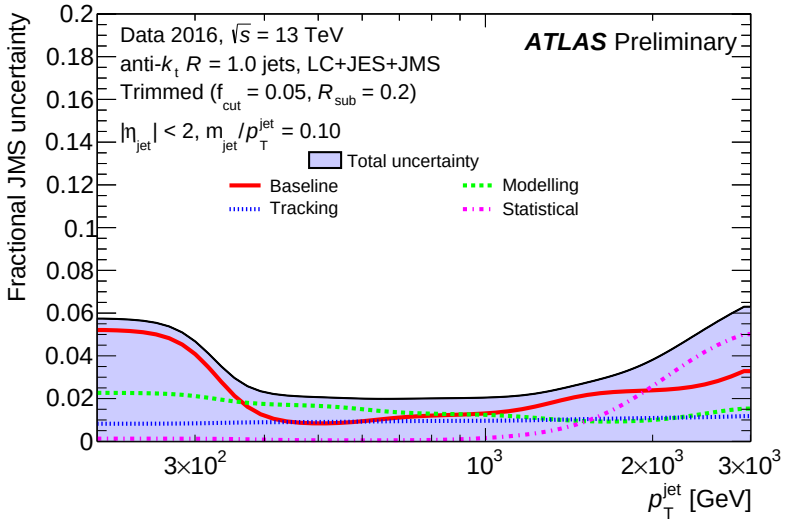

Figure 3.18: Breakdown of the systematic uncertainties on the large-R jet mass, m^{jet}, scale of fully calibrated jets with $m^{\mathrm{jet}}/p_{\mathrm{T}} = 0.1$ as a function p_{T}. Additionally, the total systematic uncertainty in the jet mass scale for the calorimeter mass is shown (black dotted line) [368].

3.3.4.3 Fixed Radius Track-Jets

In very boosted event topology, where a single large-R jet is used for the reconstruction of the Higgs boson decay products, so-called *track-jets* are used to identify the B-hadron decays, i.e. for the b-jet identification (see Section 3.3.5). Track-jets are reconstructed from at least two ID tracks by applying the anti-k_t algorithm with a fixed radius (FR) parameter of $R = 0.2$. The smaller radius parameter of 0.2, compared to the one of small-R jets with 0.4, allows to identify b-jets even when the Higgs boson becomes highly boosted.
Track-jets are uniquely matched to large-R jets by using the method of *ghost-association* [370, 371]. In this method, the ghosts are defined as jets where their p_{T} is set to an infinitesimal small value. Therefore, the four-momentum of a ghost jet is essentially only the direction of the track-jet. This ensures that during the reconstruction of the large-R jet its four-momentum is not altered by the ghosts when the calorimeter clusters and the ghosts are reclustered. All large-R jet constituents in the event, including the ghosts

are reclustered using the anti-k_t algorithm, where the large-R jet before applying the trimming procedure is used. As the ghost jets do not carry any significant momenta, the reclustered large-R jet is identical to the trimmed jet, with the addition of the associated ghosts are retained as constituents. A track-jet is said to be ghost-associated to a large-R jet, if the corresponding ghost jet is contained within the catchment area of the large-R jet. No calibration procedure is applied to track-jets. Track-jets with a fixed radius parameter are used for the mono-Higgs ($b\bar{b}$) analysis presented in Chapter 4.

3.3.4.4 Variable Radius Track-Jets

Track-jets with a variable radius parameter, so-called *VR track-jets* [372,373], provide an alternative approach for the identification of very boosted Higgs bosons with $p_{\mathrm{T}} > 1\,\mathrm{TeV}$ up to 3 TeV. For such very boosted event topologies even the fixed radius track-jets start to overlap, while the VR track-jets can still be reconstructed as two well separated track-jets as illustrated in Fig. 3.19. In particular, the radius parameters of the two track-jets are not required to be the same.

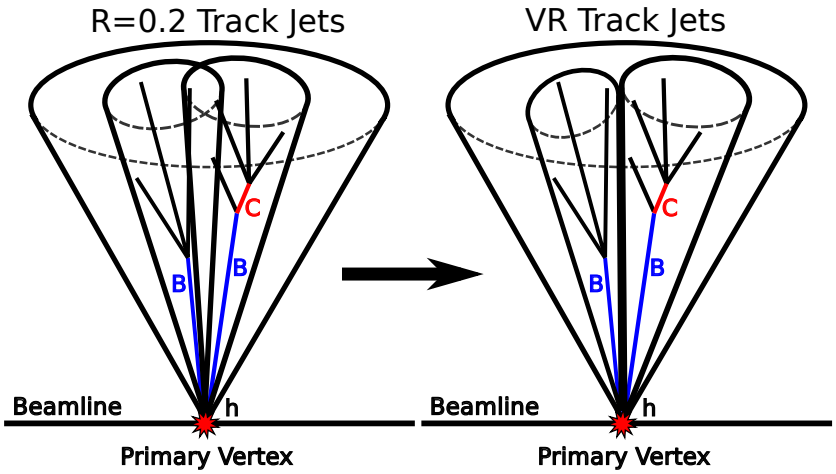

Figure 3.19: Illustration of a large-R jet with two associated track-jets with a fixed (left) and a variable (right) radius parameter [373].

VR track-jets are reconstructed from ID tracks similar as FR track-jets. The reconstruction algorithm is adjusted to provide a more flexible cone size depending on the p_{T} of the parent jet, i.e. the leading large-R jet. The maximal jet radius parameter in Eq. 3.7 is p_{T} dependent and is redefined by

$$R \longrightarrow R_{\mathrm{eff}}(p_{\mathrm{T}}) \approx \frac{\rho}{p_{\mathrm{T}}} \quad , \tag{3.11}$$

with p_{T} the transverse momentum of the large-R jet and ρ a constant with dimension of GeV. The latter defines how fast the effective cone size decreases with p_{T}. Moreover, two

boundaries on R_{eff} are imposed, namely R_{min} and R_{max}, which prevent the VR track-jets from becoming to large at low-p_{T} and from shrinking below the detector resolution at very high-p_{T}. The optimal values of these three parameters have been found to be: $\rho = 30\,\text{GeV}$, $R_{\text{min}} = 0.02$ and $R_{\text{max}} = 0.4$ (see Ref. [373]), aiming for the highest double b-jet labelling efficiency. The effective track-jet radius parameter as a function of the jet p_{T} is sketched in Fig. 3.20.

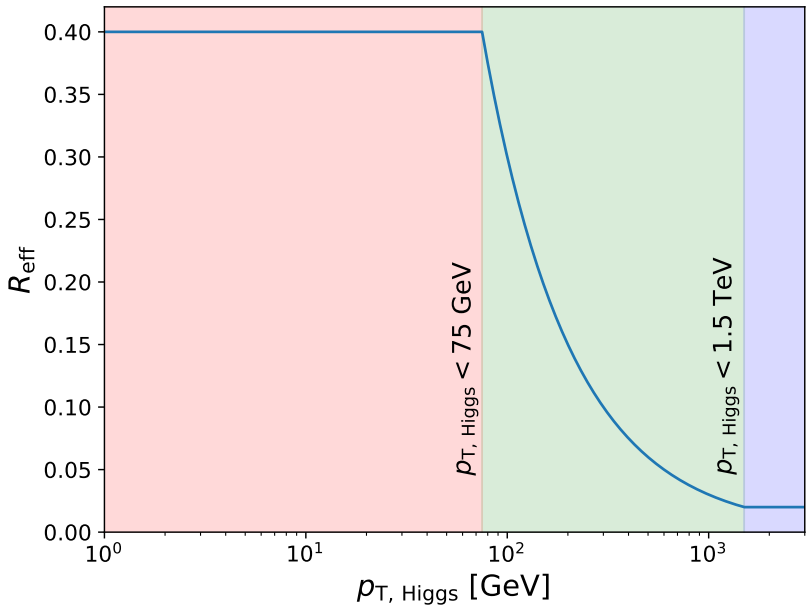

Figure 3.20: Illustration of the effective track-jet radius parameter as a function of the jet p_{T}.

Track-jets with a variable radius parameter are used in the mono-Higgs ($b\bar{b}$) analysis presented in Chapter 6.

3.3.5 *b*-jet Identification

The precise identification of the $h \to b\bar{b}$ decay is vital for the search for Dark Matter in the mono-Higgs ($b\bar{b}$) channel, in order to select signal events and to reduce background processes that contain only light-flavour jets* in the final state. Small-R jets and track-jets are used to identify the Higgs decay products for low/intermediate-pt and for high-p_{T} Higgs bosons, respectively.
A jet which is produced by B-hadron decays is called *b-jet*. The algorithms for the identification of b-jets rely on the precise reconstruction of the PV and on the determination of the impact parameters of charged particle tracks and their kinematics [374]. These variables are used by multivariate algorithms which are trained to select b-jets and to

*Light-flavour jets are referred to as jets which are not produced by decays of hadronised b or c quarks, namely produced by u, d or s quarks or gluons.

reject c-jets and light-flavour jets.
The b-jet identification is based on the relative long mean lifetime of B-hadrons of the order of 1.5 ps, which corresponds to a proper decay length of $c\tau \approx 450\,\mu$m [36]. This results in a jet signature, where a secondary vertex (SV) displaced from the PV* is expected as illustrated in Fig. 3.21.

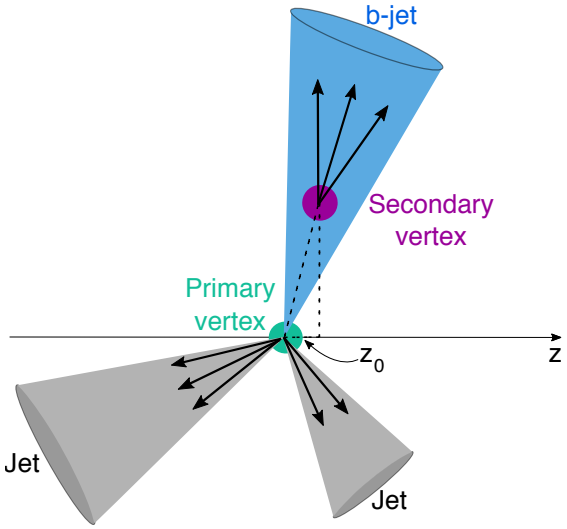

Figure 3.21: Illustration of a secondary displaced vertex produced by the decay of a B-hadron (blue) from the primary vertex of the hard interaction process. Light-flavour jets (grey) have no secondary vertex. In addition, the longitudinal impact parameter, z_0, of one track is also illustrated, while the transverse impact parameter, d_0, is not shown. Both parameters are used by the b-jet identification algorithms.

A boosted decision tree (BDT), implemented in the Toolkit for Multivariate Data Analysis (TMVA) [375], called *MV2c10* is used to decide whether a jet is identified as a b-jet or not. The BDT is trained on the output variables of three specialised algorithms: an impact parameter tagger, a SV finding algorithm and a decay chain reconstruction algorithm. The algorithms provide information about the transverse and longitudinal impact parameters of tracks which are associated with the jet and of the identification of the SV within the jet by means of a vertex fit. Furthermore, the distance between the PV and the SV is a sensitive variable for the reconstruction of the PV $\rightarrow B \rightarrow C$ – hadron decay chain. A Kalman filter [336] is used to search for a common line connecting the PV and the SV giving the B-hadron flight path (see for more details Refs. [374, 376]). The BDT training procedure is done separately for small-R jets and track-jets. The BDT output score allows to define different working points based on the required signal efficiency, i.e. the working point is related to a signal sample purity and to a misstag rate (or its inverse the background rejection). For the mono-Higgs ($b\bar{b}$) analysis a working point

*Typically, a B-hadron with a transverse momentum of 50 GeV decays on average after around 3 mm in the transverse plane, i.e. often within the ID.

corresponding to a fixed b-jet selection efficiency of 70 % is chosen for both small-R jets and track-jets, which relates to a rejection of around 380, 55 and 12 for light-flavour, τ- and c-jets, respectively [377] (τ-jets are discussed in Section 3.3.6).
The training of the BDT is performed by using jets from simulated $t\bar{t}$ events. Here, the two b-jets are assigned as the signal, and possible c-jets and light-flavour jets from W boson decays as the background. Since hadronic τ lepton decays can also be produced from W boson decays, which can mimic a b-jet, they are considered as a background as well. The background fraction used during the training of the BDT is composed of 7 % c-jets and 90 % light-flavour jets.
For the b-jet calibration, the efficiency between data and Monte-Carlo simulation is compared, and corrections with associated systematic uncertainties are derived. The calibration is performed by using dileptonic $t\bar{t}$ events with two oppositely charged leptons ($e\mu$, ee or $\mu\mu$) in the final states and by applying a combinatorial likelihood (LH) method. The selected $t\bar{t}$ events are categorised into a two and a three jet category for a better signal-to-background ratio and for deriving modelling uncertainties.
The performance of the b-jet identification algorithm for small-R jets is shown in Fig. 3.22. The efficiencies determined in data and Monte-Carlo simulation agree within their uncertainties (see Fig. 3.22a), and they are above 75 % for jet $p_{\mathrm{T}} > 50$ GeV. The resulting scale factors, defined as the ratio of the efficiencies found in data and Monte-Carlo simulation, are close to unity (see Fig. 3.22b). The data-to-simulation scale factors for track-jets

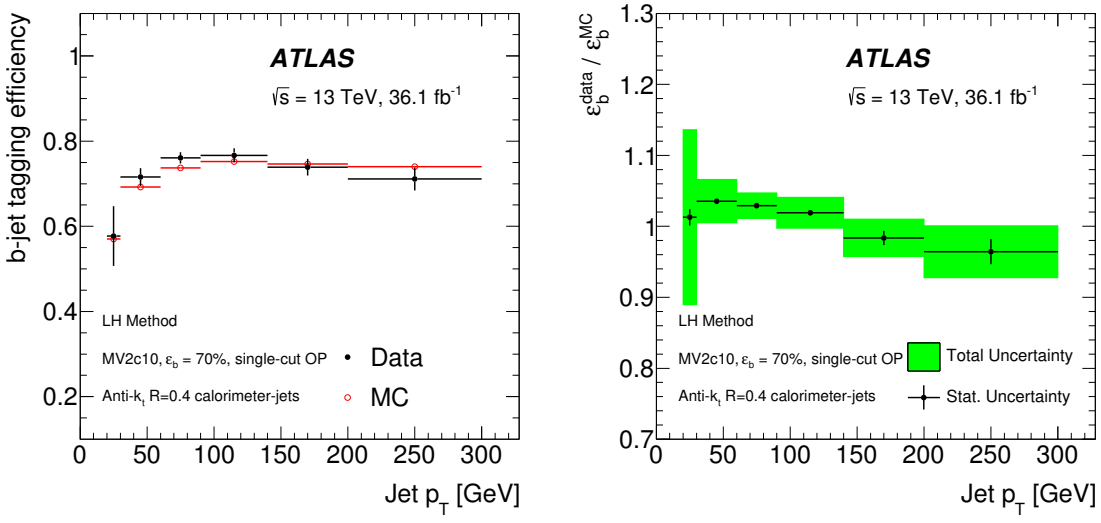

Figure 3.22: In (a) the b-jet identification efficiency for small-R jets of the 70 % working point measured in data and Monte-Carlo simulation as a function of p_{T} using the LH method and (b) the resulting data-to-simulation scale factors with their statistical uncertainties (error bars) and total uncertainties (green) [374].

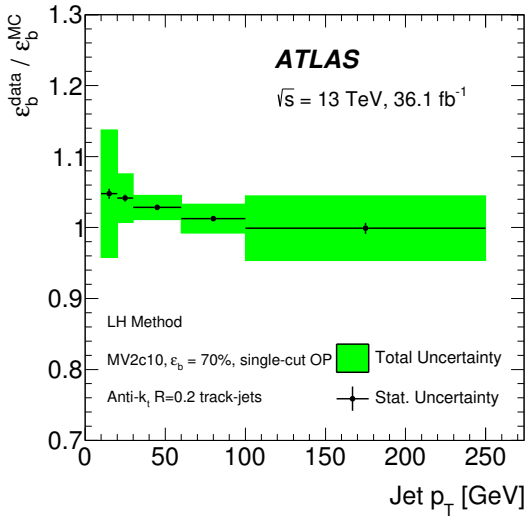

Figure 3.23: Data-to-simulation scale factors as a function of p_{T} for track-jets of the 70 % working point [374].

are shown in Fig. 3.23, which are also close to unity over the full p_{T} range. Systematic uncertainties on the scale factors are derived from comparing the predictions of different $t\bar{t}$ Monte-Carlo generators to data. The differences in the Monte-Carlo predictions are related to different descriptions of the parton shower and the hadronisation.
In addition to the calibration of b-jet efficiencies, the rate of the tagging c-jets as b-jets can be measured in single-lepton $t\bar{t}$ events, where one of the W bosons decays leptonically and the other decays via $W \to cs$ [378,379]. The rate of misidentify light-flavour jets as b-jets is measured from multijet events [380].

3.3.5.1 Energy Correction of Jets from a Semileptonic B-Hadron Decays

A jet produced by a semileptonic B-hadron decay is frequently accompanied by a nearby muon, i.e. from $b \to c\mu\nu_{\mu}$ and $b \to u\mu\nu_{\mu}$ decays. In the mono-Higgs ($b\bar{b}$) analysis, the invariant dijet mass and the mass of the leading large-R jet are of special interest, as for signal events a peak in the mass distributions around $m_h = 125\,\mathrm{GeV}$ is expected over a flat background. The resolution of the Higgs boson candidate mass can be improved by applying a jet energy correction accounting for the muon energy produced by a semileptonic decay of a B-hadron, referred to as *muon-in-jet correction*. In case of a muon nearby to a jet, the muon is often not properly taken into account in the jet four-momentum reconstruction. This results in a lower jet energy scale and poorer energy resolution, as the muon is a minimal ionising particle and deposits only a small energy in the calorimeter. There is no correction for electrons, as only 1 to 2 % [381] of the reconstructed jets have a proper reconstructed electron inside, related to their higher misidentification as jets.

Only muons passing the Medium WP (see Section 3.3.2.1) with $p_{\mathrm{T}} > 5\,\mathrm{GeV}$ are considered for the correction. The correction is applied to one of the small-R jets or to the large-R jet, if at least one small-R jet or one track-jet is identified as a b-jet, respectively, and if a muon is found within $\Delta R < 0.4$ or $\Delta R < 0.2$. At most one muon per event is considered, to avoid using fake-muons from other semileptonic non-B-hadron decays. If two close-by muons are found, the one with highest p_{T} is used. In case of a b-jet with a close-by muon, the jet energy is corrected for the muon energy deposition in the calorimeter, i.e. either of one of the small-R jets or of the leading large-R jet.
This correction translates to an improved Higgs boson candidate mass m_{jj} or m_J of the two highest-p_{T} small-R jets or of the leading large-R jet, respectively. The expected improvement of the muon-in-jet correction is illustrated in terms of the Higgs boson candidate mass distribution of Z'-2HDM signal events (see Section 2.6.3.1). Two representative Z'-2HDM models with $(m_{Z'}, m_A) = (600\,\mathrm{GeV}, 300\,\mathrm{GeV})$ and $(2600\,\mathrm{GeV}, 300\,\mathrm{GeV})$ are considered, which cover the two scenarios with a low- and a high-p_{T} Higgs boson, respectively. The distributions are shown with and without the The distributions of the Higgs boson candidate mass with and without applying the muon-in-jet corrections are shown in Fig. 3.24a and Fig. 3.24b for m_{jj} and m_J, respectively, for events with at least one b-jet. The improvements in the mass resolution are evaluated by fitting

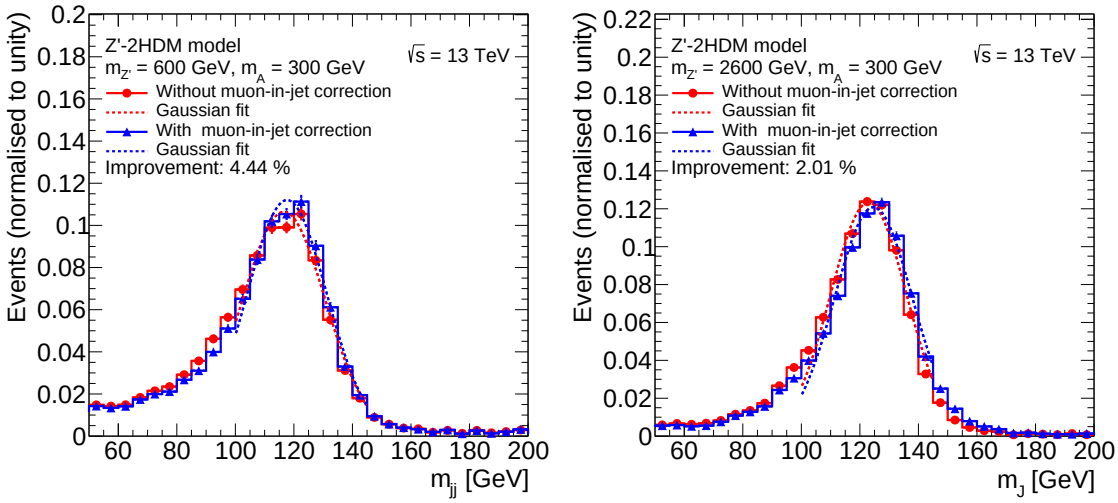

Figure 3.24: Distributions of the Higgs boson candidate mass in (a) m_{jj} and in (b) m_J with and without the muon-in-jet correction being applied for two representative Z'-2HDM signal modelsgit. The core of each mass distributions ($100\,\mathrm{GeV} < m_{jj/J} < 145\,\mathrm{GeV}$) is fitted with a Gaussian distribution and the improvement in resolution is given by comparing their widths. The uncertainties on the improvement are around 10 %.

the two distributions with a Gaussian function and by comparing the two widths with

and without the correction has been applied. They are around 4.4 % and 2.0 % for m_{jj} and m_J, respectively. The latter improvement is slightly smaller, since the chance of finding a nearby muon is smaller in case of the track-jets due to the smaller cone size. Additional signal models covering a broader spectrum of the Higgs boson p_{T} have been studied as well and similar improvements have been observed.

3.3.6 Tau Reconstruction

τ leptons are the heaviest leptons with a mass of $m_\tau = 1.77\,\mathrm{GeV}$. Due to their mean lifetime of $\tau_\tau = 290\,\mathrm{fs}$, which corresponds to a proper decay length of $c\tau = 87\,\mu\mathrm{m}$ [36], they decay inside the beam pipe of the LHC. Their decay is either leptonically ($\mathcal{B}_{\tau-\mathrm{lep}}(\tau \to \ell\nu_\ell\nu_\tau) \approx 35\,\%$ with $\ell = e,\ \mu$) or hadronically ($\mathcal{B}_{\tau-\mathrm{had}}(\tau \to \mathrm{hadrons}\,\nu_\tau) \approx 65\,\%$). Electrons or muons from τ decays cannot be distinguished from prompt ones, and, therefore, only hadronic τ decays are reconstructed by the ATLAS experiment. Hadronic τ decays (or τ-jets) are classified into the one-prong or the three-prong categories, which refers to the number of charged pions, $\pi^\pm$, in the final state. The charged pions are usually accompanied by additional neutral pions, π^0, which decay at most of the time into a pair of photons [36].

The reconstruction of τ-jets (see Refs. [382, 383]) is similar as for usual hadronic jets (see Section 3.3.4), but due to their lifetime they can also be misidentified as b-jets. The main difference between QCD jets and τ-jets is the lower track multiplicity in the latter case. Moreover, the tracks in the cone of a τ-jet are more collimated then the for a QCD jet, such that a smaller cone size can be used for the τ-jet reconstruction.

τ-jets are seeded from calorimeter clusters that are reconstructed as a QCD jet with $p_{\mathrm{T}} > 10\,\mathrm{GeV}$ and $|\eta| < 2.5$. The τ candidates in the transition region between the barrel and forward calorimeters, $1.37 < |\eta| < 1.52$, are vetoed. The τ decay vertex is defined as the ID track vertex with the largest momentum fraction from tracks within the jet core region ($\Delta R < 0.2$), while the tracks are required to have $p_{\mathrm{T}} > 1\,\mathrm{GeV}$. A Boosted Decision Tree (BDT) algorithm is used to reject quark and gluon initiated jets utilising the fact that the decay products of the τ form a narrow jet with low invariant mass and low track multiplicity. The τ-jet identification and reconstruction efficiency is measured from $Z \to \tau\tau$ events, where one τ lepton decays leptonically into a muon and neutrinos and the other decays hadronically. The efficiency is around 60 % (50 %) for 1-prong (3-prong) τ decays, in case of the least stringent selection criteria [382, 384], referred to as *Loose* working point. The efficiency is relatively low compared to the one measured for electrons and muons, given the challenge of discriminating against hadronic jets.

3.3.7 Missing Transverse Energy Reconstruction

The missing transverse energy, $\vec{E}_{\mathrm{T}}^{\mathrm{miss}}$, plays a crucial role when searching for undetected particles like Dark Matter. The principle for calculating $E_{\mathrm{T}}^{\mathrm{miss}}$ is the momentum conservation in the plane transverse to the beam axis, i.e. that the transverse momenta of all particles in the final state should sum to effectively zero. Any momentum imbalance may indicate that particles invisible to the detector systems were produced in the collision, such as neutrinos or Dark Matter particles. Both escape both the ATLAS detector without any interaction with the detector material.
The $E_{\mathrm{T}}^{\mathrm{miss}}$ reconstruction (see Refs. [385,386]) relies on the understanding of all recorded objects in the collision event. The x and y components of the missing transverse energy vector, $\vec{E}_{\mathrm{T}}^{\mathrm{miss}}$, are given by

$$E_{x(y)}^{\mathrm{miss}} = -\sum \underbrace{(E_{x(y)}^{\mathrm{miss},\,\mu} + E_{x(y)}^{\mathrm{miss},\,e} + E_{x(y)}^{\mathrm{miss},\,\gamma} + E_{x(y)}^{\mathrm{miss},\,\tau} + E_{x(y)}^{\mathrm{miss,\ small\text{-}}R\ \mathrm{jets}})}_{\text{hard-term}} - \underbrace{\sum E_{x(y)}^{\mathrm{miss,\ ID\ tracks}}}_{\text{soft-term}} \quad , \tag{3.12}$$

where each term is calculated as the negative vectorial sum of transverse energy of energy deposits or trajectories of charged particles. Moreover, the magnitude of $\vec{E}_{\mathrm{T}}^{\mathrm{miss}}$ is given by

$$E_{\mathrm{T}}^{\mathrm{miss}} = |\vec{E}_{\mathrm{T}}^{\mathrm{miss}}| = \sqrt{(E_x^{\mathrm{miss}})^2 + (E_y^{\mathrm{miss}})^2} \quad , \tag{3.13}$$

which is used as a proxy for the energy carried away by particles escaping the detector. Energy deposits in the calorimeters and tracks are matched to reconstructed objects in an order chosen to minimise double-counting of detector signals, i.e. priority is given to muons then electrons, photons[*], τ-jets and finally small-R jets. Muons are reconstructed from ID and MS tracks alone, with an small energy deposit in the calorimeter, leading to little or no signal overlap with other objects reconstructed in the calorimeter. The signals not associated with reconstructed objects in Eq. (3.12) form the *soft term*, whereas those associated with the reconstructed objects are collectively referred to as the *hard term*. In particular, only non-associated tracks are used for the calculation of the soft-term, the so-called *track based Soft Term* (TST). Since charged particles tracks are required to be matched to the PV, the soft-term is hardly sensitive to contributions from additional pp interactions and it only accounts for contributions from soft charged particles and neglects soft neutral particles and from those in the forward region $|\eta| > 2.5$. Furthermore, low-p_{T} (10 GeV $< p_{\mathrm{T}} <$ 20 GeV) and high-p_{T} ($p_{\mathrm{T}} >$ 20 GeV) jets are treated separately, such that low-p_{T} jets contribute to the soft-term and high-p_{T} jets contribute to the

[*]Details on the photon reconstruction and identification are given in Ref. [387].

hard-term, respectively.

The reconstruction of $E_{\mathrm{T}}^{\mathrm{miss}}$ is a challenging as many sub-detector systems are involved and many different physics objects in the event are contributing. For example, a mis-measurement of energy of any object can result in an imbalance of energy in the event, i.e. in a non-zero value of $E_{\mathrm{T}}^{\mathrm{miss}}$. The performance of $E_{\mathrm{T}}^{\mathrm{miss}}$ reconstruction is studied in $Z \to \mu\mu$ events, where no real $E_{\mathrm{T}}^{\mathrm{miss}}$ is expected (see Fig. 3.25a). For instance, the $pp \to ZZ \to 2\ell 2\nu$ process gives real $E_{\mathrm{T}}^{\mathrm{miss}}$ in this measurement. The dominant Standard Model background processes are compared to data and agree within 40 % for the bulk of the $E_{\mathrm{T}}^{\mathrm{miss}}$ distribution. The dominant systematic uncertainty is related to the JES. The systematic uncertainties dominate for $E_{\mathrm{T}}^{\mathrm{miss}} > 200\,\mathrm{GeV}$, while above this threshold the statistical uncertainties dominate. Good agreement between data and Monte-Carlo simulation is also found for the soft-term (see Fig. 3.25b), with differences up to 10 % below 30 GeV, while above the statistical uncertainties dominate.

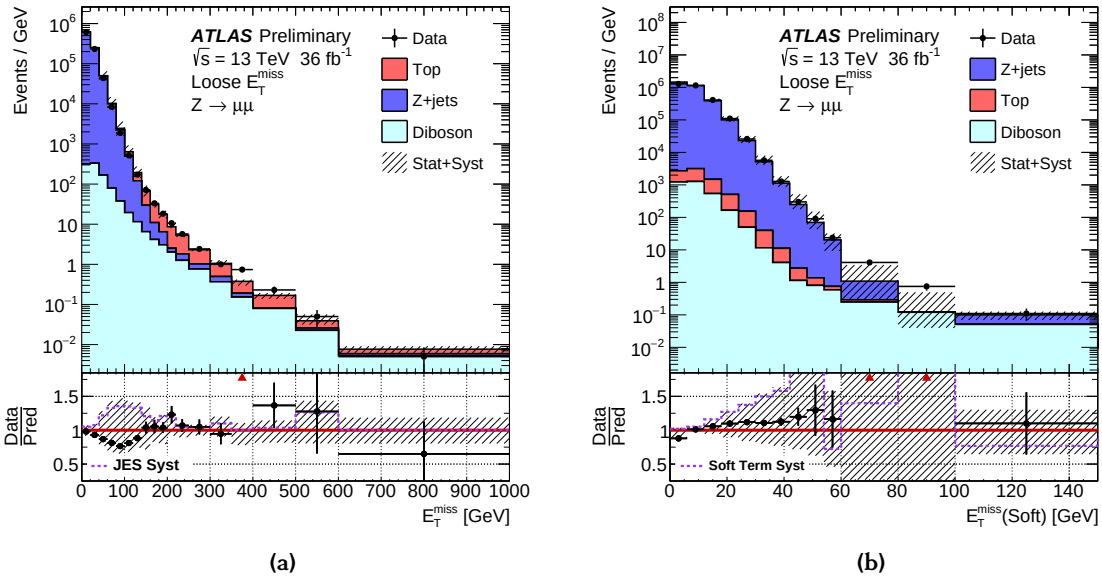

Figure 3.25: Distribution of (a) the $E_{\mathrm{T}}^{\mathrm{miss}}$ and (b) the soft-term component, $E_{\mathrm{T}}^{\mathrm{miss,\,soft\text{-}term}}$, for an inclusive sample of $Z \to \mu\mu$ events. The shaded area corresponds to the total uncertainty on the Monte-Carlo simulation. The last bin of each distribution includes the overflow [386].

In additional, the so-called *track*-$E_{\mathrm{T}}^{\mathrm{miss}}$ ($p_{\mathrm{T}}^{\mathrm{miss}}$) is used in the mono-Higgs ($b\bar{b}$) analysis, which is reconstructed from the tracks of the objects entering the hard-term of $\vec{E}_{\mathrm{T}}^{\mathrm{miss}}$. Hence, only the contributions of the charged particles are considered in the calculation. $p_{\mathrm{T}}^{\mathrm{miss}}$ is used in the analysis (see Chapter 4) to reduce beam-induced and non-collision background events.

An additional object, the so-called *object based* E_T^{miss}*-significance* [388], allows to efficiently separate events with real $E_{\mathrm{T}}^{\mathrm{miss}}$ produced by weakly interacting particles from

those with fake $E_{\mathrm{T}}^{\mathrm{miss}}$, i.e. form detector effects and mainly from mismeasured jet quantities. The object-based $E_{\mathrm{T}}^{\mathrm{miss}}$-significance, denoted as S, uses information of particles entering the $E_{\mathrm{T}}^{\mathrm{miss}}$ calculation like the energy resolution and the reconstruction efficiencies. Furthermore, S takes into account directional correlations of different particles and is given by

$$S = \frac{E_{\mathrm{T}}^{\mathrm{miss}}}{\sigma_{\mathrm{L}}^2(1-\rho_{\mathrm{LT}}^2)} \quad , \tag{3.14}$$

where σ_{L}^2 is the total variance in the longitudinal direction of $\vec{E}_{\mathrm{T}}^{\mathrm{miss}}$, and ρ_{LT}^2 is the correlation between the variances in the longitudinal and transverse directions of $\vec{E}_{\mathrm{T}}^{\mathrm{miss}}$. In case of small values of S, the event is more likely to be a multijet background event and $E_{\mathrm{T}}^{\mathrm{miss}}$ is caused by resolution effects of the jets. In contrast, S is large for events with real $E_{\mathrm{T}}^{\mathrm{miss}}$ as expected for a potential Dark Matter signal. More details on the reconstruction and the performance of the object-based $E_{\mathrm{T}}^{\mathrm{miss}}$-significance can be found in Ref. [388]. The object based $E_{\mathrm{T}}^{\mathrm{miss}}$-significance is used in the mono-Higgs ($b\bar{b}$) analysis presented in Chapter 6.

3.3.8 Overlap Removal

The objects discussed in the previous sections are reconstructed either from ID tracks, energy deposition in the calorimeters, and from tracks in the MS. For example, an electron or a jet can provide under certain circumstances a similar signature in the detector and both objects might be reconstructed from the same detector information. An algorithm resolves this object ambiguity, referred to as *overlap removal*, which avoids the double counting of such objects with a shared detector signal. The overlap removal is applied on a event basis to all reconstructed and calibrated objects. The algorithm is applied consecutively in different steps and gives priority to a certain type of object. Only the objects which are left after this procedure are considered for the signal event selection in the mono-Higgs ($b\bar{b}$) analysis (see Chapter 4).

First, the ambiguity between electrons and muons is resolved. In case of a CB muon and an electron have the an identical ID track, the electron is removed and the muon is kept, except for a CT, where it is the opposite. For a τ-jet overlapping with an electron or a muon within $\Delta R = 0.2$ the τ-jet is removed. An exception applies here, if the τ-jet p_{T} is larger then 50 GeV and the muon is not a CB muon, then the muon is removed. Small-R jets (large-R jets) are removed in cases where they overlap with electrons within $\Delta R = 0.2$ (1.2). Similarly, this is done for muons and τ-jets which overlap with small-R jets. The remaining electrons (muons) are removed if they are within $\min\Delta R(0.4, 0.04 + 10\ \mathrm{GeV}/p_{\mathrm{T}}^{\text{electron (muon)}})$ of a small-R jet.

Chapter 4

Mono-Higgs ($b\bar{b}$) Search

Searches for Dark Matter production at the LHC use so-called mono-X signatures, where Dark Matter is invisible in the detector and produced in association with a Standard Model particle, X, which often originate from initial-state-radiation (ISR) (see Section 2.5.3). The final state may involve a gluon jet, a photon, lepton pairs or heavy-flavour jets from weak gauge boson decays. After the confirmation of the existence of the Higgs boson at the LHC in 2012 [8, 9], searches for Dark Matter in association with the Higgs boson are of spatial interest. The mono-Higgs signature is complementary to other mono-X signatures as radiation of Higgs bosons in the initial state is suppressed due to the weak Yukawa couplings to u and d quarks and the Higgs boson is most likely part of the Dark Matter production.

In the following, a search for Dark Matter particles in events with large $E_{\mathrm{T}}^{\mathrm{miss}}$ and a pair of b quarks originating from the decay of a Higgs boson is presented based on a pp collision dataset of 36.1 fb^{-1} recorded by the ATLAS detector at $\sqrt{s} = 13$ TeV. Two principle improvements have been made to the previous analysis [257] using 3.2 fb^{-1}. Firstly, a new determination of the large-R jet mass has been developed with smaller systematic uncertainties for high-p_{T} jets. Secondly, improved selection criteria affecting the reduction of the $t\bar{t}$ background process are applied. The results are interpreted in terms of the simplified Z'-2HDM model describing the interaction of Dark Matter and Standard Model particles via heavy BSM mediators. The analysis results have been published in Ref. [260].

In Section 4.1, a general overview of the mono-Higgs ($b\bar{b}$) analysis is given. The particular signatures of the simplified Z'-2HDM model are discussed in Section 4.2, including the Monte-Carlo generators used for their simulation. The main background processes contributing to the mono-Higgs ($b\bar{b}$) analysis are discussed in Section 4.3. The analysed dataset and the applied triggers are discussed in Sections 4.4 and 4.5, respectively. The physical objects definitions and the event selection criteria for the mono-Higgs ($b\bar{b}$) analysis are explained in Sections 4.6 and 4.7, respectively, while the definitions of the control regions for the estimation of the main backgrounds is given in Section 4.8. The results of the mono-Higgs ($b\bar{b}$) search are discussed in Chapter 5.

4.1 General Analysis Strategy

The simplified Z'-2HDM Dark Matter model (see Section 2.6.3.1) is used as a benchmark model for the optimisation of the sensitivity of the mono-Higgs ($b\bar{b}$) search. It leads to the process $pp \to Z' \to hA \to b\bar{b}\chi\bar{\chi}$ with a pair of b quarks and large $E_{\mathrm{T}}^{\mathrm{miss}}$ in the final state. The latter originates from Dark Matter particles not interacting with the ATLAS detector. The coupling of the Higgs boson to b quarks has been confirmed by the recent observation of $h \to b\bar{b}$ decays by the ATLAS and CMS experiments [86, 87], which have the largest branching ratio of 58 % [71] for $m_h = 125\,\mathrm{GeV}$ in the Standard Model and, therefore, have been chosen for the mono-Higgs analysis.
For $E_{\mathrm{T}}^{\mathrm{miss}} < 500\,\mathrm{GeV}$, the Higgs boson decay has moderate transverse momentum and decays into two well separated small-R jets corresponding to the so-called *resolved topology* (see Fig. 4.1a). In the case of larger $E_{\mathrm{T}}^{\mathrm{miss}}$ values above 500 GeV, the Higgs boson decay is highly boosted and reconstructed as a single large-R jet with track-jet substructure, and is called *merged topology* (see Fig. 4.1b).

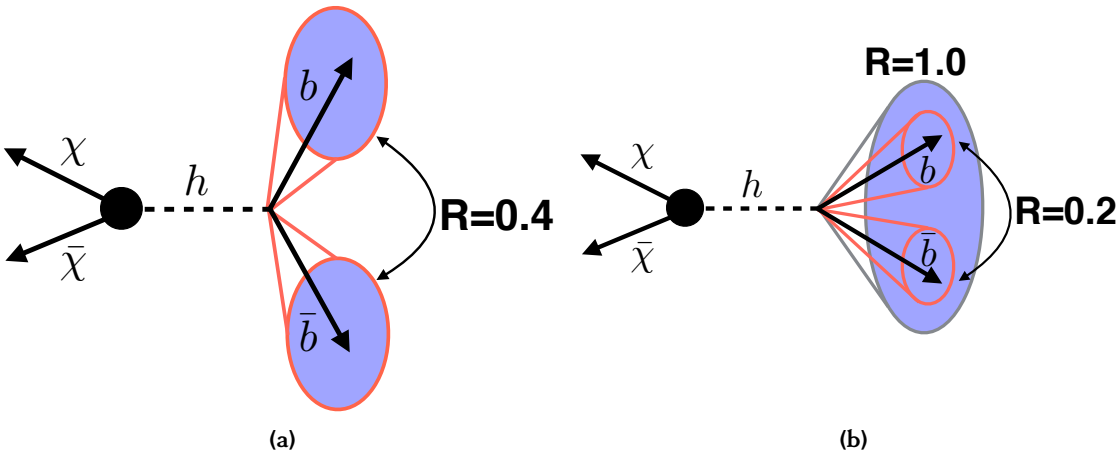

Figure 4.1: Illustration of the two event topologies studied by the mono-Higgs ($b\bar{b}$) analysis (a) the resolved topology with two well separated small-R jets recoiling against a pair of Dark Matter particles and (b) the merged topology with one large-R jet containing two associated track-jets. The objects used for b-jet identification are indicated by red circles. The jet cone sizes are described by the radius parameter R.

The division into two disjunct event topologies simplifies the analysis strategy, in particular the treatment of systematic uncertainties (see Section 5.2) and the statistical interpretation (see Chapter 5), without loosing much acceptance. The resolved and merged topologies together form the signal region (SR), which is split into four sub-regions depending on $E_{\mathrm{T}}^{\mathrm{miss}}$ each of which is divided into two regions according to the b-jet multiplicity (events with either one or two b-jets). This is done to improve the signal-to-background ratio in each sub-region by accounting for the different back-

ground compositions. The sub-region with only one b-jet is important for events with very high $E_{\mathrm{T}}^{\mathrm{miss}}$, i.e. for the merged topology, where the two track-jets are strongly collimated and start to overlap as well.
Very good discrimination between signal and background is essential at the LHC. The dominant background processes in the mono-Higgs ($b\bar{b}$) channel channel are $Z(\rightarrow \nu\nu) + \text{jets}$, $W(\rightarrow \ell\nu) + \text{jets}$ and $t\bar{t}$ production. The main backgrounds are estimated by defining signal-depleted *control regions* (CRs) which are included in a profile-likelihood fit to the data (see Chapter 5). The CRs are defined by requiring either one muon (1μ-CR) or two leptons (2ℓ-CR) in the event (see Section 4.8), while no leptons are allowed in the SR.
The final discriminating variables are $E_{\mathrm{T}}^{\mathrm{miss}}$ and the mass of the Higgs boson candidate, i.e. the invariant dijet mass m_{jj} or the mass of the leading large-R jet m_J for the resolved and the merged topology, respectively, which should peak at $m_h = 125\,\text{GeV}$ for the signal. The $E_{\mathrm{T}}^{\mathrm{miss}}$ distribution is expected to have larger tails for the signal than for the background processes.

4.2 Signal Process

In the simplified Z'-2HDM model (see Section 2.6.3.1), the heavy Z' boson is resonantly produced and decays into the Higgs boson, h, and a pseudoscalar Higgs boson, A. The latter subsequently decays into a pair of Dark Matter particles as illustrated in Fig. 2.15. This yields a characteristic back-to-back topology of the h boson against large $E_{\mathrm{T}}^{\mathrm{miss}}$ in the transverse plane. In the benchmark scenario, the masses of the Z' boson, $m_{Z'}$, and of the pseudoscalar A boson, m_A, are free parameters, while the Dark Matter particle mass is set to 100 GeV. Moreover, $\tan\beta = 1$, $g_{Z'} = 0.8$, $m_H = m_{H^\pm} = 300\,\text{GeV}$, and $\mathcal{B}(A \rightarrow \chi\bar{\chi}) \approx 100\,\%$ are assumed following the recommendations of the LHC Dark Matter Forum [215].
Monte-Carlo signal samples for the $pp \rightarrow Z' \rightarrow hA \rightarrow b\bar{b}\chi\bar{\chi}$ process are generated using `MADGRAPH` 2.2.3 [65] at LO QCD interfaced to `PYTHIA` 8.186 using the NNPDF3.0 PDF set [389] and the A14 tune [390]. Several Z'-2HDM signal samples have been generated in the $(m_{Z'}, m_A)$ parameter space with $200\,\text{GeV} < m_{Z'} < 3000\,\text{GeV}$ and $200\,\text{GeV} < m_A < 800\,\text{GeV}$. The predicted cross sections times the branching ratios for the generated final states in the Z'-2HDM signal models are shown in Fig. 4.2. The cross section decreases with increasing $m_{Z'}$ and m_A.
In the rest frame of the Z' boson, the h and A bosons are produced back-to-back with relatively large and equal transverse momenta. The missing transverse momentum due to the Dark Matter particles produced by the A boson decay thus is approximately proportional to the Higgs boson transverse momentum ($p_{\mathrm{T}}^h \approx p_{\mathrm{T}}^A \approx E_{\mathrm{T}}^{\mathrm{miss}}$) (see Fig. 4.3).

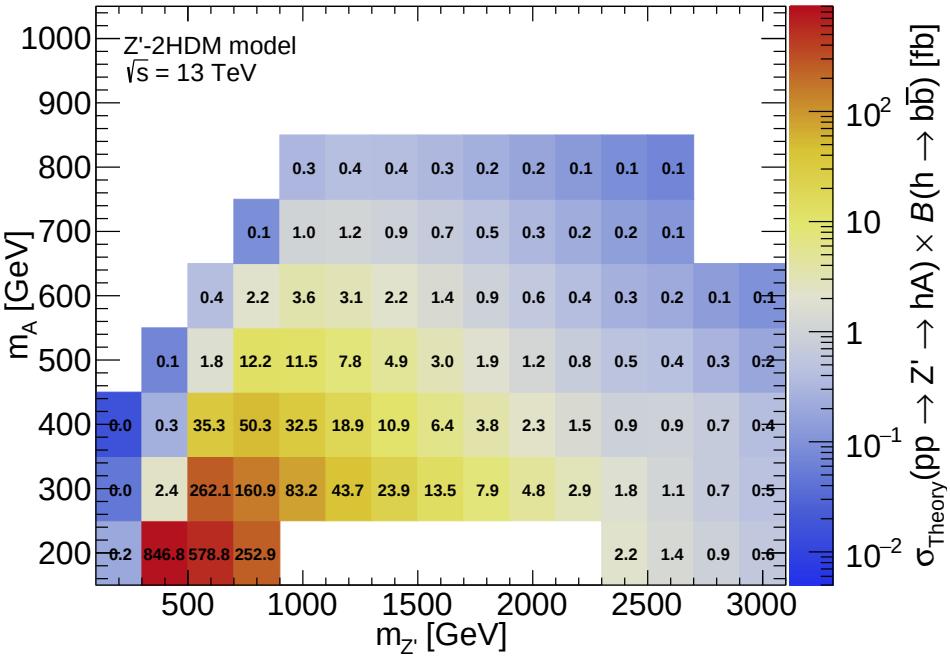

Figure 4.2: The cross section times the branching ratio in the $(m_{Z'}, m_A)$ plane for the different parameter points of the simplified Z'-2HDM model at $\sqrt{s} = 13\,\text{TeV}$ simulated by the MADGRAPH event generator at leading-order. The branching ratio of the Higgs decay into a pair of b quarks for $m_h = 125\,\text{GeV}$ is 58 % [71].

The discrimination between signal and background events strongly depends on the $E_{\text{T}}^{\text{miss}}$ distribution of the signal. The sensitivity increases with the hardness of the $E_{\text{T}}^{\text{miss}}$ spectrum, i.e. for higher $m_{Z'}$ or lower m_A values. The expected $E_{\text{T}}^{\text{miss}}$ and Higgs candidate mass before applying signal selections for different benchmark Z'-2HDM signal points are shown in Fig. 4.4 and Fig. 4.5, respectively. With increasing $m_{Z'}$, the $E_{\text{T}}^{\text{miss}}$ distribution peaks at higher values, because more energy becomes available for the A boson. For decreasing m_A values, $E_{\text{T}}^{\text{miss}}$ increases since the A boson gets more boosted and acquires higher p_{T}, and the Dark Matter particles are emitted more collimated.
For $(m_{Z'}, m_A) = (600\,\text{GeV}, 300\,\text{GeV})$, most of the events show the resolved topology due to the rather small boost of the Higgs boson. For $(2600\,\text{GeV}, 300\,\text{GeV})$, most of the events have merged topology due to the harder $E_{\text{T}}^{\text{miss}}$ and, thus, p_{T}^{h} spectra. For $(m_{Z'}, m_A) = (1400\,\text{GeV}, 600\,\text{GeV})$, events are selected both by the criteria for the resolved and for the merged topology. A peak at the Higgs boson mass of $m_h = 125\,\text{GeV}$ is expected in the dijet and leading large-R jet mass distribution. An exception is the m_J distribution for $(m_{Z'}, m_A) = (600\,\text{GeV}, 300\,\text{GeV})$, where most of the events show the resolved topology and no large-R jet with mass of the Higgs boson is found.
The angular separation, $\Delta R(b, \bar{b})$, of the two b quarks from the Higgs boson decay is shown in Fig. 4.6 as a function of p_{T}^{h} ($\approx E_{\text{T}}^{\text{miss}}$) for three Z'-2HDM benchmark signal

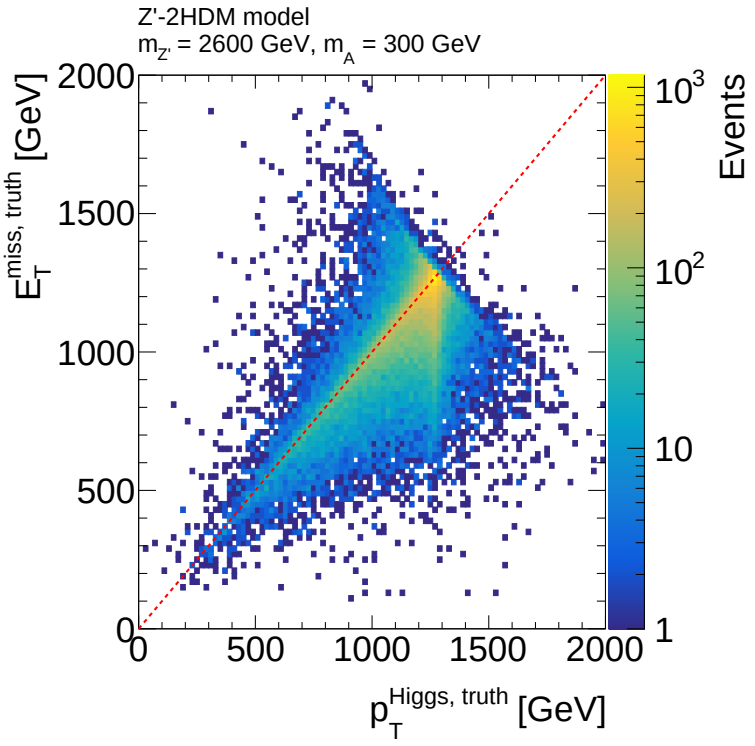

Figure 4.3: $E_{\mathrm{T}}^{\text{miss, truth}}$ from Dark Matter particles as a function of the Higgs boson transverse momentum $p_{\mathrm{T}}^{\text{Higgs, truth}}$ from Monte-Carlo simulation at particle level for a representative Z'-2HDM signal model with $(m_{Z'}, m_A) = (2600\,\text{GeV}, 300\,\text{GeV})$. The red line corresponds to $E_{\mathrm{T}}^{\text{miss, truth}} = p_{\mathrm{T}}^{\text{Higgs, truth}}$.

points. An inversely proportional dependence is seen as expected from Eq. (3.6). For low values of p_{T}^{h}, e.g. for $(m_{Z'}, m_A) = (600\,\text{GeV}, 300\,\text{GeV})$, the separation of the b quarks is large and the two b-jets can be reconstructed as two well separated small-R jets. For the signal points (1400 GeV, 600 GeV) and (2600 GeV, 300 GeV), on the other hand, the angular separation decreases below $\Delta R(b, \bar{b}) = 0.4$ for $p_{\mathrm{T}}^{h} > 500\,\text{GeV}$. Thus, the b quarks become strongly collimated and cannot be reconstructed anymore as two separated jets with radius parameter of 0.4. In this case, track-jets with radius parameter of 0.2 are used in order to identify the two b-jets within the large-R jet.

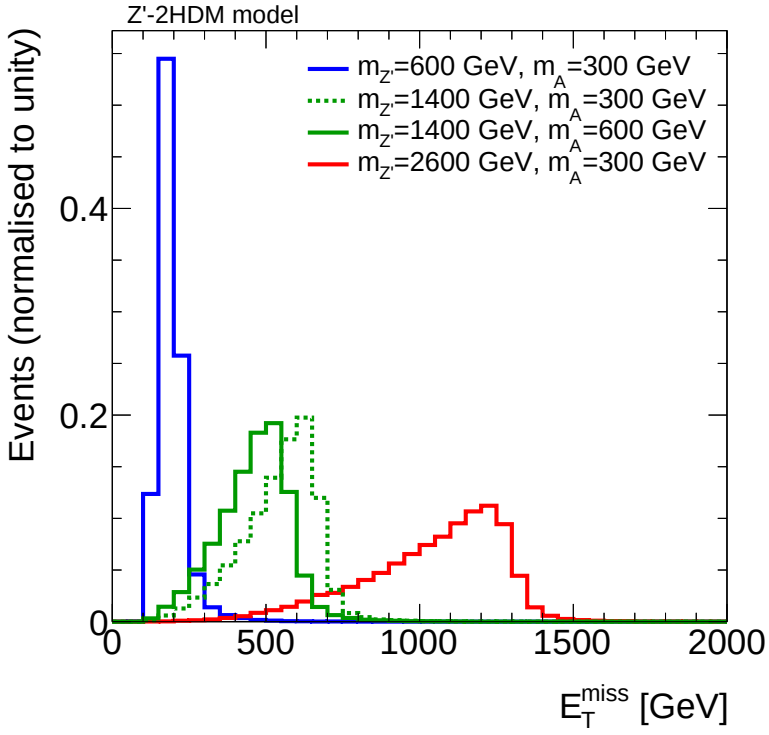

Figure 4.4: $E_{\mathrm{T}}^{\mathrm{miss}}$ distributions for four representative Z'-2HDM signal points. For fixed m_A, the $E_{\mathrm{T}}^{\mathrm{miss}}$ distribution becomes harder with increasing $m_{Z'}$. For fixed $m_{Z'}$, the $E_{\mathrm{T}}^{\mathrm{miss}}$ spectrum becomes softer with increasing m_A. All distributions are normalised to unity.

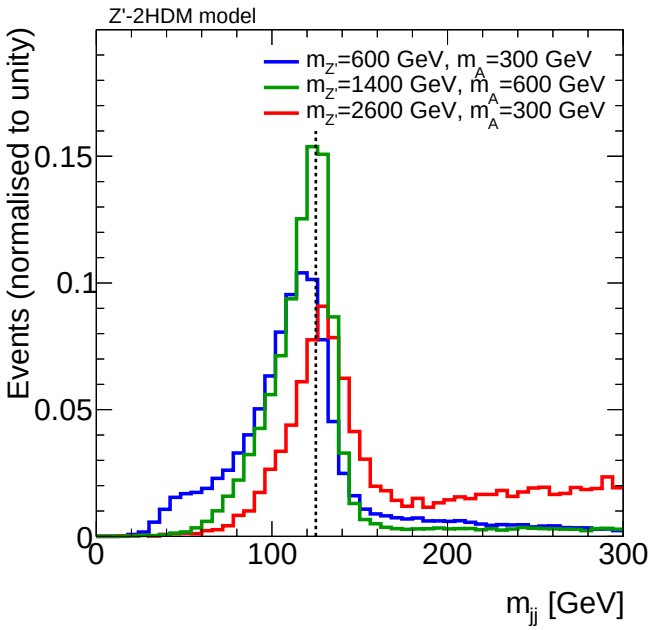

(a)

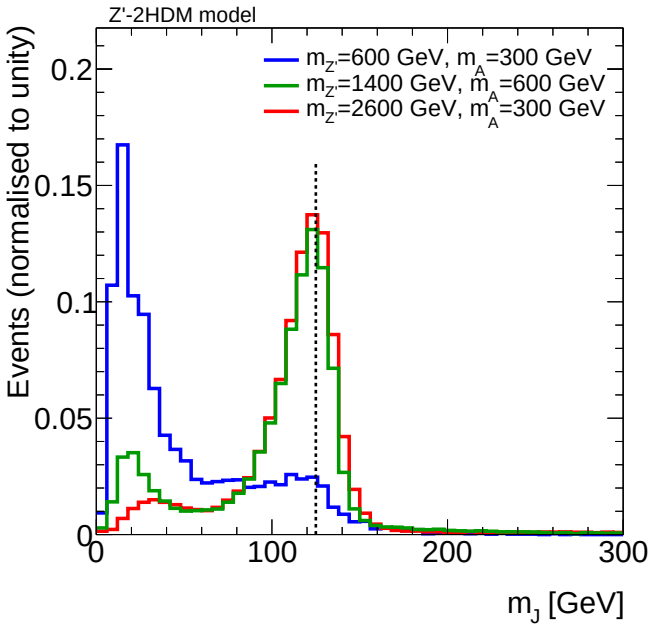

(b)

Figure 4.5: Distributions of the Higgs candidate mass defined as (a) the invariant dijet mass, m_{jj}, of the two leading central jets and (b) the leading large-R jet mass, m_J, for three representative Z'-2HDM signal points. The black dashed lines indicates the expected Higgs boson mass of $m_h = 125\,\text{GeV}$. All distributions are normalised to unity.

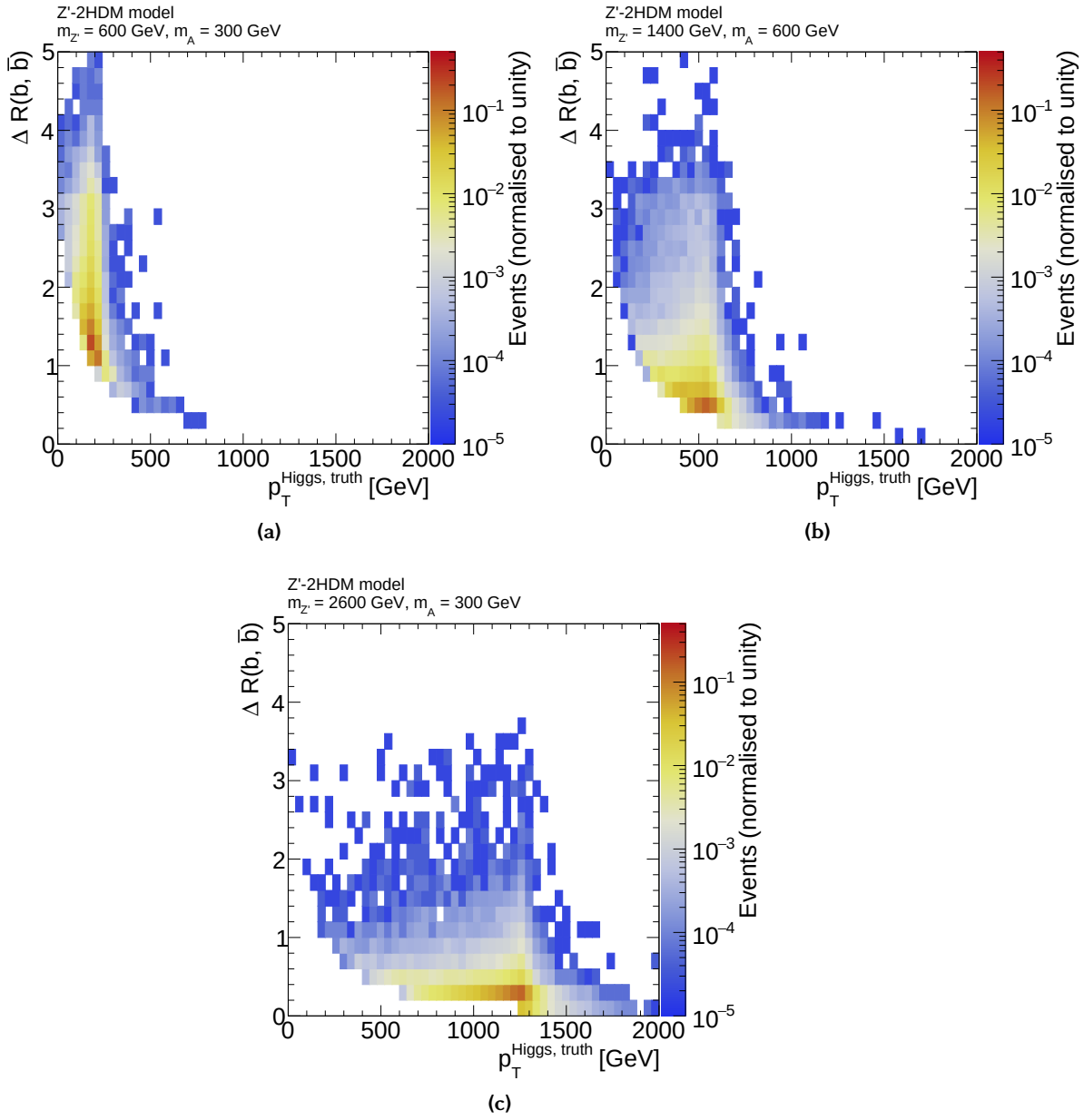

Figure 4.6: The angular separation, $\Delta R(b, \bar{b})$, of the two b quarks originating from the Higgs boson decay as a function of the Higgs boson p_{T}^{h} from Monte-Carlo truth level simulation for three representative Z'-2HDM signal models.

4.3 Background Processes

The dominant source of background are events containing neutrinos. Similar to Dark Matter particles, neutrinos do not interact in the detector and, therefore, induce large $E_{\mathrm{T}}^{\mathrm{miss}}$ values. The two main Standard Model background processes resulting in an event topology similar to the mono-Higgs ($b\bar{b}$) signal are the $t\bar{t}$ and the Z+jets production (see Fig. 4.7) with subsequent $W \to \ell\nu$ or $Z \to \nu\nu$ decays for low and high $E_{\mathrm{T}}^{\mathrm{miss}}$, respectively. They account for roughly 70 to 85 % of the total background in the SR, depending on $E_{\mathrm{T}}^{\mathrm{miss}}$ and the b-jet multiplicity.
The $t\bar{t}$ processes (see Fig. 4.7a) lead to two b-jets from $t \to Wb$ decays and are divided into three categories according to the decay modes of the two W bosons. The $t\bar{t}$ event is called *dileptonic (fully-hadronic)*, if both W bosons decay leptonically (hadronically). In the case of one W boson decaying hadronically and the other one leptonically, the event is called *semileptonic*. Fully-hadronic $t\bar{t}$ events do not contribute to the SR, since there is no genuine $E_{\mathrm{T}}^{\mathrm{miss}}$ in these events, except from neutrinos from semileptonic heavy-flavour hadron decays. The highest $E_{\mathrm{T}}^{\mathrm{miss}}$ occurs in dileptonic $t\bar{t}$ events, in which both W bosons decay to $\tau\nu$, and the two τ leptons decay leptonically. However, this contribution is rather small, as leptonic τ decays are indistinguishable from prompt electrons and muons which are both not allowed in the SR. Thus, only hadronically decaying τ leptons are relevant. The semileptonic event topology is characterised by intermediate values of $E_{\mathrm{T}}^{\mathrm{miss}}$, which increase if the lepton ($\ell = e,\ \mu$) is not reconstructed. Furthermore, additional b-jets may be reconstructed due to falsely identified c or s quarks from $W \to cs$ decays or τ-jets from $W \to \tau\nu$ decays. The main $t\bar{t}$ background contribution is from semileptonic final states with one or two hadronically decaying τ leptons.
The Z+jets process contributes to the background mainly through Z boson decays into neutrino pairs, resulting in events with high values of $E_{\mathrm{T}}^{\mathrm{miss}}$. The additional b-jets are produced via gluon splitting (see Fig. 4.7b). The contribution from $Z/\gamma \to \tau^+\tau^-$ decays is smaller, due to the six times smaller branching ratio.
A still important background is W+jets production (see Fig. 4.7c), it contributes about 9 to 18 % to the total background. As for the $t\bar{t}$ process, the amount of $E_{\mathrm{T}}^{\mathrm{miss}}$ in the events depends on the decay mode of the W boson. Large $E_{\mathrm{T}}^{\mathrm{miss}}$ results from the neutrinos from leptonic W boson decays including neutrinos from τ decays or not reconstructed electrons and muons. Events with a well reconstructed, isolated high-p_{T} electrons or muons are vetoed. Hadronic W decays do not provide sufficient $E_{\mathrm{T}}^{\mathrm{miss}}$.
The mentioned background processes provide a signal-like final state with one or two b-jets and large $E_{\mathrm{T}}^{\mathrm{miss}}$, but without a resonance in the Higgs candidate mass distribution. A less important but irreducible background process is the $Vh(\to b\bar{b})$ production with

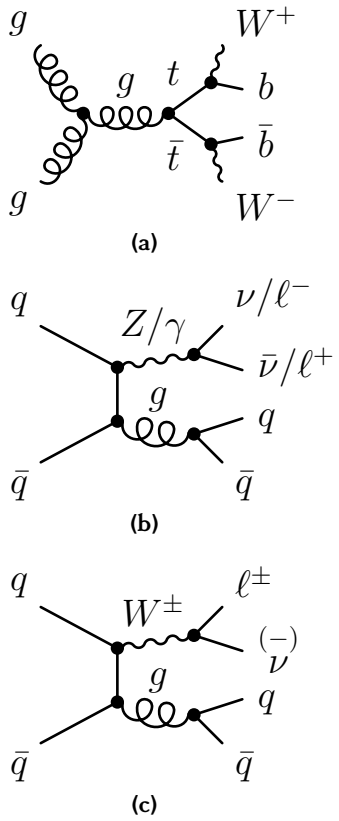

Figure 4.7: Tree-level Feynman diagrams for the three dominant background processes to the mono-Higgs ($b\bar{b}$) search: (a) $t\bar{t}$, (b) Z+jets and (c) W+jets production.

$V = W, Z$. Large $E_{\mathrm{T}}^{\mathrm{miss}}$ values are expected for the $Z \to \nu\nu$ and $W \to \ell\nu$ decays. In both cases, a peak at 125 GeV is expected in the Higgs boson candidate mass distribution.
Diboson production of $VV = WW, WZ$ or ZZ contribute to the background for leptonic decays of one of the Z or W bosons and decay to b quark pairs of the other. Furthermore, single top quark production in the t-channel, which has the highest cross section, leads to two b-jets in the final state, one from the production process and one from the top quark decay. Large $E_{\mathrm{T}}^{\mathrm{miss}}$ values result from leptonic decays of the W bosons from top decays. Associated Wt production provides even higher values of $E_{\mathrm{T}}^{\mathrm{miss}}$, but has a smaller cross section. Single top quark production in the s-channel has a still smaller cross section and causes only a small background contribution.
QCD multijet production usually is an overwhelming background at the LHC due to the large hadronic cross section but carries only small amounts of $E_{\mathrm{T}}^{\mathrm{miss}}$. It can contribute to background, if the four-momenta of one or more jets are significantly misreconstructed resulting in transverse momentum imbalance. Intermediate values of $E_{\mathrm{T}}^{\mathrm{miss}}$ in multijet events originate from semileptonic heavy-flavour hadron decays. Still, the multijet background contribution is expected to be small after the large $E_{\mathrm{T}}^{\mathrm{miss}}$ requirement. Addi-

tional *anti-QCD requirements* (see Section 4.7) efficiently reduce the remaining multijet background to an almost negligible amount. Since this process is difficult to simulate a data-driven estimation is performed (see Section 4.8.3). All other background processes are estimated from Monte-Carlo simulation. The estimation of the main background contributions from $t\bar{t}$, $W+$jets and $Z+$jets production are constrained by auxiliary measurements in signal-depleted control regions in data (see Section 4.8).

4.3.1 Background Simulation

The Monte-Carlo event generators, the PDFs and the production cross sections for the background processes in the mono-Higgs ($b\bar{b}$) search are summarised in Table 4.1.

Table 4.1: Monte-Carlo generators, parton distribution functions (PDFs) and production cross sections for the background processes contributing in the mono-Higgs ($b\bar{b}$) analysis.

Process	Generators	PDF	σ [pb]
$\boldsymbol{t\bar{t}}$	POWHEG + PYTHIA 6	CT10	831.76
Single top			
t-channel	POWHEG + PYTHIA 6	CT10	216.9
Wt-channel	POWHEG + PYTHIA 6	CT10	71.7
s-channel	POWHEG + PYTHIA 6	CT10	10.3
$\boldsymbol{V}$**+jets**			
$W(\to \ell\nu)$+jets	SHERPA 2.2.1	NNPDF3.0	15305
$Z(\to \nu\nu)$+jets	SHERPA 2.2.1	NNPDF3.0	8515
$Z/\gamma^*(\to \ell\ell)$+jets	SHERPA 2.2.1	NNPDF3.0	1577
Diboson			
WW	SHERPA 2.1	CT10	128.4
WZ	SHERPA 2.1	CT10	49.1
ZZ	SHERPA 2.1	CT10	16.9
$\boldsymbol{Vh(\to b\bar{b})}$			
$q\bar{q} \to Vh$	PYTHIA 8	NNPDF2.3	2.13
$gg \to Vh$	POWHEG + PYTHIA 8	CT10	0.13

Backgrounds from top quark pair production and single top quark production were generated at next-to-leading order (NLO) QCD with POWHEG [54–58] using CT10 PDFs [391,392] and PYTHIA 6.428 [63] for the parton shower simulation. The $t\bar{t}$ samples are normalised to the cross section calculated to next-to-next-to-leading order (NNLO) QCD including NNLO logarithmic corrections for soft-gluon radiation [393]. The single top quark processes are normalised to the NLO cross section calculation [394–398]. The V+jets background processes with $V = W, Z$ were simulated with Sherpa 2.2.1 [59] taking into account finite mass effects for b and c quarks and using NNPDF3.0 PDFs. The perturbative calculations of $V+$jets production were performed at NLO for up to two partons producing jets and at LO for up to four partons [399,400] and matched to the parton

shower [401] using the ME+PS@NLO prescription from Ref. [402]. The cross section normalisations are determined at NNLO QCD [403]. Diboson processes were simulated at NLO QCD with SHERPA 2.1.1 and with CT10 PDFs. Backgrounds from associated Vh production were generated with PYTHIA 8.186 with NNPDF3.0 PDFs for $q\bar{q} \to Vh$ at LO QCD and POWHEG interfaced to PYTHIA 8.186 with CT10 PDFs for $gg \to Vh$ at NLO QCD applying improved higher order corrections to the production cross section calculations [71] in both cases.
The effects of additional pp interactions occurring in the same and neighbouring bunch crossings (pile-up) are simulated by overlaying each hard-scatter event with additional pp interactions generated with PYTHIA 8.186 and with the MSTW2008LO PDF set [404].

4.4 Analysed Dataset

The analysed pp collision dataset at $\sqrt{s} = 13\,\text{TeV}$ has been recorded by the ATLAS detector in 2015 and 2016. Collision events are recorded for stable LHC beam conditions. Only events recorded with fully operational detector and passing *good-run quality criteria* are taken into account. These criteria take into account acquisition system inefficiencies and detector dead time when ramping up the detectors after stable beam conditions have been reached by the LHC.
With a data taking efficiency above 92 %, the ATLAS detector recorded $3.2\,\text{fb}^{-1}$ of data in 2015 and of $32.9\,\text{fb}^{-1}$ in 2016, resulting in a combined dataset of $36.1\,\text{fb}^{-1}$. The average number of pp interactions per bunch crossing was around 14 in 2015 and 25 in 2016 (see Fig. 3.2a). The uncertainty in the integrated luminosity is estimated to be 3.2 % as explained in Section 3.2.7.

4.5 Trigger Requirements

Two different types of triggers (see Section 3.2.6) are used for the mono-Higgs ($b\bar{b}$) analysis. An $E_{\text{T}}^{\text{miss}}$ trigger is used for selecting signal events. $E_{\text{T}}^{\text{miss}}$ triggers are also used for the selection of single-muon events in the 1μ-CR, while single-lepton triggers are used for 2ℓ-CR events (see Section 4.8).

4.5.1 Missing Transverse Energy Triggers

The $E_{\text{T}}^{\text{miss}}$ trigger is based on calorimeter information alone, while the offline $E_{\text{T}}^{\text{miss}}$ reconstruction (see Section 3.3.7) uses all calibrated reconstructed objects, in particular also muons which deposit only a small amount of their energy in the calorimeter. At the Level-1 (L1) trigger, muons are contributing to $E_{\text{T}}^{\text{miss}}$ like invisible particles. Trigger towers of calorimeter clusters calibrated at the EM scale are used to calculate $E_{\text{T}}^{\text{miss}}$ at

L1. For the analysis of the 2015 and 2016 dataset, a L1 $E_{\mathrm{T}}^{\mathrm{miss}}$ trigger threshold of 50 GeV was used (L1XE50 in Table 4.2).
For the high-level trigger (HLT), the $E_{\mathrm{T}}^{\mathrm{miss}}$ has been calculated with different algorithms in the two data taking periods. In 2015, the calorimeter cell based so-called *xe* algorithm was used with a threshold of 70 GeV. During 2016, $E_{\mathrm{T}}^{\mathrm{miss}}$ was defined as the negative vectorial sum of the transverse momenta of all jets in the event in the so-called *mht* algorithm. For this, jets are reconstructed from topological calorimeter clusters with radius parameter 0.4 using the anti-k_t jet finding algorithm. Pile-up subtraction and JES calibration are applied to the jets. Different HLT trigger thresholds have been used during 2016, increasing from 90 GeV to 110 GeV to adopt to the increased instantaneous luminosity provided by the LHC. The same $E_{\mathrm{T}}^{\mathrm{miss}}$ triggers for selecting signal events are also used for the selection of events in the 1μ-CR, since the trigger-level $E_{\mathrm{T}}^{\mathrm{miss}}$ is reconstructed solely from the calorimeter information and muons contribute like invisible particles. The $E_{\mathrm{T}}^{\mathrm{miss}}$ triggers used for the mono-Higgs ($b\bar{b}$) analysis are summarised in Table 4.2 for different data taking periods.
The $E_{\mathrm{T}}^{\mathrm{miss}}$ triggers are only fully efficient for a offline reconstructed $E_{\mathrm{T}}^{\mathrm{miss}} > 250$ GeV, while the search is also sensitive to signals which provide $E_{\mathrm{T}}^{\mathrm{miss}}$ values below this threshold (see Fig. 4.4). Therefore, dedicated corrections are derived accounting for the $E_{\mathrm{T}}^{\mathrm{miss}}$ trigger inefficiencies in the range $150 < E_{\mathrm{T}}^{\mathrm{miss}} < 250$ GeV and applied to Monte-Carlo simulated events in the SR and 1μ-CR (for details see Appendix B).

Table 4.2: Data taking periods with their maximum instantaneous luminosity and the lowest threshold $E_{\mathrm{T}}^{\mathrm{miss}}$ trigger used.

Data period	Max. instantaneous luminosity [10^{34} cm^{-2} s^{-1}]	$E_{\mathrm{T}}^{\mathrm{miss}}$ trigger
2015	0.49	HLT_xe70
2016 A—D3	1.0	HLT_xe90_mht_L1XE50
2016 D4—E3	1.1	HLT_xe100_mht_L1XE50
2016 F—L	1.4	HLT_xe110_mht_L1XE50

4.5.2 Single-Lepton Triggers

Events in the 2ℓ-CR are selected using single-lepton triggers as summarised in Table 4.3. Electron triggers are seeded by the L1 triggers with an electron transverse energy (E_{T}) thresholds of 18 and 20 GeV, L1EM18VH and L1EM20VH, respectively, depending on the

Table 4.3: Data taking periods, the maximal instantaneous luminosity in a given range of data taking period and the lowest single-electron and -muon triggers.

Data period	Max. instantaneous luminosity [10^{34} cm^{-2} s^{-1}]	Electron trigger	Muon trigger
2015	0.49	HLT_e24_lhmedium_L1EM18VH HLT_e24_lhmedium_L1EM20VH HLT_e60_lhmedium HLT_e120_lhloose	HLT_mu20_iloose_L1MU15 HLT_mu50
2016 A	0.34	HLT_e24_lhtight_nod0_ivarloose HLT_e60_lhmedium_nod0 HLT_e60_lhmedium HLT_e300_etcut HLT_e140_lhloose_nod0	HLT_mu24_iloose_L1MU15 HLT_mu24_iloose HLT_mu40
2016 B—E	1.1	HLT_e24_lhtight_nod0_ivarloose	HLT_mu24_ivarmedium HLT_mu50
HLT_mu24_ivarmedium 2016 F—L	1.4	HLT_e26_lhtight_nod0_ivarloose HLT_e60_lhmedium_nod0 HLT_e60_lhmedium HLT_e300_etcut HLT_e140_lhloose_nod0 HLT_e120_lhloose	HLT_mu26_ivarmedium HLT_mu50

data taking period and the increasing instantaneous luminosity. The same holds for the thresholds of the electron HLTs which range in E_{T} from 24 GeV up to 300 GeV. Additionally, different requirements on the electron identification criteria (lhloose, lhmedium and lhtight) are applied, together with requirements on the transverse impact parameter (nod0) and the track-based isolation (ivarloose) [405].
Muon triggers are seeded at L1 with a requirement of $p_{\mathrm{T}} > 15$ GeV. At the HLT level, the muon p_{T} thresholds range from 20 GeV to 50 GeV, with additional requirements of the muon track isolation (iloose and ivarmedium) [406].
A logical OR of all electron (muon) triggers is used to select events with two electrons (muons) in the 2ℓ-CR. Corrections accounting for trigger inefficiencies in data and Monte-Carlo simulation are applied to Monte-Carlo simulated events. The single-lepton trigger SFs factors are derived in a similar way as for the $E_{\mathrm{T}}^{\mathrm{miss}}$ triggers, but by selecting $Z \to \ell\ell$ events in data Monte-Carlo simulation and by applying a so-called *tag-and-probe method* [340, 342].

4.6 Object Selection

Small-R jets are required to satisfy jet-quality criteria [407, 408], which reject jets from calorimeter noise bursts and in areas of dead calorimeter modules and out-of-time jets from cosmic rays and from other non-collision backgrounds. If a single small-R jet fails such a quality criteria, the event is rejected. Small-R jets with $p_{\mathrm{T}} > 20$ GeV and $|\eta| < 2.5$

are called *central jets* and used to identify the $h \to b\bar{b}$ decay for events with resolved topology. The suppression of pile-up jets is important to correctly identify the $h \to b\bar{b}$ decay in signal events, which originate from the hard scattering processes. Spurious central jets from pile-up interactions are identified and rejected through the exploitation of their tracking information by the so-called jet vertex tagger (JVT) [355, 409]. Central jets with $20 < p_{\mathrm{T}} < 60\,\mathrm{GeV}$ have to fulfil the requirements of the medium JVT working point, which accepts 96 % of hard-scattering jets and rejects 98 % of pile-up jets. The remaining small-R jets in the region of $2.5 < |\eta| < 4.5$ are called *forward jets*, which are not used for the reconstruction of the Higgs decay products, since they do not provide tracking information needed for b-jet identification. Forward jets are required to satisfy $p_{\mathrm{T}} > 30\,\mathrm{GeV}$.

Large-R jets must satisfy $p_{\mathrm{T}} > 200\,\mathrm{GeV}$ and $|\eta| < 2.0$ and the large-R jet with highest p_{T} in the event is referred to as *the leading large-R jet*, which is considered to be the Higgs candidate for the merged topology. The leading large-R jet is required to have at least one ghost-associated track-jet with $p_{\mathrm{T}} > 10\,\mathrm{GeV}$ and $|\eta| < 2.5$. The two highest-p_{T} track-jets ghost-associated to the Higgs candidate are used for the b-jet identification [410, 411].

Jets from hadronic τ lepton decays (τ-jets) are selected, if they have exactly one or three charged tracks inside the jet cone to respect the one or three prong decay structure and must pass the loose identification working point (see Section 3.3.6). Loose-τ objects are required to satisfy $p_{\mathrm{T}} > 20\,\mathrm{GeV}$ and $|\eta| < 2.5$, while excluding the crack region $1.37 < |\eta| < 1.52$. An additional *very loose-τ object* is constructed from central small-R jets, with a relaxed requirement on the number of tracks inside the jet cone of $N_{\mathrm{tracks}} \in \{1, 2, 3, 4\}$. The associated tracks must originate from the primary vertex and satisfy $p_{\mathrm{T}} > 1\,\mathrm{GeV}$ and must be within core of the small-R jet, i.e. $\Delta R(\mathrm{small}-R\,\mathrm{jet},\,\mathrm{track}) < 0.2$ to account for the higher track collimation in a τ-jet compared to a QCD-jet. The relaxed requirement on the number of tracks accounts for the inefficiency of the track identification and for possible additional tracks from photon conversion produced by $\pi^0 \to \gamma\gamma$ decays. Furthermore, for the very loose-τ object definition a requirement on the angular separation $\Delta\Phi(\vec{E}_{\mathrm{T}}^{\mathrm{miss}}, \vec{j}) < 22.5°$ between the jet and $E_{\mathrm{T}}^{\mathrm{miss}}$ is applied. This assures that the τ object originates from a W boson decay, i.e. in $t\bar{t}$ or W+jets events, where the $E_{\mathrm{T}}^{\mathrm{miss}}$ corresponds to a neutrino produced close-by to the τ object.

Different electron and muon definitions are used in order to apply either a veto on leptons for the SR or by selecting a single-muon or lepton pairs for the 1μ-CR and 2ℓ-CR, respectively. For the SR, a veto on so-called *baseline electrons* and *muons* is applied. The baseline lepton selection is most inclusive with loose identification and loose track-based isolation requirements (see Sections 3.3.3 and 3.3.2, respectively). The baseline electrons (muons) must satisfy $p_{\mathrm{T}} > 7\,\mathrm{GeV}$ and $|\eta| < 2.47$ (2.7). For the 1μ-CR,

no baseline electrons are allowed, while tighter identification and isolation requirements are applied to muons, which are referred to as *signal muons*. For the 2ℓ-CR, either a pair of baseline electrons or muons is selected, but with more stringent requirements on the lepton p_{T} of 27 GeV and 25 GeV, respectively, referred to *high-p_{T}* baseline leptons. In addition, high-p_{T} baseline muons must satisfy $|\eta| < 2.5$.

4.7 Signal Selection

The signal selection criteria are designed to suppress background processes by exploiting the different kinematical properties of signal and background events and optimised by using the benchmark Z'-2HDM model. The events selected by the $E_{\mathrm{T}}^{\mathrm{miss}}$ triggers (see Table 4.2) are required to have offline reconstructed $E_{\mathrm{T}}^{\mathrm{miss}} > 150$ GeV to avoid the relatively poorly modelled region of the trigger turn-on curve (see Appendix B). The $E_{\mathrm{T}}^{\mathrm{miss}}$ requirement rejects already a large fraction of multijet events which have small $E_{\mathrm{T}}^{\mathrm{miss}}$. Furthermore, at least one well reconstructed primary pp collision vertex with at least two associated ID tracks with $p_{\mathrm{T}}^{\mathrm{track}} > 0.5$ GeV is required. A veto is applied against events with one or more baseline electrons or muons. Furthermore, a veto against events with a very loose and a loose τ-jet is applied (see Section 4.6 and Section C.1), which reduces mainly the $t\bar{t}$ and the $W+$jets backgrounds with $W \to \tau\nu$ decays. In case of the merged SR, the event is only rejected if a very loose τ-jet is found within $\Delta R(\vec{p}_{\text{leading large}-R\text{ jet}}, \vec{p}_{\tau}) > 1.0$.
Background contributions from non-collision events are reduced by requiring $p_{\mathrm{T}}^{\mathrm{miss}} > 30$ GeV for ID tracks. Beam interactions with the gas or the wall of the beam pipe or the shielding usually produce no ID tracks. The $p_{\mathrm{T}}^{\mathrm{miss}}$ requirement is not applied for events with two b-jets in order not to lose signal efficiency. The $p_{\mathrm{T}}^{\mathrm{miss}}$ distributions in data and Monte-Carlo simulation are shown in Fig. 4.8. The overall mismatch between data and Monte-Carlo simulation is due to missing multijet background. In the case of events with one b-jet, a particularly large difference between data and simulation is visible for $p_{\mathrm{T}}^{\mathrm{miss}} < 30$ GeV.
Multijet background is suppressed by so-called *anti-QCD requirements* based on minimum azimuthal angle differences $\min \Delta\Phi(\vec{E}_{\mathrm{T}}^{\mathrm{miss}}, \vec{j}_{1,2,3})$ between the $\vec{E}_{\mathrm{T}}^{\mathrm{miss}}$ vector and either of the three highest-p_{T} small-R jets in the event (with priority to central jets compared to forward jets) and between the azimuthal angle difference $\Delta\Phi(\vec{E}_{\mathrm{T}}^{\mathrm{miss}}, \vec{p}_{\mathrm{T}}^{\mathrm{miss}})$ between $\vec{E}_{\mathrm{T}}^{\mathrm{miss}}$ and $\vec{p}_{\mathrm{T}}^{\mathrm{miss}}$. In case of multijet events, large values of $E_{\mathrm{T}}^{\mathrm{miss}}$ mainly arise from mismeasured jet energy, such that $\vec{E}_{\mathrm{T}}^{\mathrm{miss}}$ points into the direction of the mismeasured jet leading to small $\Delta\Phi$ (see Fig. 4.9a), such that $\min \Delta\Phi(\vec{E}_{\mathrm{T}}^{\mathrm{miss}}, \vec{j}_{1,2,3}) > 20°$ is required. In events with real $E_{\mathrm{T}}^{\mathrm{miss}}$ from neutrinos or Dark Matter particles, $\vec{E}_{\mathrm{T}}^{\mathrm{miss}}$ and $\vec{p}_{\mathrm{T}}^{\mathrm{miss}}$ should align, i.e. $\Delta\Phi(\vec{E}_{\mathrm{T}}^{\mathrm{miss}}, \vec{p}_{\mathrm{T}}^{\mathrm{miss}})$ is small, except for multijet background events

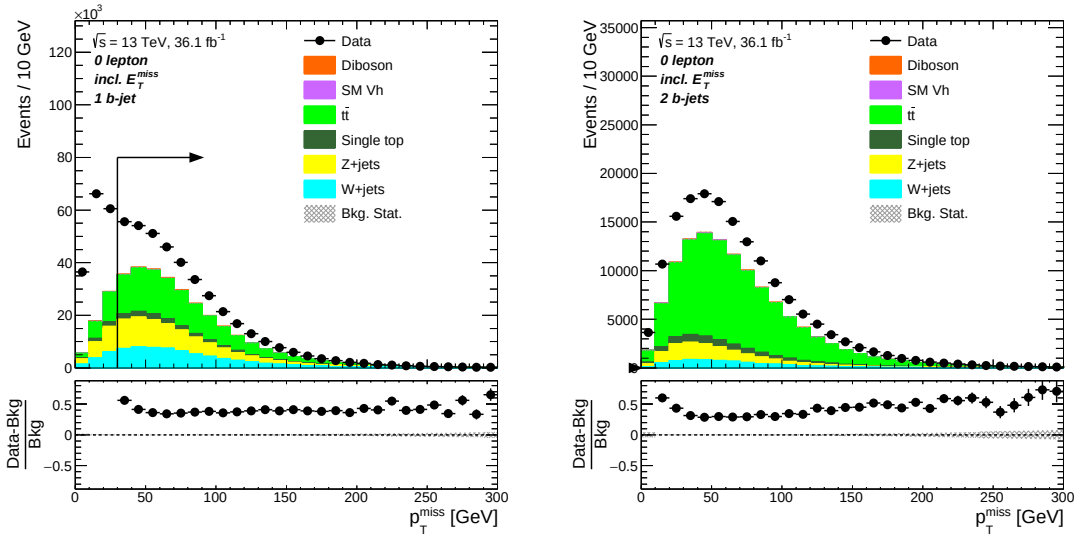

Figure 4.8: Distributions of $p_{\mathrm{T}}^{\mathrm{miss}}$ of ID tracks in signal events with (a) one and (b) two b-jets after the requirements $\min \Delta\Phi(\vec{E}_{\mathrm{T}}^{\mathrm{miss}}, \vec{j}_{1,2,3}) > 20^\circ$ and $\Delta\Phi(\vec{E}_{\mathrm{T}}^{\mathrm{miss}}, \vec{p}_{\mathrm{T}}^{\mathrm{miss}}) < 90^\circ$ to reduce multijet background. The arrow indicates the $p_{\mathrm{T}}^{\mathrm{miss}} > 30\,\mathrm{GeV}$ requirement for events with one b-jet, which is not applied to events with two b-jets.

where $\vec{E}_{\mathrm{T}}^{\mathrm{miss}}$ is expected to be aligned with one of the mismeasured jets while $\vec{p}_{\mathrm{T}}^{\mathrm{miss}}$ has no preferred direction (see Fig. 4.9b). Hence, $\Delta\Phi(\vec{E}_{\mathrm{T}}^{\mathrm{miss}}, \vec{p}_{\mathrm{T}}^{\mathrm{miss}}) < 90^\circ$ is required. The two anti-QCD requirements efficiently reduce the multijet background to a very small amount. Nevertheless, a data-driven estimation of the multijet background is performed (see Section 4.8.3) to ensure that its contribution to the total background is indeed small and well under control.

The above event selection criteria are common to all events in the SR, independent of the resolved or merged event topology. After this, the events are categorised in two disjoint categories based on a $E_{\mathrm{T}}^{\mathrm{miss}}$ requirement. Events with $E_{\mathrm{T}}^{\mathrm{miss}} < 500\,\mathrm{GeV}$ events are assigned to the resolved SR, and otherwise to the merged SR. Alternative event categorisations have been tested but no significant increase in signal sensitivity have been found.

Additional selection criteria separately applied for the resolved and for the merged SRs are described in Section 4.7.1 and Section 4.7.2, respectively. All selection criteria are summarised in Table 4.4.

4.7.1 Resolved Signal Region Selection

Events with $150\,\mathrm{GeV} < E_{\mathrm{T}}^{\mathrm{miss}} < 500\,\mathrm{GeV}$ are considered in the resolved SR. The $h \to b\bar{b}$ decay products are reconstructed from two well separated small-R jets. The two highest-

Table 4.4: Overview of the event selection criteria for the signal and the one-muon (1μ-CR) and two-lepton (2ℓ-CR) control regions. The $p_{\mathrm{T}}^{\mathrm{miss}}$ and $p_{\mathrm{T}}^{\mathrm{miss,\,no-}\mu}$ requirements are only applied to events with one b-jet.

Region	SR	1μ-CR	2ℓ-CR
Trigger	$E_{\mathrm{T}}^{\mathrm{miss}}$	$E_{\mathrm{T}}^{\mathrm{miss}}$	Single lepton
Leptons	No baseline e and μ	Exactly one signal μ No very loose and loose τ-jets	Exactly two baseline e or μ $83\,\mathrm{GeV} < m_{ee} < 99\,\mathrm{GeV}$ $71\,\mathrm{GeV} < m_{\mu^{\pm}\mu^{\mp}} < 106\,\mathrm{GeV}$
Common	$p_{\mathrm{T}}^{\mathrm{miss}} > 30\,\mathrm{GeV}$ $\min\Delta\Phi(\vec{E}_{\mathrm{T}}^{\mathrm{miss}}, \vec{j}_{1,\,2,\,3}) > 20°$ $\Delta\phi\left(\vec{E}_{\mathrm{T}}^{\mathrm{miss}}, \vec{p}_{\mathrm{T}}^{\mathrm{miss}}\right) < 90°$	$p_{\mathrm{T}}^{\mathrm{miss,\,no-}\mu} > 30\,\mathrm{GeV}$ $\min\Delta\Phi(\vec{E}_{\mathrm{T}}^{\mathrm{miss,\,no-}\mu}, \vec{j}_{1,\,2,\,3}) > 20°$ $\Delta\phi\left(\vec{E}_{\mathrm{T}}^{\mathrm{miss,\,no-}\mu}, \vec{p}_{\mathrm{T}}^{\mathrm{miss,\,no-}\mu})\right) < 90°$	— — —
Resolved	$E_{\mathrm{T}}^{\mathrm{miss}} \in [150,\,500)$ GeV — $\Delta\phi\left(\vec{E}_{\mathrm{T}}^{\mathrm{miss}}, \vec{p}_{\mathrm{h}}\right) > 120°$	$E_{\mathrm{T}}^{\mathrm{miss,\,no-}\mu} \in [150,\,500)$ GeV — Number of central small-R jets ≥ 2 Leading Higgs candidate small-R jet $p_{\mathrm{T}} > 45\,\mathrm{GeV}$ $H_{\mathrm{T,\,2\,(3)\,jets}} > 120\ (150)\,\mathrm{GeV}$ for 2 (3) jets $\Delta\phi\left(\vec{p}_h^{\,j_1}, \vec{p}_h^{\,j_2}\right) < 140°$ $\Delta R\left(\vec{p}_h^{\,j_1}, \vec{p}_h^{\,j_2}\right) < 1.8$ $\Delta\phi\left(\vec{E}_{\mathrm{T}}^{\mathrm{miss,\,no-}\mu}, \vec{p}_{\mathrm{h}}\right) > 120°$ Veto on events with > 2 b-jets H_{T}-ratio requirement (≤ 0.37) b-tagging : one or two central small-R jets **Final discriminant : dijet mass (m_{jj}) $\in$ [50, 280] GeV**	$p_{\mathrm{T}}^{\ell\ell} \in [150,\,500)$ GeV $E_{\mathrm{T}}^{\mathrm{miss}} \times \left(\sum_{\mathrm{jets,\,leptons}} p_{\mathrm{T}}\right)^{-1/2} < 3.5\,\mathrm{GeV}^{1/2}$ $\Delta\phi\left(\vec{p}_{\mathrm{T}}^{\,\ell\ell}, \vec{p}_{\mathrm{h}}\right) > 120°$
Merged	$E_{\mathrm{T}}^{\mathrm{miss}} \geq 500\,\mathrm{GeV}$	$E_{\mathrm{T}}^{\mathrm{miss,\,no-}\mu} \geq 500\,\mathrm{GeV}$ Number of large-R jets ≥ 1 Veto on b-jets not associated to large-R jet H_{T}-ratio requirement (≤ 0.57) b-tagging : one or two track-jets matched to leading large-R jet **Final discriminant : large-R jet mass (m_J) $\in$ [50, 270] GeV**	$p_{\mathrm{T}}^{\ell\ell} \geq 500\,\mathrm{GeV}$

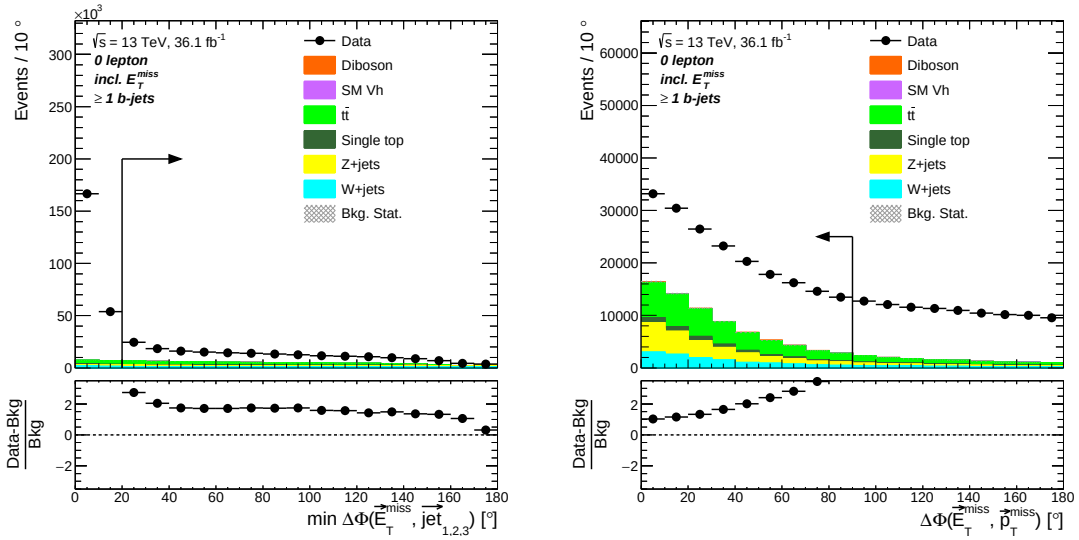

Figure 4.9: Observed and expected distributions of the two variables used for the rejection of multijet events, (a) $\min\Delta\Phi(\vec{E}_{\mathrm{T}}^{\mathrm{miss}}, \vec{j}_{1,2,3})$ and (b) $\Delta\Phi(\vec{E}_{\mathrm{T}}^{\mathrm{miss}}, \vec{p}_{\mathrm{T}}^{\mathrm{miss}})$. In both cases, the requirement of $p_{\mathrm{T}}^{\mathrm{miss}} > 30\,\mathrm{GeV}$ has been applied. In addition, the requirement $\Delta\Phi(\vec{E}_{\mathrm{T}}^{\mathrm{miss}}, \vec{p}_{\mathrm{T}}^{\mathrm{miss}}) < 90°$ is applied for (a) and the requirement $\min\Delta\Phi(\vec{E}_{\mathrm{T}}^{\mathrm{miss}}, \vec{j}_{1,2,3}) > 20°$ for (b). To good approximation, the missing multijet contribution corresponds to the difference between data and the sum of the simulated background processes. The arrows indicate the applied cuts in the two variables.

p_{T} central small-R jets, j_1 and j_2, are used for building the Higgs boson candidate with the invariant mass $m_{h,\,\mathrm{cand}} = m_{j_1 j_2}$, and for the identification of the b-jets. At least one of the small-R jets making the Higgs candidate must be identified as a b-jet and the one with highest-p_{T} must satisfy $p_{\mathrm{T}} > 45\,\mathrm{GeV}$.

Further requirements are applied on the scalar sum of jet p_{T}, $H_{\mathrm{T,\,2\,(3)\,jets}}$, of up to three jets. For this, the jets are sorted by their p_{T}, with priority to central jets compared to forward jets. For events with two (three) jets, $H_{\mathrm{T,\,2\,(3)\,jets}} > 120\ (150)\,\mathrm{GeV}$ is required. This criterion targets the region of phase space which is mismodelled in Monte-Carlo simulation due to a non-trivial dependence of the $E_{\mathrm{T}}^{\mathrm{miss}}$ trigger efficiency on the jet activity [412].

The two Higgs boson candidate jets are required to have azimuthal angle differences $\Delta\phi\left(\vec{p}_h^{\,j_1}, \vec{p}_h^{\,j_2}\right) < 140°$ to ensure that the jets are in the same detector hemisphere and close to each other. In addition, the two Higgs candidate jets are required to have an angular separation of $\Delta R\left(\vec{p}_h^{\,j_1}, \vec{p}_h^{\,j_2}\right) < 1.8$, which efficiently reduces the $t\bar{t}$ background where the top quark decay products are often back-to-back produced, i.e. with a large ΔR value between the two b-jets (for details see Section C.4). To account for the back-to-back topology of the Higgs boson candidate and $E_{\mathrm{T}}^{\mathrm{miss}}$, their azimuthal angle differences $\Delta\Phi(\vec{E}_{\mathrm{T}}^{\mathrm{miss}}, \vec{p}_{\mathrm{h}})$ is required to be larger then 120°, where $\vec{p}_{\mathrm{h}}$ is the momentum vector of

the Higgs boson candidate.
Two dedicated requirements for reducing the $t\bar{t}$ background are applied. In $t\bar{t}$ events, usually two b-jets are identified from the top quark decay products, while additional b-jets can arise from the misidentification of c quark initiated jets or τ-jets from W boson decays. Hence, a veto is applied against events with three or more b-jets (see Section C.2). Moreover, in $t\bar{t}$ events, the hadronic activity is generally higher then for signal events with $h \to b\bar{b}$ decays. Therefore, if present, the highest-p_{T} additional jet must be larger than $0.37 \times H_{\mathrm{T,\ all\ jets}}$ (see Section C.3 for more details on the so-called H_{T}-ratio requirement).
The Higgs candidate mass is required to satisfy $50 \leq m_{j_1 j_2} \leq 280\,\mathrm{GeV}$ in accordance with the Higgs boson mass and jet energy resolution. Only events with one or two b-jets are selected, and the one b-jet region is used to account for inefficiencies in the b-identification. Finally, the events are grouped into three further disjoint categories of $E_{\mathrm{T}}^{\mathrm{miss}}$ to improve the signal-to-background ratio accounting for different background compositions with increasing values of $E_{\mathrm{T}}^{\mathrm{miss}}$. The three $E_{\mathrm{T}}^{\mathrm{miss}}$ categories in the resolved SR are 150 to 200 GeV, 200 to 350 GeV and 350 to 500 GeV. The separate $E_{\mathrm{T}}^{\mathrm{miss}}$ ranges allows to be sensitivity to a variety of Z'-2HDM signal models, where the $E_{\mathrm{T}}^{\mathrm{miss}}$ distribution depends on the ($m_{Z'}$, m_A) model parameters. Together with the two categories based on the b-jet multiplicity per $E_{\mathrm{T}}^{\mathrm{miss}}$ region, this results in six disjoint resolved SRs in total.

4.7.2 Merged Signal Region Selection

The events in the merged SR are required to have $E_{\mathrm{T}}^{\mathrm{miss}} \geq 500\,\mathrm{GeV}$. At least one large-$R$ jet is required with at least one ghost-associated track-jet. In contrast to the resolved SR, the b-jet identification is done with track-jets (see Section 3.3.5) and not with small-R jets. Only the two highest-p_{T} track-jets are used for the identification of the $h \to b\bar{b}$ decay, since the jets from the Higgs boson decays are expected to be high energetic [410]. In addition, this requirement suppresses the $t\bar{t}$ background where a higher track-jet multiplicity is expected, e.g. from $t \to Wb \to csb$ decays. Events with b-jets not associated to the leading large-R jet are rejected (see Section C.2). Furthermore, the scalar sum of p_{T} of all small-R jets, $H_{\mathrm{T,\ all\ jets}}$, with $\Delta R(\vec{p}_{\text{small}-R\text{ jet}}, \vec{p}_{\text{leading large}-R\text{ jet}}) > 1.0$ is required to be smaller then $0.57 \times (H_{\mathrm{T,\ all\ jets}} + p_{\mathrm{T,\ leading\ large}-R\text{ jet}})$ (see Section C.3).
Similarly as for the resolved SRs, the events are classified into two categories with either one or two b-jets, which is particularly important for events with highly boosted Higgs bosons with $p_{\mathrm{T}} > 1\,\mathrm{TeV}$. Here, the two track-jets within the large-R jet become very collimated and can overlap, such that only one b-jet is identified instead of two.
The mass of the leading large-R jet is required to be $50 \leq m_J \leq 270\,\mathrm{GeV}$, in accordance with the Higgs boson mass and the large-R jet mass resolution.

4.7.3 Results of the Signal Region Selection

In this section, the results of the event selection prior to the combined fit are summarised. The expected and observed distributions of the Higgs boson candidate mass in the SR at pre-fit level after applying all event selection criteria are shown in Fig. 4.10 and Fig. 4.11 for events with one and two b-jets, respectively. The agreement between the data and

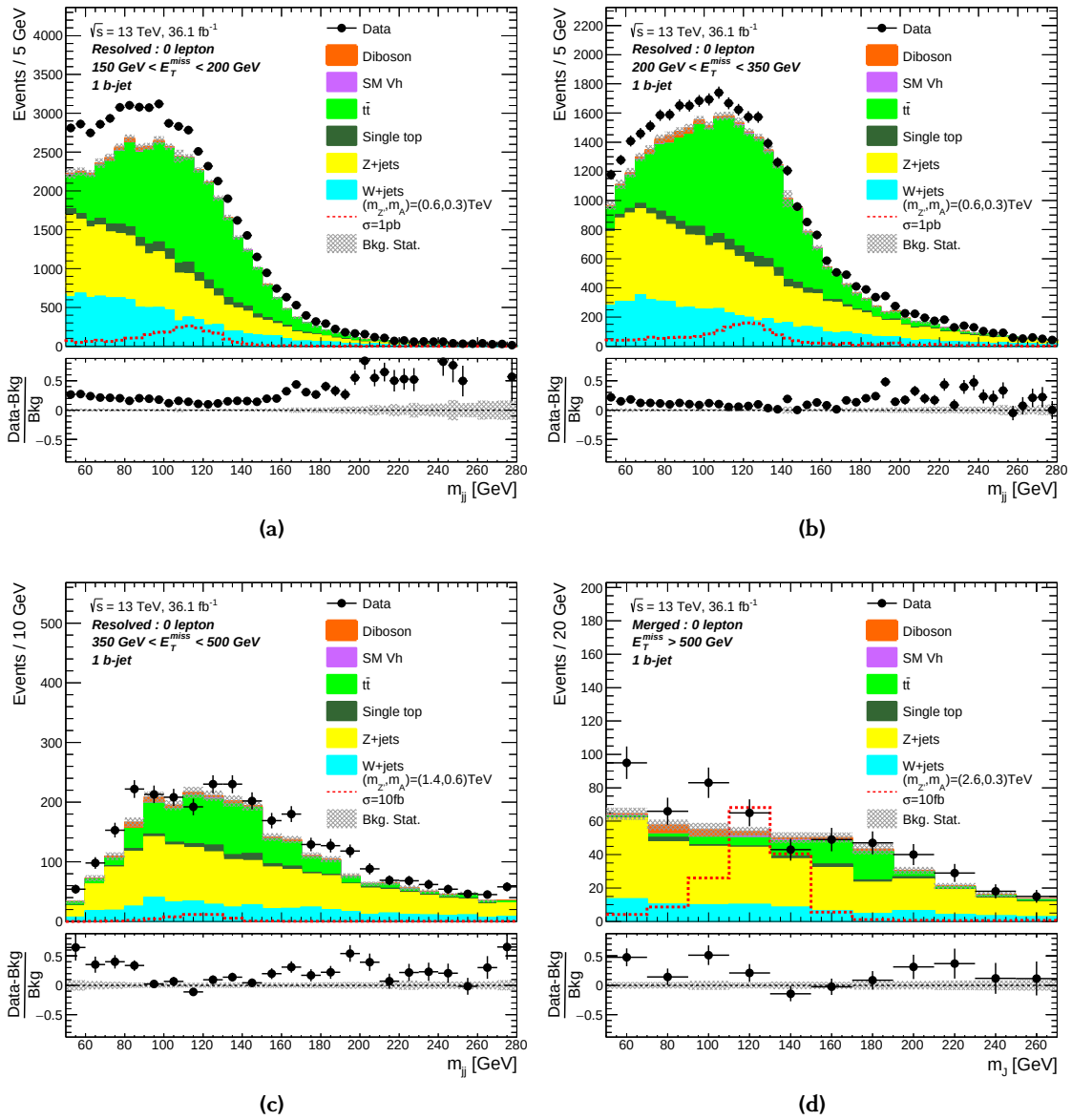

Figure 4.10: Expected and observed pre-fit distributions of the invariant mass of the Higgs boson for events with one b-jet in the four $E_{\mathrm{T}}^{\mathrm{miss}}$ categories of the signal region. The expected signal distributions are normalised to 1 pb for $(m_{Z'}, m_A) = (600\,\mathrm{GeV}, 300\,\mathrm{GeV})$ and to 10 fb for (1400 GeV, 600 GeV) and (2600 GeV, 300 GeV) for illustration.

the Monte-Carlo simulation is expected to improve once the background normalisations are adjusted within the profile-likelihood fit (see Chapter 5) and the multijet contribution is estimated. In addition, the $E_{\mathrm{T}}^{\mathrm{miss}}$ distributions at pre-fit level are shown in Fig. 4.12.

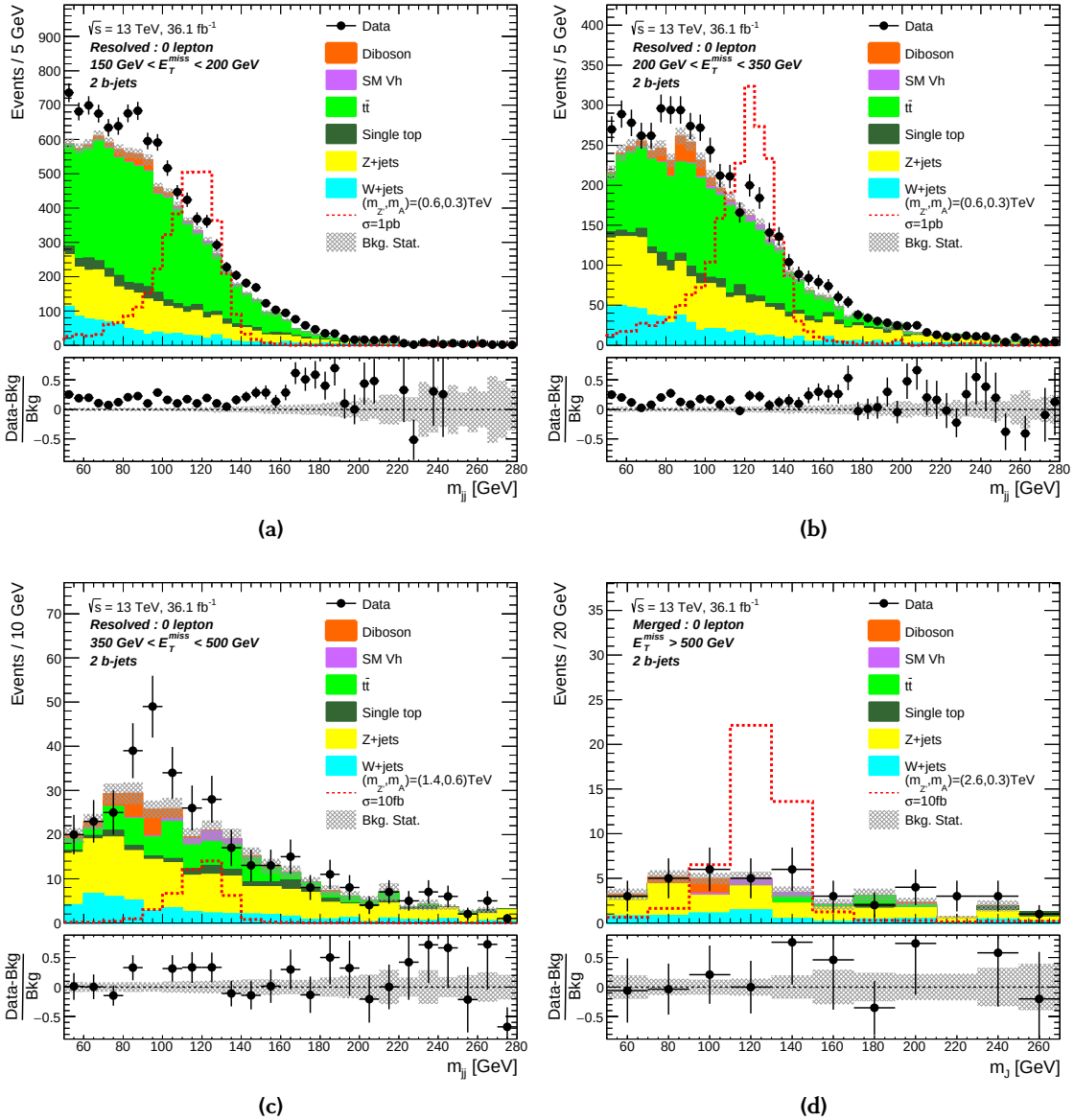

Figure 4.11: Expected and observed pre-fit distributions of the invariant mass of the Higgs boson for events with two b-jets in the four $E_{\mathrm{T}}^{\mathrm{miss}}$ categories of the signal region. The expected signal distributions are normalised to 1 pb for $(m_{Z'}, m_A) = (600\,\mathrm{GeV}, 300\,\mathrm{GeV})$ and to 10 fb for $(1400\,\mathrm{GeV}, 600\,\mathrm{GeV})$ and $(2600\,\mathrm{GeV}, 300\,\mathrm{GeV})$ for illustration.

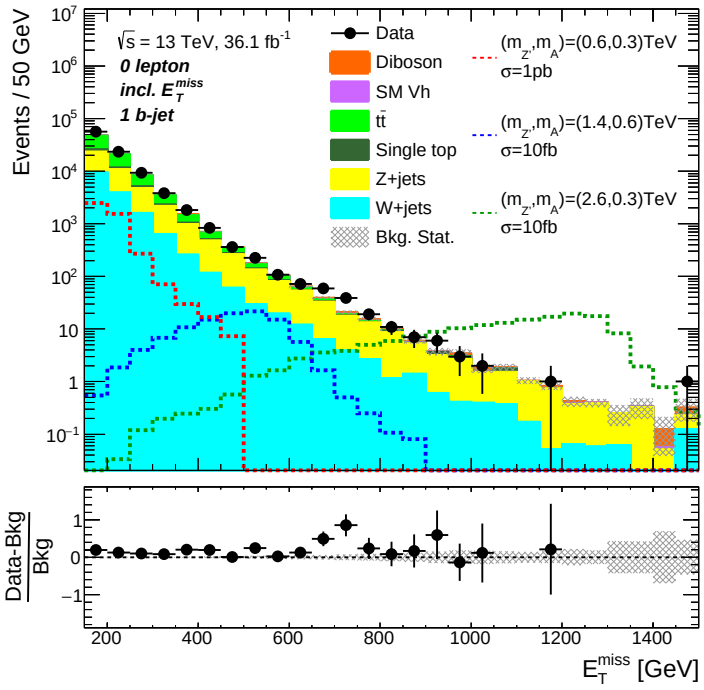

(a)

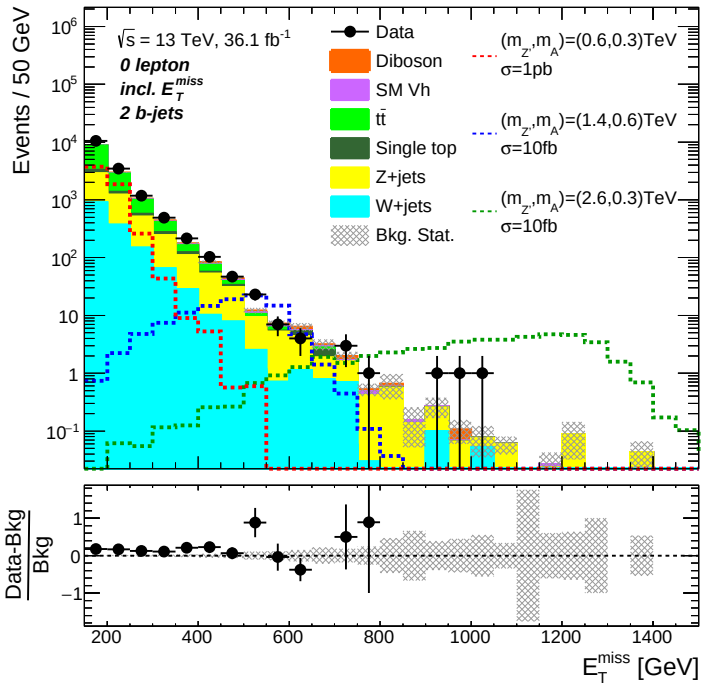

(b)

Figure 4.12: Expected and observed pre-fit distributions of $E_{\mathrm{T}}^{\mathrm{miss}}$ with (a) one and (b) two b-jets in the event in the signal region. The expected signal distributions are normalised to 1 pb for $(m_{Z'}, m_A) = (600\,\mathrm{GeV}, 300\,\mathrm{GeV})$ and to 10 fb for (1400 GeV, 600 GeV) and (2600 GeV, 300 GeV) for illustration.

4.8 Background Estimation From Control Regions

In addition to the SR (see Section 4.7), two control regions (CRs) are used for the estimation of the main backgrounds (see Section 4.3). The one-muon control region (1μ-CR) for the $t\bar{t}$ and W+jets backgrounds and the two-muon control region (2ℓ-CR) for the Z+jets background. The CRs are defined in signal-depleted regions of phase space where high purity data samples are available to constrain the background contributions in the SR. In particular, the CRs are designed by selecting disjoint sets of events based on the number of leptons and b-jets in the events and their contribution is extrapolated to the backgrounds in the SR. In addition, a dedicated multijet enriched region is defined to estimate the contribution in the SR. All SR and CRs are then used within a combined profile-likelihood fit (see Chapter 5) to extract the right normalisations of the three main backgrounds. All other backgrounds are fixed to their expectation from the Monte-Carlo simulation within assigned errors. The selection criteria in the CRs are close to ones in the SR to select kinematically similar events.

4.8.1 One-Muon Control Region

The 1μ-CR is used to constrain the normalisations of the W+jets and the $t\bar{t}$ backgrounds. Only the one-muon region is used, without selecting electrons. This allows to use the same $E_{\mathrm{T}}^{\mathrm{miss}}$ triggers (see Section 4.5.1) as in the SR. Moreover, an electron control region would require a dedicated estimate of the multijet background in the 1μ-CR, as the probability of jets faking electrons is much higher then for muons.
The 1μ-CR selects a single signal muons (see Section 4.6) produced in $W \to \mu\nu$ decays from W+jets and $t\bar{t}$ background events (see Fig. 4.7c and Fig. 4.7a, respectively), while no baseline electrons are allowed in the event. Beyond the selected muon, identical event selection criteria as for the SR are applied (see Section 4.7), except for $E_{\mathrm{T}}^{\mathrm{miss}}$ and $p_{\mathrm{T}}^{\mathrm{miss}}$. In the SR, $E_{\mathrm{T}}^{\mathrm{miss}}$ and $p_{\mathrm{T}}^{\mathrm{miss}}$ are used for the selection of signal events, while in the 1μ-CR proxies for these two variables are used. Here, the muon four-momentum is added to the four-momenta of $E_{\mathrm{T}}^{\mathrm{miss}}$ and $p_{\mathrm{T}}^{\mathrm{miss}}$ to mark the muon as invisible and to mimic the reconstructed p_{T} of the leptonically decaying W boson. The related quantities are then called $E_{\mathrm{T}}^{\mathrm{miss,\,no-}\mu}$ and $p_{\mathrm{T}}^{\mathrm{miss,\,no-}\mu}$ and their vectors are given as $\vec{E}_{\mathrm{T}}^{\mathrm{miss,\,no-}\mu}$ and $\vec{p}_{\mathrm{T}}^{\mathrm{miss,\,no-}\mu}$, respectively. In all calculations $E_{\mathrm{T}}^{\mathrm{miss}}$ and $p_{\mathrm{T}}^{\mathrm{miss}}$ are replaced by $E_{\mathrm{T}}^{\mathrm{miss,\,no-}\mu}$ and $p_{\mathrm{T}}^{\mathrm{miss,\,no-}\mu}$ and analogous their vectors, i.e. for the calculation of the anti-QCD sensitive variables (see Table 4.4). As in the SR, the events in the 1μ-CR are categorised into two b-jet regions and into four $E_{\mathrm{T}}^{\mathrm{miss,\,no-}\mu}$ categories. The $E_{\mathrm{T}}^{\mathrm{miss,\,no-}\mu}$ distributions are shown in Fig. 4.13.
The selection criteria used in the 1μ-CR are summarised in Table 4.4. In the 1μ-CR, the electric charge of the muon is used as the variable of interest entering the fit, which

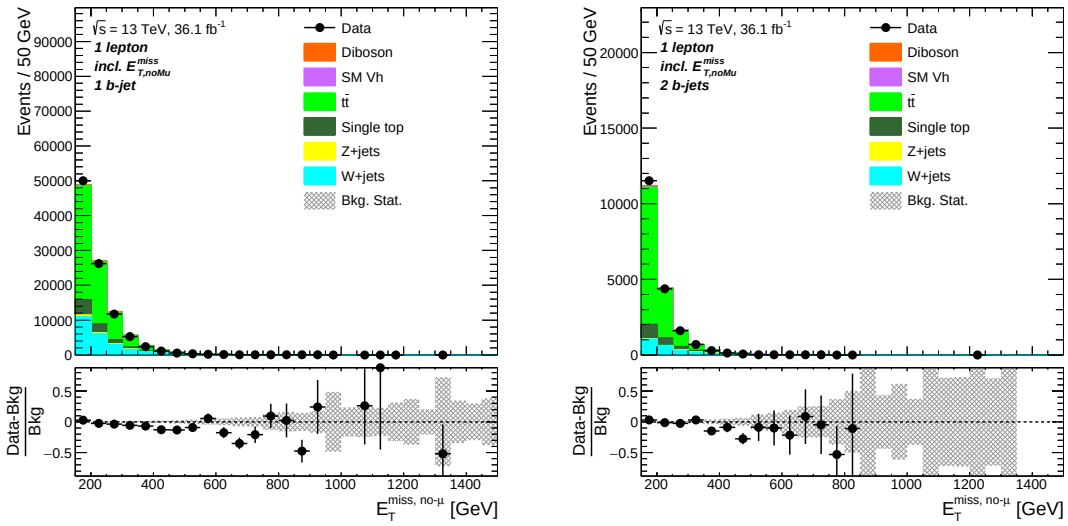

Figure 4.13: Distributions of $E_{\mathrm{T}}^{\mathrm{miss,\,no-}\mu}$ after the full 1μ-CR selection for events with (a) one and (b) two b-jets.

provides a better separation between the $t\bar{t}$ and the W+jets backgrounds compared to the Higgs boson candidate mass used in the SR. In addition, the two bins of the muon charge are sufficient to precisely predict the normalisations of the two backgrounds and no shape information about the $m_{h,\,\mathrm{cand}}$ distribution is required. The $t\bar{t}$ process provides an equal number of μ^+ and μ^- events, while for the W+jets process a prevalence of μ^+ over μ^- is expected from the proton PDFs [413] at the LHC. This charge asymmetry is directly related to the dominance of u quarks compared to d quarks in the protons. Valence u quarks interacting with sea $\bar{d}$ quarks produce within the pp collision the majority of W^++jets events, while valence d quarks interacting with sea $\bar{u}$ quarks produce most of the W^-+jets events. From the measurement of the W^+/W^- production cross section ratio in association with jets, the charge asymmetry in W+jets events is expected to be around 1.5 to 2.0 [414] depending on the jet multiplicity in the event, which is also seen in the 1μ-CR. The muon charge distribution is shown in Fig. 4.14 after applying the full 1μ-CR event selection independent of the $E_{\mathrm{T}}^{\mathrm{miss,\,no-}\mu}$ range. Here, the same amount of μ^- and μ^+ events are selected for the case of the $t\bar{t}$ process as expected, while for the W+jets process a prevalence of μ^+ events is found as expected. Overall, the data is very well described by the Monte-Carlo simulation. The Higgs boson candidate mass is illustrated in Appendix D. The purity of the Monte-Carlo templates in the 1μ-CR is given in Table 4.5. The purity of the $t\bar{t}$ template is in general higher for the two b-jet category and decreases with increasing $E_{\mathrm{T}}^{\mathrm{miss,\,no-}\mu}$. In contrast, the contribution of W+jets events increases with increasing $E_{\mathrm{T}}^{\mathrm{miss,\,no-}\mu}$ and dominates in the merged region. Similarly, for

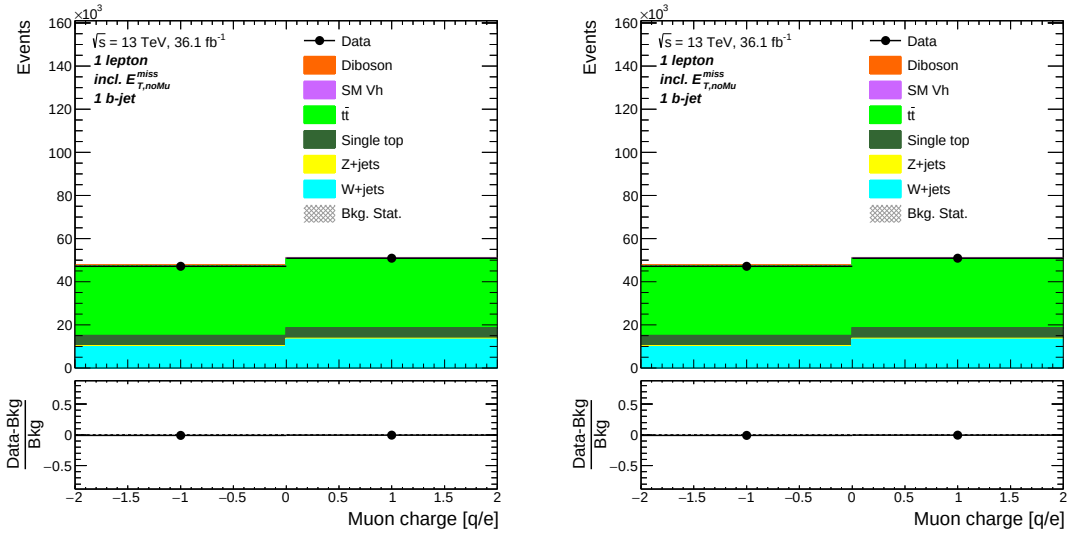

Figure 4.14: The signal muon charge after the full 1μ-CR selection for events with (a) one and (b) two b-jets.

Table 4.5: Fraction of total background events of the Monte-Carlo prediction per process in [%] in the 1μ-CR for events with one and two b-jets. Only processes with a contribution of more then 1% to the total background are given.

		Range in $E_{\mathrm{T}}^{\mathrm{miss,\,no-}\mu}$ [GeV]			
		[150, 200)	[200, 350)	[350, 500)	[500, ∞)
One b-jet	$t\bar{t}$	67	65	55	40
	Z+jets	1.1	—	—	—
	W+jets	22	23	30	42
	single-t	9.1	9.3	12	14
	Diboson	—	—	—	2.1
Two b-jets	$t\bar{t}$	81	70	42	28
	W+jets	9.1	15	27	40
	single-t	8.0	12	26	25
	Diboson	—	—	1.8	3.2
	SM $Vh(b\bar{b})$	—	—	1.1	3.2

increasing $E_{\mathrm{T}}^{\mathrm{miss,\,no-}\mu}$ also the contribution of the single top quark production increases, and has especially in the two b-jet region a large contribution of around 26 % of the total background. The contributions of the Z+jets, diboson and SM $Vh(b\bar{b})$ processes are small and in total below 6 %. Before applying the profile-likelihood fit, the W+jets Monte-Carlo sample is splitted into two templates, a heavy-flavour and a light-flavour

jet template, based on the parton-level jet flavour of the two Higgs boson candidate jets (see Appendix E).

4.8.2 Two-Lepton Control Region

The 2ℓ-CR is used to estimate the $Z(\rightarrow \nu\nu)$+jets background in the SR by selecting $Z(\rightarrow \ell^+\ell^-)$+jets events with $\ell = e, \mu$. The Z boson has for both final states the identical decay topology. In case of Z decays into a pair of charged leptons, the transverse momentum of the Z boson, $p_{\mathrm{T}}^{\ell\ell}$, is reconstructed from the two leptons, while for the Z decay into neutrinos its momentum is approximated by $E_{\mathrm{T}}^{\mathrm{miss}}$. Hence, in the 2ℓ-CR $p_{\mathrm{T}}^{\ell\ell}$ is used instead of $E_{\mathrm{T}}^{\mathrm{miss}}$ for the selection of events and for the event categories. In the 2ℓ-CR the non-collision background is expected to be small and, therefore, $p_{\mathrm{T}}^{\mathrm{miss}}$ is not used.

The dilepton events are selected by requiring the lowest single-lepton trigger (see Section 4.5.2). Furthermore, either two high-p_{T} baseline electrons or muons are required, with no additional low-p_{T} baseline leptons in the event (see Section 4.6). The two muons are required to have opposite charge, while this is not required for the electrons due to their higher rate of charge misidentification. The electron (muon) pairs are required to have an invariant mass around the Z boson mass of $83 < m_{ee} < 99\,\mathrm{GeV}$ ($71 < m_{\mu\mu} < 106\,\mathrm{GeV}$). This requirement suppresses processes having a non-resonant produced lepton-pair, i.e. dileptonic $t\bar{t}$ events. The invariant dimuon and dielectron mass distributions are shown in Fig. 4.15a and Fig. 4.15b, respectively. In both cases, good agreement between the data and the Monte-Carlo prediction is found. The amount of ee and $\mu\mu$ events is approximately the same within statistical uncertainties. In order to improve the purity of the $Z(\rightarrow \ell^+\ell^-)$+jets sample by reducing the $t\bar{t}$ background, a requirement on the so-called $E_{\mathrm{T}}^{\mathrm{miss}}$-*significance* is applied, which is defined as

$$\frac{E_{\mathrm{T}}^{\mathrm{miss}}}{\sqrt{H_{\mathrm{T}}}} \quad , \tag{4.1}$$

with H_{T} the scalar sum of transverse momenta of all small-R jets in the event and of the two leptons, and $E_{\mathrm{T}}^{\mathrm{miss}}$ the missing transverse energy in the event (in this case not $p_{\mathrm{T}}^{\ell\ell}$). The distribution of the $E_{\mathrm{T}}^{\mathrm{miss}}$-significance variable is illustrated in Fig. 4.16. The $E_{\mathrm{T}}^{\mathrm{miss}}$-significance is required to be less than $3.5\sqrt{\mathrm{GeV}}$. The $E_{\mathrm{T}}^{\mathrm{miss}}$-significance requirement reduces the $t\bar{t}$ background by around 50 to 65 %, while the other backgrounds are only marginally reduced.

The purity of $Z+$jets events in the 2ℓ-CR is given in Table 4.6. In the one b-jet resolved 2ℓ-CR, the purity of the $Z+$jets background is above 92 %, while in the two b-jet category it is above 80 % with increased contributions from the diboson, $t\bar{t}$ and $Vh(\rightarrow b\bar{b})$ backgrounds depending on the $E_{\mathrm{T}}^{\mathrm{miss}}$ range.

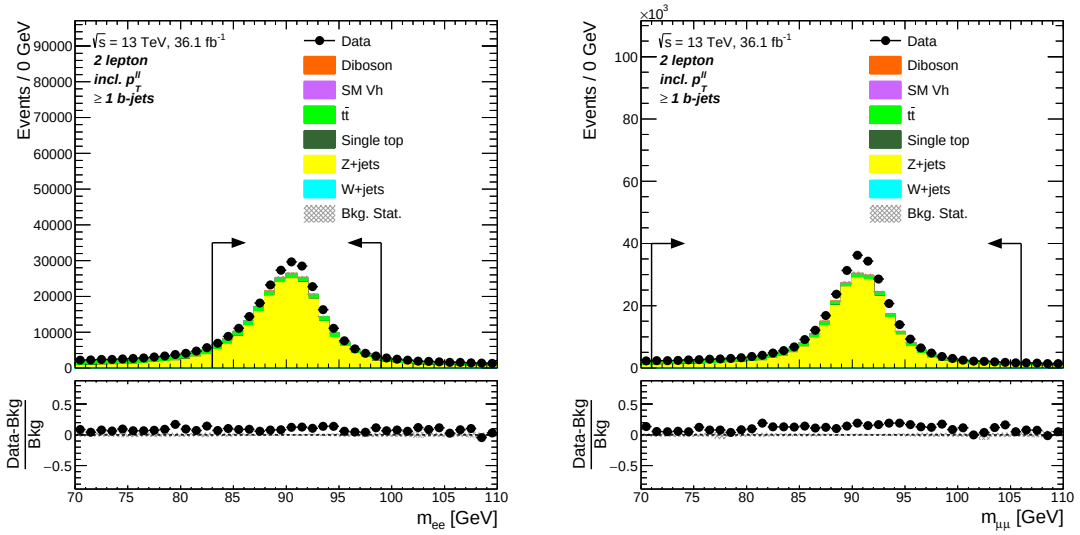

Figure 4.15: Distributions of the invariant dilepton mass in the 2ℓ-CR for (a) the ee and (b) the $\mu\mu$ final state both inclusive in the number of b-jets and in $p_{\mathrm{T}}^{\ell\ell}$.

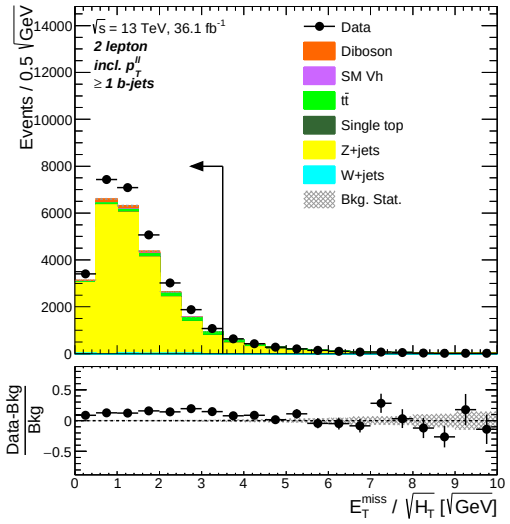

Figure 4.16: Distribution of the $E_{\mathrm{T}}^{\mathrm{miss}}$-significance in the 2ℓ-CR inclusively in the number of b-jets and $p_{\mathrm{T}}^{\ell\ell}$.

In contrast to the SR and the 1μ-CR, the common selection criteria (see Table 4.4) are not applied in the 2ℓ-CR. Especially no anti-QCD requirements are applied, due to the absence of multijet events when two isolated high-p_{T} leptons are selected.
The 2ℓ-CR events are split into two regions based on the number of b-jets and into four regions of $p_{\mathrm{T}}^{\ell\ell}$. The distributions of $p_{\mathrm{T}}^{\ell\ell}$ are shown in Fig. 4.17a and Fig. 4.17b for events with one and two b-jets, respectively.

Table 4.6: Fraction of total background events of the Monte-Carlo prediction per process in [%] in the 2ℓ-CR for events with one and two b-jets. Only processes with a contribution of more then 1% to the total background are given.

		Range in $p_{\mathrm{T}}^{\ell\ell}$ [GeV]			
		[150, 200)	[200, 350)	[350, 500)	[500, ∞)
One b-jet	$t\bar{t}$	2.9	1.3	0.44	0.30
	Z+jets	94	95	95	92
	Diboson	2.3	3.1	4.3	7.0
	SM $Vh(b\bar{b})$	0.20	0.30	0.48	0.60
Two b-jets	$t\bar{t}$	10	3.1	2.4	—
	Z+jets	82	86	84	80
	Diboson	6.0	8.0	10	14
	SM $Vh(b\bar{b})$	1.6	2.5	2.9	5.8

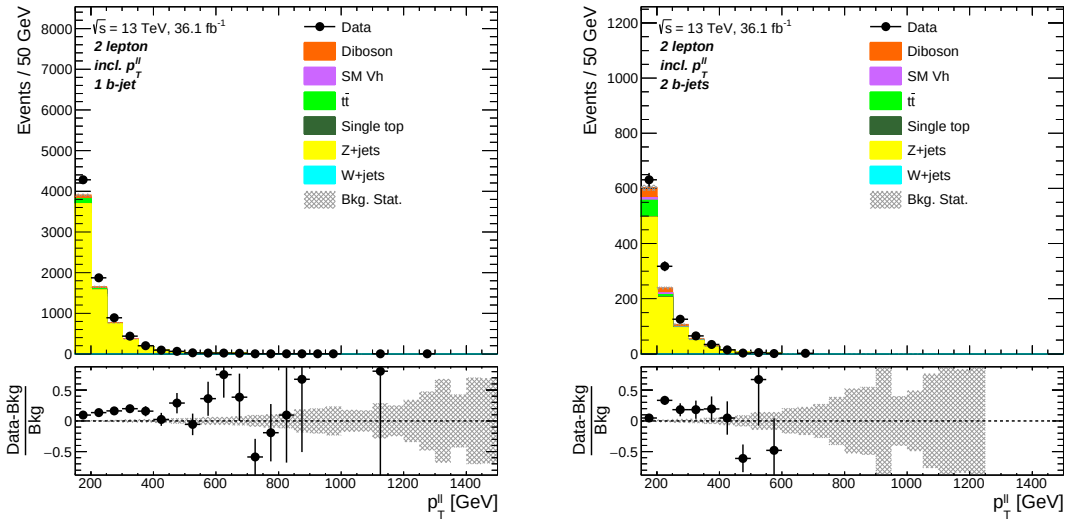

Figure 4.17: Distributions of $p_{\mathrm{T}}^{\ell\ell}$ after applying the full 2ℓ-CR event selection for events with (a) one and (b) two b-jets.

The 2ℓ-CR selection criteria are summarised in Table 4.4. As for the W+jets sample in the 1μ-CR, the Z+jets Monte-Carlo template is splitted into two sub-templates depending on the parton-level jet flavour of the two Higgs candidate jets (see Appendix E).

4.8.3 Data Driven Multijet Background Estimation

At the LHC an overwhelming large multijet background is present. Usually, in such multijet events no real $E_{\mathrm{T}}^{\mathrm{miss}}$ is present, e.g. from neutrinos or Dark Matter particles. Instead, $E_{\mathrm{T}}^{\mathrm{miss}}$ mostly originates from reconstruction effects of jets and their association energies, such that $\vec{E}_{\mathrm{T}}^{\mathrm{miss}}$ often points into the same direction as a jet. To a small amount, multijet events with real $E_{\mathrm{T}}^{\mathrm{miss}}$ can originate from jets with semileptonic heavy-flavour hadron decays where neutrinos are produced.
In the mono-Higgs ($b\bar{b}$) analysis, the multijet background is already efficiently reduced by requiring $E_{\mathrm{T}}^{\mathrm{miss}} > 150\,\mathrm{GeV}$. In addition, the anti-QCD requirements (see Section 4.7) further reduce the background. Nevertheless, the multijet background in the resolved SR is estimated in a data driven approach by using a so-called *template method*, to ensure that the background is indeed at a very small level compared to the total background. In both control regions, the multijet background is not estimated and its contribution is neglected.
Templates of the Higgs candidate mass and of $E_{\mathrm{T}}^{\mathrm{miss}}$ are used in the profile-likelihood fit for the extraction of the the signal sensitivity. The multijet background in the resolved SR is estimated separately for each of the three $E_{\mathrm{T}}^{\mathrm{miss}}$ ranges and for the two b-jet categories. A so-called *multijet region* is defined, where the multijet background is expected to be enriched, i.e. by inverting one of the anti-QCD requirements, namely $\min \Delta\Phi(\vec{E}_{\mathrm{T}}^{\mathrm{miss}}, \vec{j}_{1,\,2,\,3}) < 20°$. This region is highly dominated by multijet background events, as illustrated in Fig. 4.9a, where the multijet contribution is approximated by the difference between the data and all Standard Model backgrounds. The events in the region of $\min \Delta\Phi(\vec{E}_{\mathrm{T}}^{\mathrm{miss}}, \vec{j}_{1,\,2,\,3}) < 20°$ are used to model the shape of the $m_{h,\,\mathrm{cand}}$ distribution by taking the difference between the data and the simulated backgrounds. The derived $m_{h,\,\mathrm{cand}}$ templates of the multijet background have to be correctly normalised for every $E_{\mathrm{T}}^{\mathrm{miss}}$ range. This is done by using a second variable, the multiplicity of jets which have a muon in their vicinity, i.e. a muon within the cone of the jet $\Delta R\left(\vec{p}_{\mathrm{jet}}, \vec{p}_{\mathrm{muon}}\right) < 0.4$. Here, the muon originates from heavy-flavour hadron decays and is accompanied by neutrinos, and, therefore, real $E_{\mathrm{T}}^{\mathrm{miss}}$. The multijet template normalisations are extracted by fitting the distribution of jets with a close-by muon to data, where all non-multijet templates are allowed to float independently within their theoretical uncertainties. Finally, the multijet contribution to the total background is at most of the order of 2 % in the lowest $E_{\mathrm{T}}^{\mathrm{miss}}$ range. An additional normalisation uncertainty of 100 % is assigned to the multijet background, which is propagated as a nuisance parameter into the final profile-likelihood fit (see Chapter 5). For more details on the multijet background estimation see Appendix F.

Chapter 5

Results of the Mono-Higgs ($b\bar{b}$) Search

This Chapter summarises the results of the mono-Higgs ($b\bar{b}$) search (see Chapter 4). First, the statistical model is introduced in Section 5.1. The systematic uncertainties taken into account in the statistical model as nuisance parameters are discussed in Section 5.2. The final results of the mono-Higgs ($b\bar{b}$) search based on 36 fb^{-1} of data are discussed in in Section 5.3. The interpretation of the results in terms of upper cross section limits for the simplified Z'-2HDM model are given in Section 5.3.2.

5.1 Statistical Interpretation

The interpretation of the selected signal and background data is performed using a profile-likelihood fit of signal and background to data following Ref. [415]. The different disjoint categories depending on lepton and b-jet multiplicities and $E_{\mathrm{T}}^{\mathrm{miss}}$, and signal and control regions are combined and exclusion limits are determined in the absence of significant deviations from the Standard Model expectation (see Refs. [416–419]).
Signal predictions are derived from the Z'-2HDM model for different ($m_{Z'}$, m_A) mass points. The Higgs boson candidate mass, $m_{h,\,\mathrm{cand}}$, is used as a discriminating variable in the fit, together with four $E_{\mathrm{T}}^{\mathrm{miss}}$ bins comprising three resolved regions and one merged region.

5.1.1 Statistical Model

The statistical model uses a binned profile-likelihood fit [420] to histograms of $m_{h,\,\mathrm{cand}}$ and $E_{\mathrm{T}}^{\mathrm{miss}}$ with the likelihood function

$$\begin{aligned}\mathcal{L}(\mu,\,\vec{\theta}) \quad = \quad & \prod_{b=1}^{N_{\mathrm{bins}}} \mathcal{P}\left(n_b^{\mathrm{obs}} | \mu N_b^{\mathrm{sig}}(\theta) + N_b^{\mathrm{bkg}}(\vec{\theta})\right) \quad \times \\ & \prod_{\theta_i,\,\theta_j \in \vec{\theta},\, i<j} \mathcal{N}(\theta_i | \bar{\theta}_i,\,\sigma_{\theta_i}) \times \mathcal{LN}(\theta_j | \bar{\theta}_j,\,\sigma_{\theta_j}) \quad ,\end{aligned} \tag{5.1}$$

which is the product of the Poisson probabilities for the different bins. In Eq. (5.1), n_b^{obs} is the number of data events, N_b^{sig} and N_b^{bkg} are the numbers of expected signal and background events, respectively, in each of N_{bins} bins of all regions and categories. Moreover, μ is the signal strength parameter of interest (POI), common to all regions and defined as the ratio of measured to expected signal cross section. A zero signal strength corresponds to the background-only hypothesis and $\mu = 1$ to the signal+background hypothesis with the signal contribution as predicted by the Z'-2HDM signal model for given values of $m_{Z'}$ and m_A.
The signal and background predictions, N_b^{sig} and N_b^{bkg}, are affected by systematic uncertainties (see Section 5.2), which are taken into account in the fit as nuisance parameters (NPs), $\vec{\theta} = (\theta_i)$. N_b^{sig} and N_b^{bkg} depend on one NP θ_i for each systematic uncertainty. The probability density distributions of the nuisance parameters are normal distributions constraining the NPs to their nominal values within the corresponding systematic uncertainties. $\bar{\theta}_i$ is the mean and σ_{θ_i} the width of the distribution of the nuisance parameter θ_i. The normal distribution, $\mathcal{N}$, is multiplied with a log-normal, $\mathcal{LN}$, distribution in Eq. (5.1) to avoid negative probabilities from normalisation uncertainties. The log-normal distribution describes a random variable whose logarithm follows a normal distribution [419] (see Section G.1).
The compatibility of the data with a hypothetical Z'-2HDM signal and on the Standard Model background is tested using the profile likelihood ratio

$$\lambda(\mu) = \frac{\mathcal{L}(\mu\,, \hat{\hat{\vec{\theta}}})}{\mathcal{L}(\hat{\mu}\,, \hat{\vec{\theta}})} \quad , \tag{5.2}$$

of the two likelihood functions $\mathcal{L}(\mu, \hat{\hat{\vec{\theta}}})$ and $\mathcal{L}(\hat{\mu}, \hat{\vec{\theta}})$, where $\mathcal{L}(\mu\,, \hat{\hat{\vec{\theta}}})$ is maximised over all nuisance parameters for given μ, while the denominator, $\mathcal{L}(\hat{\mu}\,, \hat{\vec{\theta}})$, is maximised over all parameters including μ. $\hat{\mu}$ and $\hat{\vec{\theta}}$ are the *maximum likelihood estimators* of μ and $\vec{\theta}$ which maximise $\mathcal{L}(\hat{\mu}, \hat{\vec{\theta}})$, and $\hat{\hat{\vec{\theta}}}$ is the *conditional maximum likelihood estimator* of $\vec{\theta}$ which maximises the numerator in Eq. (5.2) under the condition of a given μ.
The null hypothesis can be either the background-only ($\mu = 0$) or the signal+background ($\mu > 0$) hypothesis depending on whether the significance of a potential signal or exclusion limits are to be evaluated. Different test statistics are defined based on Eq. (5.2) for the two cases. A possible excess of events above the expected Standard Model background is attributed a certain statistical significance if the background-only hypothesis

can be rejected with a corresponding probability. The test statistic is defined as

$$q_0 = \begin{cases} -2\ln\lambda(0) & \text{for } \hat{\mu} \geq 0 \quad \text{and} \\ 0 & \text{for } \hat{\mu} < 0 \quad . \end{cases} \tag{5.3}$$

$\hat{\mu} < 0$ is possible due to statistical fluctuations or systematic uncertainties. Agreement between data and background prediction, i.e. confirmation of the background-only hypothesis, corresponds to a small observed value of the test statistic q_0^{obs}, while in the case of an excess above the background the test statistics q_0^{obs} is large. The agreement between data and background is quantified by the *local* p_0*-value*, defined as

$$p_0 = \int_{q_0^{\text{obs}}}^{\infty} f(q_0|0)\mathrm{d}q_0 \quad , \tag{5.4}$$

where $f(q_0|0)$ is the probability density function of q_0. The local p_0-value gives the probability of falsely rejecting the background-only hypothesis although it is true. It is usually expressed as the statistical significance of the excess in numbers of standard deviations, Z, according to the relation

$$Z = \Phi^{-1}(1 - p_0) \tag{5.5}$$

where Φ^{-1} is the inverse of the cumulative probability distribution function of a normal distribution (see Fig. 5.1). A significance of $Z = 3$, corresponding to a p_0-value of $1.5 \cdot 10^{-3}$,

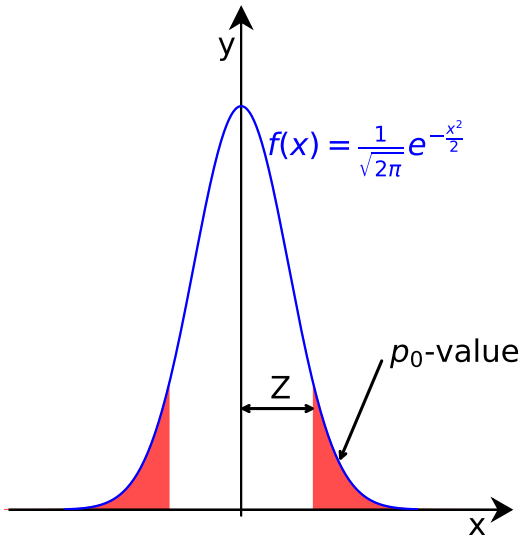

Figure 5.1: Definition of the signal significance Z from the local p_0-value assuming a normal Gaussian probability density function for the test statistic q_0.

is usually taken as evidence for a signal. For a discovery a significance of at least $Z = 5$,

corresponding to a p_0-value of $2.9 \cdot 10^{-7}$, usually is required.
For the determination of exclusion limits, the signal+background hypothesis is tested using the test statistics

$$\tilde{q}_\mu = \begin{cases} -2\ln\frac{\mathcal{L}(\mu,\hat{\hat{\vec{\theta}}}(\mu))}{\mathcal{L}(0,\hat{\hat{\vec{\theta}}}(0))} & \text{for } \hat{\mu} < 0 \quad , \\ -2\ln\frac{\mathcal{L}(\mu,\hat{\hat{\vec{\theta}}}(\mu))}{\mathcal{L}(\hat{\mu},\hat{\vec{\theta}})} & \text{for } 0 \leq \hat{\mu} \leq \mu \quad \text{and,} \\ 0 & \text{for } \hat{\mu} > \mu \quad . \end{cases} \tag{5.6}$$

resulting in small (large) values in case of high (low) compatibility of the data with the signal+background hypothesis. The requirement $\hat{\mu} \leq \mu$ prevents that an excess in the data is considered incompatible with the signal+background hypothesis. In order to set limits on μ, the p_μ-value

$$p_\mu = \int_{\tilde{q}_\mu^{\text{obs}}}^{\infty} f(\tilde{q}_\mu|\mu)\mathrm{d}\tilde{q}_\mu \quad , \tag{5.7}$$

is defined for the signal+background (null) hypothesis with $f(\tilde{q}_\mu|\mu)$ the probability density function of $\tilde{q}_\mu$ for given μ of finding the probability $\tilde{q}_\mu \geq \tilde{q}_\mu^{\text{obs}}$. The 95 % confidence level (CL) upper limit on μ is determined iteratively as the largest value for which $1 - p_\mu$ is less then 95 %.
The expected number mono-Higgs ($b\bar{b}$) signal events is rather small compared to the number of background events. To avoid excluding the signal hypothesis for small sensitivity (see the discussion in Ref. [421]), a modified frequentist method, the CL_s method [422] is used which combines the conditional probability

$$p_b = \int_{-\infty}^{\tilde{q}_\mu^{\text{obs}}} f(\tilde{q}_\mu|0)\,\mathrm{d}\tilde{q}_\mu \quad , \tag{5.8}$$

for the alternative background-only hypothesis, with the p_μ-value for the signal+background (null) hypothesis in Eq. (5.7) to the $p_\mu^{\text{CL}_\text{s}}$-value

$$p_\mu^{\text{CL}_\text{s}} = \frac{p_\mu}{1 - p_b} \quad . \tag{5.9}$$

The 95 % upper limit on the signal strength is calculated in the CL_s approach, using the asymptotic approximation of $p_\mu^{\text{CL}_\text{s}}$ [415, 423, 424] in the limit of a large sample with the largest value of μ for which $1 - p_\mu^{\text{CL}_\text{s}}$ is smaller then 95 %. Note that in contrast to the LHC limits, direct Dark Matter detection experiments use 90 % CL upper limits on the Dark Matter-nucleon cross section. For the calculation of the expected sensitivity, toy Monte-Carlo events are used in the so-called *Asimov approach* [415], which avoids the need for a large number of Monte-Carlo datasets for the estimation of the test

statistic distribution, $p_\mu^{\mathrm{CL_s}}$, and, therefore, a single Monte-Carlo dataset is chosen instead as reference data.

5.1.2 Fitted Distributions

The Z'-2HDM signal model describes a resonance in the Higgs candidate mass spectrum around $m_{h,\,\mathrm{cand}} = 125\,\mathrm{GeV}$. The sidebands of the mass peak are used to constrain the backgrounds and reduce the systematic uncertainties. The different event categories and $m_{h,\,\mathrm{cand}}$ ranges in the profile-likelihood fit are summarised in Table 5.1.

Table 5.1: Event categories entering the combined profile-likelihood fit. The signal discriminating variable in the fit is the Higgs boson candidate mass, $m_{h,\,\mathrm{cand}}$, which is either the invariant dijet mass, m_{jj}, in the resolved region or the mass of the leading large-R jet, m_J, in the merged region.

	Regions	**Signal region**	**1μ−CR**	**2ℓ−CR**
Discriminating variables	b-jet multiplicity	one or two		
	$E_{\mathrm{T}}^{\mathrm{miss}}$	$E_{\mathrm{T}}^{\mathrm{miss}}$	$E_{\mathrm{T}}^{\mathrm{miss,\,no-}\mu}$	$p_{\mathrm{T}}^{\ell\ell}$
		[150, 200), [200, 350), [350, 500), [500, ∞) GeV		
	Muon charge	—	$+1\,/\,-1$	—
	$m_{h,\,\mathrm{cand}}$	$m_{h,\,\mathrm{cand}}$ distribution	$m_{h,\,\mathrm{cand}}$ normalisation	
		$m_{jj} \in [50, 280]$ GeV (resolved)		
		$m_J \in [50, 270]$ GeV (merged)		

In the SR, equidistant binnings of $m_{h,\,\mathrm{cand}}$ are used, where the number of bins is chosen to be relatively large for high statistics in the three resolved categories and small in the rather low statistics in the merged category distinguished by $E_{\mathrm{T}}^{\mathrm{miss}}$ ranges. For the $m_{h,\,\mathrm{cand}}$ distribution in the $E_{\mathrm{T}}^{\mathrm{miss}}$ regions [150, 200) GeV and [200, 350) GeV a bin width of 5 GeV is used. For regions with higher $E_{\mathrm{T}}^{\mathrm{miss}}$ and, thus, lower statistics coarser binning is used, namely for $E_{\mathrm{T}}^{\mathrm{miss}} \in [350, 500)$ GeV and $[500, \infty)$ GeV, respectively, 10 and 20 GeV bin width.

In the 1μ-CR, separate categories with positive and negative muon charge are used in order to separate $t\bar{t}$ from W+jets events, as for the latter μ^+ events are more frequent then μ^- events in pp collisions, while in $t\bar{t}$ events both charges are equally frequent. Information about the Higgs boson candidate mass distribution is not used in the 1μ-CR and in the 2ℓ-CR for relative normalisation to the SR. In the latter case, the number of events in the whole $m_{h,\,\mathrm{cand}}$ range is used. Resulting in two bins of muon charge and one bin of $m_{h,\,\mathrm{cand}}$ for the 1μ-CR and 2ℓ-CR, respectively, per $E_{\mathrm{T}}^{\mathrm{miss}}$ range.

The events are split into regions with one and with two b-jets accounting for the different background compositions. The one-b-jet region in the 1μ-CR targets mostly W+jets events, while the two-b-jet region selects mostly $t\bar{t}$ events. In addition, the

category with one b-jet targets signal models with very high $E_{\mathrm{T}}^{\mathrm{miss}}$ and thus strongly boosted Higgs boson decays with overlapping b-jets.

5.2 Systematic Uncertainties and Nuisance Parameters

In general, the mono-Higgs ($b\bar{b}$) search is affected by two sources of uncertainties: the statistical uncertainty on the data, and the systematic uncertainty related to the detector response to the final state particles and from uncertainties in the theoretical predictions. The systematic uncertainties can influence the Monte-Carlo event yields and the shape of distributions, in particular of $m_{h,\,\mathrm{cand}}$ and of $E_{\mathrm{T}}^{\mathrm{miss}}$.
Experimental systematic uncertainties are discussed in Section 5.2.1 and uncertainties from Monte-Carlo predictions are given in Sections 5.2.3 and 5.2.2 for signal and background processes, respectively. In the final profile-likelihood fit, all uncertainties are incorporated as nuisance parameter (see Section 5.2.4). The impact of the different systematic uncertainties on the final results are evaluated in Section 5.3.1.

5.2.1 Experimental Systematic Uncertainties

A summary of all systematic uncertainties considered in the mono-Higgs ($b\bar{b}$) analysis is given in Table 5.2.

Luminosity and Pile-up
The uncertainty on the luminosity of 36.1 fb^{-1} recorded during 2015 and 2016 is 3.2 %, measured by using the methods discussed in Section 3.2.7.
Systematic uncertainties accounting for changing pile-up conditions during 2015 and 2016 are considered as well. A reweighting procedure is applied to Monte-Carlo simulated events to match the conditions in data. The uncertainties originated from the modelling of pile-up events, including uncertainties on the pp inelastic cross section. The total pile-up related uncertainty is of the order of 6 % based on a measurement done in Run 1 [339].

Electrons
Electrons are either used indirectly and vetoed in the SR and the 1μ-CR, or electron pairs are selected in the 2ℓ-CR. In the 2ℓ-CR, events are triggered by single lepton triggers. Thus, corrections and systematic uncertainties accounting for inefficiencies in the single electron triggers are applied. Furthermore, uncertainties related to the efficiency of the electron reconstruction, the identification and the isolation are used as well, which all affect the observed event yields. While, uncertainties related to the electron energy scale and resolution affect the electron kinematics and, therefore, the shape of distributions, i.e. of the $p_{\mathrm{T}}^{\ell\ell}$ distribution.

Muons

Similarly as for the case of electrons, muons are also associated with uncertainties related to the single muon trigger in the 2ℓ-CR. Moreover, the reconstruction and isolation efficiency uncertainties, as well as uncertainties of the track-to-vertex association are also used. The muon kinematics are affected by three systematics related to the momentum scale, and two for the momentum resolution measured separately in the inner detector and the muon spectrometer.

Small$-R$ Jets

Experimental uncertainties on small-R jets are related to the jet energy scale and resolution originating from the in-situ calibrations (see Section 3.3.4.1). A set of three nuisance parameters is considered for the jet energy scale, while a single nuisance parameter is used for the description of the variations on the jet energy resolution. For the small-R jet calibration, an uncertainty due to a non-closure effect of the jet response in the region of $2.4 < |\eta| < 2.5$ is considered.

Large$-R$ Jets

Uncertainties on the large-R jet (see Section 3.3.4.2) mass and energy resolution are considered as nuisance parameters in the profile-likelihood fit. Additionally, uncertainties on the mass and p_{T} scale are used as nuisance parameters. The scale uncertainties are parametrised as four components, where one accounts for the difference between the data and the predictions of `PYTHIA 8` and one due to the statistical uncertainty on the measurement. The difference in the jet energy scale found when using an alternative Monte-Carlo generators is assigned with an additional uncertainty. The fourth uncertainty is related to the track reconstruction efficiency, which impacts the combined jet mass.

Small$-R$ Jets and Track-Jet Flavour Tagging

The uncertainties on the b-jet identification efficiency of small-R jets and track-jets (see Section 3.3.5) are evaluated separately for b-, c- and light-flavour jets. The systematic uncertainties are treated as uncorrelated for the two types of jets. The uncertainties on the b-jet scale factors are parametrised as three nuisance parameters, while for the c-jets and the light-flavour jets four and five, respectively, parameters are used. Two additional uncertainties related to scale factor extrapolations on high-p_{T} jets (above 300 GeV), and for the identification of τ-jets extrapolated from c-jets are used.

$E_{\mathrm{T}}^{\mathrm{miss}}$-Trigger

The uncertainties on the $E_{\mathrm{T}}^{\mathrm{miss}}$ trigger scale factors (see Appendix B), which are used in the SR and 1μ-CR, have two components one related to the statistical uncertainty and

one related to the systematic uncertainty. For the estimation of systematic uncertainties, event final states with one and two b-jets are used and related scale factor have been derived, while their variation from the nominal scale factor serve as an uncertainty. The difference between scale factors calculated inclusively and exclusively in the number of b-jets is used as a component of uncertainty, which accounts for the difference in the $E_{\mathrm{T}}^{\mathrm{miss}}$ response for light- and heavy-flavour jets at the reconstruction and trigger level. Overall, the statistical uncertainty on the $E_{\mathrm{T}}^{\mathrm{miss}}$ trigger scale factor dominates over the systematic uncertainty.

Systematic uncertainties on the reconstructed $E_{\mathrm{T}}^{\mathrm{miss}}$, i.e. related to the $E_{\mathrm{T}}^{\mathrm{miss}}$ soft-term were missing in the generated Monte-Carlo samples and could not been used. The impact on the results has been studied for one of the main backgrounds, namely for the $t\bar{t}$ process, and for one benchmark Z'-2HDM signal model (see Section H.1), and was found to be below 5 % of the total event yield for both cases. Therefore, the $E_{\mathrm{T}}^{\mathrm{miss}}$ soft-term uncertainties have not been applied in the analysis. While the energy scale and resolution uncertainties on the jets and the leptons are propagated to the calculation of the $E_{\mathrm{T}}^{\mathrm{miss}}$ hard-term and the uncertainties are used.
A veto on τ-jets is applied in the mono-Higgs ($b\bar{b}$) analysis. The related uncertainties, i.e. the τ-jet energy scale and identification efficiency, are found to be very small, and have not been used in the analysis (see Section H.2).

5.2.2 Theoretical Background Uncertainties

Modelling uncertainties of the three main background processes, $t\bar{t}$, W+jets and Z+jets, are used to account for differences in the modelling of the reconstructed dijet mass and the $E_{\mathrm{T}}^{\mathrm{miss}}$ distributions, and have been derived by comparing the predictions of different Monte-Carlo generators. The evaluation of the theory uncertainties follows the strategy described in Ref. [425].

$t\bar{t}$ Background

Uncertainties for the $t\bar{t}$ background are derived from comparing the nominal POWHEG + PYTHIA 6 sample to alternative samples, with different parton-shower generation (POWHEG + HERWIG++ [426]), matrix-element generation (MADGRAPH5_AMC@NLO [65] + HERWIG++) and by changing settings of the nominal generator to increase or decrease the amount of gluon emission. The uncertainties are derived by comparing the shape of the $E_{\mathrm{T}}^{\mathrm{miss}}$ ($E_{\mathrm{T}}^{\mathrm{miss,\,no-}\mu}$ or $p_{\mathrm{T}}^{\ell\ell}$) distribution, depending on the selected lepton multiplicity, and of the Higgs candidate mass distribution between the different Monte-Carlo generators. The largest variation from the nominal shape is fitted with a functional form and then symmetrised (up and down variations) to define two separate modelling uncertainties

Table 5.2: Summary of the type of experimental systematic uncertainties considered in mono-Higgs ($b\bar{b}$) analysis and treated as nuisance parameters in the profile-likelihood fit

Systematic uncertainty	**Short description**
	Event
Luminosity	uncertainty on the total integrated luminosity
Pile-up reweighting	uncertainty on pile-up reweighting
	Electrons
EL_EFF_Trigger_TOTAL_1NPCOR_PLUS_UNCOR	trigger efficiency uncertainty
EL_EFF_Reco_TOTAL_1NPCOR_PLUS_UNCOR	reconstruction efficiency uncertainty
EL_EFF_ID_TOTAL_1NPCOR_PLUS_UNCOR	identification efficiency uncertainty
EL_EFF_Iso_TOTAL_1NPCOR_PLUS_UNCOR	isolation efficiency uncertainty
EG_SCALE_ALL	energy scale uncertainty
EG_RESOLUTION_ALL	energy resolution uncertainty
	Muons
MUON_EFF_TrigSystUncertainty MUON_EFF_TrigStatUncertainty	trigger efficiency uncertainties
MUON_EFF_STAT MUON_EFF_SYS	reconstruction efficiency uncertainty
MUON_ISO_STAT MUON_ISO_SYS	isolation efficiency uncertainty
MUON_TTVA_STAT MUON_TTVA_SYS	track-to-vertex association efficiency uncertainty
MUONS_SCALE	momentum scale uncertainty
MUONS_ID	momentum resolution uncertainty from the inner detector
MUONS_MS	momentum resolution uncertainty from the muon system
	Small-R Jets
JET_GroupedNP	energy scale uncertainty split into 3 components
JET_SR1_JER_SINGLE_NP	energy resolution uncertainty
JET_SR1_JET_EtaIntercalibration_NonClosure	non-closure in the jet response at $2.4 < \|\eta\| < 2.5$
	Large-R Jets
FATJET_JMR	mass resolution uncertainty
FATJET_JER	energy resolution uncertainty
JET_Comb_Baseline_Kin JET_Comb_TotalStat_Kin JET_Comb_Modelling_Kin JET_Comb_Tracking_Kin	energy scale uncertainties (p_{T} and mass scales fully correlated)
	Small-R jet and Track-Jet Flavour Tagging
FT_EFF_EIGEN_B FT_EFF_EIGEN_C FT_EFF_EIGEN_L	b-tagging efficiency uncertainties: 3 components for b-jets, 4 for c-jets and 5 for light jets
FT_EFF_EIGEN_extrapolation	b-tagging efficiency uncertainty on the extrapolation on high p_{T}-jets
FT_EFF_EIGEN_extrapolation_from_charm	b-tagging efficiency uncertainty on τ-jets
	$E_{\mathrm{T}}^{\mathrm{miss}}$-Trigger
METTrigStat METTrigSyst	trigger efficiency uncertainty

for $E_{\mathrm{T}}^{\mathrm{miss}}$ and $m_{h,\,\mathrm{cand}}$.

V+jets Background

In case of the W+jets process, the modelling uncertainties are also derived form the comparison of different Monte-Carlo generators. The uncertainties are derived by selecting one-muon events. The resulting uncertainties are given for $E_{\mathrm{T}}^{\mathrm{miss,\,no-}\mu}$ and for $m_{h,\,\mathrm{cand}}$ by comparing the distributions of the nominal SHERPA generator to those of the MADGRAPH generator. The uncertainties are only affecting the shape of the two distributions.

For the Z+jets background in contrast, a high purity region with two isolated leptons is constructed, such that the modelling uncertainties are derived from the comparison between the predictions of the SHERPA generator and the data. The modelling uncertainties, SysZPtV and SysZMbb, are parametrised in an functional way depending on the reconstructed Z boson p_{T}, $p_{\mathrm{T}}^{\ell\ell}$, and on the Higgs boson candidate mass, respectively. Here, SysZPtV effects the normalisation and the shape of the Monte-Carlo templates and SysZMbb only the shape of the Higgs boson candidate mass distribution. The uncertainties are applied to the SR and 2ℓ-CR in a fully correlated manner.

The V+jets background samples with $V = W/Z$ are subdivided into two different components based upon the jet flavours at parton-level (see Appendix E), i.e. of the two small-R jets making the Higgs candidate or of the two track-jets associated to the leading large-R jet. This is necessary, as the V+jets background composition is expected to change between the different $E_{\mathrm{T}}^{\mathrm{miss}}$ ranges and for events with one and two b-jets, and, therefore, the template normalisations are expected the behave differently within the likelihood fit. The main V+jets background contributions ($V+bb$, $V+bc$, $V+bl$ and $V+cc$) are jointly considered as the $V+$heavy-flavour (hf) background, where the label $b\,(c)$ indicates the matching of a $b\,(c)$ quark at parton-level to a jet, while l* stands for a light-flavour jet with no matching to a b or c quark. The remaining flavour components, $V+cl$ and $V+ll$, are summarised as the $V+$light-flavour (lf) background. Only the two $V+$hf normalisations, are allowed to freely float in the likelihood fit (see Section 5.2.4), while the $V+$lf normalisations are constraint within theoretical uncertainties. The $V+$lf sub-components, $V+cl$ and $V+ll$, are assigned with normalisation uncertainties of 30 % and of 10 %, respectively. The normalistions of the $Z+$hf components across the SR and the 2ℓ-CR are decorrelated within 20 %, and the same for the $W+$hf component across the SR and the 1μ-CR. These uncertainties are assigned to account for the different selection acceptances in the different event regions. Uncertainties on the relative composition of the $V+$hf sample are assigned, with respect to the smaller component. In case of the $W+$hf sample, the ratios $W+bc/W+$hf, $W+bl/W+$hf and

*The label l here indicates a light-flavour jet.

$W+cc/W+$hf are assigned each with a 20 % uncertainty which is correlated across the SR and the 1μ-CR. Furthermore, uncertainties of 20 % on the $Z+bc/Z+$hf, $Z+bl/Z+$hf and $Z+cc/Z+$hf ratios are assigned individually in the SR and the 2ℓ-CR, to allow more flexibility of the different components within the fit, with a better constraint on the $Z+$hf prediction from the high-purity 2ℓ-CR.

Beyond these systematics uncertainties, additional normalisation uncertainties are assigned to the remaining background processes. For the single top quark production in the t-channel an uncertainty of 4.4 %, in the s-channel of 4.6 % and for the associated Wt production an uncertainty of 6.2 % is assigned. The diboson production processes are assigned with uncertainties of 25 %, 26 % and 20 % for the case of $VV = WW$, WZ or ZZ, respectively, including scale variations as well as parton shower uncertainties. The $Vh(\rightarrow b\bar{b})$ production is constrained by a normalisation uncertainty of 50 %. [86,87]. The multijet normalisation is decorrelated per event category, since only for the resolved SR a data-driven estimation of the multijet background is done (see Section 4.8.3). The associated uncertainty on the multijet normalisation is 100 %, which is rather conservative but due to the small contribution to the total background it is expected to be still a small contribution. For more details on background normalisation uncertainties see Refs. [257,267,425].

5.2.3 Theoretical Signal Uncertainties

The uncertainty on the experimental acceptance for the Z'-2HDM signal model is evaluated by varying parameters of the MADGRAPH + PYTHIA generators and comparing the results by applying the analysis selection at generator level. Generator tuning, variations of parton distribution functions, and renormalisation and factorisation scale uncertainties are taken into account as nuisance parameters in the fit, for which the parameters of the Monte-Carlo generator are changed.
The default renormalisation and factorisation scales in MADGRAPH are dynamically set to $m_{\mathrm{T}}^2 + p_{\mathrm{T}}^2$, where m_{T} and p_{T} are the transverse mass and transverse momentum of the final state particles, respectively. The event-by-event scales are changed by a factor of two (up and down) coherently.
Furthermore, signal uncertainties related on the final state radiation, initial state radiation and multi-parton interactions are parametrised as a subset of parton shower tune variations providing maximal variation coverage for underlying event effects, jet structure effects and additional jet production.
The nominal NNPDF3.0 PDF set [389] is replaced by alternative PDF sets, namely by the MSTW2008LO68CL [50] and CTEQ6L1 [427] PDF sets. The related systematic uncertainty is given by the largest deviation between the two PDF sets.

The change in signal acceptance is calculated individually for each uncertainty in the four $E_{\mathrm{T}}^{\mathrm{miss}}$ bins for each ($m_{Z'}$, m_A) signal point by comparing the variations to the nominal distribution. The related up and down variations are symmetrised at the end. The change in signal acceptances are on average below 1%, although they can be slightly larger for regions with lower acceptance at either low or very high $E_{\mathrm{T}}^{\mathrm{miss}}$ (see Appendix I).

5.2.4 Treatment of Nuisance Parameters

Two different types of nuisance parameters are used to take into account systematic uncertainties with and without prior knowledge. Normalisation parameters account for uncertainties in cross sections and acceptances which are determined from data. Apart from the signal strength parameter, μ, the statistical model contains three normalisation parameters, one for each of the main backgrounds, $t\bar{t}$ and V + hf production with $V = W/Z$ (hf), which are constrained by the data in the SR and CRs. Due to the large data statistics the background contributions can be constrained without prior knowledge about their normalisation.
In addition to the normalisation parameters, the fit contains nuisance parameters which are constrained by prior knowledge, which are related to the normalisations of the remaining backgrounds, signal modelling uncertainties and experimental uncertainties. The background normalisations not described by free parameters are set to their theoretical prediction incorporated into the likelihood function by nuisance parameters following a log-normal distribution (see Eq. 5.1) to constrain their uncertainties.

In addition to the experimental and theoretical systematic uncertainties, statistical uncertainties on the Monte-Carlo simulated samples are considered as well. The limited amount of Monte-Carlo statistics is in particular pronounced for regions with a highly boosted Higgs boson and, therefore, very high $E_{\mathrm{T}}^{\mathrm{miss}}$.
Additional nuisance parameters accounting for the limited Monte-Carlo statistics of the background samples are introduced by using a light weight version of the Barlow-Beeston method [428]. This method adds an extra nuisance parameter (usually denoted as a γ parameter related to their parametrisation by the gamma distribution) representing the statistical uncertainty on the total Monte-Carlo background in each bin, which is completely uncorrelated across bins, instead of a single nuisance parameter per background component per bin. This method significantly reduces the number of nuisance parameters. Finally, a pruning and smoothing procedure of nuisance parameter is applied to reduce the effect of large statistical fluctuations in the fit (see Section G.2).

5.3 Results

The results of the mono-Higgs ($b\bar{b}$) search are based on the 2015 and 2016 dataset with an integrated luminosity of 36.1 fb^{-1} recorded at a proton-proton collision energy of 13 TeV. For illustration, two mono-Higgs ($b\bar{b}$) candidate events in data in the resolved and the merged SR are shown in Fig. 5.2 and Fig. 5.3, respectively.

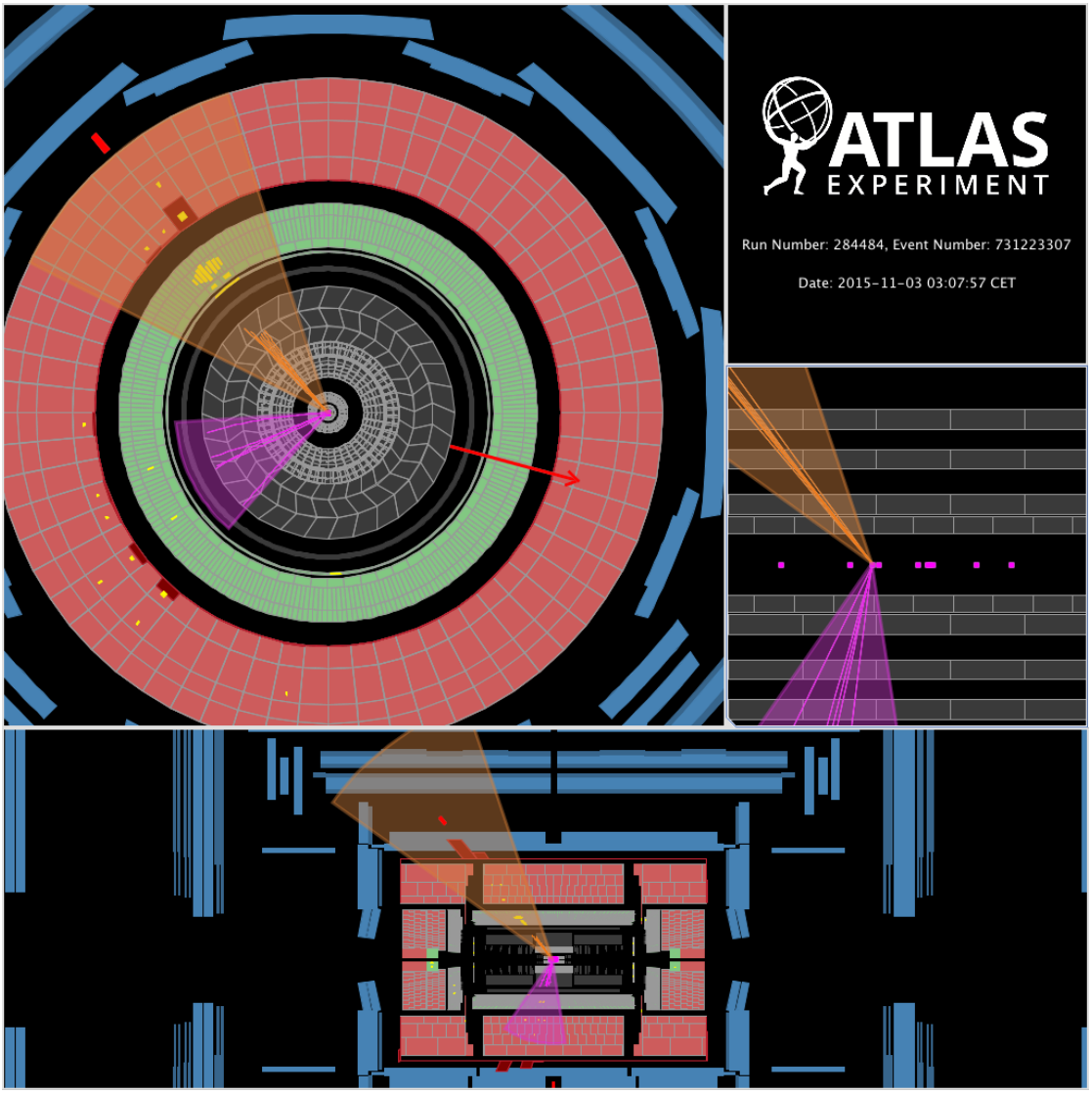

Figure 5.2: Display of a signal candidate event in the resolved signal region. The event is characterised by $E_{\mathrm{T}}^{\mathrm{miss}} = 213$ GeV and an invariant dijet mass of the two small-R jets of $m_{jj} = 120$ GeV. Both small-R jets are identified as b-jets [257].

The results are shown after the profile likelihood-fit of all SR and CRs. The Higgs boson candidate mass distributions are shown in Fig. 5.4 and Fig. 5.5 for events with one and two b-jets, respectively, for each of the four $E_{\mathrm{T}}^{\mathrm{miss}}$ ranges. The $E_{\mathrm{T}}^{\mathrm{miss}}$ distributions for

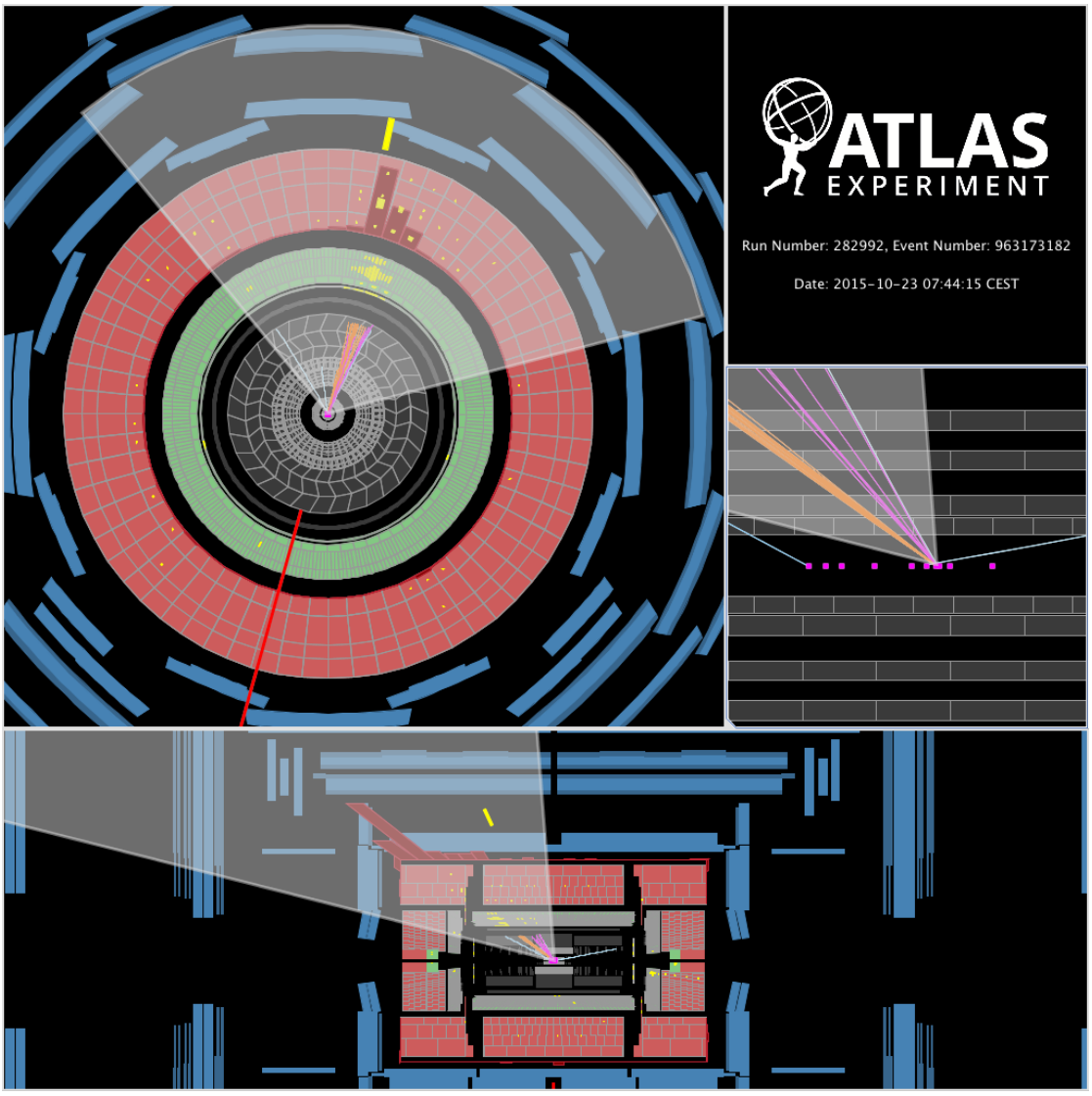

Figure 5.3: Display of a signal candidate event in the merged signal region. The event is characterised by $E_{\mathrm{T}}^{\mathrm{miss}} = 694\,\mathrm{GeV}$ and a mass of the leading large-R jet of $m_J = 106\,\mathrm{GeV}$. Both track-jets are identified as b-jets [257].

events with one and two b-jets are shown in Fig. 5.6. Very good agreement between the data and the post-fit Monte-Carlo predictions has been found within uncertainties, without any significant deviation from the predictions. The observed event yields in data are found to be in good agreement with the post-fit background predictions in all SR categories and are given in Table 5.3 and Table 5.4 for events with one and two b-jets, respectively. For $E_{\mathrm{T}}^{\mathrm{miss}} > 200\,\mathrm{GeV}$ the Z+jets background dominates, while for smaller values of $E_{\mathrm{T}}^{\mathrm{miss}}$ the $t\bar{t}$ background process has the largest contribution to the total background. In addition, for the two highest $E_{\mathrm{T}}^{\mathrm{miss}}$ ranges no event yields for the multijet background are given, as the background is negligible for large $E_{\mathrm{T}}^{\mathrm{miss}}$.

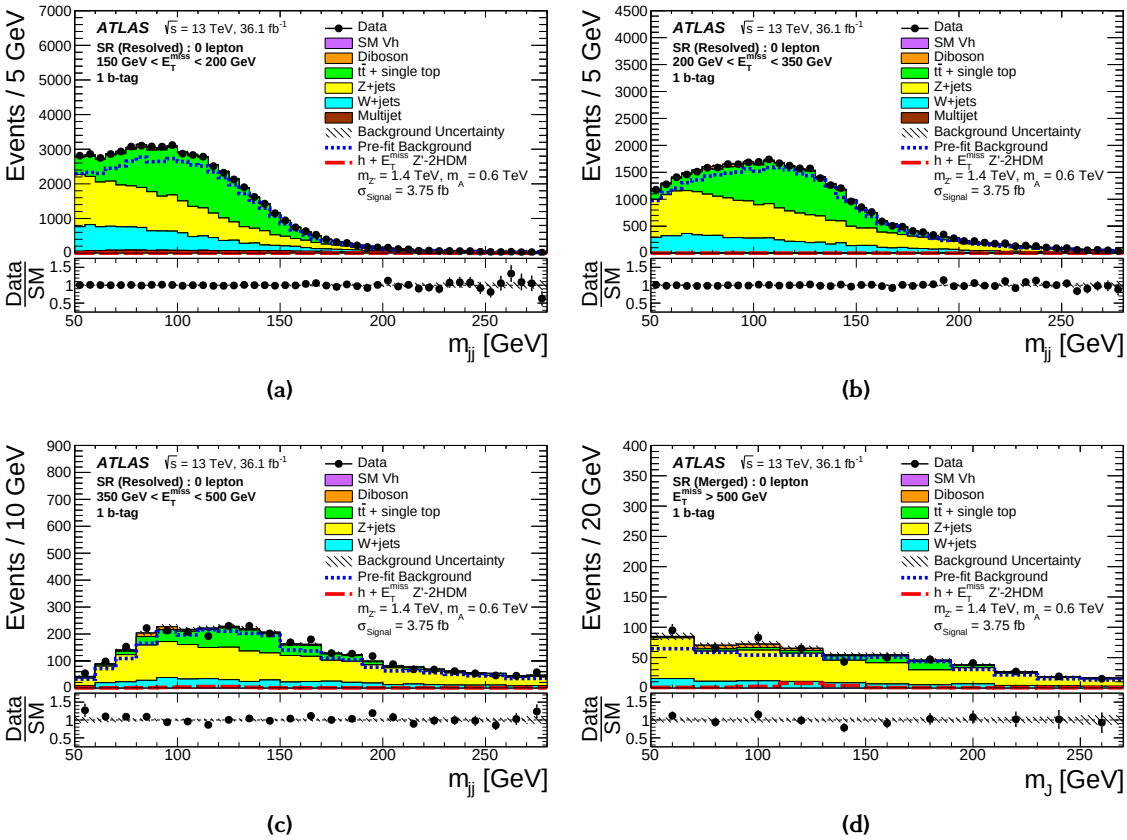

Figure 5.4: Distributions of the invariant mass of the Higgs boson candidates $m_{h,\,\mathrm{cand}} = m_{jj}$ and m_J for each of the four $E_{\mathrm{T}}^{\mathrm{miss}}$ ranges for events with one b-jet in the signal region. The upper panels show a comparison of data to the Standard Model expectation before (dashed lines) and after the fit (solid histograms). The lower panels displays the ratio of data to Standard Model expectations after the fit with the systematic uncertainties (hatched band). The expected signal from a representative Z'-2HDM model with $(m_{Z'}, m_A) = (1.4\,\mathrm{TeV}, 0.6\,\mathrm{TeV})$ assuming a production cross section of 3.75 fb is also shown (red dashed line) [258].

The W+jets contribution ranges from 9 to 18 % depending on the region of $E_{\mathrm{T}}^{\mathrm{miss}}$ and on the number of b-jets in the event. The contribution of the diboson process is above 5 % only for the two highest $E_{\mathrm{T}}^{\mathrm{miss}}$ ranges and for events with one b-jet, while the $\mathrm{Vh}(h \to b\bar{b})$ process has a small to negligible impact on the total background in all event categories.

Post-fit distributions of variables used in the CRs are given in Section D.2.

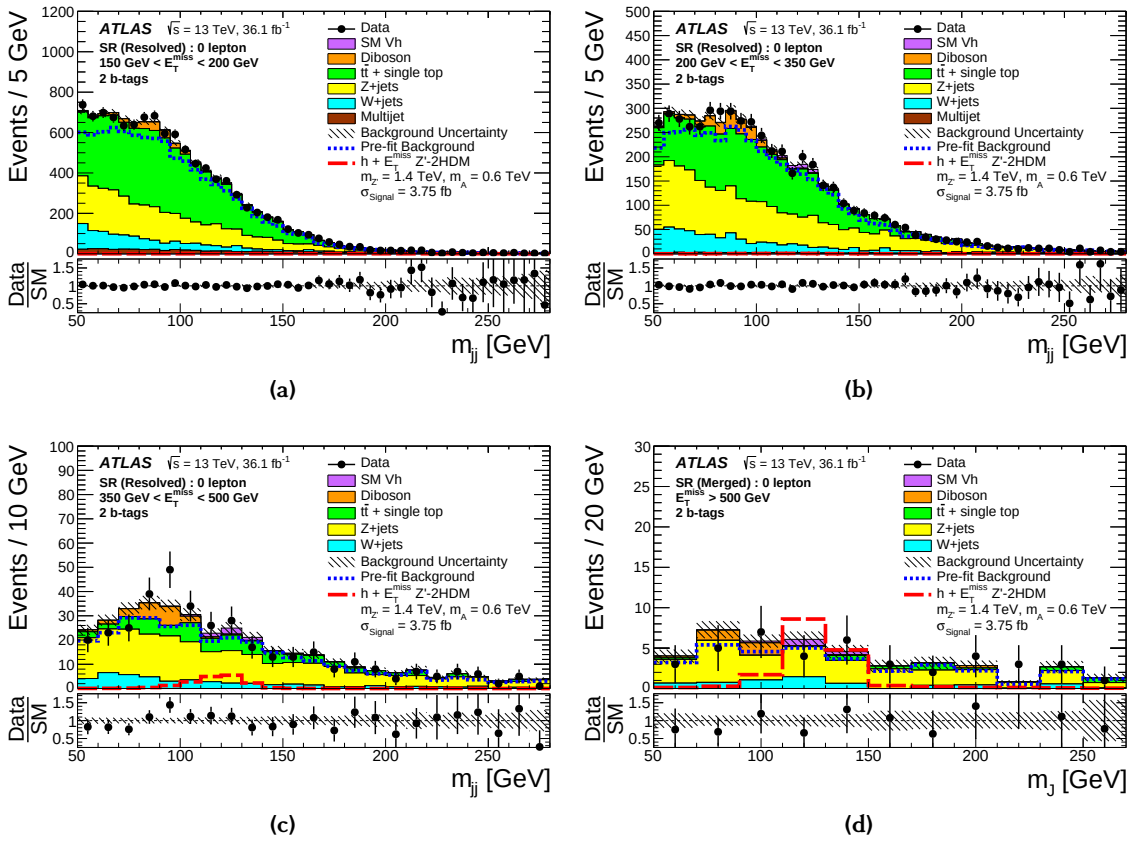

Figure 5.5: Distributions of the invariant mass of the Higgs boson candidates $m_{h,\,\mathrm{cand}} = m_{jj}$ and m_J for each of the four $E_{\mathrm{T}}^{\mathrm{miss}}$ ranges for events with two b-jets in the signal region. The upper panels show a comparison of data to the Standard Model expectation before (dashed lines) and after the fit (solid histograms). The lower panels displays the ratio of data to Standard Model expectations after the fit with the systematic uncertainties (hatched band). The expected signal from a representative Z'-2HDM model with $(m_{Z'}, m_A) = (1.4\,\mathrm{TeV}, 0.6\,\mathrm{TeV})$ assuming a production cross section of 3.75 fb is also shown (red dashed line) [258].

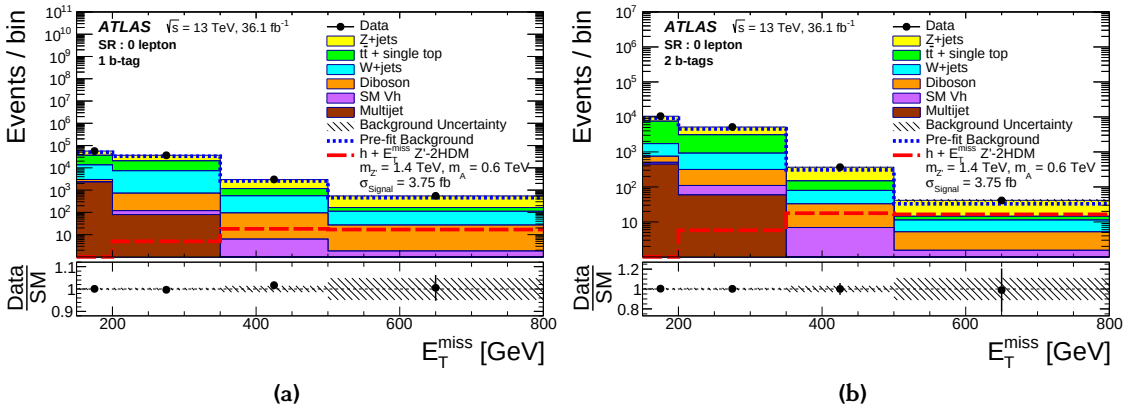

Figure 5.6: Distribution of $E_{\mathrm{T}}^{\mathrm{miss}}$ in the signal region for events with (a) one and (b) two b-jets. The upper panels show a comparison of data to the Standard Model expectation before (dashed lines) and after the fit (solid histograms) with no signal included. The lower panels display the ratio of data to Standard Model expectations after the fit, with its systematic uncertainty considering correlations between individual contributions indicated by the hatched band. The expected signal from a representative Z'-2HDM model, with $(m_{Z'}, m_A) = (1.4\,\mathrm{TeV}, 0.6\,\mathrm{TeV})$, assuming a production cross section of 3.75 fb, is also shown (red line) [258]. The rightmost bin includes overflows. The number of bin entries is divided by its width.

Table 5.3: Numbers of expected background events for each background process after the profile-likelihood fit, the sum of all background components after the fit, and observed data yields for events with one b-tag in the resolved and merged channels for each $E_{\mathrm{T}}^{\mathrm{miss}}$ region. The multijet background in the two highest-$E_{\mathrm{T}}^{\mathrm{miss}}$ ranges is negligible (indicated by '—') and not included in the fit. Statistical and systematic uncertainties are combined. The uncertainties in the total background take into account the correlation of systematic uncertainties among different background processes. The expected signal for a Z'-2HDM model with $(m_{Z'}, m_A) = (1.4\,\mathrm{TeV}, 0.6\,\mathrm{TeV})$ for $\tan\beta = 1$, $g_{Z'} = 0.8$, and $m_\chi = 100\,\mathrm{GeV}$, assuming a production cross section of 3.75 fb, is also shown [260].

Background	Range in $E_{\mathrm{T}}^{\mathrm{miss}}$ [GeV]			
	[150, 200)	[200, 350)	[350, 500)	[500, ∞)
$t\bar{t}$+single top	23 060 ± 534	13 190 ± 315	614 ± 32	53.7 ± 5.1
W+jets	10 470 ± 1280	6620 ± 812	458 ± 58	84.5 ± 13.9
Z+jets	20 000 ± 1330	16 200 ± 1070	1800 ± 120	383 ± 40
Diboson	640 ± 82	605 ± 79	87.8 ± 11.7	25.0 ± 3.6
SM $Vh(b\bar{b})$	40.1 ± 12.8	39.4 ± 14.0	6.3 ± 2.3	1.8 ± 0.7
Multijet	2310 ± 244	79.6 ± 99.3	—	—
Total Bkg.	56 570 ± 241	36 710 ± 194	2965 ± 42	548 ± 19
Data	56 611	36 584	3015	551
Exp. signal	0.2	5.0	18.2	16.9

Table 5.4: Numbers of expected background events for each background process after the profile-likelihood fit, the sum of all background components after the fit, and observed data yields for events with two b-jets in the resolved and merged channels for each $E_{\mathrm{T}}^{\mathrm{miss}}$ region. The multijet background in the two highest-$E_{\mathrm{T}}^{\mathrm{miss}}$ ranges is negligible (indicated by '—') and not included in the fit. Statistical and systematic uncertainties are combined. The uncertainties in the total background take into account the correlation of systematic uncertainties among different background processes. The expected signal for a Z'-2HDM model with $(m_{Z'}, m_A) = (1.4\,\mathrm{TeV}, 0.6\,\mathrm{TeV})$ for $\tan\beta = 1$, $g_{Z'} = 0.8$, and $m_\chi = 100\,\mathrm{GeV}$, assuming a production cross section of 3.75 fb, is also shown [260].

Background	Range in $E_{\mathrm{T}}^{\mathrm{miss}}$ [GeV]			
	[150, 200)	[200, 350)	[350, 500)	[500, ∞)
$t\bar{t}$+single top	5820 ± 168	2160 ± 76	69.2 ± 4.8	3.2 ± 0.7
W+jets	973 ± 174	605 ± 109	46.6 ± 8.7	6.1 ± 1.2
Z+jets	2940 ± 190	2070 ± 125	217 ± 13	27.0 ± 2.4
Diboson	247 ± 30	205 ± 25	25.8 ± 3.2	3.7 ± 0.6
SM $Vh(b\bar{b})$	56.4 ± 17.3	50.9 ± 17.7	6.9 ± 2.6	1.5 ± 0.6
Multijet	448 ± 116	59.1 ± 46.1	—	—
Total Bkg.	10 500 ± 101	5150 ± 62	366 ± 12	41.4 ± 3.3
Data	10 514	5160	366	41
Exp. signal	0.3	5.8	17.7	16.4

5.3.1 Impact of Different Uncertainties

In order to estimate the impact of different uncertainties on the results of the mono-Higgs ($b\bar{b}$) search, the relative uncertainty, σ_μ, on the expected signal strength is calculated, after the fit to Asimov data including a hypothetical signal. This is separately done for three representative Z'-2HDM signal points to cover all $E_{\mathrm{T}}^{\mathrm{miss}}$ ranges. The impact of each systematic uncertainty is estimated by repeating the fit without the uncertainty in question. This results in a reduced uncertainty, $\sigma_{\text{No sys}\,i}$ on the signal strength, which is subtracted quadratically from the total uncertainty $\sigma_{\text{Sys}\,i} = \sqrt{\sigma_\mu^2 - \sigma_{\text{No sys}\,i}^2}$. In order to simplify the procedure, similar sources of uncertainties are combined, e.g. all uncertainties related to the modelling of the V+jets backgrounds. The results are shown in Table 5.5.

Table 5.5: Dominant sources of uncertainty for three representative Z'-2HDM models after the fit to data with (a) $(m_{Z'}, m_A) = (600\,\text{GeV}, 300\,\text{GeV})$, (b) (1400 GeV, 600 GeV) and (c) (2600 GeV, 300 GeV). The effect is expressed as the fractional uncertainty on the signal yield. The total uncertainty is the quadrature sum of statistical and total systematic uncertainties. The impact of the luminosity uncertainty, which does not affect backgrounds with free normalizations, varies due to the changing background composition with increasing $E_{\mathrm{T}}^{\mathrm{miss}}$.

Source of uncertainty	σ_μ/μ [%]		
	(a)	(b)	(c)
Flavour tagging	5.2	12	21
Track-jets	1.4	11	17
Small-R jets	5.0	3.4	4.7
V+jets modelling	5.0	5.7	8.2
$t\bar{t}$, single-t modelling	3.2	3.0	3.9
SM $Vh(b\bar{b})$	2.2	6.9	6.9
Diboson modelling	1.1	0.7	2.3
Signal modelling	3.9	2.9	2.1
MC statistics	4.9	11	22
Luminosity	3.2	4.5	5.4
Small-R jets	1.7	3.8	2.1
Large-R jets	0.1	1.2	4.7
$E_{\mathrm{T}}^{\mathrm{miss}}$	1.3	1.3	0.3
Leptons	0.6	1.5	3.2
Total systematic uncertainty	10	21	36
Statistical uncertainty	6	38	62
Total uncertainty	12	43	71

Dominant sources of experimental systematic uncertainty arise from the calibration of the b-jet identification efficiency, the integrated luminosity, and from the energy and mass scale and resolution of jets. Dominant sources of theoretical systematic uncertainties

originate from the modelling of background processes such as the $t\bar{t}$, the V+jets, and the Vh production. For signal models resulting in very high $E_{\mathrm{T}}^{\mathrm{miss}}$ events, the statistical uncertainties on the Monte-Carlo predictions are dominant. The mono-Higgs ($b\bar{b}$) search is statistically limited for Z'-2HDM models resulting in medium and high $E_{\mathrm{T}}^{\mathrm{miss}}$, and especially in the region of $E_{\mathrm{T}}^{\mathrm{miss}} > 300\,\mathrm{GeV}$.

5.3.2 Interpretation in the Z'-2HDM Model

The expected and observed significances, as defined in Eq. (5.5), are given in Table 5.6 for three representative Z'-2HDM benchmark signal models. No experimental evidence

Table 5.6: The observed and expected significances in numbers of standard deviations, Z, for three representative Z'-2HDM signal models with $(m_{Z'}, m_A) = (600\,\mathrm{GeV}, 300\,\mathrm{GeV})$, $(1400\,\mathrm{GeV}, 600\,\mathrm{GeV})$ and $(2600\,\mathrm{GeV}, 300\,\mathrm{GeV})$ after the profile-likelihood fit.

$m_{Z'}$ [GeV]	m_A [GeV]	Z_{obs} [pb]	Z_{exp} [pb]
600	300	0.46	9.86
1400	600	0.00	2.52
2600	300	0.00	1.57

for Z'-2HDM signal models was found and, therefore, exclusion limits on the production cross section at 95 % CL are derived in the $(m_{Z'}, m_A)$ plane, where A is a pseudoscalar and Z' is the additional vector mediator. For the study, the mass, m_χ, of the Dark Matter particle is fixed to 100 GeV as the production cross section does not depend on m_χ for $m_\chi < m_A/2$. The limits are set on the signal strength parameter, μ following the details in Section 5.1. Signal models with parameters $(m_{Z'}, m_A)$ are excluded if $\hat{\mu} < 1$. The exclusion contours in the $(m_{Z'}, m_A)$ plane are shown in Fig. 5.7 and $m_{Z'}$ up to 2.6 TeV and m_A up to 0.6 TeV are excluded. This substantially extends the previous limits which are also indicated [257,260,267,429,430]. No sensitivity is found for signal models with $m_A < 200\,\mathrm{GeV}$, which corresponds to an off-shell produced A boson as the Dark Matter particle is assumed to have a mass of 100 GeV.

The sensitivity is largest in the two b-jet event category, except for signal models resulting in very high $E_{\mathrm{T}}^{\mathrm{miss}}$, i.e. for large Z' masses, where the one b-jet event category becomes important, since the track-jets start to merge. For $m_A \approx 300$ to 400 GeV and $m_{Z'} \approx 500\,\mathrm{GeV}$, where $E_{\mathrm{T}}^{\mathrm{miss}}$ is moderate, the sensitivity is mainly limited by the $E_{\mathrm{T}}^{\mathrm{miss}}$ trigger thresholds and the related $E_{\mathrm{T}}^{\mathrm{miss}} > 150\,\mathrm{GeV}$ requirement. In both cases, the systematic uncertainties in the identification of b-jets are one of the largest uncertainties, as indicated in Table 5.5.

The CMS experiment excludes Z' masses up to 3.2 TeV for $m_A = 0.32\,\mathrm{TeV}$ [431] based on a dataset of $35.9\,\mathrm{fb}^{-1}$, when using the model assumption of $m_A = m_H = m_{H^\pm}$, which

differs from the assumptions in Section 4.2 of $m_H = m_{H^\pm} = 300\,\text{GeV}$. This difference affects mainly the production cross section and changes by a small amount the decay width of the pseudoscalar Higgs boson A. In particular, for $m_A = m_H = m_{H^\pm}$ the A boson cannot decay to final states with other Higgs bosons, which is in principle possible when $m_H = m_{H^\pm} = 300\,\text{GeV}$ is assumed. The model settings used by CMS result on average in slightly higher predicted production cross sections, but for $m_A > 400\,\text{GeV}$ the cross section can be enhanced by a factor of 1.5 to 8 leading to higher mass exclusion limits.

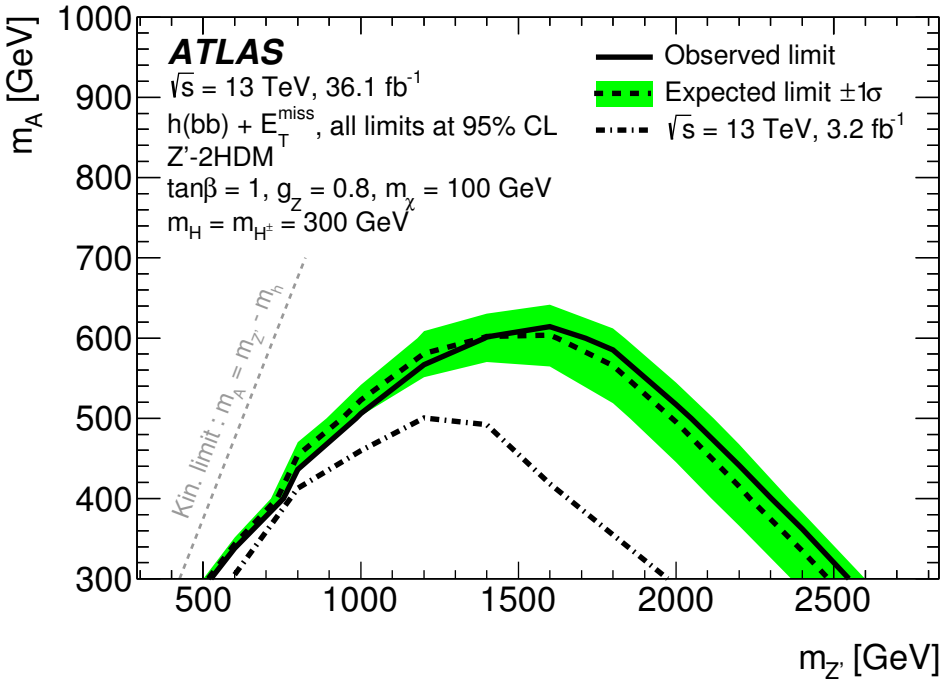

Figure 5.7: 95 % CL exclusion contours for the Z'-2HDM model in the $(m_{Z'}, m_A)$ plane for $m_\chi = 100\,\text{GeV}$, $m_H = m_{H^\pm} = 300\,\text{GeV}$, $\tan\beta = 1$ and $g_{Z'} = 0.8$ with an integrated luminosity of $36.1\,\text{fb}^{-1}$ at 13 TeV center-of-mass energy. The observed limits (solid line) are consistent with the expectation under the Standard Model-only hypothesis (dashed line) [258]. The observed exclusion contour from the previous ATLAS search with $3.2\,\text{fb}^{-1}$ at $\sqrt{s} = 13\,\text{TeV}$ (dash-dotted line) [257] are also shown.

Chapter 6

Improved Reconstruction of Boosted Higgs $b\bar{b}$ Decays

In Chapter 4, the mono-Higgs ($b\bar{b}$) analysis based on 36.1 fb^{-1} of data has been discussed. The results are given in Chapter 5.
In this Chapter, an improved reconstruction technique for highly Lorentz-boosted Higgs boson decays is discussed, based on jets reconstructed from the inner detector tracks with a variable radius parameter (see Section 3.3.4.4). The main differences between the two mono-Higgs ($b\bar{b}$) analysis are summarised in Section 6.1. The analysed data of 79.8 fb^{-1} has been recorded in 2015, 2016 and 2017. The Monte-Carlo generators used for the simulation of the background processes are discussed in Section 6.2. The analysis results are given in Section 6.3 and interpreted in the context of the simplified Z'-2HDM model.

6.1 Analysis Differences

One of the main differences between the mono-Higgs ($b\bar{b}$) searches in Chapter 4 and in this Chapter is certainly the increased dataset. The sensitivity of the mono-Higgs ($b\bar{b}$) analysis in Chapter 5 is statistically limited in the region of high $E_{\mathrm{T}}^{\mathrm{miss}}$, while the b-jet identification uncertainties (see Table 5.5) dominate for small $E_{\mathrm{T}}^{\mathrm{miss}}$ values.
In the high $E_{\mathrm{T}}^{\mathrm{miss}}$ region, the b-jet identification uncertainties are related to track-jets with a fixed radius (FR) parameter of $R = 0.2$. The track-jets were introduced to overcome the issue of overlapping small-R jets in the resolved SR, but even the track-jets are highly collimated and start to merge for highly boosted Higgs boson decays with $p_{\mathrm{T}}^{h} > 1\,\mathrm{TeV}$. Due to this, the analysis outlined in Chapter 4 relies on two event categories with one and two b-jets, such that the one b-jet event category recovers efficiency when the two FR track-jets are overlapping. An improved Higgs boson reconstruction technique overcomes this issues by using so-called track-jets with a variable radius (VR) parameter as introduced in Section 3.3.4.4. The VR track-jets allow to efficiently identify the two b-jets in the merged SR even for a very large Higgs boson $p_{\mathrm{T}}^{h} > 1\,\mathrm{TeV}$. In Fig. 6.1, the

truth sub-jet double b-labelling efficiency is shown, as a function of the Higgs boson jet p_{T} for FR and VR track-jets. The VR track-jets provide a more stable labelling efficiency

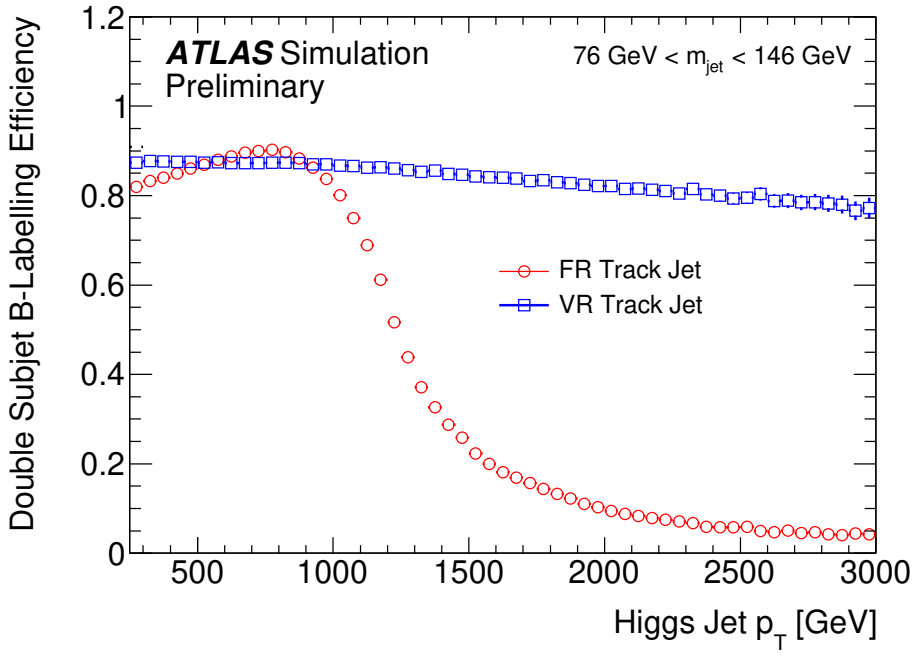

Figure 6.1: The efficiency for a Higgs jet to have its two leading associated track-jets matched to truth B-hadrons as a function of the jet p_{T}, when using track-jets with fixed (red) and variable (blue) radius parameter [373].

over the full Higgs boson p_{T} range, which is most of the time above 80 %, while for FR track-jets the efficiency decreases rapidly to below 20 % for $p_{\mathrm{T}}^{h} > 1.5$ TeV. Therefore, the VR track-jets are used for the identification of the $h \to b\bar{b}$ decays in the merged SR of the mono-Higgs ($b\bar{b}$) analysis [432].
For events with low $E_{\mathrm{T}}^{\mathrm{miss}}$ values, the object-based $E_{\mathrm{T}}^{\mathrm{miss}}$-significance (see Section 3.3.7) is used to significantly reduce the multijet background. A requirement on object-based $E_{\mathrm{T}}^{\mathrm{miss}}$-significance of $S > 16$ is placed to events in the resolved SR. The remaining multijet contribution is estimated by applying an ABCD method, compared to the template method used in Section 4.8.3 (for more details see Ref. [432]). Moreover, the muon-in-jet correction (see Section 3.3.5.1) is not applied. Besides these differences, the analysis strategy is the same as discussed in Chapter 4.

6.2 Dataset and Simulated Events

The analysed dataset of 79.8 fb^{-1} contains pp collision data recorded by the ATLAS detector in 2015, 2016 and 2017 at a centre-of-mass energy of 13 TeV. The uncertainty on the integrated luminosity is estimated to be 2.0 % using a method as outlined

in Section 3.2.7. The average number of pp interactions per bunch crossing, $< \mu >$, significantly increased over the years, related to a better performance of the LHC. In 2015, $< \mu >$ was around 13 and in 2016 around 25, and further increased during 2017 up to 38, as illustrated in Fig. 3.2b. The Monte-Carlo Simulated events are reweighted to account for different pile-up conditions found in data for different periods in time of data taking.
Compared to the background Monte-Carlo generators given in Table 4.1, the following ones have changed: the diboson processes were simulated with SHERPA 2.2.1 and with the NNPDF3.0NNLO PDF set, the single- and pair-production of top quarks were generated at NLO QCD using the POWHEG-BOX v2 interfaced to PYTHIA 8 instead of PYTHIA 6 and the NNPDF3.0 PDF set and the A14 set of tuned parameters, and the associated Vh production were generated with POWHEG-BOX v2 interfaced to PYTHIA 8 using NNPDF3.0 PDFs and the AZNLO tune [433]. The Monte-Carlo generator and settings for the generation of Z'-2HDM signal samples are unchanged (see Section 4.2).

6.3 Results

The statistical model (see Section 5.1.2) only uses the two b-jet event category, which significantly reduces the complexity of the model and also provides a better understanding of the background modelling uncertainties. The statistical model is otherwise not change with respect of Section 5.1.2, i.e the muon charge is used to separate the $t\bar{t}$ from $W+$jets background in the 1μ-CR, and a single bin of $m_{h,\,\text{cand}}$ is used in the 2ℓ-CR to extract the right event yield of the $Z+$jets process in the SR. Furthermore, the treatment of experimental and theoretical uncertainties follows the description given in Section 5.2.4.
The post-fit $m_{h,\,\text{cand}}$ distributions are shown in Fig. 6.2 for the four $E_{\text{T}}^{\text{miss}}$ ranges in the SR. The $E_{\text{T}}^{\text{miss}}$ distribution is shown in Fig. 6.3. Good data to Monte-Carlo agreement is found at the post-fit level and no significant deviation from the Standard Model expectation is found. The number of expected events for each background process after the fit, as well as the observed number of data events in each of the four $E_{\text{T}}^{\text{miss}}$ ranges, are summarised in Table 6.1. The post-fit distributions of the variables used in the CRs are shown in Section D.3.
The impact of systematic uncertainties on the physics results are discussed in Section 6.3.1. In absence of any significant deviation from the Standard Model predictions, the results are interpreted in the context of the simplified Z'-2HDM model (see Section 6.3.2).

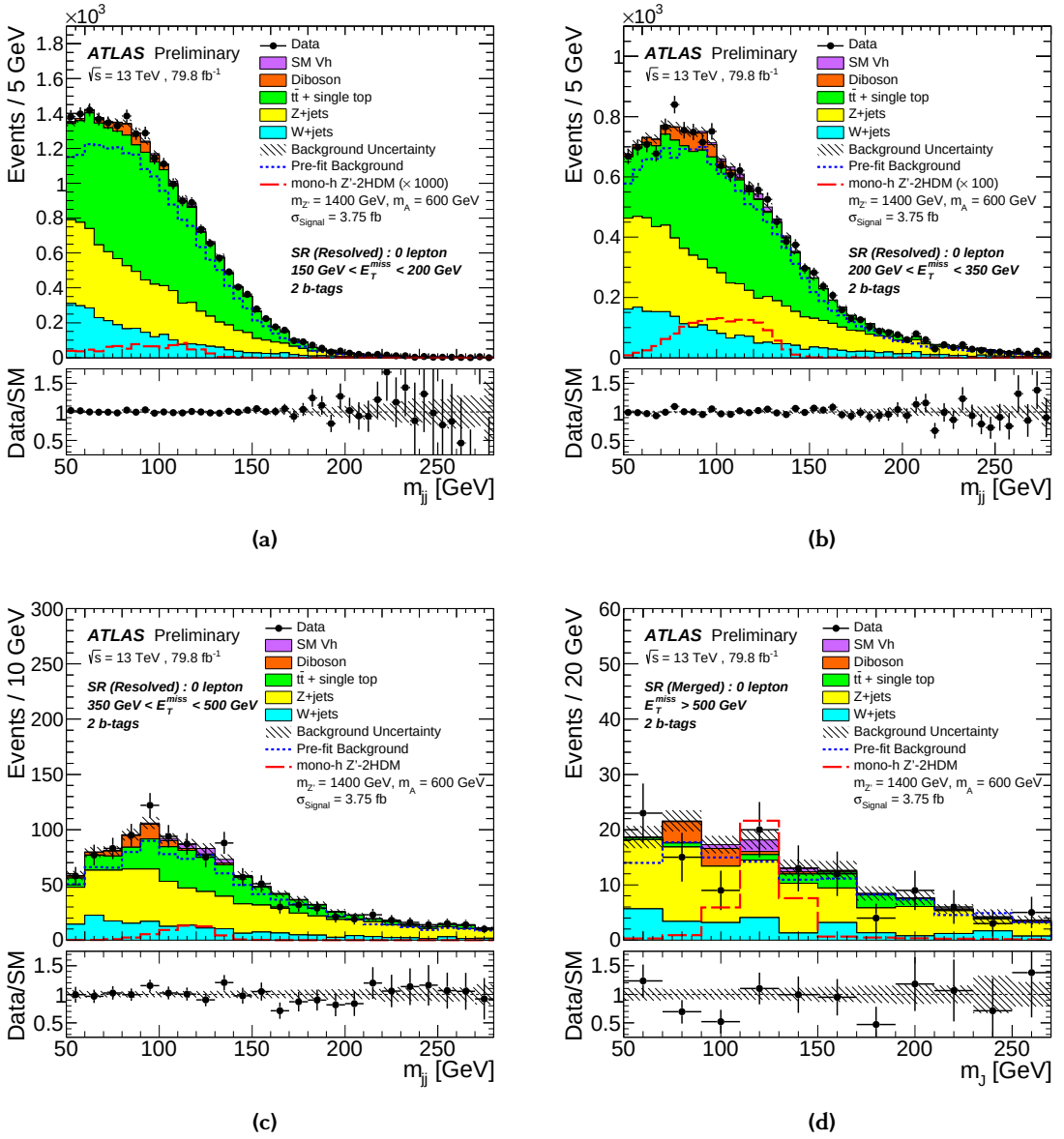

Figure 6.2: Distributions of the invariant mass of the Higgs boson candidates $m_{h,\,\mathrm{cand}} = m_{jj}$ and m_J for the four $E_{\mathrm{T}}^{\mathrm{miss}}$ categories that are used as inputs to the fit. The upper panels show a comparison of data to the Standard Model expectation before (dashed lines) and after the fit (solid histograms) with no signal included. The lower panels display the ratio of data to Standard Model expectations after the fit, with its systematic uncertainty considering correlations between individual contributions indicated by the hatched band. The expected signal from a representative Z'-2HDM model, with $(m_{Z'}, m_A) = (1.4\,\mathrm{TeV}, 0.6\,\mathrm{TeV})$, assuming a production cross section of 3.75 fb, is also shown (red dashed line) [432], and it is scaled up by a factor of 1000 to 100 for the two lowest regions of $E_{\mathrm{T}}^{\mathrm{miss}}$ (upper row), respectively, for better illustration.

6.3.1 Impact of Different Uncertainties

The systematic uncertainties considered in the mono-Higgs ($b\bar{b}$) analysis are similar to the ones discussed in Section 5.2. The experimental systematic uncertainties are

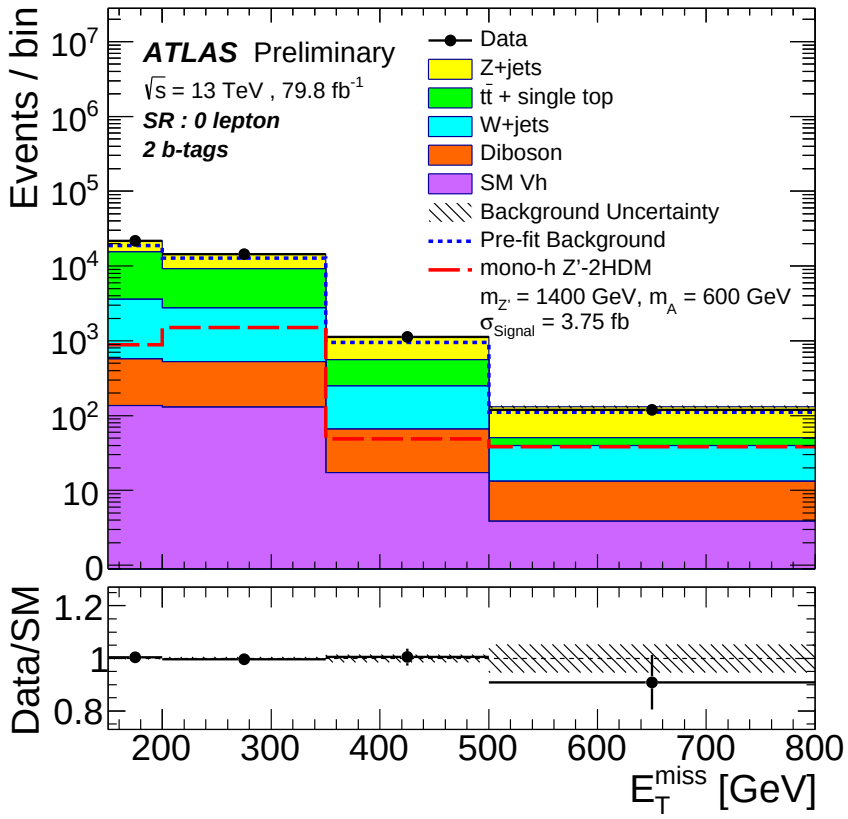

Figure 6.3: Distribution of $E_{\mathrm{T}}^{\mathrm{miss}}$ in the resolved and merged signal regions combined. The upper panels show a comparison of data to the Standard Model expectation before (dashed lines) and after the fit (solid histograms) with no signal included. The lower panels display the ratio of data to Standard Model expectations after the fit, with its systematic uncertainty considering correlations between individual contributions indicated by the hatched band. The expected signal from a representative Z'-2HDM model, with $(m_{Z'}, m_A) = (1.4\,\mathrm{TeV}, 0.6\,\mathrm{TeV})$, assuming a production cross section of 3.75 fb, is also shown (red line) [432]. The rightmost bin includes overflows. The number of bin entries is divided by its width.

expected to be smaller compared to the previous analysis iteration, due to an effort of all performance groups in ATLAS providing reduced uncertainties for all physics objects. The uncertainties on the b-jet identification efficiency for VR track-jets are implemented in the analysis and replace the ones for FR track-jets. They originate from the b-jet efficiency measurements in dileptonic $t\bar{t}$ events by applying the likelihood method as discussed in Section 3.3.5.

Compared to Section 5.2, uncertainties on the $E_{\mathrm{T}}^{\mathrm{miss}}$ soft-term resolution and scale are now taken into account, and their impact has been confirmed to be very small. Dedicated $E_{\mathrm{T}}^{\mathrm{miss}}$ trigger efficiency scale factors (see Appendix B) are re-derived for 2015 and 2016 with the latest Monte-Carlo predictions and also for the 2017 data with an increased HLT threshold of 110 GeV.

Table 6.1: Numbers of expected background events for each background process after the profile-likelihood fit, the sum of all background components after the fit, and observed data yields for events with two b-jets in the resolved and merged channels for each $E_{\mathrm{T}}^{\mathrm{miss}}$ region. The multijet background is negligible and not included in the fit. Statistical and systematic uncertainties are combined. The uncertainties in the total background take into account the correlation of systematic uncertainties among different background processes. The expected signal for a Z'-2HDM model with $(m_{Z'}, m_A) = (1.4\,\mathrm{TeV}, 0.6\,\mathrm{TeV})$ for $\tan\beta = 1$, $g_{Z'} = 0.8$, and $m_\chi = 100\,\mathrm{GeV}$, assuming a production cross-section of 3.75 fb.

Background	Range in $E_{\mathrm{T}}^{\mathrm{miss}}$ [GeV]			
	[150, 200)	[200, 350)	[350, 500)	[500, ∞)
$t\bar{t}$+single top	11 800 $\pm$ 350	6450 $\pm$200	308 $\pm$ 25	10.8 $\pm$ 2.5
W+jets	3020 $\pm$ 530	2240 $\pm$ 360	184 $\pm$ 32	26.4 $\pm$ 5.7
Z+jets	6330 $\pm$ 450	5180 $\pm$ 340	565 $\pm$ 37	80.5 $\pm$ 6.3
Diboson	438 $\pm$ 67	400 $\pm$ 59	49.0 $\pm$ 11.0	9.4 $\pm$ 1.7
SM $Vh(b\bar{b})$	136 $\pm$ 39	129 $\pm$ 37	17.3 $\pm$ 5.0	3.9 $\pm$ 1.1
Total Bkg.	21 700 $\pm$ 140	14 400 $\pm$ 110	1120 $\pm$ 25	131 $\pm$ 7
Data	21 818	14 350	1128	119
Exp. signal	0.6	10.7	35.1	29.7

Table 6.2 quantifies the dominant sources of uncertainties in terms of the relative uncertainty on the signal strength, defined as the ratio of the measured signal yield to the theory prediction, after the fit to simulated data including the signal assuming three representative Z'-2HDM scenarios. Systematic uncertainties related to b-jet identification efficiencies are treated in a fully correlated way between small-R jets and VR track-jets. Hence, a single set of nuisance parameter is used for both jet collections in the resolved and merged signal region. Thus, it is not possible to split the b-jet efficiency uncertainties into two components, one for small-R jets and track-jets. Nevertheless, the impact of the total b-jet uncertainties in Table 5.5 and Table 6.2 can be compared to each other, and the total flavour uncertainties are reduced by 23 %, 33 % and 52 % for the three representative benchmark models with $(m_{Z'}, m_A) = (600\,\mathrm{GeV}, 300\,\mathrm{GeV})$, $(1400\,\mathrm{GeV}, 600\,\mathrm{GeV})$ and $(2600\,\mathrm{GeV}, 300\,\mathrm{GeV})$, respectively. The reduction of b-jet identification uncertainties are mainly related due to reduced uncertainties for small-R jets from an improved calibration. In addition, since no one-b-jet region is used, the rate of misidentifying C-hadron decays as b-jets is smaller, and, therefore the c-jet misidentification uncertainties are much smaller. Furthermore, the uncertainties related to Monte-Carlo statistics are greatly reduced, as more Monte-Carlo events have been generated for each of the main background processes.

The total uncertainties are reduced by 45 to 65 %, depending on the benchmark signal model. Systematic uncertainties dominate in regions of low $E_{\mathrm{T}}^{\mathrm{miss}}$, while the mono-Higgs ($b\bar{b}$) search is still statistically limited for highly-boosted signatures.

Table 6.2: Dominant sources of uncertainty for three representative Z'-2HDM models after the fit to data with (a) $(m_{Z'}, m_A) = (600\,\text{GeV}, 300\,\text{GeV})$, (b) (1400 GeV, 600 GeV) and (c) (2600 GeV, 300 GeV). The effect is expressed as the fractional uncertainty on the signal yield. The total uncertainty is the quadrature sum of statistical and total systematic uncertainties. The impact of the luminosity uncertainty, which does not affect backgrounds with free normalizations, varies due to the changing background composition with increasing $E_{\text{T}}^{\text{miss}}$.

Source of uncertainty	σ_μ/μ [%]		
	(a)	(b)	(c)
Flavour tagging	4.0	8.0	10
V+jets modelling	3.5	6.0	5.0
$t\bar{t}$, single-t modelling	3.7	4.8	4.5
SM $Vh(b\bar{b})$	0.8	3.2	2.1
Diboson modelling	0.8	1.5	1.1
Signal modelling	3.0	2.5	1.5
MC statistics	1.8	5.4	4.9
Luminosity	2.0	2.5	2.5
Small-R jets	1.4	3.0	2.0
Large-R jets	0.2	1.0	2.0
$E_{\text{T}}^{\text{miss}}$	1.2	1.7	1.1
Leptons	0.2	0.8	0.7
Total systematic uncertainty	6.5	13	13
Statistical uncertainty	2.3	20	22
Total uncertainty	7	24	25

6.3.2 Interpretation in the Z'-2HDM Model

The search with improved boosted $h \to b\bar{b}$ reconstruction is interpreted in terms of 95 % CL exclusion limits on the Z'-2HDM model (analogously to Section 5.3.2). The exclusion contour in the $(m_{Z'}, m_A)$ plane shown in Fig. 6.4, extends to much higher $m_{Z'}$ and m_A values compared to Fig. 5.7. For intermediate Z' masses around 1.5 TeV, m_A is excluded up to 650 GeV, while for $m_A = 300\,\text{GeV}$ $m_{Z'}$ is excluded up to 2.8 TeV. The improvement in the exclusion limit is due to the increase of the dataset from 36.1 fb^{-1} to 79.8 fb^{-1} and from the use of VR track-jets in the merged SR, corresponding to high Z' masses and very high $E_{\text{T}}^{\text{miss}}$.

The improvement of the sensitivity using VR track-jets is demonstrated by scaling the exclusion limits derived for 36.1 fb^{-1} with FR track-jets (see Fig. 5.7) to 79.8 fb^{-1}. The resulting expected upper limits on the signal strength, μ, are shown in Fig. 6.5 as a function of $m_{Z'}$ and with $m_A = 500\,\text{GeV}$. Here, the results based on the analysis with FR track-jets combine the one and the two b-jet event categories, while the analysis with VR track-jets uses only the two b-jet category. For signals models with a very boosted Higgs boson, i.e. for $m_{Z'} > 1.5\,\text{TeV}$, the results with VR track-jets show significant

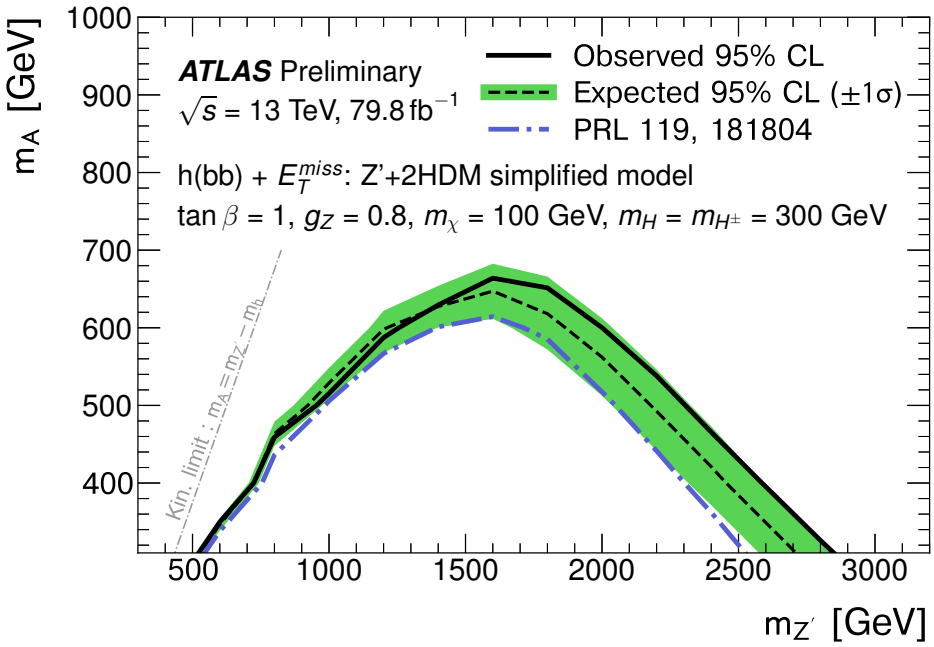

Figure 6.4: 95 % CL exclusion contours for the Z'-2HDM model in the $(m_{Z'}, m_A)$ plane for $m_\chi = 100\,\text{GeV}$, $m_H = m_{H^\pm} = 300\,\text{GeV}$, $\tan\beta = 1$ and $g_{Z'} = 0.8$ with an integrated luminosity of $79.8\,\text{fb}^{-1}$ at 13 TeV center-of-mass energy. The observed limits (solid line) are consistent with the expectation under the Standard Model-only hypothesis (dashed line) [432]. The observed exclusion contour from the previous ATLAS search with $36.1\,\text{fb}^{-1}$ at $\sqrt{s} = 13\,\text{TeV}$ (dash-dotted line) [258] are also shown.

improvement in sensitivity of up to 60 %. In the region around $m_{Z'} \approx 1\,\text{TeV}$, which translates to $E_\text{T}^\text{miss} \approx 500\,\text{GeV}$, the expected sensitivity is slightly smaller when using VR track-jets, and is reduced by around 20 % at most. The region around $E_\text{T}^\text{miss} \approx 500\,\text{GeV}$ is the transition region of the resolved and merged signal region, and, therefore, the one b-jet region recovers sensitivity in the resolved regime, where the small-R jets start to be very collimated. Nevertheless, the analysis based on VR track-jets outperforms the predecessor based on FR track jets considerably, justifying the strategy of using only events with two b-jets.

The use of VR track-jets is also applicable to other signal models in the future, introduced in Chapter 7. It improves the sensitivity in regions with very high E_T^miss and highly boosted Higgs boson decays, which is of particular interest for the analysis of the full Run 2 dataset of about $140\,\text{fb}^{-1}$ integrated luminosity.

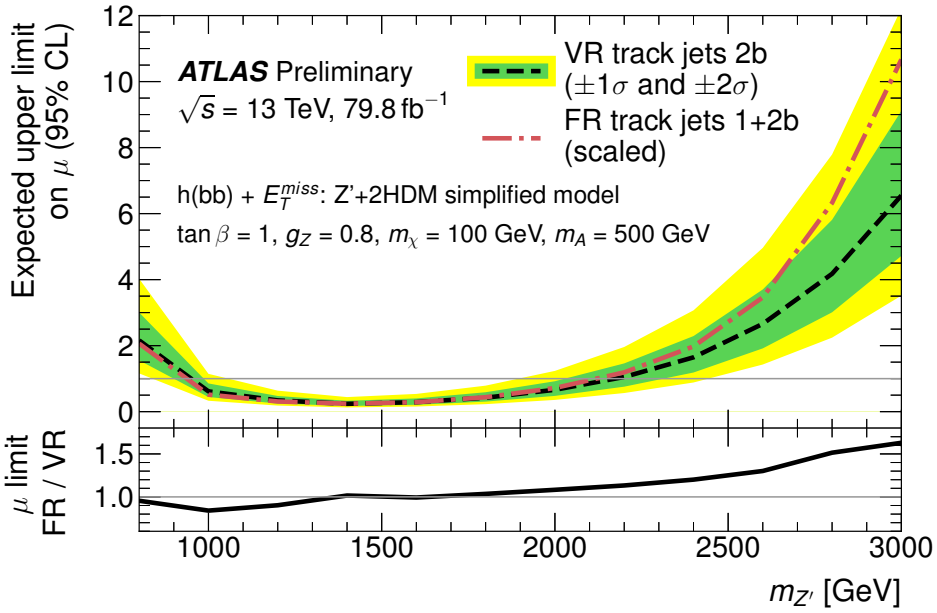

Figure 6.5: Expected 95 % CL upper limits on the signal strength, μ, as a function of $m_{Z'}$ for the analysis with variable radius (VR) track-jets (dashed line) and with fixed radius (FR) track-jets (dash-dotted line) for events with two and one+two b-jets, respectively. The expected limits with FR track-jets for 36.1 fb^{-1} are scaled up to 79.8 fb^{-1}. The limits on μ are shown for the Z'-2HDM model with fixed $m_A = 500$ GeV. The lower panel shows the ratio of the two upper limits on μ showing a significant improvement for $m_{Z'} > 1500$ GeV.

6.4 Outlook

Especially in the resolved signal region, where the data statistic is very high and precise predictions can be made but at the same time the backgrounds are extremely large, the use of machine learning techniques such as boosted decision trees, which are also used for the Standard Model $Vh(\rightarrow b\bar{b})$ analysis, or deep neural networks are expected to provide a very good background rejection and a high signal selection efficiency, by exploiting correlations between different variables. Such advanced event selection techniques are expected to improve the sensitivity in the region of low $E_{\mathrm{T}}^{\mathrm{miss}}$, where the discrimination of the background is difficult.

The study of events with low $E_{\mathrm{T}}^{\mathrm{miss}}$ is in particular interesting when looking for mediators with low masses, i.e. in case of the ϕ-2HDM model (see Section 7.2), (dark) Higgs portal models [434] or in the context of a search for Dark Energy using the mono-Higgs ($b\bar{b}$) signature [435]. Here, the use of very selective jet, b-jet or $E_{\mathrm{T}}^{\mathrm{miss}}$ triggers are required in addition. They can also be optimised by using machine learning techniques for pattern recognition of calorimeter clusters at the high-level trigger stage.

New jet objects built from both tracking and calorimeter information, referred to as Track-CaloClusters [436], similar to so-called particle flow jets, are expected to provide

improved precision of jet substructure variables, and, therefore, a better discrimination between top quark and W/Z initiated jets from Higgs boson jets for very high-p_{T} objects.

As given in Table 6.2, the $V+$jets background modelling uncertainties are one of the largest systematic uncertainties and limit the sensitivity of the mono-Higgs ($b\bar{b}$) analysis. It is expected that their impact will be reduce when using the latest Monte-Carlo generator predictions with higher-order corrections, i.e. including NNLO QCD and NLO electroweak corrections. The uncertainties can be also reduced by deriving more precise modelling uncertainties by comparing the predictions of the different Monte-Carlo generators at parton level, in particular for events with a merged topology and by applying sophisticated reweighting procedures to account for higher order corrections as proposed in Ref. [437].

The most natural choice of estimating the $Z(\rightarrow \nu\nu)$+jets background in the SR is to use the $Z(\rightarrow \mu\mu)$+jets and the $Z(\rightarrow ee)$+jets processes in the 2ℓ-CR. This approach suffers from low statistics in the high $p_{\mathrm{T}}^{\ell\ell}$ region in the 2ℓ-CR. Due to the relative branching ratios and selection acceptances, there are six times more $Z(\rightarrow \nu\nu)$+jets events than $Z(\rightarrow \ell\ell)$+jets events. To improve the $Z(\rightarrow \nu\nu)$+jets estimation in the SR, the study of a $\gamma+$jet control region is of interest, since the $\gamma+$jet process has a larger cross section then the $Z+$jets process. The $\gamma+$jet process provides a precise probe for the $Z(\rightarrow \nu\nu)+$jets process, if the photon is marked as invisible. For events in the merged region, the p_{T} of the γ and the Z boson becomes very similar, such that the $E_{\mathrm{T}}^{\mathrm{miss}}$ spectrum is almost identical. This is related to their similar production mechanism, while the effect of the non-zero Z boson mass has only a small effect at high p_{T} of the boson.

The transverse mass, which accounts for the $E_{\mathrm{T}}^{\mathrm{miss}}$ in the event in combination with the Higgs boson candidate mass, as variable of interest might have a better sensitivity for events with high $E_{\mathrm{T}}^{\mathrm{miss}}$. This have to be studied in more detail in the future and to be compared to the latest results of the CMS experiment in Ref. [431].

Furthermore, it is interesting to extend the mono-Higgs search by the $h \rightarrow c\bar{c}$ final state, i.e. for the analysis of the full Run 2 dataset and beyond, as the analysis objects are very similar. The $h \rightarrow c\bar{c}$ final state can enlarge the statistics in the high $E_{\mathrm{T}}^{\mathrm{miss}}$ range, but very selective efficient b- and c-jet identification algorithms are required.

Chapter 7

Limits on Other Dark Matter Models

In this Chapter, the results obtained in Chapter 5 with an integrated luminosity of 36.1 fb^{-1} are used to derive limits on cross sections for different Dark Matter models. The procedure for deriving upper limits is described in Section 5.1. In Section 7.1, the results are interpreted in terms of the *baryonic Z'_{B} model* and the resulting limits are compared to direct detection experiments. Limits on the *ϕ-2HDM model* with a new scalar mediator in combination with an extended Higgs sector are discussed in Section 7.2. Finally, limits with *reduced model-dependence* on the visible cross section for non-Standard Model processes with $h(\rightarrow b\bar{b}) + E_{\mathrm{T}}^{\mathrm{miss}}$ final states are derived in Section 7.3.

7.1 Interpretation in the Baryonic Z'_{B} Model

In the baryonic vector-mediator Z'_{B} model [265] it is assumed that the baryon number B is gauged under a $\mathrm{U}(1)_{\mathrm{B}}$ group with an associated Z' gauge boson and that the Dark Matter candidate carries baryon number B_χ but is neutral under Standard Model gauge symmetries. The mass of the Z'_{B} boson is generated by coupling to a scalar field, called baryonic Higgs h_{B}, which breaks the $\mathrm{U}(1)_{\mathrm{B}}$ symmetry spontaneously. After the symmetry breaking, h_{B} mixes with the Standard Model Higgs boson, h, with mixing angle θ. The Lagrangian includes three terms

$$g_q \bar{q}\gamma^\mu q Z'_\mu + g_\chi \bar{\chi}\gamma^\mu \chi Z'_\mu - g_{hZ'Z'} h Z'_\mu Z'^\mu \quad , \tag{7.1}$$

for the interaction of the Z' boson with quarks, with the Dark Matter particles (Dirac fermions) and with the Higgs boson. The Z' couples to quarks, to Dark Matter particles and to the Higgs boson with coupling strengths $g_q = g_{\mathrm{B}}/3$, $g_\chi = B_\chi g_{\mathrm{B}}$ and $g_{hZ'Z'} = m^2_{Z'} \sin\theta / v_{\mathrm{B}}$, respectively, where g_{B} is the $\mathrm{U}(1)_{\mathrm{B}}$ gauge coupling, and v_{B} the baryonic Higgs vacuum expectation value. The choice of coupling parameter and mixing angle values follows the recommendations of the LHC Dark Matter Forum [215], namely $g_q = 1/3$, $g_\chi = 1$ and $g_{hZ'Z'} = m_{Z'}$. The mixing angle is assumed to be $\sin\theta = 0.3$ to be consistent with constraints of the Standard Model Higgs boson properties [265]. The only free

model parameters are then the mass of the Z'_{B} boson, $m_{Z'}$, and the mass of the Dark Matter particle, m_χ.
The $\mathrm{U}(1)_{\mathrm{Y}}$ and $\mathrm{U}(1)_{\mathrm{B}}$ gauge bosons mix as described by an additional gauge invariant term $F_{\mathrm{Y}}^{\mu\nu} F_{\mathrm{B},\mu\nu}$ in the Lagrangian. However, the $Z - Z'$ mixing parameter is assumed to be small in order to focus on the mono-Higgs signature. The minimum decay width of the Z' mediator is assumed to be the sum of the partial widths for the decays into quarks and into the Dark Matter particles. This model offers a naturally baryonic Z'_{B} evading the constraints from dilepton resonance searches [438–440].
The Dark Matter production mechanism with mono-Higgs ($b\bar{b}$) signature in the baryonic Z'_{B} model, $pp \to Z' \to hZ'$ with subsequent Z' decay into $\chi\bar{\chi}$, is shown in Fig. 7.1. The baryonic Z'_{B} model was also studied in the previous mono-Higgs ($b\bar{b}$) analysis with $3.2\,\mathrm{fb}^{-1}$ at $\sqrt{s} = 13\,\mathrm{TeV}$ [257] and in the $\gamma\gamma$ final state [260].

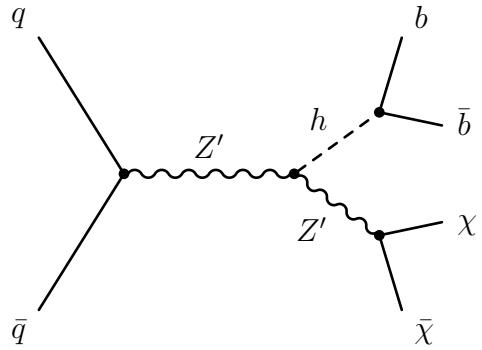

Figure 7.1: Tree-level Feynman diagram for the production of Dark Matter particles, χ, in association with the Standard Model Higgs boson in the simplified baryonic Z'_{B} model, where the Z'_{B} boson radiates a Higgs boson, h, which decays into a pair of b quarks. The Dark Matter particles are produced in the subsequent decay of the Z'_{B} boson.

7.1.1 Signal Properties

The baryonic Z'_{B} signal events are generated for $10 < m_{Z'} < 1 \cdot 10^4\,\mathrm{GeV}$ and $1 < m_\chi < 1005\,\mathrm{GeV}$ using the `MADGRAPH_AMC@NLO` 2.2.3 [65] generator at LO QCD with the `NNPDF2.3LO` PDF set. The parton shower and hadronisation is simulated by `PYTHIA` 8 with the parameter values according to ATLAS tune A14 [390]. The predicted production cross sections are given in Appendix J.
The signal sensitivity depends mainly on the $E_{\mathrm{T}}^{\mathrm{miss}}$ distribution of the signal events and, therefore, is similar as in case of the Z'-2HDM model. The harder the $E_{\mathrm{T}}^{\mathrm{miss}}$ spectrum the higher is the is the sensitivity. Figure 7.2 shows the Z'_{B} signal model $E_{\mathrm{T}}^{\mathrm{miss}}$ distributions for $m_{Z'} = 600\,\mathrm{GeV}$ and $1400\,\mathrm{GeV}$ and different Dark Matter particle masses and for comparison the $E_{\mathrm{T}}^{\mathrm{miss}}$ distribution of a Z'-2HDM model with the appropriate Z' mass. The $E_{\mathrm{T}}^{\mathrm{miss}}$ distribution for $m_{Z'} = 600\,\mathrm{GeV}$ in Fig. 7.2a does not change significantly with

increasing m_χ, expect in the off-shell regime $m_{Z'} < m_\chi/2$ where the E_T^{miss} spectrum becomes harder and the process is strongly suppressed (see Appendix J). For larger Z' masses, the E_T^{miss} spectrum becomes harder as shown in Fig. 7.2b. The distributions still peak at the same E_T^{miss} value in contrast to the Z'-2HDM model (see Fig. 7.2b) where the peak is near $m_{Z'}/2$. This is a consequence of the different Dark Matter production mechanisms in the baryonic Z'_B and the Z'-2HDM model, namely via Higgsstrahlung from the Z' in the first and via two-body Z' decay in the second case. In general, the E_T^{miss} distribution for the baryonic Z' model is softer compared to the Z'-2HDM model. Thus, the resolved SR dominates the sensitivity.

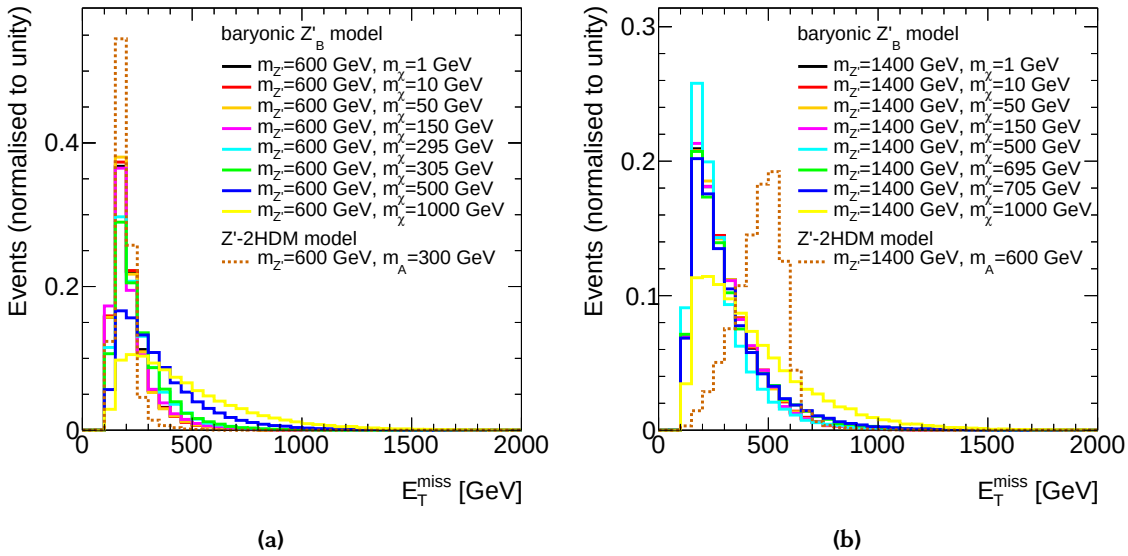

Figure 7.2: E_T^{miss} distributions with full detector simulation for the baryonic Z'_B model for two Z' mass (a) for $m_{Z'} = 600$ GeV and (b) for $m_{Z'} = 1400$ GeV and different Dark Matter particle mass, m_χ. For comparison, the E_T^{miss} distributions for two benchmark Z'-2HDM signal models $(m_{Z'}, m_A) = (600\,\text{GeV}, 300\,\text{GeV})$ and $(1400\,\text{GeV}, 600\,\text{GeV})$ are also shown. All distributions are normalised to unity.

7.1.2 Exclusion Limits

In the absence of a significant signal (see Section 5.3), exclusion limits are determined in the $(m_{Z'}, m_\chi)$ plane as shown in Fig. 7.3. The statistical analysis is performed in the same way as described for the Z'-2HDM model (see Chapter 5). For the baryonic Z'_B model no systematic uncertainties in the signal have been taken into account, as their impact on the physics results are expected to be small similarly as for the Z'-2HDM model (see Table 5.5). The limits are greatly improved compared to the previous mono-Higgs ($b\bar{b}$) analysis [257]. Z' masses below 1.9 TeV are excluded at 95 % CL for Dark Matter masses up to 200 GeV and for Dark Matter masses above 500 GeV at $m_{Z'} = 1.3$ TeV.

Sensitivity is only found where the mediator invisible decay is kinematically allowed. For comparison, the maximum observed limit on $m_{Z'}$ of the CMS experiment [441] is 1.6 TeV, and the best limit on m_χ is 430 GeV for $m_{Z'} = 1.1$ TeV.

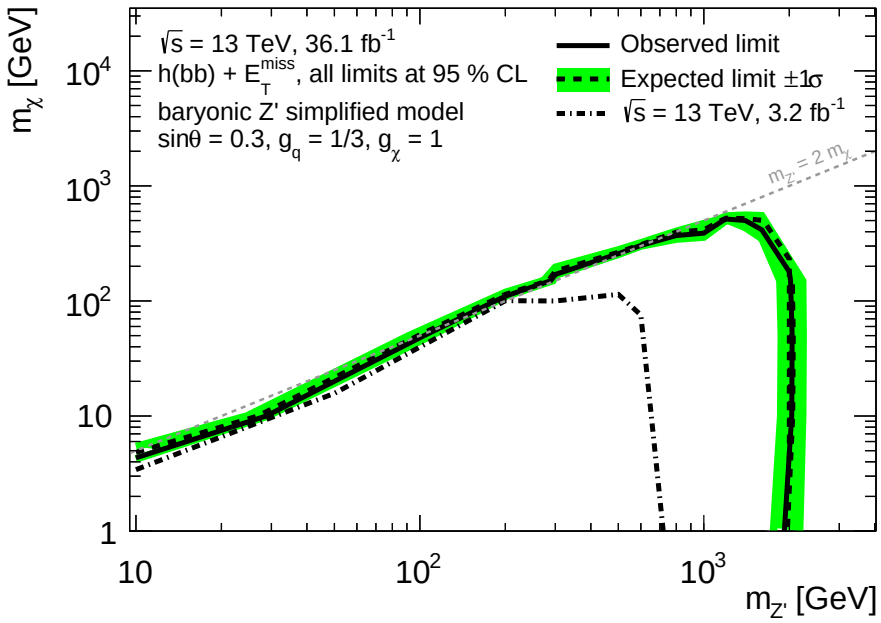

Figure 7.3: 95 % CL exclusion contours in the ($m_{Z'}$, m_χ) plane for the baryonic Z'_{B} model for $g_q = 1/3$, $g_\chi = 1$ and $\sin\theta = 0.3$. The observed limits (solid line) agree well with the expectation under the Standard Model-only hypothesis (dashed line with green uncertainty band). The observed exclusion contour from the previous ATLAS search with 3.2 fb^{-1} at $\sqrt{s} = 13$ TeV (dash-dotted line) [257] are also shown.

The limits on the simplified Z'_{B} model are used to put constraints on the spin-independent (SI) DM-nucleon cross section, $\sigma^{\mathrm{SI}}_{\chi-N}$, and compared to direct detection experiments. Following the recommendations of the LHC Dark Matter [442], the Dark Matter-nucleon cross section is calculated according to

$$\sigma^{\mathrm{SI}}_{\chi-N} = \frac{\mu^2_{\chi-N}}{\pi}(Z f_p + (A-Z) f_n)^2 \quad , \tag{7.2}$$

as a function of m_χ for vector couplings to Dark Matter [265], where $\mu_{\chi-N} = \frac{m_\chi m_n}{m_\chi + m_n}$ is the reduced mass of the Dark Matter-nucleon system with the neutron mass m_n, Z and A are the atomic and mass numbers of a nucleus, respectively, and $f_{p\,(n)}$ the couplings between Dark Matter particles and protons (neutrons). Eq. (7.2) simplifies to

$$\sigma^{\mathrm{SI}}_{\chi-N} = \frac{\mu^2_{\chi-N} f_p^2}{\pi} = \frac{9\mu^2_{\chi-N} g_q^2 g_\chi^2}{\pi m^4_{Z'}} \quad , \tag{7.3}$$

when assuming pp scattering ($A = Z = 1$) and with $f_p = \frac{3 g_q g_\chi}{m^2_{Z'}}$ [442]. The resulting 90 % CL limits on $\sigma^{\mathrm{SI}}_{\chi-N}$ for $g_q = 1/3$ and $g_\chi = 1$ are shown in Fig. 7.4 in comparison with the results from the direct detection experiments LUX [167], PandaX-II [443], SuperCDMS [444], CRESST-III [155], XENONIT [181] and DarkSide-50 [165] are also shown. The ATLAS data shows high sensitivity for Dark Matter masses below 4 GeV down to very small values of $m_\chi = 1$ GeV. The end of the exclusion curve at $m_\chi \approx 500$ GeV is due to the loss of sensitivity to the Z'_{B} model where the Dark Matter particles start to be produced off-shell. The mono-Higgs ($b\bar{b}$) search extends the limits from the mono-Higgs ($\gamma\gamma$) search [260] by almost two orders of magnitude.

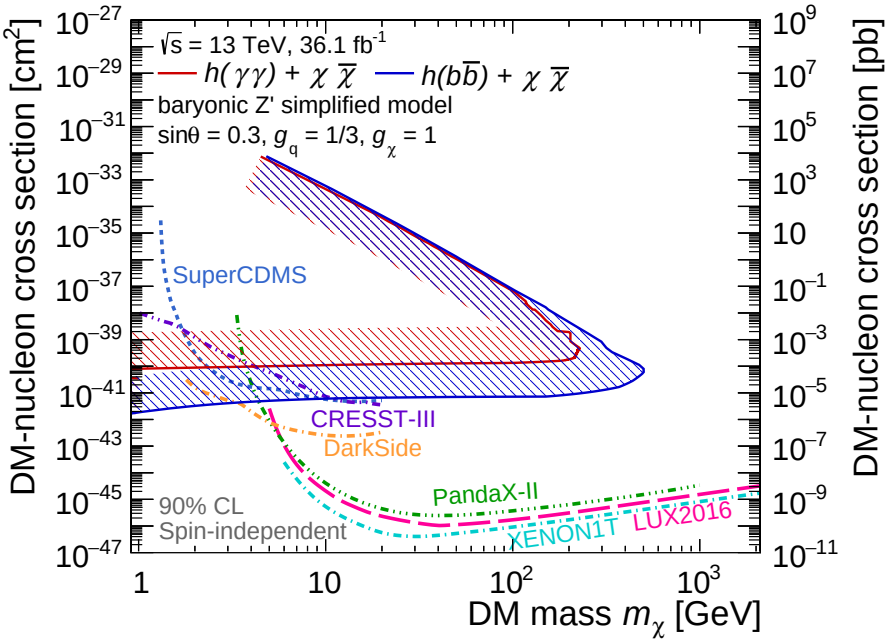

Figure 7.4: 90 % CL upper limits on the spin-independent Dark Matter-nucleon cross section as a function of the Dark Matter particle mass for the baryonic Z'_{B} signal model with vector coupling. For comparison, results from LUX [167], PandaX-II [443], SuperCDMS [444], CRESST-III [155], DarkSide-50 [165] and XENONIT [169] are shown as well as the limits from the mono-Higgs ($\gamma\gamma$) search [260].

7.1.3 Comparison to Mono-X Results

As discussed in Section 2.5.3, either the mono-X signature (see Fig. 2.10a) is used to search for Dark Matter at colliders or the dijet and the dilepton signatures (see Fig. 2.10c) are used to look for the mediators responsible for the interaction between Dark Matter and Standard Model particles. For most of the mono-X and dijet/dilepton searches simplified models are used with a vector mediator between Dark Matter and Standard Model particles (see Ref. [215]). In theses models, an additional U(1) gauge symmetry is

introduced, under which the Dark Matter particles are charged. The simplified model is then described by a set of five free parameters: the masses of the mediator and the Dark Matter particle $m_{Z'}$ and m_χ, respectively, the flavour universal coupling of the Z' boson to quarks, g_q, to leptons, g_ℓ, and to Dark Matter particles, g_χ. Here, g_χ is assumed to be fixed to one, while g_q and g_ℓ are allowed to vary and impact the sensitive of dijet or dilepton searches, respectively. Two scenarios are considered to highlight the complementary of the mono-X searches of these different final states with $(g_q, g_\ell) = (0.25, 0)$ and $(0.1, 0.01)$. The ATLAS results based on the dilepton, the dijet, the di*b*jet and the $t\bar{t}$ resonance searches together with several mono-X searches with X=jet, γ, $Z(\ell\ell)$ and W/Z(had.) (see Ref. [445]) are compared to the mono-Higgs ($b\bar{b}$) results in the context of the baryonic Z'_{B} model. The results of the mono-X searches are statistically combined. The cross section limits at 95 % CL are provided in the Dark Matter particle mass and the mediator mass plane. In Fig. 7.5, the results for a vector mediator with and without couplings to leptons are shown. The strongest limits are obtained from the dijet resonance searches (see Fig. 7.5a) which exclude mediator masses between 200 to 2600 GeV fairly independent of m_χ for $g_\ell = 0$.

The lower mass limit of the dijet search originates from limitations of the jet trigger threshold. In the region of $200 < m_{Z'} < 450$ GeV, the sensitive of the dijet resonance search is reduced due to the opening of the $Z' \to \chi\bar{\chi}$ decay channel. For $m_{Z'} < 2m_\chi$, masses of the mediator up to 2.9 TeV are excluded. The sensitive of mono-X signatures is highest in the region of $m_{Z'} > 2m_\chi$, and mediator masses up to 1.5 TeV are excluded for low m_χ. Unique coverage is provided for mediator masses below 450 GeV. The sensitivity of mono-X searches is strongly decreased in the off-shell region, as a consequence of the strongly reduced production cross section. The sensitivity is dominated by the mono-jet search, while the mono-γ search provides sensitive for very low Dark Matter masses where the mono-jet search is limited by the jet trigger threshold. Despite the different model assumptions, i.e. the different choices of coupling parameters, the mono-Higgs ($b\bar{b}$) results of the baryonic Z'_{B} model can be compared which allowed to exclude vector mediator masses below 1.9 TeV for Dark Matter masses up to 200 GeV. For non zero lepton couplings, as shown in Fig. 7.5b, and reduced couplings of the mediator to quarks, the sensitive of the dijet searches are reduced, whereas the leptonic branching ratio allows dilepton searches, e.g. via $Z' \to \ell^-\ell^+$ decays with $\ell = \mu, e$, to impose constraints for a wide range of mediator masses. The resonant searches allow to exclude mediator masses between 150 GeV and 2 TeV if $m_{Z'} < 2m_\chi$ and between 150 GeV and 350 GeV for all m_χ. The limits on the mediator masses of the mono-X searches are reduced to 1 TeV, and the mono-Higgs ($b\bar{b}$) search does not provide limits when lepton couplings are assumed.

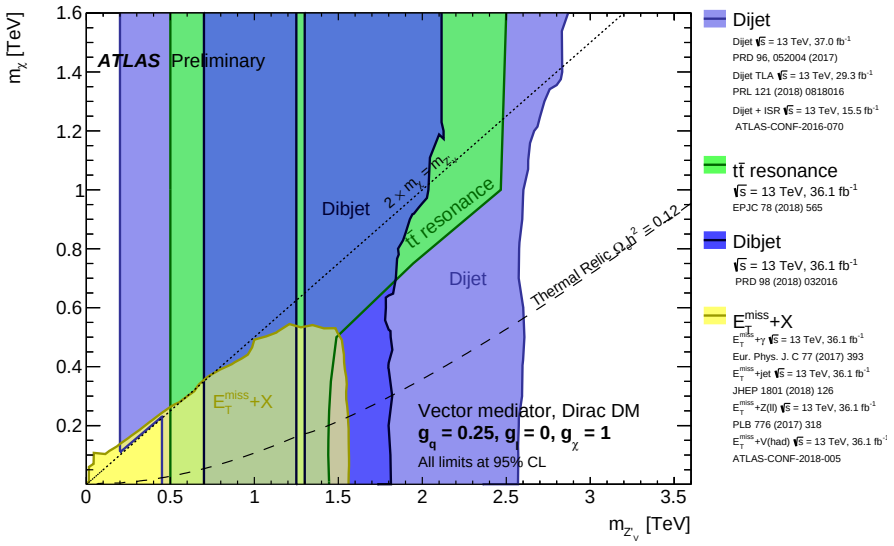

(a)

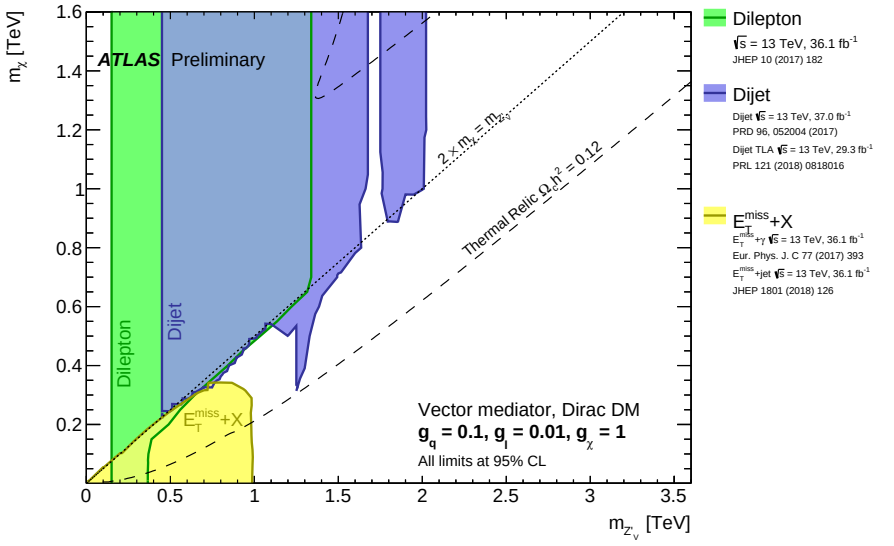

(b)

Figure 7.5: Regions in a Dark Matter mass-mediator mass plane excluded at 95 % CL by a selection of ATLAS Dark Matter searches in case of a vector mediator [445]. The exclusion contours are computed for a Dark Matter coupling parameter $g_\chi = 1.0$. In (a) a quark coupling $g_q = 0.25$ universal to all flavors and the lepton coupling $g_\ell = 0$ is used, while in (b) $g_q = 0.1$ and $g_\ell = 0.01$ is used. The dashed curves labeled *thermal relic* indicate combinations of Dark Matter and mediator mass that are consistent with the observed Dark Matter relic density. The dotted curve indicates the kinematic threshold where the mediator can decay on-shell into Dark Matter particles.

The exclusion contours in the mass-mass plane can be translated into spin-independent limits on the Dark Matter-nucleon scattering cross section (see Ref. [442]). The Dark

Matter-nucleon cross section depends on the choice of the three coupling parameters, the mediator mass and the mass of the Dark Matter particle. The comparison to direct detection experiments is only valid in the context of the specific simplified model and coupling assumptions, providing complementary but model-dependent information. The cross section limits of the ATLAS based searches are shown at 95 % CL, while those of direct detection experiments are shown at 90 %. For the comparison of the collider limits, it is assumed that the mediator does not couple to leptons, which is motivated as the Dark Matter particle scatters primarily with the nuclei within a direct detection experiment. Figure 7.6 shows the spin-independent Dark Matter-nucleon cross section as a function of m_χ for the case of a vector mediator. The collider based searches are especially sensitive in the region of low Dark Matter masses, where the direct detection experiments have less sensitivity due to very low energy recoils that such low-mass Dark Matter particles would induce. In particular, the dijet searches greatly extend the reach of collider searches to even lower Dark Matter-nucleon cross section compared to the mono-X searches. The lower edge of the sensitivity contour of the mono-X searches (see Fig. 7.6) at m_χ around 300 to 400 GeV is limited by the mediator mass reach of the analysis as the Dark Matter-nucleon scattering cross section is proportional to $m_{Z'}^{-4}$. The mono-Higgs ($b\bar{b}$) search (see Fig. 7.4) provides similar results compared to the other mono-X searches.

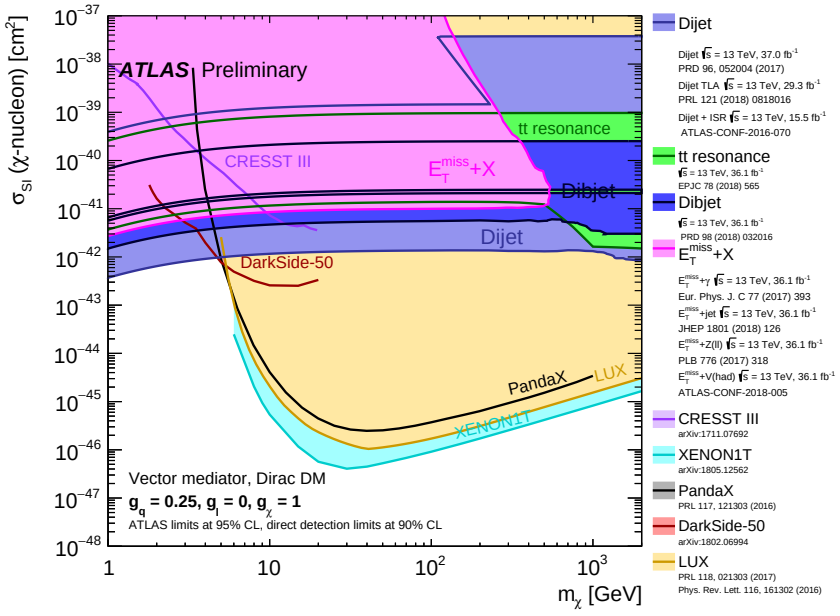

Figure 7.6: A comparison of the inferred mono-X and dijet limits to the constraints from direct detection experiments on the spin-independent Dark Matter-nucleon scattering cross section in the context of the Z'_V simplified model with vector couplings. The results from this analysis, excluding the region to the left of the contour. The ATLAS limits are shown at 95 % and direct detection limits at 90 % CL. The comparison is valid solely in the context of the simplified model, assuming a mediator width fixed by the Dark Matter mass and coupling values $g_q = 0.25$ and $g_\chi = 1$ [445].

7.2 Interpretation in the ϕ-2HDM Model

The ϕ-2HDM model [446] with pseudoscalar mediator ϕ coupling to Dark Matter has been studied for the first time in the context of the ATLAS mono-Higgs ($b\bar{b}$) search. It has been adopted as a common benchmark for ATLAS and CMS Dark Matter searches by the LHC Dark Matter Working Group [447].

The model comprises an extended Higgs sector with a pseudoscalar mediator instead of the vector mediator in the Z'-2HDM model. The Higgs self-interaction is assumed to be CP conserving and to process a softly broken Z_2 symmetry.

After electroweak symmetry breaking, the 2HDM potential yields five physical Higgs bosons, as in the case of the Z'-2HDM model, the two CP-even states h and H, the CP-odd state A, and two charged Higgs boson states $H^\pm$. The alignment limit in Eq. (2.29) is assumed, where h has couplings as predicted by the Standard Model and a mass of 125 GeV and the vacuum expectation value, $v = \sqrt{v_1^2 + v_2^2}$, is assumed to be 246 GeV. The interactions of fermionic Dark Matter particles are mediated by the pseudoscalar CP-odd field, ϕ, which mixes with the CP-odd Higgs boson A. The decay channel $\phi \to \chi\bar{\chi}$ by far dominates for $m_\phi < 2m_t$ and with these assumptions the ϕ-2HDM model is fully

described by 10 parameters. Five of them are particle masses, namely the masses of the four remaining Higgs bosons, A, H and $H^{\pm}$ with $m_{H^-} = m_{H^+}$, of the pseudoscalar mediator ϕ and of the Dark Matter particle χ. The other five are coupling parameters, the Yukawa coupling g_χ between ϕ and χ, the mixing angle $\sin\theta$ between A and ϕ, $\tan\beta$ and the quartic self couplings of the pseudoscalar, λ_3, λ_{ϕ_1} and λ_{ϕ_2}, as described in Appendix K.

For the studies, $g_\chi = 1$ and $m_\chi = 10\,\text{GeV}$ is assumed. The latter parameter has negligible effect on the final state kinematics and mostly affect the production cross section. For mixing angles $\sin\theta = 0$ or 1, no mono-X signature appears. For small $|\sin\theta|$, resonant production mode dominates, while for large $\sin\theta$ non-resonant production is more prominent. In order to produce detectable $E_{\text{T}}^{\text{miss}}$, $\sin\theta$ is chosen to be 0.35.

Constraints on the model parameters are imposed by requiring the Standard Model custodial symmetry for the tree-level Higgs potential, i.e. $m_{H^\pm} = m_H$ or $m_{H^\pm} = m_A$. $A - \phi$ mixing imposes further constraints for the case $m_{H^\pm} = m_A$. Therefore, $m_{H^\pm} = m_H = m_A$ is assumed [446]. The quartic self couplings λ_3, λ_{ϕ_1} and λ_{ϕ_2} affect all cubic Higgs interactions, e.g. of $H\phi\phi$ and $A\phi h$. In order to keep the total widths Γ_H and Γ_A small, $\lambda_3 = \lambda_{\phi_1} = \lambda_{\phi_2} = 3$ is a suitable choice.

The production mechanisms of a mono-Higgs ($b\bar{b}$) signature within the ϕ-2HDM model are either resonant ($pp \to A \to h\phi$ for $m_A > m_\phi + m_h$) or non-resonant ($gg \to h\phi$) as shown in Fig. 7.7. The resonant production via the $A\phi h$ vertex in Fig. 7.7a dominates over the top quark box contribution in Fig. 7.7b. Both interfere and the latter can be important for $m_A < 2m_t$. For $m_\phi > m_A + m_h$, the rules of A and ϕ are exchanged, and ϕ is produced resonantly.

The parameters settings have been defined by the LHC Dark Matter Working Group (see Ref. [447]).

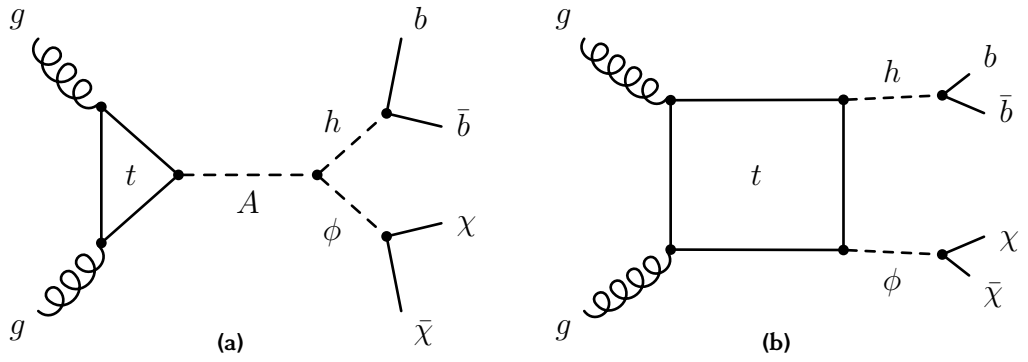

Figure 7.7: Feynman diagrams in the simplified ϕ-2HDM model for the production of Dark Matter particles, χ, in association with a Higgs boson. The Higgs boson, h, decays into a pair of b quarks, while the pseudo-scalar, ϕ, decays into a pair of Dark Matter particles. The production occurs either via the decay of the pseudoscalar Higgs boson, A, (a) or via direct coupling of h and ϕ to a top quark loop (b).

7.2.1 Signal Properties

Signal events were generated using MADGRAPH_AMC@NLO 2.4.3 [65] at NLO QCD. The parton showering and hadronisation is performed by PYTHIA 8 with parameter values according to the ATLAS tune A14 [390]. The NNPDF30_LO_AS_0130 PDF set at LO QCD with $\alpha_S(m_Z) = 0.130$ and in the five-flavor scheme with massless b-quarks is used [389]. The events were generated for fixed $\tan\beta = 1$ and varying m_A and m_ϕ, and for fixed $m_A = 600\,\text{GeV}$ and varying $\tan\beta$ and m_ϕ. The production cross sections for different ϕ-2HDM signal model points are summarised in Appendix K.
In Figs. 7.8 and 7.9, the E_T^miss distributions of the signal events are shown for different combinations of m_A, m_ϕ and $\tan\beta$. For fixed m_A, the E_T^miss spectra become narrower and

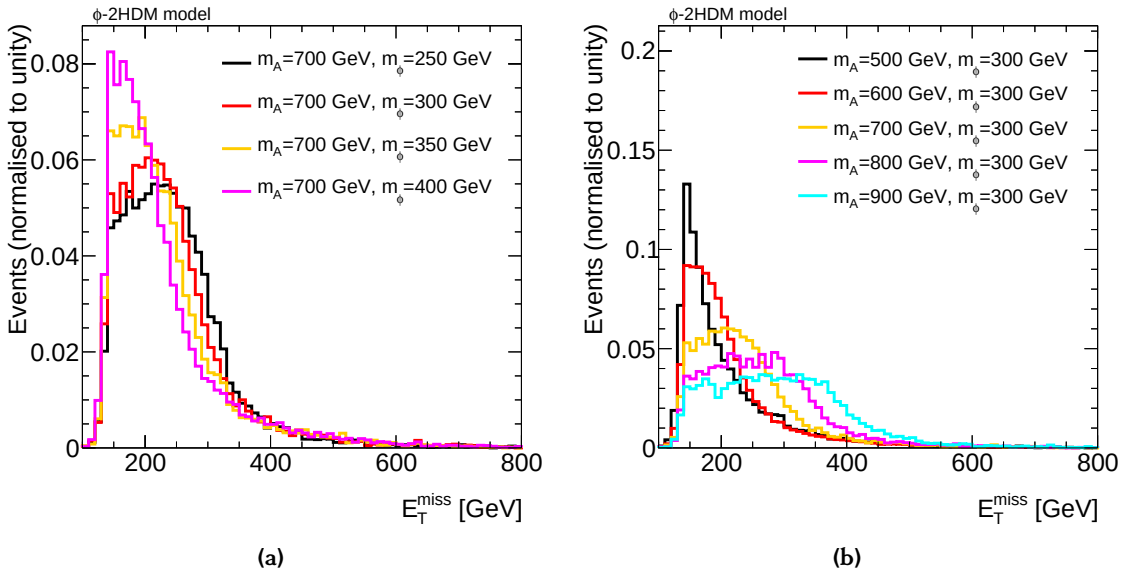

Figure 7.8: E_T^miss distributions with full detector simulation for the ϕ-2HDM model with $\tan\beta = 1$, $\sin\theta = 0.35$ and $m_\chi = 10\,\text{GeV}$ for (a) fixed $m_A = 700\,\text{GeV}$ and varying m_ϕ and (b) fixed $m_\phi = 300\,\text{GeV}$. All distributions are normalised to unity.

shifted to lower values with decreasing m_ϕ. For fixed m_ϕ, the spectra become broader and harder with increasing m_A, until the end-point of the Jacobian peak is reached, which is smeared out due to detector and E_T^miss resolution. The E_T^miss distribution is also broader and softer for the non-resonant production mechanism (see Fig. 7.7b).
The impact of varying $\tan\beta$ on the E_T^miss distribution is shown in Fig. 7.9. It is small for $\tan\beta \geq 1$, while for values of $\tan\beta < 1$ the E_T^miss spectrum becomes softer.

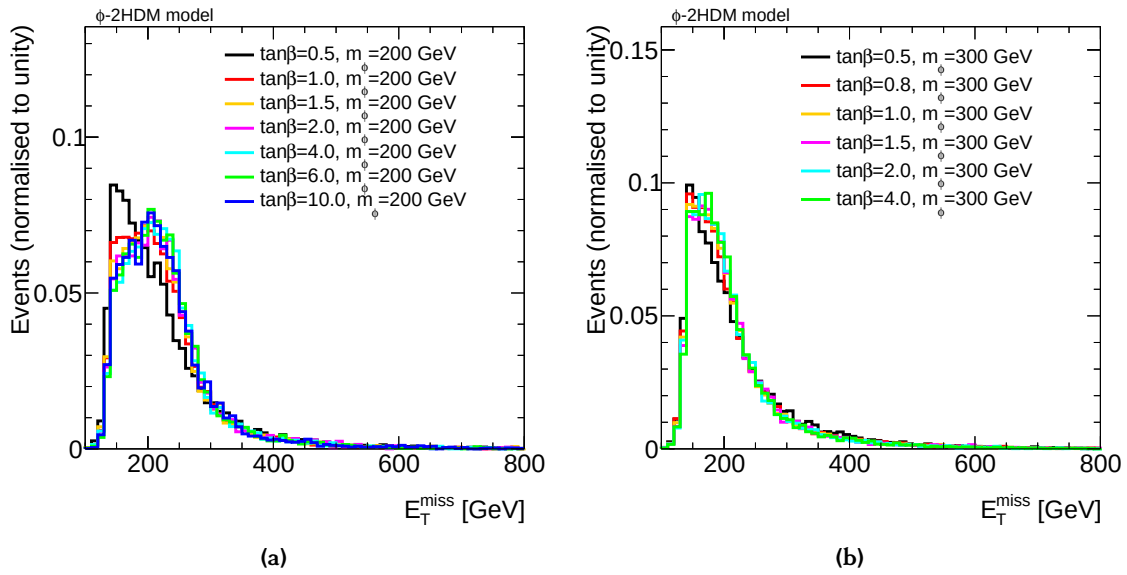

Figure 7.9: $E_{\mathrm{T}}^{\mathrm{miss}}$ distributions with full detector simulation for the ϕ-2HDM model with $\sin\theta = 0.35$, $m_\chi = 10\,\mathrm{GeV}$ and $m_A = 600\,\mathrm{GeV}$ for fixed $m_\phi = 200\,\mathrm{GeV}$ (a) and 300 GeV (b) for varying $\tan\beta$. All distributions are normalised to unity.

7.2.2 Exclusion Limits

Limits on the cross section are determined in the (m_ϕ, m_A) plane with the constraint $m_A = m_H = m_{H^\pm}$ and for fixed values of $g_\chi = 1$, $\sin\theta = 0.35$, $\tan\beta = 1$ and $m_\chi = 10\,\mathrm{GeV}$ (see Fig. 7.10). Signal uncertainties have been again neglected, as their impact on the physics results are expected to be small also for the ϕ-2HDM model (see Table 5.5). Values of m_A between 300 and 1350 GeV are excluded at 95 % CL for small m_ϕ. The uncertainties on the limits are increasing with m_A, because $E_{\mathrm{T}}^{\mathrm{miss}}$ increases and also the statistical uncertainty in the $E_{\mathrm{T}}^{\mathrm{miss}}$ measurement.

Cross section limits are also determined in the ($\tan\beta$, m_ϕ) plane for fixed $m_A = m_H = m_{H^\pm} = 600\,\mathrm{GeV}$ (see Fig. 7.11). Values of $\tan\beta$ between 0.5 and 2.8 and m_ϕ between 100 to 260 GeV are excluded at 95 % CL. The exclusion was not investigated for $\tan\beta < 0.5$, due to the non-trivial dependency of the width with respect to $\tan\beta$ when the $H/A \to t\bar{t}$ decay becomes important. sensitivity is found for signal models with $\tan\beta < 0.5$.

In comparison, the CMS experiment excludes masses $500 < m_A < 900\,\mathrm{GeV}$ for $m_\phi = 150\,\mathrm{GeV}$ and $\tan\beta$ values between 0.5 and 2.0 for $m_\phi = 100\,\mathrm{GeV}$ [441].

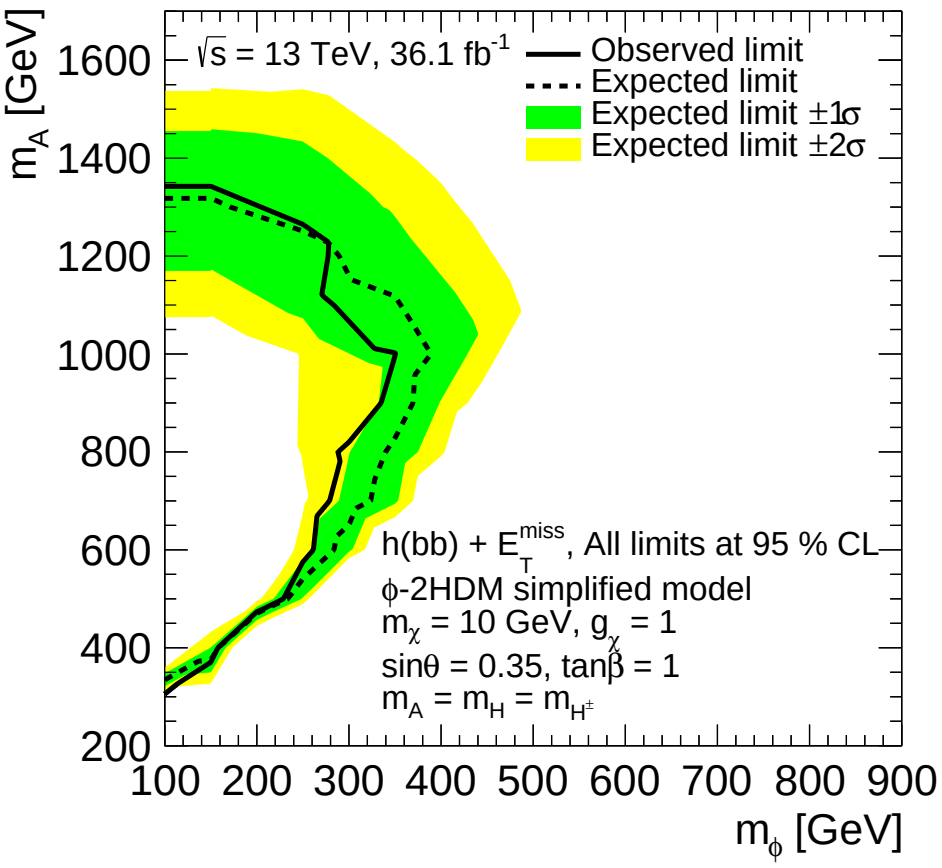

Figure 7.10: 95 % CL exclusion contours in the (m_ϕ, m_A) plane for the ϕ-2HDM model with $m_A = m_H = m_{H^\pm}$ and for $g_\chi = 1$, $\sin\theta = 0.35$, $\tan\beta = 1$ and $m_\chi = 10$ GeV. The observed limits (solid line) are consistent with the expectation under the Standard Model-only hypothesis (dashed line) within one standard deviation (green filled band).

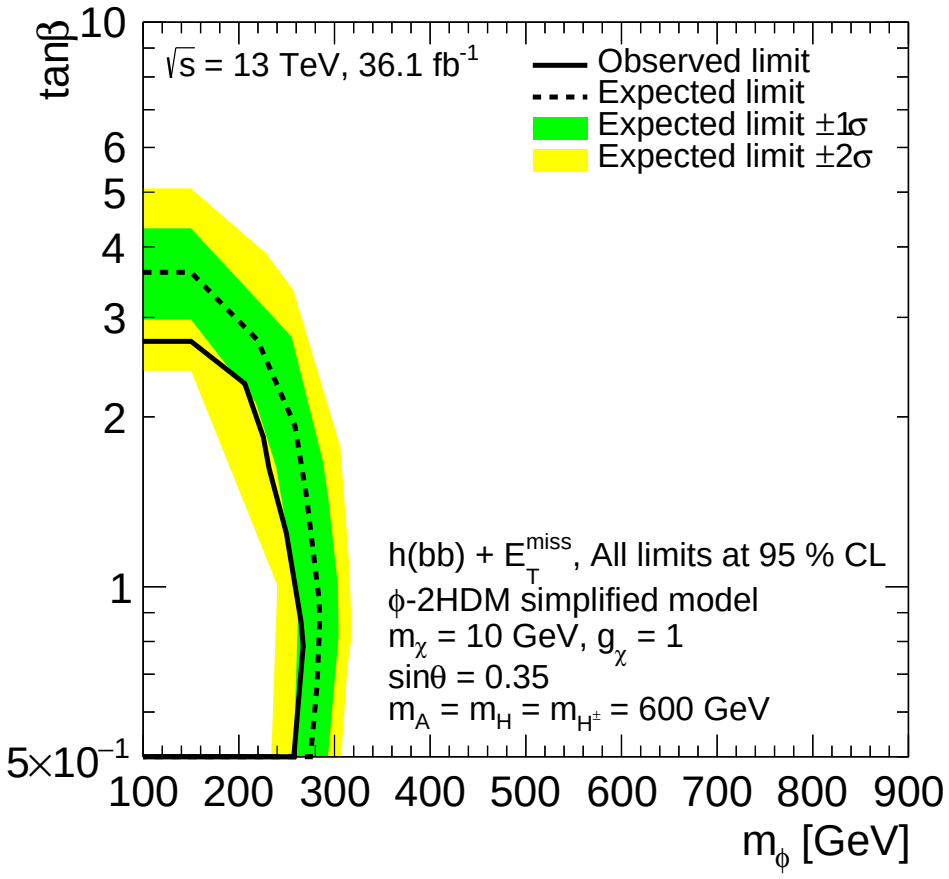

Figure 7.11: 95 % CL exclusion contours in the ($\tan\beta$, m_ϕ) plane for the ϕ-2HDM model with for $g_\chi = 1$, $\sin\theta = 0.35$, $m_\chi = 10\,\text{GeV}$ and $m_A = m_H = m_{H^\pm} = 600\,\text{GeV}$. The observed limits (solid line) are consistent with the expectation under the Standard Model-only hypothesis (dashed line) within one to two standard deviations (green and yellow filled bands).

7.3 Less Model-Dependent Limits

Finally, the mono-Higgs ($b\bar{b}$) search results are used to set limits on the visible cross section for $h(\rightarrow b\bar{b})$ $+E_{\mathrm{T}}^{\mathrm{miss}}$ production as a function of $E_{\mathrm{T}}^{\mathrm{miss}}$ as given by

$$\sigma_{\mathrm{vis},\, h(b\bar{b})+\mathrm{DM}} = \sigma_{h+\mathrm{DM}} \times \mathcal{B}(h \rightarrow b\bar{b}) \times \mathcal{A} \times \varepsilon(E_{\mathrm{T}}^{\mathrm{miss}}) \quad , \tag{7.4}$$

where $\sigma_{h+\mathrm{DM}}$ is the generic $h + \mathrm{DM}$ production cross section, $\mathcal{B}$ the branching ratio of the Standard Model Higgs boson decay into a pair of b quarks and $\mathcal{A} \times \varepsilon(E_{\mathrm{T}}^{\mathrm{miss}})$ the kinematic acceptance times the probability for an event to be reconstructed in the same $E_{\mathrm{T}}^{\mathrm{miss}}$ bin as generated and to pass all selection criteria except the cuts on m_h and the b-jet multiplicity. In particular, no separation of events into the one and two b-jet categories is done, in order to reduce the dependence on the b-tagging efficiency.
The obtained cross section limits have reduced $h + \mathrm{DM}$ model assumptions, i.e that the Higgs boson is produced in a back-to-back configuration relative to $\vec{E}_{\mathrm{T}}^{\mathrm{miss}}$ from Dark Matter particles. In order to reduce the model dependence on the $E_{\mathrm{T}}^{\mathrm{miss}}$ distribution, the statistical interpretation (see Chapter 5) of the mono-Higgs ($b\bar{b}$) analysis is modified to analyse only one $E_{\mathrm{T}}^{\mathrm{miss}}$ range of the signal region at a time.
The $\mathcal{A} \times \varepsilon(E_{\mathrm{T}}^{\mathrm{miss}})$ values are derived from the benchmark Z'-2HDM signal model, which provides a sufficient event population in all of the four $E_{\mathrm{T}}^{\mathrm{miss}}$ ranges depending on the combinations of ($m_{Z'}$, m_A) together with a generic $h + \mathrm{DM}$ signal event topology. A range of up to ten ($m_{Z'}$, m_A) signal model points that yield a sizable contribution of $\approx 10\,\% \times \sigma_{h+\mathrm{DM}} \times \mathcal{B}(h \rightarrow b\bar{b})$ in a given $E_{\mathrm{T}}^{\mathrm{miss}}$ bin are used for the derivation of $A \times \varepsilon$. Here, $A \times \varepsilon$ as a function of $E_{\mathrm{T}}^{\mathrm{miss}}$ for a certain ($m_{Z'}$, m_A) signal point is given by

$$\mathcal{A} \times \varepsilon(E_{\mathrm{T}}^{\mathrm{miss}}) = \frac{N_{\mathrm{events}}^{\mathrm{after}}(E_{\mathrm{T,\,truth}}^{\mathrm{miss}} \text{ and } E_{\mathrm{T,\,reco}}^{\mathrm{miss}})}{N_{\mathrm{events}}^{\mathrm{before}}(E_{\mathrm{T,\,truth}}^{\mathrm{miss}})} \quad , \tag{7.5}$$

with $N_{\mathrm{events}}^{\mathrm{after}}(E_{\mathrm{T,\,truth}}^{\mathrm{miss}}$ and $E_{\mathrm{T,\,reco}}^{\mathrm{miss}})$ the number of events which end up in the same $E_{\mathrm{T}}^{\mathrm{miss}}$ bin as generated after applying all selection criteria and $N_{\mathrm{events}}^{\mathrm{before}}(E_{\mathrm{T,\,truth}}^{\mathrm{miss}})$ the number of events with $E_{\mathrm{T,\,truth}}^{\mathrm{miss}}$ value at parton-level before applying any of the event selection criteria. The lowest $A \times \varepsilon$ value for a range of ($m_{Z'}$, m_A) signal model points in a given $E_{\mathrm{T}}^{\mathrm{miss}}$ region is quoted in Fig. 7.12. The individual $\mathcal{A} \times \varepsilon(E_{\mathrm{T}}^{\mathrm{miss}})$ values for each ($m_{Z'}$, m_A) combination can be found in Appendix L. The $A \times \varepsilon$ values range between 15 to 40 % in the resolved region and around 55 % in the merged region. The signal selection efficiency in the resolved region is smaller related to the $E_{\mathrm{T}}^{\mathrm{miss}}$ trigger and $E_{\mathrm{T}}^{\mathrm{miss}} > 150\,\mathrm{GeV}$ requirement, which rejects Z'-2HDM signal events produced with low $E_{\mathrm{T}}^{\mathrm{miss}}$ values.
Exemplarily, the limits on $\sigma_{\mathrm{vis},\, h(b\bar{b})+\mathrm{DM}}$ for a range of Z'-2HDM models in the lowest $E_{\mathrm{T}}^{\mathrm{miss}}$

bin are shown in Table 7.1 (for the limits in the other three $E_{\mathrm{T}}^{\mathrm{miss}}$ bins see Appendix L). The derived upper limits on $\sigma_{\mathrm{vis},\, h(b\bar{b})+\mathrm{DM}}$ at 95 % CL for each $E_{\mathrm{T}}^{\mathrm{miss}}$ bin are given

Table 7.1: 95 % observed and expected limits on $\sigma_{\mathrm{vis},\, h(b\bar{b})+\mathrm{DM}}$ for h + DM events in the [150, 200) GeV $E_{\mathrm{T}}^{\mathrm{miss}}$ bin derived from a range of Z'-2HDM models. Also shown are the up and down variations ($\pm 1\,\sigma$) by one standard deviation on the expected limit. All expected limits are within 25 % of each other. To avoid any model dependence, the parameter set $(m_{Z'},\, m_A) = (400\,\mathrm{GeV},\, 400\,\mathrm{GeV})$ with weakest expected limit (in bold) is used for setting limits with reduced model-dependence.

$m_{Z'}$ [GeV]	m_A [GeV]	σ_{obs} [fb]	σ_{exp} [fb]	$-1\,\sigma$ [fb]	$+1\,\sigma$ [fb]
400	**400**	19.12	18.34	13.22	25.53
600	200	14.46	12.93	9.32	18.00
600	400	17.02	16.98	12.24	23.64
600	600	11.38	12.69	9.14	17.66
800	300	19.18	14.44	10.40	20.09
800	500	12.71	12.21	8.79	16.99
800	600	11.99	12.66	9.12	17.62
800	700	13.26	13.30	9.58	18.50
1000	800	13.73	13.21	9.52	18.39

in Fig. 7.12, with the least stringent limit has being quoted for a range of $(m_{Z'},\, m_A)$ combinations (see Table 7.1). The cross sections limits on $\sigma_{\mathrm{vis},\, h(b\bar{b})+\mathrm{DM}}$ range from 1.7 to 19.1 fb and decrease with increasing $E_{\mathrm{T}}^{\mathrm{miss}}$. The limits become stronger with increasing $E_{\mathrm{T}}^{\mathrm{miss}}$ due to the rapidly decreasing Standard Model backgrounds for high $E_{\mathrm{T}}^{\mathrm{miss}}$.

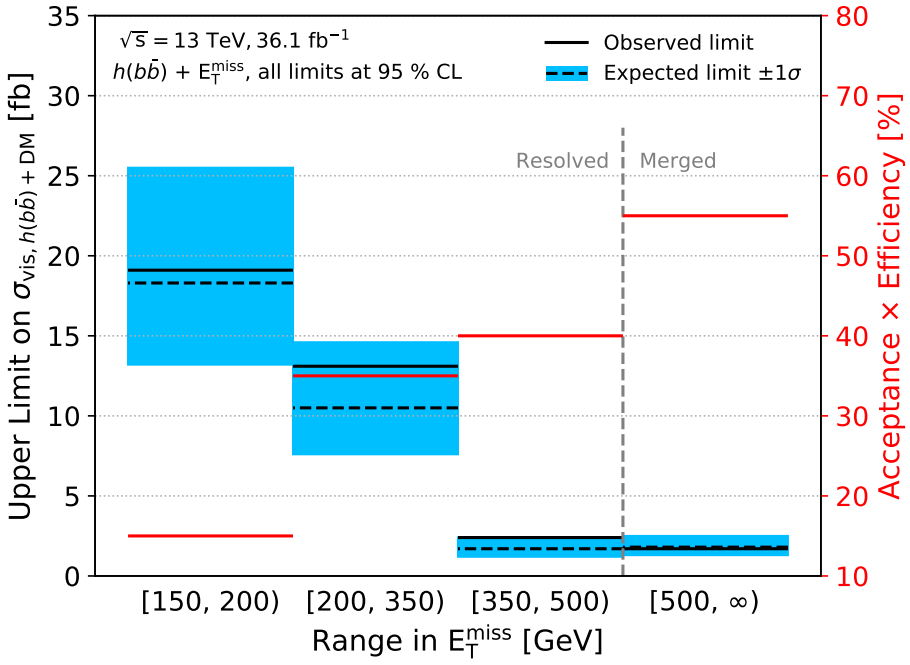

Figure 7.12: 95 % CL upper limits on the visible cross section, $\sigma_{\text{vis},\, h(b\bar{b})+\text{DM}}$, for $h+\text{DM}$ events with $h \to b\bar{b}$ decays separately for the four $E_{\text{T}}^{\text{miss}}$ ranges inclusive in the number of b-jets. The observed limits (solid line) are consistent with the expectations under the Standard Model-only hypothesis (dashed line) within the uncertainties (coloured band). In addition, the acceptance times efficiency, i.e. the probability to select an event in the same $E_{\text{T}}^{\text{miss}}$ bin as generated, is shown (red line).

Summary

The Standard Model (SM) of particle physics provides a consistent and precise description of all known elementary particles and their interactions via the strong, the weak and the electromagnetic force. The discovery of the Higgs boson by the ATLAS and CMS experiments at the Large Hadron Collider (LHC) completed the SM particle content.

Nonetheless, the SM leaves many questions unanswered. In particular, it provides no explanation for the existence and nature of Dark Matter (DM). The existence of DM is supported by many astrophysical and cosmological observations based on its gravitational effects. Little is known about the particle nature of DM and whether it is affected by any other force than gravity. It is generally assumed that DM particles do not interact electromagnetically and strongly. DM particles may, however, couple weakly to SM particles. The most favoured DM particle candidate is a Weakly Interacting Massive Particle (WIMP), which is stable over the lifetime of the Universe and has a mass in the GeV to TeV range. The concept is supported by the fact that WIMP particles would be naturally produced in the required abundance during the formation of the Universe. This so-called WIMP miracle is based on the assumption that DM and SM particles were in thermal equilibrium in the early Universe and DM froze-out at a certain point in time in the evolution of the Universe. WIMP DM particles can be searched for in underground direct detection experiments, in ground- or space-based indirect detection experiments and at the LHC.

In this thesis, a search for DM particles in the so-called mono-Higgs ($b\bar{b}$) channel has been performed. The Higgs boson is produced in association with DM particles and decays into a pair of b quarks. The decay of the SM Higgs boson with a mass of 125 GeV into b quark pairs has the highest branching ratio. The Higgs boson candidates are produced in a characteristic back-to-back topology, where the Higgs boson recoils against large missing transverse energy ($E_{\mathrm{T}}^{\mathrm{miss}}$) associated with the pair produced DM particles. The mono-Higgs ($b\bar{b}$) search is based on datasets of 36.1 fb^{-1} and 79.8 fb^{-1} recorded by the ATLAS detector at a center-of-mass energy of 13 TeV in 2015-2016 and in 2017, respectively, during Run 2 of the LHC.

The mono-Higgs channel provides a complementary signature to other mono-X DM searches. Due to the small Yukawa couplings of the Higgs boson to light quarks, its production as initial-state radiation is strongly suppressed compared to other SM particles. It must rather originate from the production vertex of the DM particles. It is a reasonable assumption that DM particles, like SM particles, couple to the Higgs boson because of their mass. The production mechanism in extensions of the SM usually involves a new heavy mediator of the interaction between SM and DM particles. The Higgs bosons are then produced with large Lorentz boosts back-to-back to the pair produced DM particles. The most frequent Higgs decays into into collimated b-jet pairs are efficiently reconstructed by using jet substructure analysis. The selection of mono-Higgs ($b\bar{b}$) $+E_{\mathrm{T}}^{\mathrm{miss}}$ events was optimised assuming them to arise from the Z'-two-Higgs-doublet model (Z'-2HDM), where the $h(\rightarrow b\bar{b}) + E_{\mathrm{T}}^{\mathrm{miss}}$ final states are produced via $pp \rightarrow Z' \rightarrow hA \rightarrow b\bar{b}\chi\bar{\chi}$ with the pseudoscalar Higgs boson A decaying solely into a DM particle pair $\chi\bar{\chi}$. The first analysis was performed using the 36.1 fb^{-1} of ATLAS data recorded in 2015 and 2016. Background contributions with hadronically decaying τ leptons or a third b-jet had to be suppressed in particular.
In the absence of a significant deviation from the SM expectation, 95 % CL lower limits on $m_{Z'}$ and m_A of 2600 GeV and 600 GeV, respectively, have been derived for a DM particle mass of 100 GeV. The sensitivity of the mono-Higgs ($b\bar{b}$) search is limited by systematic uncertainties in the b-jet identification efficiency and statistically at high $E_{\mathrm{T}}^{\mathrm{miss}}$ values.
For very high $E_{\mathrm{T}}^{\mathrm{miss}}$ and corresponding large Lorentz-boost of the Higgs, the signal selection efficiency has been increased by using an improved b-jet reconstruction based on track-jets with variable cone radius. The improved search has been applied to 79.8 fb^{-1} of data taken in 2017, allowing for the exclusion of a substantial additional parameter space of the Z'-2HDM models, i.e. $m_{Z'}$ up to 2800 GeV and m_A up to 680 GeV.

The results based on the 36.1 fb^{-1} dataset have also been interpreted in the context of a Z'_{B} vector boson mediator model with baryonic U(1)$_{\mathrm{B}}$ charge excluding Z'_{B} masses up to 1.9 TeV at 95 % CL for DM mass $m_\chi = 1$ GeV, Z'_{B} couplings to quarks and DM particles of $g_q = 1/3$ and $g_\chi = 1$, respectively, and a mixing angle $\sin\theta = 0.3$ between the SM Higgs and the baryonic Higgs from spontaneous U(1)$_{\mathrm{B}}$ breaking. The limits on the Z'_{B} model were used to derive constraints on the spin-independent DM-nucleon cross section at 90 % CL which can be compared to those from direct detection experiments. The mono-Higgs ($b\bar{b}$) search is especially competitive for DM masses from 1 GeV up to 450 GeV. Both have, however, different model dependences. In addition, the results have been interpreted in an extended 2HDM with pseudoscalar mediator ϕ coupling to DM and SM particles. Masses of the pseudoscalar mediator are excluded up to 300 GeV for

$m_\chi = 10\,\text{GeV}$, $g_\chi = 1$, $\tan\beta = 1$ and mixing angle $\sin\theta = 0.35$ between h and ϕ. Values of $\tan\beta$ between 0.6 and 2.8 are excluded for m_ϕ between 100 and 260 GeV. Finally, stringent upper limits on the visible production cross section for non-SM events with $h + E_{\text{T}}^{\text{miss}}$ signature with reduced model dependence have been determined at 95 % CL, which range from 1.7 to 19.1 fb and decrease with increasing $E_{\text{T}}^{\text{miss}}$.

In the near future, the complete Run 2 dataset with additional $60\,\text{fb}^{-1}$ from 2018 will improve the sensitivity of the mono-Higgs ($b\bar{b}$) analysis at high $E_{\text{T}}^{\text{miss}}$. Algorithms combining tracking and calorimeter information to construct improved large-R jet substructure observables can also improve the sensitivity at high $E_{\text{T}}^{\text{miss}}$. Multivariate techniques may allow to extend the analysis to lower $E_{\text{T}}^{\text{miss}}$ where the background is higher. These techniques will be even more important for Run-3 and the High-Luminosity LHC.

Appendix A

Brief History of the Universe

Eq. (2.6) implies that Ω is time-dependent, because a and H are time-dependent too, where any deviation from one can be thought of as a present-day contribution of the curvature $\Omega_k = \frac{-k}{a_0^2 H_0^2}$ to the total matter-energy density of the Universe.
From Ref. [97], one can see that the different Ω_i components evolve differently in time, depending on the equation of state of that component. In general, the expansion rate can be derived as:

$$\frac{H^2(z)}{H_0^2} = \left[\Omega_X(1+z)^{3(1+\alpha_x)} + \Omega_k(1+z)^2 + \Omega_M(1+z)^3 + \Omega_R(1+z)^4\right] \quad , \qquad \text{(A.1)}$$

where M and R are the labels for matter and radiation, respectively, and X refers to a generic component with equation of state $p_X = \alpha_X \rho_X$, e.g. for the energy density of the vacuum with $\alpha_X = -1$. z is the redshift*. When studying the abundance of each of the different species in Eq. (A.1) at the present day, projections to the past are possible even approaching the Big Bang itself. A very short summary of the evolution of the Universe is provided below:

- $t < 10^{-43}\,\text{s}\,; \quad T > m_{\text{Pl}} = 10^{19}\,\text{GeV}$:
  The Planck epoch, where quantum gravitational interactions either dominated or were part of a grand unified theory. At the end of this epoch, the gravitational force loses relevance, and the strong, weak, and electromagnetic forces were likely unified into a single theory.
- $t < 10^{-36}\,\text{s}\,; \quad T > 10^{16}\,\text{GeV}$:
  The three forces of the Standard Model are assumed to be unified into a single theory.
- $t < 10^{-32}\,\text{s}\,; \quad T > 10^{14}\,\text{GeV}$:
  The inflationary epoch, where the volume of the Universe has grown by a factor of 10^{78}. The three forces separated into the strong and electroweak forces. While the density of particles, which existed before the epoch began were enormously diluted and due to this rapid expansion, the break-down of the enormous potential

*For an emitted wavelength λ_{emit} and an observed wavelength λ_{obs}, the redshift parameter z is defined by $1 + z = \frac{\lambda_{\text{obs}}}{\lambda_{\text{emit}}}$. In the standard FLRW metric of cosmology, the redshift can be related to the change in the scale factor $a(t)$ through $1 + z = \frac{a(t_{\text{obs}})}{a(t_{\text{emit}})}$.

energy of the inflationary field repopulated the expanded Universe with a very dense admixture of quarks, anti-quarks and gluons.

- $t < 10^{-12}\,\mathrm{s}\,; \quad T > 10^{2}\,\mathrm{GeV}$:
  The electroweak epoch, where electroweak symmetry breaking occurs, leaving the strong and the electromagnetic forces.
- $t < 10^{-6}\,\mathrm{s}\,; \quad T > 0.3\,\mathrm{GeV}$:
  The quark epoch, when free quarks exist, but not being able to form hadrons due to the high temperature. They build together with gluons a so-called *quark-gluon-plasma*.
- $t < 1\,\mathrm{s}\,; \quad T > 1\,\mathrm{meV}$:
  The hadron epoch, when no free quarks exist anymore and the QCD phase transition occurs, when confinement comes into play. The build hadrons and anti-hadrons are in thermal equilibrium.
- $t < 10\,\mathrm{s}\,; \quad T > 100\,\mathrm{keV}$:
  The lepton epoch, when hadrons and anti-hadrons have annihilated, while leptons and anti-leptons still exist in thermal equilibrium. The epoch is lately after neutrinos ceased interacting with baryonic matter.
- $t < 10^{3}\,\mathrm{s}\,; \quad T > 1\,\mathrm{keV}$:
  The epoch of Big Bang nucleosynthesis epoch, when $^{1}\mathrm{H}, ^{4}\mathrm{He}, ^{2}\mathrm{H}, ^{3}\mathrm{He}$ and $^{7}\mathrm{Li}$ are produced. All heavier elements than lithium were created much later, by stellar nucleosynthesis in evolving and exploding stars.
- $t < 380\,\mathrm{ka}\,; \quad T > 1\,\mathrm{eV}$:
  The photon epoch, when the Universe consists of a plasma of nuclei, electrons and photons. The temperatures remain still too high for the binding of electrons to nuclei. Later, electrons and atomic nuclei first become bound to form neutral atoms. Photons are no longer in thermal equilibrium with matter and the Universe first becomes transparent. The photons of the cosmic microwave background (CMB) radiation originate at this time.
- $t \approx 13.8\,\mathrm{Ga}\,; \quad T \approx 0.1\,\mathrm{meV}$:
  The energy of the Universe has dropped to 2.7 K, the energy of CMB photons.

Appendix B

Efficiency Measurement of the $E_{\mathrm{T}}^{\mathrm{miss}}$ Triggers

The $E_{\mathrm{T}}^{\mathrm{miss}}$ triggers used in the mono-Higgs ($b\bar{b}$) search given in Table 4.2 are all fully efficient for a reconstructed $E_{\mathrm{T}}^{\mathrm{miss}} > 250\,\mathrm{GeV}$, while the search is also sensitive to signal models which provide $E_{\mathrm{T}}^{\mathrm{miss}}$ values below this threshold (see Fig. 4.4). The low $E_{\mathrm{T}}^{\mathrm{miss}}$ region can partly exploited measuring the $E_{\mathrm{T}}^{\mathrm{miss}}$ trigger efficiencies in data and Monte-Carlo simulation. The so-called *scale factors* (SFs) are derived by comparing the two efficiencies, which are at the end applied to Monte-Carlo simulation. The $E_{\mathrm{T}}^{\mathrm{miss}}$ trigger efficiencies are measured separately for all used $E_{\mathrm{T}}^{\mathrm{miss}}$ triggers.
The efficiencies are measured in single-muon events from $W \to \mu\nu$ decays, where the muons is required to be a signal muon (see Section 4.6) and the event is triggered by single-muon triggers (see Section 4.5.2). Since muons do not contribute to the $E_{\mathrm{T}}^{\mathrm{miss}}$ calculation at trigger-level, there is no bias from the muon trigger imposed in the measurement. The $E_{\mathrm{T}}^{\mathrm{miss}}$ trigger efficiencies are measured as a function of a modified offline $E_{\mathrm{T}}^{\mathrm{miss}}$, so-called $E_{\mathrm{T}}^{\mathrm{miss,\,no-}\mu}$, which is the common reconstructed $E_{\mathrm{T}}^{\mathrm{miss}}$ but without the muon contribution to emulate the trigger-level definition of $E_{\mathrm{T}}^{\mathrm{miss}}$. The $E_{\mathrm{T}}^{\mathrm{miss}}$ trigger efficiency is defined as the ratio

$$\varepsilon(E_{\mathrm{T}}^{\mathrm{miss}} - \text{trigger},\, E_{\mathrm{T}}^{\mathrm{miss,\,no-}\mu}) = \frac{N_{\text{Passed selection and trigger}}}{N_{\text{Passed selection}}} \quad , \tag{B.1}$$

with $N_{\text{Passed selection and trigger}}$ the number of events passing the single-muon selections and the $E_{\mathrm{T}}^{\mathrm{miss}}$ trigger requirement and $N_{\text{Passed selection}}$ the number of events passing only the single-muon selection requirements but without the one for the $E_{\mathrm{T}}^{\mathrm{miss}}$ trigger. The measured trigger efficiencies for all four $E_{\mathrm{T}}^{\mathrm{miss}}$ triggers are shown in Fig. B.1 inclusively in the number of b-jets in the events.
Good agreement between the efficiencies in data and Monte-Carlo simulation is observed for $E_{\mathrm{T}}^{\mathrm{miss,\,no-}\mu} > 250\,\mathrm{GeV}$, where the $E_{\mathrm{T}}^{\mathrm{miss}}$ triggers are fully efficient and the scale factors are one. In the turn-on region between 150 to 250 GeV, the efficiencies are above 85 %

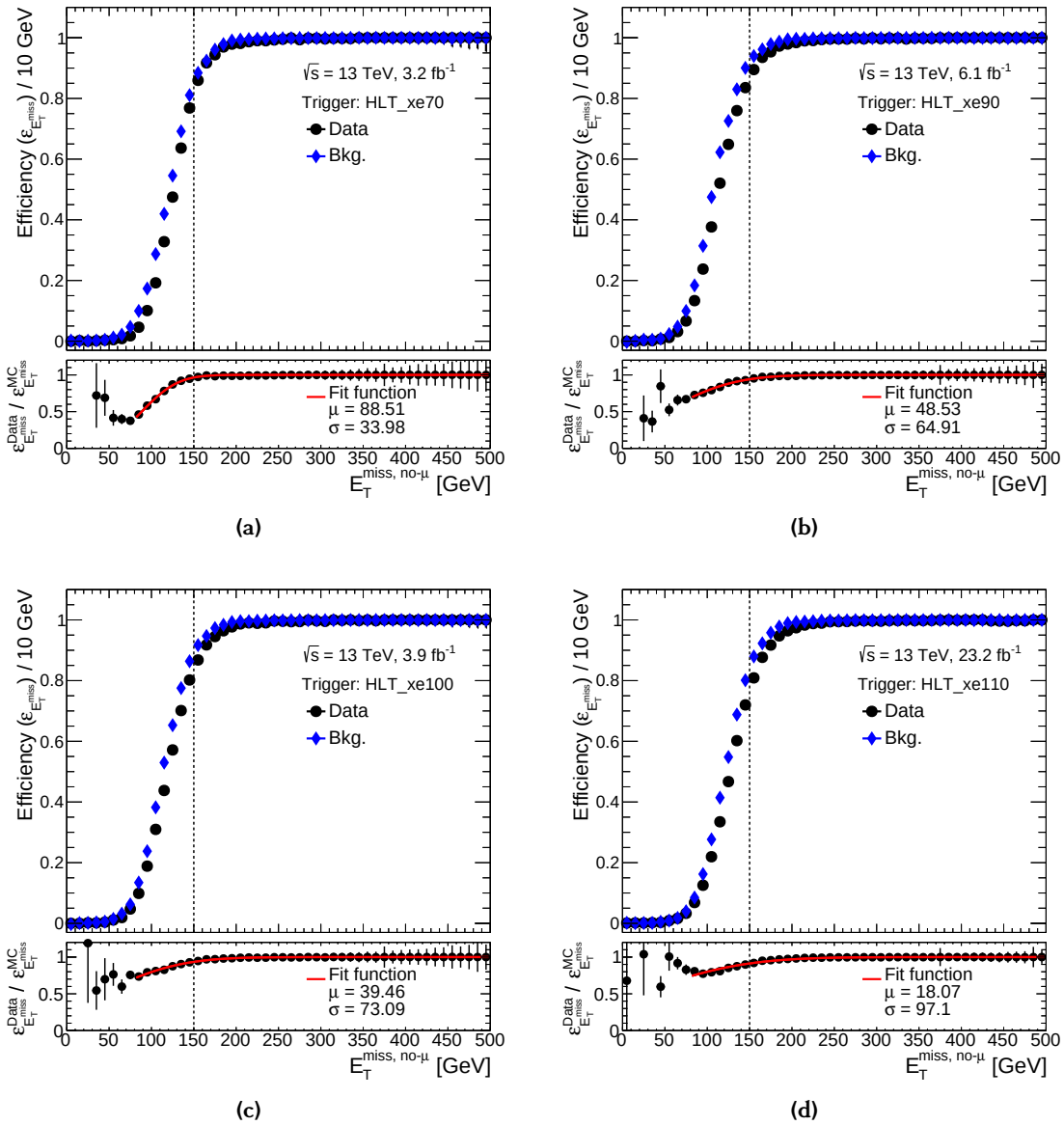

Figure B.1: The measured $E_{\mathrm{T}}^{\mathrm{miss}}$ trigger efficiencies (upper pad) in data and Monte-Carlo simulation and the related scale factors (lower pad) both as a function of $E_{\mathrm{T}}^{\mathrm{miss,\,no-}\mu}$ for the four $E_{\mathrm{T}}^{\mathrm{miss}}$ triggers (a) HLT_xe70, (b) HLT_xe90_mht_L1XE50, (c) HLT_xe100_mht_L1XE50 and (d) HLT_xe110_mht_L1XE50. The distribution of scale factors is fitted with an error function with expectation value μ and standard deviation σ. The vertical dashed line indicates the minimal offline $E_{\mathrm{T}}^{\mathrm{miss}}$ requirement in the mono-Higgs ($b\bar{b}$) search.

for all triggers both in data and Monte-Carlo simulation. The inefficiencies in this region is a result of the finite calorimeter resolution.

Corrections accounting for the difference between data and Monte-Carlo simulation are defined by the ratio of their efficiencies (see the lower pad in Fig. B.1). The SFs as a

function of $E_{\mathrm{T}}^{\mathrm{miss,\,no-}\mu}$ are fitted with an error function

$$f\left(E_{\mathrm{T}}^{\mathrm{miss,\,no-}\mu}\right) = 0.5 \cdot \left[1 + \mathrm{erf}\left(\frac{E_{\mathrm{T}}^{\mathrm{miss,\,no-}\mu} - \mu}{\sqrt{2}\sigma}\right)\right] \quad , \tag{B.2}$$

with μ the expectation value and σ the standard deviation. The SFs are applied to Monte-Carlo simulated events to match their prediction to data in the SR and 1μ-CR. In the region $E_{\mathrm{T}}^{\mathrm{miss,\,no-}\mu} < 150\,\mathrm{GeV}$, larger deviations between data and simulation are seen. Moreover, a large impact of multijet events is expected in this region, such that events with $E_{\mathrm{T}}^{\mathrm{miss}}\,(E_{\mathrm{T}}^{\mathrm{miss,\,no-}\mu}) < 150\,\mathrm{GeV}$ are not considered in the mono-Higgs ($b\bar{b}$) analysis. No corrections are applied in the merged region since $E_{\mathrm{T}}^{\mathrm{miss}} > 500\,\mathrm{GeV}$ is required.

Appendix C

Optimisation of the Signal Region Selection

Apart from the $Z(\rightarrow \nu\nu) + b\bar{b}$ process, the $t\bar{t}$ production is one of the dominant backgrounds. It contributes by about 30 % to 80 % to the total background depending on the number of b-jets in the event and the $E_{\mathrm{T}}^{\mathrm{miss}}$ interval. Requirements efficiently reducing the $t\bar{t}$ process are discussed here, which significantly improve the signal sensitivity. The selection criteria are outlined in the following, after a short discussion of the $t\bar{t}$ final states at parton-level. The results are summarised in Section C.5.
As discussed in Section 4.3, the $t\bar{t}$ background events entering the SR are either of fully-leptonic or of semileptonic nature, i.e. with at least one W boson decaying leptonically. Fully-hadronic $t\bar{t}$ events usually don't have large $E_{\mathrm{T}}^{\mathrm{miss}}$ and are mostly rejected by the requirement of $E_{\mathrm{T}}^{\mathrm{miss}} > 150\,\mathrm{GeV}$. Even in the case of $W \rightarrow \ell\nu$ decays (with $\ell = e, \mu$), most of the $t\bar{t}$ events are rejected due to the veto on baseline e and μ. Nevertheless, such an event can enter the SR in case of soft electrons or muons with $p_{\mathrm{T}} < 7\,\mathrm{GeV}$ or in the case that the leptons are outside of the detector acceptance, but their contribution is expected to be small. The dominant $t\bar{t}$ background process includes events with $W \rightarrow \tau\nu$ decays, resulting in an additional $E_{\mathrm{T}}^{\mathrm{miss}}$ from the τ decay products. Additional b-jets in the final state can be falsely reconstructed from the τ decay or in a semileptonic $t\bar{t}$ final state in which one of the W bosons decays hadronically, in particular via the $W \rightarrow cs$ decay. The fraction of various $t\bar{t}$ final states at the parton-level are illustrated in Fig. C.1 for Monte-Carlo simulated $t\bar{t}$ events with at least one leptonically decaying W boson. The event fractions are shown only for events passing the SR selection criteria in Section 4.7 of both the resolved and merged region. Around 75 % of all $t\bar{t}$ events in the SR contain at least one τ lepton at the particle-level, while around 44 % of all events include one W boson which decays into cs quarks. The hadronically decaying τ-leptons and jets from $W \rightarrow cs$ decays can be misidentified as b-jets.
The event selection introduces vetoes on events with τ-jets and a third b-jet in the event, described in Section C.1 and Section C.2, respectively. Furthermore, a so-called H_{T}-ratio

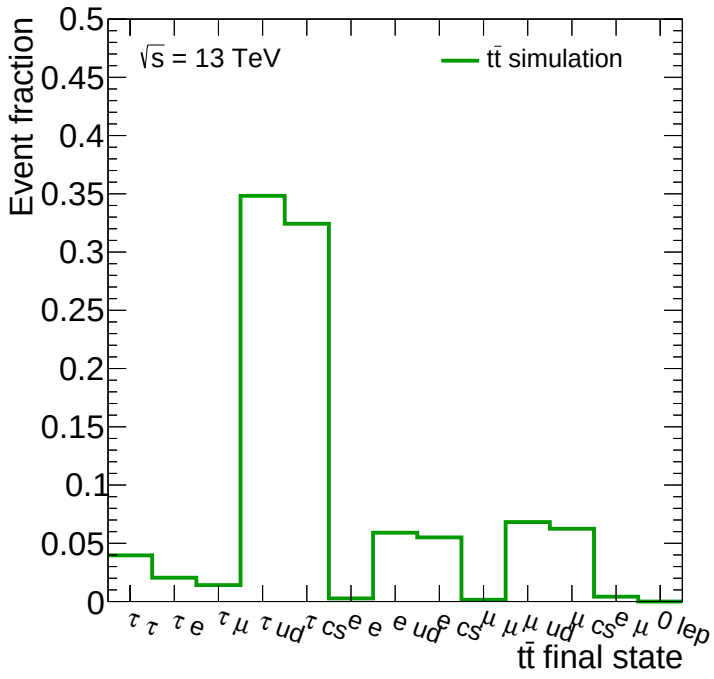

Figure C.1: Fraction of different $tt \to WbWb$ final states at the particle-level for $t\bar{t}$ events in the signal region. The labels on the x-axis indicate the decay mode of both W bosons, with $\ell = e, \mu, \tau$ indicating leptonic $W \to \ell\nu_\ell$ decays and with ud or cs for hadronic W decays. The last bin shows the fraction of events with no truth lepton in the event.

requirement is applied, which accounts for higher hadronic activity in $t\bar{t}$ compared to signal events is described in Section C.3. Finally, a requirement on the angular separation of the two leading small-R jets from the Higgs boson candidate in the resolved region is applied (see Section C.4).

C.1 Veto Against Hadronic Tau Decays

A veto on events with hadronically decaying τ-leptons is applied to reduce a large fraction of $t\bar{t}$ background (see Fig. C.1), while leaving the signal almost unaffected. A veto on leptonically decaying τ-leptons is not applied, since these are indistinguishable from prompt electrons and muons, which would mainly contribute to the 1μ-CR and 2ℓ-CR. The described $\tau-$veto not only reduces the $t\bar{t}$ background, but also the contributions from the single top quark and $W+$jets production. The τ objects used for applying a veto are defined in Section 4.6.

First, a veto on events with loose τ-jets is applied. The loose τ-jets identification working point (see Section 3.3.6) has an efficiency of about 60 % (50 %) for simulated hadronically decaying τ-leptons with one (three) charged tracks, while having a false identification rate for quark- and gluon-initiated jets of below 6 % (1 %) [382].

In the resolved signal region, events with a loose-τ are vetoed. A similar veto on events with a loose-τ is applied in the merged region, if the τ-jet is not overlapping with the leading large-R jet (J), i.e. if $\Delta R(\vec{J}, \vec{\tau}) \geq 1.0$. This additional requirement in the merged region is used to keep the signal efficiency high. The distributions of the number of loose-τ-jets in the resolved and merged region are shown in Fig. C.2a and Fig. C.2b, respectively. Most of the signal events have no loose τ-jets, while there is a significant

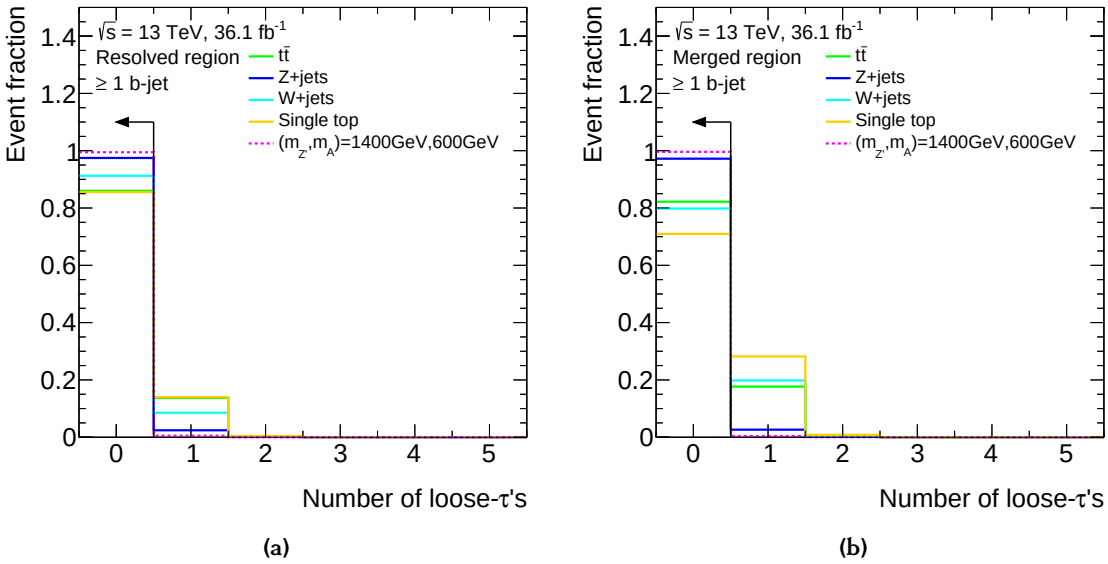

Figure C.2: Multiplicity of loose τ-jets in events with at least one b-jet for (a) the resolved and (b) for the merged region. Shown are the distributions for the main background processes as well for one representative Z'-2HDM signal model with $(m_{Z'}, m_A) = (1400\,\text{GeV}, 600\,\text{GeV})$. All distributions are normalised to unity. The arrows indicate the selection requirements.

fraction of background events with one loose-τ object. The veto on events with loose τ-jets reduces the $t\bar{t}$, W+jets and single top quark background processes in the resolved region by 14.0 %, 8.74 % and 14.5 %, respectively, while in the merged region these backgrounds are reduced by 17.8 %, 20.2 % and 29.0 %. The veto has almost no impact on the signal selection, with a loss in signal efficiency of less then 1 %.

An additional background rejection is achieved by applying a veto on events with a very loose-τ object (see Section 4.6), with relaxed track multiplicity requirements. The veto is applied separately in the resolved and the merged SR. In the merged region, the event is vetoed if a very loose-τ object is found outside the leading large-R jet. The distributions of the number of very loose τ-jets is shown in Fig. C.3a and Fig. C.3b for the resolved and merged region, respectively. The fraction of $t\bar{t}$, W+jets and single top quark background events in the resolved region including a very loose-τ object is 13.3 %, 7.27 % and 11.4 %, before applying the veto on events with a loose-τ object. In

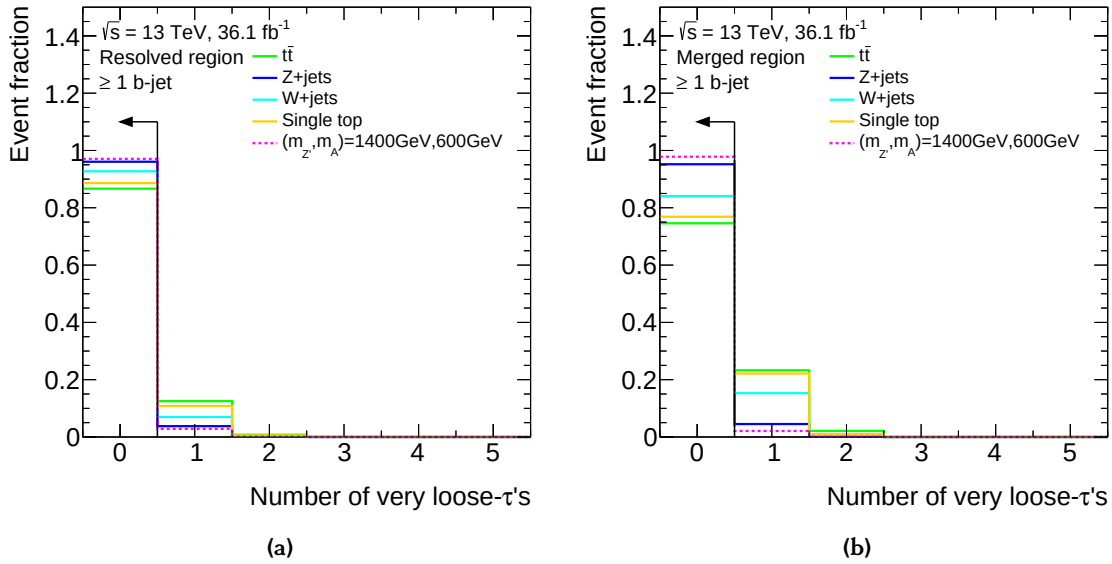

Figure C.3: Multiplicity of very loose τ-jets in events with at least one b-jet for (a) the resolved and (b) for the merged region. Shown are the distributions for the main background processes as well for one representative Z'-2HDM signal model with $(m_{Z'}, m_A) = (1400\,\text{GeV}, 600\,\text{GeV})$. All distributions are normalised to unity. The arrows indicate the selection requirements.

the merged region, the fractions of such events are 25.4 %, 15.9 % and 23.1 % for the $t\bar{t}$, W+jets and single top quark background processes, respectively. The fraction of signal events rejected by the very loose-τ veto is below 2 % for all signal models.

C.2 Veto Against Additional b-Jets

The mono-Higgs signal events are characterised by exactly two b-jets in the final state from the Higgs boson decay, while for example the $t\bar{t}$ processes may provide higher b-jet multiplicities. In $t\bar{t}$ events, the two b quarks originating from the decay of the two top quarks will most likely correctly be identified as b-jets, while additional b-jets can arise from the misidentification of c quark initiated jets or τ-jets from semileptonic $t\bar{t}$ decays (see Fig. C.1). Events with more then two b-jets can also arise from single top quark production, e.g. via the s-channel production. The distributions of the fractional b-jet multiplicity in the resolved region are shown in Fig. C.4a, for event with either one or two b-jets. The veto on events with more then two b-jets rejects up to 3 % of $t\bar{t}$ and up to 1.5 % of single top quark background events.

The b-jet veto in the merged region is slightly different than in the resolved region due to the different decay topology of the signal and background processes. The top quarks in a $t\bar{t}$ event are mostly produced back-to-back. In the merged region, one of the two

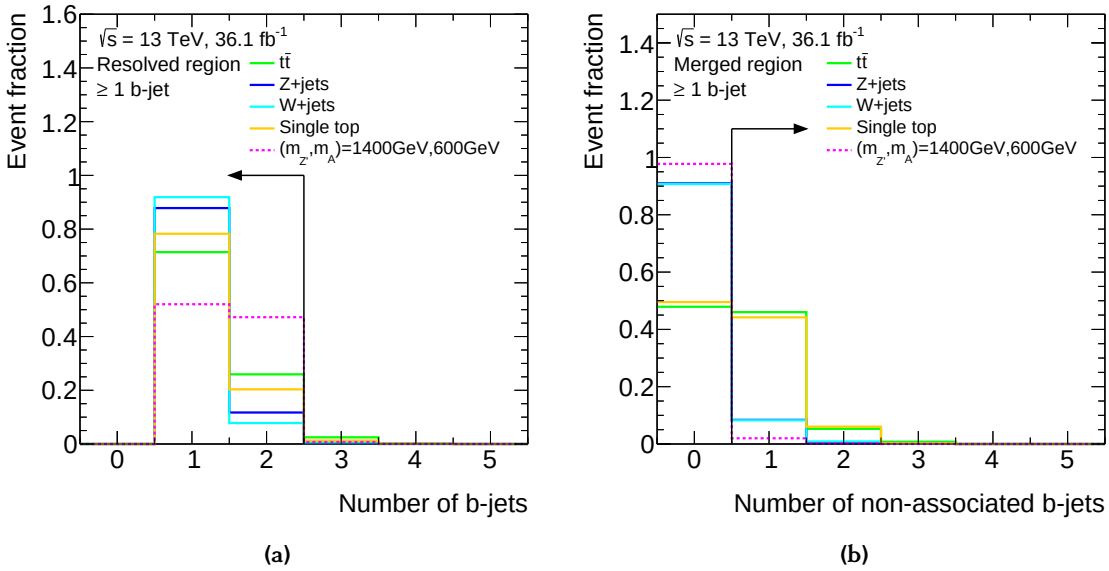

Figure C.4: Multiplicity of b-jets in events with at least one b-jet for (a) the resolved and (b) for the merged region. Shown are the distributions for the main background processes as well for one representative Z'-2HDM signal model with $(m_{Z'}, m_A) = (1400\,\text{GeV}, 600\,\text{GeV})$. All distributions are normalised to unity. The arrows indicate the selection requirements.

top quarks will carry most of the p_T and will be reconstructed as the leading large-R jet, which is considered as the Higgs boson candidate. The decay products of the second top quark (with smaller p_T) will be usually reconstructed as small-R jets. Therefore, one of the two b-jets identified through their association to track-jets is expected to be outside of the leading large-R jet, as opposed to the signal with both b-tagged track-jets within the large-R jet. Thus, a veto on b-tagged track-jets not associated to the leading large-R jet is applied. The distribution of non-associated b-jets is shown in Fig. C.4b. For the signal, less than 2 % of the events contain additional b-jets. At the same time, around 52 % of all $t\bar{t}$ events have one or even two non-associated b-jets in the final state and can be rejected. Additionally, the contribution of the single top quark background processes can be reduced by around 50 %.

C.3 H_T-Ratio Requirement

Apart from the Higgs boson decay products, additional hadronic activity in mono-Higgs events can arise from ISR initiated jets. These have in general a rather soft p_T compared to the two jets from the Higgs boson decay.
In $t\bar{t}$ events, the hadronic activity is generally higher then for signal events. In addition to the two b quarks from the top quark decays, the hadronic activity originates from

hadronic W boson decays or from ISR. Jets from the W boson decays are likely to have on average a similar p_{T} as the b-jets from the top quark decay. The p_{T} of the Higgs boson candidate reconstructed in $t\bar{t}$ events, usually the two b-jets, is smaller or about equal to the sum of the transverse momenta of the jets originating from the W boson decays and additional ISR jets.
A measure of the hadronic activity in an event is the scalar sum of transverse momenta of all jets in the event, denoted as H_{T}. In the resolved region, the signal can be discriminated from background by the so-called $H_{\mathrm{T}}^{\mathrm{resolved}}$-ratio variable given as

$$H_{\mathrm{T}}^{\mathrm{resolved}}\text{-ratio} = \frac{\sum\limits_{i=4} p_{\mathrm{T},i}}{\sum\limits_{i=1} p_{\mathrm{T},i}} \quad , \tag{C.1}$$

where the jets are sorted in decreasing order in p_{T}. $\sum\limits_{i=4} p_{\mathrm{T},i}$ is the scalar sum of transverse momenta of small-R jets (starting from the fourth jet in the event) and $\sum\limits_{i=1} p_{\mathrm{T},i}$ is the sum over all small-R jets in the event. The third jet is not counted in the nominator, since in signal events such jets with third-highest p_{T} can also be present, and usually corresponds to an ISR-induced jet. The distribution of $H_{\mathrm{T}}^{\mathrm{resolved}}$-ratio is shown in Fig. C.5a. Most of the

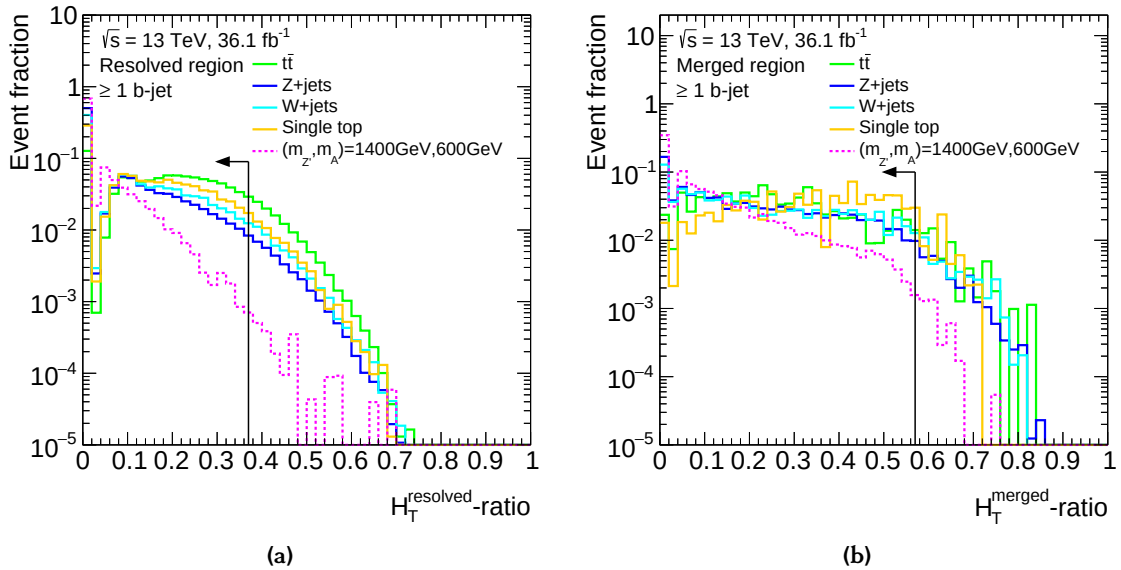

Figure C.5: Expected distributions of the H_{T}-ratio variable in events with at least one b-jet for (a) the resolved and (b) the merged region. Shown are the distributions for the main background processes as well for one representative Z'-2HDM signal model with $(m_{Z'}, m_A) = (1400\,\mathrm{GeV}, 600\,\mathrm{GeV})$. All distributions are normalised to unity. The arrows indicate the selection requirements.

signal events are located at small values of $H_{\mathrm{T}}^{\mathrm{resolved}}$-ratio, while most of the background

events populate larger values. A requirement of $H_{\mathrm{T}}^{\mathrm{resolved}}$-ratio < 0.37 provides the best signal sensitivity and is applied to events in the resolved signal region. The $t\bar{t}$ background is reduced by around 12 %. For other background processes the reduction ranges from 3 to 6 %. The corresponding loss of signal events is below 1 %.
For the merged region, the $H_{\mathrm{T}}^{\mathrm{merged}}$-ratio variable is used and is given as

$$H_{\mathrm{T}}^{\mathrm{merged}}\text{-ratio} = \frac{\sum\limits_{i=1} p_{\mathrm{T},i}^{\text{not-matched}}}{p_{\mathrm{T}}^{J} + \sum\limits_{i=1} p_{\mathrm{T},i}^{\text{not-matched}}} \quad , \tag{C.2}$$

where $p_{\mathrm{T},i}^{\text{not-matched}}$ is the transverse momentum of the ith small-R jet not-matched to the leading large-R jet, i.e. $\Delta R(\vec{p}_{\mathrm{T},i}^{\text{not-matched}}, \vec{p}^{J}) \geq 1.0$, and p_{T}^{J} is the transverse momentum of the leading large-R jet in the event. The distributions of $H_{\mathrm{T}}^{\mathrm{merged}}$-ratio for the most dominant background processes as well as for three benchmark signal models are shown in Fig. C.5b. A requirement of $H_{\mathrm{T}}^{\mathrm{merged}}$-ratio < 0.57 is applied for optimal signal sensitivity. The corresponding loss of signal efficiency is below 0.5 % for most of the signal models, while the $t\bar{t}$ and single top quark background can be reduced by around 7.2 % and 8.2 %, respectively. Furthermore, the contribution of V+jets backgrounds is reduced by 5.0 % and 3.8 % for $V = W$ and Z, respectively.

C.4 Angular Separation of b-Jets

In the merged regime, a jet with a sufficiently large cone size of $R = 1.0$ is used to account for all of the decay products of the Higgs boson.
The Higgs boson candidate in the resolved region consists of the two highest p_{T} central small-R jets in the event, $\vec{p}_h^{\,j_1}$ and $\vec{p}_h^{\,j_2}$, where at least one of them is identified as a b-jet. The angular separation of the two jets is approximately given by Eq. (3.6), indicating that even for a moderate Higgs boson p_{T} the two small-R jets from its decay are collimated. For example, for a Higgs transverse momentum of 150 GeV, which corresponds to the lower $E_{\mathrm{T}}^{\mathrm{miss}}$ bound in the resolved region, the angular separation of the two jets is expected at $\Delta R\left(\vec{p}_h^{\,j_1}, \vec{p}_h^{\,j_2}\right) \approx 1.7$ (see Eq. (3.6)). In contrast, for most of the background processes the separation of the two highest-p_{T} small-R jets is larger. For example, the two top quarks in $t\bar{t}$ events and the corresponding decay products are often back-to-back produced. This results in a rather large angular separation of the two b quarks. In Fig. C.6, the distribution of $\Delta R\left(\vec{p}_h^{\,j_1}, \vec{p}_h^{\,j_2}\right)$ of the two small-R jets with highest-p_{T} is shown. An optimal requirement of $\Delta R\left(\vec{p}_h^{\,j_1}, \vec{p}_h^{\,j_2}\right) < 1.8$ is found, resulting in a signal loss of only below 6 % and a significant reduction of backgrounds by approximately 50 % each.

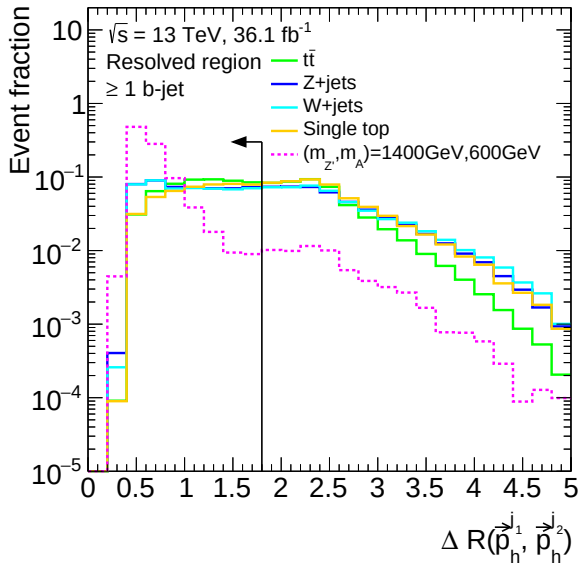

Figure C.6: Distributions of $\Delta R\left(\vec{p}_h^{\,j_1}, \vec{p}_h^{\,j_2}\right)$ for events with more then one b-jet of the main background processes as well for one representative Z'-2HDM signal model with $(m_{Z'}, m_A) = (1400\,\text{GeV}, 600\,\text{GeV})$ in the resolved signal region for. All distributions are normalised to unity. The arrow indicates the selection requirements.

C.5 Results of the Optimised Event Selection

The results of the event selection prior to the combined fit are summarised in this section. The selection efficiency of the Z'-2HDM signal events is investigated to make sure that the optimised selection criteria target mostly the reduction of background processes and do not strongly affect the signal.

The number of signal events passing the selection criteria are compared to the number of events passing the selection without the specific ones for the $t\bar{t}$ reduction. The signal efficiency for various Z'-2HDM signal points is given in Fig. C.7. For most of the signal points, the signal efficiency is around 96 % after applying the optimised selection criteria. The signal efficiency is slightly reduced in the off-shell region, where the signal events tend to have smaller values of $E_{\text{T}}^{\text{miss}}$. The signal sensitivity in this region is anyhow small. The backgrounds processes, on the other hand are highly reduced in both the resolved and the merged SRs.

The total background selection efficiency is 36 %, 38 %, 45 % and 70 % in the $E_{\text{T}}^{\text{miss}}$-bins [150, 200) GeV, [200, 350) GeV, [350, 500) GeV and [500, ∞) GeV, respectively.

The signal significance, Z, is estimated using the following definition [415]

$$Z = \sqrt{2\left[(s+b)\ln(1+s/b) - s\right]} \quad , \tag{C.3}$$

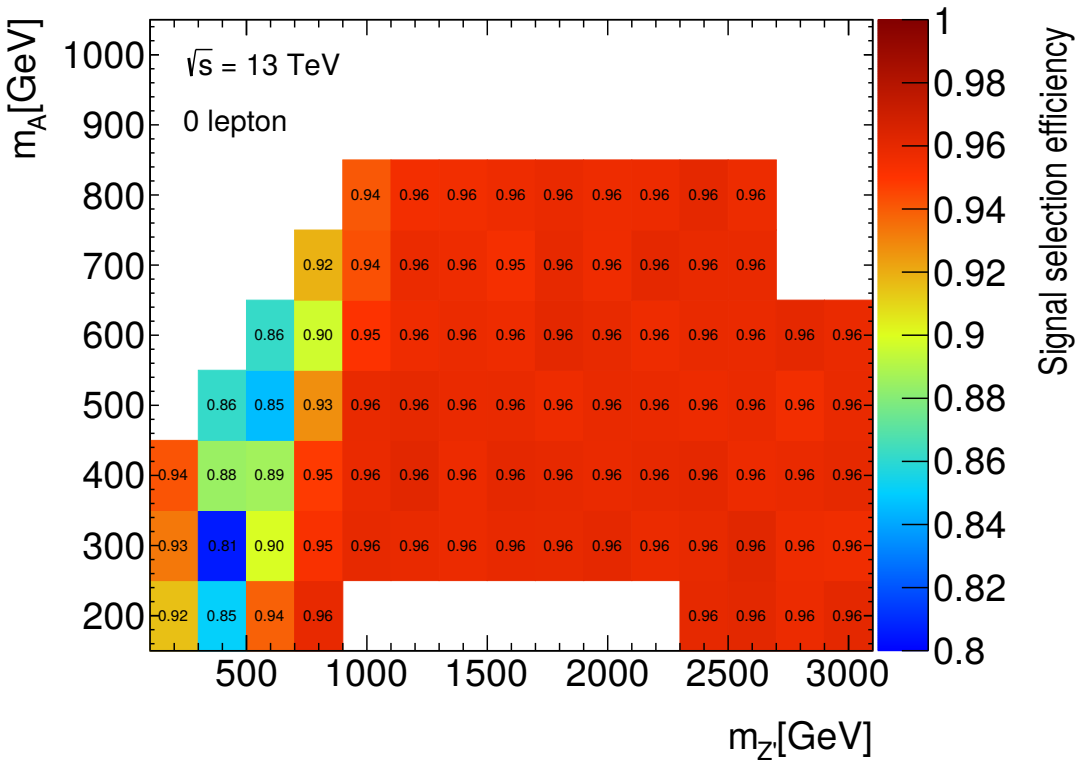

Figure C.7: The selection efficiencies of Z'-2HDM signal events after the optimised selection with respect to the baseline selection. The resolved and the merged signal regions are combined.

where s is the number of signal and b the total number of expected background events. In Fig. C.8, the ratio of the signal significance obtained after the optimised selection to the signal significance obtained by the baseline event selection is shown. The signal significance for the Z'-2HDM signal points is increased by up to 50 %. The gain in significance is larger for models with lower $m_{Z'}$ which contribute mostly to the resolved signal region. In particular, the gain in significance is up to 50 % in the region of $m_{Z'} < 1000$ GeV for all values of m_A. For signal models with a larger $E_{\mathrm{T}}^{\mathrm{miss}}$, related to $m_{Z'} > 1400$ GeV, the gain in significance is in the range of 8 to 14 %.
The optimised selection criteria are also applied to the 1μ-CR and the 2ℓ-CR to ensure the selection of similar events, i.e. that the kinematic properties of events cover the same region of phase space as the SR events.

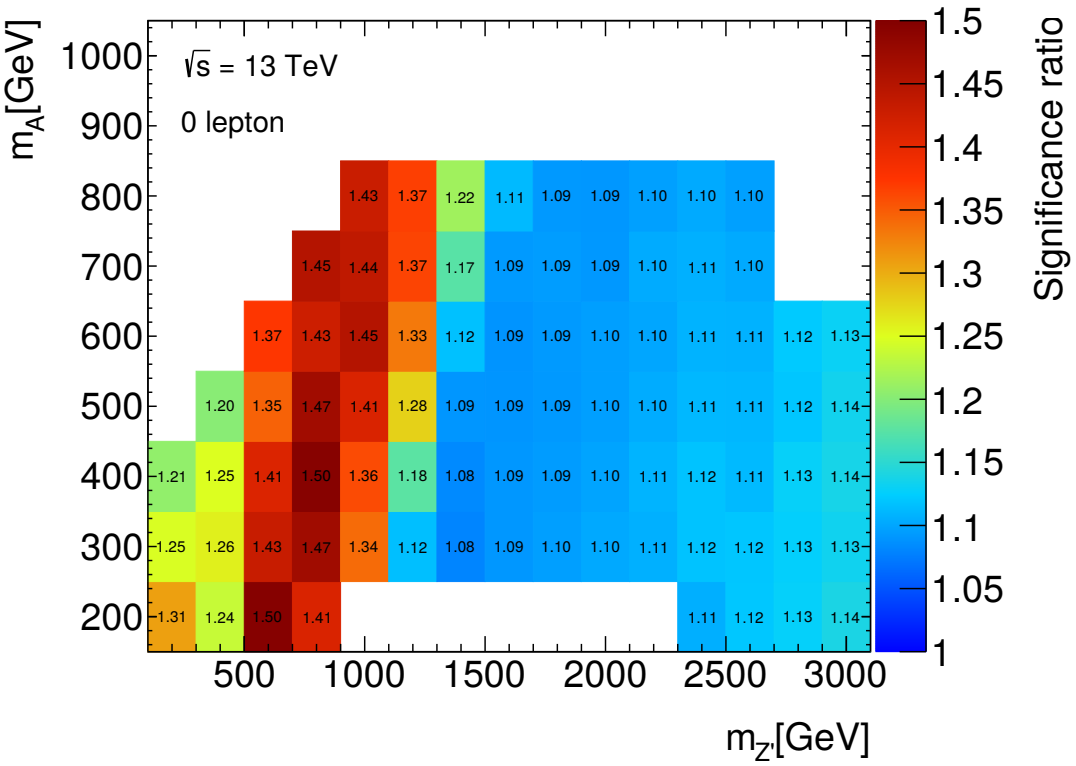

Figure C.8: The ratios between the significance upon applying the optimisation selections and the significance of the former baseline event selection for Z'-2HDM signal models, when combining the resolved and merged region inclusive of the number of b-jets. The significance gain of Z'-2HDM signal models reaches values up to 50 % due to the optimisation selection criteria. The signal models are normalised to their theoretical cross section.

Appendix D

Control Region Distributions

In this Chapter, the Higgs boson candidate mass ($m_{h,\,\text{cand}} = m_{jj}$ and m_J) and $E_{\text{T}}^{\text{miss}}$ distributions are shown for the 1μ-CR and 2ℓ-CR. In both cases, $m_{h,\,\text{cand}}$ is used for selecting events, and in particular the muon charge for the 1μ-CR. In the 2ℓ-CR a single bin of $m_{h,\,\text{cand}}$ is used without exploiting the shape information of the distribution, as only the normalisation of the Z+jets process in the signal region is constrained. The distributions related to the mono-Higgs ($b\bar{b}$) analysis in Chapter 4 with 36 fb^{-1} are shown in Sections D.1 and D.2, while for the analysis in Chapter 6 with 79.8 fb^{-1} they are given in Section D.3.

D.1 Pre-Fit Distributions with 36 fb^{-1}

The Higgs boson candidate mass distributions in the 1μ-CR at the pre-fit level are illustrated in Fig. D.1 and Fig. D.2 for events with one and two b-jets, respectively. Similarly, the $m_{h,\,\text{cand}}$ distributions in the 2ℓ-CR at the pre-fit level are illustrated in Fig. D.3 and Fig. D.4. Good data to Monte-Carlo agreement is found for all distributions within statistical uncertainties.

D.2 Post-Fit Distributions with 36 fb^{-1}

In Fig. D.5 and Fig. D.6, the distributions of $E_{\text{T}}^{\text{miss,\,no}-\mu}$ in the 1μ-CR are illustrated for events with one and two b-jets, respectively. Good agreement between data and the Standard Model prediction is found. The separation power of the muon charge for $t\bar{t}$ and W+jets events is illustrated in Fig. D.7, where the fraction of the total background events is given as a function of $E_{\text{T}}^{\text{miss,\,no}-\mu}$. The fraction of $t\bar{t}$ events for muons with negative and positive electric charges are the same within uncertainties as expected. In contrast, for W+jets events predominance of muons with positive electric charge is seen, as expected for proton-proton collisions at the LHC.
The post-fit $p_{\text{T}}^{\ell\ell}$ distributions in the 2ℓ-CR are shown in Fig. D.8a for events with one b-jet and in Fig. D.8a for events with two b-jets. Here, each $p_{\text{T}}^{\ell\ell}$ bin is equivalent to

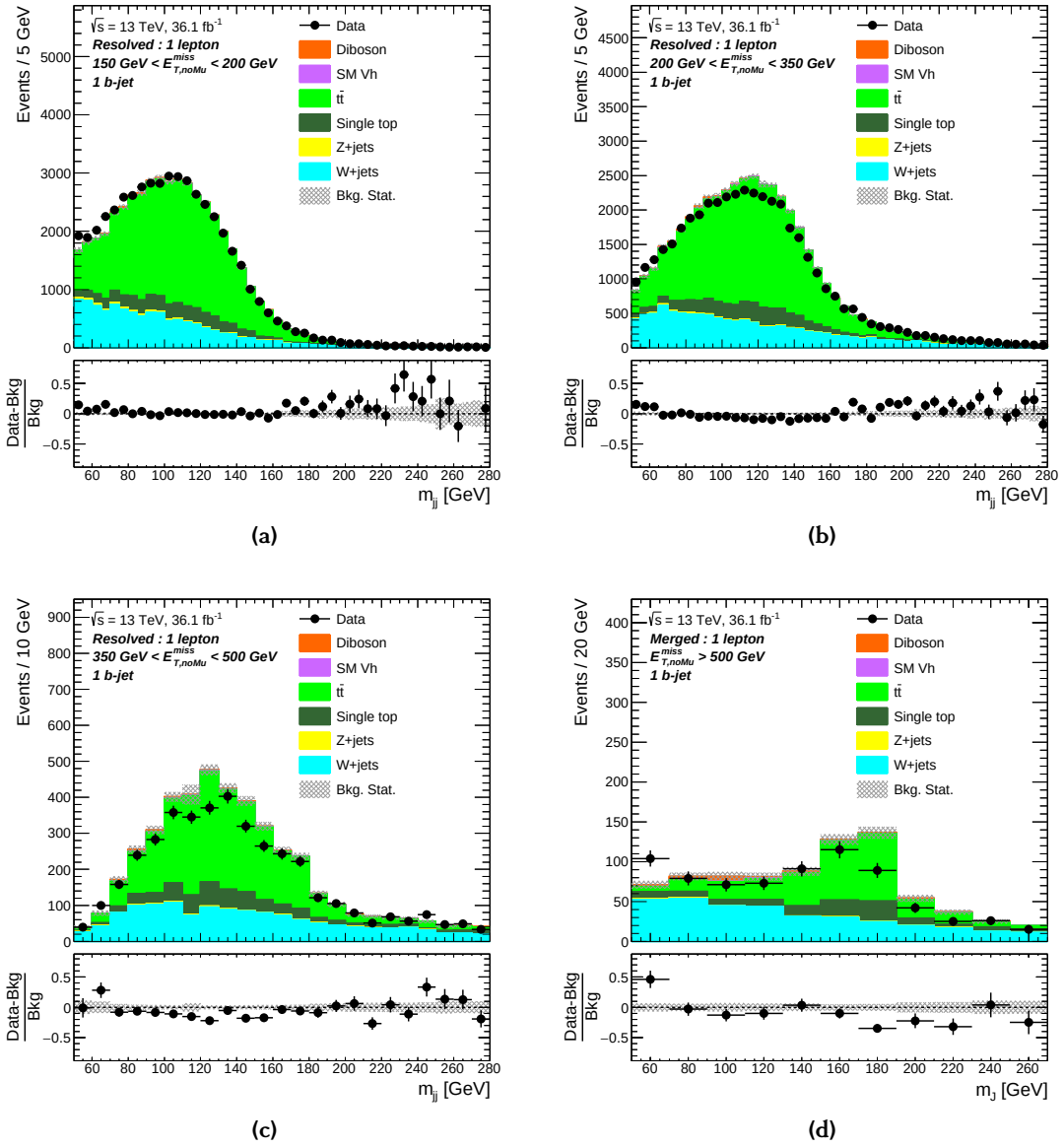

Figure D.1: Pre-fit distributions of the invariant mass of the Higgs boson candidates $m_{h,\,\mathrm{cand}} = m_{jj}$, m_J for events one b-jet in the 1μ-CR for the four $E_{\mathrm{T}}^{\mathrm{miss,\,no-}\mu}$ categories.

the used $m_{h,\,\mathrm{cand}}$ bin, since no shape information of the $m_{h,\,\mathrm{cand}}$ distribution was used during the profile-likelihood fit. Very good agreement between the data and Monte-Carlo prediction is found, with uncertainties below 20 %.

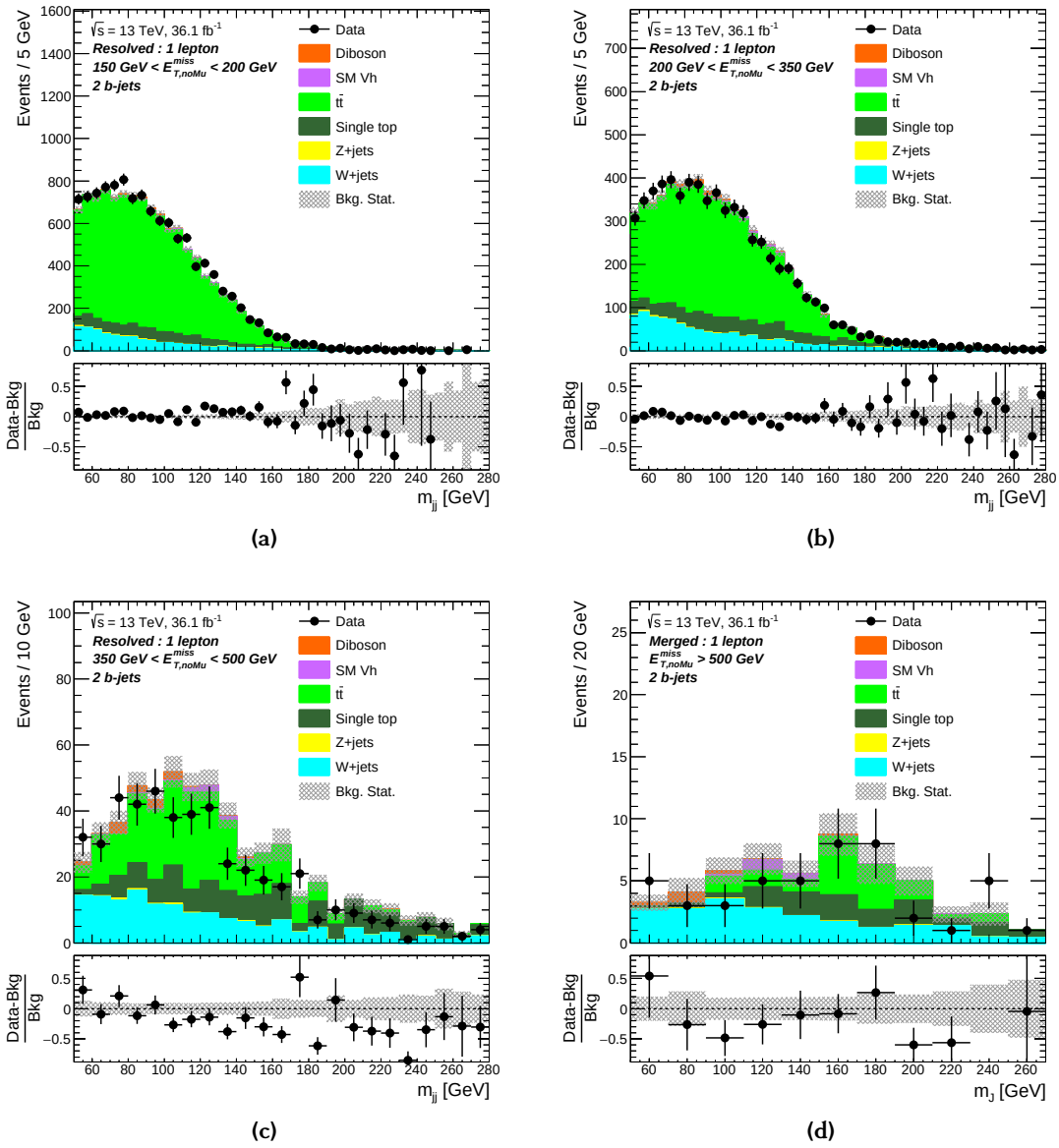

Figure D.2: Pre-fit distributions of the invariant mass of the Higgs boson candidates $m_{h,\,\mathrm{cand}} = m_{jj}$, m_J for events two b-jets in the 1μ-CR for the four $E_{\mathrm{T}}^{\mathrm{miss,\,no-}\mu}$ categories.

D.3 Post-Fit Distributions with 79.8 fb^{-1}

This section provides post-fit distribution of $E_{\mathrm{T}}^{\mathrm{miss,\,no-}\mu}$ and $p_{\mathrm{T}}^{\ell\ell}$ in the 1μ-CR and 2ℓ-CR, respectively, based on the mono-Higgs ($b\bar{b}$) analysis given in Chapter 6 with an integrated luminosity of 79.8 fb^{-1}.

In Fig. D.9a and Fig. D.9b, the distributions of $E_{\mathrm{T}}^{\mathrm{miss,\,no-}\mu}$ in the 1μ-CR for muons with positive and negative electric charge, respectively, are illustrated. Good agreement

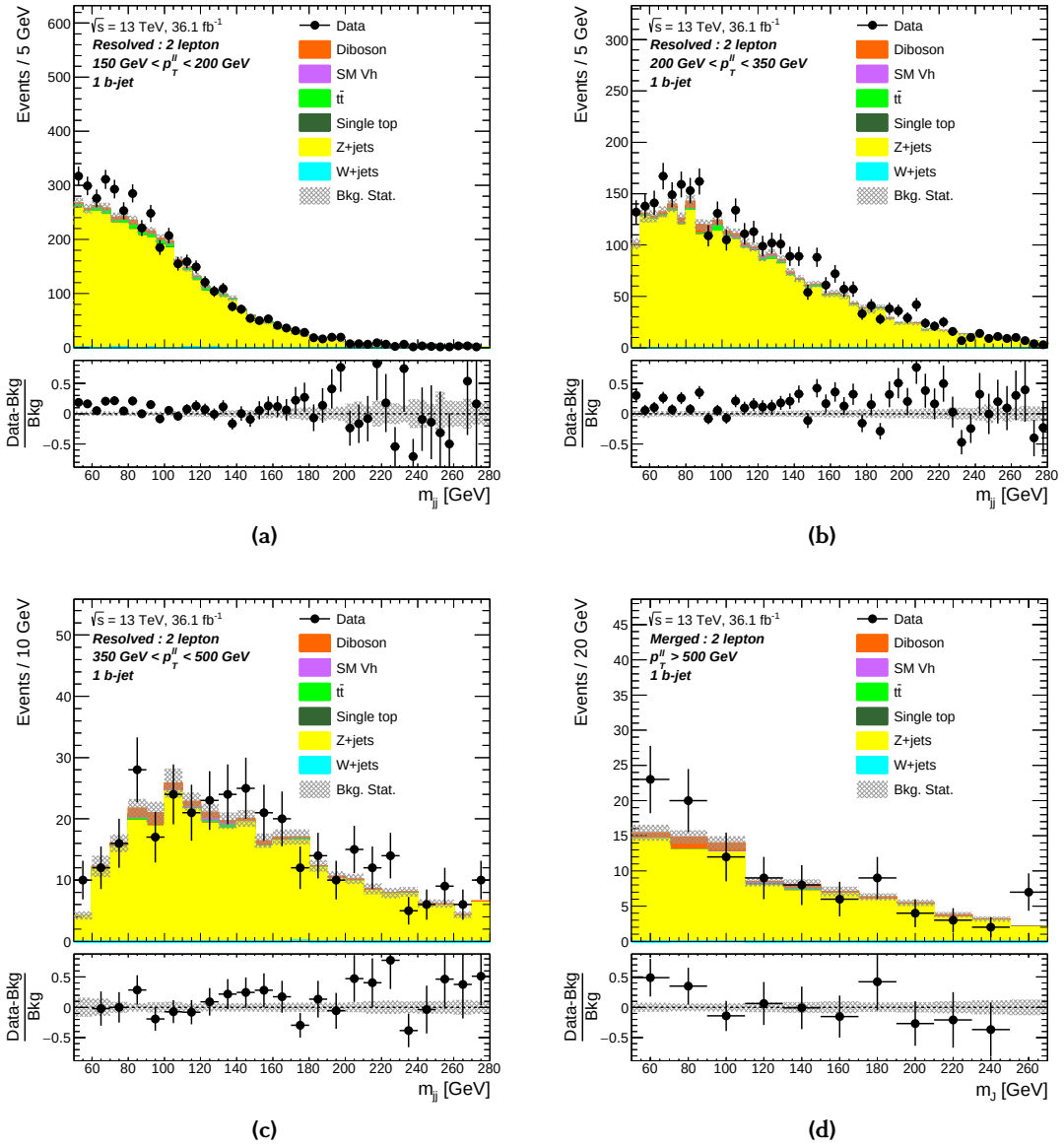

Figure D.3: Pre-fit distributions of the invariant mass of the Higgs boson candidates $m_{h,\,\mathrm{cand}} = m_{jj}$, m_J for events one b-jet in the 2ℓ-CR for the four $p_{\mathrm{T}}^{\ell\ell}$ categories.

between data and the Standard Model predictions is found. The separation power of the muon charge for $t\bar{t}$ and W+jets events is and a predominance of muons with positive electric charge is seen, as expected for proton-proton collisions at the LHC.
The post-fit $p_{\mathrm{T}}^{\ell\ell}$ distributions in the 2ℓ-CR are shown in Fig. D.10. Very good agreement between the data and Monte-Carlo prediction is found.

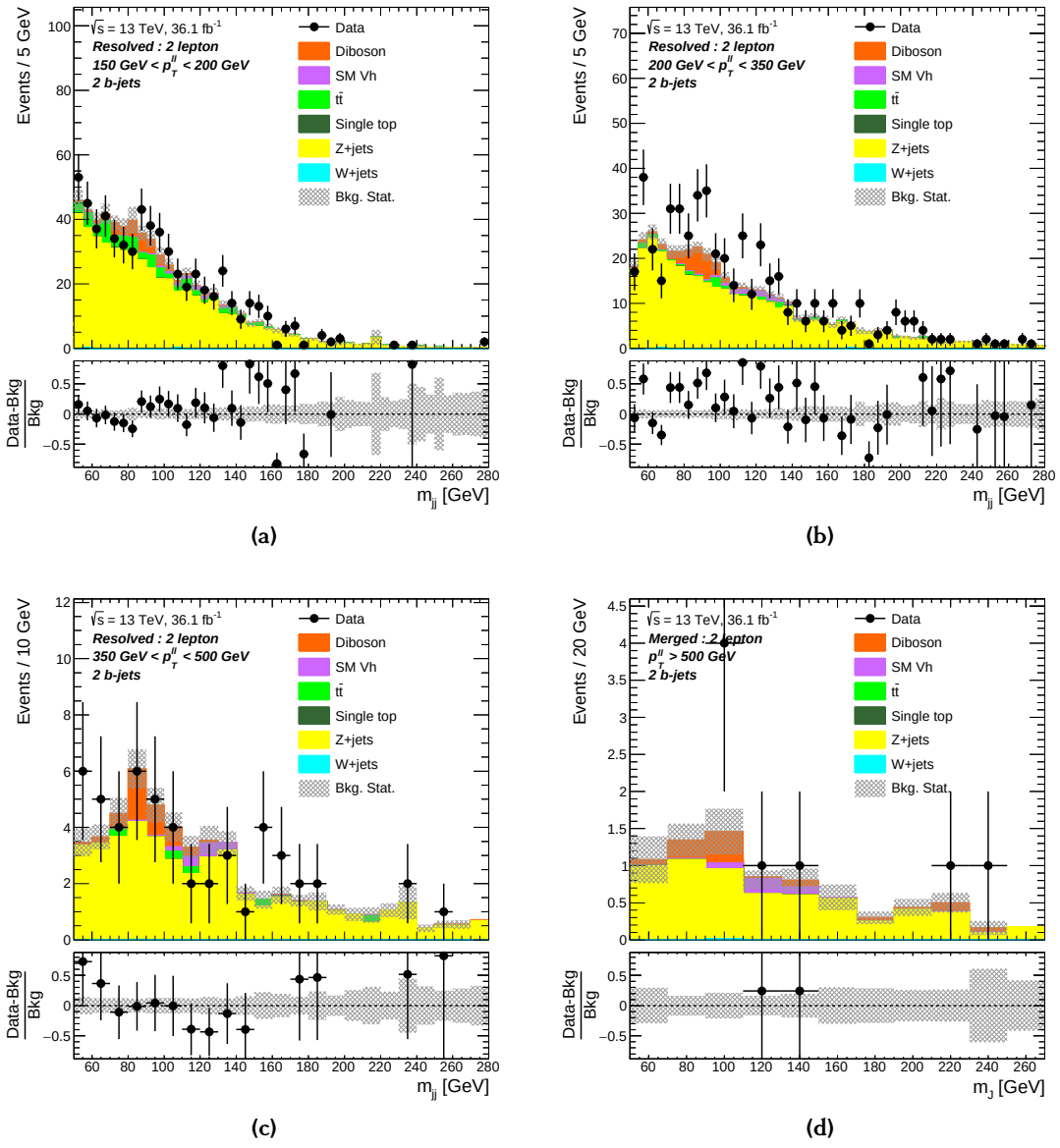

Figure D.4: Pre-fit distributions of the invariant mass of the Higgs boson candidates $m_{h,\,\mathrm{cand}} = m_{jj}$, m_J for events two b-jets in the 2ℓ-CR for the four $p_{\mathrm{T}}^{\ell\ell}$ categories.

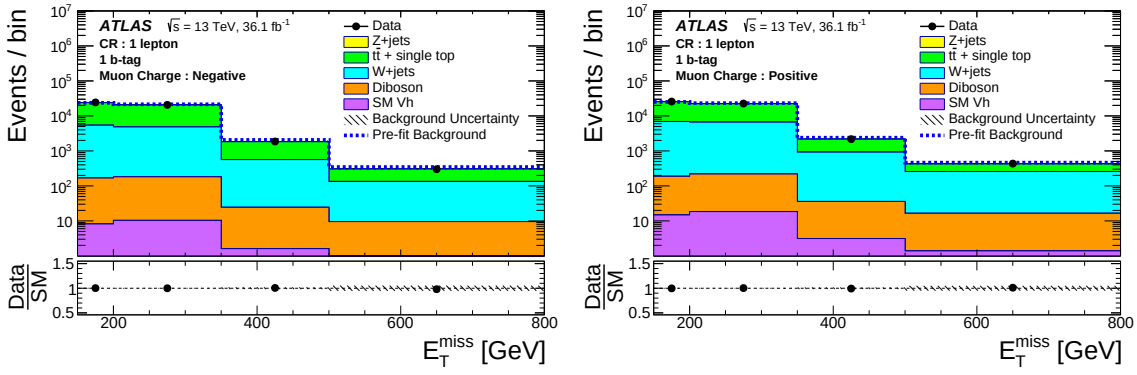

(a) (b)

Figure D.5: Distribution of $E_{\mathrm{T}}^{\mathrm{miss,\,no-}\mu}$ in the one muon control region in case of (a) a muon with negative charge and in (b) with positive charge is selected for events with one b-jet. The muon four momenta is not considered in the $E_{\mathrm{T}}^{\mathrm{miss}}$ calculation. For all figures, the upper panels show a comparison of data to the Standard Model expectation before (dashed lines) and after the fit (solid histograms). The lower panels display the ratio of data to Standard Model expectations after the fit, with its systematic uncertainty considering correlations between individual contributions indicated by the hatched band [258]. The rightmost bin includes overflows. The number of bin entries is divided by its width.

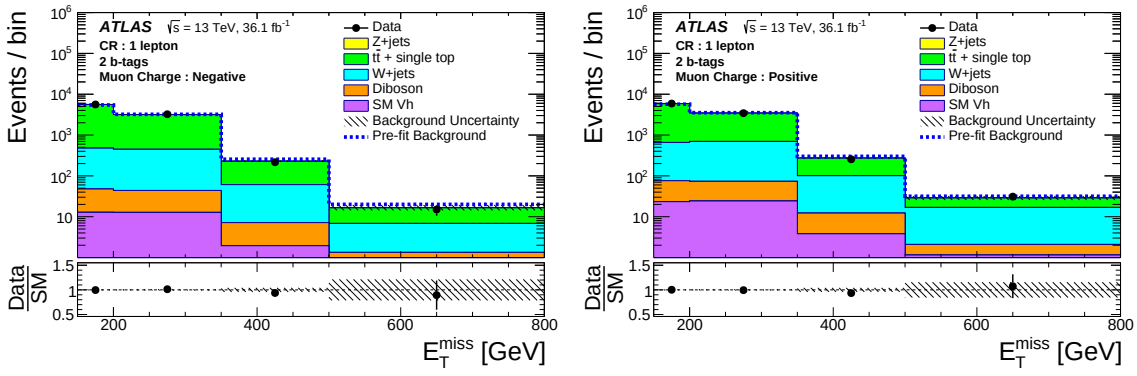

(a) (b)

Figure D.6: Distribution of $E_{\mathrm{T}}^{\mathrm{miss,\,no-}\mu}$ in the one muon control region in case of (a) a muon with negative charge and in (b) with positive charge is selected for events with two b-jets. The muon four momenta is not considered in the $E_{\mathrm{T}}^{\mathrm{miss}}$ calculation. For all figures, the upper panels show a comparison of data to the Standard Model expectation before (dashed lines) and after the fit (solid histograms). The lower panels display the ratio of data to Standard Model expectations after the fit, with its systematic uncertainty considering correlations between individual contributions indicated by the hatched band [258]. The rightmost bin includes overflows. The number of bin entries is divided by its width.

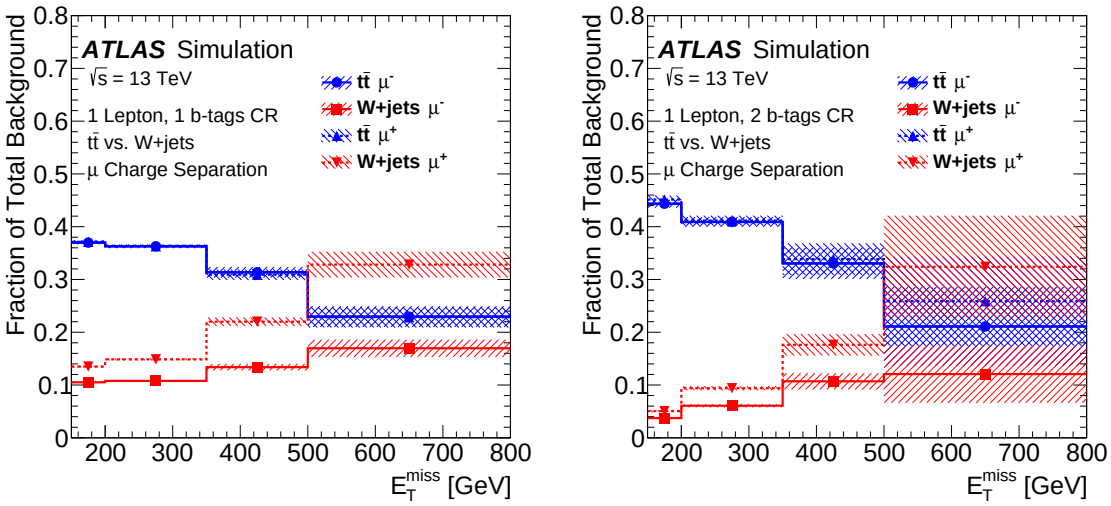

Figure D.7: Fraction of the $t\bar{t}$ and W+jets processes to the total sum of backgrounds as a function of $E_{\mathrm{T}}^{\mathrm{miss}}$ for events with (a) one and (b) two b-jets, while the former is symmetric in the muon charge, the latter shows an asymmetry which allows to separate the two processes. The quadratic sum of statistical and systematic uncertainties is indicated by the hatched band [258].

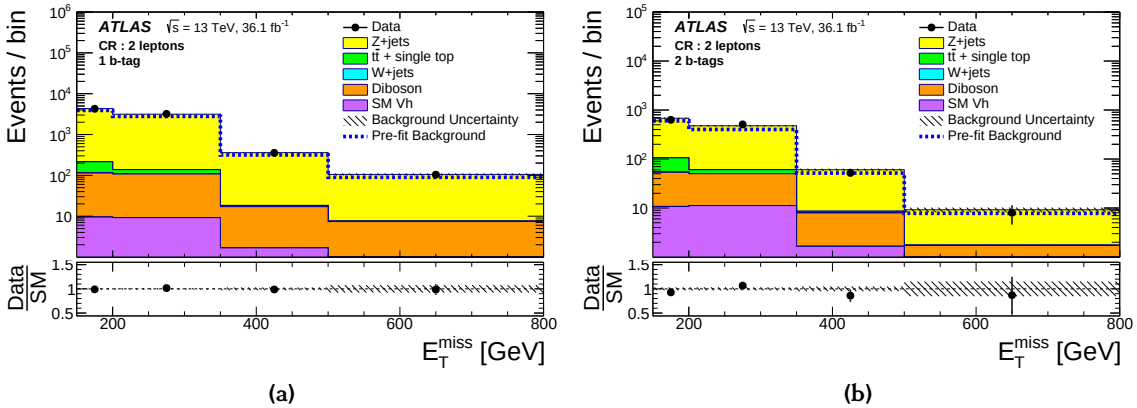

Figure D.8: Distribution of $p_{\mathrm{T}}^{\ell\ell}$ in the two lepton control region, where $E_{\mathrm{T}}^{\mathrm{miss}}$ corresponds to the transverse momenta of the Z boson, for events with (a) one and (b) two b-jets. The upper panels show a comparison of data to the Standard Model expectation before (dashed lines) and after the fit (solid histograms). The lower panels display the ratio of data to Standard Model expectations after the fit, with its systematic uncertainty considering correlations between individual contributions indicated by the hatched band [258]. The rightmost bin includes overflows. The number of bin entries is divided by the bin width.

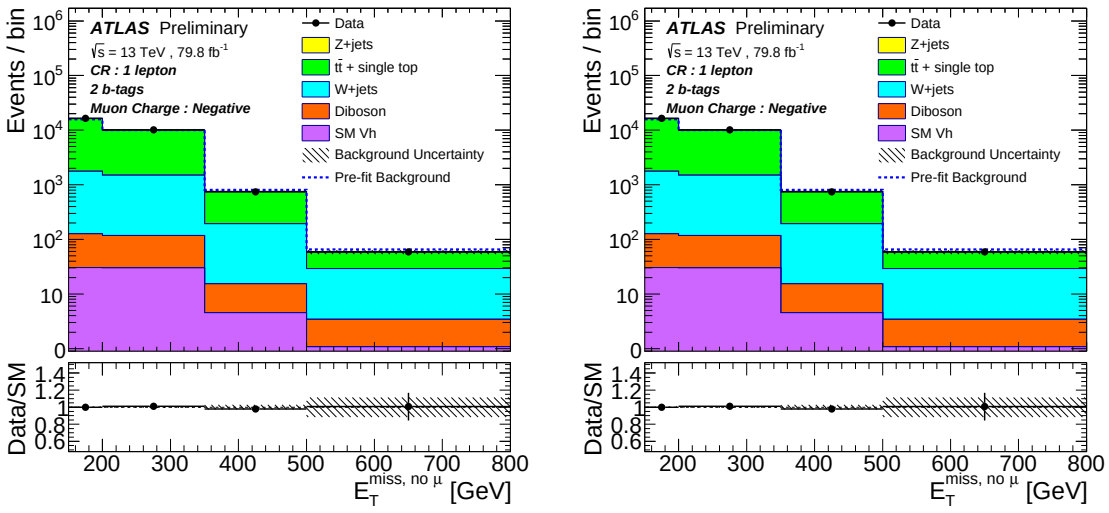

Figure D.9: Distribution of $E_{\mathrm{T}}^{\mathrm{miss,\,no-}\mu}$ in the one muon control region in case of (a) a muon with negative charge and in (b) with positive charge. For all figures, the upper panels show a comparison of data to the Standard Model expectation before (dashed lines) and after the fit (solid histograms). The lower panels display the ratio of data to Standard Model expectations after the fit, with its systematic uncertainty considering correlations between individual contributions indicated by the hatched band [432]. The rightmost bin includes overflows. The number of bin entries is divided by its width.

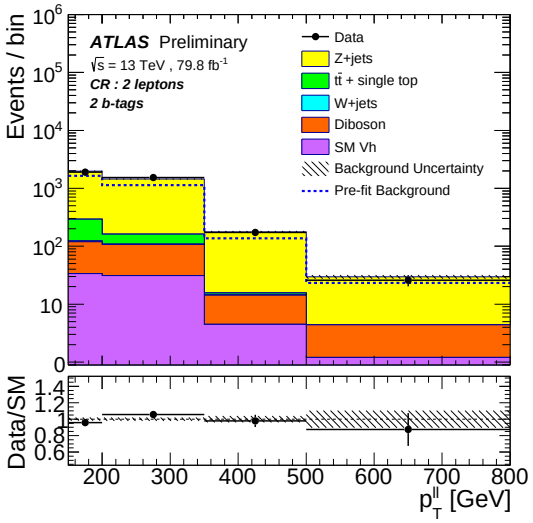

Figure D.10: Distribution of $p_{\mathrm{T}}^{\ell\ell}$ in the two lepton control region, where $p_{\mathrm{T}}^{\ell\ell}$ corresponds to the transverse momenta of the Z boson. The upper panels show a comparison of data to the Standard Model expectation before (dashed lines) and after the fit (solid histograms). The lower panels display the ratio of data to Standard Model expectations after the fit, with its systematic uncertainty considering correlations between individual contributions indicated by the hatched band [432]. The rightmost bin includes overflows. The number of bin entries is divided by the bin width.

Appendix E

Truth-Level Jet Flavour Labelling

The W+jets and Z+jets processes, summarised in the following as V+jets, are simulated with the SHERPA Monte-Carlo generator. In order to get sufficiently large event statistics of with large $E_{\mathrm{T}}^{\mathrm{miss}}$ and heavy-flavour jets, filters are applied at generator level. For each of the two processes $Z \to \ell^+\ell^-/\nu\nu$ + jets and $\ell^+\nu^-$ + jets with $\ell = e, \mu, \tau$, the Monte-Carlo samples are sliced in the variable $\max[H_{\mathrm{T}}, p_{\mathrm{T}}^V]$, where p_{T}^V is the p_{T} of the weak vector boson build from the two truth-level leptons and H_{T} is given by the scalar sum of p_{T} of all parton-level jets with $p_{\mathrm{T}} > 20\,\mathrm{GeV}$ to populate $E_{\mathrm{T}}^{\mathrm{miss}}$ intervals. For $\max[H_{\mathrm{T}}, p_{\mathrm{T}}^V]$ below 500 GeV, the Monte-Carlo samples are also filtered according to their B- and C-hadron content at particle level [448] to populate the one and two b-jet region.

The simulated V+jets background samples are further decomposed according to the truth-flavour of the jets used for identifying the Higgs boson decay products. This is necessary as the V+jets background composition changes between different $E_{\mathrm{T}}^{\mathrm{miss}}$ regions and for the one and two b-region, such that different normalisations of the templates are expected in the final profile likelihood fit (see Chapter 5). The jet truth-flavour labelling is done for both small-R jets and track-jets based on a cone matching of truth-hadrons to the jets within a cone with radius parameter of $R_{\mathrm{max}} = 0.3$. If a decaying B-hadron is found within $\Delta R < R_{\mathrm{max}}$ of a jet, the jet is labeled as a truth b-jet. In case of no nearby B-hadron to a jet, but instead a C-hadron is found within $\Delta R < R_{\mathrm{max}}$ of a jet, the jet is labeled as a truth c-jet. The jet is truth-labeled as a τ-jet if a τ lepton is found within ΔR and no B- or C-hadrons. In case of multiple matching objects to a jet, priority is given to the closest. All remaining jets are labeled as light-jets. For the labelling of the Higgs boson candidate the two highest-p_{T} small-R jets or track-jets are used. For events where only on b-jet is found, the non b-jet with highest-p_{T} is considered as well. This approach results in six sub-samples for each of the W+jets and Z+jets samples, and templates of the Higgs boson candidate mass are build. In case of two jets truth-labeled as b-jets (c-jets) the template is denoted as $V + bb$ ($V + cc$). If one of the jets is labeled as a b-jet while the other as a c-jet, the template is denoted as $V + bc$. For cases where one jet is labeled as a b-jets or c-jets, while the other is a

truth light-jet the sample is assigned to $V + bl$ or $V + cl$, respectively. If both jets are labeled as truth light-jets, the template is denoted as $V + ll$. The $V + bb$, bc bl and cc are summarised as $V +$ heavy-flavour (hf). The light-flavour components, $V + cl$ and $V + ll$, are summarised as $V +$ light-flavour (lf). The resulting templates are used within a profile-likelihood fit, see Chapter 5.

The composition of the $W+$jets and $Z+$jets background samples are given in Table E.1 and Table E.3 for events with one b-jet and in Table E.2 and Table E.4 for two b-jets. Here, the numbers correspond to the samples after applying the full signal region event selection (see Section 4.7). For events with two b-jets the $V+$jets template is mostly composed from the $W +$ hf part, with a fraction of more then 95 %. In case of events with one b-jet the total $W+$jets sample is half made of the $W +$ hf and half of $W +$ lf, expect for the merged region, where around 62 % are from the $W +$lf component. While for $Z+$jets events with one b-jet the component of $Z +$ lf is increased up to 70 %, and shared with $Z +$ hf for the merged region. For events with one b-jet the dominant component originates from $V + bb$, expect for the merged region of $W+$jets events, where $W + cl$ provides the leading contribution to the total background sample. The $V + bb$ component dominates in case of events with two b-jets for both background samples.

Table E.1: Composition [%] of the $W+$jets background sample after applying truth-Level jet flavour labelling for events with one b-jet in the signal region. The heavy-flavour component, $W +$ hf, is given by the sum of the $W + bb$, bc bl and cc components, while the light-flavour component, $W+$lf, is given by the sum of $W+cl$ and $W+ll$. The shown uncertainties correspond to the statistical uncertainty of the template.

Z+jets component	$E_{\mathrm{T}}^{\mathrm{miss}}$ region [GeV]			
	[150, 200)	[200, 350)	[350, 500)	[500, ∞)
$W + bb$	3.82 ±0.12	4.49 ±0.17	6.34 ±0.54	5.32 ± 1.23
$W + bc$	2.46 ±0.10	2.91 ±0.12	2.82 ±0.33	1.41 ±0.50
$W + bl$	42.78 ±0.54	43.57 ±0.50	42.03 ± 1.67	26.77 ± 2.74
$W + cc$	3.46 ±0.31	3.76 ±0.27	3.53 ±0.70	4.65 ± 1.27
$W + cl$	29.35 ±0.82	29.09 ±0.90	32.28 ± 2.32	35.46 ± 3.32
$W + ll$	18.14 ± 1.36	16.18 ±0.84	12.99 ± 1.40	26.39 ± 2.88
$W +$ hf	52.52 ±0.64	54.73 ±0.60	54.73 ± 1.92	38.15 ± 3.3
$W +$ lf	47.48 ± 1.59	45.27 ± 1.23	45.27 ± 2.71	61.85 ± 4.4

Table E.2: Composition [%] of the W+jets background sample after applying truth-Level jet flavour labelling for events with two b-jets in the signal region. The heavy-flavour component, W + hf, is given by the sum of the $W + bb$, bc bl and cc components, while the light-flavour component, W+lf, is given by the sum of $W+cl$ and $W+ll$. The shown uncertainties correspond to the statistical uncertainty of the template.

Z+jets component	$E_{\mathrm{T}}^{\mathrm{miss}}$ region [GeV]			
	[150, 200)	[200, 350)	[350, 500)	[500, ∞)
$W + bb$	83.80± 1.96	82.99 ± 2.09	82.60± 5.55	66.72 ±14.40
$W + bc$	5.60±0.66	5.42 ±0.53	7.95 ± 2.33	3.15 ± 2.15
$W + bl$	3.72 ±0.57	4.21 ±0.59	3.87 ± 1.77	12.58 ± 7.28
$W + cc$	4.11 ± 1.26	3.39 ±0.77	3.17 ± 1.74	12.25 ± 7.28
$W + cl$	2.27 ± 1.07	3.75 ± 1.27	0.23 ± 2.36	2.81 ± 2.81
$W + ll$	0.50 ±0.24	0.25 ±0.46	2.63 ± 1.61	2.48 ± 2.15
W + hf	97.23 ± 2.49	96.01 ± 2.36	97.60± 6.51	94.70 ±17.84
W + lf	2.77 ± 1.10	3.99 ± 1.35	2.40 ± 2.85	5.30 ± 3.54

Table E.3: Composition [%] of the Z+jets background sample after applying truth-Level jet flavour labelling for events with one b-jet in the signal region. The heavy-flavour component, Z + hf, is given by the sum of the $Z + bb$, bc bl and cc components, while the light-flavour component, Z+lf, is given by the sum of $Z+cl$ and $Z+ll$. The shown uncertainties correspond to the statistical uncertainty of the template.

Z+jets component	$E_{\mathrm{T}}^{\mathrm{miss}}$ region [GeV]			
	[150, 200)	[200, 350)	[350, 500)	[500, ∞)
$Z + bb$	5.27 ±0.09	5.90±0.08	6.77 ±0.21	5.22 ±0.35
$Z + bc$	3.45 ±0.07	3.52 ±0.06	3.56 ±0.15	2.29 ±0.26
$Z + bl$	56.85 ±0.32	53.94 ±0.27	50.24 ±0.53	37.27 ±0.99
$Z + cc$	4.14 ±0.17	3.87 ±0.13	4.62 ±0.38	5.23 ±0.43
$Z + cl$	20.41 ±0.35	21.77 ±0.34	23.25 ±0.91	25.84 ± 1.58
$Z + ll$	9.88 ±0.41	11.01 ±0.58	11.56 ±0.69	24.14 ± 1.21
Z + hf	69.71 ±0.38	67.22 ±0.32	65.19 ±0.7	50.01 ± 1.17
Z + lf	30.29 ±0.54	32.78 ±0.67	34.81 ± 1.14	49.99 ± 1.99

Table E.4: Composition [%] of the Z+jets background sample after applying truth-Level jet flavour labelling for events with two b-jets in the signal region. The heavy-flavour component, Z + hf, is given by the sum of the $Z + bb$, bc bl and cc components, while the light-flavour component, Z+lf, is given by the sum of $Z+cl$ and $Z+ll$. The shown uncertainties correspond to the statistical uncertainty of the template.

Z+jets component	$E_{\mathrm{T}}^{\mathrm{miss}}$ region [GeV]			
	[150, 200)	[200, 350)	[350, 500)	[500, ∞)
$Z + bb$	87.09±0.96	87.00±0.87	85.15 ± 2.17	70.61 ± 4.43
$Z + bc$	5.65 ±0.33	6.10 ±0.32	6.95 ±0.64	8.53 ± 1.82
$Z + bl$	2.96 ±0.21	3.33 ±0.20	3.43 ±0.48	0.61 ± 2.10
$Z + cc$	2.71 ±0.33	2.61 ±0.37	2.52 ±0.75	6.20± 1.65
$Z + cl$	1.20±0.28	1.29 ±0.35	1.40 ±0.52	4.89 ± 1.88
$Z + ll$	0.39 ±0.23	0.33 ±0.49	0.56 ±0.34	0.17 ± 1.25
Z + hf	98.41 ± 1.09	99.04± 1.02	98.04 ± 2.43	94.94 ± 5.49
Z + lf	1.59 ±0.36	0.96 ±0.60	1.96 ±0.62	5.06± 2.25

Appendix F

Estimation of the Multijet Background

At the LHC an overwhelming large multijet background is present. Usually, in multijet events no real $E_{\mathrm{T}}^{\mathrm{miss}}$, e.g. from neutrinos or Dark Matter particles, is available. Instead, $E_{\mathrm{T}}^{\mathrm{miss}}$ mostly originates from reconstruction effects of jets and their energies, such that $\vec{E}_{\mathrm{T}}^{\mathrm{miss}}$ often points into the same direction as a jet and to a small amount from semileptonic heavy-flavour hadron decays where neutrinos are produced.
Multijet events can efficiently be reduced by requiring a large $E_{\mathrm{T}}^{\mathrm{miss}}$, e.g. above 150 GeV, and by applying anti-QCD cuts, as introduced in Section 4.7, which take into account the characteristic event topology of multijet events. Nevertheless, the multijet background is estimated by using da data driven approach in the SR to guarantee that the process is understood and its contribution is under control. The estimation of the multijet background is only done for the resolved signal region, while for the merged signal region the multijet background is expected to be negligible due to the high $E_{\mathrm{T}}^{\mathrm{miss}}$ requirement of $E_{\mathrm{T}}^{\mathrm{miss}} > 500$ GeV. Nevertheless, the anti-QCD requirements are applied to both events in the resolved and in the merged signal region. In the control regions, the contribution of the multijet background is neglected.
The multijet process is challenging to model in Monte-Carlo simulation since the production of sufficiently high amount of events is very computing intense. Therefore, this background is estimated in the SR in a data driven way by using a so-called *template method*. Templates of the multijet background of e.g. the Higgs boson candidate mass are used in the final profile-likelihood fit for extracting the signal sensitivity. The multijet estimation is only done for the resolved region, as the multijet contribution is expected to be negligible once a $E_{\mathrm{T}}^{\mathrm{miss}}$ of more then 500 GeV is required as for the merged region (see Appendix F). Even in the resolved region the multijet background is expected to be a minor contribution to the overall amount of selected events, especially in regions with one or two b-jets. Due to the relatively small contribution, the estimation of multijet contributions can come with a relatively large uncertainty, without diminishing the sensitivity of the analysis to Dark Matter signals.
The multijet background in the resolved region is estimated separately for each of the

three $E_{\mathrm{T}}^{\mathrm{miss}}$ regions and for events with one or two b-jets. Dedicated regions of phase space is defined, where multijet events are enriched, so-called *multijet regions*, to derive templates of distributions of different variables of interest like $E_{\mathrm{T}}^{\mathrm{miss}}$ and $m_{h,\,\mathrm{cand}}$. Events are selected in the multijet region by requiring to pass the $E_{\mathrm{T}}^{\mathrm{miss}}$ trigger requirement, no leptons and by inverting one of the anti-QCD cuts, namely $\min\Delta\Phi(\vec{E}_{\mathrm{T}}^{\mathrm{miss}},\,\vec{j}_{\mathrm{l},\,2,\,3}) < 20°$. This region is dominated by multijet background events, as illustrated in Fig. F.1, where the multijet distribution is given as the difference of data and all Standard Model background processes.

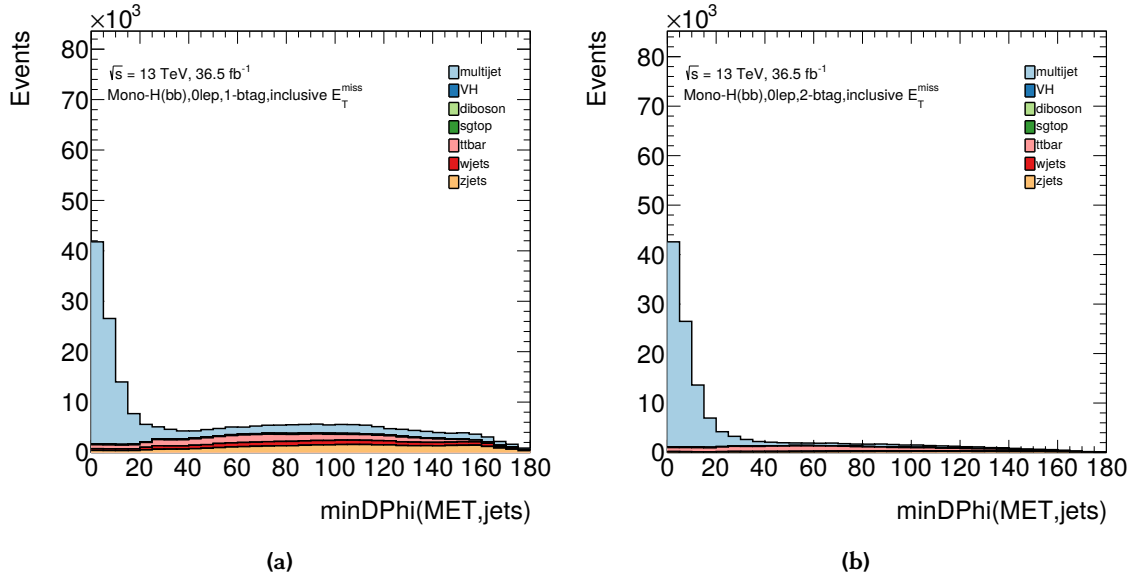

Figure F.1: Distribution of $\min\Delta\Phi(\vec{E}_{\mathrm{T}}^{\mathrm{miss}},\,\vec{j}_{\mathrm{l},\,2,\,3})$ for events with (a) one and (b) two b-jets and inclusively in $E_{\mathrm{T}}^{\mathrm{miss}}$, showing that the region below $\min\Delta\Phi(\vec{E}_{\mathrm{T}}^{\mathrm{miss}},\,\vec{j}_{\mathrm{l},\,2,\,3}) < 20°$ is dominated by multijet background events. The shown multijet background (blue) is the difference between data and all Standard Model background processes.

In the region of $\min\Delta\Phi(\vec{E}_{\mathrm{T}}^{\mathrm{miss}},\,\vec{j}_{\mathrm{l},\,2,\,3}) < 20°$, the difference between data and simulated non-multijet backgrounds is used as a model of the shape of different variables ($E_{\mathrm{T}}^{\mathrm{miss}}$ and $m_{h,\,\mathrm{cand}}$) of the multijet background. These templates must be correctly normalised in order to be used in the resolved region for the three different categories of $E_{\mathrm{T}}^{\mathrm{miss}}$. The normalisation is performed within a fit of the multijet templates and the remaining simulated Standard Model backgrounds to data. The variable which is used to perform the fit, resulting in the multijet normalisation, is the multiplicity of jets which contain a muon. This choice is motivated by the fact that many of the multijet events come with no real $E_{\mathrm{T}}^{\mathrm{miss}}$ and in case of events with $E_{\mathrm{T}}^{\mathrm{miss}}$, it is caused by neutrinos which originate from heavy-flavour hadron decays, which are reconstructed as jets. In addition to neutrinos, muons are produced as well within the cone of the small-R jet. Thus, multijet events

accumulate at higher multiplicities of the distribution of jets which contain muons. Within this fit, all simulated non-multijet backgrounds are allowed to float independently within theoretical uncertainties with one overall normalisation factor that controls the normalisation of non-multijet components in the fit. Finally, statistical uncertainties are taken into account separately for each component in the fit. The normalisation of the multijet template is left to float freely and is the parameter of interest that is measured to provide estimates of the normalisation of the multijet contribution. The multijet contribution after the full SR selection is quite small. In order to have reasonable and converging fits, the event selection in the multijet region is relaxed compared to the full selection. More precisely, anti-QCD cuts ($\Delta\phi\left(\vec{E}_{\mathrm{T}}^{\mathrm{miss}}, \vec{p}_{\mathrm{T}}^{\mathrm{miss}}\right) < 90°$, $\Delta\phi\left(\vec{E}_{\mathrm{T}}^{\mathrm{miss}}, \vec{p}_{\mathrm{h}}\right) > 120°$) and $\Delta R\left(\vec{p}_h^{\,j_1}, \vec{p}_h^{\,j_2}\right) < 1.8$ cuts are not applied in order to increase the amount of multijet events, so that fits can provide robust results regarding the multijet normalisation. Since this fit selection is similar to the SR, events around the Higgs boson mass of 70 to 140 GeV are not taken into account. The results of the fit of the distribution of jets with muons are given in Fig. F.2 and Fig. F.3 for events with one and two b-jets, respectively, separately for each $E_{\mathrm{T}}^{\mathrm{miss}}$ interval. In the second highest $E_{\mathrm{T}}^{\mathrm{miss}}$ category of [200, 350) GeV, the multijet contribution is at the level of 1 to 2 % depending on the number of b-jets and is neglected due to its minor impact. Finally, for each of the two remaining $E_{\mathrm{T}}^{\mathrm{miss}}$ intervals and for each b-tag multiplicity, a multijet template of the Higgs boson candidate mass distribution is derived and used in the final fit for estimating the dominant backgrounds (see Chapter 5). An uncertainty of 100 % is assumed for the multijet normalisation, to guarantee that any statistical deviation within the template method is covered and the multijet background process is well under control. Even under the conservative normalisation uncertainty, the contribution is still very small and at most of the order of 4 % of the total background.

In order to validate that the multijet contribution in the merged region is indeed negligible, a multijet enriched region is build by considering events with $\min\Delta\Phi(\vec{E}_{\mathrm{T}}^{\mathrm{miss}}, \vec{j}_{1,\,2,\,3}) < 20°$ and no requirement of $E_{\mathrm{T}}^{\mathrm{miss}} > 500\,\mathrm{GeV}$. The shape of the $E_{\mathrm{T}}^{\mathrm{miss}}$ distribution is used to providing an estimate in the merged region by extrapolating the distribution to higher $E_{\mathrm{T}}^{\mathrm{miss}}$.

The event selection of the merged region is applied in the same way as it is done for defining the signal region. After inverting the $\min\Delta\Phi(\vec{E}_{\mathrm{T}}^{\mathrm{miss}}, \vec{j}_{1,\,2,\,3})$ requirement, templates of the $E_{\mathrm{T}}^{\mathrm{miss}}$ distribution of multijet events are derived, which are then normalised within a profile-likelihood fit with all other non-multijet background processes to the data. The resulting $E_{\mathrm{T}}^{\mathrm{miss}}$ distributions after the fit has been applied are shown in Fig. F.4. The multijet contribution above $E_{\mathrm{T}}^{\mathrm{miss}} > 500\,\mathrm{GeV}$ is vanishingly small independent of the number of b-jets. The fraction of multijet events in merged region calculated from this fits is less than 1 %, such that its contribution is neglected in the merged region.

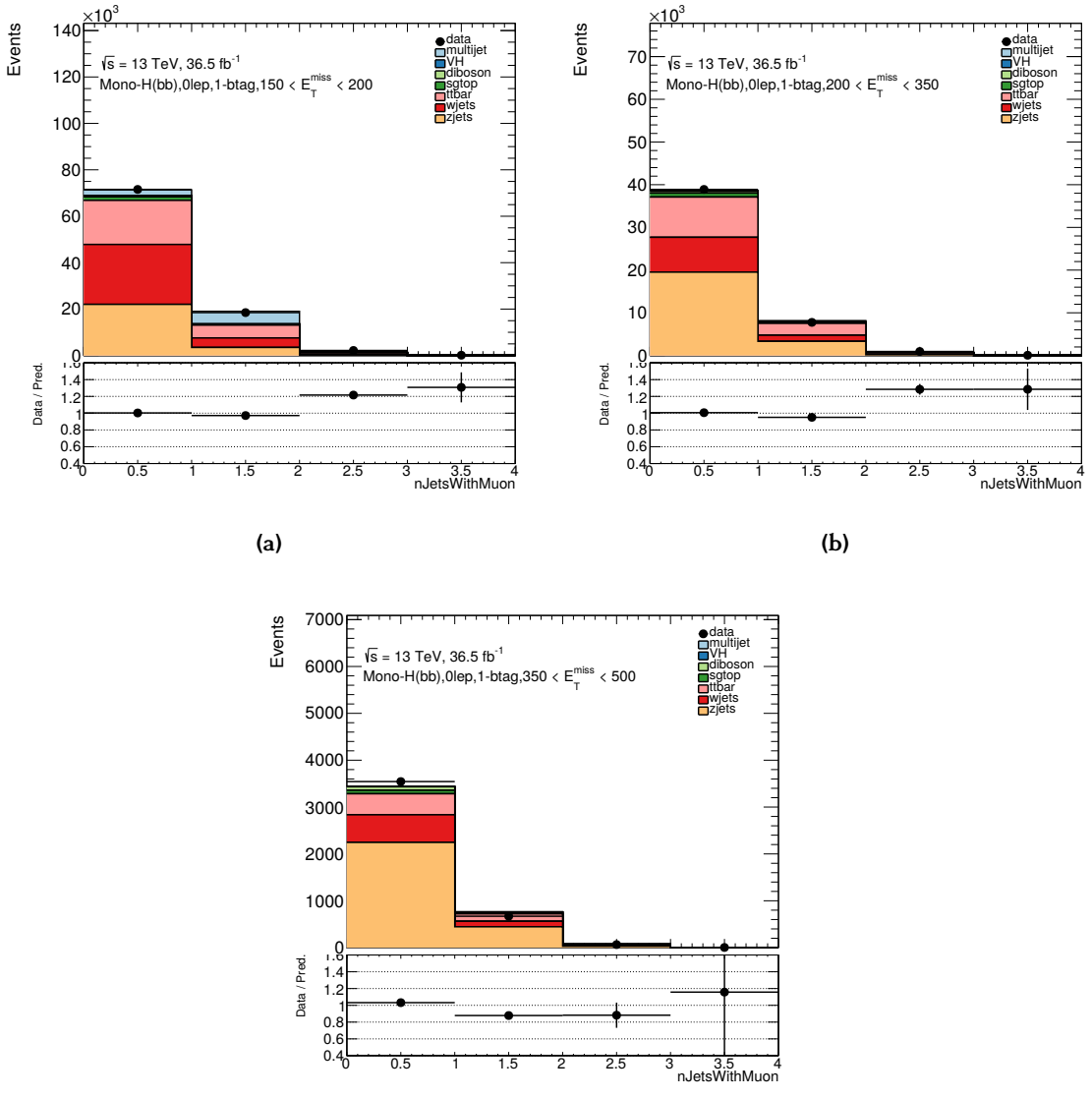

Figure F.2: Post-fit distributions of the number of small-R jets containing a muon for events with one b-jet for the three $E_{\mathrm{T}}^{\mathrm{miss}}$ categories in the resolved signal region.

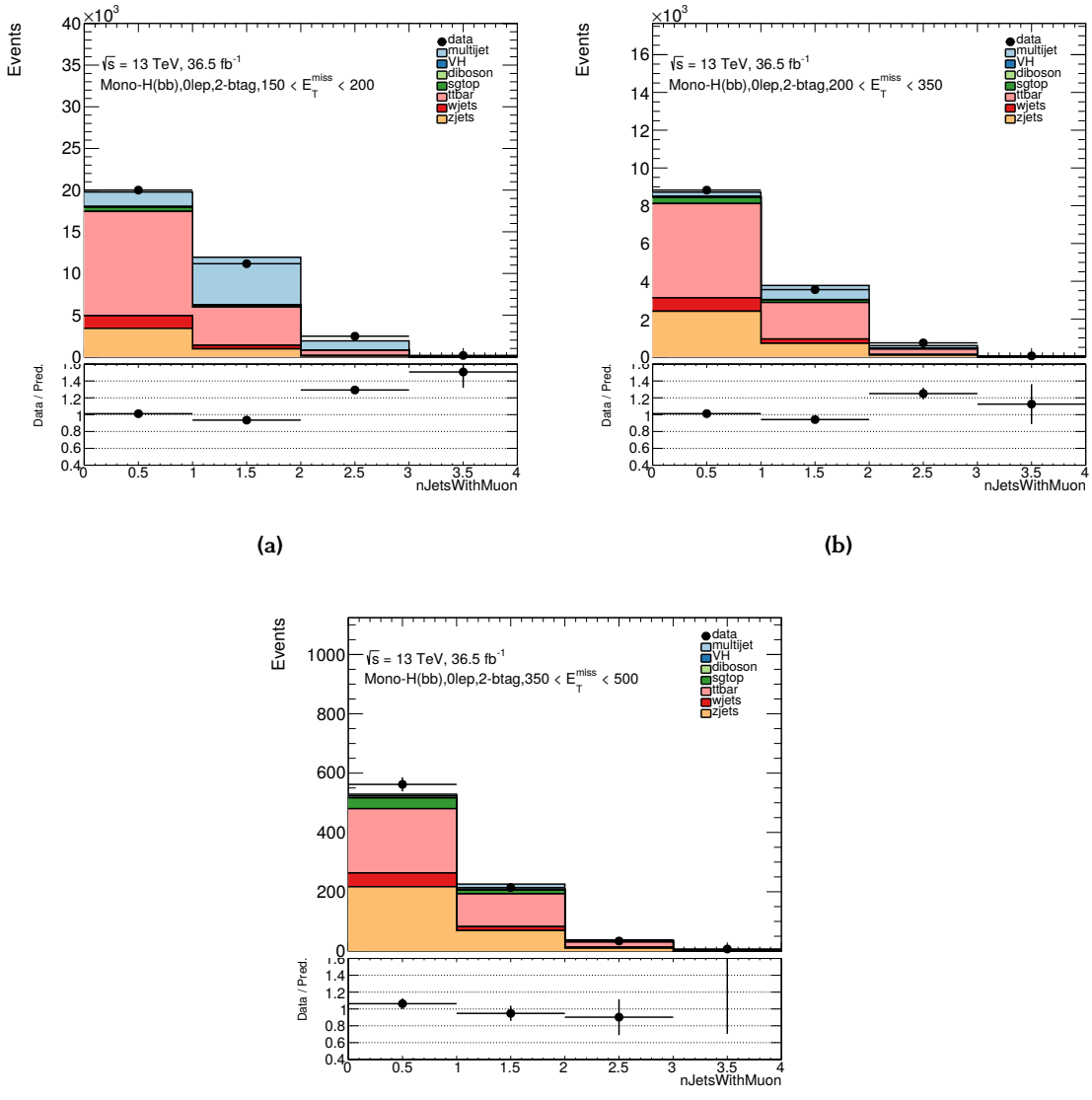

Figure F.3: Post-fit distributions of the number of small-R jets that containing a muon for events with two b-jets for the three $E_{\mathrm{T}}^{\mathrm{miss}}$ categories in the resolved region.

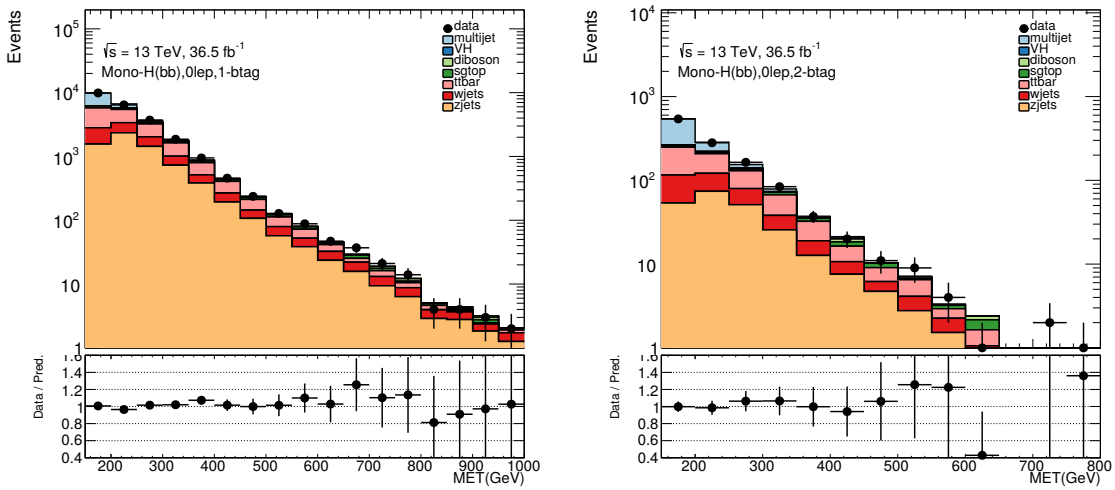

(a) **(b)**

Figure F.4: Distribution of $E_{\mathrm{T}}^{\mathrm{miss}}$ for events with (a) one and (b) two b-jets after applying the selection requirements of the merged region.

Appendix G

Statistical Methods

This Chapter provides information about the log-normal distribution (see Section G.1), which is used in the likelihood definition in Eq. (5.1) for the description of nuisance parameters related to background normalisation uncertainties, and about the pruning and smoothing procedures of nuisance parameters (see Section G.2).

G.1 The Log-Normal Probability Density Function

The log-normal distribution [449] (see Fig. G.1) describes a random variable, whose logarithm follows a normal distribution, and is given by

$$\mathcal{LN}(x|\mu,\,\sigma) = \frac{1}{x\sigma\sqrt{2\pi}} \exp\left[-\frac{(\ln x - \mu)^2}{2\sigma^2}\right] \tag{G.1}$$

with μ the mean value, σ the standard deviation and x the random variable with $x > 0$. Compared to a normal distribution, which is usually used for the parametrisation of experimental systematic uncertainties, the log-normal distribution has a longer tail and goes to zero at $x = 0$, such that the normalisation of a template is constrained to be always positive.

G.2 Pruning and Smoothing of Nuisance Parameters

Some of the systematics uncertainties discussed in Section 5.2.1 are expected to have only a negligible effect on the final results, i.e. change the shape or the normalisation of a distribution only by little. Moreover, a large number of nuisance parameter makes the statistical model more complex, and impact the robustness of the model. In addition, the fit may diverge for cases where the Monte-Carlo templates have low statistics and large fluctuations are observed, i.e. for high $E_{\mathrm{T}}^{\mathrm{miss}}$. Therefore, some uncertainties are not considered in the likelihood-fit and *pruned* away, if their impact on the nominal distribution is smaller then a certain threshold. Furthermore, for Monte-Carlo templates with very low statistics a *smoothing* procedure to the bins with low statistics is applied.

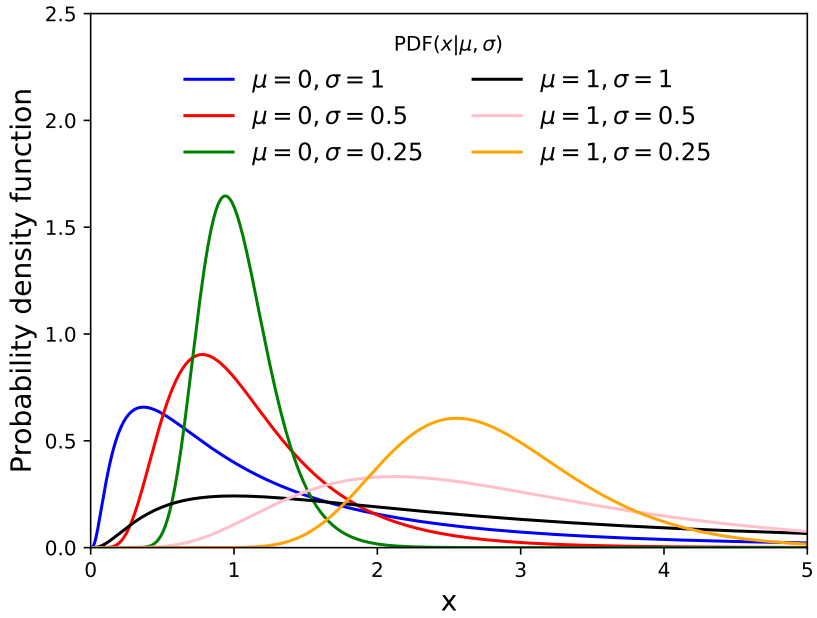

Figure G.1: Overview of different log-normal probability density functions defined for different mean values, μ, and standard deviations, σ.

The *pruning* algorithm is applied, in a way that a systematic uncertainty is excluded for a template in a certain region, if not one single bin has a deviation of more than 0.5 % form the nominal case. The impact of the pruning algorithm is varified by reducing the threshold from 0.5 % to 0.1 %, and the sensitivity is estimated for the benchmark $(m_{Z'}, m_A) = (1400\,\text{GeV}, 600\,\text{GeV})$ signal point. Here, the impact on the expected significance was found to be below 1 %.

In order to reduce statistical fluctuations within the fit, a *smoothing* procedure to nuisance parameters which change the shape of distributions is applied. For example, nuisance parameters which are related to systematic uncertainties of the jet energy scale and resolution. These shape uncertainties can result in bin-to-bin migrations of events, i.e. when the energy of a jet is shifted by $\pm\sigma$, such that the event passes or fails a certain selection requirement or ends up in a different bin of a histogram. To reduce this effect, the ratio of the nominal and the systematically varied histogram is built. Then, the ratio histogram rebinned that at most only one local extrema exists in the distribution. The remaining bins are merged in order to reduce statistical fluctuations until the statistical uncertainty of each of the merged bins is smaller then 5 %. Second, the bins resulting from this first algorithm are used to define an appropriate ratio of the nominal and systematically varied histogram. Then the latter is replaced by the product of the nominal histogram and the computed ratio histogram and its integral is set to its original value.

Appendix H

Study of Further Systematic Uncertainties

In this Chapter, the impact of systematic uncertainties neglected in the mono-Higgs ($b\bar{b}$) analysis (see Chapter 4) is discussed, which are related to the $E_{\mathrm{T}}^{\mathrm{miss}}$ soft-term (see Section H.1) and to the τ-jet identification their kinematics (see Section H.2).

H.1 Systematic Uncertainties in $E_{\mathrm{T}}^{\mathrm{miss}}$

Four systematic uncertainties related to the $E_{\mathrm{T}}^{\mathrm{miss}}$ soft-term (see Table H.1) were not available when the mono-Higgs ($b\bar{b}$) analysis has been performed, and, therefore, were not considered as nuisance parameters in the profile-likelihood fit. The impact of the missing

Table H.1: Qualitative summary of the missing $E_{\mathrm{T}}^{\mathrm{miss}}$ systematic uncertainties.

Systematic uncertainty	Short description
MET_JetTrk_Scale	scale uncertainty due to tracks in jets
MET_SoftTrk_ResoPerp	transversal resolution uncertainty on track-based soft-term
MET_SoftTrk_ResoPara	longitudinal resolution uncertainty on track-based soft-term
MET_SoftTrk_Scale	longitudinal scale uncertainty on track-based soft-term

uncertainties have been studied by using Monte-Carlo samples, which arrived later in time, of all backgrounds and one benchmark Z'-2HDM signal model with $(m_{Z'}, m_A) = (1400\,\mathrm{GeV}, 600\,\mathrm{GeV})$. The nominal distributions of the Higgs boson candidate mass are compared with the up and down variations, considering the overall change in the event yield and shape of the distribution. The uncertainty MET_SoftTrk_ResoPerp and MET_SoftTrk_ResoPara are only parametrised as an up variation of the nominal distribution. The distributions for the total background and one representative Z'-2HDM signal model are shown in Fig. H.1-H.8 and Fig. H.9-H.16, respectively, in each of the four different $E_{\mathrm{T}}^{\mathrm{miss}}$ bins and for events with one and two b-jets.
In all regions of $E_{\mathrm{T}}^{\mathrm{miss}}$ and independent of the number of b-jets in the event, the deviation

from the nominal distributions is less then 5 % for each of the four missing $E_{\mathrm{T}}^{\mathrm{miss}}$ systematic uncertainties given as up and down variations for both the total background and a benchmark signal model. Thus, it is expected that the physical results are not significantly changed when the $E_{\mathrm{T}}^{\mathrm{miss}}$ systematic uncertainties are neglected as nuisance parameters.

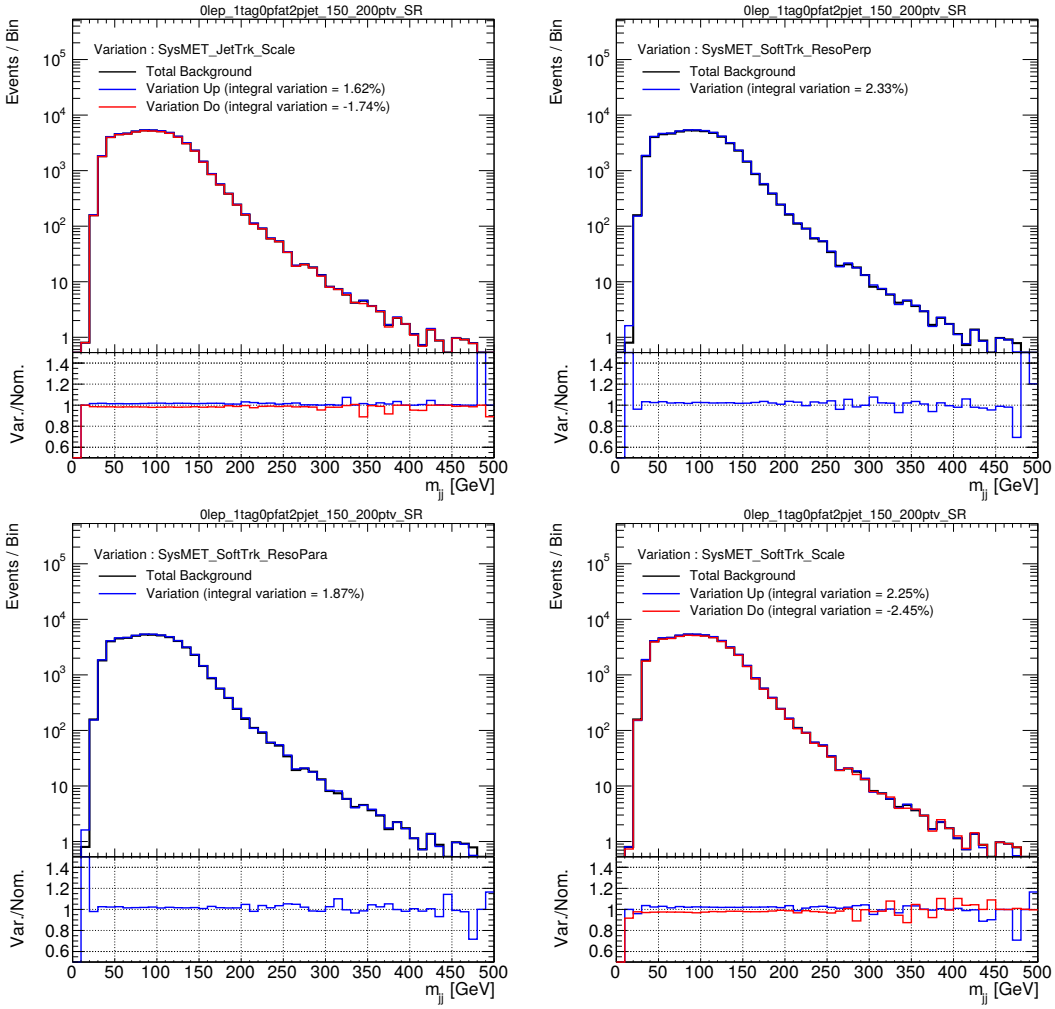

Figure H.1: Nominal distribution (black) of the Higgs boson candidate mass and the effect of the four $E_{\mathrm{T}}^{\mathrm{miss}}$ systematic uncertainties as up (blue) and down (red) variations (one and two-sided) for the summed pre-fit background for events with one b-jet and $E_{\mathrm{T}}^{\mathrm{miss}} \in [150, 200)$ GeV.

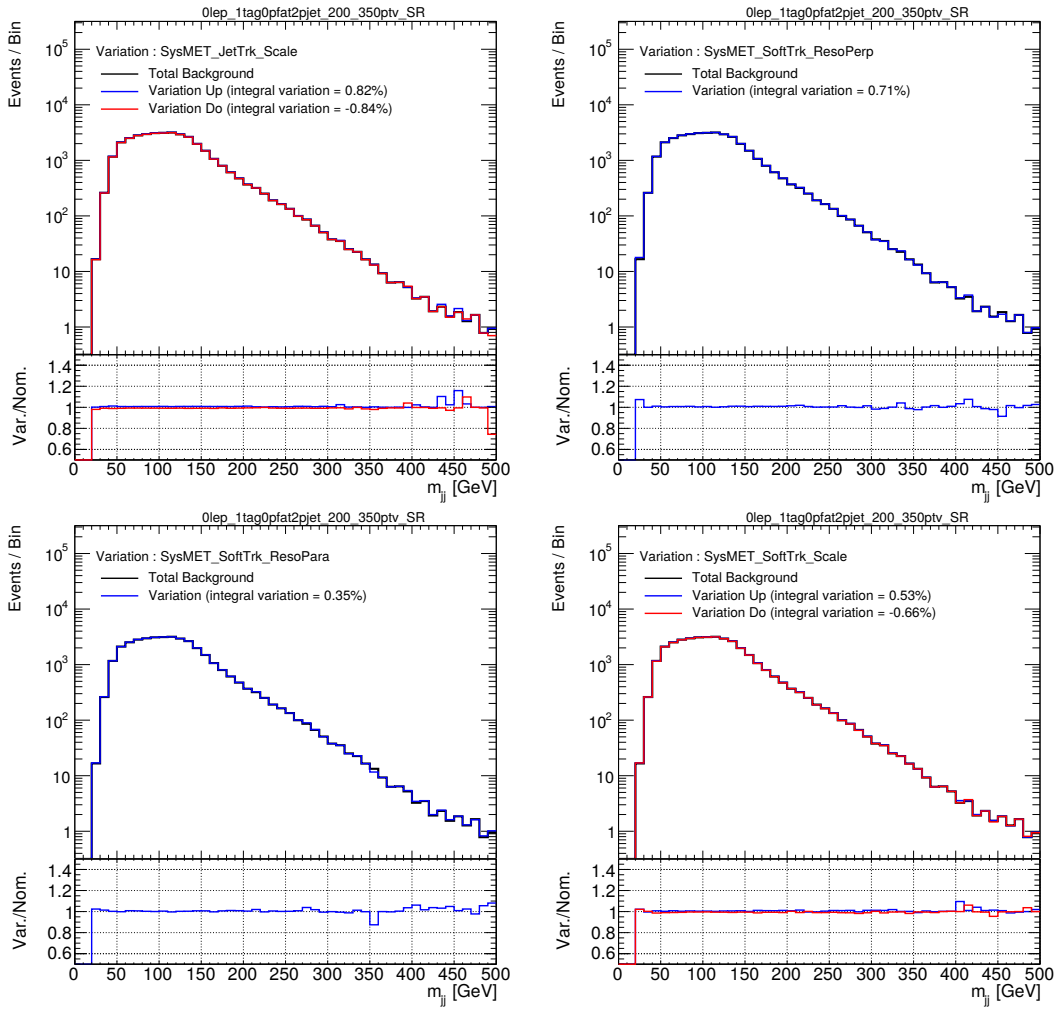

Figure H.2: Nominal distribution (black) of the Higgs boson candidate mass and the effect of the four $E_{\mathrm{T}}^{\mathrm{miss}}$ systematic uncertainties as up (blue) and down (red) variations (one and two-sided) for the summed pre-fit background for events with one b-jet and $E_{\mathrm{T}}^{\mathrm{miss}} \in [200, 350)$ GeV.

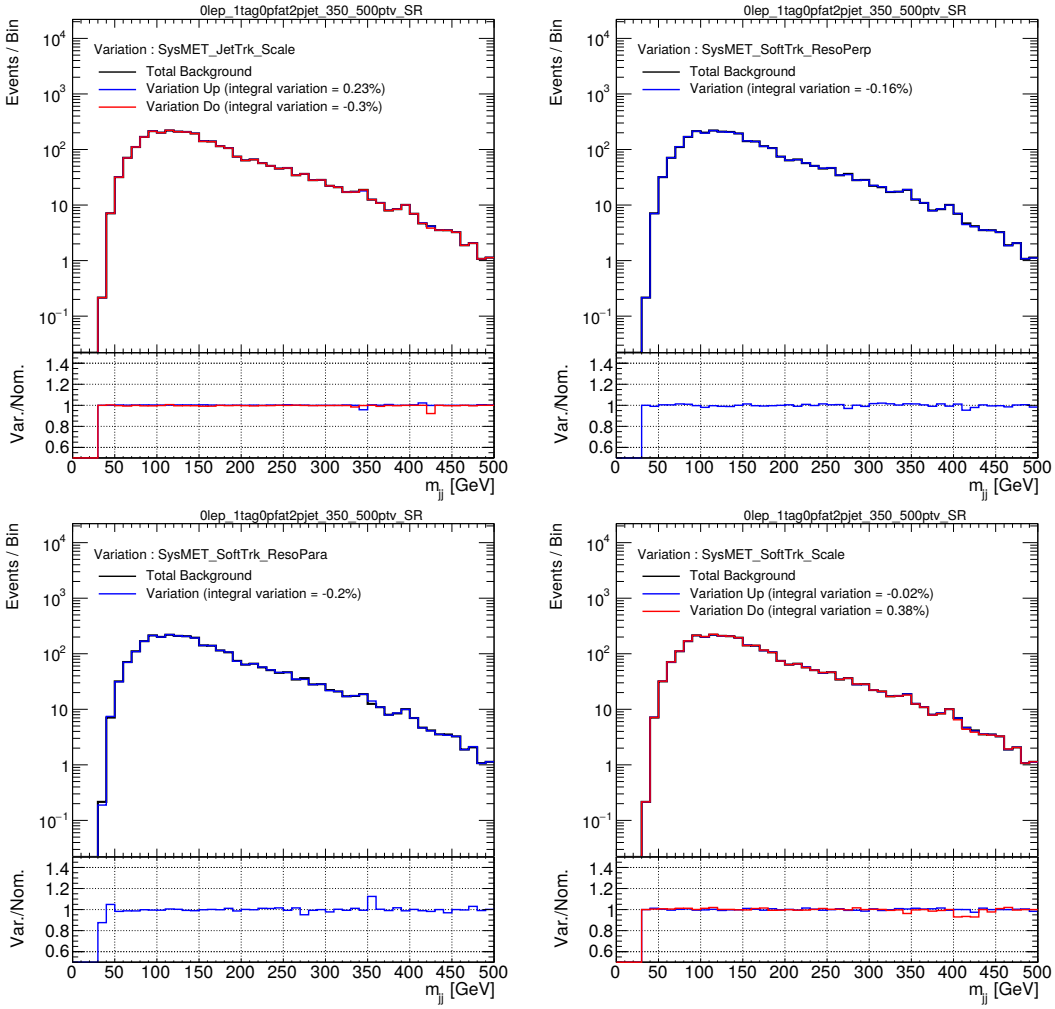

Figure H.3: Nominal distribution (black) of the Higgs boson candidate mass and the effect of the four $E_{\mathrm{T}}^{\mathrm{miss}}$ systematic uncertainties as up (blue) and down (red) variations (one and two-sided) for the summed pre-fit background for events with one b-jet and $E_{\mathrm{T}}^{\mathrm{miss}} \in [350, 500)$ GeV.

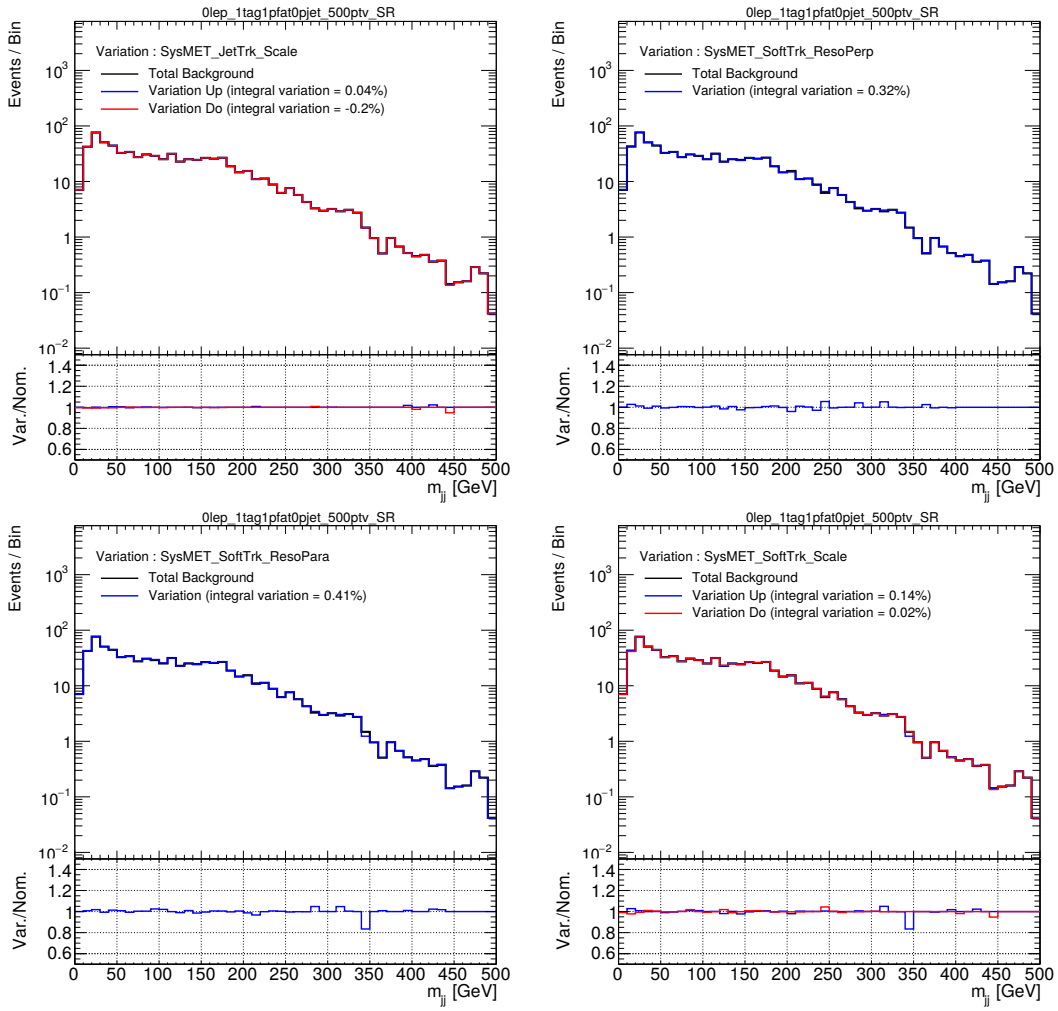

Figure H.4: Nominal distribution (black) of the Higgs boson candidate mass and the effect of the four $E_{\mathrm{T}}^{\mathrm{miss}}$ systematic uncertainties as up (blue) and down (red) variations (one and two-sided) for the summed pre-fit background for events with one b-jet and $E_{\mathrm{T}}^{\mathrm{miss}} \in [500, \infty)$ GeV.

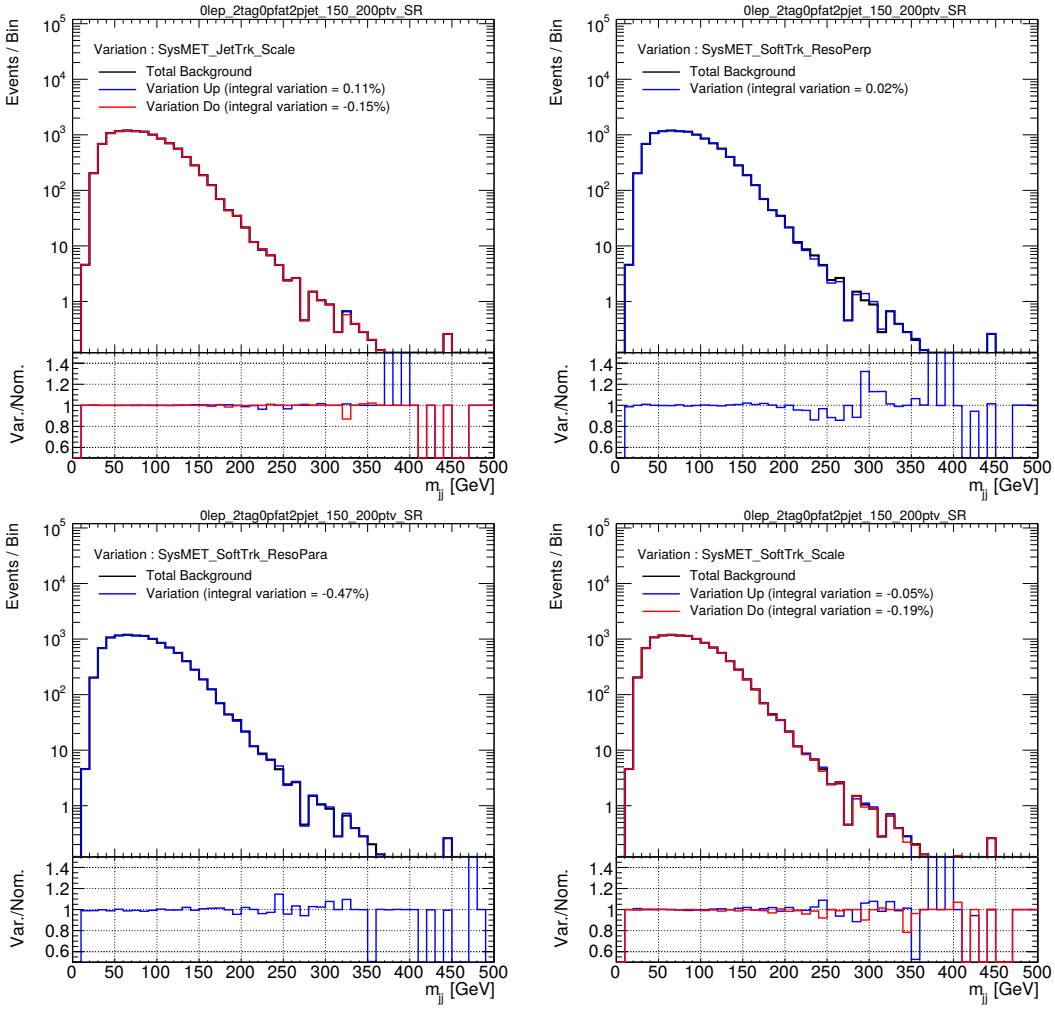

Figure H.5: Nominal distribution (black) of the Higgs boson candidate mass and the effect of the four $E_{\mathrm{T}}^{\mathrm{miss}}$ systematic uncertainties as up (blue) and down (red) variations (one and two-sided) for the summed pre-fit background for events with two b-jets and $E_{\mathrm{T}}^{\mathrm{miss}} \in [150, 200)$ GeV.

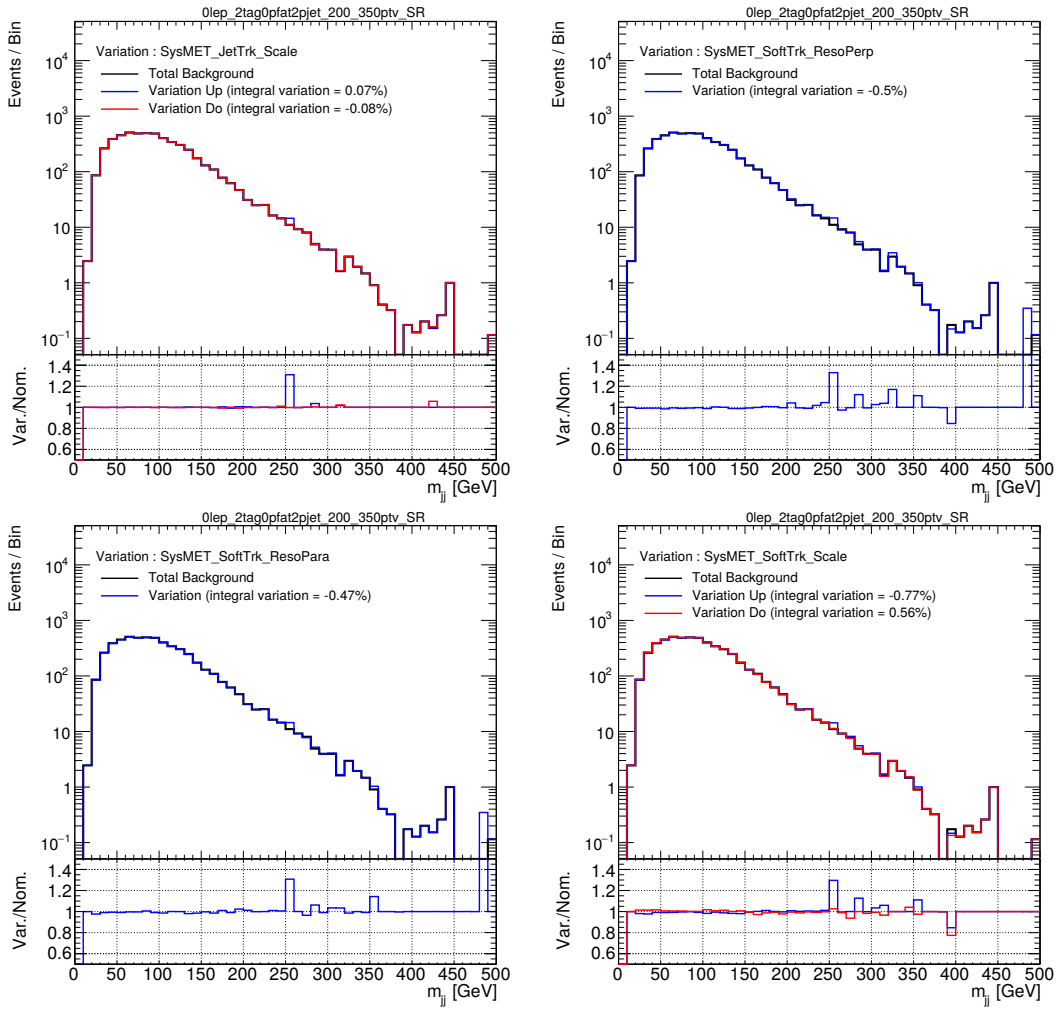

Figure H.6: Nominal distribution (black) of the Higgs boson candidate mass and the effect of the four $E_{\mathrm{T}}^{\mathrm{miss}}$ systematic uncertainties as up (blue) and down (red) variations (one and two-sided) for the summed pre-fit background for events with two b-jets and $E_{\mathrm{T}}^{\mathrm{miss}} \in [200, 350)$ GeV.

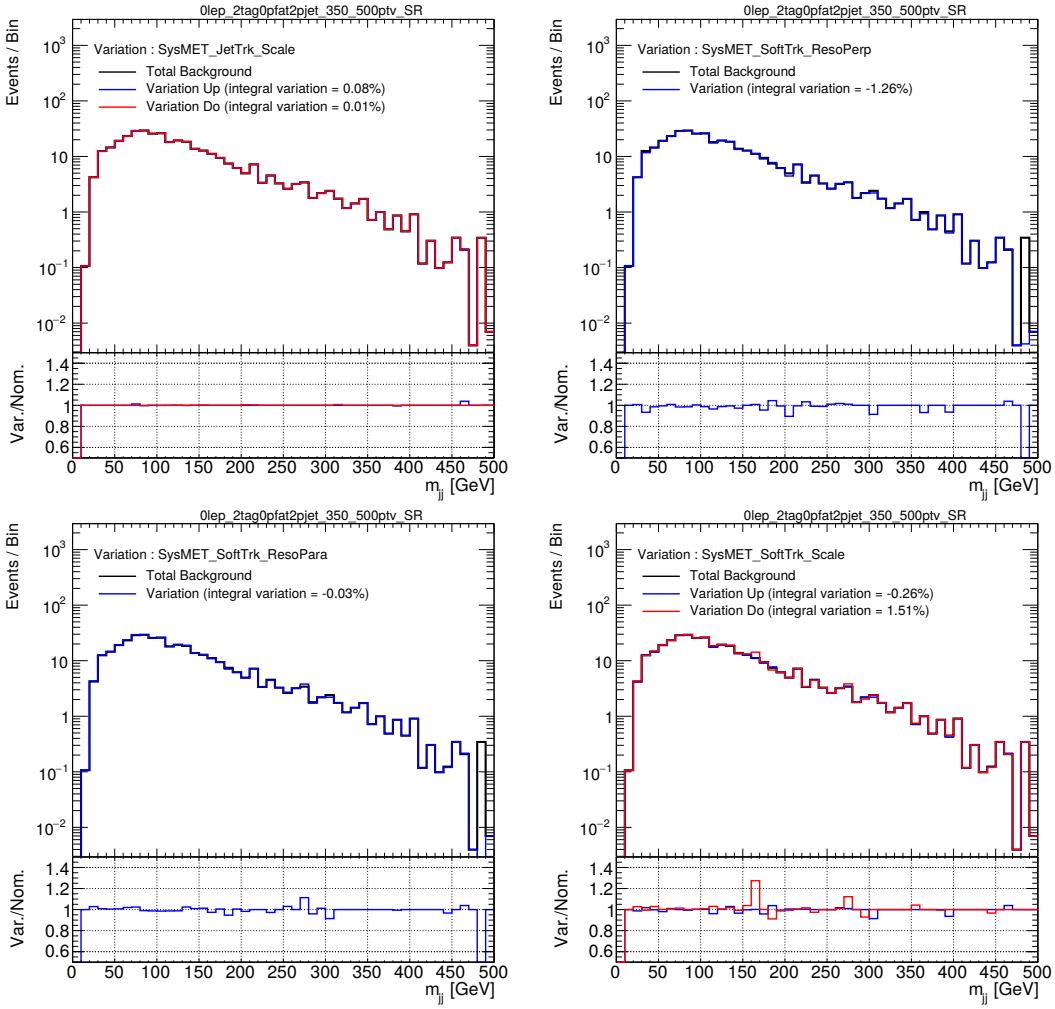

Figure H.7: Nominal distribution (black) of the Higgs boson candidate mass and the effect of the four $E_{\mathrm{T}}^{\mathrm{miss}}$ systematic uncertainties as up (blue) and down (red) variations (one and two-sided) for the summed pre-fit background for events with two b-jets and $E_{\mathrm{T}}^{\mathrm{miss}} \in [350, 500)$ GeV.

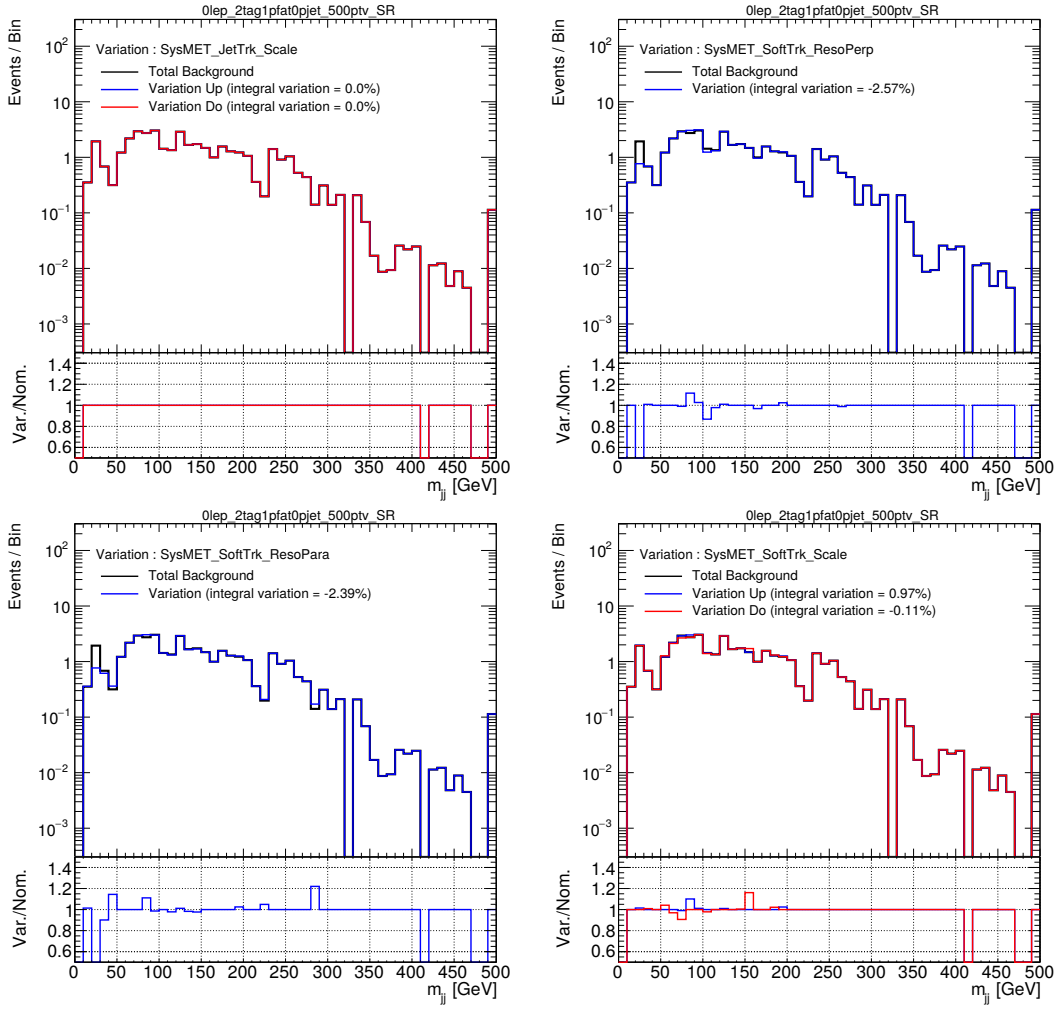

Figure H.8: Nominal distribution (black) of the Higgs boson candidate mass and the effect of the four $E_{\mathrm{T}}^{\mathrm{miss}}$ systematic uncertainties as up (blue) and down (red) variations (one and two-sided) for the summed pre-fit background for events with two b-jets and $E_{\mathrm{T}}^{\mathrm{miss}} \in [500, \infty)$ GeV.

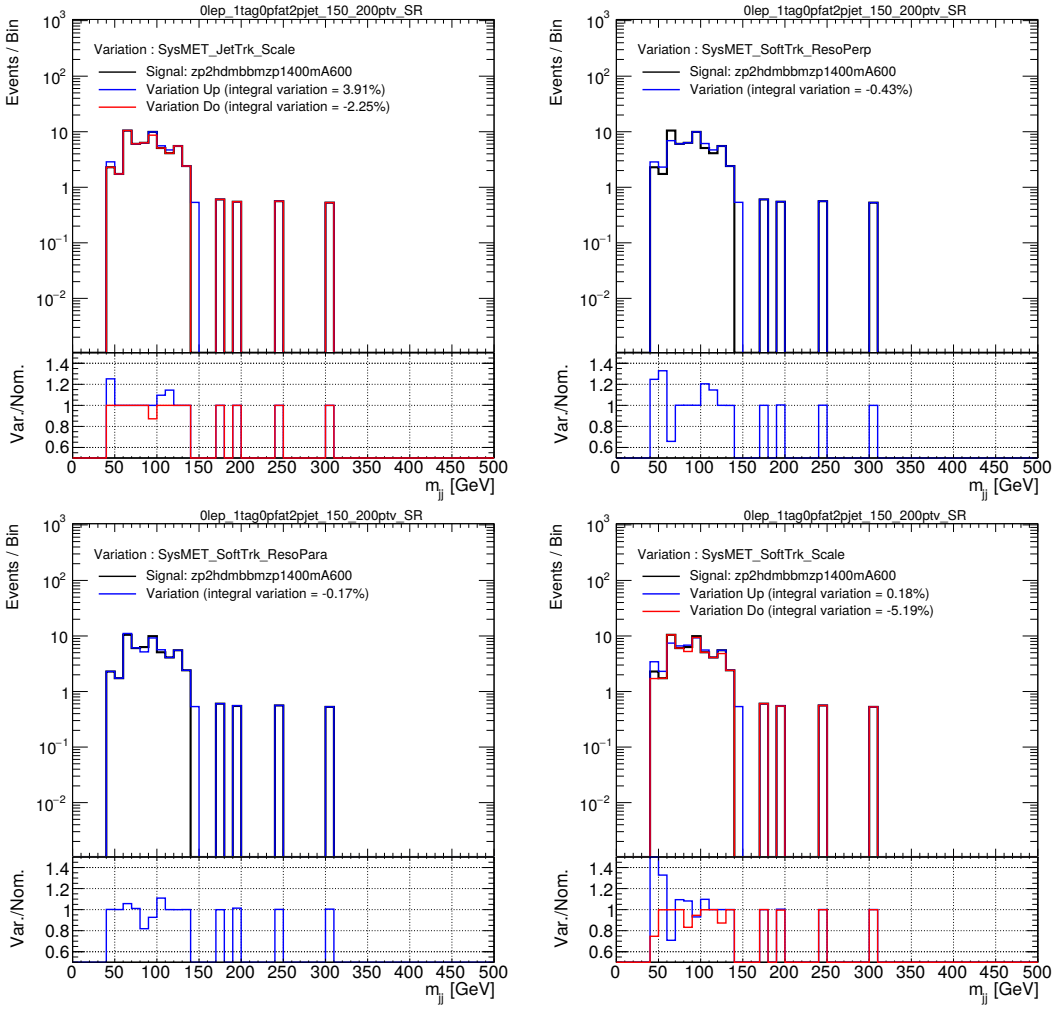

Figure H.9: Nominal distribution (black) of the Higgs boson candidate mass and the effect of the four $E_{\mathrm{T}}^{\mathrm{miss}}$ systematic uncertainties as up (blue) and down (red) variations (one and two-sided) for one benchmark signal point with $(m_{Z'}, m_A) = (1400\,\mathrm{GeV}, 600\,\mathrm{GeV})$ for events with one b-jet and $E_{\mathrm{T}}^{\mathrm{miss}} \in [150, 200)$ GeV.

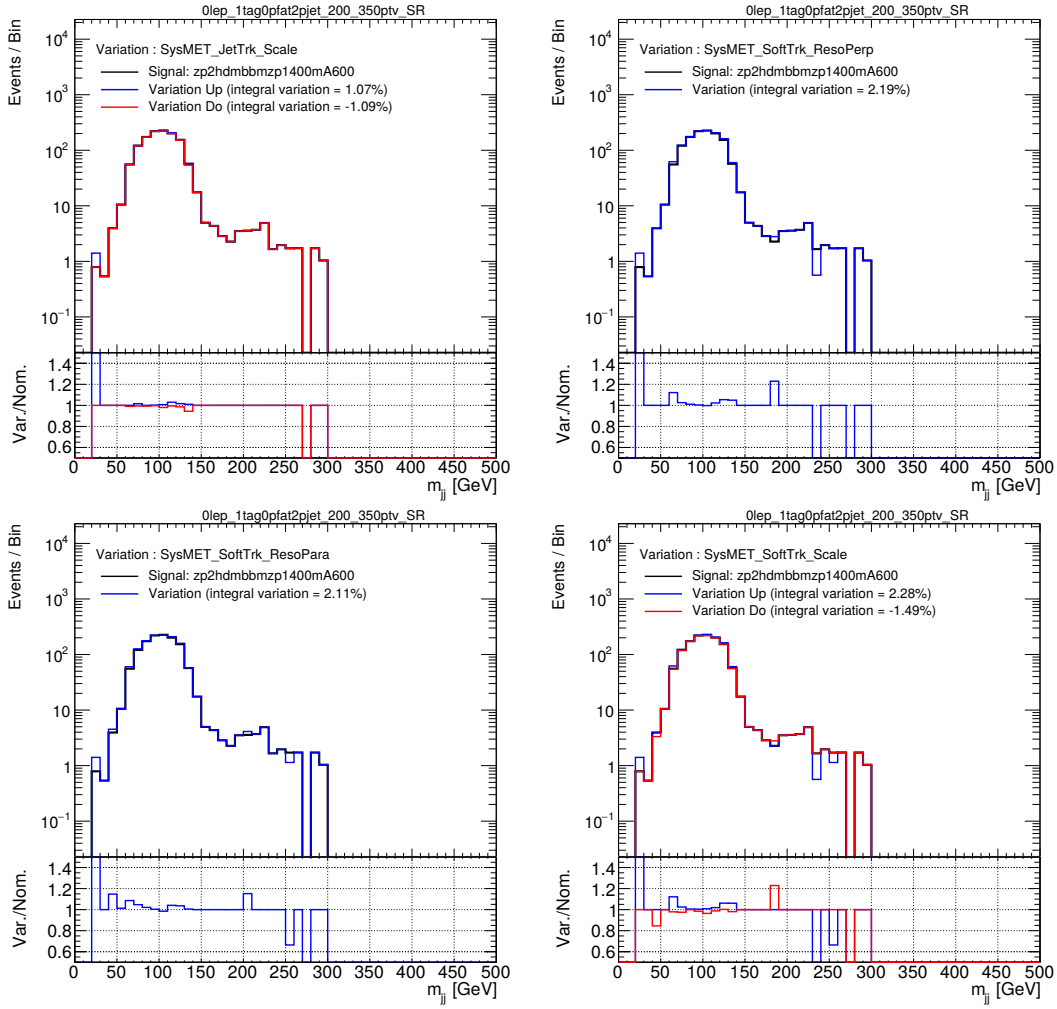

Figure H.10: Nominal distribution (black) of the Higgs boson candidate mass and the effect of the four $E_{\mathrm{T}}^{\mathrm{miss}}$ systematic uncertainties as up (blue) and down (red) variations (one and two-sided) for one benchmark signal point with $(m_{Z'}, m_A) = (1400\,\mathrm{GeV}, 600\,\mathrm{GeV})$ for events with one b-jet and $E_{\mathrm{T}}^{\mathrm{miss}} \in [200, 350)$ GeV.

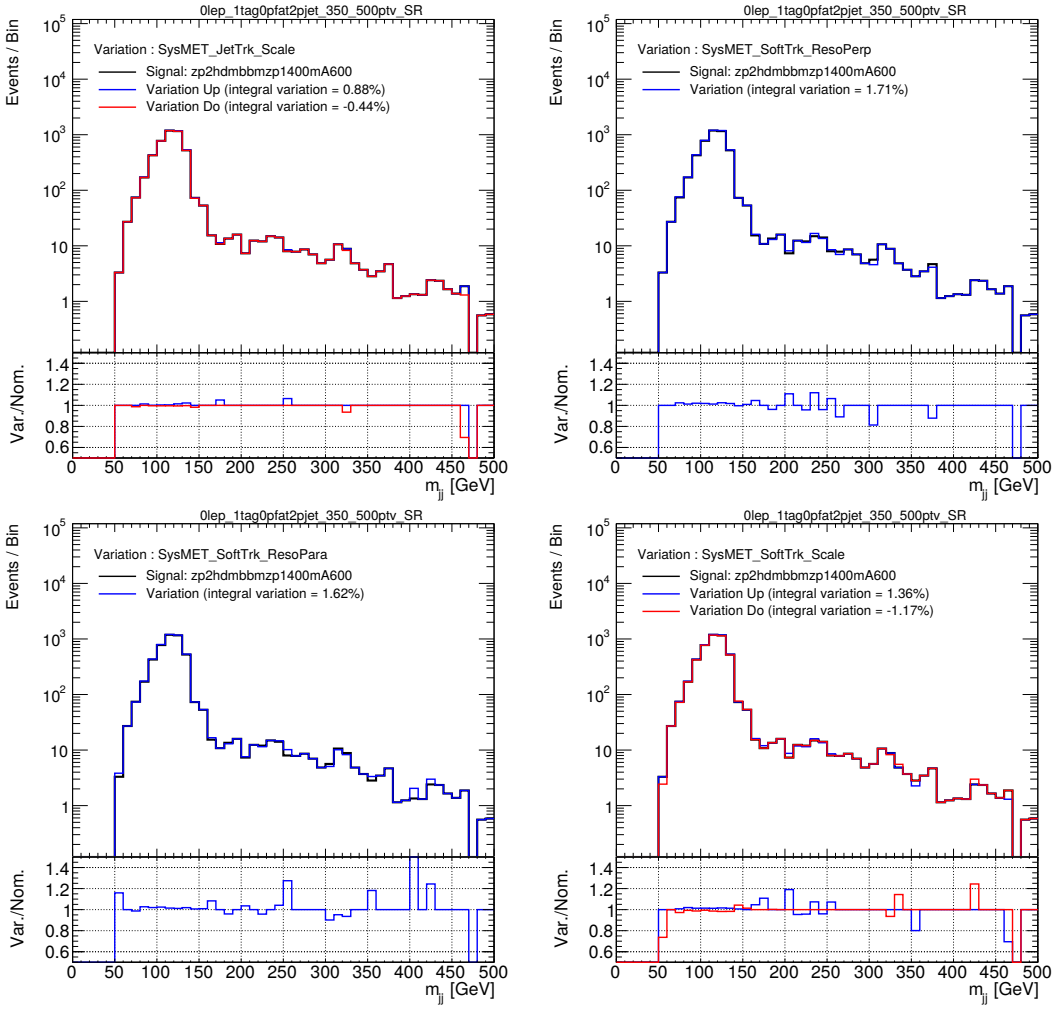

Figure H.11: Nominal distribution (black) of the Higgs boson candidate mass and the effect of the four $E_{\mathrm{T}}^{\mathrm{miss}}$ systematic uncertainties as up (blue) and down (red) variations (one and two-sided) for one benchmark signal point with $(m_{Z'}, m_A) = (1400\,\mathrm{GeV}, 600\,\mathrm{GeV})$ for events with one b-jet and $E_{\mathrm{T}}^{\mathrm{miss}} \in [350, 500)$ GeV.

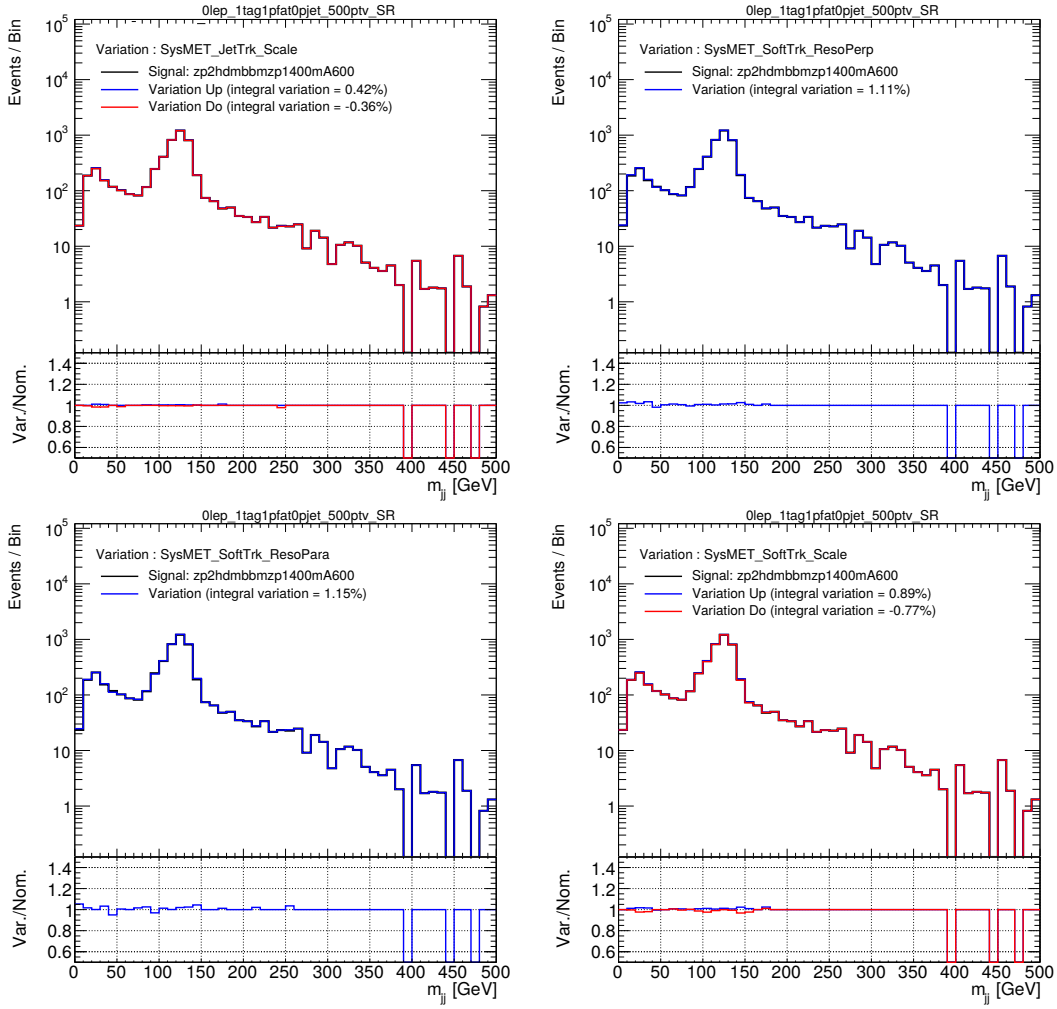

Figure H.12: Nominal distribution (black) of the Higgs boson candidate mass and the effect of the four $E_{\mathrm{T}}^{\mathrm{miss}}$ systematic uncertainties as up (blue) and down (red) variations (one and two-sided) for one benchmark signal point with $(m_{Z'}, m_A) = (1400\,\mathrm{GeV}, 600\,\mathrm{GeV})$ for events with one b-jet and $E_{\mathrm{T}}^{\mathrm{miss}} \in [500, \infty)$ GeV.

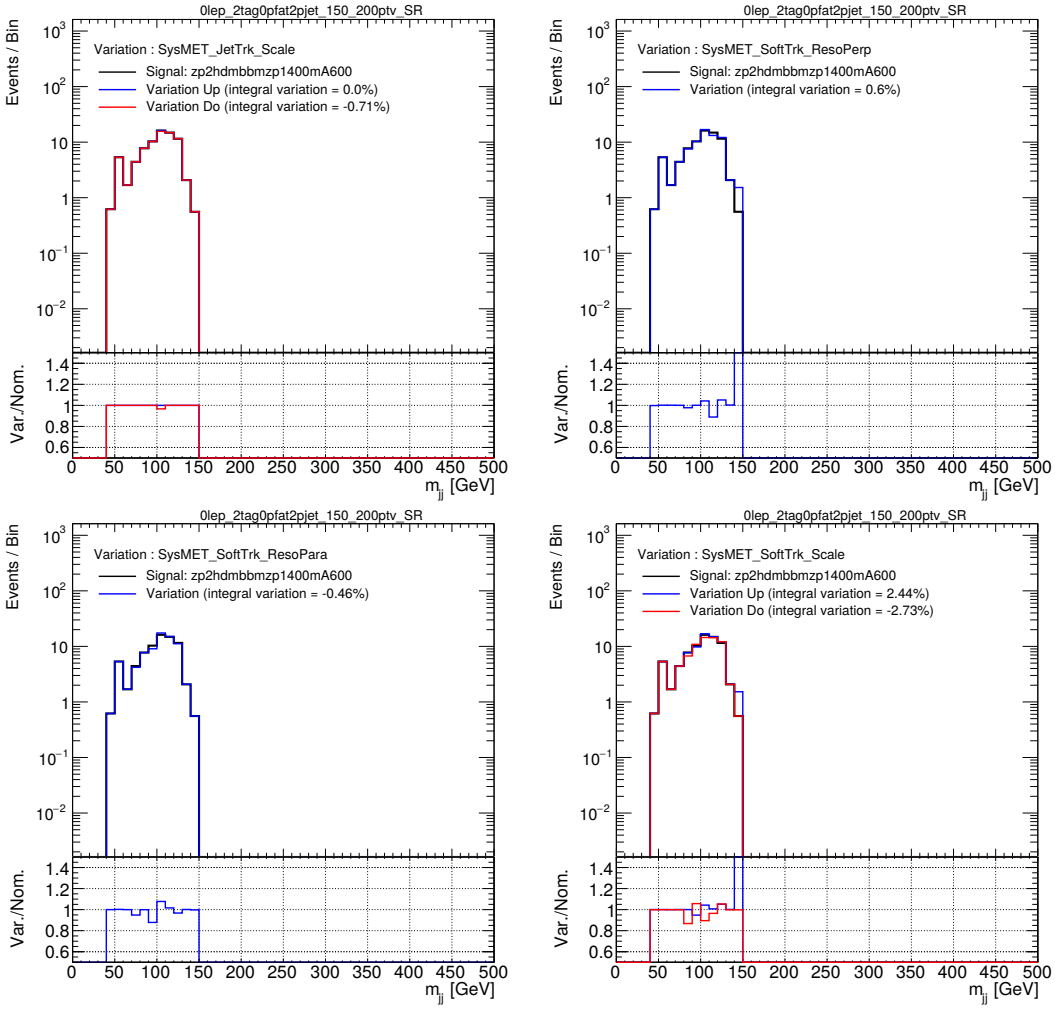

Figure H.13: Nominal distribution (black) of the Higgs boson candidate mass and the effect of the four $E_{\mathrm{T}}^{\mathrm{miss}}$ systematic uncertainties as up (blue) and down (red) variations (one and two-sided) for one benchmark signal point with $(m_{Z'}, m_A) = (1400\,\mathrm{GeV}, 600\,\mathrm{GeV})$ for events with two b-jets and $E_{\mathrm{T}}^{\mathrm{miss}} \in [150, 200)$ GeV.

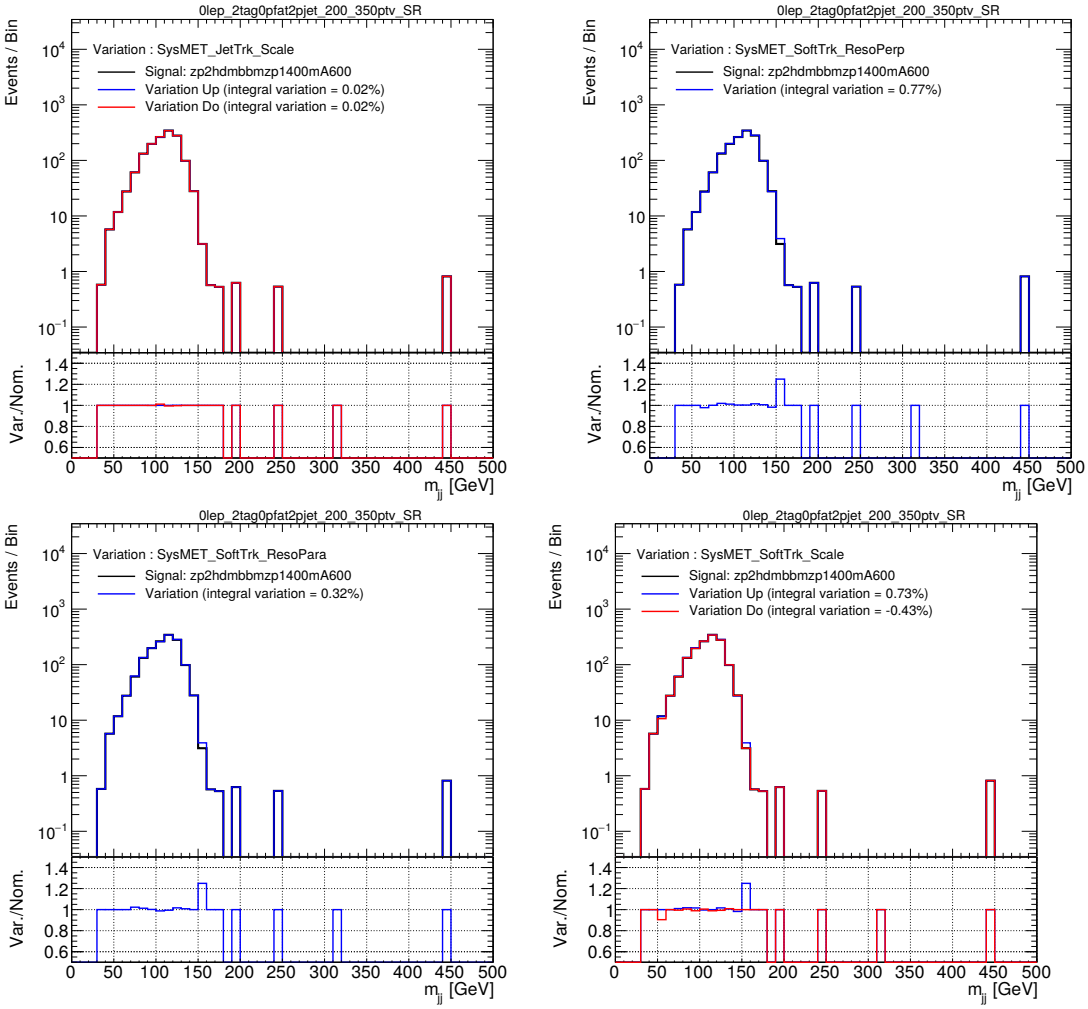

Figure H.14: Nominal distribution (black) of the Higgs boson candidate mass and the effect of the four $E_{\mathrm{T}}^{\mathrm{miss}}$ systematic uncertainties as up (blue) and down (red) variations (one and two-sided) for one benchmark signal point with $(m_{Z'}, m_A) = (1400\,\mathrm{GeV}, 600\,\mathrm{GeV})$ for events with two b-jets and $E_{\mathrm{T}}^{\mathrm{miss}} \in [200, 350)$ GeV.

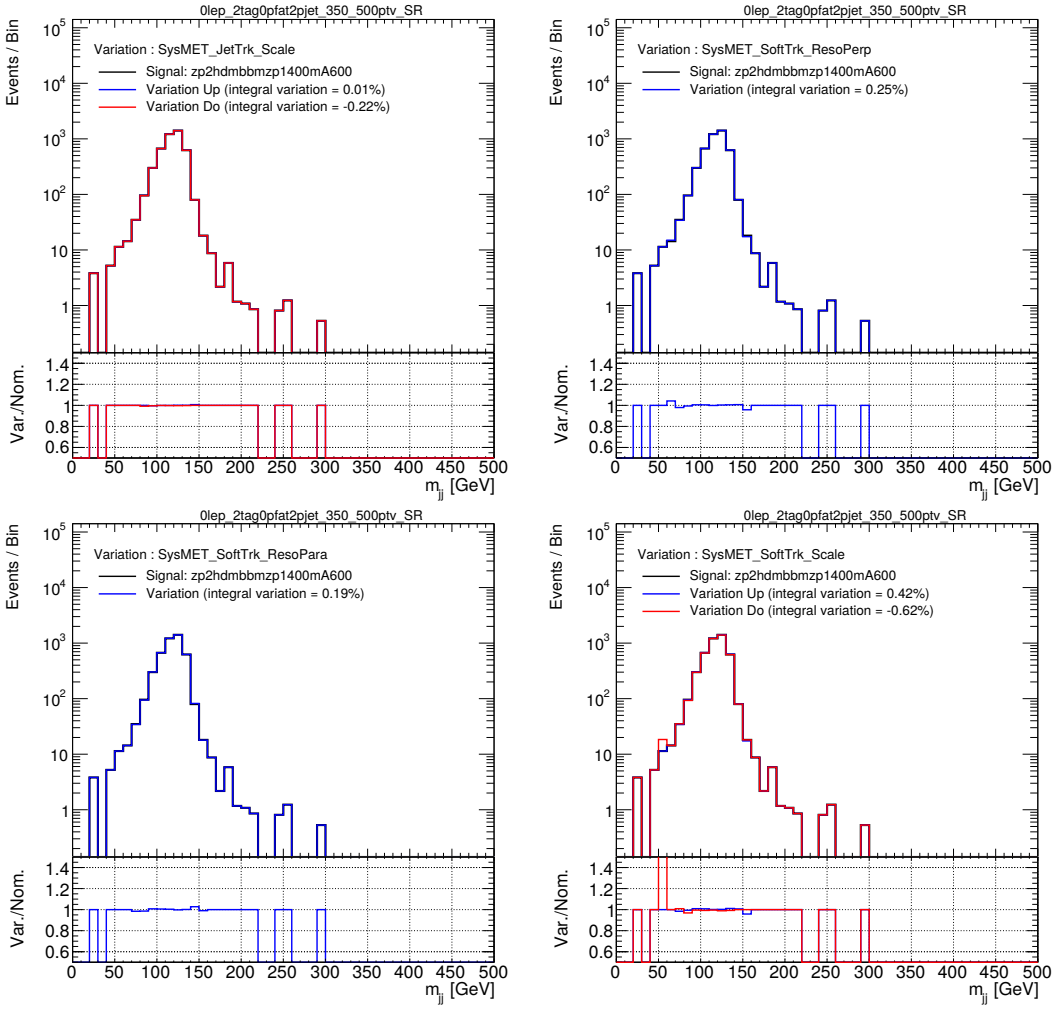

Figure H.15: Nominal distribution (black) of the Higgs boson candidate mass and the effect of the four $E_{\mathrm{T}}^{\mathrm{miss}}$ systematic uncertainties as up (blue) and down (red) variations (one and two-sided) for one benchmark signal point with $(m_{Z'}, m_A) = (1400\,\mathrm{GeV}, 600\,\mathrm{GeV})$ for events with two b-jets and $E_{\mathrm{T}}^{\mathrm{miss}} \in [350, 500)$ GeV.

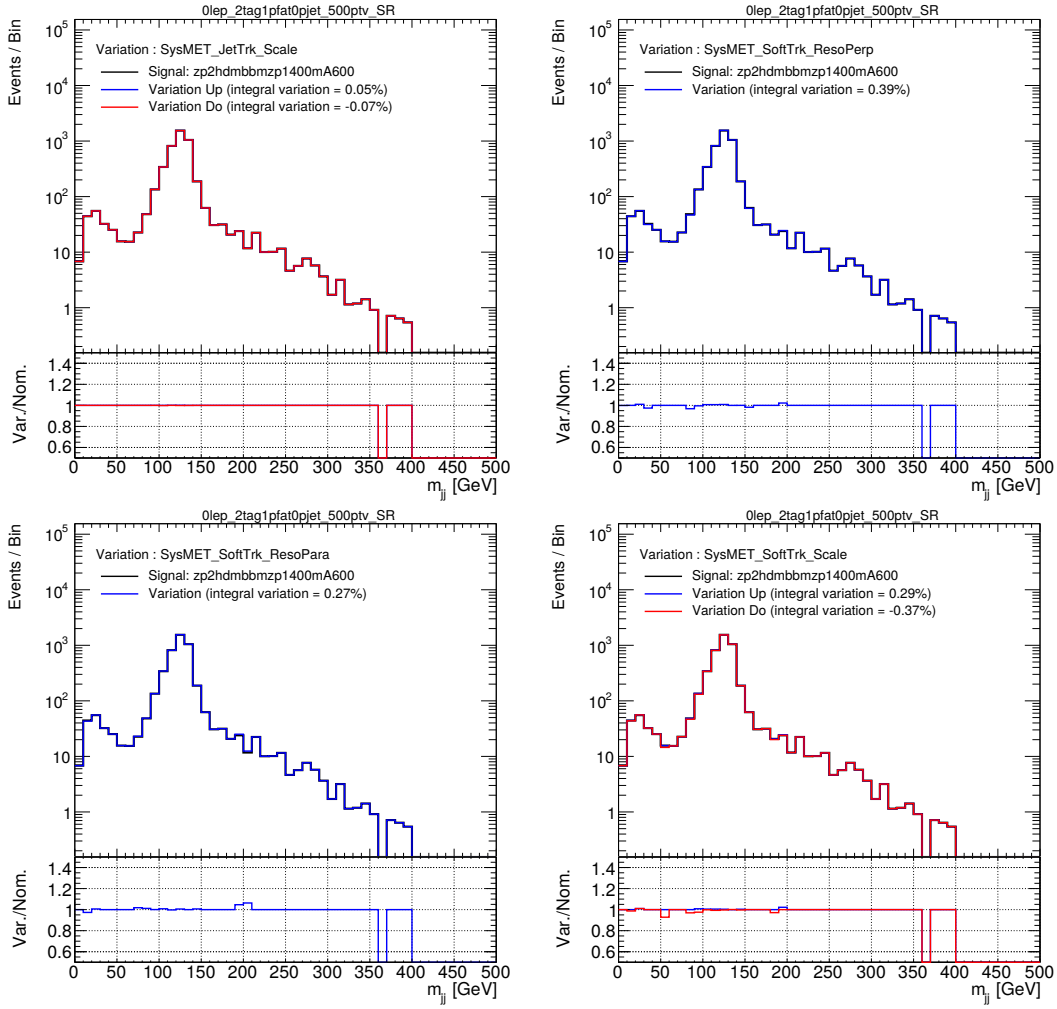

Figure H.16: Nominal distribution (black) of the Higgs boson candidate mass and the effect of the four $E_{\mathrm{T}}^{\mathrm{miss}}$ systematic uncertainties as up (blue) and down (red) variations (one and two-sided) for one benchmark signal point with $(m_{Z'}, m_A) = (1400\,\mathrm{GeV}, 600\,\mathrm{GeV})$ for events with two b-jets and $E_{\mathrm{T}}^{\mathrm{miss}} \in [500, \infty)$ GeV.

H.2 Systematic Uncertainties in the Tau Identification

Within the mono-Higgs ($b\bar{b}$) analysis, a veto on hadronic τ's is applied in the signal and control regions, which increased the sensitivity of the search significantly. The τ veto is composite of the veto on very loose-τ's (a self-built τ identification) and a veto on loose-τ's (the standard ATLAS BDT based identification), as described in Section C.1. For the latter case, the two veto requires the introduction of specific τ-jet systematic uncertainties, related to the identification and reconstruction efficiency as well for the energy. For the veto on very loose-τ's specific tracking uncertainties should be considered. No experimental systematic uncertainties for τ-jets are being considered so far, and are not included as nuisance parameters in the profile-likelihood fit. The impact of the missing uncertainties are studied by using the $t\bar{t}$ background sample, which arrived later in time. The application of the τ systematics should have the largest impact on the $t\bar{t}$ background. In the following, the impact of τ uncertainties on the $t\bar{t}$ yields in the signal region is studied. In Table H.2, the τ uncertainties considered for our τ vetoes are presented. The first three τ uncertainties correspond to τ energy scale (TES) uncertainties, which affect the τ object selection by modifying the p_{T} cut. The last two τ uncertainties correspond to the track efficiency reconstruction and fake track uncertainties, which affect the very loose self-built τ identification, by selecting a certain number of tracks in the core of small-R jets. The standard τ objects are required to have a p_{T} above of 20 GeV. In

Table H.2: Qualitative summary of the missing τ-jet systematic uncertainties.

Systematic uncertainty	**Short description**
TAUS_TRUEHADTAU_SME_TES_DETECTOR	τ energy scale
TAUS_TRUEHADTAU_SME_TES_INSITU	τ energy scale
TAUS_TRUEHADTAU_SME_TES_MODEL	τ energy scale
TRK_EFF_LOOSE_TIDE	track efficiency reconstruction uncertainty
TRK_FAKE_RATE_LOOSE	fake track reconstruction uncertainty

order to see the effect of TES up variations, one needs to shift the p_{T} cut on τ objects at object selection. Based on Fig. H.17, which shows the mean p_{T} of τ-jets in $t\bar{t}$ events in the signal region as function of the τ uncertainties. The variation in p_{T} is around 2 %, which has a very little effect to the final physical results since the τ objects are not directly used and since the $t\bar{t}$ background is anyways highly reduced when applying the other optimised selection criteria discussed in Appendix C. Furthermore, in Fig. H.18, the change of the $t\bar{t}$ event yield when applying τ uncertainties with respect to the nominal case are shown. The effect of τ uncertainties on the $t\bar{t}$ yields is less than one percent. Therefore, τ uncertainties have a negligible impact on the $t\bar{t}$ normalisation uncertainty used in the fit configuration and one expects, that they would be pruned away by the

pruning algorithm. This satisfies that the neglection of τ uncertainties will not changing the physics results.

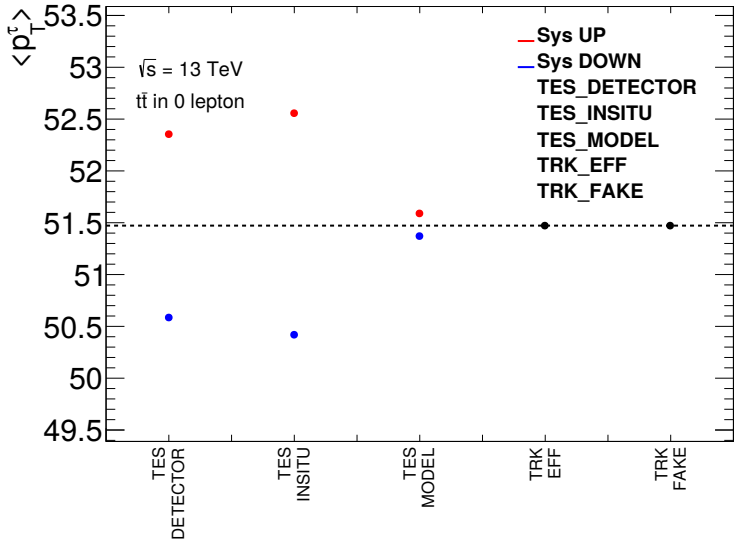

Figure H.17: Mean p_T of τ-jets in $t\bar{t}$ background events depending on the different τ uncertainties. The mean shift in p_T is about 1.2 GeV.

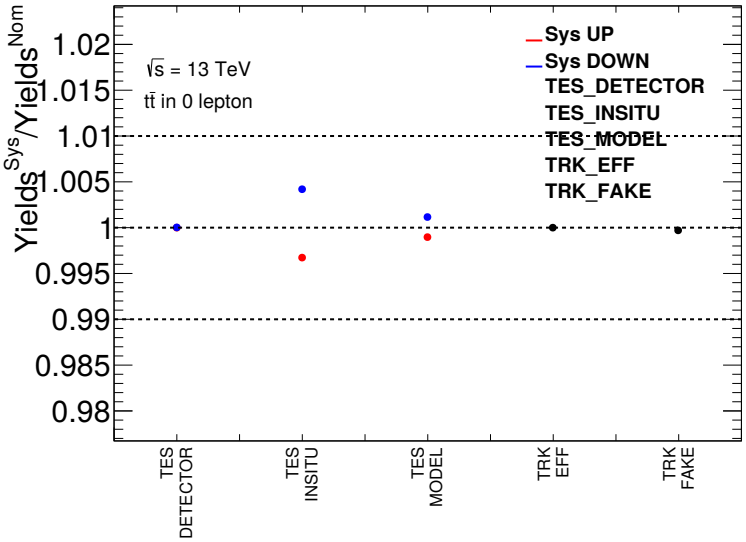

Figure H.18: Nominal $t\bar{t}$ yields and the effect of τ-jet uncertainties normalised to the $t\bar{t}$ nominal yields in the signal region. The effect of τ uncertainties on $t\bar{t}$ yields is less than a percent.

Appendix I

Z'-2HDM Signal Model Acceptance Uncertainties

The change in Z'-2HDM signal acceptances for variations of the hadronisation and renormalisation scales (see Table I.1), parton-shower tunes (see Table I.2) and PDFs (see Table I.3) in the MADGRAPH generator are listed below for each of the four $E_{\mathrm{T}}^{\mathrm{miss}}$ bins and for each signal point.

The acceptances are calculated at truth level, and defined as the ratio of events which pass a truth-level event selection, which is as close as possible to the event selection at reconstruction level, divided by the number of generated events. This is done to avoid running the full detector simulation for each parameter setting of the generator, considered as a systematic. The impact of each uncertainty is then given as the change of the acceptance by the uncertainty compared to the nominal one.

Table I.1: Impact of signal uncertainties on the acceptance [%] for the Z'-2HDM model due to renormalisation and factorisation scales variations in MADGRAPH for the four regions of $E_{\mathrm{T}}^{\mathrm{miss}}$. In case of an impact of less than 1% on the acceptance the errors are not shown and denoted by '—'.

$m_{Z'}$ [GeV]	m_A [GeV]	Range in $E_{\mathrm{T}}^{\mathrm{miss}}$ [GeV]			
		$[150, 200)$	$[200, 350)$	$[350, 500)$	$[500, \infty)$
400	200	0.88	1.93	—	—
600	200	0.79	0.28	—	—
600	300	0.33	1.14	1.22	8.00
600	400	1.18	1.98	8.99	8.37
600	500	0.44	2.06	—	—
600	600	0.29	0.96	—	—
800	200	2.23	0.86	0.94	—
800	300	2.09	0.31	1.31	4.80
800	400	1.48	0.46	9.01	3.70
800	500	0.48	0.47	7.18	23.20
800	600	0.58	0.47	1.02	10.90
800	700	1.23	0.47	8.62	—
1000	300	3.48	0.38	0.32	1.44
1000	400	5.78	0.47	0.52	2.08
1000	500	1.20	0.27	0.48	1.38
1000	600	2.68	0.45	0.58	0.48
1000	700	0.36	0.60	0.75	10.30

$m_{Z'}$ [GeV]	m_A [GeV]	Range in $E_{\mathrm{T}}^{\mathrm{miss}}$ [GeV] $[150,200)$	$[200,350)$	$[350,500)$	$[500,\infty)$
1000	800	0.60	0.73	2.04	4.21
1200	300	8.84	3.80	1.27	0.69
1200	400	15.60	2.40	0.38	0.85
1200	500	4.76	0.65	0.29	1.62
1200	600	2.94	0.97	0.63	2.15
1200	700	1.14	0.80	1.14	1.62
1200	800	0.99	0.61	1.03	1.08
1400	300	3.81	2.84	1.20	0.32
1400	400	2.49	2.53	0.15	0.35
1400	500	6.80	3.46	0.56	0.33
1400	600	4.64	0.88	0.85	0.38
1400	700	3.43	1.01	0.45	0.65
1400	800	0.20	0.92	0.67	0.95
1600	300	—	—	2.06	0.15
1600	400	—	8.54	3.72	0.24
1600	500	—	4.16	4.91	0.27
1600	600	—	3.25	1.93	0.52
1600	700	—	1.54	2.33	0.17
1600	800	—	1.30	1.74	0.29
1800	300	—	—	—	0.13
1800	400	—	—	—	0.44
1800	500	—	—	4.69	0.18
1800	600	—	2.20	5.57	0.18
1800	700	—	1.97	5.04	0.12
1800	800	—	2.00	3.63	0.17
2000	300	—	—	—	0.07
2000	400	—	—	—	0.28
2000	500	—	—	—	0.17
2000	600	—	—	—	0.09
2000	700	—	—	—	0.12
2000	800	—	—	—	0.41
2200	300	—	—	—	0.10
2200	400	—	—	—	0.31
2200	500	—	—	—	0.08
2200	600	—	—	—	0.38
2200	700	—	—	—	0.17
2200	800	—	—	—	0.24
2400	200	—	—	—	0.15
2400	300	—	—	—	0.01
2400	400	—	—	—	0.20
2400	500	—	—	—	0.23
2400	600	—	—	—	0.21
2400	700	—	—	—	0.13
2400	800	—	—	—	0.13
2600	200	—	—	—	0.16
2600	300	—	—	—	0.19
2600	400	—	—	—	0.11
2600	500	—	—	—	0.10
2600	600	—	—	—	0.05
2600	700	—	—	—	0.25
2600	800	—	—	—	0.06
2800	200	—	—	—	0.23
2800	300	—	—	—	0.30
2800	400	—	—	—	0.11
2800	500	—	—	—	0.14
2800	600	—	—	—	0.26
3000	200	—	—	—	0.14
3000	300	—	—	—	0.37
3000	400	—	—	—	0.21
3000	500	—	—	—	0.16
3000	600	—	—	—	0.22

Table I.2: Impact of signal uncertainties on the acceptance [%] for the Z'-2HDM model due to parton-shower tune variations in MADGRAPH for the four regions of $E_{\mathrm{T}}^{\mathrm{miss}}$. In case of an impact of less than 1% on the acceptance the errors are not shown and denoted by '—'.

$m_{Z'}$ [GeV]	m_A [GeV]	Range in $E_{\mathrm{T}}^{\mathrm{miss}}$ [GeV]			
		$[150, 200)$	$[200, 350)$	$[350, 500)$	$[500, \infty)$
400	200	9.24	10.70	—	—
600	200	3.51	1.33	—	—
600	300	2.77	4.64	8.99	53.30
600	400	6.17	7.97	24.90	25.30
600	500	1.61	4.80	—	—
600	600	2.40	3.37	—	—
800	200	6.74	4.46	6.29	—
800	300	6.51	1.31	10.10	17.10
800	400	5.43	1.21	16	25.40
800	500	2.60	1.04	12.30	55.80
800	600	2.90	1.59	12.10	16.60
800	700	3.69	2.79	13.50	—
1000	300	10.40	3.71	1.81	7.57
1000	400	10.90	2.39	0.61	10.60
1000	500	7.64	1.66	1.57	16.50
1000	600	4.82	1.20	3.08	13.70
1000	700	4.21	1.53	5.03	16
1000	800	2.63	1.24	2.12	11.70
1200	300	16.30	8.46	3.70	1.53
1200	400	15.70	6.33	2.28	1.91
1200	500	7.75	4.95	1.62	5.50
1200	600	10.10	2.88	1.57	8.25
1200	700	6.35	2.70	1.15	5.64
1200	800	4.48	1.87	2.19	6.11
1400	300	18.30	8.79	4.76	1.30
1400	400	18.20	7.52	4.73	1.49
1400	500	26.80	9.24	3.41	1.44
1400	600	15.50	4.78	2.74	1.75
1400	700	9.82	5.35	2.10	2.24
1400	800	4.74	3.48	1.71	2.55
1600	300	—	—	8.94	1.08
1600	400	—	10.30	7.20	1.48
1600	500	—	6.96	5.54	1.30
1600	600	—	6.21	7.28	1.35
1600	700	—	6.25	5.44	1.44
1600	800	—	4.70	5.37	1.22
1800	300	—	—	—	1.18
1800	400	—	—	—	1.08
1800	500	—	—	9.32	1.14
1800	600	—	11.80	7.88	1.33
1800	700	—	8.51	9.08	1.30
1800	800	—	6.07	7.89	1.36
2000	300	—	—	—	1.04
2000	400	—	—	—	1.02
2000	500	—	—	—	1.14
2000	600	—	—	—	0.92
2000	700	—	—	—	1.00
2000	800	—	—	—	1.03
2200	300	—	—	—	1.00
2200	400	—	—	—	0.87
2200	500	—	—	—	0.78
2200	600	—	—	—	0.99
2200	700	—	—	—	0.71
2200	800	—	—	—	1.27
2400	200	—	—	—	1.08
2400	300	—	—	—	1.00
2400	400	—	—	—	1.24

$m_{Z'}$ [GeV]	m_A [GeV]	Range in $E_{\mathrm{T}}^{\mathrm{miss}}$ [GeV] $[150,200)$	$[200,350)$	$[350,500)$	$[500,\infty)$
2400	500	—	—	—	0.98
2400	600	—	—	—	1.16
2400	700	—	—	—	1.11
2400	800	—	—	—	0.94
2600	200	—	—	—	1.20
2600	300	—	—	—	1.13
2600	400	—	—	—	1.24
2600	500	—	—	—	1.14
2600	600	—	—	—	1.05
2600	700	—	—	—	1.12
2600	800	—	—	—	0.95
2800	200	—	—	—	1.06
2800	300	—	—	—	0.96
2800	400	—	—	—	1.20
2800	500	—	—	—	1.05
2800	600	—	—	—	1.08
3000	200	—	—	—	1.04
3000	300	—	—	—	0.94
3000	400	—	—	—	1.30
3000	500	—	—	—	1.02
3000	600	—	—	—	1.03

Table I.3: Impact of signal uncertainties on the acceptance [%] for the Z'-2HDM model due to PDFs variations in MADGRAPH for the four regions of $E_{\mathrm{T}}^{\mathrm{miss}}$. In case of an impact of less than 1% on the acceptance the errors are not shown and denoted by '—'.

$m_{Z'}$ [GeV]	m_A [GeV]	Range in $E_{\mathrm{T}}^{\mathrm{miss}}$ [GeV] $[150,200)$	$[200,350)$	$[350,500)$	$[500,\infty)$
400	200	1.84	0.64	—	—
600	200	1.08	0.19	—	—
600	300	0.03	1.82	7.23	76
600	400	3.04	2.79	16	6.90
600	500	1.50	1.25	—	—
600	600	1.51	1.16	—	—
800	200	2.25	1.14	2.97	—
800	300	0.95	0.84	0.81	3.52
800	400	1.24	0.43	11.40	7.41
800	500	1.51	0.61	3.28	44.70
800	600	1.25	0.03	7.22	16.80
800	700	0.90	0.47	8.44	—
1000	300	5.54	0.93	1.11	3.96
1000	400	6.57	0.98	0.85	4.72
1000	500	2.25	0.35	1.38	5.19
1000	600	3.01	0.07	0.15	2.14
1000	700	1.98	0.53	1.79	16.50
1000	800	—	—	—	—
1200	300	8.42	5.34	2.12	0.49
1200	400	20.10	3.24	1.38	2.15
1200	500	5.29	1.42	1.06	3.46
1200	600	5.73	0.95	0.84	4.42
1200	700	2.16	0.58	0.65	1.88
1200	800	4.11	0.56	1.30	2.61
1400	300	3.57	4.23	0.24	0.07
1400	400	14.10	3.36	1.14	0.63
1400	500	11.70	2.18	0.70	0.74
1400	600	4.27	3.54	0.87	1.13
1400	700	4.34	3.03	0.73	1.65
1400	800	1.27	0.71	0.08	1.50

$m_{Z'}$ [GeV]	m_A [GeV]	Range in $E_{\mathrm{T}}^{\mathrm{miss}}$ [GeV] $[150, 200)$	$[200, 350)$	$[350, 500)$	$[500, \infty)$
1600	300	—	—	1.04	0.39
1600	400	—	8.39	2.40	0.30
1600	500	—	0.68	4.61	0.63
1600	600	—	5.94	3.62	0.52
1600	700	—	1.23	5.24	0.60
1600	800	—	4.47	2.72	0.50
1800	300	—	—	—	0.35
1800	400	—	—	—	0.77
1800	500	—	—	9.91	0.03
1800	600	—	6.97	5.82	0.48
1800	700	—	5.00	4.99	0.51
1800	800	—	3.51	8.38	1.28
2000	300	—	—	—	0.41
2000	400	—	—	—	0.21
2000	500	—	—	—	0.54
2000	600	—	—	—	0.36
2000	700	—	—	—	0.14
2000	800	—	—	—	0.34
2200	300	—	—	—	0.29
2200	400	—	—	—	0.58
2200	500	—	—	—	0.10
2200	600	—	—	—	0.48
2200	700	—	—	—	0.24
2200	800	—	—	—	0.35
2400	200	—	—	—	0.46
2400	300	—	—	—	0.32
2400	400	—	—	—	0.39
2400	500	—	—	—	0.50
2400	600	—	—	—	0.49
2400	700	—	—	—	0.11
2400	800	—	—	—	0.25
2600	200	—	—	—	0.30
2600	300	—	—	—	0.63
2600	400	—	—	—	0.23
2600	500	—	—	—	0.31
2600	600	—	—	—	0.28
2600	700	—	—	—	0.37
2600	800	—	—	—	0.39
2800	200	—	—	—	0.18
2800	300	—	—	—	0.25
2800	400	—	—	—	0.24
2800	500	—	—	—	0.28
2800	600	—	—	—	0.25
3000	200	—	—	—	0.30
3000	300	—	—	—	0.44
3000	400	—	—	—	0.43
3000	500	—	—	—	0.16
3000	600	—	—	—	0.24

Appendix J

The Baryonic Z'_{B} Model

The cross sections calculated by the MADGRAPH event generator at leading-order QCD for the $\sigma(pp \to h\chi\bar{\chi})$ process of the baryonic Z'_{B} model are given in Table J.1, with $g_q = 1/3$, $g_\chi = 1$, $g_{hZ'Z'} = m_{Z'}$ and $\sin\theta = 0.3$.

Table J.1: Cross sections (σ_{theo}) for the $\sigma(pp \to h\chi\bar{\chi})$ process for each of the baryonic Z'_{B} signal model points. The cross sections do not include the branching ratio of the Higgs boson to $b\bar{b}$ decay.

$m_{Z'}$ [GeV]	m_χ [GeV]	σ_{theo} [pb]	$m_{Z'}$ [GeV]	m_χ [GeV]	σ_{theo} [pb]	$m_{Z'}$ [GeV]	m_χ [GeV]	σ_{theo} [pb]
10	1	2.64	500	245	$1.22 \cdot 10^{-1}$	1400	1	$5.44 \cdot 10^{-2}$
10	50	$3.59 \cdot 10^{-4}$	500	255	$5.07 \cdot 10^{-2}$	1400	10	$5.44 \cdot 10^{-2}$
10	10	$2.10 \cdot 10^{-2}$	500	500	$3.52 \cdot 10^{-5}$	1400	50	$5.44 \cdot 10^{-2}$
10	150	$5.50 \cdot 10^{-6}$	500	1000	$1.00 \cdot 10^{-7}$	1400	150	$5.38 \cdot 10^{-2}$
10	500	$7.71 \cdot 10^{-9}$	600	1	$7.27 \cdot 10^{-1}$	1400	500	$3.36 \cdot 10^{-2}$
10	1000	$4.66 \cdot 10^{-11}$	600	10	$7.27 \cdot 10^{-1}$	1400	695	$3.64 \cdot 10^{-3}$
15	10	$7.32 \cdot 10^{-2}$	600	50	$7.20 \cdot 10^{-1}$	1400	705	$2.49 \cdot 10^{-3}$
20	1	2.75	600	150	$5.79 \cdot 10^{-1}$	1400	1000	$4.30 \cdot 10^{-6}$
50	1	3.29	600	295	$7.33 \cdot 10^{-2}$	1600	1	$3.14 \cdot 10^{-2}$
50	10	3.24	600	305	$3.43 \cdot 10^{-2}$	1600	10	$3.14 \cdot 10^{-2}$
50	20	2.63	600	500	$6.97 \cdot 10^{-5}$	1600	50	$3.13 \cdot 10^{-2}$
50	30	$1.19 \cdot 10^{-1}$	600	1000	$2.00 \cdot 10^{-7}$	1600	150	$3.11 \cdot 10^{-2}$
50	50	$1.26 \cdot 10^{-2}$	800	1	$3.53 \cdot 10^{-1}$	1600	500	$2.38 \cdot 10^{-2}$
95	50	$3.10 \cdot 10^{-1}$	800	10	$3.53 \cdot 10^{-1}$	1600	795	$2.00 \cdot 10^{-3}$
100	1	3.20	800	50	$3.52 \cdot 10^{-1}$	1600	805	$1.42 \cdot 10^{-3}$
100	10	3.19	800	150	$3.28 \cdot 10^{-1}$	1600	1000	$1.15 \cdot 10^{-5}$
100	45	1.96	800	395	$3.02 \cdot 10^{-2}$	1995	1000	$5.47 \cdot 10^{-4}$
100	55	$1.70 \cdot 10^{-1}$	800	405	$1.65 \cdot 10^{-2}$	2000	1	$1.12 \cdot 10^{-2}$
100	150	$6.64 \cdot 10^{-4}$	800	500	$3.58 \cdot 10^{-4}$	2000	10	$1.12 \cdot 10^{-2}$
200	1	2.62	800	1000	$5.00 \cdot 10^{-7}$	2000	50	$1.12 \cdot 10^{-2}$
200	50	2.09	995	500	$1.00 \cdot 10^{-2}$	2000	150	$1.11 \cdot 10^{-2}$
200	95	$9.18 \cdot 10^{-1}$	1000	1	$1.81 \cdot 10^{-1}$	2000	500	$9.88 \cdot 10^{-3}$
200	105	$1.59 \cdot 10^{-1}$	1000	150	$1.75 \cdot 10^{-1}$	2000	995	$6.54 \cdot 10^{-4}$
200	150	$5.54 \cdot 10^{-3}$	1000	495	$1.39 \cdot 10^{-2}$	2000	1005	$4.93 \cdot 10^{-4}$
295	150	$1.77 \cdot 10^{-1}$	1000	505	$8.44 \cdot 10^{-3}$	2500	1	$3.38 \cdot 10^{-3}$
300	1	2.28	1000	1000	$9.00 \cdot 10^{-7}$	2500	10	$3.38 \cdot 10^{-3}$
300	50	1.98	1200	1	$9.74 \cdot 10^{-2}$	2500	50	$3.38 \cdot 10^{-3}$
300	145	$4.51 \cdot 10^{-1}$	1200	150	$9.58 \cdot 10^{-2}$	2500	150	$3.37 \cdot 10^{-3}$
300	150	$2.70 \cdot 10^{-1}$	1200	500	$3.60 \cdot 10^{-2}$	2500	1000	$1.69 \cdot 10^{-3}$
300	155	$1.15 \cdot 10^{-1}$	1200	595	$6.93 \cdot 10^{-3}$	3000	1	$1.10 \cdot 10^{-3}$
300	500	$8.50 \cdot 10^{-6}$	1200	605	$4.50 \cdot 10^{-3}$	10000	1	$1.60 \cdot 10^{-8}$
500	1	1.06	1200	1000	$1.90 \cdot 10^{-6}$			
500	50	1.04						
500	150	$6.58 \cdot 10^{-1}$						

Appendix K

The ϕ-2HDM Model

The ϕ-2HDM model [446], with an extended Higgs sector of type-II with the two Higgs doublets H_1 and H_2, introduces an additional pseudoscalar singlet ϕ. A Z_2 symmetry is imposed, with transformation of the Higgs fields $H_1 \to H_1$ and $H_2 \to -H_2$, to guarantee the absence of flavour-changing neutral currents at tree-level which are not observed in the Standard Model.
The mediator between the Dark Matter and the Standard Model particles is a superposition of the CP-odd components of H_1 and H_2 and of ϕ. The most general and renormalisable scalar potential is given by

$$V = V_{\text{Higgs}} + V_{\text{Higgs}-\phi} + V_{\phi} \quad , \tag{K.1}$$

with the Higgs potential

$$\begin{aligned} V_{\text{Higgs}} = {} & \mu_1 H_1^\dagger H_1 + \mu_2 H_2^\dagger H_2 + \left(\mu_3 H_1^\dagger H_2 + \text{h.c.}\right) + \lambda_1 \left(H_1^\dagger H_1\right)^2 + \lambda_2 \left(H_2^\dagger H_2\right)^2 \\ & + \lambda_3 \left(H_1^\dagger H_1\right)\left(H_2^\dagger H_2\right) + \lambda_4 \left(H_1^\dagger H_2\right)\left(H_2^\dagger H_1\right) + \left[\lambda_5 \left(H_1^\dagger H_2\right)^2 + \text{h.c.}\right] \quad , \end{aligned} \tag{K.2}$$

the potential terms connecting the doublets and the singlet

$$V_{\text{Higgs}-\phi} = \phi \left(i b_\phi H_1^\dagger H_2 + \text{h.c.}\right) + \phi^2 \left(\lambda_{\phi_1} H_1^\dagger H_1 + \lambda_{\phi_2} H_2^\dagger H_2\right) \quad , \tag{K.3}$$

and the singlet potential

$$V_\phi = \frac{1}{2} m_\phi^2 \phi^2 \quad , \tag{K.4}$$

where the $\left(\mu_3 H_1^\dagger H_2 + \text{h.c.}\right)$ term in Eq. (K.2) softly breaks the Z_2 symmetry for real values of μ_3. A diagonalisation of the mass-squared matrices of the scalar states relates the free parameters μ_i (with $i = 1, 2, 3$), λ_j (with $i = 1, ..., 5$), $\lambda_{\phi_{1,2}}$ and b_ϕ after EW symmetry breaking to mixing angles, the EW vacuum expectation value v and particle masses, except for three remaining quartic self-couplings of ϕ. The ϕ-2HDM model is described by 14 free parameters: three mixing angles α, β, θ, v, the remaining quartic

couplings λ_3, λ_{ϕ_1}, λ_{ϕ_2} and the masses m_h, m_H, m_A, $m_{H^\pm}$ and m_ϕ. Furthermore, the mass of the Dark Matter particle, m_χ, and its Yukawa coupling constant, g_χ.
Predicted cross sections for the $\sigma(pp \to h\chi\bar{\chi})$ process for each of the ϕ-2HDM signal model points calculated by the MADGRAPH event generator at next-to-leading-order QCD are given in Table K.1, with $g_\chi = 1$, $\sin\theta = 0.35$, $m_A = m_H = m_{H^\pm}$ and $m_\chi = 10\,\text{GeV}$.

Table K.1: Cross sections (σ_{theo}) for the $\sigma(pp \to h\chi\bar{\chi})$ process for each of the ϕ-2HDM signal model points. The cross sections do not include the branching ratio of the Higgs boson to $b\bar{b}$ decay.

$\tan\beta$	$\sin\theta$	m_A [GeV]	m_ϕ [GeV]	σ_{theo} [pb]
1.0	0.35	200	100	$3.98 \cdot 10^{-1}$
1.0	0.35	200	150	$3.57 \cdot 10^{-1}$
1.0	0.35	300	100	3.28
1.0	0.35	300	150	1.81
1.0	0.35	400	100	1.46
1.0	0.35	400	150	1.06
1.0	0.35	400	200	$6.46 \cdot 10^{-1}$
1.0	0.35	400	250	$2.47 \cdot 10^{-1}$
1.0	0.35	500	150	$5.34 \cdot 10^{-1}$
1.0	0.35	500	200	$3.87 \cdot 10^{-1}$
1.0	0.35	500	250	$2.46 \cdot 10^{-1}$
1.0	0.35	500	300	$1.35 \cdot 10^{-1}$
1.0	0.35	600	200	$2.37 \cdot 10^{-1}$
1.0	0.35	600	250	$1.70 \cdot 10^{-1}$
1.0	0.35	600	300	$1.18 \cdot 10^{-1}$
1.0	0.35	600	350	$7.93 \cdot 10^{-2}$
1.0	0.35	700	250	$1.11 \cdot 10^{-1}$
1.0	0.35	700	300	$8.45 \cdot 10^{-2}$
1.0	0.35	700	350	$6.62 \cdot 10^{-2}$
1.0	0.35	700	400	$4.30 \cdot 10^{-2}$
1.0	0.35	800	250	$7.08 \cdot 10^{-2}$
1.0	0.35	800	300	$5.68 \cdot 10^{-2}$
1.0	0.35	800	350	$4.84 \cdot 10^{-2}$
1.0	0.35	800	400	$3.46 \cdot 10^{-2}$
1.0	0.35	800	500	$1.60 \cdot 10^{-2}$
1.0	0.35	900	300	$3.71 \cdot 10^{-2}$
1.0	0.35	900	350	$3.34 \cdot 10^{-2}$
1.0	0.35	900	400	$2.52 \cdot 10^{-2}$
1.0	0.35	900	500	$1.40 \cdot 10^{-2}$
1.0	0.35	1000	150	$4.29 \cdot 10^{-2}$
1.0	0.35	1000	250	$2.72 \cdot 10^{-2}$
1.0	0.35	1000	350	$2.20 \cdot 10^{-2}$
1.0	0.35	1000	400	$1.72 \cdot 10^{-2}$
1.0	0.35	1000	500	$1.07 \cdot 10^{-2}$
1.0	0.35	1100	250	$1.58 \cdot 10^{-2}$
1.0	0.35	1100	350	$1.39 \cdot 10^{-2}$
1.0	0.35	1100	500	$7.59 \cdot 10^{-3}$
1.0	0.35	1200	150	$1.02 \cdot 10^{-2}$
1.0	0.35	1200	250	$9.14 \cdot 10^{-3}$
1.0	0.35	1200	350	$8.49 \cdot 10^{-3}$
1.0	0.35	1200	500	$5.17 \cdot 10^{-3}$
1.0	0.35	1300	150	$9.09 \cdot 10^{-3}$
1.0	0.35	1300	250	$6.71 \cdot 10^{-3}$
1.0	0.35	1300	350	$5.48 \cdot 10^{-3}$
1.0	0.35	1300	500	$3.42 \cdot 10^{-3}$
1.0	0.35	1400	150	$1.94 \cdot 10^{-2}$
1.0	0.35	1400	250	$8.72 \cdot 10^{-3}$
1.0	0.35	1400	350	$4.76 \cdot 10^{-3}$
1.0	0.35	1400	450	$2.68 \cdot 10^{-3}$
1.0	0.35	1500	150	$4.30 \cdot 10^{-2}$
1.0	0.35	1500	250	$1.54 \cdot 10^{-2}$
1.0	0.35	1500	400	$3.49 \cdot 10^{-3}$
1.0	0.35	1600	150	$8.21 \cdot 10^{-2}$
1.0	0.35	1600	250	$2.73 \cdot 10^{-2}$
1.0	0.35	1600	350	$1.09 \cdot 10^{-2}$
0.5	0.35	600	200	$4.41 \cdot 10^{-1}$
0.5	0.35	600	250	$2.67 \cdot 10^{-1}$
0.5	0.35	600	300	$1.63 \cdot 10^{-1}$
0.5	0.35	600	350	$1.05 \cdot 10^{-1}$
0.8	0.35	600	250	$1.98 \cdot 10^{-1}$
0.8	0.35	600	300	$1.33 \cdot 10^{-1}$
0.8	0.35	600	350	$8.77 \cdot 10^{-2}$
1.5	0.35	600	200	$1.59 \cdot 10^{-1}$
1.5	0.35	600	250	$1.22 \cdot 10^{-1}$
1.5	0.35	600	300	$8.98 \cdot 10^{-2}$
2.0	0.35	600	150	$1.36 \cdot 10^{-1}$
2.0	0.35	600	200	$1.13 \cdot 10^{-1}$
2.0	0.35	600	250	$8.96 \cdot 10^{-2}$
2.0	0.35	600	300	$6.85 \cdot 10^{-2}$
2.0	0.35	600	350	$4.91 \cdot 10^{-2}$
4.0	0.35	600	150	$4.40 \cdot 10^{-2}$
4.0	0.35	600	200	$3.82 \cdot 10^{-2}$
4.0	0.35	600	250	$3.20 \cdot 10^{-2}$
4.0	0.35	600	300	$2.59 \cdot 10^{-2}$
6.0	0.35	600	150	$2.00 \cdot 10^{-2}$
6.0	0.35	600	200	$1.75 \cdot 10^{-2}$
6.0	0.35	600	250	$1.48 \cdot 10^{-2}$
10.0	0.35	600	150	$6.47 \cdot 10^{-3}$
10.0	0.35	600	200	$5.69 \cdot 10^{-3}$
10.0	0.35	600	250	$4.73 \cdot 10^{-3}$

Appendix L

Less Model-Dependent Limits

The Z'-2HDM model is used to derive the limits on the visible cross section for $h+\text{DM}$ events. The statistical model (see Chapter 5) is modified to analyse one $E_{\text{T}}^{\text{miss}}$ bin of the signal region at a time. The Z'-2HDM signal model with different combinations of ($m_{Z'}$, m_A) is used to model the dependence on the $E_{\text{T}}^{\text{miss}}$ distribution. An ensemble of nine to ten ($m_{Z'}$, m_A) combinations are used, and the one with the weakest expected cross section limit is used for setting limits with reduced model dependence as shown in Fig. 7.12.
The full $A \times \varepsilon$, required for calculating limits with reduced model-dependence in Eq. (7.4), is not accessible, since a pre-selection stage at generator level is involved which applies a $E_{\text{T}}^{\text{miss}}$ requirement of 140 GeV. Thus, $A \times \varepsilon$ is factorised into two components

$$A \times \varepsilon \equiv (A \times \varepsilon)_{\text{presel}} \times (A \times \varepsilon)_{\text{sel}} \quad , \tag{L.1}$$

where $(A \times \varepsilon)_{\text{presel}}$ is the acceptance times efficiency at the pre-selection stage involving events with $E_{\text{T}}^{\text{miss}} < 140\,\text{GeV}$ and $(A \times \varepsilon)_{\text{sel}}$ the one calculated at the event selection level. The measured values of

$$(A \times \varepsilon)_{\text{sel}}(E_{\text{T}}^{\text{miss}} > 140) = \frac{N_{\text{events}}(E_{\text{T, truth}}^{\text{miss}} \text{ and } E_{\text{T, reco}}^{\text{miss}}) \text{ after the event selection}}{N_{\text{events}}(E_{\text{T, truth}}^{\text{miss}}) \text{ before the event selection}} \quad , \tag{L.2}$$

are given in Table L.1 for each $E_{\text{T}}^{\text{miss}}$ bin. In Table L.1, $(A \times \varepsilon)_{\text{presel}}$ is approximated as

$$(A \times \varepsilon)_{\text{prese}}(E_{\text{T}}^{\text{miss}} < 140) = \frac{\sigma_{\text{theo}} \times \mathcal{L} - N_{\text{events}}(E_{\text{T, truth}}^{\text{miss}} > 140) \text{ before the event selection}}{\sigma_{\text{theo}} \times \mathcal{L}} \quad , \tag{L.3}$$

where $\sigma_{\text{theo}} \times \mathcal{L}$ is the number of expected signal events for a given production cross section σ_{theo} and with an integrated luminosity, $\mathcal{L}$, of $36.1\,\text{fb}^{-1}$.
The limits on $\sigma_{\text{vis},\, h(b\bar{b})+\text{DM}}$ for a range of Z'-2HDM models for three different $E_{\text{T}}^{\text{miss}}$ bins are given in Tabs. L.2-L.4.

Table L.1: The $(A \times \varepsilon)_{\text{sel}}$ [%] values per $E_{\text{T}}^{\text{miss}}$ bin, as well as $(A \times \varepsilon)_{\text{presel}}$ [%] averaged over all $E_{\text{T}}^{\text{miss}}$ bins, for all Z'-2HDM models.

$m_{Z'}$ [GeV]	m_A [GeV]	$(A \times \varepsilon)_{\text{sel}}$ [%] in ranges of $E_{\text{T}}^{\text{miss}}$ [GeV]				$(A \times \varepsilon)_{\text{presel}}$ [%]
		$[150, 200)$	$[200, 350)$	$[350, 500)$	$[500, \infty)$	
200	200	33.00	52.60	57.40	69.90	57.60
200	300	34.30	54.60	57.40	66.90	72.90
200	400	33.50	54.40	58.50	71.40	79.60
400	200	13.10	14.30	9.80	4.60	10.10
400	300	16.50	27.40	38.10	50.30	28.10
400	400	19.40	42.20	52.90	68.80	36.70
400	500	16.50	37.50	51.40	71.70	32.30
600	200	31.70	54.00	39.60	16.70	82.10
600	300	37.10	41.30	25.20	19.50	62.20
600	400	26.40	26.00	12.60	15.20	17.10
600	500	34.70	39.50	19.30	20.40	43.10
600	600	34.90	42.60	25.10	25.20	50.20
800	200	26.70	54.20	54.60	19.30	92.30
800	300	26.70	59.20	52.00	26.30	91.40
800	400	30.80	59.70	47.00	16.00	86.30
800	500	36.80	52.90	37.60	20.30	71.60
800	600	35.90	52.80	36.30	16.70	52.90
800	700	35.90	54.20	42.90	19.40	70.60
1000	300	24.90	48.90	65.30	44.90	95.80
1000	400	25.00	51.60	63.90	32.30	93.70
1000	500	25.00	55.20	59.10	26.90	92.00
1000	600	28.90	58.60	56.70	21.90	88.80
1000	700	34.30	57.30	58.00	23.20	81.20
1000	800	33.60	56.20	59.80	24.70	78.00
1200	300	22.20	45.80	53.80	68.80	97.40
1200	400	19.00	46.40	56.40	64.40	97.10
1200	500	23.80	48.00	61.70	58.70	95.20
1200	600	22.80	50.80	63.70	51.40	95.20
1200	700	28.10	54.70	62.30	46.10	93.80
1200	800	32.40	56.40	61.90	50.30	90.90
1400	300	14.50	40.40	45.90	73.90	98.10
1400	400	15.40	42.50	47.70	73.30	98.00
1400	500	19.60	43.10	50.10	72.40	96.40
1400	600	19.20	46.20	54.50	70.30	97.50
1400	700	25.00	48.60	58.60	67.00	95.30
1400	800	28.10	51.30	60.10	65.30	95.80
1600	300	23.50	38.60	42.20	75.90	98.40
1600	400	20.60	41.90	44.10	76.00	97.10
1600	500	14.40	41.20	44.50	75.30	97.20
1600	600	20.20	43.10	46.90	74.60	97.30
1600	700	21.10	42.80	50.70	73.30	96.80
1600	800	23.90	46.60	54.20	72.30	97.60
1800	300	13.60	37.00	38.30	76.90	98.70
1800	400	18.30	35.30	41.90	77.20	97.30
1800	500	18.50	39.80	42.00	76.70	98.70
1800	600	23.00	39.10	44.20	76.30	98.50
1800	700	20.40	38.50	44.80	76.10	97.20
1800	800	24.40	44.60	48.40	75.30	98.30
2000	300	14.70	32.20	41.20	78.20	97.50
2000	400	7.30	32.30	38.80	78.30	97.40
2000	500	15.50	36.70	39.00	77.80	97.80
2000	600	17.90	34.90	41.70	77.60	97.70
2000	700	18.90	38.50	41.30	77.10	99.70
2000	800	24.50	39.80	44.40	76.50	97.30
2200	300	42.40	38.60	38.60	78.90	97.60
2200	400	7.50	36.70	40.90	78.60	97.90
2200	500	34.80	34.90	39.80	78.40	98.90
2200	600	16.10	36.00	39.20	78.40	97.50
2200	700	12.40	37.50	42.00	78.20	97.70

$m_{Z'}$ [GeV]	m_A [GeV]	$(A \times \varepsilon)_{\text{sel}}$ [%] in ranges of $E_{\text{T}}^{\text{miss}}$ [GeV]				$(A \times \varepsilon)_{\text{presel}}$ [%]
		$[150, 200)$	$[200, 350)$	$[350, 500)$	$[500, \infty)$	
2200	800	15.50	37.30	42.80	77.80	98.70
2400	200	19.50	30.90	36.70	79.40	99.00
2400	300	11.70	32.20	35.10	78.70	98.00
2400	400	6.80	27.80	37.20	79.30	97.70
2400	500	9.00	29.90	34.50	78.60	98.90
2400	600	12.60	29.80	39.30	78.80	98.30
2400	700	2.70	38.50	40.70	78.40	97.60
2400	800	30.10	33.70	41.50	78.30	98.20
2600	200	9.00	40.30	38.90	79.10	99.00
2600	300	0.00	45.60	40.70	79.30	99.10
2600	400	23.50	30.60	34.80	79.20	99.00
2600	500	15.60	32.60	35.00	79.30	97.70
2600	600	5.20	37.00	36.50	79.30	98.50
2600	700	24.40	36.20	44.20	78.60	99.00
2600	800	12.30	34.20	37.30	79.10	99.00
2800	200	34.90	28.50	41.30	79.40	99.10
2800	300	7.00	28.10	36.90	79.50	97.80
2800	400	0.00	28.80	37.80	79.80	97.70
2800	500	42.50	37.50	37.60	79.20	99.00
2800	600	10.30	29.00	36.50	79.40	99.10
3000	200	19.40	26.00	33.10	80.00	97.80
3000	300	27.50	26.50	30.60	79.50	99.00
3000	400	40.00	24.50	36.20	79.50	99.10
3000	500	0.00	17.30	38.80	79.20	99.00
3000	600	5.60	25.20	37.30	79.70	99.10

Table L.2: 95 % observed and expected limits on $\sigma_{\text{vis},\, h(b\bar{b})+\text{DM}}$ for h + DM events in the [200, 350) GeV $E_{\text{T}}^{\text{miss}}$ bin derived from a range of Z'-2HDM models. Also shown are the up and down variations ($\pm 1\ \sigma$) by one standard deviation on the expected limit. All expected limits are within 15 % of each other. To avoid any model dependence, the parameter set $(m_{Z'},\, m_A) =$ (600 GeV, 500 GeV) with weakest expected limit (in bold) is used for setting limits with less model dependence.

$m_{Z'}$ [GeV]	m_A [GeV]	σ_{obs} [fb]	σ_{exp} [fb]	$-1\ \sigma$ [fb]	$+1\ \sigma$ [fb]
400	500	14.64	10.50	7.56	14.61
600	200	10.92	8.18	5.90	11.39
600	**500**	13.12	10.52	7.58	14.64
800	300	10.47	7.87	5.67	10.95
800	500	11.31	8.67	6.24	12.06
800	700	10.84	8.31	5.99	11.56
1000	400	11.18	8.56	6.17	11.92
1000	600	10.59	7.97	5.74	11.09
1000	800	10.72	8.18	5.90	11.39
1200	800	11.13	8.23	5.93	11.45

Table L.3: 95 % observed and expected limits on $\sigma_{\text{vis},\, h(b\bar{b})+\text{DM}}$ for h + DM events in the [350, 500) GeV $E_{\text{T}}^{\text{miss}}$ bin derived from a range of Z'-2HDM models. Also shown are the up and down variations ($\pm 1\ \sigma$) by one standard deviation on the expected limit. All expected limits are within 10 % of each other. To avoid any model dependence, the parameter set $(m_{Z'}, m_A) =$ (1400 GeV, 600 GeV) with weakest expected limit (in bold) is used for setting limits with less model dependence.

$m_{Z'}$ [GeV]	m_A [GeV]	σ_{obs} [fb]	σ_{exp} [fb]	$-1\ \sigma$ [fb]	$+1\ \sigma$ [fb]
800	200	1.91	1.45	1.05	2.02
1000	400	1.90	1.45	1.05	2.02
1000	600	2.05	1.53	1.10	2.12
1200	300	2.41	1.68	1.21	2.34
1200	500	2.02	1.51	1.08	2.10
1200	800	2.00	1.48	1.07	2.07
1200	800	2.00	1.48	1.07	2.07
1400	**600**	2.42	1.71	1.23	2.38
1400	800	2.15	1.56	1.13	2.18
1600	800	2.43	1.70	1.23	2.37

Table L.4: 95 % observed and expected limits on $\sigma_{\text{vis},\, h(b\bar{b})+\text{DM}}$ for h + DM events in the [500, ∞) GeV $E_{\text{T}}^{\text{miss}}$ bin derived from a range of Z'-2HDM models. Also shown are the up and down variations ($\pm 1\ \sigma$) by one standard deviation on the expected limit. All expected limits are within 70 % of each other. To avoid any model dependence, the parameter set $(m_{Z'}, m_A) =$ (3000 GeV, 300 GeV) with weakest expected limit (in bold) is used for setting limits with less model dependence.

$m_{Z'}$ [GeV]	m_A [GeV]	σ_{obs} [fb]	σ_{exp} [fb]	$-1\ \sigma$ [fb]	$+1\ \sigma$ [fb]
1200	300	0.74	0.71	0.51	0.98
1400	600	0.75	0.71	0.51	0.99
1800	800	0.80	0.77	0.55	1.07
2000	300	0.96	0.94	0.68	1.31
2200	300	1.06	1.04	0.75	1.45
2400	600	1.07	1.07	0.77	1.48
2600	400	1.35	1.34	0.96	1.86
2800	200	1.61	1.60	1.15	2.23
3000	**300**	1.73	1.77	1.27	2.46

References

[1] F. Zwicky, *Die Rotverschiebung von extragalaktischen Nebeln*, Helv. Phys. Acta **6** (1933) 110–127.

[2] K. G. Begeman, A. H. Broeils, and R. H. Sanders, *Extended rotation curves of spiral galaxies: Dark haloes and modified dynamics*, MNRAS **249** (1991) 523.

[3] Planck Collaboration, P. A. R. Ade et al., *Planck 2013 results. I. Overview of products and scientific results*, Astron. Astrophys. **571** (2014) A1, arXiv:1303.5062 [astro-ph.CO].

[4] A. A. Penzias and R. W. Wilson, *A Measurement of Excess Antenna Temperature at 4080 Mc/s.*, Astrophys. J. **142** (1965) 419–421.

[5] R. H. Dicke et al., *Cosmic Black-Body Radiation.*, Astrophys. J. **142** (1965) 414–419.

[6] A. N. Taylor et al., *Gravitational lens magnification and the mass of abell 1689*, Astrophys. J. **501** (1998) 539, arXiv:astro-ph/9801158.

[7] D. Clowe et al., *A direct empirical proof of the existence of dark matter*, Astrophys. J. **648** (2006) 109–113, arXiv:astro-ph/0608407.

[8] ATLAS Collaboration, G. Aad et al., *Observation of a new particle in the search for the Standard Model Higgs boson with the ATLAS detector at the LHC*, Phys. Lett. B **716** (2012) 1.

[9] CMS Collaboration, S. Chatrchyan et al., *Observation of a new boson at a mass of 125 GeV with the CMS experiment at the LHC*, Phys. Lett. B **716** (2012) 30.

[10] M. E. Peskin and D. V. Schroeder, *An Introduction to quantum field theory*. Addison-Wesley, 1995.

[11] W. Hollik, *Quantum field theory and the Standard Model*, arXiv:1012.3883 [hep-ph].

[12] S. Glashow, *Partial symmetries of weak interactions*, Nucl. Phys. **22** (1961) 579.

[13] S. Weinberg, *A Model of Leptons*, Phys. Rev. Lett. **19** (1967) 1264.

[14] A. Salam, *Weak and Electromagnetic Interactions*, Conf. Proc. C **680519** (1968) 367–377.

[15] G. 't Hooft and M. Veltman, *Regularization and renormalization of gauge fields*, Nucl. Phys. B **44** (1972) 189.

[16] S. Sternberg, *Group Theory and Physics*. Cambridge University Press, 2008.

[17] C. N. Yang and R. L. Mills, *Conservation of Isotopic Spin and Isotopic Gauge Invariance*, Phys. Rev. **96** (1954) 191.

[18] G. Zweig, *An SU(3) model for strong interaction symmetry and its breaking*, CERN-TH-401, CERN, 1964.

[19] H. Fritzsch and M. Gell-Mann, *Current algebra: Quarks and what else?*, eConf **C720906V2** (1972) 135–165, `arXiv:hep-ph/0208010`.

[20] H. Fritzsch, M. Gell-Mann, and H. Leutwyler, *Advantages of the color octet gluon picture*, Phys. Lett. B **47** (1973) 365.

[21] A. Salam and J. C. Ward, *Electromagnetic and weak interactions*, Phys. Lett. **13** (1964) 168.

[22] S. Tomonaga, *On a relativistically invariant formulation of the quantum theory of wave fields*, Prog. Theor. Phys. **1** (1946) 27.

[23] J. S. Schwinger, *Quantum electrodynamics. I. A covariant formulation*, Phys. Rev. **74** (1948) 1439.

[24] J. S. Schwinger, *On quantum electrodynamics and the magnetic moment of the electron*, Phys. Rev. **73** (1948) 416.

[25] R. Feynman, *Mathematical formulation of the quantum theory of electromagnetic interaction*, Phys. Rev. **80** (1950) 440.

[26] R. Feynman, *The theory of positrons*, Phys. Rev. **76** (1949) 749.

[27] R. Feynman, *Space - time approach to quantum electrodynamics*, Phys. Rev. **76** (1949) 769.

[28] F. Englert and R. Brout, *Broken symmetry and the mass of gauge vector mesons*, Phys. Rev. Lett. **13** (1964) 321–323.

[29] P. W. Higgs, *Broken symmetries, massless particles and gauge fields*, Phys. Lett. **12** (1964) 132–133.

[30] P. W. Higgs, *Broken symmetries and the masses of gauge bosons*, Phys. Rev. Lett. **13** (1964) 508–509.

[31] G. Guralnik, C. Hagen, and T. Kibble, *Global conservation laws and massless particles*, Phys. Rev. Lett. **13** (1964) 585.

[32] P. W. Higgs, *Spontaneous symmetry breakdown without massless bosons*, Phys. Rev. **145** (1966) 1156.

[33] T. Kibble, *Symmetry breaking in non-Abelian gauge theories*, Phys. Rev. **155** (1967) 1554–1561.

[34] G. 't Hooft, *Renormalizable Lagrangians for massive Yang-Mills fields*, Nucl. Phys. B **35** (1971) 167–188.

[35] M. Veltman and G. 't Hooft, *Combinatorics of gauge fields*, Nucl. Phys. B **50** (1972) 318–353.

[36] Particle Data Group Collaboration, M. Tanabashi et al., *Review of Particle Physics*, Phys. Rev. D **98** (2018) 030001.

[37] M. Gell-Mann, *The interpretation of the new particles as displaced charge multiplets*, Nuovo Cimento **4** (1956) 848–866.

[38] T. Nakano and K. Nishijima, *Charge Independence for V-particles*, Progr. Theor. Exp. Phys. **10** (1953) 581–582.

[39] M. Dine, *TASI lectures on the strong CP problem*, arXiv:hep-ph/0011376.

[40] Y. Nambu and G. Jona-Lasinio, *Dynamical Model of Elementary Particles Based on an Analogy with Superconductivity. I*, Phys. Rev. **122** (1961) 345–358.

[41] Y. Nambu and G. Jona-Lasinio, *Dynamical Model of Elementary Particles Based on an Analogy with Superconductivity. II*, Phys. Rev. **124** (1961) 246–254.

[42] J. Goldstone, *Field theories with superconductor solutions*, Nuovo Cimento **19** (1961) 154–164.

[43] J. Goldstone, A. Salam, and S. Weinberg, *Broken symmetries*, Phys. Rev. **127** (1962) 965.

[44] FAST Collaboration, A. Barczyk et al., *Measurement of the Fermi Constant by FAST*, Phys. Lett. B **663** (2008) 172–180, arXiv:0707.3904 [hep-ex].

[45] S. P. Martin, *A Supersymmetry primer*, Adv. Ser. Direct. High Energy Phys. **18** (1998) 1, arXiv:hep-ph/9709356.

[46] K. D. Lane, *Technicolor 2000*, Frascati Phys. Ser. **18** (2000) 235–280, arXiv:hep-ph/0007304.

[47] J. C. Collins and D. E. Soper, *The Theorems of Perturbative QCD*, Ann. Rev. Nucl. Part. Sci. **37** (1987) 383–409.

[48] S. Dulat et al., *New parton distribution functions from a global analysis of quantum chromodynamics*, Phys. Rev. D **93** (2016) 033006, arXiv:1506.07443 [hep-ph].

[49] W. J. Stirling, *private communication*,. https://www.hep.ph.ic.ac.uk/~wstirlin/plots/plots.html. [Online; accessed 23-January-2018].

[50] A. Martin et al., *Parton distributions for the LHC*, Eur. Phys. J. C **63** (2009) 189.

[51] M. R. Whalley, D. Bourilkov, and R. C. Group, *The Les Houches accord PDFs (LHAPDF) and LHAGLUE*, arXiv:hep-ph/0508110.

[52] ATLAS Collaboration, G. Aad et al., *The ATLAS simulation infrastructure*, Eur. Phys. J. C **70** (2010) 823–874, arXiv:1005.4568 [physics.ins-det].

[53] GEANT4 Collaboration, S. Agostinelli et al., *GEANT4: A simulation toolkit*, Nucl. Instr. Meth. A **506** (2003) 250.

[54] P. Nason, *A new method for combining NLO QCD with shower Monte Carlo algorithms*, JHEP **11** (2004) 040, arXiv:hep-ph/0409146.

[55] S. Frixione, P. Nason, and C. Oleari, *Matching NLO QCD computations with Parton Shower simulations: the POWHEG method*, JHEP **11** (2007) 070, arXiv:0709.2092 [hep-ph].

[56] S. Alioli et al., *A general framework for implementing NLO calculations in shower Monte Carlo programs: the POWHEG BOX*, JHEP **06** (2010) 043, arXiv:1002.2581 [hep-ph].

[57] S. Alioli et al., *NLO single-top production matched with shower in POWHEG: s- and t-channel contributions*, JHEP **09** (2009) 111, arXiv:0907.4076 [hep-ph].

[58] E. Re, *Single-top Wt-channel production matched with parton showers using the POWHEG method*, Eur. Phys. J. C **71** (2011) 1547, arXiv:1009.2450 [hep-ph].

[59] T. Gleisberg et al., *Event generation with SHERPA 1.1*, JHEP **0902** (2009) 7.

[60] J. Alwall et al., *MadGraph/MadEvent v4: The new web generation*, JHEP **0709** (2007) 28.

[61] J. Alwall et al., *MadGraph 5 : Going beyond*, JHEP **1106** (2011) 128.

[62] R. C. Gray et al., *Backgrounds to Higgs boson searches from $W\gamma^* \to \ell\nu\ell(\ell)$ asymmetric internal conversion*, arXiv:1110.1368 [hep-ph].

[63] T. Sjostrand, S. Mrenna, and P. Z. Skands, *PYTHIA 6.4 physics and manual*, JHEP **0605** (2006) 26.

[64] T. Sjostrand, S. Mrenna, and P. Z. Skands, *A brief introduction to PYTHIA 8.1*, Comp. Phys. Comm. **178** (2008) 852.

[65] J. Alwall et al., *The automated computation of tree-level and next-to-leading order differential cross sections, and their matching to parton shower simulations*, JHEP **07** (2014) 079, arXiv:1405.0301 [hep-ph].

[66] A. Buckley et al., *General-purpose event generators for LHC physics*, Phys. Rept. **504** (2011) 145–233, arXiv:1101.2599 [hep-ph].

[67] ATLAS, CMS Collaboration, G. Aad et al., *Combined Measurement of the Higgs Boson Mass in pp Collisions at $\sqrt{s} = 7$ and 8 TeV with the ATLAS and CMS Experiments*, Phys. Rev. Lett. **114** (2015) 191803, arXiv:1503.07589 [hep-ex].

[68] M. Aaboud et al., *Measurement of the Higgs boson mass in the $H \to ZZ^* \to 4\ell$ and $H \to \gamma\gamma$ channels with $\sqrt{s} = 13$ TeV pp collisions using the ATLAS detector*, Phys. Lett. B **784** (2018) 345–366, arXiv:1806.00242 [hep-ex].

[69] CMS Collaboration, A. M. Sirunyan et al., *Measurements of properties of the Higgs boson decaying into the four-lepton final state in pp collisions at $\sqrt{s} = 13$ TeV*, JHEP **11** (2017) 047, arXiv:1706.09936 [hep-ex].

[70] A. Djouadi, *The anatomy of electro-weak symmetry breaking. I: The Higgs boson in the standard model*, Phys. Rept. **457** (2008) 1.

[71] LHC Higgs Cross Section Working Group Collaboration, D. de Florian et al., *Handbook of LHC Higgs Cross Sections: 4. Deciphering the Nature of the Higgs Sector*, arXiv:1610.07922 [hep-ph].

[72] ATLAS, CMS Collaboration, G. Aad et al., *Measurements of the Higgs boson production and decay rates and constraints on its couplings from a combined ATLAS and CMS analysis of the LHC pp collision data at $\sqrt{s} = 7$ and 8 TeV*, JHEP **08** (2016) 045, arXiv:1606.02266 [hep-ex].

[73] CMS Collaboration, A. M. Sirunyan et al., *Observation of the Higgs boson decay to a pair of τ leptons with the CMS detector*, Phys. Lett. B **779** (2018) 283–316, arXiv:1708.00373 [hep-ex].

[74] ATLAS Collaboration, M. Aaboud et al., *Cross-section measurements of the Higgs boson decaying to a pair of tau leptons in proton-proton collisions at $\sqrt{s} = 13$ TeV with the ATLAS detector*, ATLAS-CONF-2018-021, CERN, 2018, https://cds.cern.ch/record/2621794.

[75] ATLAS Collaboration, G. Aad et al., *Combined measurements of the Higgs boson production and decay rates in $H \to ZZ^* \to 4\ell$ and $H \to \gamma\gamma$ final states using pp collision data at $\sqrt{s} = 13$ TeV in the ATLAS experiment*, ATLAS-CONF-2016-081, CERN, 2016, https://cds.cern.ch/record/2206272.

[76] CMS Collaboration, A. M. Sirunyan et al., *Measurement of differential fiducial cross sections for Higgs boson production in the diphoton decay channel in pp collisions at $\sqrt{s} = 13$ TeV*, CMS-PAS-HIG-17-015, CERN, 2017, https://cds.cern.ch/record/2257530.

[77] ATLAS Collaboration, M. Aaboud et al., *Combined measurements of Higgs boson production and decay using up to 80 fb^{-1} of proton-proton collision data at $\sqrt{s} = 13$ TeV collected with the ATLAS experiment*, ATLAS-CONF-2018-031, CERN, 2018, https://cds.cern.ch/record/2629412.

[78] L. Landau, *On the angular momentum of a two-photon system*, Dokl. Akad. Nauk Ser. Fiz. **60** (1948) 207.

[79] C.-N. Yang, *Selection Rules for the Dematerialization of a Particle Into Two Photons*, Phys. Rev. **77** (1950) 242.

[80] ATLAS Collaboration, G. Aad et al., *Study of the spin and parity of the Higgs boson in diboson decays with the ATLAS detector*, Eur. Phys. J. C **76** (2016) 152, arXiv:1506.05669 [hep-ex].

[81] CMS Collaboration, V. Khachatryan et al., *Constraints on the spin-parity and anomalous HVV couplings of the Higgs boson in proton collisions at 7 and 8 TeV*, Phys. Rev. D **92** (2015) 012004, arXiv:1411.3441 [hep-ex].

[82] ATLAS Collaboration, M. Aaboud et al., *Constraints on off-shell Higgs boson production and the Higgs boson total width in $ZZ \to 4\ell$ and $ZZ \to 2\ell 2\nu$ final states with the ATLAS detector*, Phys. Lett. B **786** (2018) 223–244, arXiv:1808.01191 [hep-ex].

[83] ATLAS Collaboration, M. Aaboud et al., *Observation of Higgs boson production in association with a top quark pair at the LHC with the ATLAS detector*, Phys. Lett. B **784** (2018) 173–191, arXiv:1806.00425 [hep-ex].

[84] CMS Collaboration, A. M. Sirunyan et al., *Observation of $t\bar{t}H$ Production*, Phys. Rev. Lett. **120** (2018) 231801, arXiv:1804.02610 [hep-ex].

[85] CDF, D0 Collaboration, T. Aaltonen et al., *Evidence for a particle produced in association with weak bosons and decaying to a bottom-antibottom quark pair in Higgs boson searches at the Tevatron*, Phys. Rev. Lett. **109** (2012) 071804, arXiv:1207.6436 [hep-ex].

[86] ATLAS Collaboration, M. Aaboud et al., *Observation of $H \to b\bar{b}$ decays and VH production with the ATLAS detector*, ATLAS-CONF-2018-036, CERN, 2018, https://cds.cern.ch/record/2630338.

[87] CMS Collaboration, A. M. Sirunyan et al., *Observation of Higgs boson decay to bottom quarks*, CMS-PAS-HIG-18-016, CERN, 2018, https://cds.cern.ch/record/2633415.

[88] G. Bertone, D. Hooper, and J. Silk, *Particle dark matter: Evidence, candidates and constraints*, Phys. Rept. **405** (2005) 279–390, arXiv:hep-ph/0404175.

[89] E. Hubble, *A relation between distance and radial velocity among extra-galactic nebulae*, Proc. Natl. Acad. Sci. **15** (1929) 168–173.

[90] A. G. Lemaître, *A Homogeneous Universe of Constant Mass and Increasing Radius accounting for the Radial Velocity of Extra-galactic Nebulae*, MNRAS **91** (1931) 483–490.

[91] A. Einstein, *Kosmologische Betrachtungen zur allgemeinen Relativitätstheorie*, Sitzungsberichte der Königlich Preußischen Akademie der Wissenschaften (1917) 142–152.

[92] A. G. Riess et al., *The Farthest Known Supernova: Support for an Accelerating Universe and a Glimpse of the Epoch of Deceleration*, Astrophys. J. **560** (2001) 49.

[93] P. J. E. Peebles and B. Ratra, *The Cosmological constant and dark energy*, Rev. Mod. Phys. **75** (2003) 559–606, arXiv:astro-ph/0207347.

[94] A. Friedman, *Über die Krümmung des Raumes*, Z. Physik **10** (1922) 377–386.

[95] A. Friedmann, *Über die Möglichkeit einer Welt mit konstanter negativer Krümmung des Raumes*, Z. Physik **21** (1924) 326–332.

[96] Planck Collaboration, P. A. R. Ade et al., *Planck 2015 results. XIII. Cosmological parameters*, Astron. Astrophys. **594** (2016) A13, arXiv:1502.01589 [astro-ph.CO].

[97] L. Bergstrm, *Nonbaryonic dark matter: Observational evidence and detection methods*, Rept. Prog. Phys. **63** (2000) 793, arXiv:hep-ph/0002126.

[98] J. L. Feng, *Dark Matter Candidates from Particle Physics and Methods of Detection*, Annu. Rev. Astron. Astrophys. **48** (2010) 495–545.

[99] J. H. Oort, *The force exerted by the stellar system in the direction perpendicular to the galactic plane and some related problems*, Bulletin of the Astronomical Institutes of the Netherlands **6** (1932) 249.

[100] U. G. Briel and J. P. Henry, *An x-ray temperature map of coma*, arXiv:astro-ph/9711237.

[101] V. C. Rubin and W. K. Ford, *Rotation of the Andromeda Nebula from a Spectroscopic Survey of Emission Regions*, Astrophys. J. **159** (1970) 379.

[102] M. Milgrom, *MOND theory*, Can. J. Phys. **93** (2015) 107–118, arXiv:1404.7661 [astro-ph.CO].

[103] J. D. Bekenstein, *Relativistic gravitation theory for the modified Newtonian dynamics paradigm*, Phys. Rev. D **70** (2004) 083509.

[104] M. Markevitch, *Chandra observation of the most interesting cluster in the universe*, ESA Spec. Publ. **604** (2006) 723, arXiv:astro-ph/0511345.

[105] M. Markevitch et al., *Direct constraints on the dark matter self-interaction cross-section from the merging galaxy cluster 1E0657-56*, Astrophys. J. **606** (2004) 819–824, arXiv:astro-ph/0309303.

[106] T. Bringmann et al., *Strong constraints on self-interacting dark matter with light mediators*, Phys. Rev. Lett. **118** (2017) 141802, arXiv:1612.00845 [hep-ph].

[107] J. Zavala, M. Vogelsberger, and M. G. Walker, *Constraining self-interacting dark matter with the Milky Way's dwarf spheroidals*, MNRAS Lett. **431** (2013) 20–24.

[108] D. J. Fixsen, *The Temperature of the Cosmic Microwave Background*, Astrophys. J. **707** (2009) 916.

[109] R. A. Alpher, H. Bethe, and G. Gamow, *The Origin of Chemical Elements*, Phys. Rev. **73** (1948) 803–804.

[110] G. Gamow, *The Origin of Elements and the Separation of Galaxies*, Phys. Rev. **74** (1948) 505–506.

[111] Planck Collaboration, *Picture Gallery*, 2018. https://www.cosmos.esa.int/web/planck/picture-gallery. [Online; accessed 5-April-2018].

[112] Planck Collaboration, P. A. R. Ade et al., *Planck 2013 results. XV. CMB power spectra and likelihood*, Astron. Astrophys. **571** (2014) A15, arXiv:1303.5075 [astro-ph.CO].

[113] M. Boylan-Kolchin et al., *Resolving cosmic structure formation with the Millennium-II Simulation*, MNRAS **398** (2009) 1150–1164.

[114] K. Freese, B. Fields, and D. Graff, *Limits on stellar objects as the dark matter of our halo: nonbaryonic dark matter seems to be required*, Nucl. Phys. Proc. Suppl. **80** (2000) 0305, arXiv:astro-ph/9904401.

[115] M. Drewes, *The Phenomenology of Right Handed Neutrinos*, Int. J. Mod. Phys. E **22** (2013) 1330019, arXiv:1303.6912 [hep-ph].

[116] S. Dodelson and L. M. Widrow, *Sterile-neutrinos as dark matter*, Phys. Rev. Lett. **72** (1994) 17–20, arXiv:hep-ph/9303287.

[117] ALEPH, DELPHI, L3, OPAL and SLD Collaboration, S. Schael et al., *Precision electroweak measurements on the Z resonance*, Phys. Rept. **427** (2006) 257, arXiv:hep-ex/0509008.

[118] A. de Gouvêa and A. Kobach, *Global Constraints on a Heavy Neutrino*, Phys. Rev. D **93** no. 3, (2016) 033005, arXiv:1511.00683 [hep-ph].

[119] S. Weinberg, *A New Light Boson?*, Phys. Rev. Lett. **40** (1978) 223–226.

[120] F. Wilczek, *Problem of Strong P and T Invariance in the Presence of Instantons*, Phys. Rev. Lett. **40** (1978) 279–282.

[121] G. G. Raffelt, *Axions: Motivation, limits and searches*, J. Phys. A **40** (2007) 6607–6620, arXiv:hep-ph/0611118.

[122] G. G. Raffelt, *Astrophysical axion bounds*, Lect. Notes Phys. **741** (2008) 51–71, arXiv:hep-ph/0611350.

[123] ADMX Collaboration, S. J. Asztalos et al., *SQUID-Based Microwave Cavity Search for Dark-Matter Axions*, Phys. Rev. Lett. **104** (2010) 041301.

[124] MADMAX Collaboration, B. Majorovits et al., *MADMAX: A new road to axion dark matter detection*, in *15th International Conference on Topics in Astroparticle and Underground Physics (TAUP 2017) Sudbury, Ontario, Canada*. 2017. arXiv:1712.01062 [physics.ins-det].

[125] B. W. Lee and S. Weinberg, *Cosmological Lower Bound on Heavy-Neutrino Masses*, Phys. Rev. Lett. **39** (1977) 165–168.

[126] J. E. Gunn et al., *Some astrophysical consequences of the existence of a heavy stable neutral lepton*, Astrophys. J. **223** (1978) 1015–1031.

[127] E. John et al., *Supersymmetric relics from the big bang*, Nucl. Phys. B **238** (1984) 453–476.

[128] G. Steigman and M. S. Turner, *Cosmological constraints on the properties of weakly interacting massive particles*, Nucl. Phys. B **253** (1985) 375–386.

[129] K. Griest and M. Kamionkowski, *Unitarity limits on the mass and radius of dark-matter particles*, Phys. Rev. Lett. **64** (1990) 615–618.

[130] G. Jungman, M. Kamionkowski, and K. Griest, *Supersymmetric dark matter*, Phys. Rep. **267** (1996) 195–373.

[131] T. Falk, K. A. Olive, and M. Srednicki, *Heavy sneutrinos as dark matter*, Phys. Lett. B **339** (1994) 248–251, `arXiv:hep-ph/9409270`.

[132] J. L. Feng, A. Rajaraman, and F. Takayama, *Superweakly interacting massive particles*, Phys. Rev. Lett. **91** (2003) 011302, `arXiv:hep-ph/0302215`.

[133] S. Dimopoulos and H. Georgi, *Softly broken supersymmetry and SU(5)*, Nucl. Phys. B **193** (1981) 150–162.

[134] S. Dimopoulos, S. Raby, and F. Wilczek, *Supersymmetry and the scale of unification*, Phys. Rev. D **24** (1981) 1681–1683.

[135] N. Sakai, *Naturalnes in supersymmetric GUTS*, Z. Phys. C **11** (1981) 153–157.

[136] L. Ibáñez and G. Ross, *Low-energy predictions in supersymmetric grand unified theories*, Phys. Lett. B **105** (1981) 439–442.

[137] T. Kaluza, *Zum Unitätsproblem der Physik*, Sitzungsber. Preuss. Akad. Wiss. Berlin (Math. Phys.) K **1** (1921) 966–972, `arXiv:1803.08616 [physics.hist-ph]`.

[138] T. Appelquist, H.-C. Cheng, and B. A. Dobrescu, *Bounds on universal extra dimensions*, Phys. Rev. D **64** (2001) 035002, `arXiv:hep-ph/0012100`.

[139] N. Arkani-Hamed, A. G. Cohen, and H. Georgi, *Electroweak symmetry breaking from dimensional deconstruction*, Phys. Lett. B **513** (2001) 232–240, `arXiv:hep-ph/0105239`.

[140] N. Arkani-Hamed et al., *Phenomenology of electroweak symmetry breaking from theory space*, JHEP **08** (2002) 020, `arXiv:hep-ph/0202089`.

[141] N. Arkani-Hamed et al., *The Littlest Higgs*, JHEP **07** (2002) 034, `arXiv:hep-ph/0206021`.

[142] N. Arkani-Hamed et al., *The Minimal moose for a little Higgs*, JHEP **08** (2002) 021, `arXiv:hep-ph/0206020`.

[143] F. Sannino, *Dynamical Stabilization of the Fermi Scale: Phase Diagram of Strongly Coupled Theories for (Minimal) Walking Technicolor and Unparticles*, `arXiv:0804.0182 [hep-ph]`.

[144] S. Chang, C. Coriano, and A. E. Faraggi, *Stable superstring relics*, Nucl. Phys. B **477** (1996) 65–104, arXiv:hep-ph/9605325.

[145] E. W. Kolb, D. J. H. Chung, and A. Riotto, *WIMPzillas!*, AIP Conf. Proc. **484** (1999) 91–105, arXiv:hep-ph/9810361.

[146] A. Kusenko et al., *Experimental signatures of supersymmetric dark matter Q balls*, Phys. Rev. Lett. **80** (1998) 3185–3188, arXiv:hep-ph/9712212.

[147] A. Kusenko and M. E. Shaposhnikov, *Supersymmetric Q balls as dark matter*, Phys. Lett. B **418** (1998) 46–54, arXiv:hep-ph/9709492.

[148] D. N. Spergel and P. J. Steinhardt, *Observational evidence for selfinteracting cold dark matter*, Phys. Rev. Lett. **84** (2000) 3760–3763, arXiv:astro-ph/9909386.

[149] R. Dave et al., *Halo properties in cosmological simulations of selfinteracting cold dark matter*, Astrophys. J. **547** (2001) 574–589, arXiv:astro-ph/0006218.

[150] W. Hu, R. Barkana, and A. Gruzinov, *Cold and fuzzy dark matter*, Phys. Rev. Lett. **85** (2000) 1158–1161, arXiv:astro-ph/0003365.

[151] A. M. Green, *Astrophysical uncertainties on direct detection experiments*, Mod. Phys. Lett. A **27** (2012) 1230004, arXiv:1112.0524 [astro-ph.CO].

[152] T. Marrodán Undagoitia and L. Rauch, *Dark matter direct-detection experiments*, J. Phys. G **43** (2016) 013001, arXiv:1509.08767 [physics.ins-det].

[153] M. Klasen, M. Pohl, and G. Sigl, *Indirect and direct search for dark matter*, Prog. Part. Nucl. Phys. **85** (2015) 1–32, arXiv:1507.03800 [hep-ph].

[154] CRESST Collaboration, G. Angloher et al., *Results on light dark matter particles with a low-threshold CRESST-II detector*, Eur. Phys. J. C **76** (2016) 25, arXiv:1509.01515 [astro-ph.CO].

[155] CRESST Collaboration, F. Petricca et al., *First results on low-mass dark matter from the CRESST-III experiment*, in *15th International Conference on Topics in Astroparticle and Underground Physics (TAUP 2017) Sudbury, Canada*. 2017. arXiv:1711.07692 [astro-ph.CO].

[156] CDEX Collaboration, H. Jiang et al., *Limits on Light Weakly Interacting Massive Particles from the First 102.8 kg $\times$ day Data of the CDEX-10 Experiment*, Phys. Rev. Lett. **120** (2018) 241301, arXiv:1802.09016 [hep-ex].

[157] EDELWEISS Collaboration, L. Hehn et al., *Improved EDELWEISS-III sensitivity for low-mass WIMPs using a profile likelihood approach*, Eur. Phys. J. C **76** (2016) 548, arXiv:1607.03367 [astro-ph.CO].

[158] DAMIC Collaboration, J. Barreto et al., *Direct Search for Low Mass Dark Matter Particles with CCDs*, Phys. Lett. B **711** (2012) 264–269, arXiv:1105.5191 [astro-ph.IM].

[159] D. Yu. Akimov et al., *WIMP-nucleon cross-section results from the second science run of ZEPLIN-III*, Phys. Lett. B **709** (2012) 14–20, arXiv:1110.4769 [astro-ph.CO].

[160] CDMS Collaboration, R. Agnese et al., *Silicon Detector Dark Matter Results from the Final Exposure of CDMS II*, Phys. Rev. Lett. **111** (2013) 251301, arXiv:1304.4279 [hep-ex].

[161] SuperCDMS Collaboration, R. Agnese et al., *Search for Low-Mass Weakly Interacting Massive Particles with SuperCDMS*, Phys. Rev. Lett. **112** (2014) 241302, arXiv:1402.7137 [hep-ex].

[162] SuperCDMS Collaboration, R. Agnese et al., *New Results from the Search for Low-Mass Weakly Interacting Massive Particles with the CDMS Low Ionization Threshold Experiment*, Phys. Rev. Lett. **116** (2016) 071301.

[163] PICO Collaboration, C. Amole et al., *Dark matter search results from the PICO-60 CF_3I bubble chamber*, Phys. Rev. D **93** (2016) 052014, arXiv:1510.07754 [hep-ex].

[164] PICO Collaboration, C. Amole et al., *Dark Matter Search Results from the PICO-60 C_3F_8 Bubble Chamber*, Phys. Rev. Lett. **118** (2017) 251301, arXiv:1702.07666 [astro-ph.CO].

[165] DarkSide Collaboration, P. Agnes et al., *Low-Mass Dark Matter Search with the DarkSide-50 Experiment*, Phys. Rev. Lett. **121** (2018) 081307, arXiv:1802.06994 [astro-ph.HE].

[166] DarkSide Collaboration, P. Agnes et al., *DarkSide-50 532-day Dark Matter Search with Low-Radioactivity Argon*, arXiv:1802.07198 [astro-ph.CO].

[167] LUX Collaboration, D. S. Akerib et al., *Results from a search for dark matter in the complete LUX exposure*, Phys. Rev. Lett. **118** (2017) 021303, arXiv:1608.07648 [astro-ph.CO].

[168] PandaX-II Collaboration, X. Cui et al., *Dark Matter Results From 54-Ton-Day Exposure of PandaX-II Experiment*, Phys. Rev. Lett. **119** (2017) 181302, arXiv:1708.06917 [astro-ph.CO].

[169] XENON Collaboration, E. Aprile et al., *Dark Matter Search Results from a One Ton-Year Exposure of XENON1T*, Phys. Rev. Lett. **121** (2018) 111302, arXiv:1805.12562 [astro-ph.CO].

[170] DAMA/LIBRA Collaboration, R. Bernabei et al., *First results from DAMA/LIBRA and the combined results with DAMA/NaI*, Eur. Phys. J. C **56** (2008) 333–355, arXiv:0804.2741 [astro-ph].

[171] DAMA/LIBRA Collaboration, R. Bernabei et al., *DAMA/LIBRA results and perspectives*, EPJ Web Conf. **136** (2017) 05001, arXiv:1612.01387 [hep-ex].

[172] J. Billard, L. Strigari, and E. Figueroa-Feliciano, *Implication of neutrino backgrounds on the reach of next generation dark matter direct detection experiments*, Phys. Rev. D **89** (2014) 023524, arXiv:1307.5458 [hep-ph].

[173] K. Freese, M. Lisanti, and C. Savage, *Colloquium: Annual modulation of dark matter*, Rev. Mod. Phys. **85** (2013) 1561–1581, arXiv:1209.3339 [astro-ph.CO].

[174] R. Bernabei et al., *First Model Independent Results from DAMA/LIBRA-Phase 2*, Universe **4** (2018) 116, arXiv:1805.10486 [hep-ex].

[175] J. Amare et al., *The ANAIS-112 experiment at the Canfranc Underground Laboratory*, in *15th International Conference on Topics in Astroparticle and Underground Physics (TAUP 2017) Sudbury, Ontario, Canada*. 2017. arXiv:1710.03837 [physics.ins-det].

[176] G. Adhikari et al., *Initial Performance of the COSINE-100 Experiment*, Eur. Phys. J. C **78** (2018) 107, arXiv:1710.05299 [physics.ins-det].

[177] G. Angloher et al., *The COSINUS project - perspectives of a NaI scintillating calorimeter for dark matter search*, Eur. Phys. J. C **76** (2016) 441, arXiv:1603.02214 [physics.ins-det].

[178] SABRE Collaboration, G. D'Imperio, *Dark matter search with the SABRE experiment*, arXiv:1807.00584 [physics.ins-det].

[179] DM-Ice Collaboration, W. C. Pettus, *DM-Ice: Current Status and Future Prospects*, in *Proceedings, 12th Conference on the Intersections of Particle and Nuclear Physics (CIPANP 2015): Vail, Colorado, USA*. 2015. arXiv:1510.00378 [physics.ins-det].

[180] CoGeNT Collaboration, C. E. Aalseth et al., *CoGeNT: A Search for Low-Mass Dark Matter using p-type Point Contact Germanium Detectors*, Phys. Rev. D **88** (2013) 012002, arXiv:1208.5737 [astro-ph.CO].

[181] XENON Collaboration, E. Aprile et al., *First Dark Matter Search Results from the XENON1T Experiment*, Phys. Rev. Lett. **119** (2017) 181301, arXiv:1705.06655 [astro-ph.CO].

[182] COUPP Collaboration, E. Behnke et al., *First Dark Matter Search Results from a 4-kg CF_3I Bubble Chamber Operated in a Deep Underground Site*, Phys. Rev. D **86** (2012) 052001, arXiv:1204.3094 [astro-ph.CO].

[183] PICASSO Collaboration, E. Behnke et al., *Final Results of the PICASSO Dark Matter Search Experiment*, Astropart. Phys. **90** (2017) 85–92, arXiv:1611.01499 [hep-ex].

[184] SIMPLE Collaboration, M. Felizardo et al., *Final Analysis and Results of the Phase II SIMPLE Dark Matter Search*, Phys. Rev. Lett. **108** (2012) 201302, arXiv:1106.3014 [astro-ph.CO].

[185] CDMS Collaboration, Z. Ahmed et al., *Search for Weakly Interacting Massive Particles with the First Five-Tower Data from the Cryogenic Dark Matter Search at the Soudan Underground Laboratory*, Phys. Rev. Lett. **102** (2009) 011301, arXiv:0802.3530 [astro-ph].

[186] XENON100 Collaboration, E. Aprile et al., *XENON100 Dark Matter Results from a Combination of 477 Live Days*, Phys. Rev. D **94** (2016) 122001, arXiv:1609.06154 [astro-ph.CO].

[187] KIMS Collaboration, S. C. Kim et al., *New Limits on Interactions between Weakly Interacting Massive Particles and Nucleons Obtained with CsI(Tl) Crystal Detectors*, Phys. Rev. Lett. **108** (2012) 181301.

[188] IceCube Collaboration, R. Abbasi et al., *Limits on a Muon Flux from Neutralino Annihilations in the Sun with the IceCube 22-String Detector*, Phys. Rev. Lett. **102** (2009) 201302.

[189] IceCube Collaboration, M. G. Aartsen, , et al., *Search for Dark Matter Annihilations in the Sun with the 79-String IceCube Detector*, Phys. Rev. Lett. **110** (2013) 131302.

[190] IceCube Collaboration, M. G. Aartsen et al., *Search for annihilating dark matter in the Sun with 3 years of IceCube data*, Eur. Phys. J. C **77** (2017) 146, arXiv:1612.05949 [astro-ph.HE].

[191] T. R. Slatyer, *TASI Lectures on Indirect Detection of Dark Matter*, MIT-CTP-4946, MIT, 2017, arXiv:1710.05137 [hep-ph].

[192] H. Haghi and V. Amiri, *Testing modified gravity with dwarf spheroidal galaxies*, MNRAS **463** (2016) 1944–1951.

[193] H.E.S.S. Collaboration, A. Abramowski et al., *Search for dark matter annihilation signatures in H.E.S.S. observations of Dwarf Spheroidal Galaxies*, Phys. Rev. D **90** (2014) 112012, arXiv:1410.2589 [astro-ph.HE].

[194] H.E.S.S. Collaboration, H. Abdallah et al., *Search for dark matter annihilations towards the inner Galactic halo from 10 years of observations with H.E.S.S*, Phys. Rev. Lett. **117** (2016) 111301, arXiv:1607.08142 [astro-ph.HE].

[195] H.E.S.S. Collaboration, L. Rinchiuso et al., *Dark matter gamma-ray line searches toward the Galactic Center halo with H.E.S.S. I*, PoS **ICRC2017** (2017) 893, arXiv:1708.08358 [astro-ph.HE].

[196] J. Aleksiffj et al., *Optimized dark matter searches in deep observations of Segue 1 with MAGIC*, JCAP **1402** (2014) 008, arXiv:1312.1535 [hep-ph].

[197] P. Giammaria et al., *Latest results on searches for dark matter signatures in galactic and extragalactic selected targets by the MAGIC Telescopes*, JPCS **718** (2016) 042024.

[198] Fermi-LAT, MAGIC Collaboration, M. L. Ahnen et al., *Limits to dark matter annihilation cross-section from a combined analysis of MAGIC and Fermi-LAT observations of dwarf satellite galaxies*, JCAP **1602** (2016) 039, arXiv:1601.06590 [astro-ph.HE].

[199] MAGIC Collaboration, V. A. Acciari et al., *Constraining Dark Matter lifetime with a deep gamma-ray survey of the Perseus Galaxy Cluster with MAGIC*, Phys. Dark Univ. **22** (2018) 38–47, arXiv:1806.11063 [astro-ph.HE].

[200] T. Arlen et al., *Constraints on Cosmic Rays, Magnetic Fields, and Dark Matter from Gamma-Ray Observations of the Coma Cluster of Galaxies with VERITAS and Fermi*, Astrophys. J. **757** (2012) 123.

[201] VERITAS Collaboration, S. Archambault et al., *Dark Matter Constraints from a Joint Analysis of Dwarf Spheroidal Galaxy Observations with VERITAS*, Phys. Rev. D **95** (2017) 082001, arXiv:1703.04937 [astro-ph.HE].

[202] J. Conrad, J. Cohen-Tanugi, and L. E. Strigari, *WIMP searches with gamma rays in the Fermi era: challenges, methods and results*, J. Exp. Theor. Phys. **121** (2015) 1104–1135, arXiv:1503.06348 [astro-ph.CO].

[203] Fermi-LAT Collaboration, M. Ackermann et al., *Searching for Dark Matter Annihilation from Milky Way Dwarf Spheroidal Galaxies with Six Years of Fermi Large Area Telescope Data*, Phys. Rev. Lett. **115** (2015) 231301, arXiv:1503.02641 [astro-ph.HE].

[204] Super-Kamiokande Collaboration, C. Kachulis et al., *Search for Boosted Dark Matter Interacting With Electrons in Super-Kamiokande*, Phys. Rev. Lett. **120** (2018) 221301, arXiv:1711.05278 [hep-ex].

[205] ANTARES Collaboration, A. Albert et al., *Results from the search for dark matter in the Milky Way with 9 years of data of the ANTARES neutrino telescope*, Phys. Lett. B **769** (2017) 249–254.

[206] IceCube Collaboration, M. G. Aartsen et al., *Search for Neutrinos from Dark Matter Self-Annihilations in the center of the Milky Way with 3 years of IceCube/DeepCore*, Eur. Phys. J. C **77** (2017) 627, arXiv:1705.08103 [hep-ex].

[207] PAMELA Collaboration, O. Adriani et al., *An anomalous positron abundance in cosmic rays with energies 1.5-100 GeV*, Nature **458** (2009) 607–609, arXiv:0810.4995 [astro-ph].

[208] Fermi-LAT Collaboration, M. Ackermann et al., *Measurement of Separate Cosmic-Ray Electron and Positron Spectra with the Fermi Large Area Telescope*, Phys. Rev. Lett. **108** (2012) 011103.

[209] AMS Collaboration, M. Aguilar et al., *First Result from the Alpha Magnetic Spectrometer on the International Space Station: Precision Measurement of the Positron Fraction in Primary Cosmic Rays of 0.5-350 GeV*, Phys. Rev. Lett. **110** (2013) 141102.

[210] K. Blum, B. Katz, and E. Waxman, *AMS-02 Results Support the Secondary Origin of Cosmic Ray Positrons*, Phys. Rev. Lett. **111** (2013) 211101, arXiv:1305.1324 [astro-ph.HE].

[211] HAWC Collaboration, A. U. Abeysekara et al., *Extended gamma-ray sources around pulsars constrain the origin of the positron flux at Earth*, Science **358** (2017) 911–914, arXiv:1711.06223 [astro-ph.HE].

[212] D. Hooper et al., *HAWC Observations Strongly Favor Pulsar Interpretations of the Cosmic-Ray Positron Excess*, Phys. Rev. D **96** (2017) 103013, arXiv:1702.08436 [astro-ph.HE].

[213] F. Kahlhoefer, *On the LHC sensitivity for non-thermalised hidden sectors*, Phys. Lett. B **779** (2018) 388–392, arXiv:1801.07621 [hep-ph].

[214] D. Bauer et al., *Dark matter in the coming decade: Complementary paths to discovery and beyond*, Phys. Dark Univ. **7–8** (2015) 16–23, arXiv:1305.1605 [hep-ph].

[215] D. Abercrombie et al., *Dark Matter Benchmark Models for Early LHC Run-2 Searches: Report of the ATLAS/CMS Dark Matter Forum*, arXiv:1507.00966 [hep-ex].

[216] P. J. Fox et al., *Missing Energy Signatures of Dark Matter at the LHC*, Phys. Rev. D **85** (2012) 056011, arXiv:1109.4398 [hep-ph].

[217] O. Buchmueller, M. J. Dolan, and C. McCabe, *Beyond Effective Field Theory for Dark Matter Searches at the LHC*, JHEP **01** (2014) 025, arXiv:1308.6799 [hep-ph].

[218] M. Cirelli, E. Del Nobile, and P. Panci, *Tools for model-independent bounds in direct dark matter searches*, JCAP **1310** (2013) 019, arXiv:1307.5955 [hep-ph].

[219] J. Abdallah et al., *Simplified Models for Dark Matter Searches at the LHC*, Phys. Dark Univ. **9–10** (2015) 8–23, arXiv:1506.03116 [hep-ph].

[220] G. Busoni et al., *On the Validity of the Effective Field Theory for Dark Matter Searches at the LHC*, Phys. Lett. B **728** (2014) 412–421, arXiv:1307.2253 [hep-ph].

[221] ATLAS Collaboration, M. Aaboud et al., *Measurement of detector-corrected observables sensitive to the anomalous production of events with jets and large missing transverse momentum in pp collisions at $\sqrt{s} = 13$ TeV using the ATLAS detector*, Eur. Phys. J. C **77** (2017) 765, arXiv:1707.03263 [hep-ex].

[222] ATLAS Collaboration, M. Aaboud et al., *Search for dark matter and other new phenomena in events with an energetic jet and large missing transverse momentum using the ATLAS detector*, JHEP **01** (2018) 126, arXiv:1711.03301 [hep-ex].

[223] CMS Collaboration, A. M. Sirunyan et al., *Search for new physics in final states with an energetic jet or a hadronically decaying W or Z boson and transverse momentum imbalance at $\sqrt{s} = 13$ TeV*, Phys. Rev. D **97** (2018) 092005, arXiv:1712.02345 [hep-ex].

[224] ATLAS Collaboration, M. Aaboud et al., *Search for dark matter at $\sqrt{s} = 13$ TeV in final states containing an energetic photon and large missing transverse momentum with the ATLAS detector*, Eur. Phys. J. C **77** (2017) 393, arXiv:1704.03848 [hep-ex].

[225] CMS Collaboration, A. M. Sirunyan et al., *Search for new physics in final states with a single photon and missing transverse momentum in proton-proton collisions at $\sqrt{s} = 13$ TeV*, Submitted to: JHEP (2018), arXiv:1810.00196 [hep-ex].

[226] ATLAS Collaboration, M. Aaboud et al., *Search for dark matter in events with a hadronically decaying vector boson and missing transverse momentum in pp collisions at $\sqrt{s} = 13$ TeV with the ATLAS detector*, JHEP **10** (2018) 180, arXiv:1807.11471 [hep-ex].

[227] ATLAS Collaboration, M. Aaboud et al., *Search for an invisibly decaying Higgs boson or dark matter candidates produced in association with a Z boson in pp collisions at $\sqrt{s} = 13$ TeV with the ATLAS detector*, Phys. Lett. B **776** (2018) 318–337, arXiv:1708.09624 [hep-ex].

[228] CMS Collaboration, A. M. Sirunyan et al., *Search for new physics in events with a leptonically decaying Z boson and a large transverse momentum imbalance in proton-proton collisions at $\sqrt{s} = 13$ TeV*, Eur. Phys. J. C **78** (2018) 291, arXiv:1711.00431 [hep-ex].

[229] ATLAS Collaboration, M. Aaboud et al., *Search for dark matter produced in association with bottom or top quarks in $\sqrt{s} = 13$ TeV pp collisions with the ATLAS detector*, Eur. Phys. J. C **78** (2018) 18, arXiv:1710.11412 [hep-ex].

[230] ATLAS Collaboration, M. Aaboud et al., *Search for top-squark pair production in final states with one lepton, jets, and missing transverse momentum using 36 fb^{-1} of $\sqrt{s} = 13$ TeV pp collision data with the ATLAS detector*, JHEP **06** (2018) 108, arXiv:1711.11520 [hep-ex].

[231] ATLAS Collaboration, M. Aaboud et al., *Search for large missing transverse momentum in association with one top-quark in proton-proton collisions at $\sqrt{s} = 13$ TeV with the ATLAS detector*, Submitted to: JHEP (2018), arXiv:1812.09743 [hep-ex].

[232] CMS Collaboration, A. M. Sirunyan et al., *Search for dark matter in events with energetic, hadronically decaying top quarks and missing transverse momentum at $\sqrt{s} = 13$ TeV*, JHEP **2018** (2018) 27.

[233] CMS Collaboration, A. M. Sirunyan et al., *Search for dark matter produced in association with heavy-flavor quark pairs in proton-proton collisions at $\sqrt{s} = 13$ TeV*, Eur. Phys. J. C **77** (2017) 845, arXiv:1706.02581 [hep-ex].

[234] CMS Collaboration, A. M. Sirunyan et al., *Search for dark matter in events with energetic, hadronically decaying top quarks and missing transverse momentum at $\sqrt{s} = 13$ TeV*, JHEP **06** (2018) 027, arXiv:1801.08427 [hep-ex].

[235] CMS Collaboration, A. M. Sirunyan et al., *Search for dark matter particles produced in association with a top quark pair at $\sqrt{s} = 13$ TeV*, Submitted to: Phys. Rev. Lett. (2018), arXiv:1807.06522 [hep-ex].

[236] ATLAS Collaboration, M. Aaboud et al., *Search for new phenomena in dijet events using 37 fb^{-1} of pp collision data collected at $\sqrt{s} = 13$ TeV with the ATLAS detector*, Phys. Rev. D **96** (2017) 052004, arXiv:1703.09127 [hep-ex].

[237] ATLAS Collaboration, M. Aaboud et al., *Search for light resonances decaying to boosted quark pairs and produced in association with a photon or a jet in proton-proton collisions at $\sqrt{s} = 13$ TeV with the ATLAS detector*, Submitted to: Phys. Lett. B (2018), arXiv:1801.08769 [hep-ex].

[238] ATLAS Collaboration, M. Aaboud et al., *Search for low-mass dijet resonances using trigger-level jets with the ATLAS detector in pp collisions at $\sqrt{s} = 13$ TeV*, Phys. Rev. Lett. **121** (2018) 081801, arXiv:1804.03496 [hep-ex].

[239] ATLAS Collaboration, M. Aaboud et al., *Search for resonances in the mass distribution of jet pairs with one or two jets identified as b-jets in proton-proton collisions at $\sqrt{s} = 13$ TeV with the ATLAS detector*, Phys. Rev. D **98** (2018) 032016, arXiv:1805.09299 [hep-ex].

[240] ATLAS Collaboration, M. Aaboud et al., *Search for dijet resonances in events with an isolated lepton using $\sqrt{s} = 13$ TeV proton-proton collision data collected by the ATLAS detector*, ATLAS-CONF-2018-015, CERN, 2018, https://cds.cern.ch/record/2621126.

[241] ATLAS Collaboration, M. Aaboud et al., *Search for low-mass resonances decaying into two jets and produced in association with a photon using pp collisions at $\sqrt{s} = 13$ TeV with the ATLAS detector*, Submitted to: Phys. Lett. (2019), arXiv:1901.10917 [hep-ex].

[242] CMS Collaboration, A. M. Sirunyan et al., *Searches for dijet resonances in pp collisions at $\sqrt{s} = 13$ TeV using data collected in 2016.*, CMS-PAS-EXO-16-056, CERN, 2017, https://cds.cern.ch/record/2256873.

[243] CMS Collaboration, A. M. Sirunyan et al., *Search for low mass vector resonances decaying into quark-antiquark pairs in proton-proton collisions at $\sqrt{s} = 13$ TeV*, JHEP **01** (2018) 097, arXiv:1710.00159 [hep-ex].

[244] CMS Collaboration, A. M. Sirunyan et al., *Search for new physics in dijet angular distributions using proton-proton collisions at $\sqrt{s} = 13$ TeV and constraints on dark matter and other models*, Eur. Phys. J. C **78** (2018) 789, arXiv:1803.08030 [hep-ex].

[245] CMS Collaboration, A. M. Sirunyan et al., *Search for narrow and broad dijet resonances in proton-proton collisions at $\sqrt{s} = 13$ TeV and constraints on dark matter mediators and other new particles*, JHEP **08** (2018) 130, arXiv:1806.00843 [hep-ex].

[246] ATLAS Collaboration, M. Aaboud et al., *Search for new high-mass phenomena in the dilepton final state using 36 fb^{-1} of proton-proton collision data at $\sqrt{s} = 13$ TeV with the ATLAS detector*, JHEP **10** (2017) 182, arXiv:1707.02424 [hep-ex].

[247] S. Kanemura et al., *Can WIMP Dark Matter overcome the Nightmare Scenario?*, Phys. Rev. D **82** (2010) 055026, arXiv:1005.5651 [hep-ph].

[248] A. Djouadi et al., *Implications of LHC searches for Higgs-portal dark matter*, Phys. Lett. B **709** (2012) 65–69, arXiv:1112.3299 [hep-ph].

[249] A. Djouadi et al., *Direct Detection of Higgs-Portal Dark Matter at the LHC*, Eur. Phys. J. C **73** (2013) 2455, arXiv:1205.3169 [hep-ph].

[250] ATLAS Collaboration, G. Aad et al., *Search for invisible decays of a Higgs boson using vector-boson fusion in pp collisions at $\sqrt{s} = 8$ TeV with the ATLAS detector*, JHEP **01** (2016) 172, arXiv:1508.07869 [hep-ex].

[251] CMS Collaboration, V. Khachatryan et al., *Searches for invisible decays of the Higgs boson in pp collisions at $\sqrt{s}$ = 7, 8, and 13 TeV*, JHEP **02** (2017) 135, arXiv:1610.09218 [hep-ex].

[252] ATLAS Collaboration, G. Aad et al., *Search for invisible decays of the Higgs boson produced in association with a hadronically decaying vector boson in pp collisions at $\sqrt{s}$ = 8 TeV with the ATLAS detector*, Eur. Phys. J. C **75** (2015) 337, arXiv:1504.04324 [hep-ex].

[253] ATLAS Collaboration, M. Aaboud et al., *Search for invisible Higgs boson decays in vector boson fusion at $\sqrt{s} = 13$ TeV with the ATLAS detector*, Submitted to: Phys. Lett. (2018), arXiv:1809.06682 [hep-ex].

[254] ATLAS Collaboration, M. Aaboud et al., *Combination of searches for invisible Higgs boson decays with the ATLAS experiment*, ATLAS-CONF-2018-054, CERN, 2018, https://cds.cern.ch/record/2649407.

[255] ATLAS Collaboration, G. Aad et al., *Constraints on new phenomena via Higgs boson couplings and invisible decays with the ATLAS detector*, JHEP **11** (2015) 206, arXiv:1509.00672 [hep-ex].

[256] CMS Collaboration, A. M. Sirunyan et al., *Search for invisible decays of the Higgs boson produced through vector boson fusion at $\sqrt{s} = 13$ TeV*, CMS-PAS-HIG-17-023, CERN, 2018, https://cds.cern.ch/record/2308434.

[257] ATLAS Collaboration, M. Aaboud et al., *Search for dark matter in association with a Higgs boson decaying to b-quarks in pp collisions at $\sqrt{s} = 13$ TeV with the ATLAS detector*, Phys. Lett. B **765** (2017) 11–31, arXiv:1609.04572 [hep-ex].

[258] ATLAS Collaboration, M. Aaboud et al., *Search for Dark Matter Produced in Association with a Higgs Boson Decaying to $b\bar{b}$ using 36 fb^{-1} of pp collisions at $\sqrt{s} = 13$ TeV with the ATLAS Detector*, Phys. Rev. Lett. **119** (2017) 181804, arXiv:1707.01302 [hep-ex].

[259] CMS Collaboration, A. M. Sirunyan et al., *Search for associated production of dark matter with a Higgs boson that decays to a pair of bottom quarks*, CMS-PAS-EXO-16-050, CERN, 2018, https://cds.cern.ch/record/2628473.

[260] ATLAS Collaboration, M. Aaboud et al., *Search for dark matter in association with a Higgs boson decaying to two photons at $\sqrt{s} = 13$ TeV with the ATLAS detector*, Phys. Rev. D **96** (2017) 112004, arXiv:1706.03948 [hep-ex].

[261] CMS Collaboration, A. M. Sirunyan et al., *Search for Dark Matter Produced in Association with a Higgs Boson Decaying to Two Photons*, CMS-PAS-EXO-16-054, CERN, 2017, https://cds.cern.ch/record/2264691.

[262] CMS Collaboration, A. M. Sirunyan et al., *Search for dark matter produced in association with a Higgs boson decaying to $\gamma\gamma$ or $\tau^+\tau^-$ at $\sqrt{s} = 13$ TeV*, JHEP **09** (2018) 046, arXiv:1806.04771 [hep-ex].

[263] ATLAS Collaboration, G. Aad et al., *Measurements of the Higgs boson production cross section at 7, 8 and 13 TeV centre-of-mass energies and search for new physics at 13 TeV in the $H \to ZZ^* \to \ell^+\ell^-\ell'^+\ell'^-$ final state with the ATLAS detector*, ATLAS-CONF-2015-059, CERN, 2015, https://cds.cern.ch/record/2114825.

[264] A. A. Petrov and W. Shepherd, *Searching for dark matter at LHC with Mono-Higgs production*, Phys. Lett. B **730** (2014) 178–183, arXiv:1311.1511 [hep-ph].

[265] L. Carpenter et al., *Mono-Higgs-boson: A new collider probe of dark matter*, Phys. Rev. D **89** (2014) 075017, arXiv:1312.2592 [hep-ph].

[266] A. Berlin, T. Lin, and L.-T. Wang, *Mono-Higgs Detection of Dark Matter at the LHC*, JHEP **1406** (2014) 078, arXiv:1402.7074 [hep-ph].

[267] ATLAS Collaboration, G. Aad et al., *Search for dark matter produced in association with a Higgs boson decaying to two bottom quarks in pp collisions at $\sqrt{s} = 8$ TeV with the ATLAS detector*, Phys. Rev. D **93** (2016) 072007, arXiv:1510.06218 [hep-ex].

[268] J. McDonald, *Gauge singlet scalars as cold dark matter*, Phys. Rev. D **50** (1994) 3637–3649, arXiv:hep-ph/0702143.

[269] C. P. Burgess, M. Pospelov, and T. ter Veldhuis, *The Minimal model of nonbaryonic dark matter: A Singlet scalar*, Nucl. Phys. B **619** (2001) 709–728, arXiv:hep-ph/0011335.

[270] B. Patt and F. Wilczek, *Higgs-field portal into hidden sectors*, arXiv:hep-ph/0605188.

[271] Y. G. Kim and K. Y. Lee, *The Minimal model of fermionic dark matter*, Phys. Rev. D **75** (2007) 115012, arXiv:hep-ph/0611069.

[272] J. March-Russell et al., *Heavy Dark Matter Through the Higgs Portal*, JHEP **07** (2008) 058, arXiv:0801.3440 [hep-ph].

[273] I. Low et al., *The dark side of the Higgs boson*, Phys. Rev. D **85** (2012) 015009, arXiv:1110.4405 [hep-ph].

[274] L. Lopez-Honorez, T. Schwetz, and J. Zupan, *Higgs portal, fermionic dark matter, and a Standard Model like Higgs at 125 GeV*, Phys. Lett. B **716** (2012) 179–185, arXiv:1203.2064 [hep-ph].

[275] G. Belanger et al., *Status of invisible Higgs decays*, Phys. Lett. B **723** (2013) 340–347, arXiv:1302.5694 [hep-ph].

[276] XENON100 Collaboration, E. Aprile et al., *Implications on inelastic dark matter from 100 live days of XENON100 data*, Phys. Rev. D **84** (2011) 061101.

[277] J.-Y. Chen, E. W. Kolb, and L.-T. Wang, *Dark matter coupling to electroweak gauge and Higgs bosons: an effective field theory approach*, Phys. Dark Univ. **2** (2013) 200–218, arXiv:1305.0021 [hep-ph].

[278] G. Busoni et al., *On the Validity of the Effective Field Theory for Dark Matter Searches at the LHC, Part II: Complete Analysis for the s-channel*, JCAP **1406** (2014) 060, arXiv:1402.1275 [hep-ph].

[279] A. Askew et al., *Searching for Dark Matter at Hadron Colliders*, Int. J. Mod. Phys. A **29** (2014) 1430041, arXiv:1406.5662 [hep-ph].

[280] J. L. Hewett and T. G. Rizzo, *Low-energy phenomenology of superstring-inspired E6 models*, Phys. Rep. **183** (1989) 193–381.

[281] M. Cvetic and P. Langacker, *Implications of Abelian extended gauge structures from string models*, Phys. Rev. D **54** (1996) 3570–3579, arXiv:hep-ph/9511378.

[282] M. Carena et al., *Z' gauge bosons at the Tevatron*, Phys. Rev. D **70** (2004) 093009, arXiv:hep-ph/0408098.

[283] P. Langacker, *The Physics of Heavy Z' Gauge Bosons*, Rev. Mod. Phys. **81** (2009) 1199–1228, arXiv:0801.1345 [hep-ph].

[284] A. Leike, *The Phenomenology of extra neutral gauge bosons*, Phys. Rept. **317** (1999) 143–250, arXiv:hep-ph/9805494.

[285] D. Suematsu and Y. Yamagishi, *Radiative symmetry breaking in a supersymmetric model with an extra U(1)*, Int. J. Mod. Phys. A **10** (1995) 4521–4536, arXiv:hep-ph/9411239.

[286] G. C. Branco et al., *Theory and phenomenology of two-Higgs-doublet models*, Phys. Rept. **516** (2012) 1–102, arXiv:1106.0034 [hep-ph].

[287] N. Craig, J. Galloway, and S. Thomas, *Searching for Signs of the Second Higgs Doublet*, arXiv:1305.2424 [hep-ph].

[288] J. Bernon et al., *Scrutinizing the alignment limit in two-Higgs-doublet models: $m_h = 125$ GeV*, Phys. Rev. D **92** (2015) 075004, arXiv:1507.00933 [hep-ph].

[289] M. Misiak and M. Steinhauser, *Weak radiative decays of the B meson and bounds on $M_{H^\pm}$ in the Two-Higgs-Doublet Model*, Eur. Phys. J. C **77** (2017) 201, arXiv:1702.04571 [hep-ph].

[290] J. Bernon, L. Bian, and Y. Jiang, *A new insight into the phase transition in the early Universe with two Higgs doublets*, arXiv:1712.08430 [hep-ph].

[291] P. Sikivie et al., *Isospin breaking in technicolor models*, Nucl. Phys. B **173** (1980) 189–207.

[292] O. S. Brüning et al., *LHC design report. 1. The LHC main ring*, CERN-2004-003-V-1, CERN, 2004, https://cds.cern.ch/record/782076.

[293] O. S. Brüning et al., *LHC design report. 2. The LHC infrastructure and general services*, CERN-2004-003-V-2, CERN, 2004, https://cds.cern.ch/record/782076.

[294] M. Benedikt et al., *LHC design report. 3. The LHC injector chain*, CERN-2004-003, CERN, 2004, https://cds.cern.ch/record/823808.

[295] L. Evans and P. Bryant, *LHC machine*, JINST **3** (2008) S08001.

[296] LEP Collaboration, *LEP design report*, CERN-LEP-84-01, CERN, 1984, https://cds.cern.ch/record/102083.

[297] ATLAS Collaboration, G. Aad et al., *The ATLAS Experiment at the CERN Large Hadron Collider*, JINST **3** (2008) S08003.

[298] CMS Collaboration, P. Aarnio et al., *CMS technical proposal*, CERN-LHCC-94-38, CERN, 1994, https://cds.cern.ch/record/290969.

[299] ALICE Collaboration, S. Ahmad et al., *ALICE: Technical proposal for a large ion collider experiment at the CERN LHC*, CERN-LHCC-95-71, CERN, 1995, https://cds.cern.ch/record/293391.

[300] LHCb Collaboration, S. Amato et al., *LHCb technical proposal*, CERN-LHCC-98-004, CERN, 1998, https://cds.cern.ch/record/622031.

[301] W. Commons, *The free media repository*, 2018. https://commons.wikimedia.org/w/index.php?title=File:Cern-accelerator-complex.svg&oldid=224873166. [Online; accessed 1-March-2018, modified version].

[302] CMS-TOTEM Collaboration, M. Albrow et al., *CMS-TOTEM Precision Proton Spectrometer*, TOTEM-TDR-003, CERN, 2014, https://cds.cern.ch/record/1753795.

[303] LHCf Collaboration, O. Adriani et al., *LHCf experiment: Technical Design Report*, LHCF-TDR-001, CERN, 2006, https://cds.cern.ch/record/926196.

[304] MoEDAL Collaboration, J. Pinfold et al., *Technical Design Report of the MoEDAL Experiment*, MoEDAL-TDR-001, CERN, 2009, https://cds.cern.ch/record/1181486.

[305] M. Lamont, *Status of the LHC*, J. Phys. Conf. Ser. **455** (2013) 012001.

[306] ATLAS Collaboration, Z. Marshall, *Simulation of Pile-up in the ATLAS Experiment*, J. Phys. Conf. Ser. **513** (2014) 022024. https://stacks.iop.org/1742-6596/513/i=2/a=022024.

[307] ATLAS Collaboration, M. Aaboud et al., *Luminosity Public Results Run 2*, 2017. https://twiki.cern.ch/twiki/bin/view/AtlasPublic/LuminosityPublicResultsRun2. [Online; accessed 5-April-2018].

[308] ATLAS Collaboration, A. Airapetian et al., *ATLAS detector and physics performance: Technical Design Report, 1*, CERN-LHCC-99-014, CERN, 1999, https://cds.cern.ch/record/391176.

[309] ATLAS Collaboration, G. Aad et al., *The ATLAS Inner Detector commissioning and calibration*, Eur. Phys. J. C **70** (2010) 787.

[310] ATLAS Collaboration, Z. Meng, *Performance of the ATLAS liquid argon calorimeter*, DESY-PROC-2010-01, DESY, 2010, https://inspirehep.net/record/891081/.

[311] ATLAS Collaboration, N. Nikiforou, *Performance of the ATLAS Liquid Argon Calorimeter after three years of LHC operation and plans for a future upgrade*, arXiv:1306.6756 [physics.ins-det].

[312] ATLAS Collaboration, G. Aad et al., *Measurement of the muon reconstruction performance of the ATLAS detector using 2011 and 2012 LHC proton-proton collision data*, Eur. Phys. J. C **74** (2014) 3130, arXiv:1407.3935 [hep-ex].

[313] ATLAS Collaboration, N. C. Benekos et al., *ATLAS Inner Detector Performance*, ATL-INDET-2004-002, CERN, 2003, https://cds.cern.ch/record/688762.

[314] ATLAS Collaboration, G. Aad et al., *ATLAS inner detector: Technical Design Report, 1*, CERN-LHCC-97-016, CERN, 1997, https://cds.cern.ch/record/331063.

[315] ATLAS Collaboration, M. Aaboud et al., *Track Reconstruction Performance of the ATLAS Inner Detector at $\sqrt{s} = 13$ TeV*, ATL-PHYS-PUB-2015-018, CERN, 2015, https://cds.cern.ch/record/2037683.

[316] ATLAS Collaboration, M. Aleksa et al., *Measurement of the ATLAS solenoid magnetic field*, JINST **3** (2008) P04003.

[317] ATLAS Collaboration, G. Aad et al., *ATLAS pixel detector electronics and sensors*, JINST **3** (2008) P07007.

[318] ATLAS Collaboration, M. Capeans et al., *ATLAS Insertable B-Layer Technical Design Report*, CERN-LHCC-2010-013, CERN, 2010, https://cds.cern.ch/record/1291633.

[319] ATLAS Collaboration, G. Aad et al., *ATLAS Liquid-Argon Calorimeter: Technical Design Report*, CERN-LHCC-96-041, CERN, 1996, https://cds.cern.ch/record/331061.

[320] ATLAS Collaboration, G. Aad et al., *ATLAS Tile Calorimeter: Technical Design Report*, CERN-LHCC-96-042, CERN, 1996, https://cds.cern.ch/record/331062.

[321] ATLAS Collaboration, G. Aad et al., *ATLAS muon spectrometer: Technical Design Report*, CERN-LHCC-97-022, CERN, 1997, https://cds.cern.ch/record/331068.

[322] ATLAS Collaboration, J. Pequenao, *Computer generated image of the ATLAS Muons subsystem*, 2008. https://cds.cern.ch/record/1095929. [Online; accessed 24-April-2018].

[323] A. Yamamoto et al., *The ATLAS central solenoid*, Nucl. Instrum. Methods Phys. Res. Sec. A **584** (2008) 53–74.

[324] ATLAS Collaboration, M. Aaboud et al., *Performance of the ATLAS Trigger System in 2015*, Eur. Phys. J. C **77** (2017) 317, arXiv:1611.09661 [hep-ex].

[325] R. Achenbach et al., *The ATLAS Level-1 Calorimeter Trigger*, J. Instrum. **3** (2008) P03001.

[326] ATLAS Collaboration, D. Kobayashi, *Performance of the ATLAS Muon Trigger in Run I and Upgrades for Run II*, J. Phys. Conf. Ser. **664** (2015) 092016.

[327] ATLAS Collaboration, M. Aaboud et al., *Luminosity determination in pp collisions at $\sqrt{s}$ = 8 TeV using the ATLAS detector at the LHC*, Eur. Phys. J. C **76** (2016) 653, arXiv:1608.03953 [hep-ex].

[328] P. Jenni and M. Nessi, *ATLAS Forward Detectors for Luminosity Measurement and Monitoring*, CERN-LHCC-2004-010, CERN, 2004, https://cds.cern.ch/record/721908.

[329] P. Jenni et al., *ATLAS Forward Detectors for Measurement of Elastic Scattering and Luminosity*. Technical Design Report ATLAS. CERN, 2008. https://cds.cern.ch/record/1095847.

[330] S. van der Meer, *Calibration of the effective beam height in the ISR*, CERN-ISR-PO-68-31, CERN, 1968, https://cds.cern.ch/record/296752.

[331] C. Rubbia, *Measurement of the luminosity of $p\bar{p}$ collider with a (generalized) Van der Meer method*, CERN-$p\bar{p}$-Note-38, CERN, 1977, https://cds.cern.ch/record/1025746.

[332] ATLAS Collaboration, G. Aad et al., *ATLAS computing: technical design report*, CERN-LHCC-2005-022, CERN, 2005, https://cds.cern.ch/record/837738.

[333] ATLAS Collaboration, T. Cornelissen et al., *The new ATLAS track reconstruction (NEWT)*, J. Phys. Conf. Ser. **119** (2008) 032014.

[334] ATLAS Collaboration, T. Cornelissen et al., *Concepts, design and implementation of the ATLAS New Tracking (NEWT)*, ATL-SOFT-PUB-2007-007, CERN, 2007, https://cds.cern.ch/record/1020106.

[335] ATLAS Collaboration, M. Aaboud et al., *Performance of the ATLAS Track Reconstruction Algorithms in Dense Environments in LHC Run 2*, Eur. Phys. J. C **77** (2017) 673, arXiv:1704.07983 [hep-ex].

[336] R. Fruhwirth, *Application of Kalman filtering to track and vertex fitting*, Nucl. Instr. Meth. A **262** (1987) 444.

[337] ATLAS Collaboration, I. Gavrilenko, *Description of Global Pattern Recognition Program (XKalman)*, ATL-INDET-97-165, CERN, 1997, https://cds.cern.ch/record/686017.

[338] G. Piacquadio, K. Prokofiev, and A. Wildauer, *Primary vertex reconstruction in the ATLAS experiment at LHC*, J. Phys. Conf. Ser. **119** (2008) 032033.

[339] ATLAS Collaboration, M. Aaboud et al., *Reconstruction of primary vertices at the ATLAS experiment in Run 1 proton-proton collisions at the LHC*, Eur. Phys. J. C **77** (2017) 332, arXiv:1611.10235 [physics.ins-det].

[340] ATLAS Collaboration, G. Aad et al., *Muon reconstruction performance of the ATLAS detector in proton-proton collision data at $\sqrt{s} = 13$ TeV*, Eur. Phys. J. C **76** (2016) 292, arXiv:1603.05598 [hep-ex].

[341] ATLAS Collaboration, M. Aaboud et al., *ATLAS Muon Combined Performance with the full 2016 dataset*, 2017. https://atlas.web.cern.ch/Atlas/GROUPS/PHYSICS/PLOTS/MUON-2017-001/. [Online; accessed 28-January-2018].

[342] ATLAS Collaboration, G. Aad et al., *Electron efficiency measurements with the ATLAS detector using the 2015 LHC proton-proton collision data*, ATLAS-CONF-2016-024, CERN, 2016, https://cds.cern.ch/record/2157687.

[343] ATLAS Collaboration, G. Aad et al., *Electron and photon energy calibration with the ATLAS detector using data collected in 2015 at $\sqrt{s} = 13$ TeV*, ATL-PHYS-PUB-2016-015, CERN, 2016, https://cds.cern.ch/record/2203514.

[344] ATLAS Collaboration, W. Lampl et al., *Calorimeter Clustering Algorithms: Description and Performance*, ATL-LARG-PUB-2008-002, CERN, 2008, https://cds.cern.ch/record/1099735.

[345] ATLAS Collaboration, G. Aad et al., *Improved electron reconstruction in ATLAS using the gaussian sum filter-based model for bremsstrahlung*, ATLAS-CONF-2012-047, CERN, 2012, https://cds.cern.ch/record/1449796.

[346] ATLAS Collaboration, G. Aad et al., *Electron reconstruction and identification efficiency measurements in 2016 Data*,. https://atlas.web.cern.ch/Atlas/GROUPS/PHYSICS/PLOTS/EGAM-2017-003/. [Online; accessed 15-May-2018].

[347] ATLAS Collaboration, M. Aaboud et al., *Electron and photon energy calibration with the ATLAS detector using 2015-2016 LHC proton-proton collision data*, Submitted to: JINST (2018), arXiv:1812.03848 [hep-ex].

[348] J. M. Butterworth et al., *Jet substructure as a new Higgs search channel at the LHC*, Phys. Rev. Lett. **100** (2008) 242001, arXiv:0802.2470 [hep-ph].

[349] M. Cacciari, G. P. Salam, and G. Soyez, *The anti-k_t jet clustering algorithm*, JHEP **04** (2008) 63.

[350] ATLAS Collaboration, G. Aad et al., *Jet energy measurement and its systematic uncertainty in proton-proton collisions at $\sqrt{s} = 7$ TeV with the ATLAS detector*, Eur. Phys. J. C **75** (2015) 17, arXiv:1406.0076 [hep-ex].

[351] ATLAS Collaboration, M. Aaboud et al., *Jet energy scale measurements and their systematic uncertainties in proton-proton collisions at $\sqrt{s} = 13$ TeV with the ATLAS detector*, Phys. Rev. D **96** (2017) 072002, arXiv:1703.09665 [hep-ex].

[352] M. Cacciari and G. P. Salam, *Dispelling the N^3 myth for the k_t jet-finder*, Phys. Lett. B **641** (2006) 57.

[353] M. Cacciari, G. P. Salam, and G. Soyez, *FastJet user manual*, Eur. Phys. J. C **72** (2012) 1896.

[354] ATLAS Collaboration, G. Aad et al., *Topological cell clustering in the ATLAS calorimeters and its performance in LHC Run 1*, Eur. Phys. J. C **77** (2017) 490, arXiv:1603.02934 [hep-ex].

[355] ATLAS Collaboration, G. Aad et al., *Performance of pile-up mitigation techniques for jets in pp collisions at $\sqrt{s} = 8$ TeV using the ATLAS detector*, Eur. Phys. J. C **76** (2016) 581, arXiv:1510.03823 [hep-ex].

[356] ATLAS Collaboration, G. Aad et al., *Jet global sequential corrections with the ATLAS detector in proton-proton collisions at $\sqrt{s} = 8$ TeV*, ATLAS-CONF-2015-002, CERN, 2015, https://cds.cern.ch/record/2001682.

[357] ATLAS Collaboration, M. Aaboud et al., *JES Public Plots for Moriond 2017*, 2017. https://atlas.web.cern.ch/Atlas/GROUPS/PHYSICS/PLOTS/JETM-2017-003/. [Online; accessed 28-January-2018].

[358] ATLAS Collaboration, G. Aad et al., *Jet energy resolution in proton-proton collisions at $\sqrt{s} = 7$ TeV recorded in 2010 with the ATLAS detector*, Eur. Phys. J. C **73** (2013) 2306.

[359] ATLAS Collaboration, G. Aad et al., *Monte Carlo Calibration and Combination of In-situ Measurements of Jet Energy Scale, Jet Energy Resolution and Jet Mass in ATLAS*, ATLAS-CONF-2015-037, CERN, 2015, https://cds.cern.ch/record/2044941.

[360] ATLAS Collaboration, T. Barillari et al., *Local Hadronic Calibration*, ATL-LARG-PUB-2009-001-2., CERN, 2008, https://cds.cern.ch/record/1112035.

[361] ATLAS Collaboration, G. Aad et al., *Jet energy measurement with the ATLAS detector in proton-proton collisions at $\sqrt{s} = 7$ TeV*, Eur. Phys. J. C **73** (2013) 2304, arXiv:1112.6426 [hep-ex].

[362] ATLAS Collaboration, G. Aad et al., *Performance of jet substructure techniques for large-R jets in proton-proton collisions at $\sqrt{s}$ = 7 TeV using the ATLAS detector*, JHEP **09** (2013) 076, arXiv:1306.4945 [hep-ex].

[363] S. D. Ellis, C. K. Vermilion, and J. R. Walsh, *Techniques for improved heavy particle searches with jet substructure*, Phys. Rev. D **80** (2009) 051501, arXiv:0903.5081 [hep-ph].

[364] D. Krohn, J. Thaler, and L.-T. Wang, *Jet Trimming*, JHEP **02** (2010) 084, arXiv:0912.1342 [hep-ph].

[365] S. Catani et al., *Longitudinally-invariant anti-k_t clustering algorithms for hadron-hadron collisions*, Nucl. Phys. B **406** (1993) 187–224.

[366] ATLAS Collaboration, G. Aad et al., *Determination of the jet energy scale and resolution at ATLAS using Z/γ-jet events in data at $\sqrt{s} = 8$ TeV*, ATLAS-CONF-2015-057, CERN, 2015, https://cds.cern.ch/record/2059846.

[367] ATLAS Collaboration, G. Aad et al., *Data-driven determination of the energy scale and resolution of jets reconstructed in the ATLAS calorimeters using dijet and multijet events at $\sqrt{s} = 8$ TeV*, ATLAS-CONF-2015-017, CERN, 2015, https://cds.cern.ch/record/2008678.

[368] ATLAS Collaboration, M. Aaboud et al., *In-situ measurements of the ATLAS large-radius jet response in 13 TeV pp collisions*, ATLAS-CONF-2017-063, CERN, 2017, https://cds.cern.ch/record/2275655.

[369] ATLAS Collaboration, M. Aaboud et al., *Jet mass reconstruction with the ATLAS Detector in early Run 2 data*, ATLAS-CONF-2016-035, CERN, 2016, https://cds.cern.ch/record/2200211.

[370] M. Cacciari and G. P. Salam, *Pileup subtraction using jet areas*, Phys. Lett. B **659** (2008) 119.

[371] M. Cacciari, G. P. Salam, and G. Soyez, *The Catchment Area of Jets*, JHEP **04** (2008) 005, arXiv:0802.1188 [hep-ph].

[372] D. Krohn, J. Thaler, and L.-T. Wang, *Jets with Variable R*, JHEP **06** (2009) 059, arXiv:0903.0392 [hep-ph].

[373] ATLAS Collaboration, M. Aaboud et al., *Variable Radius, Exclusive-k_T, and Center-of-Mass Subjet Reconstruction for Higgs($\to b\bar{b}$) Tagging in ATLAS*, ATL-PHYS-PUB-2017-010, CERN, 2017, https://cds.cern.ch/record/2268678.

[374] ATLAS Collaboration, M. Aaboud et al., *Measurements of b-jet tagging efficiency with the ATLAS detector using $t\bar{t}$ events at $\sqrt{s} = 13$ TeV*, JHEP **08** (2018) 089, arXiv:1805.01845 [hep-ex].

[375] A. Höcker et al., *TMVA - Toolkit for Multivariate Data Analysis*, PoS **ACAT** (2007) 040, arXiv:physics/0703039.

[376] ATLAS Collaboration, G. Aad et al., *Performance of b-Jet Identification in the ATLAS Experiment*, JINST **11** (2016) 04008, arXiv:1512.01094 [hep-ex].

[377] ATLAS Collaboration, G. Aad et al., *Optimisation of the ATLAS b-tagging performance for the 2016 LHC Run*, ATL-PHYS-PUB-2016-012, CERN, 2016, https://cds.cern.ch/record/2160731.

[378] ATLAS Collaboration, M. Aaboud et al., *Measurement of b-tagging Efficiency of c-jets in $t\bar{t}$ Events Using a Likelihood Approach with the ATLAS Detector*, ATLAS-CONF-2018-001, CERN, 2018, https://cds.cern.ch/record/2306649.

[379] ATLAS Collaboration, M. Aaboud et al., *Calibration of the b-tagging eflciency on charm jets using a sample of $W + c$ events with $\sqrt{s}$ = 13 TeV ATLAS data*, ATLAS-CONF-2018-055, CERN, 2018, https://cds.cern.ch/record/2652195.

[380] ATLAS Collaboration, M. Aaboud et al., *Calibration of light-flavour jet b-tagging rates on ATLAS proton-proton collision data at $\sqrt{s} = 13$ TeV*, ATLAS-CONF-2018-006, CERN, 2018, https://cds.cern.ch/record/2314418.

[381] ATLAS Collaboration, A. Buzatu and W. Wang, *Object selections for SM Higgs boson produced in association with a vector boson in which $H \to bb$ and V decays leptonically with Run-2 data: Object support note for VH(bb) 2015+2016 dataset publication*, ATL-COM-PHYS-2016-1674, CERN, 2016, https://cds.cern.ch/record/2233686.

[382] ATLAS Collaboration, G. Aad et al., *Reconstruction, Energy Calibration, and Identification of Hadronically Decaying Tau Leptons in the ATLAS Experiment for Run-2 of the LHC*, ATL-PHYS-PUB-2015-045, CERN, 2015, https://cds.cern.ch/record/2064383.

[383] ATLAS Collaboration, M. Aaboud et al., *Measurement of the tau lepton reconstruction and identification performance in the ATLAS experiment using pp collisions at $\sqrt{s} = 13$ TeV*, ATLAS-CONF-2017-029, CERN, 2017, https://cds.cern.ch/record/2261772.

[384] ATLAS Collaboration, G. Aad et al., *Identification and energy calibration of hadronically decaying tau leptons with the ATLAS experiment in pp collisions at $\sqrt{s}$=8 TeV*, Eur. Phys. J. C **75** (2015) 303, arXiv:1412.7086 [hep-ex].

[385] ATLAS Collaboration, M. Aaboud et al., *Performance of missing transverse momentum reconstruction with the ATLAS detector using proton-proton collisions at $\sqrt{s} = 13$ TeV*, Eur. Phys. J. C **78** (2018) 903, arXiv:1802.08168 [hep-ex].

[386] ATLAS Collaboration, M. Aaboud et al., *E_T^{miss} performance in the ATLAS detector using 2015-2016 LHC p-p collisions*, ATLAS-CONF-2018-023, CERN, 2018, https://cds.cern.ch/record/2625233.

[387] ATLAS Collaboration, M. Aaboud et al., *Measurement of the photon identification efficiencies with the ATLAS detector using LHC Run 2 data collected in 2015 and 2016*, Submitted to: Eur. Phys. J. (2018), arXiv:1810.05087 [hep-ex].

[388] ATLAS Collaboration, M. Aaboud et al., *Object-based missing transverse momentum significance in the ATLAS detector*, ATLAS-CONF-2018-038, CERN, 2018, https://cds.cern.ch/record/2630948.

[389] NNPDF Collaboration, R. D. Ball et al., *Parton distributions for the LHC Run II*, JHEP **04** (2015) 040, arXiv:1410.8849 [hep-ph].

[390] ATLAS Collaboration, G. Aad et al., *ATLAS Run 1 Pythia 8 tunes*, ATL-PHYS-PUB-2014-021, CERN, 2014, https://cds.cern.ch/record/1966419.

[391] H.-L. Lai et al., *New parton distributions for collider physics*, Phys. Rev. D **82** (2010) 074024, arXiv:1007.2241.

[392] J. Gao et al., *CT10 next-to-next-to-leading order global analysis of QCD*, Phys. Rev. D **89** (2014) 033009, arXiv:1302.6246 [hep-ph].

[393] M. Czakon, P. Fiedler, and A. Mitov, *The total top quark pair production cross-section at hadron colliders through $O(\alpha_S^4)$*, Phys. Rev. Lett. **110** (2013) 252004, arXiv:1303.6254 [hep-ph].

[394] Bordes, G. and van Eijk, B., *Calculating QCD corrections to single top production in hadronic interactions*, Nucl. Phys. B **435** (1995) 23.

[395] T. Stelzer, Z. Sullivan, and S. Willenbrock, *Single-top-quark production via W-gluon fusion at next-to-leading order*, Phys. Rev. D **56** (1997) 5919.

[396] T. Stelzer, Z. Sullivan, and S. Willenbrock, *Single top quark production at hadron colliders*, Phys. Rev. D **58** (1998) 094021, arXiv:hep-ph/9807340.

[397] M. C. Smith and S. Willenbrock, *QCD and Yukawa corrections to single top quark production via $q\bar{q} \to t\bar{b}$*, Phys. Rev. D **54** (1996) 6696, arXiv:hep-ph/9604223.

[398] N. Kidonakis, *Top Quark Production*, arXiv:1311.0283 [hep-ph].

[399] T. Gleisberg and S. Höche, *Comix, a new matrix element generator*, JHEP **12** (2008) 039, arXiv:0808.3674 [hep-ph].

[400] F. Cascioli, P. Maierhofer, and S. Pozzorini, *Scattering Amplitudes with Open Loops*, Phys. Rev. Lett. **108** (2012) 111601, arXiv:1111.5206 [hep-ph].

[401] S. Schumann and F. Krauss, *A Parton shower algorithm based on Catani-Seymour dipole factorisation*, JHEP **03** (2008) 038, arXiv:0709.1027 [hep-ph].

[402] S. Höche et al., *QCD matrix elements + parton showers: The NLO case*, JHEP **04** (2013) 027, arXiv:1207.5030 [hep-ph].

[403] K. Melnikov and F. Petriello, *Electroweak gauge boson production at hadron colliders through $\mathcal{O}(\alpha_s^2)$*, Phys. Rev. D **74** (2006) 114017, arXiv:hep-ph/0609070.

[404] G. Watt and R. Thorne, *Study of Monte Carlo approach to experimental uncertainty propagation with MSTW 2008 PDFs*, JHEP **08** (2012) 052, arXiv:1205.4024 [hep-ph].

[405] ATLAS Collaboration, M. Aaboud et al., *Public Egamma Trigger Plots for Collision Data*, 2018. https://twiki.cern.ch/twiki/bin/view/AtlasPublic/EgammaTriggerPublicResults/. [Online; accessed 09-August-2018].

[406] ATLAS Collaboration, M. Aaboud et al., *Muon Trigger Public Results*, 2018. https://twiki.cern.ch/twiki/bin/view/AtlasPublic/MuonTriggerPublicResults/. [Online; accessed 09-August-2018].

[407] ATLAS Collaboration, G. Aad et al., *Data-Quality Requirements and Event Cleaning for Jets and Missing Transverse Energy Reconstruction with the ATLAS Detector in Proton-Proton Collisions at a Center-of-Mass Energy of $\sqrt{s} = 7$ TeV*, ATLAS-CONF-2010-038, CERN, 2010, https://cds.cern.ch/record/1277678.

[408] ATLAS Collaboration, G. Aad et al., *Selection of jets produced in 13 TeV proton-proton collisions with the ATLAS detector*, ATLAS-CONF-2015-029, CERN, 2015, https://cds.cern.ch/record/2037702.

[409] ATLAS Collaboration, G. Aad et al., *Tagging and suppression of pileup jets with the ATLAS detector*, ATLAS-CONF-2014-018, CERN, 2014, https://cds.cern.ch/record/1700870.

[410] G. Aad et al., *Flavor Tagging with Track Jets in Boosted Topologies with the ATLAS Detector*, ATL-PHYS-PUB-2014-013, CERN, 2014, https://cds.cern.ch/record/1750681.

[411] ATLAS Collaboration, G. Aad et al., *Expected Performance of Boosted Higgs ($\to b\bar{b}$) Boson Identification with the ATLAS Detector at $\sqrt{s} = 13$ TeV*, ATL-PHYS-PUB-2015-035, CERN, 2015, https://cds.cern.ch/record/2042155.

[412] ATLAS Collaboration, G. Aad et al., *Search for the $b\bar{b}$ decay of the Standard Model Higgs boson in associated $(W/Z)H$ production with the ATLAS detector*, JHEP **01** (2015) 069, arXiv:1409.6212 [hep-ex].

[413] C.-H. Kom and W. J. Stirling, *Charge asymmetry in W+jets production at the LHC*, Eur. Phys. J. C **69** (2010) 67–73.

[414] ATLAS Collaboration, M. Aaboud et al., *Measurement of differential cross sections and W^+/W^- cross-section ratios for W boson production in association with jets at $\sqrt{s} = 8$ TeV with the ATLAS detector*, JHEP **05** (2018) 077, arXiv:1711.03296 [hep-ex].

[415] G. Cowan et al., *Asymptotic formulae for likelihood-based tests of new physics*, Eur. Phys. J. C **71** (2011) 1554.

[416] I. Antcheva et al., *ROOT - A C++ framework for petabyte data storage, statistical analysis and visualization*, Comput. Phys. Commun. **182** (2011) 1384–1385.

[417] W. Verkerke and D. Kirkby, *The RooFit toolkit for data modeling*, 2003. arXiv:physics/0306116 [physics.data-an].

[418] K. Cranmer et al., *The RooStats Project*, in *Proceedings, 13th International Workshop on Advanced Computing and Analysis Techniques in Physics Research (ACAT 2010): Jaipur, India*. 2010. arXiv:1009.1003 [physics.data-an].

[419] ROOT Collaboration, K. Cranmer et al., *HistFactory: A tool for creating statistical models for use with RooFit and RooStats*, CERN-OPEN-2012-016, CERN, 2012, https://cds.cern.ch/record/1456844.

[420] J. Neyman and E. S. Pearson, *On the Problem of the Most Efficient Tests of Statistical Hypotheses*, Phil. Trans. R. Soc. Lond. A **231** (1933) 289–337.

[421] G. J. Feldman and R. D. Cousins, *Unified approach to the classical statistical analysis of small signals*, Phys. Rev. D **57** (1998) 3873–3889.

[422] A. L. Read, *Presentation of search results: The CL(s) technique*, J. Phys. G **28** (2002) 2693.

[423] S. S. Wilks, *The Large-Sample Distribution of the Likelihood Ratio for Testing Composite Hypotheses*, Ann. Math. Statist. **9** (1938) 60–62.

[424] A. Wald, *Tests of statistical hypotheses concerning several parameters when the number of observations is large*, Trans. Amer. Math. Soc. **54** (1943) 426–482.

[425] ATLAS Collaboration, M. Aaboud et al., *Evidence for the $H \to b\bar{b}$ decay with the ATLAS detector*, JHEP **12** (2017) 024, arXiv:1708.03299 [hep-ex].

[426] M. Bähr et al., *Herwig++ physics and manual*, Eur. Phys. J. C **58** (2008) 639–707.

[427] J. Pumplin et al., *New generation of parton distributions with uncertainties from global QCD analysis*, JHEP **0207** (2002) 012, arXiv:hep-ph/0201195.

[428] R. Barlow and C. Beeston, *Fitting using finite Monte Carlo samples*, Comput. Phys. Commun. **77** (1993) 219–228.

[429] ATLAS Collaboration, G. Aad et al., *Search for Dark Matter in Events with Missing Transverse Momentum and a Higgs Boson Decaying to Two Photons in pp Collisions at $\sqrt{s} = 8$ TeV with the ATLAS Detector*, Phys. Rev. Lett. **115** (2015) 131801, arXiv:1506.01081 [hep-ex].

[430] CMS Collaboration, A. M. Sirunyan et al., *Search for associated production of dark matter with a Higgs boson decaying to $b\bar{b}$ or $\gamma\gamma$ at $\sqrt{s} = 13$ TeV*, JHEP **10** (2017) 180, arXiv:1703.05236 [hep-ex].

[431] CMS Collaboration, A. M. Sirunyan et al., *Search for heavy resonances decaying into a vector boson and a Higgs boson in final states with charged leptons, neutrinos and b quarks at $\sqrt{s} = 13$ TeV*, JHEP **11** (2018) 172, arXiv:1807.02826 [hep-ex].

[432] ATLAS Collaboration, M. Aaboud et al., *Search for Dark Matter Produced in Association with a Higgs Boson decaying to $b\bar{b}$ at $\sqrt{s} = 13$ TeV with the ATLAS Detector using 79.8 fb^{-1} of proton-proton collision data*, ATLAS-CONF-2018-039, CERN, 2018, https://cds.cern.ch/record/2632344.

[433] ATLAS Collaboration, G. Aad et al., *Measurement of the Z/γ^* boson transverse momentum distribution in pp collisions at $\sqrt{s}$ = 7 TeV with the ATLAS detector*, JHEP **09** (2014) 145, arXiv:1406.3660 [hep-ex].

[434] C. Burrage et al., *Fifth forces, Higgs portals and broken scale invariance*, JCAP **1811** (2018) 036, arXiv:1804.07180 [hep-th].

[435] P. Brax et al., *LHC Signatures Of Scalar Dark Energy*, Phys. Rev. D **94** (2016) 084054, arXiv:1604.04299 [hep-ph].

[436] ATLAS Collaboration, M. Aaboud et al., *Improving jet substructure performance in ATLAS using Track-CaloClusters*, ATL-PHYS-PUB-2017-015, CERN, 2017, https://cds.cern.ch/record/2275636.

[437] J. M. Lindert et al., *Precise predictions for $V+$ jets dark matter backgrounds*, Eur. Phys. J. C **77** (2017) 829, arXiv:1705.04664 [hep-ph].

[438] CMS Collaboration, V. Khachatryan et al., *Search for leptophobic Z bosons decaying into four-lepton final states in proton-proton collisions at $\sqrt{s} = 8$ TeV*, Phys. Lett. B **773** (2017) 563–584, arXiv:1701.01345 [hep-ex].

[439] CMS Collaboration, A. M. Sirunyan et al., *Search for high-mass resonances in dilepton final states in proton-proton collisions at $\sqrt{s} = 13$ TeV*, JHEP **2018** (2018) 120, arXiv:1803.06292 [hep-ex].

[440] ATLAS Collaboration, M. Aaboud et al., *Combination of searches for heavy resonances decaying into bosonic and leptonic final states using 36 fb^{-1} of proton-proton collision data at $\sqrt{s} = 13$ TeV with the ATLAS detector*, Phys. Rev. D **98** (2018) 052008, arXiv:1808.02380 [hep-ex].

[441] CMS Collaboration, A. M. Sirunyan et al., *Search for dark matter produced in association with a Higgs boson decaying to a pair of bottom quarks in proton-proton collisions at $\sqrt{s} = 13$ TeV*, Submitted to: Eur. Phys. J. (2018), arXiv:1811.06562 [hep-ex].

[442] LHC Dark Matter Working Group Collaboration, G. Busoni et al., *Recommendations on presenting LHC searches for missing transverse energy signals using simplified s-channel models of dark matter*, arXiv:1603.04156 [hep-ex].

[443] PandaX-II Collaboration, A. Tan et al., *Dark Matter Results from First 98.7 Days of Data from the PandaX-II Experiment*, Phys. Rev. Lett. **117** (2016) 121303, arXiv:1607.07400 [hep-ex].

[444] SuperCDMS Collaboration, R. Agnese et al., *New Results from the Search for Low-Mass Weakly Interacting Massive Particles with the CDMS Low Ionization Threshold Experiment*, Phys. Rev. Lett. **116** (2016) 071301, arXiv:1509.02448 [astro-ph.CO].

[445] ATLAS Collaboration, M. Aaboud et al., *Constraints on mediator-based dark matter models using $\sqrt{s} = 13$ TeV pp collisions at the LHC with the ATLAS detector*, ATLAS-CONF-2018-051, CERN, 2018, https://cds.cern.ch/record/2646248.

[446] M. Bauer, U. Haisch, and F. Kahlhoefer, *Simplified dark matter models with two Higgs doublets: I. Pseudoscalar mediators*, JHEP **05** (2017) 138, arXiv:1701.07427 [hep-ph].

[447] LHC Dark Matter Working Group Collaboration, T. Abe et al., *LHC Dark Matter Working Group: Next-generation spin-0 dark matter models*, arXiv:1810.09420 [hep-ex].

[448] ATLAS Collaboration, M. Aaboud et al., *ATLAS simulation of boson plus jets processes in Run 2*, ATL-PHYS-PUB-2017-006, CERN, 2017, https://cds.cern.ch/record/2261937.

[449] J. Aitchison and J. A. C. Brown, *The lognormal distribution : with special reference to its uses in economics*. Cambridge University Press, 1957.

List of Figures

List of Tables